Journal of Turbomachinery

Published Quarterly by ASME

VOLUME 132 • NUMBER 2 • APRIL 2010

RESEARCH PAPERS

(Contents continued on inside back cover)

This journal is printed on acid-free paper, which exceeds the ANSI Z39.48-1992 specification for permanence of paper and library materials. ♾™
♻ 85% recycled content, including 10% post-consumer fibers.

Journal of Turbomachinery Volume 132, Number 2 APRIL 2010

The ASME Journal of Turbomachinery is abstracted and indexed in the following:

Aluminum Industry Abstracts, Aquatic Science and Fisheries Abstracts, Ceramics Abstracts, Chemical Abstracts, Civil Engineering Abstracts, Compendex (The electronic equivalent of Engineering Index), Corrosion Abstracts, Current Contents, Ei EncompassLit, Electronics & Communications Abstracts, Energy Information Abstracts, Engineered Materials Abstracts, Engineering Index, Environmental Science and Pollution Management, Excerpta Medica, Fluidex, Fuel and Energy Abstracts, INSPEC, Index to Scientific Reviews, Materials Science Citation Index, Mechanical & Transportation Engineering Abstracts, Mechanical Engineering Abstracts, METADEX (The electronic equivalent of Metals Abstracts and Alloys Index), Metals Abstracts, Oceanic Abstracts, Pollution Abstracts, Referativnyi Zhurnal, Shock & Vibration Digest, Steels Alert

Enhancement of Impingement Cooling in a High Cross Flow Channel Using Shaped Impingement Cooling Holes

Andrew C. Chambers

David R. H. Gillespie
e-mail: david.gillespie@eng.ox.ac.uk

Department of Engineering Science,
University of Oxford,
Parks Road,
Oxford OX1 3PJ, UK

Peter T. Ireland
Rolls-Royce plc.,
P.O. Box 31,
Derby DE24 8BJ, UK

Robert Kingston
Rolls-Royce plc.,
P.O. Box 3, Filton,
Bristol BS34 7QE, UK

Impingement systems are common place in many turbine cooling applications. Generally these systems consist of a target plate that is cooled by the impingement of multiple orthogonal jets. While it is possible to achieve high target surface heat transfer with this configuration, the associated pressure drop is generally high and the cooling efficiency low. Furthermore, especially in large impingement arrays, the buildup of cross flow from upstream jets can be significant and results in deflection of downstream impingement jets reducing the resultant heat transfer coefficient distribution. This paper presents a computational and experimental investigation into the use of shaped elliptical or elongated circular impingement holes designed to improve the penetration of the impinging jet across the coolant passage. This is of particular interest where there is significant cross flow. Literature review and computational investigations are used to determine the optimum aspect ratio of the impingement jet. The improved heat transfer performance of the modified design is then tested in an experimental rig with varying degrees of cross flow at engine representative conditions. In all cases, a 16% increase in the Nusselt number on the impingement target surface in the downstream half of the cooling passage was achieved. Under the first four impingement holes, a Nusselt number enhancement of 28–77% was achieved, provided no additional cross flow was present in the passage. When appropriately aligned, a significant reduction in the stress concentration factor caused by the addition of a hole can be achieved using this design.
[DOI: 10.1115/1.3140282]

Keywords: impingement blade cooling

1 Introduction

Many modern high pressure turbine blades are cooled by passing air bled from the compressor through the blade, before feeding it to the external surface to form cooling films. The heat removed by convection is dependent on both the temperature of the flow and the heat transfer coefficient. Cooling by impingement is of particular interest as it provides heat transfer coefficient enhancement over an ordinary plane passage, while the continual injection of coolant keeps the driving gas temperature difference high to ensure locally high heat fluxes. Improvements in casting technology have increased the useful heat transfer area and flow path length of impingement cooling systems while maintaining a robust design. Figure 1 indicates a cross section of a prototype turbine blade cooled using impingement channels integrally cast into the blade wall.

This paper is concerned with the heat transfer characteristics of one such long low aspect ratio ($z/d=1.54$) channel, and the effect of shaping the impingement holes. While mostly earlier impingement channel cross sections have tended to be of high aspect ratio and had several rows of impingement holes spread across their width [1–3], the current study models integrally cast passages of a race track cross-sectional geometry oriented radially in the turbine blade. Typically the passage includes about 19 impingement holes. This is much longer than impingement passages previously tested, and results in changed flow conditions. Experimental measurements of the Nusselt number and jet effectiveness distributions in a large scale Perspex model of the cooling passage were reported in Ref. [4]. In that configuration, circular holes were employed. Details of the experimental rig, which is modified for the current study, are shown in Fig. 2. A reduction in impinging jet penetration across the cooling passage with increasing cross flow was seen to dominate the levels of heat transfer obtained, particularly toward the end of the passage. While other workers have investigated the use of passage roughness elements to increase heat transfer in both leading edge [5] and midspan [6] applications, the aim of the current study was to investigate whether impinging jet penetration could be improved by shaping the impingement holes. It was hoped that this technique would be associated with minimal additional passage pressure drop.

Round jets have been used almost universally in impingement systems because of their ease of manufacture. When the impinging jet has to traverse a cross flow, the impingement properties of the jet become a function of the momentum ratio, the velocity ratio, and the aspect ratio of the channel, z/D. Measurements by Abramovich [7] and Wooler et al. [8] showed that a free jet in cross flow undergoes considerable deflection and does not remain round even at low cross flow to jet mass velocity ratios ($G_c/G_j > 0.25$). The development of the jet shape consists of the initial transition from a circular to an elliptical profile, and then a steady increase in the jet diameter at a constant aspect ratio. The dilution of a jet by the surrounding flow and the reduction in its ability to reach the target plate are primarily determined by the following properties.

- *Jet drag.* The component of the cross flow perpendicular to the jet's axis causes form drag that deflects the jet down-

Contributed by the Turbomachinery Division of ASME for publication in the JOURNAL OF TURBOMACHINERY. Manuscript received June 9, 2006; final manuscript received March 23, 2009; published online December 31, 2009. Review conducted by David Wisler. Paper presented at the ASME Turbo Expo 2006: Land, Sea and Air (GT2006), Barcelona, Spain, May 8–11, 2006.

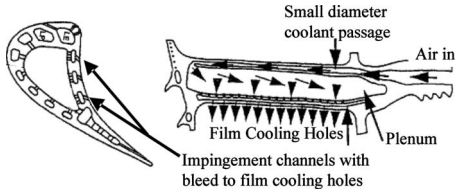

Fig. 1 Schematic cross section of a turbine blade

stream. The drag coefficient, C_D, for a circular jet is approximately equal to 1.8 [9].

- *Entrainment.* The jet mixes with the surrounding cross flow. This "dilutes" the jet cooling potential and erodes the potential core region. The transfer of momentum from the surrounding flow also creates a force on the jet deflecting it downstream [10]. Estimates of the entrained mass flow can be made from the work of Hill [11], who performed experiments using a variable collar arrangement surrounding a jet to measure the local entrainment rate in the presence of cross flow.

The listed reasons above suggest that, in cross flow, an appropriately shaped jet would have improved impingement, when compared with that of a round jet. A streamlined jet could be designed to have a reduced drag coefficient, C_D, and thus very low form drag, but the surface area of its circumference would be greater than that of a circular jet of the same cross-sectional area. A circular jet of the same area has the smallest possible perimeter and hence the lowest entrainment drag, but would suffer more from form drag as the projected area is greater than that of a streamlined jet.

Very little data exist into the impingement performance of noncircular jets. Callaghan and Bowden [12] made measurements of elliptical, square, and circular jets using heated jets in a free cross flow. Somewhat surprisingly, it was found that square jets provided the best penetration performance, followed by that of circular jets, and then that of an elliptical jet with a 2:1 aspect ratio. Manufacturing and lifeing constraints dictate that a square jet is not feasible in a hot engine component, and the current authors conclude that the optimum aspect ratio of an elliptical jet lies somewhere between that of a circular jet and a 2:1 aspect ratio.

2 CFD Analysis

Computational fluid dynamics (CFD) was used to investigate the impingement performance of shaped jets at a G_c/G_j ratio of 0.707, this being the asymptotic and maximum value of G_c/G_j for a cooling passage with the impingement hole area to passage cross-sectional area ratio being used in this study. The flow field was modeled for jets with an aspect ratio of 1, 1.2, 1.5, and 2, and for circular jet with a hole axis inclined by 30 deg upstream into the oncoming channel flow. Angling of the hole has been shown to improve jet penetration [13,14], but is difficult to achieve in the short holes (typically $l/d=1-1.5$) used in engine applications because of flow separation through the holes, and nonreattachment over the length of the hole. The jet cross-sectional area, the jet Reynolds number, and the channel dimensions were the same for all the geometries investigated.

The discharge coefficient of a jet orifice is dependent on its shape and, therefore, for a fixed cross-sectional area and mass flow rate, the pressure drop will vary between geometries. A comparison at identical flow conditions would require matching both the mass flow rate and the pressure drop, which could only be achieved by varying the hole cross-sectional area. This would require prior knowledge of the discharge coefficient, and presuming this was known, the jet areas should be varied in accordance to the ratio

$$\frac{A_{\text{shaped}}}{A_{\text{round}}} = \sqrt{\frac{C_{d\ \text{round}}}{C_{d\ \text{shaped}}}} \tag{1}$$

However there are no reports of the discharge coefficient of such shaped holes in cross flow in the literature, and therefore the experiments were performed with mass flow rate and hole cross-sectional area matched. While this implies that the impingement supply pressure will vary slightly between the different cases tested, this pressure is rarely marginal in the engine (particularly toward the blade tip where improved jet penetration is required), and will not change the performance ranking of the different configurations. In any case, the CFD performed here was used as a comparative tool, and promising potential geometries were subsequently tested experimentally.

2.1 Model Geometry and Running Conditions. A model of a generic impingement channel onto which various impingement hole designs could be superimposed was constructed using GAMBIT 1.3.0. The cooling passage modeled was of the aspect ratio of

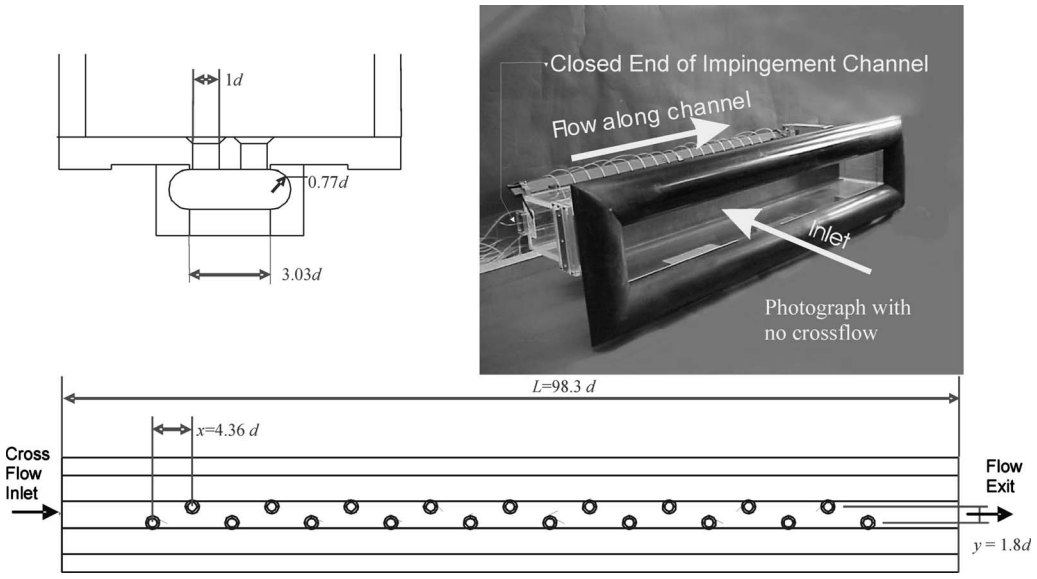

Fig. 2 Impingement channel geometry

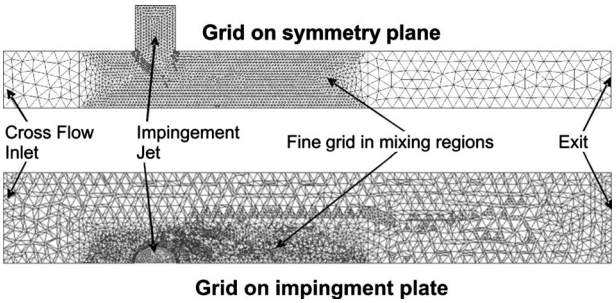

Fig. 3 Grid used for CFD analysis of impinging channel

1.54:1 to match the impingement channel described above, however the impingement hole was located centrally in the passage, allowing symmetry conditions to be applied and hence reducing computational demands. Figure 3 shows the initial mesh before grid adaptation.

Tetrahedral elements were employed throughout and the boundary layers modeled using nonequilibrium wall functions. The flow fields were solved using FLUENT 5 with a realizable k-ε turbulence model. This was chosen as it is considered more accurate for flows with high shear rates, such as those found at the jet boundaries. Nonequilibrium wall functions are based on the y^* (the nondimensional wall cell thickness) value, which ranged from 52.5 to 68.6 on the wall adjacent cells on the target surface. This is within the limits recommended by the code developers. A uniform velocity boundary condition was applied at the channel entrance and a jet Reynolds number of 20,000 was used to set a mass flow inlet boundary condition at the entrance of the hole. The authors recognize that a more accurate simulation might have been achieved by modeling a plenum upstream of the impingement hole, however, the heat transfer results near the jet axis and the nature of the boundary layer within the hole are strong functions of the precise geometry of this plenum [15]. The effect of the latter boundary condition is to eliminate flow separation in the holes, and hence to focus the CFD investigation on the relative degradation of the jet due to drag from, and entrainment of, the passage cross flow. As the results of the simulations are being used merely to investigate the relative jet effectiveness and velocity field, no formal grid sensitivity study is presented below.

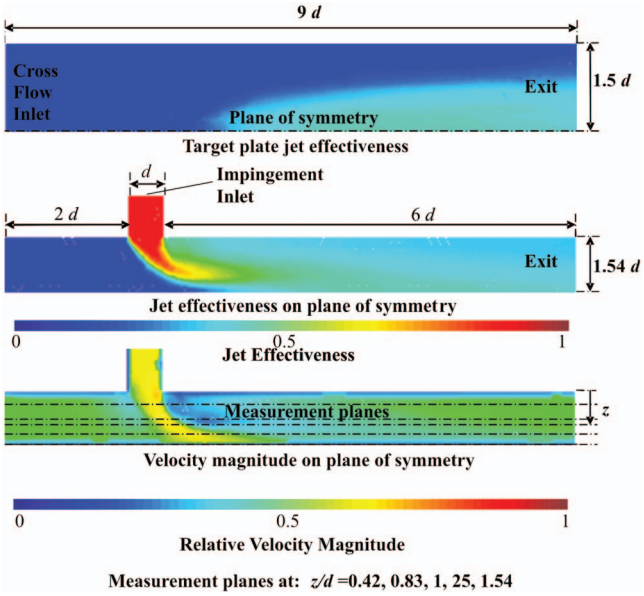

Fig. 4 Flow field for jet aspect ratio=1.0

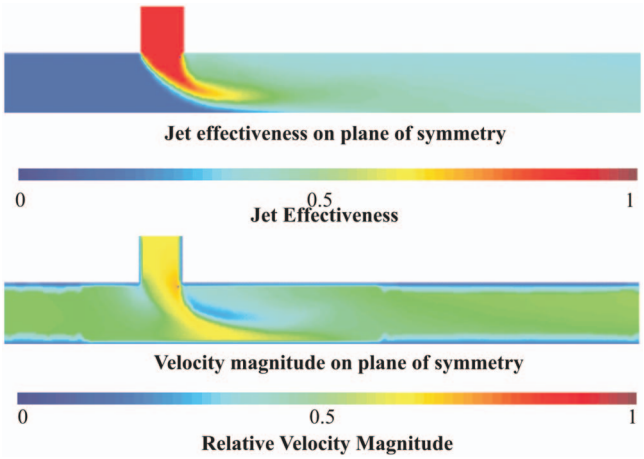

Fig. 5 Flow field for jet aspect ratio=1.2

2.2 CFD Results. Results from the CFD calculations are presented in Figs. 4–8. For all cases, the target plate wall adjacent jet effectiveness appears to be very similar, and is shown only for the circular hole. Although the potential core of none of the impingement holes considered reaches all the way across the passage to strike the target surface, along the centerline, the potential core of the angled jet appears to have best penetration. There are small

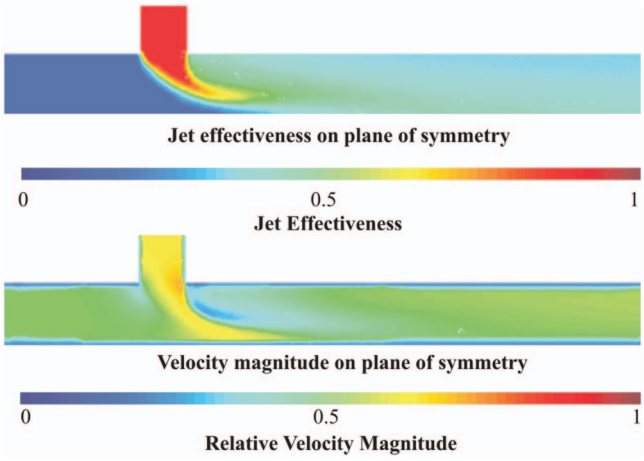

Fig. 6 Flow field for jet aspect ratio=1.5

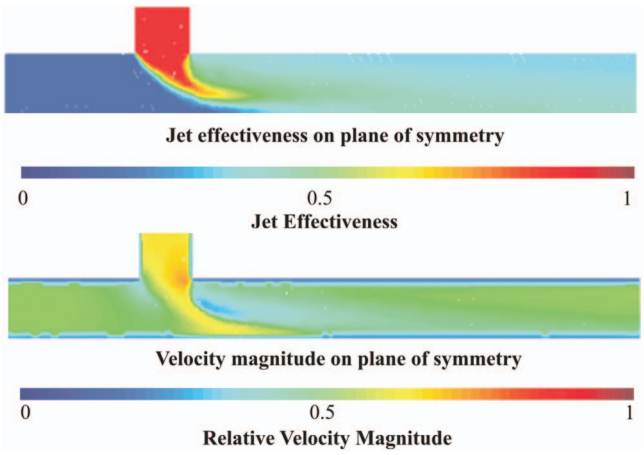

Fig. 7 Flow field for jet aspect ratio=2

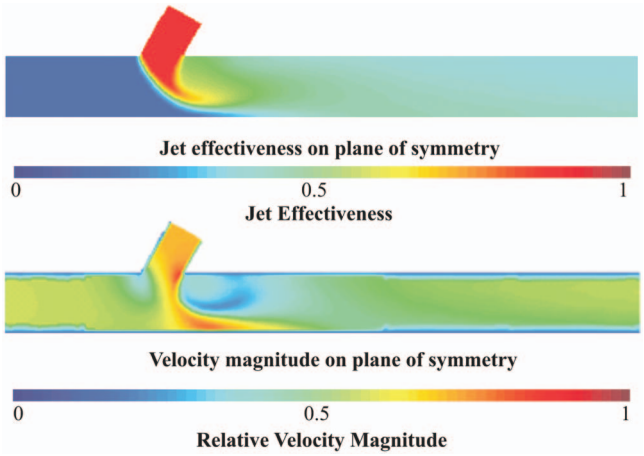

Fig. 8 Flow field for jet aspect ratio=1.0,30 deg upstream injection

changes in the flow field around the jet as the elliptical holes aspect ratio is increased: the midpassage region of low velocity air downstream of the jet is reduced, confirming that the form drag of the jet is reduced, and the velocity of the air in the near wall region from the hole axis moving $1d-2d$ downstream is progressively higher. The highest velocities seen for the angled jet are close to the wall, but they are in a region of low jet effectiveness.

To quantify the effect of hole shape on impingement potential a number of measurement planes were defined parallel to the impingement plate at distances of $0.43d$, $0.83d$, $1d$, $1.25d$, and $1.54d$ from the holed surface (as shown in Fig. 4). Particle lines emerging from the impingement jet were traced and the number of particle lines that crossed each measurement plane calculated as a fraction of the total jet particle lines. The results of this calculation are presented in Fig. 9.

An indication of the relative jet performance is given by the fraction of the total particle lines that cross any given measurement plane. No particle lines cross the $1.54d$ plane, as this represents the target plate. Of particular interest is the $1.25d$ plane, as this is closest to the target plate, and thus the results on this plane are likely to be indicative of the relative performance of each hole design. The results indicate that a jet with an aspect ratio of 1.2 should provide the greatest impingement enhancement. Nearly four times as many jet particle lines cross the $1.25d$ plane from the

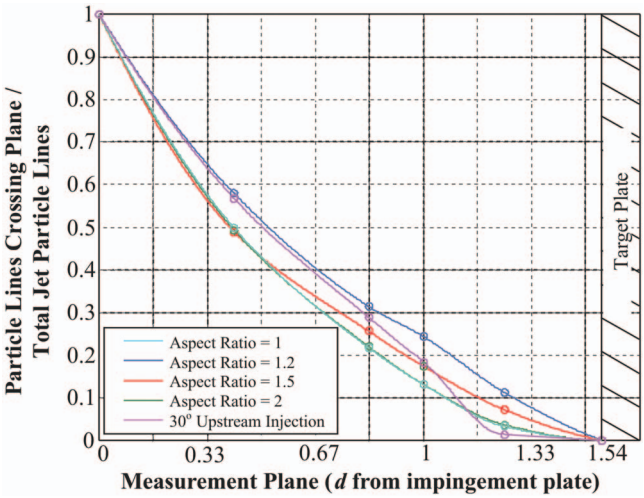

Fig. 9 Particle lines crossing a measurement plane as a fraction of the total jet particle lines

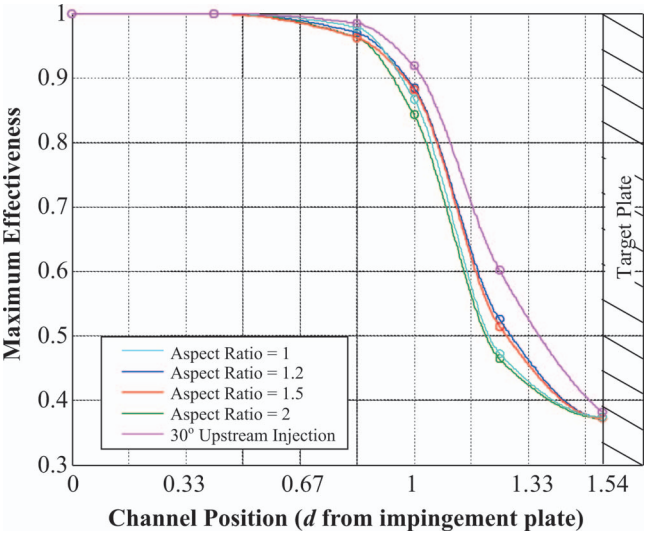

Fig. 10 Maximum effectiveness on a plane

jet with an aspect ratio of 1.2 as do from a circular jet. The results show that a jet with an aspect ratio of 1.5 would appear to offer the next best impingement performance.

The relative performance of the impingement jets was also ranked using the maximum effectiveness that occurred on the measurement planes detailed in Fig. 4. This interpretation of the results is presented in Fig. 10.

These results indicate that the greatest impingement enhancement would occur using a jet that is inclined at 30 deg upstream followed by that of an elliptical jet with an aspect ratio of 1.2. However, the 30 deg inclined jet was ranked as the worst performer in the previous measure, suggesting a highly nonuniform behavior away from the passage centerline. All the jets resulted in a similar maximum target plate effectiveness of 0.37; the reasons for these are not as yet fully understood, however, nonuniform velocity profiles in the impingement is likely to aid the shaped holes to punch through the cross flow and raise their actual effectiveness. The results on both the $1d$ and $1.25d$ planes support the conclusions of Fig. 9 that, of the elliptical jets, an aspect ratio of 1.2 provides the greatest impingement enhancement. The jet angled 30 deg upstream results in the highest local maximum effectiveness on any of the given measurement planes. For this condition, the CFD results show that a "tongue" of the impingement gas penetrates the flow leading to the high effectiveness, while the majority of the jet flow is stripped by the cross flow. These results are in line with those of Ward et al. [14], where it was shown experimentally that a jet angled 30 deg upstream would produce the highest peak heat transfer coefficient (for a range of jet inclination from 0 deg to 60 deg. As a high *average* effectiveness was required, the angled jet was discounted, and only elliptical jets were considered further.

3 Additional Benefits of Shaped Jets

Elliptically or racetrack shaped impingement holes have the independent advantage that when the major axis of the machined hole is aligned with the direction of the predominant blade stress, there is a reduction in the resulting stress concentration factor. Comparison between elliptical and circular holes located in an infinite plate loaded in tension in which the major axis of the elliptical hole aligned with direction of axial tension shows a reduction in the theoretical stress concentration factor by between 11% and 22% for elliptical holes of aspect ratio 1.2 and 1.5, respectively (after Ref. [16]). High aspect ratio elongated holes have been investigated for leading edge applications by other workers [7]. The impingement channel detailed in this report is

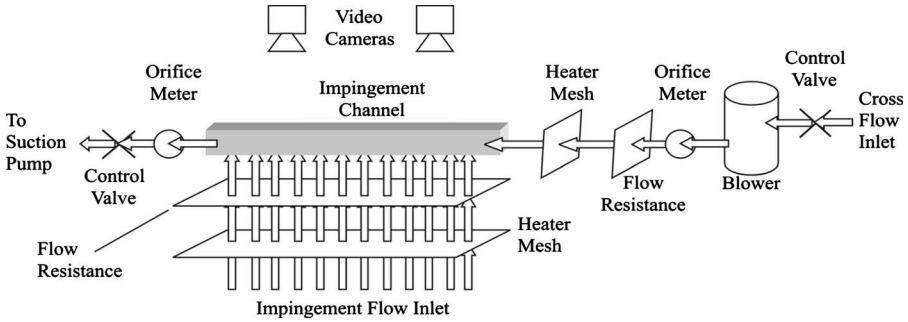

Fig. 11 Schematic diagram showing the layout of the experimental apparatus

aligned with the radial axis of the blade, and thus the use of streamlined holes would result in reduced stress concentration factors, which would lead to blade life improvements. This is of particular benefit in integrally cast systems where inspection of internal features is difficult. For this reason alone such holes should be considered as a serious contender in future cooling system designs.

4 Experimental Tests

4.1 Experimental Considerations. Experiments were performed on a candidate racetrack shaped hole impingement configuration using the test rig shown schematically in Fig. 11, and a modified impingement plate, Fig. 12. The channel used is constructed from Perspex and coated with a single narrow band thermochromic liquid crystal displaying peak intensity at 33.0°C. Cross flow may be introduced at one end of the channel, while air impinges from a separate source through a single staggered row of 19 evenly spaced holes along the length of the channel, spacing $x/d=4.36$, $y/d=\pm 1.8$. In both cases, the turbulence intensity of the air in the plena is less than 0.1%. The air exhausts at the far end of the channel via a control valve to a vacuum pump. The proportion of cross flow is controlled by a variable speed blower. Independent heating of each gas stream is achieved by passing the air through two planar mesh heaters [17]. Both the Nusselt number, $\mathrm{Nu}=hd/k$, and the local jet effectiveness, $e=T_{\mathrm{aw}}-T_{\mathrm{cross}}/T_{\mathrm{imp}}-T_{\mathrm{cross}}$, are found using a two test strategy, which ensures a well conditioned experiment. A full description of the specific transient heat transfer technique employed in these tests can be found in Refs. [18,19], where the root sum square (rss) experimental uncertainties in heat transfer coefficient and effectiveness are quoted as 8.85% and 16.37%, respectively, after [20]. The apparatus is able to reproduce engine representative Reynolds numbers based on impingement hole diameter, $\mathrm{Re}_{\mathrm{jet}}=10{,}000-35{,}000$, and cross flow of up to 10% of the total mass flow rate. The uncertainty in mass flow rate measurements made using two British Standard 1042 orifice meters was similarly determined and found to be 1.90% for the impingement flow and 1.68% in the case of the additional cross flow. This infers that for nominal cross flows of 5% and 10% of the total mass flow rate, values lying in the ranges 4.83–5.17% and 9.68–10.32% are achieved, respectively.

The aim was to determine if the shaped hole would lead to increased target plate heat transfer. To facilitate manufacture, it was decided to approximate the elliptical hole by an elongated circular hole. The CFD results indicate that the optimum hole geometry has an aspect ratio lying between 1.2 and 1.5. The width (and diameter) of the elongated circular hole were chosen by matching the length of the major axes and the cross-sectional area of the hole. These parameters form a quadratic equation that was solved to find the required aspect ratio. Elliptical holes, with aspect ratios of 1.2 and 1.5, had an equivalent elongated hole aspect ratio of 1.27 and 1.66, respectively. A design aspect ratio of 1.35 was chosen, as this lies a third of the way between these values, being closer to the better performing aspect ratio of 1.2. The impingement plate with elongated holes was identical to the standard impingement plate in all, but the hole shape (Fig. 12). While the circular holes had an inlet chamfer of $0.167d$ this was considered to be unrepresentatively large for the narrower elongated holes, and instead a $0.083d$ chamfer was used. Experiments were carried out at four flow conditions using both round and elongated holes. These were impingement into the channel with flow exiting through one end, and (1) and (2) no additional cross flows, average jet Reynolds numbers of $\mathrm{Re}_{\mathrm{jet}}=20{,}000$ and 35,000, (3) 5% additional cross flow, $\mathrm{Re}_{\mathrm{jet}}=20{,}000$, and (4) 10% additional cross flow, $\mathrm{Re}_{\mathrm{jet}}=20{,}000$. The cross flow is quoted as a percentage of the total impingement flow entering the channel.

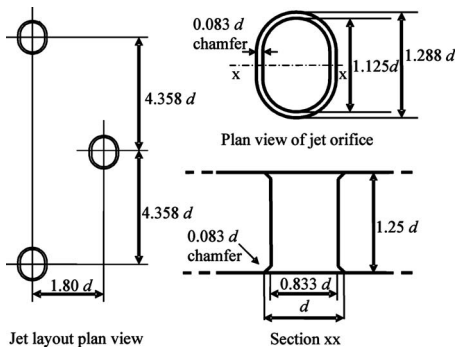

Fig. 12 Details of the elongated hole impingement plate and the hole geometry

5 Experimental Results

5.1 Local Nusselt Number and Effectiveness. Local Nusselt number and jet effectiveness maps are presented in Figs. 13 and 14, for the tests carried out at an average jet Reynolds number of $\mathrm{Re}_{\mathrm{jet}}=20{,}000$ and an initial channel cross flow equal to 5% of the total impingement flow with both round and elongated holes. The Nusselt number and Reynolds number data presented were calculated in all cases using the circular hole diameter, d, as the characteristic dimension. For the elongated hole, the hydraulic diameter is $0.985d$ (i.e., a 1.5% difference), however, the use of a single characteristic dimension means that a comparison of Nusselt number relates directly to a comparison of local heat flux at the same mass flow rate. These Nusselt number data are normalized by the chordwise (y-direction) averaged Nusselt number measured at $x/L=0.95$, for round holes, with 10% cross flow. This was the maximum average Nusselt number achieved using round impingement holes at $\mathrm{Re}_{\mathrm{jet}}=20{,}000$, and is denoted hereafter by $\mathrm{Nu}_{\mathrm{max}}$. This method of normalization has been chosen to allow comparison between different hole and cross flow configurations while maintaining the underlying variation in the level of Nusselt

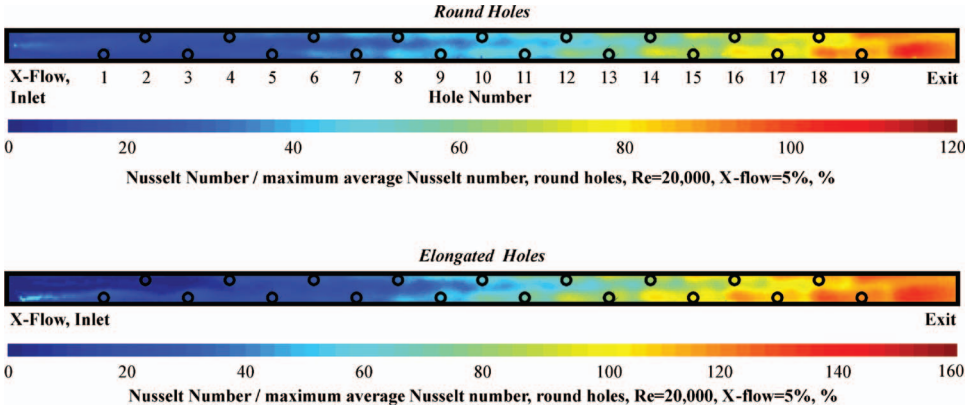

Fig. 13 Local $\underline{Nu}/\overline{Nu}_{max}$, cross flow=5%, Re_{jet}=20,000

number along the passage. It clearly shows the improvement in impingement performance through the use of shaped holes. The effectiveness measurements indicate $\varepsilon=0$ when the heat transfer is driven solely by flow originating in the cross flow, and $\varepsilon=1$ where the impinging jet flow drives heat transfer. Full details of the local heat transfer coefficient and effectiveness distributions for the round hole case are reported in Ref. [19]. The effectiveness measurements are very similar, being slightly lower in the case of the elongated hole in the early part of the passage (compare the value directly under hole 5), the changes reflect small changes in the flow distribution and jet velocities. This, however, does not indicate identical flow fields as the levels of normalized Nusselt number are quite different. The Nusselt number distributions show the same general pattern but the level is clearly higher for the elongated holes, suggesting that more of the high cooling potential jet flow reaches the target surface. Interestingly this is the case along the entire passage length, suggesting an unexpected change in the character of the jets where there is little or no cross flow.

5.2 Average Nusselt Number. Further insight can be gained into the mechanisms driving the improved heat transfer by considering the chord wise averaged Nusselt number, similarly normalized, as presented in Fig. 15, for all tests conducted at Re_{jet} =20,000.

With no additional cross flow, impingement flow, which fully penetrates across the passage, occurs in the upstream portion of the channel (holes 1–3). The average and peak Nusselt number enhancement factors compared with the equivalent round holed case for the first four impingement holes are detailed in Table 1. The average is calculated over an area that extends across the full target plate width and two diameters upstream and two diameters downstream of the center of the impingement hole in question. The experimental results show that shaped jets resulted in a 28–77% increase in the Nusselt number in this region. This cannot be due to the protection against entrainment that the elongated hole was designed to provide, as there is little cross flow in this region. The pattern with no cross flow is extremely similar at Re_{jet} =35,000, with the only difference being the small increase in the level of Nusselt number enhancement in the upstream part of the passage as noted in the table.

The peak Nusselt number increases with hole position until the fourth hole where it drops despite the mass flow rate through the holes increasing with downstream position. This is explained by the build up of cross flow deflecting the impingement jet before it strikes the surface resulting in a decrease in the peak Nusselt number. This trend and the mechanism driving are precisely the same as those previously reported for circular holes [4]. The key features are the reduction in the peak Nusselt number when the potential core of the jet no longer strikes the surface, and the underlying increase in the average Nusselt number along the passage as the mass flow rate in the passage and the flow through each impingement hole increases. In the downstream half of the passage flow through the impingement holes acts to accelerate the passage flow under the obstacle presented by the emerging jet. This increased velocity, and the improved cooling potential of the flow is responsible for the ripple in Nusselt number seen in this region.

The change in the peak value of Nusselt number in the jets known to impinge on the surface suggests that the peak velocity of the jet is increased at the same hole position for the same average jet Reynolds number, when the array of elongated holes is used.

This infers a decrease in the hole discharge coefficient. The impingement plate is the same thickness for both the circular and elongated holes and it is thought that the reduced ratio of the minor diameter to plate thickness of the elongated holes results in a reduced discharge coefficient due to separation effects, Fig. 16. Furthermore, the elongated holes were machined with a smaller inlet chamfer to that of the round holes, which may have resulted in a slight additional reduction in C_d. Chambers et al. [19] measured the discharge coefficient for a circular hole and showed that

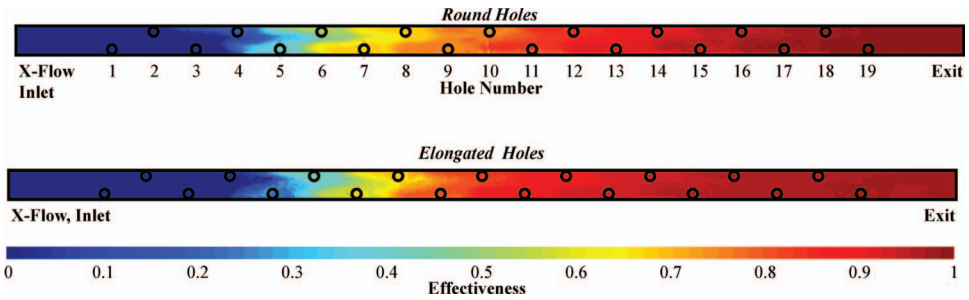

Fig. 14 Local jet effectiveness, cross flow=5%, Re_{jet}=20,000

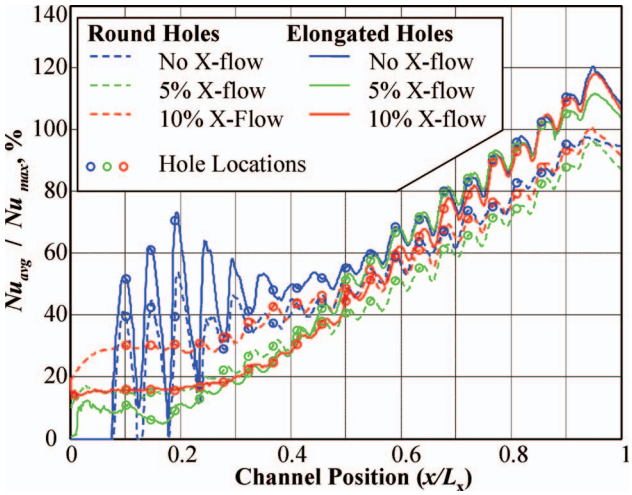

Fig. 15 $Nu_{avg}/\overline{Nu}_{max}$, $Re_{jet}=20{,}000$

it remained constant for a G_c/G_j ratio of up to 0.85. It is assumed that shaped holes exhibit similar performance in the presence of cross flow, and C_d is constant along the passage. There are two mechanisms through which a change in discharge coefficient affects the Nusselt number distributions. First, the flow distribution in the passage is changed. A reduction in discharge coefficient reduces the effective size of the impingement holes. Thus, for a given total mass flow rate in the passage, this results in a more uniform flow distribution between each of the injection holes, as the drop in pressure required to pass the flow through the holes is increased relative to the drop in pressure as the flow moved from the first impingement hole toward the passage exit. This acts to increase flow through upstream holes and would lead to increased Nusselt numbers in this region.

The effect of changing hole discharge coefficient can be analytically assessed using a distributed injection model of impingement, as first proposed by Florschuetz et al. [21]. Figure 17 shows

Table 1 Heat transfer enhancement for the upstream impingement holes (holes 1–4)

		Enhancement	
Re	Hole	Avg	Peak
20k	1	1.66	1.3
	2	1.39	1.29
	3	1.43	1.45
	4	1.28	1.28
35k	1	1.77	1.4
	2	1.43	1.41
	3	1.48	1.56
	4	1.36	1.3

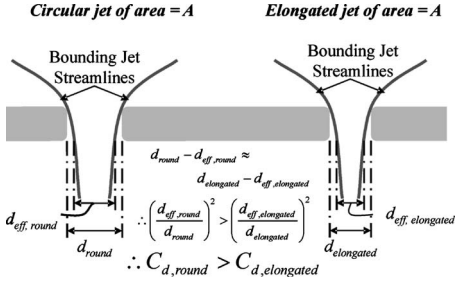

Fig. 16 Reduction in effective area caused by separation at impingement holes (view of the *y-z* plane)

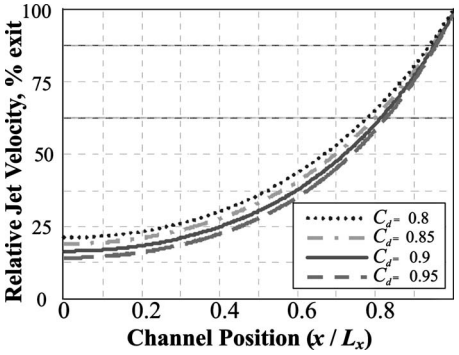

Fig. 17 The effect of C_d on relative jet velocity for the 19 hole impingement channel

relative jet velocity for discharge coefficients in the range $C_d = 0.8-0.95$. This confirms that the relative velocity near the passage increases as the discharge coefficient drops.

The second possible reason for an increase Nu_{avg} in holes 1–4 is an increase in the peak jet velocity caused by increased flow separation and the associated reduction in the jet effective area. It is, of course, impossible to uncouple the two effects above to determine which is dominant. It is noticeable that there is a reduction in Nusselt number in this region with either 5% or 10% initial cross flow. In the case of no cross flow, the enhancement seen is caused by higher local impinging jet velocities, however, with additional cross flow, although the jet velocities will still be higher, the effective area of the jets is reduced. The authors speculate that in this region where the cross flow is dominant and the jets fail to cross the passage, enhancement is caused by the acceleration of the cross flow near the target surface. The reduction in the effective area of the impinging jet, particularly the jet width (y-direction), reduces this local acceleration and thus the average Nusselt number observed. In these cases, the changed geometry of the first impingement hole unexpectedly has an effect on the level of the target plate Nusselt number far upstream (almost to the passage entrance), the precise cause of this is not fully understood.

In the downstream half of the passage, regardless of the initial cross flow rate or test Reynolds number, the impingement plate with elongated holes resulted in an approximately 16% increase in Nusselt number. As the cross flow in this region is dominated by the flow from upstream holes, which will be proportionally higher for the elongated holes (if the assumption of lower C_d is sensibly correct), the improved heat transfer performance must be caused by the reduced drag and entrainment of the shaped jets, and the higher peak jet velocity caused by the reduced hole discharge coefficient.

It is clear that a lower discharge coefficient for all of the holes implies a higher driving pressure difference across the impingement system, and the improved heat transfer has not been gained without some additional pressure penalty.

6 Summary and Conclusions

Computational simulations have been used to show that shaped holes and directed cooling jets in an impingement channel are able to offer enhanced heat transfer performance through the improved ability of the jets to penetrate the cross flow. Experimental tests of an elongated hole, with semicircular ends and an aspect ratio of 1.35, confirmed the changes in behavior predicted by the CFD and provided reliable measurements of the Nusselt number enhancement.

From the tests performed it may be concluded that:

- a low aspect ratio hole, of axes ratio 1.2–1.5, is required to obtain heat transfer enhancement;
- average Nusselt number enhancement in the early part of the

channel (low cross flow) lies between 28% and 77%, and is a weak function of the jet Reynolds number being driven by a drop in the hole discharge coefficient;
- average Nusselt number enhancement in the cross flow dominated region was 16% and independent of Re_{jet} at the limited number of Reynolds numbers tested.

An additional benefit of the shaped holes is a reduction in stress concentration factors. When appropriately aligned, these are reduced by 10–20% over the range of aspect ratios recommended above.

Acknowledgment

This work was supported by Rolls-Royce plc. and the DTI CARAD program. The experimental rigs were constructed by Mr. Pat Timms. Insight into practical issues facing the gas turbine designer was gained from discussions with Mr. Geoff Dailey. Their support is greatly appreciated.

Nomenclature

A = area, m^2
d = round hole diameter, m
D = passage hydraulic diameter, m
C_d = discharge coefficient
C_D = drag coefficient
G_c = cross flow mass velocity (density × velocity), kg m^{-1} s^{-1}
G_j = jet mass velocity (density × velocity), kg m^{-1} s^{-1}
h = heat transfer coefficient, W m^{-2} K^{-1}
k = conductivity, W m^{-1} K^{-1}
l = length of impingement hole, m
L = passage length, m
N = total number of holes
Nu = Nusselt number, $Nu = hd/k$
Nu_{avg} = Nusselt number averaged across target surface in the y-direction
$\overline{Nu}_{max}$ = maximum value of Nu_{avg} for a given Re_{jet} at all cross flows (0%, 5%, and 10%)
Re_{jet} = average jet Reynolds number, $Re_{jet} = 4\dot{m}/\pi\mu dN$
T_{cross} = cross flow temperature, K
T_{aw} = local adiabatic wall temperature, K
T_{imp} = impingement jet temperature, K
x = distance along passage, m
y = distance across passage, m
y^* = nondimensional wall cell thickness
z = holed surface to target surface spacing, m
ε = jet effectiveness, $\varepsilon = T_{gas} - T_{cross}/T_{imp} - T_{cross}$
μ = dynamic viscosity, Pa s

Subscripts

avg = average values
elongated = elongated hole with semicircular ends
round = circular hole
shaped = hole of arbitrary cross section and inclination

References

[1] Dailey, G. M., 2000, "Aero-Thermal Performance of Integral Cooling Systems in Turbomachines: Design and Calculation Issues," VKI Lecture Series, Feb. 28–Mar. 3.
[2] Van Treuren, K. V., Wang, Z., Ireland, P. T., and Jones, T. V., 1994, "Detailed Measurements of Local Heat Transfer Coefficient and Adiabatic Wall Temperature Beneath an Array of Impinging Jets,"ASME J. Turbomach., **116**, pp. 369–374.
[3] Florschuetz, L. W., Metzger, D. E., Takeuichi, D. I. and Berry, R. A., 1980, "Multiple Jet Impingement Heat Transfer Characteristics—Experimental Investigation of In-line and Staggered Arrays With Cross Flow," NASA Contractor Report No. 3217.
[4] Chambers, A. C., Gillespie, D. R. H., and Ireland, P. T., 2002, "A Novel Transient Liquid Crystal Technique to Determine Heat Transfer Coefficient Distributions and Adiabatic Wall Temperature in a Three Temperature Problem," ASME Paper No. 2002-GT-30533.
[5] Taslim, M., 2002, "Experimental Racetrack Shaped Jet Impingement on a Roughened Leading-Edge Wall With Film Holes," ASME Paper No. 2002-GT-30477.
[6] Son, C. M., Gillespie D. R. H., and Ireland, P. T., 2005, "An Investigation of the Application of Roughness Elements to Enhance Heat Transfer in an Impingement Cooling System," ASME GT2005-68504.
[7] Abramovich, G. N., 1963, *The Theory of Turbulent Jets*, MIT, Cambridge, MA.
[8] Burghart, G. H., Gallager, J. T., and Wooler, P. T., 1967, "Pressure Distribution on a Rectangular Wing With a Jet Exhausting Normally Into an Airstream," J. Aircr., **4**, pp. 537–543.
[9] Stoy, R. L., and Ben-Haim, Y., 1973, "Turbulent Jets in Cross Flow," ASME J. Fluids Eng., **95**, pp. 551–556.
[10] Platten, J. L., and Keffer, J. F., 1968, "Entrainment in Deflected Axisymmetric Jets at Various Angles to the Stream," University of Toronto, Mechanical Engineering Department, Report No. UTME-TP-6808.
[11] Hill, B. J., 1972, "Measurement of Local Entrainment Rate in the Initial Region of Axisymmetric Turbulent Jets," J. Fluid Mech., **51**, pp. 773–779.
[12] Callaghan, E., and Bowden, D. T., 1949, "Investigation of Flow Coefficient of Circular, Square, and Elliptical Orifices at High Pressure Ratios," Lewis Flight Propulsion Laboratory, Cleveland, OH, NASA Technical Report No. 1947.
[13] Jackson, T. W., 1980, "Two-Dimensional, Inclined 'Jet-Impingement' Heat Transfer in Confined Cross-Flow," M.Sc. thesis, School of Mechanical Engineering, Cranfield Institute of Technology.
[14] Ward, J., Oladiran, M. T., and Hammond, G. P., 1991, "The Effect of Nozzle Inclination on Jet-Impingement Heat Transfer in a Cross-Flow," ASME Paper No. 91-HTD.
[15] Gillespie, D. R. H., Guo S. M., Wang, Z., Ireland, P. T., and Kohler, S. T., 1996, "A Comparison of Full Surface Local Heat Transfer Coefficient and Flow Field Studies Beneath Sharp-Edged and Radiused Entry Impinging Jets," ASME Paper No. 96-GT-428.
[16] Peterson, R. E., 1974, *Stress Concentration Factors*, Wiley, New York.
[17] Gillespie, D. R. H., 1996, "Intricate Internal Cooling Systems for Gas Turbine Blading," Ph.D. thesis, Department of Engineering Science, Oxford University.
[18] Chambers, A. C., Gillespie, D. R. H., and Ireland, P. T., 2003, "A Novel Transient Liquid Crystal Technique to Determine Heat Transfer Coefficient Distributions and Adiabatic Wall Temperature in a Three Temperature Problem," ASME J. Turbomach., **125**(3), pp. 538–546.
[19] Chambers, A. C., Gillespie, D. R. H., Ireland, P. T., and Dailey, G. M., 2005, "The Effect of Initial Cross Flow on the Cooling Performance of a Narrow Impingement Channel," ASME J. Heat Transfer, **127**(4), pp. 358–365.
[20] Moffat, R. J., 1990, "Contributions to the Theory of Single Sample Uncertainty Analysis," ASME J. Fluids Eng., **104**, pp. 250–260.
[21] Florschuetz, L., Metzger, D., Su, C., Isoda, Y. and Tseng, H., 1982, "Jet Array Impingement Flow Distributions and Heat Transfer Characteristics—Effects of Initial Cross Flow and Non Uniform Array Geometry," NASA Contractor Report No. 3630.

Detailed Heat Transfer Measurements in a Model of an Integrally Cast Cooling Passage

Ioannis Ieronymidis

David R. H. Gillespie
e-mail: david.gillespie@eng.ox.ac.uk

Department of Engineering Science,
University of Oxford,
Parks Road,
Oxford OX1 3PJ, UK

Peter T. Ireland

Robert Kingston
e-mail: robert.kingston@rolls-royce.com

Rolls-Royce plc.,
P.O. Box 3,
Filton,
Bristol BS34 7QE, UK

Detailed measurements of the heat transfer coefficient (htc) distributions on the internal surfaces of a novel gas turbine blade cooling configuration were carried out using a transient liquid crystal technique. The cooling geometry, in which a series of racetrack passages are connected to a central plenum, provides high heat transfer coefficients in regions of the blade in good thermal contact with the outer blade surface. The Reynolds number changes along its length because of the ejection of fluid through a series of 19 transfer holes in a staggered arrangement, which are used to connect ceramic cores during the casting process. Heat transfer coefficient distributions on these holes surface are particularly important in the prediction of blade life, as are heat transfer coefficients within the hole. The results at passage inlet Reynolds numbers of 21,667, 45,596, and 69,959 are presented along with in-hole htc distributions at $Re_{hole}=5930$, *12,479, 19,147; and suction ratios of 0.98, 1.31, 2.08, and 18.67, respectively. All values are engine representative. Characteristic regions of high heat transfer downstream of the transfer holes were observed with enhancement of up to 92% over the Dittus–Boelter level. Within the transfer holes, the average htc level was strongly affected by the cross-flow at the hole entrance. htc levels were low in these short* $(l/d=1.5)$ *holes fed from regions of developed boundary layer.* [DOI: 10.1115/1.3140283]

1 Introduction

The heat transfer performance of internal cooling passages inside gas turbine blades is of great importance to the designer because higher cooling effectiveness generally allows higher turbine inlet temperatures, which results in increased power output from the engine. Many strategies including impingement cooling, film cooling, and ribbed serpentine passages have previously been employed to maximize the heat transferred from the blade to the coolant. In all such designs, many regions, which are unable to lower the external blade surface temperature, are heavily cooled. Figure 1 shows spanwise and chordwise cross sections through a prototype turbine blade, in which the cooling features are located in the blade wall, providing good conduction paths between the external (heated) and internal (cooled) surfaces. The coolant is fed from a series of racetrack channels to a central plenum through a series of transfer holes. Subsequently the flow impinges through further holes into a second series of racetrack channels. Finally the air is ejected onto the pressure surface through conventional film-cooling holes.

This paper presents experimentally measured heat transfer coefficient distributions on the internal surface of an inlet racetrack cooling passage used in this design. The passage modeled is connected to the central plenum through a series of 19 transfer holes in a staggered configuration. The local heat transfer coefficient distribution in a number of these holes is also presented. Knowledge of the thermal stresses inside such holes can help in the design of blades with greatly extended life. Currently there are very little such data available in the literature.

The use of thermochromic liquid crystals has enabled researchers to measure full surface heat transfer coefficient distributions of very complex shapes with very little flow intrusion. The transient technique was used for the experimental work because it allows full surface data acquisition while reducing errors introduced by lateral conduction and nonuniformity in the heating of the model surface.

Heat transfer measurements using liquid crystals is a technique that has been used since early 1980s. It was established by Ireland and Jones [2], and only a short description is given here. For the technique to produce useful results, the experimental test section should be manufactured from a transparent material with low thermal diffusivity, such as Perspex. The liquid crystals are sprayed on the surface of the test section using an air brush and the thickness of the coating is between 5 μm and 10 μm. In a typical transient heat transfer experiment, the flow temperature is subject to a sudden change and the optical response of the liquid crystal surface coating is monitored using digital video cameras. From these data, the temperature history of the model surface and hence the heat transfer coefficient distribution are determined.

Although several previous workers have made detailed measurements of the flow distribution in manifolds, their studies have mainly been limited to investigations of manifolds with long inlet and outlet ducts in which the flow always becomes attached over the length of the duct. The most comprehensive of these, Miller [3], studied flow distributions in dividing manifolds, correlating loss coefficients in the feed and dividing ducts to the ducts' area and flow ratios. Importantly he noted that by varying the branch and manifold areas and modifying branch junctions to adjust branch loss coefficients, it is possible to obtain any required flow distribution, provided the resultant pressure losses are acceptable.

Heat transfer coefficient distributions in branched passages and manifolds have been measured, usually at low resolution by a number of other workers. Wesley and Sparrow [4] measured local and circumferentially averaged turbulent heat transfer coefficients in a tube downstream of a tee. They found that heat transfer coefficients in the thermal entranced region of the passage were very much higher than those for conventional axisymmetric turbulent tube flows, and also noted that circumferential variations of the Nusselt number were found to be confined to the initial part of the entrance region, with circumferential uniformity being attained at a downstream length of about 8 diameters. Ainsworth and Jones [5] used a transient technique based on point measurements from

Contributed by the Turbomachinery Division of ASME for publication in the JOURNAL OF TURBOMACHINERY. Manuscript received June 9, 2006; final manuscript received June 21, 2006; published online December 31, 2009. Review conducted by David Wisler.

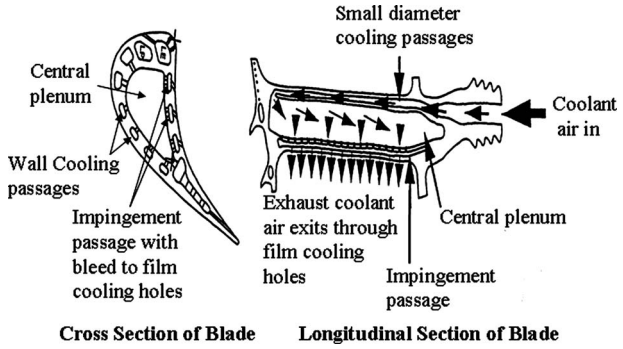

Fig. 1 Typical sections of a turbine blade [1]

thin film gauges to examine the effect of mass removal through discrete holes from a circular duct representative of a turbine cooling passage. They observed that the enhancement was doubled downstream of the hole and that it increased proportionately with the bleed rate of flow. Sparrow and Kemink [6] made a similar study of flow downstream of a branch takeoff, measuring heat transfer enhancement factors of up to 5 using a steady state technique.

Byerley [7] studied the heat transfer coefficients near film-cooling holes angled at 30 deg, 90 deg, and 150 deg to the oncoming flow, using a transient liquid crystal technique. For all configurations, they found that the peak level of enhancement is located at the downstream hole edge. Average heat transfer enhancement factors of up to 6 were found in up to 3 hole diameters downstream of the holes. Shen et al. [8] extended this work to investigate a blade midchord convergent cooling passage with single and multiple holes. Once again they concluded that heat transfer is always enhanced downstream of the film-cooling hole. They also found that the diameter of the film-cooling hole has an effect on the heat transfer coefficient, with smaller hole diameters yielding larger enhancement. In a related study Gillespie et al. [9] measured the effect of cross-flow on the inside surface of single holes inclined at 90 deg and 150 deg to the flow direction. They concluded that the effect of cross-flow is considerable and produces a Nusselt number distribution within the 90 deg hole, which is far from symmetrical about the 90 deg line. Along the 0 deg line there is always a region of low heat transfer due to the separation on the upstream edge of the inlet in both geometries. They also found that the overall circumferentially averaged Nusselt number for the 150 deg hole is higher than that for the 90 deg hole, but lower than that predicted by the tried and tested sharp-edged hole entry enhancement correlation of Boelter et al. [10].

Goldstein et al. [11] investigated the flow and mass transfer coefficient distributions in a duct feeding three short holes perpendicular to the duct flow direction using the naphthalene sublimation technique. By changing the number of open holes used, the effects of neighboring holes, hole spacing, distance to end of the duct, and duct height were investigated. They concluded that the flow into a hole (for one open hole) can be thought of as the combination of flow along a 90 deg tube bend and a sink flow (a sudden contraction). The Sherwood number around the circumference of the inside hole surface varies considerably due to the secondary flows. The Sherwood number near the trailing edge side of the hole entrance is about two times that on the leading edge. However, the Sherwood number is quite uniform near the exit of the hole. Although the local Sherwood number is very nonuniform around the circumference of the hole, the circumferential average Sherwood number inside the hole is only about 6% lower than that for open sink flow. It is suggested that the average mass transfer rate in the hole for a sink flow can be used to approximate that for duct flow, however, the thermal boundary conditions for these two cases are quite different.

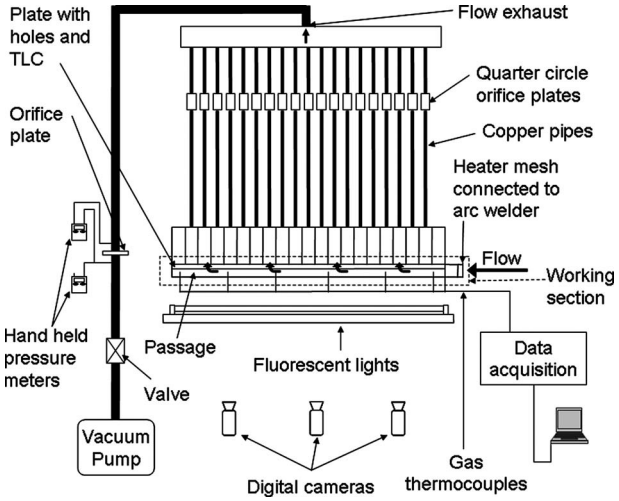

Fig. 2 Schematic of experimental setup (not to scale)

2 Experimental Apparatus

A large scale rig of a single cooling passage was constructed. The working section was built from Perspex, which ensured good optical access and low thermal diffusivity. Figure 2 shows a schematic of the rig. Figure 3 describes in detail the working section of the rig. The model is approximately $20\times$ engine scale. This scale was chosen to allow both the inlet and hole Reynolds numbers and suction ratio SR (defined as $u_{\text{hole}}/u_{\text{passage}}$), to be matched to engine conditions. It was not necessary to match the Mach number as it was less than 0.2 over the full range of engine representative conditions [12]. The air intake is atmospheric. Hole centers are located $y/d=\pm 1.77$ from the passage centerline; the hole pitch is $x/d=6.54$ along the passage axis. The first hole is located at $x/d=13.08$, and the total passage length is $x/d=147.5$. The holes are orientated at 90 deg to the oncoming flow. The length of the holes was $1.5d$. A 45 deg casting representative chamfer $0.125d$ deep is included on the passage side of the holes. Flow entering the passage is bled through these holes resulting in a reduction in the cross-flow passage velocity with distance from the inlet. The passage has a characteristic racetrack shape in cross section. The flow through each hole in the manifold was separately metered, and additionally the total mass flow rate was measured at the rig exit using orifice meters designed in accordance with BS1042. Temperature data were obtained using T-type thermocouples and thermochromic liquid crystal coatings. The color change in the coated surfaces was monitored using a number of

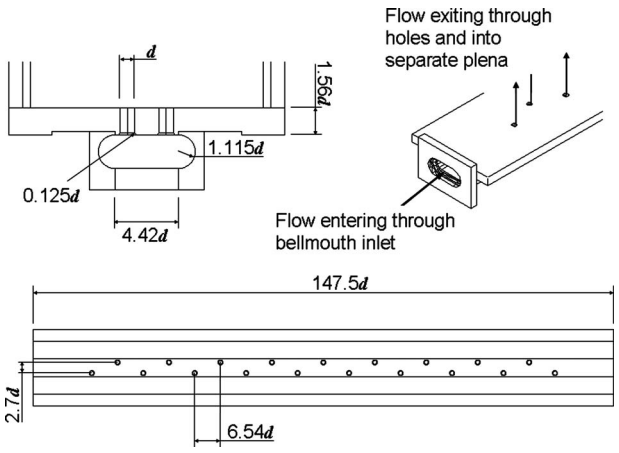

Fig. 3 Detailed description of working section geometry

digital video cameras. The gas temperature transient required for heat transfer tests was produced by a planar heater mesh located at the passage inlet.

3 Transient Heat Transfer Technique

Local heat transfer coefficient distributions were determined using the transient liquid crystal technique as briefly described above. Narrow-band thermochromic liquid crystals (TLCs) were used as full surface thermometers; these experience a full scale color change over a range of 1°C and are insensitive to both illumination and viewing angle. The liquid crystal color play was calibrated prior to testing. The full method of solution of the transient liquid crystal technique employed in this study is described by Abu Talib et al. [13].

Experimental intensity histories are produced by using digital video cameras to capture the crystal color change when the model is subjected to a sudden gas temperature change. These intensity histories are compared with analytical intensity histories generated for a range of heat transfer coefficients; the one with the minimum variance is selected as a solution.

As the passage is long in this series of tests, it is appropriate to base the heat transfer coefficient on the local passage centerline temperature. The gas temperature history was calculated for every column of pixels by linearly interpolating between temperatures measured by the gas thermocouples positioned at seven points along the passage. In-hole htc measurements were also based on the local passage centerline temperature as inferred at the entrance of each hole. Since the diameter of the hole is small, all pixels on the inside surface of the holes were processed using the same driving gas temperature history.

Two different temperature liquid crystals were used to obtain temperature history data in the passage; however, these were applied as two separate coatings. Approximately three-quarters of the passage (from the passage entrance to half way between holes 14 and 15) was sprayed with a liquid crystal displaying its maximum intensity at 40°C, and the rest of the passage and the interior of the impingement holes were sprayed with a 30°C crystal. This allowed high quality intensity signals to be obtained over the full passage surface in a single test as the inlet gas temperature could be controlled so that the liquid crystals at the beginning of the passage reacted slowly enough for the cameras to capture the characteristic signature of the color play with sufficient resolution, and quickly enough toward the end of the passage so that the crystal color play occurred within the experimentally valid test time.

For the test surface to behave as a semi-infinite solid, the time taken for the full liquid crystal color play to occur must be relatively short compared with the time taken for the thermal pulse to travel through the wall of the test rig and begin dissipating heat to the surrounding environment. Schultz and Jones [14] showed that the time t taken for the thermal pulse to travel across a wall of depth d is calculated by

$$t = \frac{d^2}{16\alpha} \tag{1}$$

where α is the thermal diffusivity of the material and has a value of 1.08×10^{-7} m^2/s for Perspex. With a Perspex plate depth of 0.0125 m, the maximum test time was thus calculated to be 90.42 s.

For the in-hole htc measurements, a single 30°C liquid crystal was used since the inlet gas temperature could be very easily controlled, and separate tests were carried out for each hole. Two cameras were used for the in-hole htc experiments. Each viewed half of the hole through the Perspex plate. The area of each pixel was subsequently adjusted to take account of the effect of the curvature of the hole on the projected image.

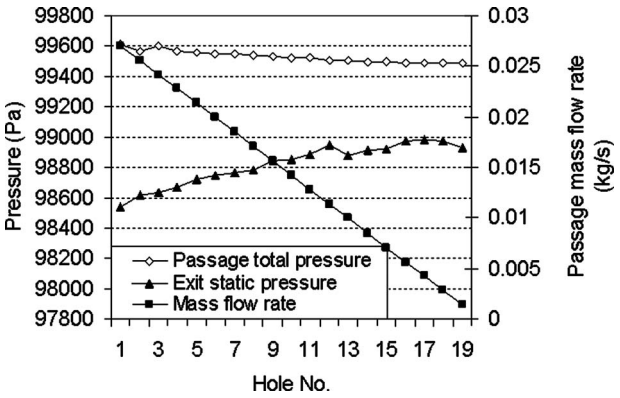

Fig. 4 Typical pressure and mass flow rate distributions within the passage, Re_{inlet}=45,596

4 Results

A total of 15 heat transfer tests are reported below. Three experiments were used to characterize heat transfer on the holed surface performed at different inlet Reynolds numbers: Re_{inlet} =21,667, 45,596 and 69,959. While full details of the flow characteristics of this cooling system can be found in the work of Ieronymidis et al. [15], typical pressure and mass flow rate distributions are included at a single inlet Reynolds number Re_{inlet} =45,596 (Fig. 4) to aid interpretation of the heat transfer results. The mass flow rate through each hole was separately measured, and it was found that these were almost identical at a constant inlet Reynolds number. For the three experimental inlet Reynolds numbers the corresponding average hole Reynolds numbers were 5930, 12,479 and 19,147, respectively.

4.1 Passage Heat Transfer Coefficient Results. The camera view and lighting arrangement for the passage htc experiments are shown in Fig. 5. The black region is the surface upon which the liquid crystals were sprayed. Heat transfer coefficient distributions measured at three inlet Reynolds numbers are shown in Fig. 6. Because the cooling holes are arranged in a staggered configuration, some asymmetry was expected between the upper and lower rows of holes. The htc range has been clipped in Fig. 6 to allow greater resolution of the htc distribution. The highest heat transfer coefficient recorded was ~1300 W/m^2 K in small regions immediately downstream of the holes farthest from the passage inlet.

The distribution of heat transfer coefficient can be sensibly explained by the expected flow field. Flow enters the passage through the bell mouth inlet from a rectangular plenum, along the walls of which a boundary layer is formed. It is thought that the variation in the path length from the mesh heater to the passage circumference where $x/d=0$ may explain the two patches of low htc at the top and bottom of the passage near the entrance. Flow that enters the passage at midheight is initially accelerated toward hole 1, creating a high htc patch as it approaches the hole. Not all flow that is accelerated toward hole 1 is ejected through that hole, and the remaining flow is re-accelerated toward hole 2 creating an

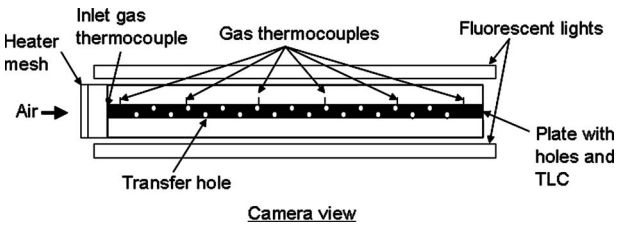

Fig. 5 Camera view and lighting arrangement for passage htc experiments (not to scale)

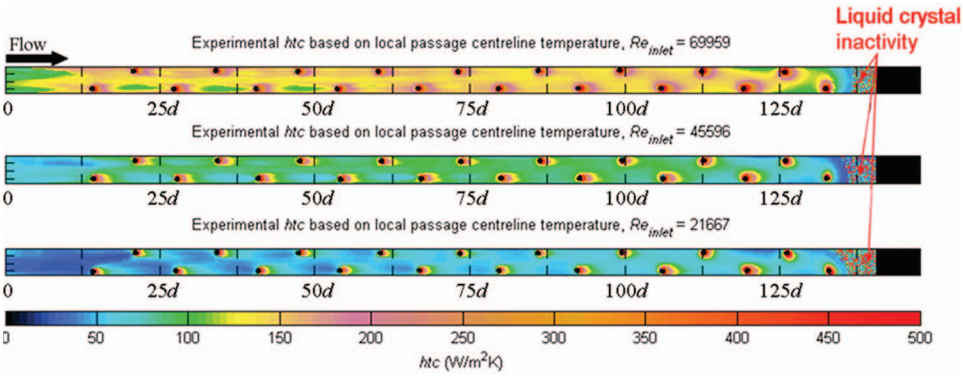

Fig. 6 Passage htc results using narrower scale for better understanding of results

enhanced patch of high htc on the surface between the holes. The staggered configuration of the cooling holes means that this htc enhancement is repeated along the entire passage in an oscillating pattern. Figure 7 shows an image of path lines released along the passage centerline in a Reynolds averaged Navier-Stockes computational fluid dynamics (CFD) simulation of the experiment (2.2×10^6 cells, realizable k-ε turbulence model). The flow oscillations from one hole to the other are clearly visible.

This flow travels down the center of the passage and forms a thicker boundary layer than in the region immediately downstream of the transfer holes from which the boundary layer has been stripped, decreasing the relative level of heat transfer coefficient. This is clearly seen in the low htc patch between the two rows of holes in Fig. 6. At the beginning of the passage the strong cross-flow limits the amplitude of the oscillating flow in the middle of the passage. Toward the passage end, however, the flow slows and with longer residence time in the passage the pressure field can produce larger oscillations. It is clear in Fig. 7, that the path lines show a preferential acceleration of the flow toward the top row of holes. This again is caused by the staggered configuration of the holes and can be seen in the asymmetry of the heat transfer distribution in the passage. Figure 8 shows a more detailed view of CFD path lines colored by the velocity on the x-axis. The CFD study of the geometry is more fully described by Ieronymidis et al. [15] and is used here only for flow diagnosis. The red patch shows the flow being pulled toward the top row of holes and the blue patch toward the opposite side. For holes 13–15 the increased amplitude of the oscillations is clearly demonstrated.

As the flow is accelerated toward the first hole, the boundary layer becomes thinner and the htc rises; the flow entering the first hole is drawn mainly from the boundary layer. The boundary layer immediately downstream of the hole is restarted and this gives rise to a region of high heat transfer. The flow that passes directly over the hole diffuses and re-attaches forming a new boundary layer. Some of the flow close to the holed surface, which was initially accelerated toward hole 1 but passed on either side of the first hole, is reaccelerated toward hole 3 and ejected through it as indicated on Fig. 8. The low htc patch in front of hole 3, that extends in a spanwise direction upstream by an entire hole-to-hole pitch, suggests that the majority of the flow being ejected comes from the passage sides and the center of passage. This phenomenon is most pronounced where the cross-flow is relatively high in the channel (holes 1–9) and is seen at all inlet Reynolds numbers.

For holes 10–16, the flow behaves as expected. The boundary layer is stripped and restarts downstream of the holes, creating an area of htc enhancement and then re-attaches forming a boundary layer. Where the suction ratio quickly increases in the final three holes, there is clear evidence that the flow ejected through the holes not only originates upstream of the hole but also from areas to either side. The pattern of htc around the last hole of the flow resembles a sink flow and the ring of enhanced htc around the hole indicates that ejected air enters from all around the circumference of the hole. This, along with the increase in htc around the last hole, agrees with the findings of Goldstein et al. [11]. But the level of *mass transfer coefficient* is substantially higher in their experimental results. This may be explained by the different geometries, different hole arrangements, absence of a chamfered inlet, and the difficulty of creating an analog of the thermal boundary layer in mass transfer experiments. For the rest of the passage, results cannot be compared because as Goldstein et al. [11] suggested, the flow pattern around an off-center hole, even with minor asymmetry, can be very different from that of a centered hole.

The area of noisy data, downstream of the last hole, is an area in which the liquid crystals did not change color during the transient tests. This is an evidence of very low htc in this region. This region extended to the final hole in the case of the lowest inlet Reynolds number tested.

Figure 9 shows averaged htc across the passage in the area between the holes. Heat transfer coefficient distributions are nota-

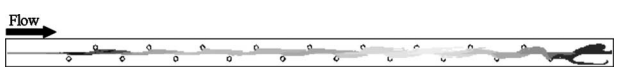

Fig. 7 CFD path lines released from a surface along the passage centerline (x/d=0) showing flow oscillations

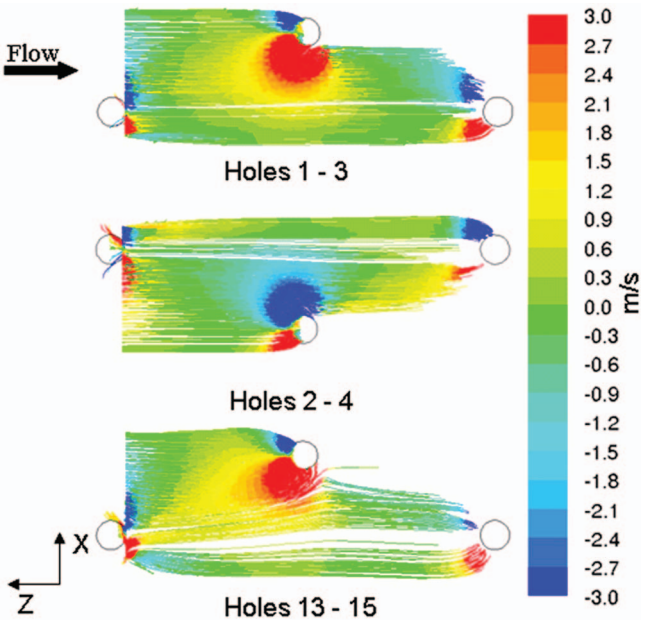

Fig. 8 CFD path lines colored by the x-axis velocity

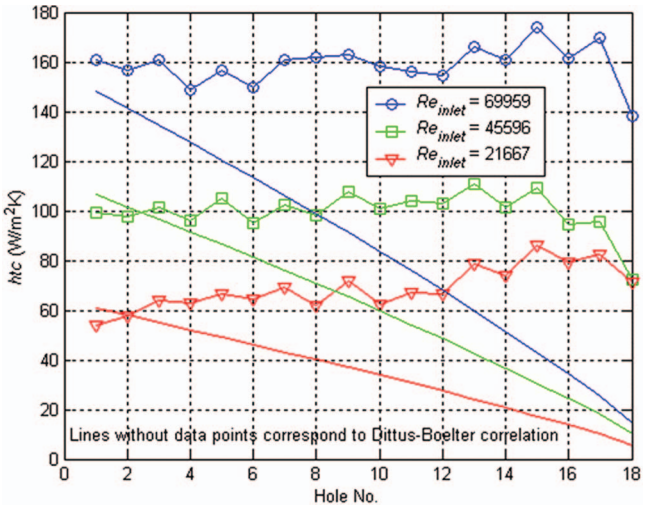

Fig. 9 Average experimental htc and Dittus–Boelter correlation for surfaces between holes

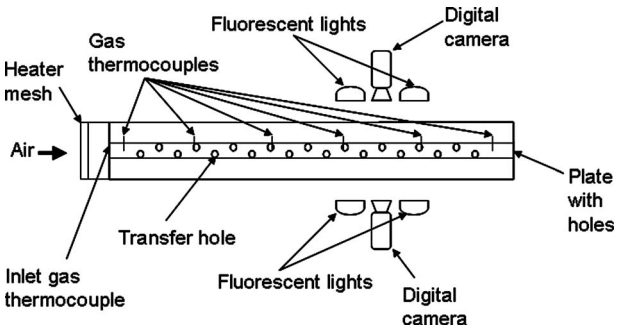

Fig. 10 Camera and lighting arrangement for in-hole htc experiments (not to scale)

bly flat for a given inlet Reynolds number in spite of the rapidly dropping local Reynolds number. The average level of heat transfer coefficient at $Re_{inlet}=21{,}667$ and $Re_{inlet}=45{,}596$ is 43% and 62% of the level obtained at $Re_{inlet}=69{,}959$. This is highlighted by a comparison to the Dittus–Boelter correlation for turbulent flow in pipes as follows:

$$Nu_{DB} = 0.023\ Re^{0.8}\ Pr^{0.4} \tag{2}$$

Here the local Reynolds number in the channel is used to calculate the Nusselt number, and the characteristic length used for both Nusselt and Reynolds numbers is the hydraulic diameter of the passage. It is clear that the average value is dominated by the presence of the transfer holes, and despite variations in the local heat transfer coefficient distribution around each hole the average htc is nearly constant for a set mass flow rate through the holes.

Figure 9 also shows that at $Re_{inlet}=21{,}667$ the passage htc level increases between holes 13 and 17, compared with the first three values, by much more than for the other two cases. This can be explained by the lower cross-flow velocity in the passage. Because the flow travels at lower speeds it is more strongly affected by flow acceleration across the passage. This means that instead of being a region of undisturbed fluid, the fluid close to the wall is now relatively fast moving, zigzagging from one hole to the next, and creating a corresponding region of elevated heat transfer coefficient. This is confirmed by the visible patch of elevated htc connecting holes 13–17 at $Re_{inlet}=21{,}667$ seen in Fig. 6. It should be noted that the chamfer plays a very important role in shaping the flow as it enters the cooling holes. However, htc results from the chamfer area should be treated with caution as the htc may be slightly lower than measured. This is because heat conduction has been assumed to be 1D in the analysis used, and this is not the case near the apexes of the chamfer.

4.2 In-Hole Heat Transfer Coefficient Results. Additional tests were carried out using two cameras to measure the heat transfer coefficient inside holes 1, 6, 11, and 19 at the same inlet Reynolds number as in the passage htc experiments. Hole 16, situated in the upper half of the passage, was also investigated at one inlet Reynolds number to check for any differences in htc levels and patterns between the top and bottom rows of holes.

The modified camera view and lighting arrangement for the in-hole htc experiments is shown in Fig. 10. While the hole Reynolds number is equal through each of the transfer holes for a given inlet Reynolds number, the cross-flow velocity decreases with distance into the cooling passage and this results in increasing values of suction ratio. Hence the suction ratio for holes 1, 6, 11, 16, and 19 are SR=0.98, 1.31, 2.08, 4.49, and 18.67, respectively. These values are unchanged with changing inlet Reynolds number as the discharge coefficients of the transfer holes are a very weak function of hole Reynolds number [15].

The schematic in Fig. 12 shows the angular notation θ used around the circumference of each hole.

Figure 11 shows the htc distribution in each of the holes at an inlet Reynolds number of $Re_{inlet}=69{,}959$. It is evident that the flow inside the hole, and hence the level of the heat transfer coefficient, is strongly affected by the suction ratio. However, there are strong common features, less clearly seen in the final hole, which are described below. Looking at hole 1, the separation zone dominates the region between $\theta=\pm 60$ deg. This is because of the high cross-flow in the passage; flow entering the hole would have to turn through a small radius of curvature to travel in the axial hole direction. As this turning requires a high pressure gradient, which is not available, the flow separates, and at the highest cross-flow (smallest suction ratio, SR=0.98) it appears not to re-attach over the entire length of the hole along the $\theta=0$ deg line. This behavior was previously noted by Goldstein et al. [11]. The majority of the flow re-attaches to the hole surface $\sim 0.6d$ downstream of the hole entrance, but the resulting htc remains very low. On the surface between $\theta=\pm 120$ deg (via 180 deg) maximum htc is observed. This is the downstream surface of the hole, where the flow impinges and high htcs are expected. In this region, maxima are observed between $l/d=0$ and $l/d=0.6$ from the hole entrance where the developing boundary layer is thinnest and the near wall velocities are highest. Between the separation zone and the high htc area noted above, there is a tongue of high heat transfer coefficient, which is associated with re-attachment at the edge of the separated region. This is similar to local htc distributions seen by Gillespie et al. [9] in film-cooling holes of larger l/d. Toward the hole exit, there are regions of low heat transfer coefficient seen in all cases with significant cross-flow. These are centered at ± 90 deg; they seem to occur between the area immediately downstream of the developing impingement flow, and the area into which the re-attached flow has been accelerated. Although the heat transfer coefficient distribution is nearly symmetrical about the 0 deg line, a slightly higher overall heat transfer performance is seen over the $\theta=+ve$ half of the hole surface. It should be remembered that the upstream conditions on either side of the hole axis are quite different, as discussed for the *in-passage* htc results above. Additional evidence that the tongue of high htc may be attributed to flow accelerating around the separated zone was gained from a CFD simulation (fully reported by Ieronymidis et al. [15]). Path lines close to the surface of the hole, shown in Fig. 12, indicate attached high speed flow in the region surrounding the ± 90 deg line. A schematic of the flow field is shown in Fig. 11.

Holes 6, 11, and 19 behave similarly, but there are some important differences. Interestingly, the overall level of heat transfer coefficient increases with increasing suction ratio, even though the

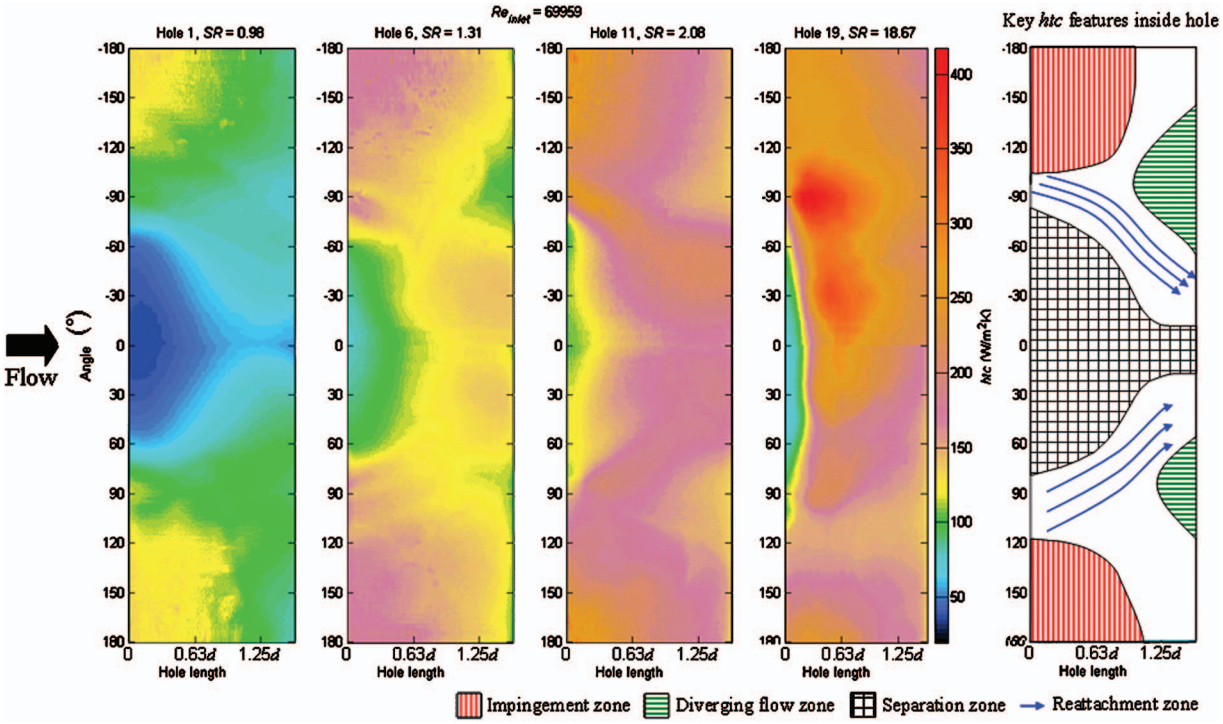

Fig. 11 In-hole htc distribution, $Re_{inlet}=69{,}959$

hole Reynolds number is unchanged. This is associated with a continuous reduction in the separation zone and an increase in the level of heat transfer coefficient in the area surrounding it. The high streak of htc associated with flow re-attachment can be seen particularly clearly for hole 11. The flow regime in hole 19 is rather different from the other holes, as all the remaining flow in the passage exits through this hole. A separation zone is still present between $\theta=\pm 60$ deg, but it extends only $0.25d-0.38d$ into the hole. There is a ring of high htc downstream of this, although the heat transfer is somewhat unsteady in this region, and because flow enters the hole from across the entire passage the distribution is not as symmetrical as before. Circular patches of high heat transfer seen at ~ -80 deg and -30 deg are mirrored on the other half of the hole, but are smaller in size and about 35% lower in htc level. Between 100 deg and 140 deg, there is a region of low htc, which is not as pronounced on any of the other holes tested.

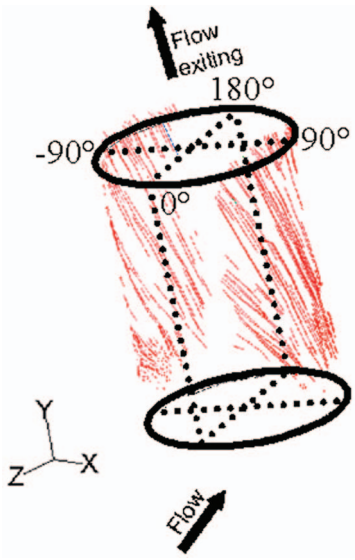

Fig. 12 In-hole angle notation and path lines close to the surface of the hole colored by the *z*-axis velocity

At lower inlet Reynolds numbers, the htc patterns are very similar to the $Re_{inlet}=69{,}959$ case. All key features as identified in the annotated sketch of Fig. 11 are present. Some differences exist in the size of the separation and re-attachment zones and level of htc, but these are minor; for a given SR, the separation zone becomes larger with decreasing Reynolds number, especially for $SR>1$. Local htc distributions are not reported here.

Average htc values are presented in two formats. Figure 13 shows values grouped by hole number (identical suction ratio) and Fig. 14 by inlet/hole Reynolds number. Values were averaged circumferentially over $0.063d$ steps into the hole. Note the nonzero axes on the figures.

With the exception of hole 1, a slight movement of the position of the peak in average htc toward the hole entrance can be seen for all holes as the Reynolds number is increased. In hole 1, the heat transfer is greatly enhanced at high Reynolds number and this appears to be caused by a considerable increase in the level of htc in the cross-flow impingement zone. The highest heat transfer coefficient is measured in hole 19, however, here, there is less uniformity along the length of the hole.

The htc increase in each hole is proportional to $Re_{hole}^{0.59-0.62}$ (excluding hole 1, $Re_{inlet}=69{,}959$). When compared at the same hole Reynolds number, the effect of changing suction ratio is clearly seen. In holes 1, 6, and 11, there is a steady increase in htc with suction ratio as the size of the inlet separation is progressively reduced. In holes 16 and 19, a change in the shape of the average htc distribution is seen. As the flow now separates around the entire circumference of the hole on entry, the cross-flow impingement region is eliminated, and the flow separation actually increases from hole 16 (SR=4.49) to hole 19 (SR=18.67). A peak in htc is seen where the flow re-attaches further into the hole. As the behavior is more circumferentially uniform than at low suction ratio, this peak is more pronounced. The overall heat transfer co-

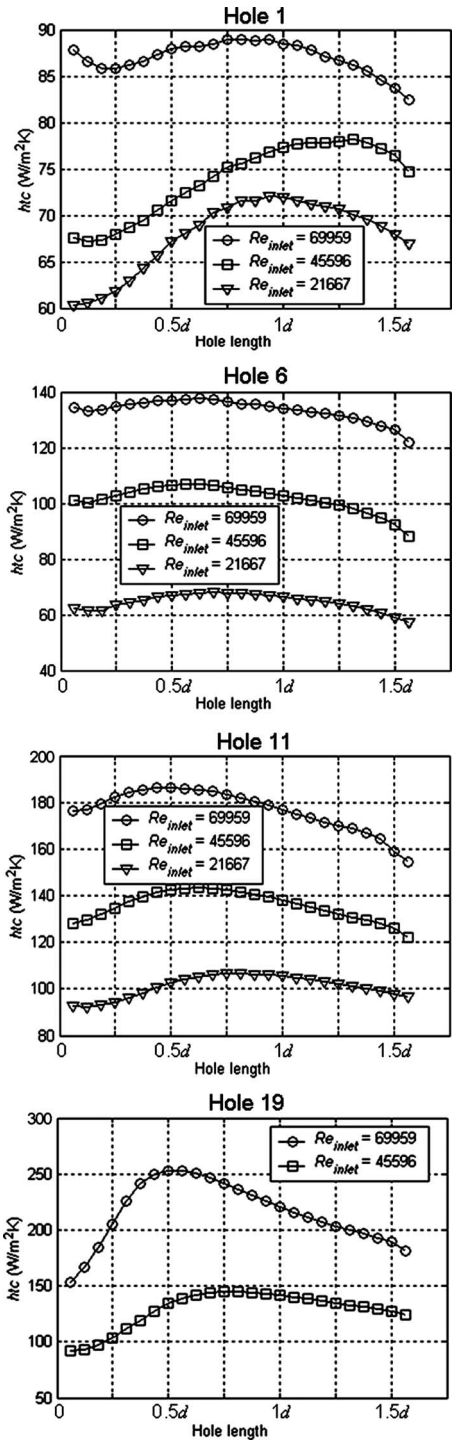

Fig. 13 Circumferentially averaged in-hole htc for same hole and different Re_{inlet}

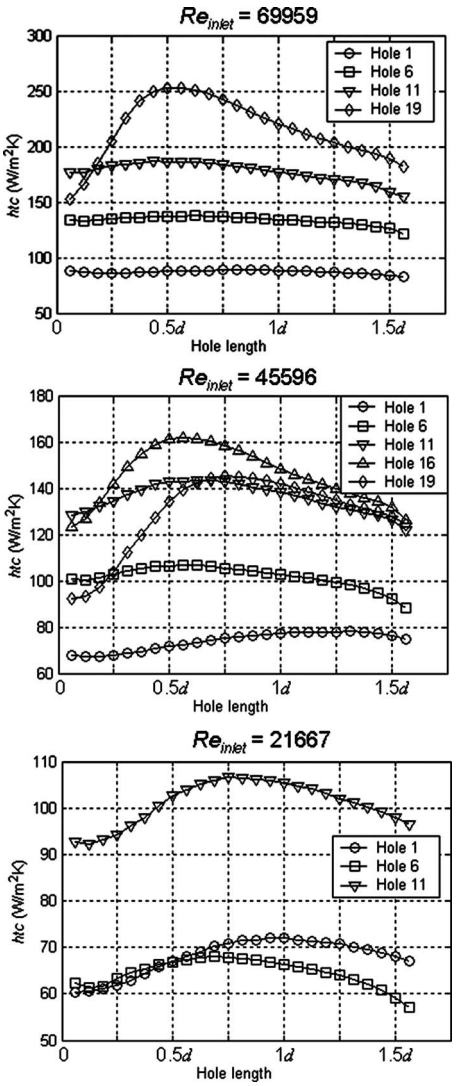

Fig. 14 Circumferentially averaged in-hole htc for same Re_{inlet} and different hole

efficient is higher in hole 16 than hole 19; this is thought to be due to the optimally sized small separation around the circumference of the hole, which allows early flow re-attachment within the hole.

Comparing these results to those obtained by Goldstein et al. [11] in a three hole manifold, great similarity in the pattern of heat/mass transfer coefficients was seen, particularly for holes 1 and 6 where the oscillating motion of the flow is least pronounced. The effect of the chamfer in the current study is to limit the extent of the separation zone to the upstream edge of the hole. Interestingly Goldstein et al. [11] observed the highest htc values in the first hole, while this study shows that the holes near the closed end of the passage give the highest average htc value. This difference may in part be due to the asymmetry of the holes or the changed flow distribution in the much shorter manifold used by Goldstein et al. [11]. The most noticeable variation between the current data and that of Goldstein et al. [11] is that the levels of htc do not agree. While the previous work has been carried out with meticulous care, this infers that there is considerable difficulty in making an analogy between heat and mass transfers for such a geometry, as the heat transfer coefficient, while based on a mixed bulk parameter, may be driven by the temperature of the air in the boundary layer and this requires the boundary layer in the entire passage to be modeled. This is rarely the case for mass transfer coefficient tests, where discrete pockets within the working section are cast with subliming material. As the flow is separating and transition occurs, it is also difficult to assign a scaling exponent to the Schmidt/Prandtl number in the entire passage. They predicted a maximum Sherwood number of around 400 for the first hole, which translates to a Nusselt number of 240 for $Re_{hole}=15{,}700$. In this study, for $Re_{hole}=19{,}147$, the last hole (highest htc) only achieves a maximum Nusselt number of 117, which is approximately 50% lower but with an 18% higher mass flow rate through the hole.

The level of in-hole htc compares slightly better to those by Gillespie et al. [9], for a single longer hole ($l/d=8$), fed from a

Table 1 Uncertainty analysis for heat transfer coefficient measurements

Parameters	Typical values	Typical error	Low htc error (%)	High htc error (%)
$T_{initial}$(°C)	17.3	±0.3	1.14	1.01
T_{gas}(°C)	67.0	±0.3	1.44	1.88
$T_{crystal}$(°C)	39.9	±0.3	2.61	2.87
$t_{crystal}$(s)	14.9	±0.04	0.17	1.13
$\sqrt{\rho ck}$	569	±29	5.07	4.71
Base value of htc (W/m^2 K)	-	-	143	417
RSS error (%)			6.00	6.03
Worst case (%)			10.43	11.62

fully developed boundary layer in a high aspect ratio channel. The Nusselt number is still considerably lower: the ratio of Nu/Nu_{DB} is found to be 1.55 in Ref. [9] and 1.0 for this study.

Uncertainty analysis was carried out using the method outlined by Moffat [16]. This shows that the root sum square error in the heat transfer coefficient measurements is between 6.00% and 6.03% depending on the heat transfer coefficient level, and in the worst case this rises between 10.43% and 11.62%. Table 1 shows the uncertainty ascribed to each measure and the results of the uncertainty analysis. Note that the uncertainty in the measured gas temperature takes account of possible effects of radiation from the mesh heater at all thermocouple locations along the passage. Although the mesh heater is in close proximity to the first thermocouple, because of the high convective efficiency of the heater mesh (0.3–0.5 dependent on flow velocity), the temperature of the heater wires lies between 100°C and 160°C. Thus even at the lowest flow rate the first thermocouple will merely over-read the inlet gas temperature by ~0.01°C. No correction was applied to the reading to take account of this.

5 Summary and Conclusion

Detailed heat transfer coefficient measurements were made in a model of a cooling manifold integrally cast into the wall of a turbine blade.

In the passage, the flow was strongly influenced by the staggered configuration of the cooling holes, which caused oscillating flow between the holes along the length of the passage. Importantly the level of heat transfer coefficient appears to be set by the local Reynolds number of flow entering the transfer holes rather than the average passage Reynolds number. Slight asymmetry in heat transfer coefficient is observed between two halves of the passage suggesting that the secondary flow setup by the first hole persists along the passage length.

In-hole heat transfer coefficients on the other hand are strong functions of the local hole suction ratio, increasing with increasing suction ratio at a given hole Reynolds number. Three factors dictate the pattern of htc inside the holes. These are the size of separation, which is inversely proportional to the suction ratio; the size of cross-flow impingement region; and the size of re-attached region. Additionally, the size of the separation on the upstream edge of the hole is reduced as the hole Reynolds number increases at a given suction ratio. This allows a near linear relationship between hole Reynolds number and heat transfer coefficient. Circumferentially averaged htc increases with suction ratio for all holes; the only exception to this being the final hole. The last hole, which has the highest suction ratio and whose flow field is unconstrained by holes further downstream in the passage, produces the highest htc.

The authors argue that the in-hole htc values measured are lower than those by both Goldstein et al. [11] and Gillespie et al. [9], because of differences in the experimental technique used and the short $l/d=1.5$ hole geometry being tested, respectively.

Acknowledgment

This work has been carried out with the support of Rolls-Royce plc., the continuance of which is greatly appreciated. The experimental apparatus was manufactured by Mr. Pat Timms and Mr. Nigel Brett.

Nomenclature

A = cross-sectional area (m^2)
D_h = hydraulic diameter of passage=4 A/P(m)
d = hole diameter or depth of experimental substrate (m)
h, htc = heat transfer coefficient (W/m^2 K)
l = length of hole (m)
n = number of holes
Nu = Nusselt number=hd/k
P = perimeter of cross section of passage (m)
Pr = Prandtl number
p = pressure (Pa)
Re = Reynolds number=$\rho ud/\mu$
Sh = Sherwood number=$h \times d/D_{naph}$ (h is the mass transfer coefficient, D_{naph} is the mass diffusion coefficient for naphthalene vapor in air)
T = temperature (K)
t = time (s)
u = velocity (m/s)
x,y,z = distance along passage (m)

Greek

Θ = angular notation for in-hole htc results
μ = dynamic viscosity (N s/m^2)
ρ = density (kg/m^3)

Subscripts

0 = total
DB = Dittus–Boelter
e = exit
i = inlet
s = static

References

[1] Dailey, G.M., 2000, "Aero-Thermal Performance of Integral Cooling Systems in Turbomachines: Design and Calculation Issues," VKI Lecture Series, Feb. 28–Mar. 3.
[2] Ireland, P. T., and Jones, T. V., 1986, "Detailed Measurements of Heat Transfer on and Around a Pedestal in Fully Developed Channel Flow," *Proceedings of the Eighth International Heat Transfer Conference*, San Francisco, CA, pp. 975–986.
[3] Miller, D. S., 1990, *Internal Flow Systems*, 2nd. ed., BHR Group Ltd., Cranfield, UK.
[4] Wesley, D. A., and Sparrow, E. M., 1976, "Circumferentially Local and Average Turbulent Heat-Transfer Coefficients in a Tube Downstream of a Tee," Int. J. Heat Mass Transfer, **19**, pp. 1205–1214.
[5] Ainsworth, R.W., and Jones, T.V., 1979, "Measurement of Heat Transfer in Circular, Rectangular, and Triangular Ducts, Representing Typical Turbine

Blade Internal Cooling Passages Using Transient Techniques," ASME Paper No. 79-GT-40.
[6] Sparrow, E.M., and Kemink, R.G., 1979, "Heat Transfer Downstream of a Fluid Withdrawal Branch in a Tube," ASME J. Heat Transfer, **101**, 23–28.
[7] Byerley, A. R., 1989, "Heat Transfer Near the Entrance to a Film Cooling Hole in a Gas Turbine Blade," Ph.D. thesis, Department of Engineering Science, University of Oxford, Oxford, UK.
[8] Shen, J.R., Ireland, P.T., Wang, Z., and Jones, T., 1991, "Heat Transfer Coefficient Enhancement in a Gas Turbine Blade Cooling Passage Due to Film Cooling Holes," *Turbomachinery: Latest Developments in a Changing Scene*, IMechE, London, pp. 219–226.
[9] Gillespie, D. R. H., Byerley, A. R., Wang, Z., Ireland, P. T., Jones, T. V., and Kohler, S. T., 1996, "Detailed Measurements of Local Heat Transfer Coefficient in the Entrance to Normal and Inclined Film Cooling Holes," ASME J. Turbomach., **118**, pp. 285–290.
[10] Boelter, L. M. K., Young, G., and Iversen, H. W., 1948, "An Investigation of Aircraft Heaters XXVII: The Distribution of Heat Transfer Rate in the Entrance Region of a Circular Tube," NACA Report No. TN 1451.
[11] Goldstein, R. J., Cho, H. H., and Jabbari, M. Y., 1997, "Effect of Plenum Crossflow on Heat (Mass) Transfer Near and Within the Entrance of Film Cooling Holes," ASME J. Turbomach., **119**, pp. 761–769.
[12] Andrews, G. E., and Mkpadi, M. C., 1983, "Full Coverage Discrete Hole Wall Cooling: Discharge Coefficients," International Gas Turbine Conference and Exhibit, Phoenix, AZ, Mar.
[13] Abu Talib, A.R., Ireland, P.T., Neely, A.J., and Mullender, A.J., 2003, "A Novel Liquid Crystal Image Processing Technique Using Multiple Gas Temperature Tests to Determine Heat Transfer Coefficient Distribution and Adiabatic Wall Temperature," ASME Paper No. GT2003-38198.
[14] Schultz, D.L., and Jones, T.V., 1973, "Heat Transfer Measurements in Short Duration Hypersonic Facilities," AGARDograph No. 165.
[15] Ieronymidis, I., Gillespie, D. R. H., Ireland, P. T., and Kingston, R., 2006, "Experimental and Computational Flow Field Studies of an Integrally Cast Cooling Manifold With and Without Rotation," Turbo Expo 2006: Power for Land, Sea & Air, Barcelona, Spain, May 8–11.
[16] Moffat, R. J., 1988, "Describing the Uncertainties in Experimental Results," Exp. Therm. Fluid Sci., **1**, pp. 3–17.

Experimental Reduction of Transonic Fan Forced Response by Inlet Guide Vane Flow Control

S. Todd Bailie[1]
e-mail: samuel.bailie@wpafb.af.mil

Wing F. Ng
e-mail: wng@vt.edu

Department of Mechanical Engineering,
Virginia Polytechnic Institute and State University,
Blacksburg, VA 24061

William W. Copenhaver
Propulsion Directorate,
Air Force Research Laboratory,
WPAFB,
OH 45433
e-mail: william.copenhaver@wpafb.af.mil

The main contributor to the high cycle fatigue of compressor blades is the response to aerodynamic forcing functions generated by an upstream row of stators or inlet guide vanes. Resonant response to engine order excitation at certain rotor speeds can be especially damaging. Studies have shown that flow control by trailing edge blowing (TEB) can reduce stator wake strength and the amplitude of the downstream rotor blade vibrations generated by the unsteady stator-rotor interaction. In the present study, the effectiveness of TEB to reduce forced fan blade vibrations was evaluated in a modern single-stage transonic fan rig. Data were collected for multiple uniform full-span TEB conditions over a range of rotor speeds including multiple modal resonance crossings. Resonant response sensitivity was generally characterized by a robust region of strong attenuation. The baseline resonant amplitude of the first torsion mode, which exceeded the endurance limit on the critical blade, was reduced by more than 80% with TEB at 1.0% of the total rig flow. The technique was also found to be modally robust; similar reductions were achieved for all tested modal crossings, including more than 90% reduction in the second leading-edge bending response using 0.7% of the rig flow.
[DOI: 10.1115/1.3140823]

1 Introduction

The occurrence of high cycle fatigue (HCF) failures in military turbine engines has increased dramatically in the past 25 years. HCF has been cited as the cause of 56% of United States Air Force engine-related Class-A failures between 1982 and 1996. Additionally, HCF-related maintenance costs are estimated at more than USD 400 million per year [1]. In response to this alarming trend, many recent research efforts have focused on understanding and mitigating HCF problems in turbine engines.

Compressor and turbine rotor blades are particularly prone to HCF damage as they experience continuous forced excitation. This excitation is primarily the result of unsteady flow interactions with neighboring blade rows [2,3]. As rotor blades pass through the wakes shed by upstream stator vanes, they experience highly unsteady aerodynamic loading, inducing forced blade vibrations. Because potential flow interactions present an additional forcing function, downstream vanes can also excite rotor blade vibration. Both of these aerodynamic excitations occur at the fundamental vane passing frequency (VPF) and its harmonics, thus corresponding to fixed engine orders.

Operation at a resonance crossing, where the rotor speed is such that an engine order excitation coincides with a blade natural frequency, can be especially damaging. Because load cycles are rapidly accumulated at the high rotational speeds typical in turbomachinery, high-amplitude resonant vibrations can quickly lead to fatigue failure. Thus it is a standard, and often iterative, design practice to try to locate blade modes such that resonance crossings do not occur near the intended steady operating speed(s) of the rotor. However, rotor blades will experience multiple resonance crossings during engine run-up and run-down [2]. Accumulation of damage is consequently inevitable and, in the event that this damage exceeds material limits, failure will occur.

Accordingly, a specific objective of the National HCF Science and Technology Program has been to damp resonant stress by 60% in fans [1]. There are two basic approaches to alter a component's forced response—either the component itself (that is, in this case, the fan blades) or the force input to the component (the stimulus) can be modified. While simply thickening the rotor blades can increase damage tolerance, the associated weight and dynamic load penalties are often unacceptable. Many research efforts have attempted to modify the system by adding damping, in various forms, to the rotor blades. While this approach has produced promising results, implementation without reducing the structural integrity of the rotor remains a challenge [4].

The stimulus can be modified in several ways. One such method, employed by von Flotow et al. [4], is to impose an additional forcing function, out of phase with the original modal excitation, to produce some response cancellation. This new variable forcing function is generated by selectively extending rods into the flow between blade rows to introduce additional wakes. The technique has been shown to be highly effective but must be calibrated to target specific modes, and as such would generally be implemented only after a fatigue problem has been encountered and its origin determined. Also, to produce and control the additional forcing function, engine system complexity and performance penalties are typically increased.

An alternate method, which can be implemented without a priori knowledge of the critical resonance crossings, is to attempt to reduce the amplitude of the dominant forcing function, which is the set of wakes shed by the upstream vane row. Waitz et al. [5] discussed the feasibility of various flow control techniques for wake reduction on curved airfoil shapes. The study concluded that the TEB technique should be more effective than boundary layer suction for reduction of viscous wakes. In this technique, air is ejected from the trailing edge of wake sources, such as the inlet guide vanes (IGVs) upstream of a fan, to reduce the mean velocity deficit and turbulent velocity fluctuations in the wake region.

Implementation of the TEB technique also requires some degree of increased system complexity. However, it is common that the front frames and IGVs of military engines are already plumbed with a bleed air recirculation system for de-icing pur-

[1]Present address: Propulsion Directorate Air Force Research Laboratory.

Contributed by the International Gas Turbine Institute of ASME for publication in the JOURNAL OF TURBOMACHINERY. Manuscript received July 1, 2005; final manuscript received March 7, 2008; published online December 31, 2009. Review conducted by David Wisler. Paper presented at the ASME Turbo Expo 2004: Land, Sea, and Air (GT2004), Vienna, Austria, June 14–17, 2004.

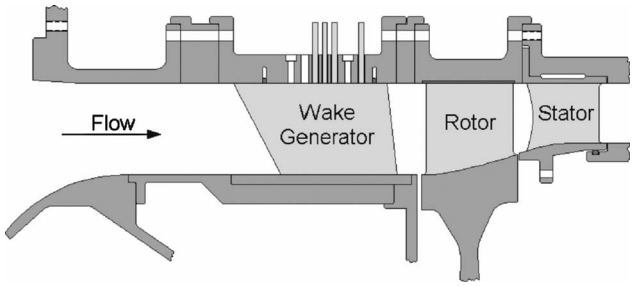

Fig. 1 Cross section of SMI transonic compressor rig

poses. There also exists the potential that such a wake-filling system could be passively scheduled without requiring special tuning with respect to individual resonance crossings.

Morris et al. [6] studied TEB effects in a linear cascade of stator vanes and subsequently implemented TEB in a 17-in. (43.2 cm) scaled fan rig, the blades of which were instrumented with strain gages. Rotor blade stress reductions of as much as 90% were reported with TEB mass flow for 20 IGVs at 1.4% of the total rig flow. However, shock interaction was not present, as the rotor was operated at subsonic conditions [7].

In comparison with the experiments previously discussed by Bailie et al. [8], the present study similarly applies the TEB technique in a modern compressor rig but with a different stage installed. Both stages are transonic designs with close stage row spacings. Thus strong shock-wake interactions are present, which have been observed to substantially increase wake depth [9]. The fan stage of the current study is more highly loaded than the core stage of the earlier investigation. A much more extensive set of blade forced response data was obtained in the latter experiments, including a broad range of full- and part-span IGV TEB conditions at multiple modal resonance crossings. The present discussion is limited to the full-span TEB results.

2 Description of Experiment

2.1 Stage Matching Investigation Rig. Experiments were conducted in the stage matching investigation (SMI) transonic compressor rig at the Air Force Research Laboratory (AFRL). The rig consists of a high-speed highly loaded rotor followed by a row of stator vanes. A row of wake generator (WG) vanes, similar to IGVs, is installed upstream of the rotor to simulate an embedded stage. The rig was originally designed to investigate upstream wake influences on stage flow matching [10]. However, with the adjustability of the WG forcing function and the addition of rotor-mounted strain gages, the rig was recently proven useful for forced response experiments.

A schematic of the SMI rig flow path with WGs installed is provided in Fig. 1. The fan is a 19-in. (48.3 cm) diameter integrally bladed disk (or blisk) with 28 blades of 0.916 average aspect ratio. The rotor has a design speed of 16,400 rpm, with hub and tip relative Mach numbers of 1.10 and 1.39, respectively. The stator row is composed of 49 vanes with 0.824 average aspect ratio. Design flow capacity is 34.5 lb/s (15.6 kg/s) and design pressure ratio for the stage is 2.13. Additional details concerning the SMI rig design are provided in Ref. [10].

2.2 Wake Generators. The wake generators, which provide the baseline aerodynamic forcing function in the present work, are symmetric airfoils without camber. They have a blunt trailing edge and are intended to produce wakes that are representative of the wakes shed from modern highly loaded low-aspect-ratio front stages. Such wakes are deeper and broader and decay more slowly than those shed by high-aspect-ratio stages [11]. WG vane counts of 0 (clean inlet), 12, 24, or 40 may be chosen. In addition, the axial distance between the WG row and the rotor can be adjusted, via interchangeable spacers, to 12%, 26%, or 56% of the mean

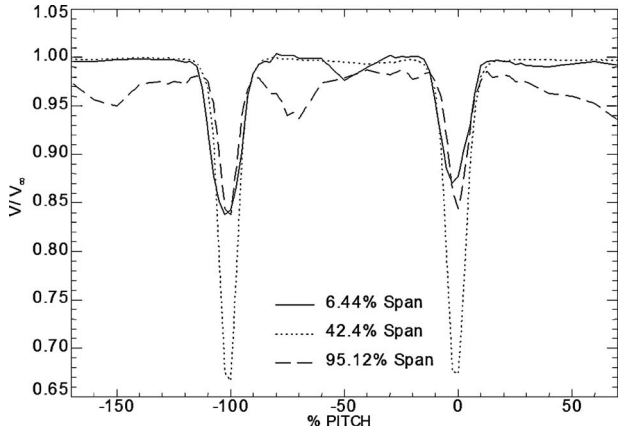

Fig. 2 SMI 24-WG wake velocity profiles at 26% axial spacing (from Ref. [12])

WG chord, which is 3.5 in. (89 mm).

In the present study, the 26% chord spacing was chosen as being representative of axial gaps found in modern fans and compressors [11]. Figure 1 illustrates this spacing, while Fig. 2 shows the deep wakes in the form of steady velocity measurements by Gorrell [12] at the same relative spacing in the 24-WG configuration. The wake data were collected at design speed but without rotor-shock effects, as the axial gap between rows was increased to accommodate the traversing measurement rake assembly. To minimize the complexity of the TEB system plumbing and external compressed air consumption, the 12-WG configuration was selected. The WGs thus produce a strong aerodynamic gust forcing function at the 12th engine order (12E) and higher harmonics (24E, 36E, etc.).

2.3 Trailing Edge Blowing System. The TEB design was developed from a series of experiments in a small transonic blowdown wind tunnel at Virginia Tech. Steady velocity field measurements were taken downstream of the WG to assess the influence of discrete TEB hole size, shape, and pitchwise spacing on the wake-filling effectiveness. The tests were conducted at an inlet Mach number of 0.55. These experiments confirmed the feasibility of TEB at high-subsonic speeds and close axial distances and led to the selection of a final TEB hole configuration for the subsequent compressor rig experiments.

In order to minimize unsteady rotor blade loading, it is desirable to promote as much circumferential flow field uniformity as possible. As such it was deemed unnecessary, even undesirable, to place TEB holes within the end wall boundary layers, which are present for the entire circumference and lead to reduced wake depth near the end walls (refer to Fig. 2). The selected TEB design, illustrated in Fig. 3, consisted of seven blowing holes per WG, with both trailing-edge (TE) thickness-to-diameter and hole pitch-to-diameter ratios of 2.5, which provided effective coverage for most of the span between the end wall boundary layers.

While complete wake-filling would maximize circumferential flow field uniformity, the compressor bleed air requirement to achieve this may be prohibitively costly to overall engine performance. It was desired to characterize the sensitivity of the forced response to the flowrate of TEB air and its spanwise distribution. Thus the TEB plumbing was designed to permit independent adjustment of flow to different spanwise sectors of holes. As shown in Fig. 3, four independent lines supplied the seven holes. One line was used to supply a single tip hole, while the remaining six holes were fed through three additional supply lines. Thus a single line was used for each remaining pair of TEB holes, with the maximum mass flowrate variation between the paired holes estimated to be 5%.

The single-stage compressor rig did not have sufficient pressure

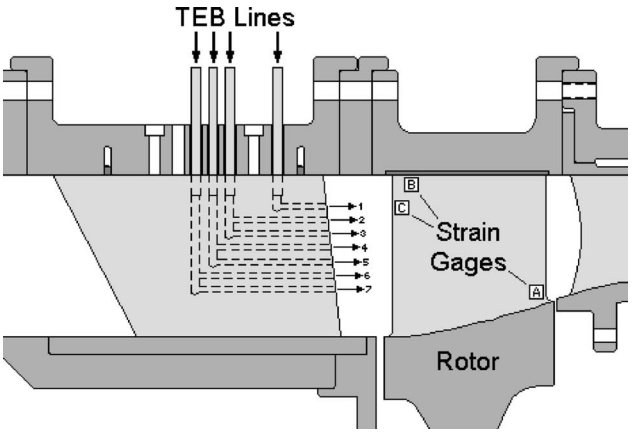

Fig. 3 Detail of SMI rig showing trailing edge blowing configuration and strain gage locations

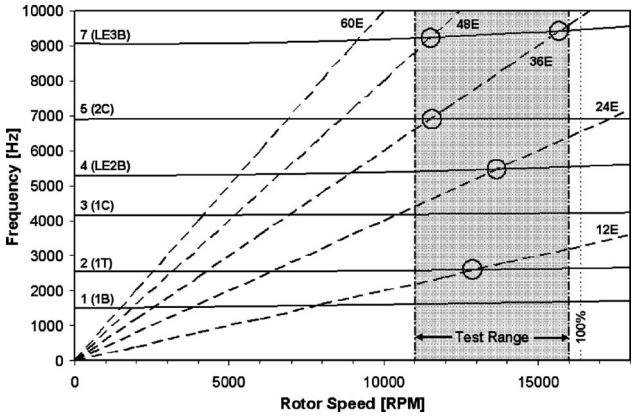

Fig. 5 SMI fan Campbell diagram showing 12-WG harmonic excitations (dashed) and resonance crossings (circled) within the test range

ratio to feed the flow control system by bleed recirculation, so high-pressure air was supplied for TEB from external storage tanks. The flow was throttled to a typical settling tank pressure of 100 psig (690 kPa) and then independently regulated to four rig-mounted plenums, as shown in Fig. 4. Each plenum, with a typical pressure of 60 psig (414 kPa), distributed flow evenly to the same radial sector of TEB holes of all 12 WGs. Because the plumbing was designed for installation ease and experimental flexibility rather than for minimizing pressure losses, it should be noted that this high TEB supply pressure is not representative of requirements for engine implementation. A pressure ratio of 2–3, typically achieved within two modern stages, should be adequate for implementing an efficient TEB design.

2.4 Measurements and Data Analysis. As documented by Cheatham and Tyner [10], critical blade modes and their natural frequencies were identified by NASTRAN finite element analysis (FEA), impact testing, and holography. Stress pattern analysis using thermal emissions (SPATE) was also employed to identify areas of maximum vibratory stress for modes of interest. Three gage locations, which offered sufficient sensitivity to the expected critical modes, were selected for vibration monitoring during subsequent rig tests. A recent finite element analysis of a higher fidelity model by Blackwell [13] included rotational effects.

Strain gages were surface mounted on the pressure side of nine rotor blades at each of the three locations, which are depicted in Fig. 3. The strain gage bridge circuitry was zero balanced and calibrated for 10 ksi (69 MPa) per signal volt. As required to maintain effective resolution of the dynamic signals while avoiding voltage saturation due to high steady loading, the gages were rebalanced at 80% rotor speed. The strain signals were extracted from the rotor via a slip ring. These and other dynamic signals, such as a once-per-revolution key-phaser, were simultaneously recorded with a high-speed 28-channel analog tape recorder.

Several resonance crossings were identified from the Campbell diagram, shown in Fig. 5, as being potential HCF drivers for the 12-WG configuration. The fundamental 12E crossing of the first torsional mode (1T/12E) near 12,800 rpm was known to be particularly severe. Harmonic crossings were also of interest, including those of the second leading-edge (LE) bending mode (LE2B/24E) near 13,600 rpm and the second chordwise bending mode (2C/36E) near 11,600 rpm. These crossings, as well as a pair of Mode 7 crossings, are indicated by circles in the figure. To encompass these and higher order modal crossings, a test range from 11,000 rpm to 16,000 rpm (67–97% of design speed) was selected. As predicted by FEA, the 1T and LE2B mode shapes are illustrated in Fig. 6.

Rotor speed sweeps were conducted for a range of full- and part-span TEB flowrates. The present discussion includes only the full-span TEB results, which correspond to uniform flow to all seven holes on each WG, with overall flowrates ranging from 0.3% to 1.0% of the rig design flow capacity. For each test case, data was recorded for a 45-second period, during which the rotor speed was gradually increased through the test range. This corresponds to a nominal sweep rate of 110 rpm/second, which was found to be sufficiently slow to eliminate transient effects, such that maximum vibration amplitude was reached at resonance crossings.

Rotor forced response data were then digitized and postprocessed with engine order tracking tools developed for this investigation. Using the key-phaser to establish the position of the rotor, the original time-sampled data were resampled at fixed rotor angle steps. As such, the resampled data always include the same

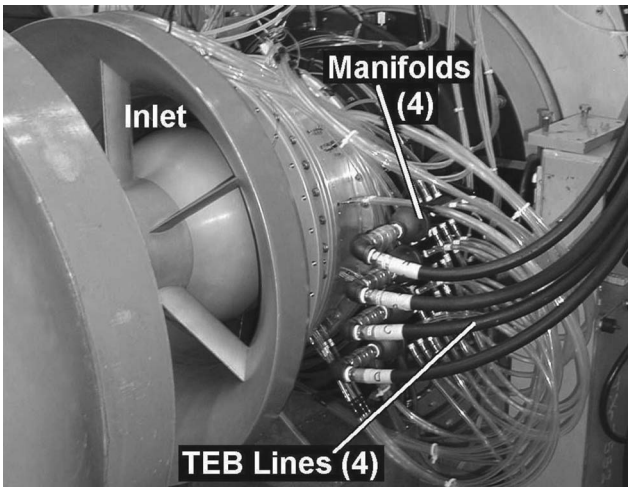

Fig. 4 SMI rig assembly with TEB plumbing installed

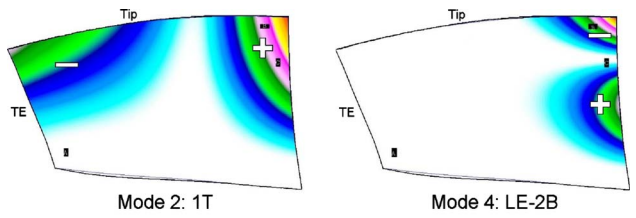

Fig. 6 Selected SMI fan blade displacement mode shapes with signs indicating relative phase

number of points per revolution, regardless of rotor speed. Upon subsequent fast Fourier transform (FFT) analysis, spectral lines correspond to fixed engine orders, or multiples of the shaft rotational frequency. Thus the effective sampling frequency, and hence the frequency associated with each spectral line, is scaled linearly with the rotational frequency. This order analysis approach has the advantage of providing precise amplitude and phase tracking of the response to known engine order excitations (i.e., the WG wakes), as well as their higher harmonics. A detailed discussion of the computed order tracking technique is provided by Fyfe and Munck [14].

The test rotor is randomly mistuned due to geometric variations in blade machining. Standard deviation in individual blade natural frequencies ranged up to 2% of the mean for the various modes evaluated. As a result typical of low-aspect-ratio bladed disks, there are substantial variations in the individual blade resonant responses. Even with directly comparable data only being available for 4 of the 28 blades, the peak 1T/12E response varied from blade to blade by a factor of about 3. The variations are consistent with numerous analytical studies, including that of a transonic compressor by Kahl [15]. To simplify the discussion, attention is primarily focused on the highest responding blade, hereafter dubbed the *critical* blade, at each respective modal resonance crossing.

2.5 Uncertainty. Basic measurement accuracy was very high, and errors added from the computed order tracking technique were found to be minimal. Absolute stress measurement errors, including those due to gage position errors, were not quantified since data interpretation was based on comparison to the measured baseline response at each gage location. Quantization error, based on one-half of the least significant bit (LSB), was rather small at 0.02 ksi peak-to-peak (p-p).

Repeatability errors proved to be more significant than instrumentation errors. Thus repeatability in resonance crossing amplitude was used to quantify overall uncertainty in the blade stress measurements. Considering multiple rotor speed sweeps, resonance crossing amplitude was found to be repeatable within ±3% for back-to-back data. However, comparisons are made between data involving independent adjustments of the exit throttle, used to set the stage loading to the same nominal operating line. Baseline blade response appeared to be sensitive to small errors in throttle positioning, which implies that small changes in the time-averaged flow field can have a significant effect on response amplitude. It is noted that application of TEB presumably also changes the time-averaged flow field. However, the data currently available do not permit the effects of flow field changes (whether from throttle position or TEB) to be treated independently from the forced response data. Consequently, overall uncertainty for the normalized stress results presented herein is estimated to be ±8%.

The overall uncertainty in the reported total TEB flowrate, including measurement uncertainty and actual variations in flowrate over the course of a given rotor speed sweep, is within ±2%. Though not confirmed by direct measurements, it is believed that the manifolds and consistent tubing length were effective in providing each WG with the same amount of TEB flow (i.e., 1/12 of the total flow).

3 Results

The effectiveness of the order tracking technique for analysis of synchronous vibrations is demonstrated in Fig. 7. The various lines in the figure represent selected order components, corresponding to known aerodynamic forcing functions, from a single strain gage signal during a single speed run-up at baseline (no TEB) conditions. As is the case for all forced response data presented here, stage loading was set by an exit flow throttle to represent a design operating line.

The data in the figure are taken from a noncritical blade and the "B" location gage (refer to Fig. 3), which is shown here because it was responsive to more modes than other gage locations. Accordingly, multiple resonance crossings are clearly characterized in the figure. In conjunction with the predicted Campbell diagram, modes could be readily identified, as labeled in the figure. It is noted that some modes exhibit sharp single resonance peaks, while other modes show broader multipeaked resonances. This behavior, with widely varying shape and amplitude characteristics for each blade evaluated, implies mode localization to certain blades as a consequence of mistuning.

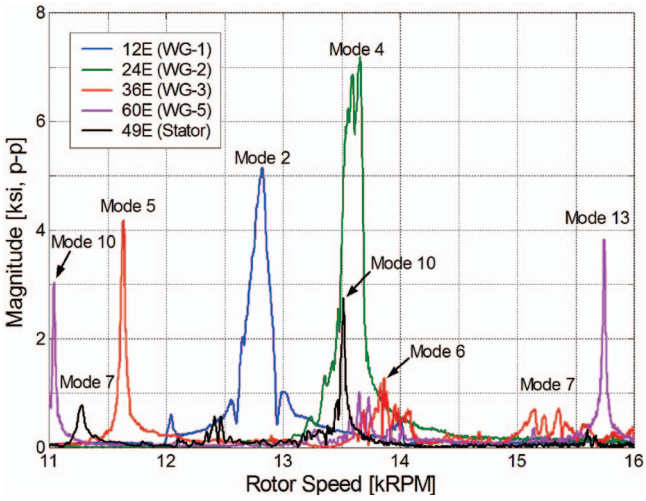

Fig. 7 Baseline order tracks showing multiple modal resonances due to upstream WG and downstream stator excitations

Though not apparent from Fig. 7 because the "B" gages are less responsive to torsional vibrations than to other modes, the 1T/12E crossing ("Mode 2" in the figure) was the highest amplitude resonance within the test range. For comparison, the critical blade response of the 1T/12E crossing reached 39.7 ksi (274 MPa) p-p at the "A" gage location (refer to Figs. 8 and 9).

Based on stress ratios obtained from the finite element analysis of Blackwell [13], this corresponds to a maximum 1T/12E alternating stress amplitude on the critical blade of 191.5 ksi (1322 MPa) p-p. Even without considering the addition of mean stresses or any strength-reducing factors, this large response amplitude exceeds the titanium alloy's endurance limit by 10%, thereby indicating the strong possibility of an HCF failure being prompted by baseline 1T/12E damage accumulation.

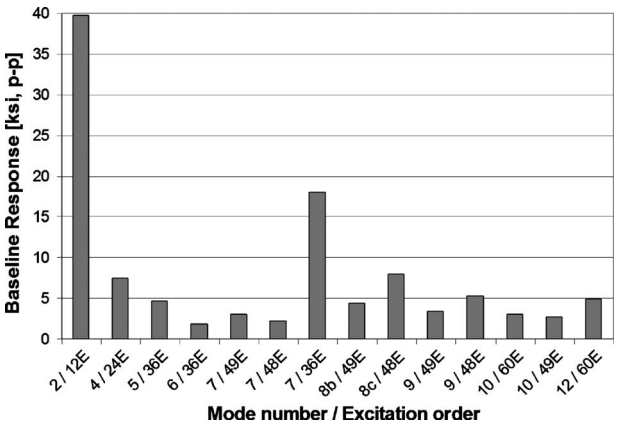

Fig. 8 Baseline critical gage response for various modal resonance crossings

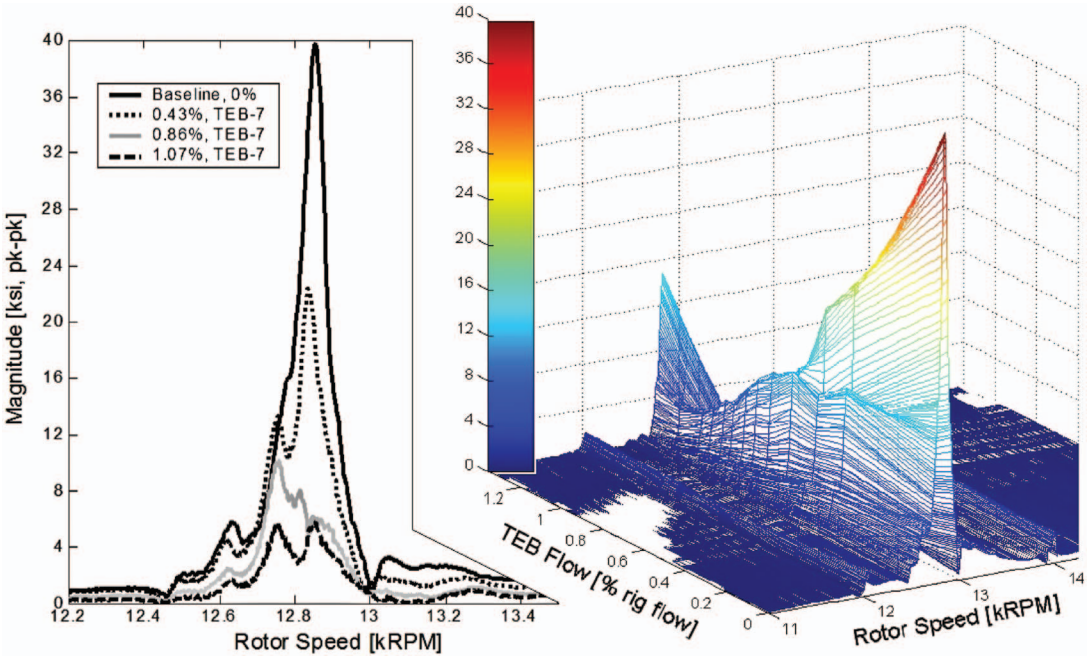

Fig. 9 Effect of TEB on critical blade response at the 1T/12E resonance crossing

Figure 8 summarizes the critical blade responses for various modal resonance crossings within the test range. Amplitudes shown correspond to the highest responding gage location, which generally does *not* represent the maximum stress location. Responses denoted "49E" correspond to fundamental excitation by the potential field of the downstream stator row, while all other crossings correspond to harmonic excitations from the upstream WGs. Not surprisingly, it is noted that the 49E potential excitation was generally weaker in effect than the viscous excitation originating upstream of the rotor. The response to the fundamental stator excitation was typically of the same order as that produced by the fourth (48E) or fifth (60E) WG harmonics, which contain less energy than the WG fundamental (12E).

Many of the amplitudes presented in the figure are small and hence generate little concern for fatigue damage. However, it should be stressed that the designer does not generally know before build (or even extensive field service) which modes will be most responsive or which ones may ultimately lead to a fatigue failure. For example, it was rather surprising that the third WG harmonic (36E) crossing of Mode 7 (third LE bending or LE3B) generated a substantial response on the critical blade. This finding suggests the importance of considering mistuning effects and multiple harmonics of vortical forcing functions in the aeromechanical design of turbomachinery. Also, many of the lower amplitude modes in the present investigation are likely to be more responsive under fundamental excitation (as opposed to the higher WG harmonics of this study), such as may be present in a similar compressor with more upstream vanes.

By stacking 12E order tracks for successive TEB flowrates against the baseline data, as shown in Fig. 9, the strong effect of flow control on resonant response of the critical blade is demonstrated. The surface plot on the right provides an overview of the entire test domain, with the baseline 1T/12E resonance dominating in the foreground. The line plot on the left compares selected slices of the same data to provide a more detailed view of the local effects at resonance.

Application of increasing TEB flowrate is shown to progressively attenuate the first torsion response. Using a total of 1.07% of the rig inlet flow at the crossing speed, the critical 1T gage response was limited to 5.8 ksi (40MPa) p-p, a reduction of 85%.

Resonant amplitude data from four blades were normalized and averaged for the 1T/12E and LE2B/24E crossings, as presented in Figs. 10 and 11, respectively. Amplitudes are normalized by the baseline crossing amplitude for each respective gage used in the average, while TEB flowrates are normalized by the corrected rig inlet flow for the speed at which the respective crossing occurs. In addition to the four-blade-average data, critical blade data are indicated. Bars are included to illustrate the range of responses for the measured blades. It is noted that the maximum attenuation occurs on the critical blade for both crossings.

As clearly illustrated in Figs. 9–11, the resonant response amplitude exhibits a saddle-type trend over the range of TEB flowrates. For increasing TEB flow, resonant response is attenuated until a minimum crossing response is achieved, at what is considered the optimal flowrate for that particular resonance crossing. If flow is further increased beyond this saddle point, referred to as "mechanical overblowing," the mechanical (that is, vibratory) response of the crossing begins to increase. In the event of substantial overblowing, the response can exceed that of the baseline case.

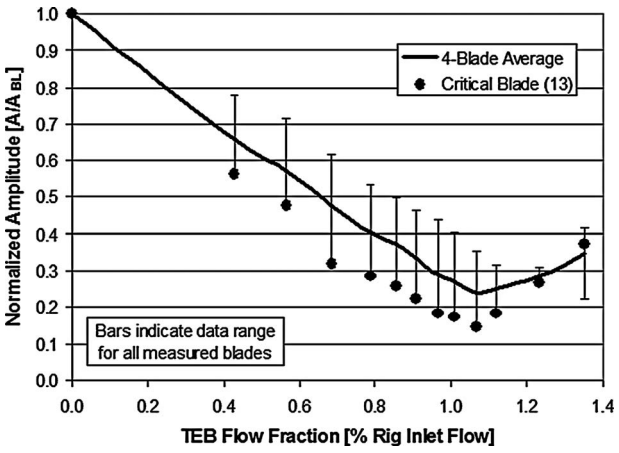

Fig. 10 Effect of total TEB flowrate on 1T/12E resonant response

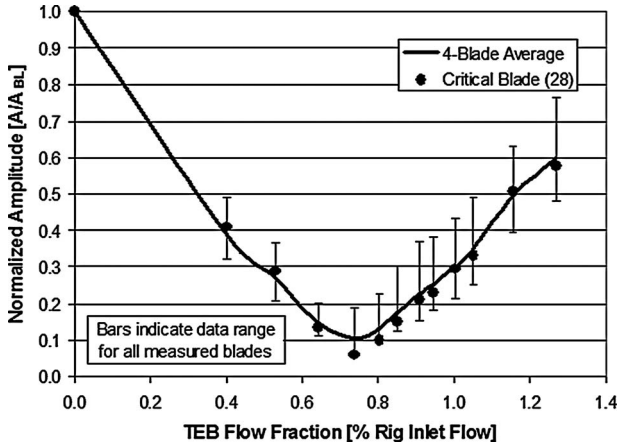

Fig. 11 Effect of total TEB flowrate on LE2B/24E resonant response

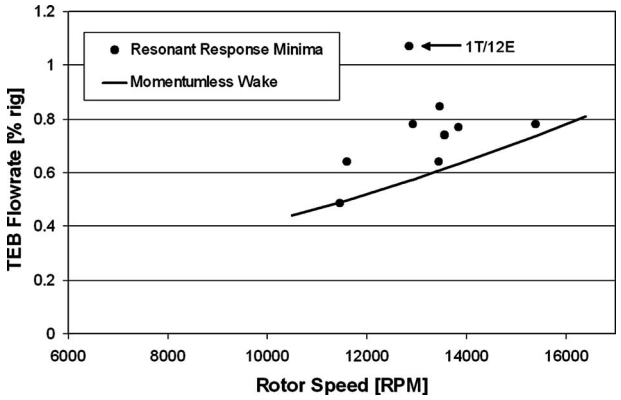

Fig. 13 Comparison of optimal TEB flowrates based on resonance crossing data and aerodynamic estimates

This inflection behavior, which was generally noted for all the measured crossings, is expected. The saddle point occurs when the offending forcing function harmonic passes through minimum amplitude. It was expected that the inflection point should approximately coincide with the wake velocity deficit being minimized. For increasing TEB flowrate, the original wake velocity deficit would eventually be replaced with a surplus. This point will be discussed later in more detail.

It is noted that substantial attenuation in resonant amplitude, roughly proportional to the TEB flowrate, is achieved at less-than-optimal flowrates. This point should not be lost on the designer seeking an appropriate compromise between forced response mitigation and engine performance.

Figure 12 shows the effect of full-span TEB on response amplitude for multiple WG-induced resonance crossings documented in the test range. By stacking so many data series together, the robustness of the full-span TEB approach is demonstrated. *All* of the mode crossings are seen to be attenuated for some range of TEB. Specifically, for a flowrate ranging from 0.5% to 0.9% of the rig flow (normalized with respect to each crossing), the response at all crossings is reduced by at least 32%. Moreover, for the most responsive crossings, indicated by the heavy solid lines and symbols, the response reduction was at least 50% over the same flowrate range. While greater reductions in the high 1T/12E response are achieved at higher flowrates, the response at other crossings (e.g., Mode 5/36E) begins to be amplified due to substantial overblowing.

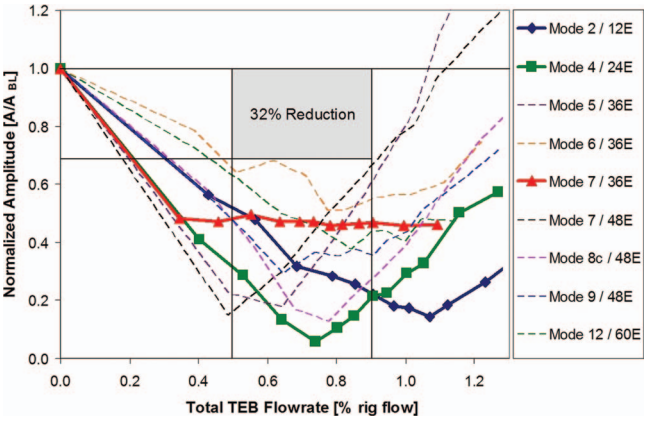

Fig. 12 Effect of TEB flowrate on multiple modal resonances showing region of substantial attenuation

In addition to the modal and flowrate robustness illustrated in the figure, it is also clear that the optimal TEB flowrate varies for the different modal crossings. Since the crossings occur at different speeds, it was a point of interest to see if the optimal TEB flowrates could be better correlated as a function of rotor speed. Such a correlation would be rather convenient, as it would make implementation of a basic TEB control system relatively easy. Thus, for the available family of resonance crossing minima, the corresponding full-span TEB flowrates are plotted in Fig. 13 against the associated crossing speeds.

Also included in the figure is an approximate characteristic of the TEB requirement to achieve "momentumless wakes." The momentumless wake condition exists when some momentum addition (in this case, by TEB) to the wake region is adjusted to balance the momentum deficit corresponding to the wake drag [16]. Two-dimensional velocity profiles in the near field of a momentumless wake will generally have multiple inflection points [17], usually with a "W" shape and with the centerline velocity exceeding that of the free-stream.

Several assumptions are involved in the estimation of the present momentumless characteristic. First, the thrust of the TEB jets are equated to the WG vane drag force for the span affected by TEB. Though mixing losses will generally require jet thrust to exceed drag for far field wakes to be momentumless, the small axial gap between WGs and rotor did not allow for substantial mixing. The drag coefficient of the WG is estimated from the wake momentum deficit, which is found by integration of the baseline wake velocity profile. The midspan profile was measured in a blowdown wind tunnel at design flow conditions and approximately the same relative axial location as the fan face. The drag coefficient is assumed to be constant, which is a reasonable approximation since the flow remains turbulent for the range of interest.

The jets and core flow are assumed to be isothermal and ideal gases. The jets are further taken to be choked, which was the case throughout the present investigation. Under these assumptions the following relationship for momentumless wakes can be derived:

$$\text{TEB flowrate } (\%\ \text{rig}) = B \cdot C_D \cdot M_1 \cdot 100\% \tag{1}$$

where C_D is the effective WG drag coefficient and M_1 is the WG inlet Mach number, which has a slightly nonlinear characteristic as measured along the rig operating line. B is a constant given by

$$B = \frac{\#\ \text{TEB holes} \times \text{hole pitch} \times \text{WG chord}}{2 \cdot \text{rig inlet area}} \tag{2}$$

It is noted in Fig. 13 that there is substantial scatter in the family of crossing minima. However, most of the points (except 1T/12E) seem to be clustered along a characteristic slope, indeed a slope similar to that of the momentumless wake characteristic.

The momentumless characteristic also seems to effectively bound the response minima, suggesting the validity of the momentum balance approach.

If TEB, properly adjusted for each given rig operating condition, were capable of eliminating the wake over the entire span, a more defined minimum response trend with respect to rotor speed might be expected. That is, there would likely be less scatter in the data, and the mechanically optimal trend should be roughly coincident with some aerodynamically optimal TEB characteristic. However, the forced response minima are generally seen to require *more* flow than was estimated to be near optimal in the local aerodynamic sense.

Exact agreement with the aerodynamic predictions is not expected for several reasons. First, the most appropriate metric(s) for an aerodynamic optimum are not well-defined and will likely be difficult to predict or measure with current tools. The simple integrated momentum balance presently used appears to provide a good first approximation, but blade response is expected to be sensitive to other factors excluded from the momentum analysis, such as the unsteady velocity field and its harmonic content as experienced by the rotor. The steady baseline wake measurements, from which the momentum deficit was estimated, also do not include the rotor-shock passing effects present in the rig tests, effects which have been noted to substantially influence the unsteady wake structure [9,18]. These and other factors contribute to the unsteady blade loading characteristics that ultimately drive the mechanical response.

The momentum analysis also does not take into account the fact that the rotor blades respond to unsteady loading input over their entire surface, not just in the region affected by the TEB flow. Despite the "full-span" label, the TEB jets only cover about 60% of the span. There is also likely to be some reduction in wake-filling effectiveness between holes. Even if TEB effectively eliminated the wake over this 60% of the span, substantial wake-induced forcing would be present for the remaining 40% (though the unsteady loading is somewhat reduced by end wall effects for 10–15% of the span). For this reason, a TEB flowrate resulting in the minimum unsteady blade loading for the TEB-affected portion of the span *may not* correspond to the overall minimum blade response.

Thus, as a consequence of the incomplete spanwise TEB coverage, it is reasonable to expect that higher TEB flowrates may be required to minimize forced response. This point can be interpreted as a need to provide a local momentum surplus in the TEB sector (designated "aerodynamic overblowing") to compensate for the momentum deficit that remains in the spanwise wake sector(s) without TEB. While a local momentum surplus will yield a local unsteady gust blade load, this load will be in an opposing direction to that generated by a momentum deficit elsewhere on the blade span.

The degree of aerodynamic overblowing that may be necessary to minimize blade response will depend on the TEB spanwise location and extent, as well as the particular blade mode in question. Different blade modes have differing sensitivities to the spanwise loading distribution. For instance, the 1T mode is rather sensitive to loading along the entire span, while the first chordwise mode will tend to be much more sensitive at the tip than the hub. This implies that the 1T mode may require more aerodynamic overblowing than other modes to compensate for its sensitivity to the wake momentum deficit near the hub, where TEB was not applied. These hypotheses regarding aerodynamic overblowing seem to be supported by the scatter of the forced response minima in Fig. 13 and the requirement of substantially more TEB flow to minimize the 1T/12E response than at other crossings.

It is also noteworthy that modes with one or more spanwise nodes (e.g., LE3B, 2T, etc.) are sensitive to the phase pattern of the spanwise loading distribution. For example, the LE2B has a nodal line along the leading edge near 75% span, with the blade motion on either side having opposite phase (refer to Fig. 6). In the case of such modes, care should be taken in applying TEB to avoid undesirable spanwise phase matching between the wake forcing function and the mode shape, such as by tip-only blowing, which could result in response amplification.

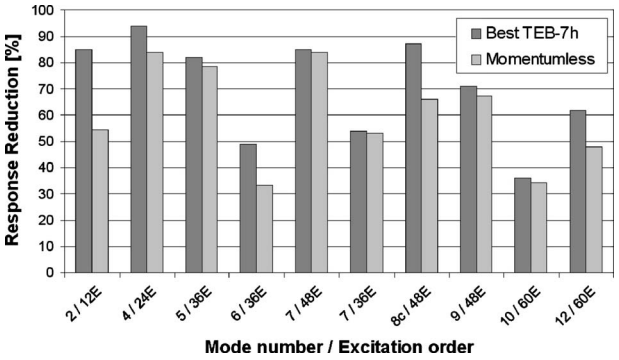

Fig. 14 Comparison of modal resonant response reductions by TEB

Figure 14 summarizes the maximum reductions in critical blade response achieved by TEB for various modal crossings. In most cases the 60% attenuation goal established for the National HCF Program [1] was exceeded. It is noted that 100% reductions by TEB are not considered feasible, since, even if complete wake-filling were achieved, a potential forcing function would still be generated by the upstream vanes.

The figure further demonstrates the robustness of full-span TEB by presenting the reductions achieved with a TEB schedule following the momentumless wake characteristic established in Fig. 13. Even though more TEB flow than this aerodynamic estimate was usually required to minimize the respective resonant amplitudes, it is evident from Fig. 14 that substantial reductions are still achieved for all of the modes (at least 64% of the maximum reduction). This finding indicates that, while greater reductions in forced response may be realizable, the simple momentum balance approach may be sufficient for scheduling TEB in similar applications.

Significant TEB sensitivity is only expected for resonance crossings involving excitation orders associated with the wake forcing function directly modified by TEB. Correspondingly, resonant responses caused by downstream stator vane excitation were not expected to be affected by the application of TEB.

However, it was noted with some surprise that the LE3B/49E crossing amplitude was attenuated by as much 32% with TEB. Conversely, some 49E crossings were amplified by up to 15%. The baseline amplitudes for the 49E crossings were relatively small, so this unexpected finding does not appear to be consequential in terms of HCF for the present study. However, it is suggestive that either the stage operating point or, less likely, the downstream stator potential field has been altered by the TEB application.

Despite close blade row spacing and the presence of strong rotor bow shocks, substantial stress reductions were achieved at multiple resonance crossings in the present study. These results also compare favorably to those previously documented. Morris et al. [6] reported stress reductions on a high-subsonic rotor of 90% for chordwise bending (1C) and 43% for the third leading-edge bending mode (LE3B). While the total TEB-to-rig mass flow ratio for the Morris experiments was greater than the optimal flowrates determined in the present study, the flow ratio was similar on a per-vane basis.

4 Conclusions

The TEB flow control technique was implemented in a row of WG vanes, placed just upstream of a modern highly loaded transonic fan stage. The WGs produced fundamental and harmonic

engine order excitations that caused numerous resonance crossings in the tested range of the compressor. Rotor stress measurements confirmed that the TEB technique can be quite effective for reducing resonant rotor response, even with close blade row spacing and strong rotor bow shocks sweeping the WG trailing edge.

Full-span TEB was found to be *modally robust*, as resonant amplitudes of all documented modal crossings were attenuated substantially. In most cases the National HCF Program's goal of 60% reduction in fan resonant response was exceeded. Reductions of as much as 85% and 94% were achieved by TEB for the first torsion and second LE bending modes, respectively. Moreover, all modal responses were reduced at least 32% for the robust TEB flow range of 0.5–0.9% of the rig flow. Reductions were approximately linear for suboptimal flowrates.

While the optimal TEB flowrates for the various modal resonance crossings only correlated loosely with rotor speed, the data followed a similar slope and were bounded by a TEB schedule based on a jet-wake momentum balance. Though more TEB flow was generally required to minimize forced response, large reductions were still achieved using this simple aerodynamic approximation. Ultimately, the substantial response reductions by TEB should allow significant gains in blade life.

Acknowledgment

The authors gratefully acknowledge the support of Mr. Oral Mehmed and NASA Glenn Research Center (GRC). The authors are especially indebted to the entire staff of the Compressor Aero Research Laboratory for their many useful suggestions as well as patient assistance provided during experiments. The support afforded the primary author by an NSF Graduate Research Fellowship is also duly acknowledged.

References

[1] Air Force Research Laboratory, 2001, "High Cycle Fatigue (HCF) Science and Technology Program 2000 Annual Report," WPAFB Technical Report No. AFRL-PR-WP-TR-2001-2010.
[2] Rao, J. S., 1991, *Turbomachine Blade Vibration*, Wiley, New York.
[3] Manwaring, S. R., and Wisler, D. C., 1993, "Unsteady Aerodynamic and Gust Response in Compressors and Turbines," ASME J. Turbomach., **115**, pp. 724–740.
[4] von Flotow, A., Tappert, P., and Mercadal, M., 2001, "HCF Active Control: An Active Wake Management Implementation Manual," *Proceedings of the 6th National Turbine Engine High Cycle Fatigue (HCF) Conference*.
[5] Waitz, I. A., Brookfield, J. M., Sell, J., and Hayden, B. J., 1996, "Preliminary Assessment of Wake Management Strategies for Reduction of Turbomachinery Fan Noise," J. Propul. Power, **12**(5), pp. 958–966.
[6] Morris, R. J., Benedict, B. K., and Cowles, B. A., 1998, "Active Structural Control for Gas Turbine Engines," ASME Paper No. 98-GT-514.
[7] Benedict, B. K., 2001, personal communication.
[8] Bailie, S. T., Ng, W. F., Wicks, A. L., and Copenhaver, W. W., 2002, "Effects of Flow Control on Forced Response and Performance of a Transonic Compressor," ASME Paper No. GT-2002-30008.
[9] Kozak, J. D., 2000, "Steady and Unsteady Aerodynamic Investigation of Inlet Guide Vane Trailing-Edge Blowing Flow Control in a F109 Turbofan Engine," Ph.D. thesis, Virginia Polytechnic Institute & State University, Blacksburg, VA.
[10] Cheatham, J. G., and Tyner, T. M., 1992, "Stage Matching Investigation," Wright Laboratory, WPAFB Technical Report No. WL-TR-91-2098.
[11] Gorrell, S. E., Copenhaver, W. W., and Chriss, R. M., 2001, "Upstream Wake Influences on the Measured Performance of a Transonic Compressor Stage," J. Propul. Power, **17**(1), pp. 43–48.
[12] Gorrell, S. E., 2001, "An Experimental and Numerical Investigation of Stator-Rotor Interactions in a Transonic Compressor," Ph.D. thesis, Iowa State University, Ames, IA.
[13] Blackwell, C. M., 2002, personal communication.
[14] Fyfe, K. R., and Munck, E. D. S., 1997, "Analysis of Computed Order Tracking," Mech. Syst. Signal Process., **11**(2), pp. 187–205.
[15] Kahl, G., 2003, "Mistuning and Coupling Effects in Turbomachinery Bladings," *Proceedings of the 10th International Symposium on Unsteady Aerodynamics, Aeroacoustics, and Aeroelasticity of Turbomachinery (ISUAAAT)*, Duke University, Durham, NC, Sept. 8–11.
[16] Park, W. J., and Cimbala, J., 1991, "The Effects of Jet Injection Geometry on Two-Dimensional Momentumless Wakes," J. Fluid Mech., **224**, pp. 29–47.
[17] Schetz, J. A., 1980, "Injection and Mixing in Turbulent Flow," *Progress in Aeronautics and Astronautics*, Vol. 68, American Institute of Aeronautics and Astronautics, New York.
[18] Gorrell, S. E., 2002, personal communication.

A Review of Surface Roughness Effects in Gas Turbines

J. P. Bons
Department of Aerospace Engineering,
Ohio State University,
2300 West Case Road,
Columbus, OH 43017

The effects of surface roughness on gas turbine performance are reviewed based on publications in the open literature over the past 60 years. Empirical roughness correlations routinely employed for drag and heat transfer estimates are summarized and found wanting. No single correlation appears to capture all of the relevant physics for both engineered and service-related (e.g., wear or environmentally induced) roughness. Roughness influences engine performance by causing earlier boundary layer transition, increased boundary layer momentum loss (i.e., thickness), and/or flow separation. Roughness effects in the compressor and turbine are dependent on Reynolds number, roughness size, and to a lesser extent Mach number. At low Re, roughness can eliminate laminar separation bubbles (thus reducing loss) while at high Re (when the boundary layer is already turbulent), roughness can thicken the boundary layer to the point of separation (thus increasing loss). In the turbine, roughness has the added effect of augmenting convective heat transfer. While this is desirable in an internal turbine coolant channel, it is clearly undesirable on the external turbine surface. Recent advances in roughness modeling for computational fluid dynamics are also reviewed. The conclusion remains that considerable research is yet necessary to fully understand the role of roughness in gas turbines. [DOI: 10.1115/1.3066315]

1 Introduction

The degradation of gas turbines with service is a serious problem that must be appropriately addressed for efficient and safe operation of both land-based (power) and aeropropulsion gas turbines. Due to the importance of this topic, there have been a number of excellent review articles addressing its root causes and exploring preventive measures [1,2]. Technical advancements in the design and manufacture of gas path turbomachinery components over the past two decades have only heightened the significance of understanding the effects of flowpath degradation on gas turbine operation. For example, surface coatings in both the compressor and turbine, more aggressive airfoil shapes, advanced rotor tip and passage endwall designs, and an increased number of bleeds to feed more intricate film cooling hole geometries are among the technologies that have created an increased urgency for fundamental research into the root causes and effects of degradation. As evidence of this increased emphasis, Fig. 1 shows the number of degradation-related journal articles that have been published each year in three of the leading publications for gas turbine research. The rising trend evidenced in the figure is likely to continue for the foreseeable future as gas turbines continue to command an impressive market share in both the power generation and transportation industries.

Degradation in gas turbines is caused by a wide variety of operational and environmental factors. Perhaps the most common sources are ingested aerosols, namely, salt spray from marine applications [3–6], airborne dust, sand [7,8], pollen, combustion products [5,9], and even volcanic ash [10]. Occasionally, larger objects can be ingested (e.g., inlet nacelle ice accumulation [11] or birdstrikes) at times resulting in significant component damage (FOD). From within the gas turbine itself, oil leaks, rust or scale, and even dirty fuels (for power turbines) [12,13] can result in fouled gas path surfaces and clogged bleed systems. These various degradation sources influence gas turbine performance in different ways depending on the interaction with the wetted surfaces in the engine. Foreign particulate that deposits on the surface can result in modified airfoil shapes (e.g., at the leading edge [6,7]), increased surface roughness [14–17], and clogged film cooling holes [10,16,18] and fuel nozzles. Figure 2 shows an example of deposition on a nozzle guide vane due to inadequately cleaned fuel used in a land-based turbine. In extreme cases such as this, deposition can significantly reduce the flowpath area and alter the operating point of the engine. Surface erosion, typically caused by larger particles (e.g., desert sand), can be equally damaging. Erosion at the airfoil leading edge reduces the effective chord of the blade or vane, limiting the aerodynamic turning and changing the incidence angle. Rotor blades often show the effects of erosion at their tip, thus increasing the tip gap flow and associated secondary losses [7,19,20]. An example of compressor rotor tip wear due to sand ingestion is shown in Fig. 3. Perhaps most importantly, erosion can result in the removal of critical thermal barrier coatings in the turbine (i.e., coating spallation), thus exposing the underlying metal to excessive gas temperatures. Finally, many of the sources that cause degradation contain corrosive elements that promote rapid deterioration of metal components in the gas path, potentially leading to catastrophic failure.

Unless frequent boroscopic evaluations are made to detect and assess surface damage, gas turbine operators will likely see a gradual drop in performance (thrust or power output) as the first sign of degradation. Upon closer inspection, an increase in specific fuel consumption (SFC) will be evident as component efficiencies (for the compressor and/or turbine) decline. As degradation worsens, excessive temperatures may occur in the turbine due to coating loss or flow restriction. In the most severe case of excessive deposition buildup, loss of compressor stall margin may make safe operation of the gas turbine altogether impossible [1,2,4,20–22]. Fortunately, there are a number of preventive measures that, if implemented properly, can mitigate unacceptable losses in performance and/or availability [1]. For example, deposit buildup on compressor blading has traditionally been removed using abrasive chaff (e.g., nutshells). With the advent of coated compressor blades in the past decade, compressor maintenance has moved to on-line water washing, possibly with detergents [3,13,21,23,24]. More stubborn deposits can be removed with off-line (crank) washing of both compressor and turbine blading. Dirty fuels (e.g., biomass or high ash-bearing heavy fuel oils [12]) can be safely used with adequate cold and/or hot gas cleanup,

Contributed by the Turbomachinery Division of ASME for publication in the JOURNAL OF TURBOMACHINERY. Manuscript received December 13, 2007; final manuscript received September 10, 2008; published online January 11, 2010. Review conducted by Gregory J. Walker.

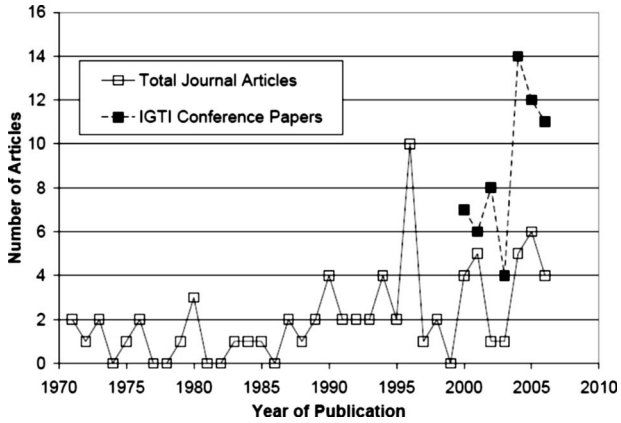

Fig. 1 Gas turbine roughness-related journal articles published in ASME Journal of Turbomachinery, ASME Journal of Engineering for Gas Turbines and Power, and AIAA Journal of Propulsion and Power, AIAA Journal of Aircraft, and AIAA Journal (numbers are not comprehensive prior to 1990). Also, roughness-related IGTI conference papers from 2000–2006.

although these auxiliary systems can be expensive and require regular maintenance as well. Ultimately, the most severe cases of degradation (erosion and corrosion, in particular) may necessitate a major engine overhaul with significant downtime. Only then can individual blades or vane sectors be removed for refurbishment and resurfacing to recover lost performance margin.

Since many of these preventive measures are costly and negatively impact availability, operators must be equipped with accurate cost and benefit estimates to maintain efficient gas turbine operation. A number of recent studies have proposed system-level models aimed at determining optimum maintenance intervals and procedures to maximize gas turbine availability and performance [13,21,24–27]. These models account for system degradation through performance decrements associated with component efficiency loss and/or changes in massflow (increase for erosion and decrease for deposition). Specific numerical values for these decrements are obtained from reported degradation losses available in the open literature [1,2]. For example, Zwebek and Pilidis accounted for turbine fouling (deposition) in their system-level analysis by assuming a 1% reduction in nondimensional mass flow and a 0.5% reduction in turbine efficiency [25,26]. With this component-level input, their model predicts a drop in gas turbine power output and efficiencies of 1.2% and 1%, respectively. Models have also been developed to predict specific component-level performance losses with degradation. For instance, Millsaps et al. [28] evaluated the effect of fouled airfoil surfaces due to deposits on a three-stage axial compressor. They assumed a doubling of

Fig. 2 Deposition on first stage vane of utility gas turbine after approximately 8000 h of service. Firing temperature 1150°C.

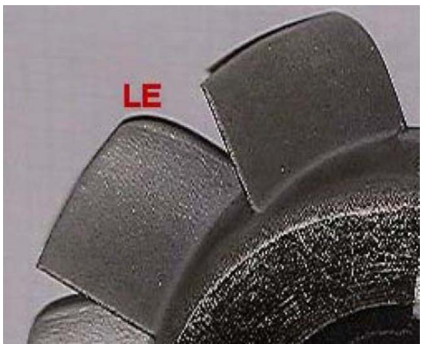

Fig. 3 Eroded test rotor blades due to sand ingestion near design point during 9 h (Fig. 9 from Ghenaiet et al. [20])

blade profile losses and predicted a 1.5% drop in π_c and η_c with a 1% drop in massflow. Component-level model predictions such as this can then be used as building blocks in a larger system-level model [25].

While such models are useful to indicate trends, their ability to accurately predict changes in overall gas turbine system performance for a given installation is dependent on the accuracy of the numeric decrements employed. Determining these quantitative adjustments is complicated by the diversity of degradation sources and turbomachinery designs. There have been some attempts to test the accuracy of these system-level models using accelerated deposition testing, for example, with interim measurements of deposit thickness and surface roughness levels [3,4,6–8,29]. However, even with measurements of surface roughness in hand, there is still a significant leap from centerline averaged roughness (Ra) measurements to predicting compressor efficiency (η_c). In practice, this chasm is often spanned using empirical correlations to convert measured roughness (e.g., Ra or Rq) to an "equivalent sandgrain" (k_s) value. This k_s value can then be used to predict local changes in boundary layer parameters (e.g., θ and c_f) leading to profile loss estimates, again using empirical correlations [22,30–34]. Finally, summing profile losses through multiple stages (using a stage-stacking model, for example [29]) yields the desired estimate for an efficiency decrement ($\Delta\eta_c$). The remainder of this article will review research studies that have been conducted to bridge this gap between actual surface measurements and predicted performance decrements, specifically for the case of surface roughness caused by degradation.

2 Background: Surface Roughness

The use of roughness correlations dates back three quarters of a century to the turbulent pipe flow study of Nikuradse [35]. His pressure loss data, taken with sand-roughened pipe walls, manifested different dependencies on Reynolds number and roughness for different flow regimes (Fig. 4). Nikuradse defined a dimensionless roughness parameter, $k^+ = k_s u_\tau / \nu$, using the actual sandgrain diameter (k_s), the measured friction or shear velocity (u_τ), and kinematic viscosity (ν). He found that for values of this parameter greater than 70, the pipe loss coefficient was only a function of k_s, while for $5 < k^+ < 70$, both Re and k_s were important. These regimes are termed "completely" or "fully" rough and "transitionally" rough, respectively. For k^+ values below 5, roughness was found to have no effect on pressure loss since the roughness peaks were wholly immersed in the laminar sublayer of the turbulent boundary layer. Thus, this regime is declared "hydraulically smooth." Nikuradse observed that the turbulent boundary layer "law of the wall" ($u^+ = 1/\kappa^* \ln y^+ + B$) was still valid for rough surfaces except that the constant B was shown to be dependent on k^+. For "completely rough" surfaces, this dependency can be approximated as $B = 5.5 - 1/\kappa\{\ln(1 + 0.3k^+)\}$ [36]. Note that the constant in this expression varies between 5 and 5.5 in the litera-

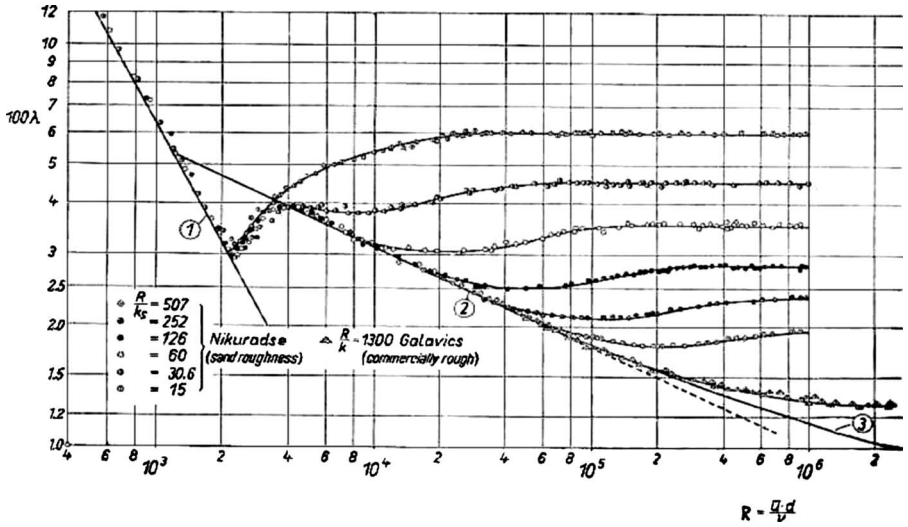

Fig. 4 Nikuradse's original sand-roughened pipe flow data (Fig. 20.18 from Schlichting [39])

ture and care should be taken to consistently employ the same expression when comparing various models. In this way, k^+ can be used (in a boundary layer calculation, for example, Ref. [37]) to calculate skin friction for a rough wall. Schlichting [38] subsequently used Nikuradse's data to correlate various types of "non-sand" roughness (e.g., rivets, bumps, and protuberances). In so doing, Schlichting [39] coined the term "equivalent sandgrain roughness" to connote a roughness feature (and spacing) that has the "equivalent" effect on skin friction losses as a uniform layer of actual sandgrains of diameter k_s. Though Schlichting's quantitative results have since been disputed by Coleman et al. [40], his equivalent sandgrain methodology has gained universal acceptance. Until recently, practically every roughness correlation for skin friction, convective heat transfer, and even boundary layer transition utilized k_s [36,39,41–44].

In roughness work related to gas turbines, various correlations have been employed to convert measurable surface roughness parameters (Ra, Rq, or Rz) to equivalent sandgrain roughness (k_s), following the Schlichting model. Table 1 contains a survey from the open literature. The first thing that is apparent from the table is the wide variety of proposed correlations. Since many of the correlations vary by up to a factor of 5, the uninitiated would be hard pressed to select an appropriate value for a new application [54].

Table 1 Roughness correlations for k_s determination of gas turbine roughness

Year	Reference	k_s relation	Surface type
1962	Speidel [45]	$k_s=Rz/5$	Milled surface with grooves parallel (within 10 deg) to flow (Rz=groove height)
		$k_s=Rz/2.56$	Milled surface with grooves greater than 10 deg from flow-aligned
1967	Forster [46]	$k_s\approx 2Ra$	Machined surfaces
		$k_s\approx 7Ra$	Emery papers
1976	Koch and Smith [32]	$k_s\approx 6Ra$	Sandgrains
1976	Bammert and Sandstede [47]	$k_s\approx 2.2Ra^{0.88}$	Mechanically produced surface and emery grain surface
1980	Schaffler [48]	$k_s\approx 8.9Ra$	Forged and machined blades
1984	Simon and Bulskamper [33]	$k_s\approx 2Ra$	Machined surfaces
1990	Sigal and Danberg [49] (as used by Boyle and Civinskas [50] and Bogard et al. [16])	$0.5<k_s/k<5$ as $f(\Lambda_s)$	Isolated 2D and 3D roughness elements of height k
1997	Barlow and Kim [51]	$k_s\approx 2.7k$ or $k_s\approx 16Ra$	Ordered array of pedestals of height k
1996	Hoffs et al. [52]	$k_s=Rz$	Liquid crystal surface
1998	Guo et al. [53]	$k_s=Rz$	Liquid crystal surface
1998	Bogard et al. [16]	$k_s\approx 4Ra$	Turbine vane surface roughness
1998	Abuaf et al. [54]	$Ra<k_s<10Ra$	Cast and polished metal surfaces
1998	Kind et al. [34]	$2.4<k_s/k<6.1$ as $f(\lambda)$	Sparsely distributed sandgrains of average size k
2001	Boyle et al. [55]	$k_s\approx 2.1Rq$	Research vane surface
2003	Boyle and Senyitko [43]	$k_s\approx 4.8Rq$	ZrO spray-on roughness particles
2003	Bunker [56]	$k_s\approx 10Ra$	Polished TBC
2004	Shabbir and Turner [57]	$k_s=8.9Ra$	Turbine roughness
2004	Zhang and Ligrani [58]	$k_s\approx 1.9Rz$ as $f(\Lambda_s)$	20–150 μm Ni particles
2005	Bons [59]	$0.5<k_s/Rz<3.5$ as $f(\alpha_f)$	Scaled turbine blade roughness
2005	Syverud et al. [6]	$0.4<k_s/k<2$ as $f(\lambda)$ [47]	Salt grains from sea-spray ingestion
2005	Stripf et al. [60]	$2<k_s/k<5$ as $f(k,t)$	Ordered arrays of truncated cones of height, k, and spacing, t
2005	Hummel et al. [61]	$k_s\approx 5.2Ra$	Correlation with various surfaces
2006	Yuan and Kind [62]	$k_s\approx 1.8k$	Sparsely distributed sandgrains of average size k

Several of those identified in the table have lamented over this morass of data, ultimately taking matters into their own hands by defining their own correlation. For example, Hummel et al. [61] used a turbine blade loss model from Traupel [63] to correlate estimated blade row losses versus Ra/c from several previous experiments (including some of their own data) and arrived at a best fit using $k_s=5.2Ra$. Boyle and Senyitko [43] provide a detailed evaluation of a number of the leading correlations showing how estimates for k_s can vary up to an order of magnitude depending on the method used. Of course, part of the problem with defining a single universal correlation is the variety of roughness characterizations: machined, sandgrain, ordered arrays of identical roughness elements (e.g., cones), and finally actual degraded surface roughness. Recognizing this difficulty, many have proposed correlations based on something other than the standard roughness metrics (Ra, Rq, or Rz). Parameters that account for the individual shape and density of roughness elements (e.g., Λ_s, λ, and α_f) have broader appeal but still fall short of being universal [6,34,49,59,60]. Moreover, the vast majority of these correlations are defined using "artificial" or "simulated" roughness rather than "real" roughness. Bons [64] studied scaled models of real roughness samples taken from in-service turbine hardware and found a markedly different k_s correlation when compared with ordered arrays of deterministic roughness elements (e.g., cones, hemispheres, or sandgrains). One final difficulty with defining a single universal k_s correlation for all roughness characterizations is that while Schlichting defined k_s from the perspective of aerodynamic drag equivalence, it has since been adopted for convective heat transfer equivalence as well. Fundamental issues with this ill-conceived "adoption" from aerodynamics to heat transfer are addressed below in further detail.

In many cases, the gas turbine operator is solely concerned with ensuring that the surface roughness is below the hydraulically smooth limit. Schlichting [39] plotted skin friction data for turbulent boundary layer flow over sand-roughened plates (again based on Nikuradse's pipe flow data) and noted the first evidence of roughness influence for $k_s \cong 100\nu/U_\infty$. For gas turbine roughness on airfoils, it is most convenient to represent this admissible level of roughness ($k_{s,\mathrm{adm}}$) relative to the blade (or vane) chord, c:

$$\frac{k_{s,\mathrm{adm}}}{c} \leq \frac{100}{\mathrm{Re}_c} \tag{1}$$

For a typical chord Reynolds number of 1×10^6 and blade chord of 5 cm, this represents a $k_{s,\mathrm{adm}}$ of 5 μm. Given the range of correlations in Table 1 ($1<k_s/Ra<10$), this explains industry-wide specifications for surface finish ($Ra\leq1$ μm. The dimensionless roughness parameter, $U_\infty k_s/\nu$, (sometimes called the "roughness Reynolds number" or Re_k) is often reported relative to the "100" threshold for admissible roughness. A review of gas turbine roughness literature shows a broad acceptance of Eq. (1) as a design guideline [30,31,48,61,65,66], although anecdotal evidence of temporary SFC reductions immediately following surface refurbishment on aeroengines well below the 100 threshold has been supported by recent research into "ultrapolishing" [67]. Nevertheless, the roughness Reynolds number (Re_k) is the most commonly reported roughness parameter in the open literature and is routinely used in the scaling of research facilities for roughness research [37,68–70].

At issue then is how far above $k_{s,\mathrm{adm}}$ can the surface roughness be tolerated before maintenance is necessary. Unfortunately, to answer this question requires an understanding of two of the most intractable problems in the fluid dynamics of wall-bounded flows, namely, boundary layer separation and transition. The limited scope of this article cannot possibly do justice to these two subjects. Hopefully, the reader will forgive the meager illustration provided here.

Boundary layer transition is influenced by a wide assortment of flow and surface parameters in addition to surface roughness (e.g., Reynolds number, freestream turbulence level and lengthscale, surface heating or cooling, pressure gradient, upstream history, blowing or suction, Mach number, shocks, and curvature). As an example of surface roughness effects on transition, Feindt [71] studied boundary layer transition on a sand-roughened wall and found the critical sandgrain dimension that induced early transition to be $Uk_s/\nu\approx120$. The same threshold was noted for a modest range of adverse and favorable freestream pressure gradients. This criterion is very close to the $k_{s,\mathrm{adm}}$ relation for turbulent boundary layers (Eq. (1)), which should be good news for gas turbine operators. Unfortunately, there are at least two complicating factors that must be taken into account. First, Feindt's data show a smooth-wall transition Reynolds number ($\mathrm{Re}_{x,\mathrm{tr}}$) of 6.6×10^5, which is considerably less than values that can be obtained experimentally using clean/quiet wind tunnels ($\mathrm{Re}_{x,\mathrm{tr}}>3\times10^6$). Thus, Feindt's criterion of $Uk_s/\nu<120$ must be adjusted for flows with other mitigating factors that influence transition (e.g., higher or lower freestream turbulence levels). The only component in a gas turbine engine that would likely have a more "disturbance-free" environment than Feindt's experimental facility is the engine inlet or nacelle. Thus, the roughness criterion for transition would be more stringent (less than 120) in this case. Embedded blade rows in compressors and turbines are rife with disturbances (e.g., wakes and shocks) and thus may have significantly higher thresholds for roughness to effect transition. Braslow [44] reviewed boundary layer development with distributed roughness and suggested a criterion of $k^+>19$ for roughness-induced transition. For the Re_c values typical of gas turbine airfoils, this corresponds to a roughness Reynolds number criterion of $Uk_s/\nu<500$. This is close to the threshold of 600 suggested by White [36] for an isolated roughness element. Indeed, transition is generally considered to be a significant factor in turbomachinery for chord Reynolds numbers above $(2–4)\times10^5$ [43,48]. Roughness can also promote earlier transition in separated free shear layers, thus reducing the size of separation bubbles, as noted by Roberts and Yaras [72]. Prior to boundary layer transition, roughness has no perceptible influence on local values of aerodynamic drag (Fig. 4) or heat transfer [73,74].

The second complicating factor with using a universal k_s/c criterion for both turbulent and laminar boundary layers is what happens once the threshold is exceeded. For a turbulent boundary layer, exceeding $k_{s,\mathrm{adm}}$ may mean a modest increase in blade profile losses (Fig. 4). For a laminar boundary layer, if exceeding $k_{s,\mathrm{adm}}$ causes transition, the profile loss could increase by up to a factor of 2 [43] (and the local heat transfer coefficient up to a factor of 8 [73]). On the other hand, if the laminar boundary layer was already prone to separation, roughness-induced transition could minimize or eliminate separation and actually reduce profile losses [75] (as in the golf ball flow). Thus, the effects of transition and separation are coupled in many turbomachinery flows.

3 Real Gas Turbine Roughness Characterizations

The majority of roughness studies referenced thus far were conducted using sand-roughened walls. Indeed, this is the most common roughness characterization employed historically for gas turbine research as well as in other industries. Before reviewing gas turbine roughness research in more detail, it is instructive to evaluate how closely actual degradation-induced gas turbine surface roughness compares to sandgrains. There are relatively few studies of this type in the open literature. Dunn et al. [10] showed pictures of compressor rotor blades subjected to "simulated" volcanic-ash ingestion with varying levels of erosion. Although the images do not allow an up-close assessment of surface character, it is evident that the erosion is not spatially uniform. Erosion is primarily evident in the leading edge and tip regions. Accelerated salt-spray ingestion tests by Kacprzynski et al. [3] and Syverud et al. [6] show similar spatial variation. A picture of second stage compressor vanes shows 0.5 mm thick salt deposits

at the vane leading edge, with a strong preference for the hub versus the tip annulus [6]. A boroscope image of a first stage compressor blade shown in Ref. [3] has regions with pronounced ridge-lines of salt deposit as well as regions without any obvious deposit. Finally, a magnified image of salt grains on a first stage vane pressure surface shows a nonuniform distribution of salt grains with sizes from $3<k<30$ μm (mean grain size=22 μm and mean grain spacing=88 μm). In 2000, Leipold et al. [70] studied roughness on precision forged compressor blades and found sparsely distributed roughness elements (similar to those studied by Kind et al. [34] for turbines) rather than the close-packed elements typical of sandgrain characterizations.

For turbines, Taylor [15] measured surface roughness on two sets of first stage turbine vanes, 30 from a TF-39 and 30 from an F-100 engine. He found that the roughness level varied by an order of magnitude around the blades on average ($1<Ra<10$ μm), with degradation favoring the leading edge suction surface for one engine and the trailing edge pressure surface for the other. In addition, individual traces showed the roughness to be highly non-Gaussian in many cases (nonzero skewness and kurtosis). Tarada and Suzuki [14] reported on a survey of 58 used turbine blades from aero-, marine, and industrial engines. Peak roughness levels (Ra) ranged from 50 μm to 160 μm in the most severely degraded portions of the blades, particularly in the leading edge region. Bogard et al. [16] studied the oxidized and deposited turbine vanes from two military aeroengines and reported that the surface character bore greater similarity to "scale" rather than the sand grit typically used to model roughness. Finally, Bons et al. [17] reported on a study of over 100 different used industrial turbine components, showing examples of deposition, corrosion, erosion, and coating spallation (Fig. 5). Spatial nonuniformity of roughness character was the norm for all blades, and transitions between rough and smooth surface conditions were at times abrupt. Differences between the roughness signatures of various degradation mechanisms (e.g., deposition versus spallation) led the authors to conclude that no single characterization (e.g., sand, cones, and hemispheres) can accurately capture the range of diverse features exhibited by the various forms of surface roughness on serviced turbine blades. Given this assessment, it is perhaps inconceivable that any roughness parameter (e.g., k_s or Re_k) could ever be effectively used to characterize roughness from such diverse samples. Yet, Bons [59] later reported that both Λ_s and α_f provided reasonable correlation for c_f and St enhancement caused by roughness for a broad spectrum of surface features.

Observed spatial variations in roughness for in-service turbomachinery components are of particular significance since the sand-roughness experiments of Nikuradse [35] (and many since then) have studied the effects of uniform distributions of closely packed sandgrains of a similar size. All three of these characterizations ("uniform," "closely packed," and "similar size") appear to be contradicted by actual surface measurements in gas turbines. Also, roughness modeling algorithms in commercially available computational fluid dynamics (CFD) codes that typically apply a uniform k_s roughness level to all wetted surfaces may produce misleading results when compared with real turbine airfoils with degraded leading edges but smooth surfaces elsewhere. In addition, experimental work by Pinson and Wang [76] showed that abrupt changes in roughness size can have a significant effect on transition location. Specifically, abrupt streamwise changes from large roughness to a smooth-wall condition exhibited earlier transition than changes from large to small roughness.

The remainder of this article will focus on roughness studies of compressor and turbine airfoils. The turbine section will also address roughness effects on film cooling. Finally, some comments regarding the state of the art in roughness modeling for CFD will be addressed. Though considerable effort has been made to canvas the literature, these reviews are by no means comprehensive. Rather, they are intended to provide a sampling of past and current research in a very active and difficult area of study.

(*a*)

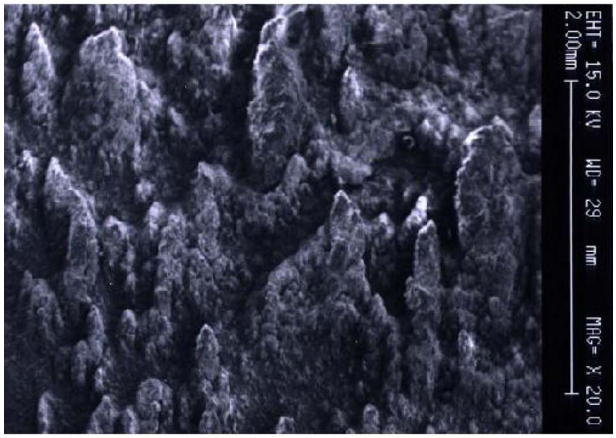

(*b*)

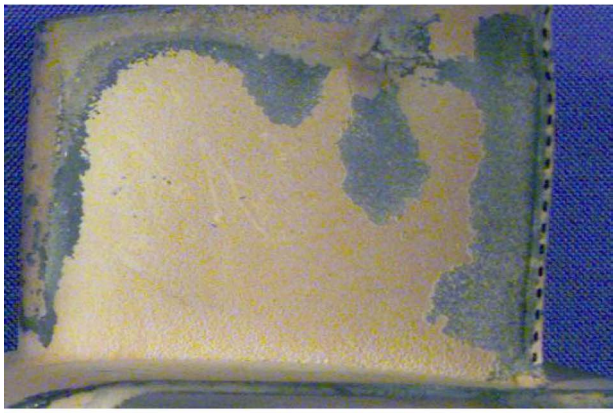

(*c*)

Fig. 5 Samples of erosion, deposition, and TBC spallation on turbine blading. (*a*) Erosion sample from suction surface leading edge region (7×10 mm^2). (*b*) Fuel deposition sample from pressure surface trailing edge region (3×4 mm^2). (*c*) Spallation on turbine blade pressure surface.

4 Roughness in Compressors

A review of the past 30 years of compressor roughness research shows nearly an equal interest in axial and centrifugal machines. Since the two devices experience different fluid mechanics issues, they will be treated separately here, although the primary focus is on axial machines. The role of the compressor is to increase the total pressure of the gas prior to combustion. This is done by imparting kinetic energy to the fluid and subsequently decelerating it to collect static pressure. Thus, compressor airfoils are de-

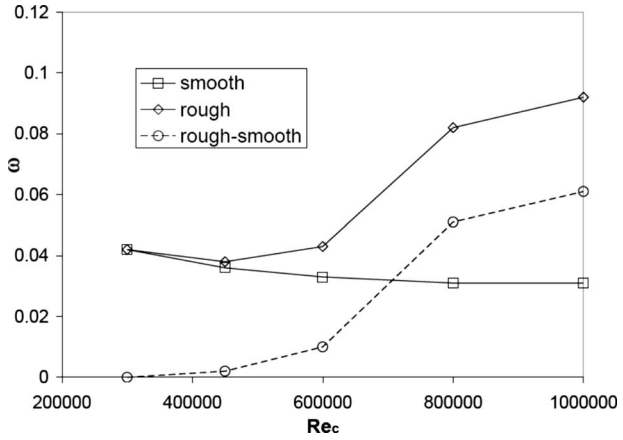

Fig. 6 Compressor cascade loss measurements for rough and smooth blades versus Re_c (Fig. 8 from Leipold et al. [70])

signed with considerable care due to the inherent adverse streamwise pressure gradient. Overly aggressive blade camber can result in boundary layer separation (particularly at low flow rates, i.e., high positive incidence angles), which reduces stage efficiency and can ultimately lead to compressor stall and/or surge. As such, circular arc camber lines with maximum thickness to chord ratios of less than 8% are typical. Controlled diffusion airfoils (front-loaded airfoils that take advantage of laminar flow prior to the suction peak and control boundary layer diffusion to avoid separation) are also widely used in multistage compressors. Since the pressure rise scales with the rotor rotational frequency, substantial benefit can be derived from operating at higher speeds, creating the potential for transonic flow in the compressor passages. Supersonic compressor airfoils are designed with sharp leading edges to reduce shock-induced losses. As such, they are even more sensitive to changes in leading edge shape. Because of the critical role of boundary layer separation (both for sub- and supersonic airfoil designs) in determining profile losses, it is important to ensure that compressor roughness research is conducted with the appropriate range of dimensionless parameters: Reynolds and Mach numbers.

The critical role of Reynolds number is well illustrated in the experimental work of Leipold et al. [70]. They studied the effects of typical blade forging roughness using a high pressure cascade facility over a range of Re_c from 3×10^5 to 1×10^6 (based on inlet conditions). The inlet Mach number to the cascade was set to 0.67, with a peak isentropic Mach number near 1 at the highest Re_c (i.e., the flow was shock free). Figure 6 shows their wake measurements of total pressure loss taken at midspan (span/chord=1.67) for both the smooth and artificially roughened airfoils. The roughness to chord ratio was $Rz/c=4\times10^{-4}$, which just exceeds the $k_{s,\mathrm{adm}}$ threshold (Eq. (1)) at $Re_c=2.5\times10^5$ (assuming $Rz\approx k_s$ for this case). The trend for the smooth airfoil in Fig. 6 follows the conventional wisdom that losses fall (efficiency rises) as Re_c increases up to a plateau around $Re_c=5\times10^5$. The rough blade losses show the opposite trend of increasing losses above this Re_c threshold. Boundary layer measurements confirmed that this rise in profile loss was due to the turbulent boundary layer separation on the airfoil suction surface. As Re_c increases, the thinning boundary layer creates a more pronounced roughness effect (increasing k_s/δ). As such, roughness-induced momentum losses in the turbulent boundary layer at midchord cannot overcome the diffusion on the aft portion of the blade. While roughness does eliminate a small laminar separation bubble at moderate Re_c, the added viscous drag more than makes up for this in the aggregate profile loss measurement. This finding is particularly relevant since a large aeroengine at cruise experiences core compressor Reynolds numbers from $(1-2)\times10^6$ (higher still at take-off conditions). Schaffler [48] emphasized this same trend of increased loss with inlet Reynolds number using polytropic efficiency measurements from a five-stage high pressure compressor rig. For blade surfaces with a roughness Reynolds number only 60% higher than the admissible threshold, Schaffler reported lower efficiencies (compared with smooth blades) beginning at $Re_c=3.1\times10^5$ (first stage rotor Re_c). Since Re_c increased by a factor of 2 through Schaffler's five-stage high pressure compressor, the last stage was clearly above the "knee" in the profile loss curve reported by Leipold et al. (Fig. 6). Thus, roughness effects that would not be evident from a low Reynolds number compressor cascade test can become critical during actual engine operation.

In 1972, Bammert and Milsch [30] published an oft-referenced study operating a low-speed compressor cascade with five sandgrain roughness levels: $2.3\times10^{-4}<k_s/c<5.6\times10^{-3}$. The inlet Reynolds number was fixed at $Re_c=4.3\times10^5$ and the Mach number was 0.11. They reported increases in profile losses from 2% to 10% over this range of roughness, largely due to trailing edge separation on the suction surface. They also noted reduced turning with increased roughness, which would certainly affect the efficiency of the subsequent blade row by altering the incidence angle. Thus, a follow-on study by Bammert and Woelk [77] using a three-stage axial compressor with comparable sandgrain roughness levels on all three stages of airfoils produced a 6–13% loss in efficiency and up to 30% loss in overall pressure ratio. Similar cascade profile loss increases were reported by Elrod and King [78] although their sand roughness $(2\times10^{-3}<k_s/c<9\times10^{-3})$ was only applied to the leading 25% of the suction surface (to simulate regions typically affected by erosion). Elrod et al. also found that roughness effects were overshadowed at elevated freestream turbulence levels (up to 5%). This finding runs counter to the observations of Schreiber et al. [79] who studied roughness effects on transition in a compressor cascade using liquid crystals $(0.7\times10^6<Re_c<3\times10^6)$. They noted that elevated freestream turbulence (up to 4%) actually increased the frequency of turbulent wedges forming in the wake of discrete roughness elements in an otherwise laminar boundary layer. Thus, the effects of roughness and freestream turbulence on transition were complementary or synergistic. Incidentally, the study of Leipold et al. was conducted with 2–3.5% turbulence while Bammert and Milsch's facility had less than 1%. Schreiber et al. also visually corroborated previous findings that an increasing flow Re_c amplifies the effect of roughness on early transition, thus reducing laminar separation zones.

One of the few compressor roughness studies on a transonic rotor, by Suder et al. [80], concluded that roughness decreases performance by increasing shock losses. Roughness laden paints were applied to a research rotor (relative tip Mach number=1.48 at design speed) with roughness Reynolds numbers more than five times the threshold value of 100. At design speed, roughness and increased blade thickness (due to the paint thickness) both produced efficiency decrements of 3% (with a combined 9% reduction in pressure ratio). By systematically applying the paints to the rotor blade leading edges and then trailing edges only, Suder et al. determined that the effect of roughness on the shock-boundary layer interaction at the leading edge of the airfoil was responsible for the measured losses in performance. Roughness (and added paint thickness) over the first 2% of blade chord caused a thickening of the boundary layer. Subsequent interaction of this thickened boundary layer with the rotor passage shock created increased blockage and reduced diffusion in the blade passage. The effect of roughness was much less pronounced at lower operating speeds (only 1–2% effect on efficiency at 60% design) as would be expected due to the lower Re (lower k_s/δ) and the absence of shocks.

The critical role of compressor blade leading edge modification due to degradation (erosion or deposition) has been well researched [3,7,65,67,81], usually without considering the compli-

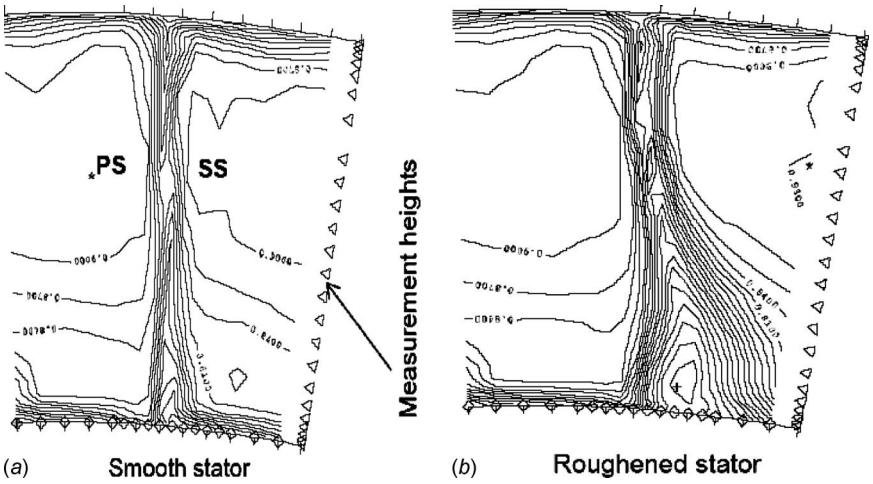

Fig. 7 Contours of total pressure rise coefficient at the exit of compressor stator for (*a*) smooth and (*b*) LE roughness only conditions. $Re_c=2.7\times10^5$ (Fig. 2 from Gbadebo et al. [37]).

cating effects of surface roughness. One exception to this is the recent work by Gbadebo et al. [37] who studied roughness effects on endwall separation in a low-speed single-stage compressor facility ($Re_c=2.7\times10^5$). The first 20% chord on the stator blades was modified by attaching emery paper with a grain size to match the roughness Reynolds number of a modern turbofan engine at takeoff with a typical surface condition of $Ra\approx2$ μm. Measurements showed significant increases in hub endwall losses (up to 15%) on the suction side of the airfoil due to three-dimensional endwall separation triggered by the leading edge roughness. The affected region extended to 30% span (Fig. 7). At the same time, midspan profile losses and tip endwall losses were virtually unaffected. Roughness applied downstream of the suction peak had no perceptible effect on profile or endwall losses.

Centrifugal compressors have considerably higher single-stage pressure ratios (2–4) compared with axial compressors (1.2–1.5) and the flow is generally not transonic. Efficient compressor performance is often dictated by the interaction of the impeller with the diffuser and collector. Useful one-dimensional models have been developed by Wiesner [31], Simon and Bulskamper [33], and Benra et al. [82] among others. The results show similar trends to those cited above, namely, an increased detrimental effect of roughness with increasing Reynolds number. Relative roughness size is referenced to the impeller discharge height (b_2) or hydraulic diameter (d_h), and roughness effects become significant for $k_s/d_h>3\times10^{-4}$. Roughness influences centrifugal compressor loss through the same fluid mechanisms of earlier transition, increased boundary layer losses, and flow separation.

5 Roughness in Turbines

Axial flow turbines are distinguished from compressors by several key design features. First, they are designed to extract work from an expanding flow. Since the static pressure is falling in the flow direction, boundary layer separation is (generally) not as critical and blade designs can be much more aggressive (i.e., higher turning) than in an axial flow compressor stage. Consequently, there are far fewer turbine stages than compressor stages since the stagnation enthalpy drop through one turbine stage can be used to drive three to five compressor stages. Higher blade loading requires thicker airfoils; hence turbine airfoils can have maximum thickness to chord ratios in excess of 25%. Because of this, airfoil trailing edges are thicker creating larger wake losses. Also, the flow in many first stage (high pressure) turbines is transonic, with choked nozzles during normal operation. Thus maintaining minimum passage (throat) areas is critical for efficient operation at the design flow coefficient. The other distinctive feature of turbines is their proximity to the combustor exit. Turbine inlet temperatures for modern gas turbines regularly exceed material limits of the most exotic single crystal Ni-based alloys. Thus, since the 1960s, hollow turbine vanes and blades have been fed with compressor discharge air to alleviate the effects of thermal fatigue. In the past two decades, this internal cooling has been augmented with elaborate film cooling passages and external thermal barrier coatings (TBCs) to protect the structural metal. Designers now routinely depend on these "thermal management" systems to allow higher firing temperatures ($\sim$1800 K) than turbine metals can withstand. Due to these added complexities, turbines now account for a disproportionate amount of the overall gas turbine cost, both in terms of R&D and operating costs. It is perhaps no surprise then that most of the gas turbine roughness research in recent years has been devoted to turbine applications. For example, over three times as many turbine roughness articles (compared with compressor roughness articles) were used in the preparation of this review, and roughly half of them are related to heat transfer as opposed to aerodynamic loss. The following is a summary of major findings from these articles. Surface roughness effects on turbine film cooling are addressed in Sec. 6.

While compressors must deal with ingested foreign matter including aerosols, airborne salts, pollutants, and foreign objects that may deposit or cause erosion, any large particles are generally broken up into micron-sized dust (<7 μm) by the time they reach the turbine [83]. However, this does not mean that the turbine is a pristine environment without its own degradation mechanisms. Ash bearing fuels used in land-based turbines can rapidly clog cooling holes and reduce choked passage throats [84,85]. Also, due to the high turbine inlet temperatures, many of the airborne contaminants that pass through the compressor can become molten in the turbine, agglomerating in significant quantities [83]. As deposits adhere to ceramic turbine coatings (TBCs), coating removal by delamination (or spallation) can occur creating local roughness features comparable to the boundary layer dimensions (0.2–0.5 mm) [17,86,87]. Thus, it is critical to understand both the aerodynamic and thermal penalties associated with surface roughness in turbines.

Perhaps because of the mitigating factors outlined above (i.e., elevated operating temperatures), there have been relatively few roughness studies on actual operating turbines compared with compressors. In 1972, Bammert and Sandstede [88] applied emery grain roughness to a 703 kW four-stage research turbine and reported a 10% drop in overall efficiency for $k_s/c=0.00765$. An

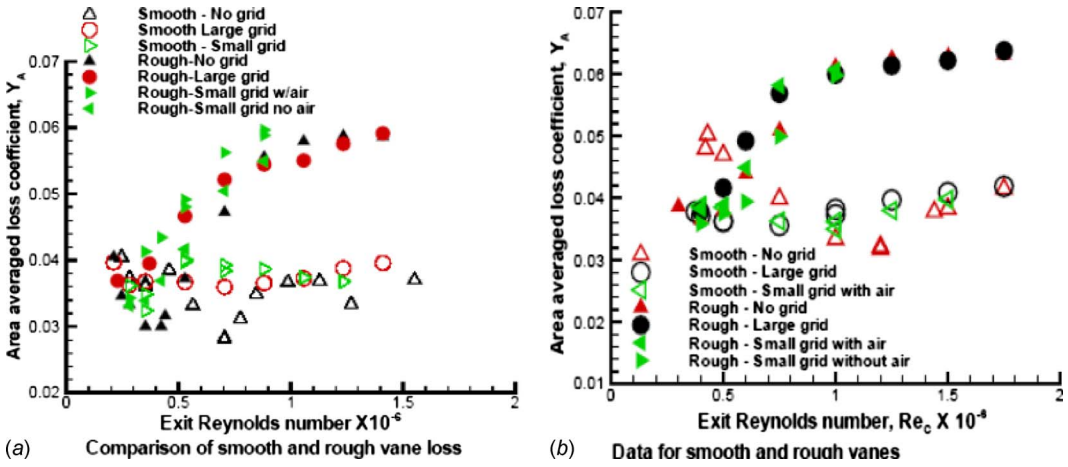

Fig. 8 Area-averaged loss coefficient versus Re_c for HP vane cascade at exit Mach number=0.5 and 0.9 (Figs. 6(*a*) and 4(*a*) from Boyle and Senyitko [43]). ($Re_{cx} \approx 0.5\ Re_c$).

additional 3% efficiency loss was attributed to the increased blade thickness (emery grains plus the adhesive layer). They recommended maintaining turbine surfaces to a finish below k_s/c of 0.001 ($Re_k < 500$). Recently, Yun et al. [89] conducted a similar study by adding sandpaper roughness to a single-stage 15 kW research turbine. By carefully matching the blade thickness for the smooth and rough test cases, they measured efficiency losses due only to surface roughness that was slightly larger than the findings reported by Bammert and Sandstede (up to 19% drop in η for $k_s/c=0.0067$). Another full turbine rig test with roughness was conducted by Boynton et al. [90] with the Rocketdyne Space Shuttle Main Engine (SSME) two-stage fuel side turbine (axial chord $\approx$2 cm). Polishing the rotor and stator airfoil surfaces from $Rq=10$ μm down to 0.76 μm yielded a 2.5% increase in turbine efficiency. A series of follow-on experiments was conducted by Blair [69] and Dunn et al. [91] to discern whether the same benefit could be expected for blade surface heat transfer. Blair applied large grain sand ($k_s/c \approx 0.004$) to a large scale ($c \approx 15$ cm) stage and a half research turbine and found dramatic increases in local heat transfer compared with the smooth-wall case. The most significant effect (100% increase in local St) was caused by early roughness-induced transition on the suction surface. Stanton number increases in turbulent boundary layer regimes (e.g., on the pressure surface) were a more modest 20–30%. Dunn et al. [91] subsequently measured surface heat transfer on a replica of the same SSME turbine used by Boynton et al. [90] but with a surface roughness of $Rq=15$ μm and $Rz=84$ μm ($Rz/c \approx 0.004$). Lacking a smooth-blade data set for direct comparison, Dunn et al. used a CFD calculation of Boyle and Civinskas [50] to conclude that the surface was not rough enough to produce a measurable increase in heat transfer. Although Taylor et al. [92] later argued that the use of smooth heat flux gauges of Dunn et al. may be inappropriate for accurate rough surface heat transfer measurement, the primary factors leading to this apparent contradiction between the results of Blair [69] and Dunn et al. [91] can be explained by dimensional scaling arguments. Although the sandgrain size employed by Blair ($Rz=k_s=660$ μm) was selected to be an eight times geometric scaling of the measured turbine roughness used by Dunn et al. ($Rq=15$ μm and $Rz=84$ μm) to match the different blade chord ratios, Boyle and Civinskas [50] postulated that sand roughness and blade forging roughness do not have the same k_s/Rz conversion. In addition, the study by Blair operated at a higher Reynolds number (5.8×10^5) than the experiment of Dunn et al. (3.8×10^5). Both Re_{cx} values were significantly lower than that used in the aerodynamic study of Boynton et al. (8.9×10^5).

Thus we again see the critical role that Reynolds number plays in determining the significance of surface roughness effects in turbines (as was outlined above for compressors). There are several excellent studies that document the synergies between Re_{cx} and roughness effects in turbines [52,54,56,93]. One of the more cogent discussions is provided by Boyle and Senyitko [43] who applied a ZrO-laden spray-on coating to a high pressure turbine vane cascade. The average Rq were 1.6 μm and 18.2 μm for the smooth and rough vanes, respectively (estimated $k_s/c=0.00084$ for the rough vane). The test facility had the capability of varying Mach and Reynolds numbers independently. Figure 8 contains two of the wake loss coefficient plots from this study, for exit Mach numbers of 0.5 and 0.9. Note that the Re_c based on true chord shown in the figure can be adjusted down to the Re_{cx} based on axial chord by multiplying by 0.5. Symbols are shown for several levels of freestream turbulence: 1% (no grid), 4.5% (small grids no air), 8% (small grids with air), and 17% (large grids with air). All of the data show a trend of increasing roughness effect on vane losses with increasing Reynolds number (up to a 50–60% loss increase at the higher Re_c). The increased loss is attributed to both roughness-induced transition and increased turbulent boundary layer momentum losses. For some low Re_c cases, roughness-induced transition actually prevented laminar boundary layer separation on the suction surface thus lowering the overall vane losses compared with the smooth-wall case. The threshold for a rough-wall loss benefit occurred near $Re_c=5 \times 10^5$ for $M_{ex}=0.9$ (slightly lower at $M_{ex}=0.5$) (Fig. 8). Hummel et al. [61] explored a similar exit Re_{cx} range $(5.6–11) \times 10^5$ in a linear rotor blade cascade with spanwise grooves applied to the blade surfaces. Their grooved surface roughness height was smaller ($0.8 \times 10^{-5} < Ra/c < 8 \times 10^{-5}$) than the range used by Boyle and Senyitko ($1.2 \times 10^{-5} < Ra/c < 14 \times 10^{-5}$) and they found a correspondingly smaller profile loss increase (20–50% versus 40–60%). At the lowest Reynolds number tested ($Re_{cx}=5.6 \times 10^5$), Hummel et al. did not find a region of roughness benefit. The low Re benefit only occurs if a smooth-wall laminar separation is prevented by roughness-induced transition, which depends strongly on the airfoil profile and loading. Low pressure turbine airfoils are more prone to experience this benefit, as will be discussed later. The blade profiles used by Hummel et al. are significantly different from the nozzle guide vanes in Boyle and Senyitko's cascade, which may explain the different observations. It is possible that the low Re roughness benefit may be muted when considering multiple blade rows or multistage effects since neither Bammert and Sandstede [88] ($3 \times 10^5 < Re_c < 6 \times 10^5$) nor Yun et al. [89] ($Re_c \cong 2 \times 10^5$) found evidence of this phenomenon in their full rig tests cited above.

The Boyle and Senyitko [43] data shown in Fig. 8 also include

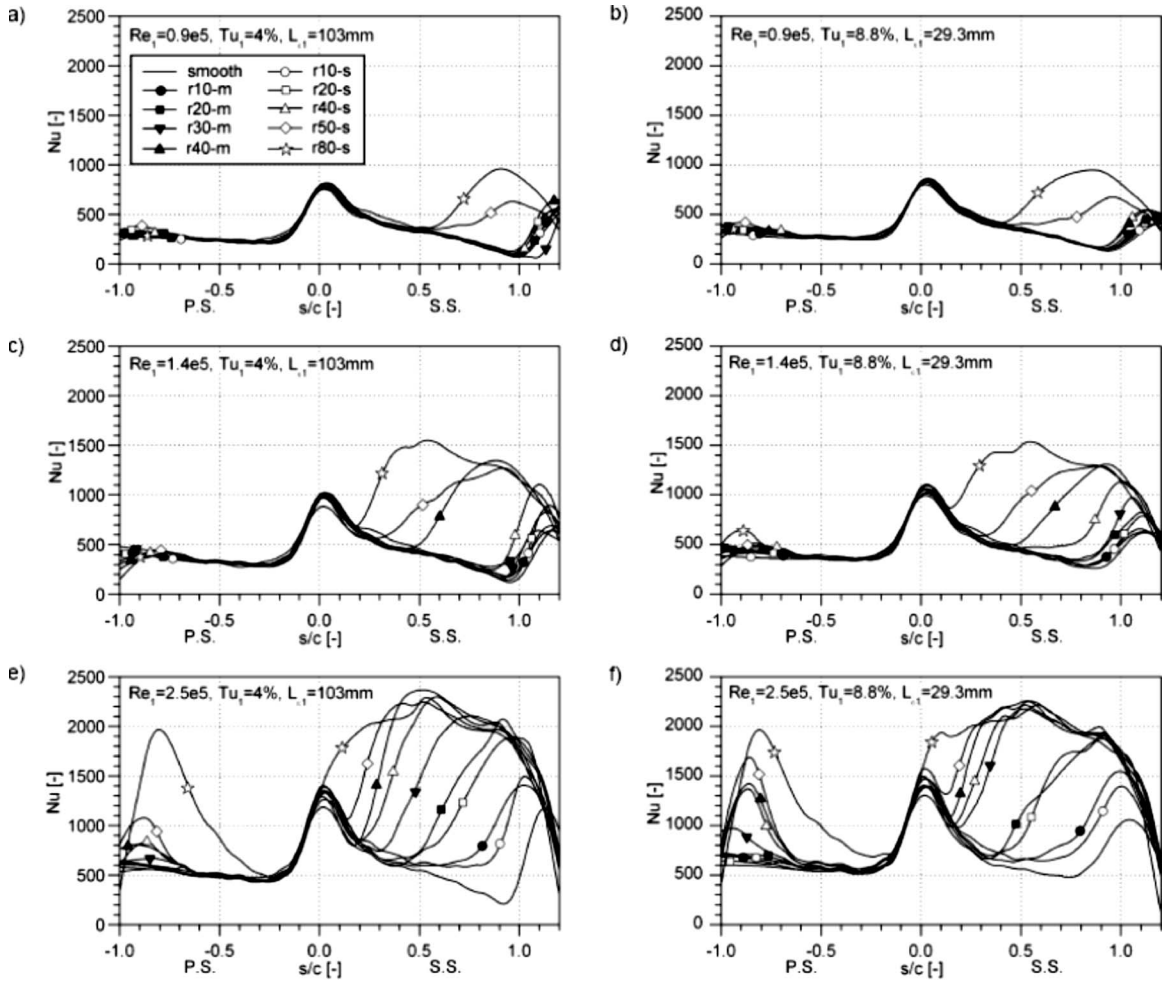

Fig. 9 Vane Nu data for various Re and Tu. (Fig. 6 from Stripf et al. [60].) ($1.6\ Re_1 \approx Re_{cx}$)

the combined effect of roughness with freestream turbulence. For the conditions studied (1–17% turbulence), turbulence alone appears to have some of the same low and high Reynolds number effects on losses as roughness; however, roughness effects dominate when the two are present simultaneously. This is not a universal finding, as a number of other studies have shown. In flat plate wind tunnel studies, Bogard et al. [16] found the two effects (roughness and freestream turbulence) to be additive for heat transfer augmentation, meaning that the increased heat transfer with both roughness and turbulence present was approximately equal to the sum of the heat transfer increase measured with each one alone. Bons [64] described a synergistic effect of combined roughness and turbulence on c_f due to the fuller turbulent boundary layer producing higher momentum loss on the protruding roughness peaks. Bunker [93] measured vane heat transfer in a linear cascade with both roughness and freestream turbulence (4–12%) at much higher Re_{cx} ($(2-5)\times 10^6$) and found the effects to be at least additive. Zhang and Ligrani [58] ($Re_{cx}=6\times 10^5$) report similar results for cascade aerodynamic losses with combined roughness and freestream turbulence (up to 8%). The Boyle and Senyitko [43] data (Fig. 8) also show roughness-induced losses to be fairly insensitive to cascade exit Mach number. This finding is corroborated in the data sets of Yuan and Kind [62] and Zhang et al. [94] as well as the low pressure turbine work of Vera et al. [75]. Thus, roughness effects deduced from low-speed experiments are relevant as long as the Reynolds number, roughness scaling, and freestream turbulence levels are representative of engine conditions.

The aerodynamic loss studies referenced above universally identify the suction surface as the region most susceptible to roughness effects. In fact, several researchers applied roughness exclusively to the suction surface to demonstrate this fact conclusively [34,89,95]. As explained previously, losses generated on the suction side are strongly dependent on the interplay between separation and transition, and roughness can have a significant effect on both of these phenomena. While the efficiency of a turbine stage depends on the mass-averaged losses at the exit, heat transfer is a phenomenon of local concern. For example, if roughness-induced transition prevents separation on the suction surface at low Re, it may ultimately reduce the stage losses and improve efficiency. However, local levels of heat transfer at the transition location will see an increase of up to a factor of 2–3 compared with the smooth-wall condition where laminar separation was present. Vane heat transfer data from Stripf et al. [60] shown in Fig. 9 provides an excellent example of the local heat transfer augmentation caused by roughness-induced transition. Note that the Re_1 values shown in the figure are based on true chord and inlet velocity. It is estimated that the corresponding Re_{cx} values would be 60% larger. The data were acquired in a HP vane cascade with truncated cones of various geometries and spacings etched onto the surface. The legend contains the identifier for each roughness case. The two numerical digits indicate the height of the cones in microns ($k=Rz$), while the $-s$ indicates a sparse separation and a $-m$ is a closer spacing (e.g., $r40$-s is roughness with 40 μm high truncated cones at sparse spacing). The vane chord

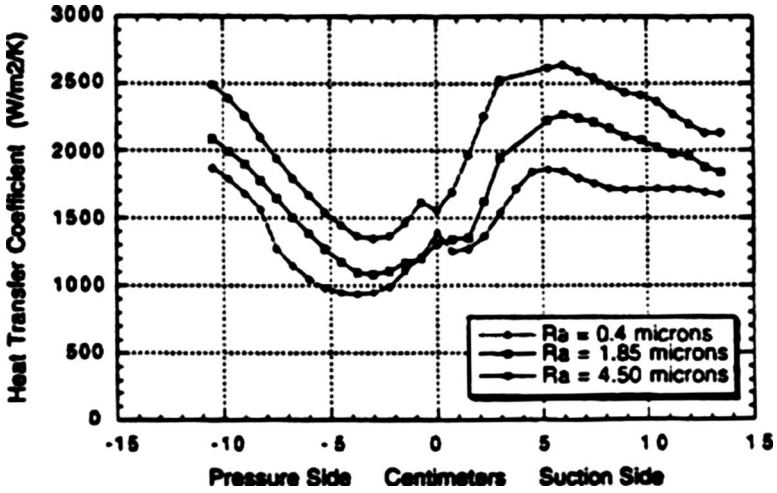

Fig. 10 Vane heat transfer coefficient data for various *Ra* at $Re_{cx}=4.7\times10^6$ and Tu=9% (Fig. 12 from Bunker [93]).

was 94 mm so the largest Rz/c ratio was 8.5×10^{-4}. Using a correlation derived from Waigh and Kind [96], Stripf et al. estimated $k_s/Rz\cong2$ for the $-s$ cases and $k_s/Rz\cong5$ for the $-m$ cases. At low freestream turbulence, the authors indicate that transition on the suction surface takes place via a short laminar separation bubble while the flow is completely laminar on the pressure surface due to the strong flow acceleration there. Roughness has the effect of eliminating the suction side separation in favor of a bypass transition mode that moves upstream with roughness size. The effect is more pronounced at higher Reynolds numbers and freestream turbulence levels. Roughness contributed to early boundary layer transition on the pressure surface only at the highest Re_1 tested (2.5×10^5). Stagnation point heat transfer also shows an increase with roughness, up to 25% for the largest roughness considered. Bunker [93] reported similar trends for an order of magnitude higher Reynolds number in his transonic linear vane cascade ($c=12.75$ cm). Figure 10 shows the heat transfer coefficients measured at $Re_{cx}=4.7\times10^6$ and Tu=9%. As with the data set of Stripf et al., transition moves forward on the suction surface as roughness level is increased by an order of magnitude from $Ra=0.4$ μm ($Rz/c=1.8\times10^{-5}$) to 4.5 μm ($Rz/c=2.2\times10^{-4}$). Stagnation heat transfer showed a slight increase, although this was within the experimental uncertainty. Outside of the leading edge and transition regions, Bunker found that heat transfer scaled roughly as $Rz^{0.25}$ for all of the turbulent boundary layer results. The heat transfer increases of 20–40% shown in Fig. 10 are consistent with rough-wall turbulent boundary layer heat transfer studies conducted in numerous flat plate wind tunnel facilities [16,56,64,92].

Two recent studies have explored the influence of roughness on end-wall secondary flows in turbines. Matsuda et al. [95] measured the profile and endwall total pressure losses in a large-scale vane cascade with varying degrees of surface polish ($0.8\times10^{-5}<Rz/c<8.4\times10^{-4}$). The freestream turbulence level in the tunnel was low (0.5%) and Re_c was varied $(0.3-1)\times10^6$. Figure 11 contains a summary of profile loss measurements from their study. Roughness causes a significant rise in loss for $Rz/c>2.5\times10^{-4}$. Incidentally, Matsuda et al. also found a roughness benefit at low Re similar to Boyle and Senyitko [43] for $Re_c<4\times10^5$ (not shown). Contour maps of pressure loss (Fig. 12) show a marked rise in endwall losses as well for the large roughness cases (a net increase of up to 50% for the largest roughness case). When roughness is added to the endwall (for the largest roughness case), an additional 30% net loss is measured. The authors attribute this increased loss to secondary flows (vortices) that roll up roughness-effected low momentum fluid from the boundary layer. The magnitude of endwall loss increase is larger than that reported by Gbadebo et al. [37] for compressors. It's unlikely that the effect is due to separation losses on the endwall since Fig. 12 shows no appreciable movement of the endwall loss structure away from the hub (as was observed by Gbadebo et al., Fig. 7). Using the same linear vane cascade cited earlier [60], Stripf et al. [73] explored vane surface heat transfer in the endwall-effected region (with smooth endwalls and a spanwise boundary layer trip near the vane leading edge). Similar to Matsuda et al. [95], they found that vane roughness did not appreciably alter the size of the endwall-effected region. However, turbulent heat transfer in this region increased up to 80% with the largest vane roughness ($k/c>3.2\times10^{-4}$), compared with 40% at midspan ($Re_{cx}\approx4\times10^5$ and Tu=4% and 8%). Without a leading edge boundary layer trip, the midspan heat transfer increase was over 600% due to the roughness-induced transition at this low Re_{cx}, whereas the endwall heat transfer increase was still only 80%. Roughness-induced endwall heat transfer increases are of particular concern for turbine designers since the rotor endwall is a region of aggravated mechanical stress as well.

As with the compressor, many of degradation mechanisms that produce surface roughness in the turbine also result in undesirable

	C1	C2	C3	C4	C5	C6	C7
$Rz/c\times10^5$	0.8	5.2	6	17	36	63	84
URz/v	10.4	67.7	78.1	224	468	817	1093

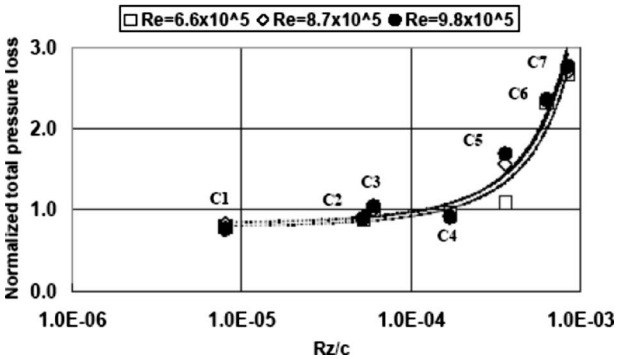

Fig. 11 Turbine vane total pressure loss data from Matsuda et al. [95] for various *Rz/c* for three values of Re_c and Tu=0.5%. ($Re_{cx}\approx0.7$ Re_c) (Fig. 7).

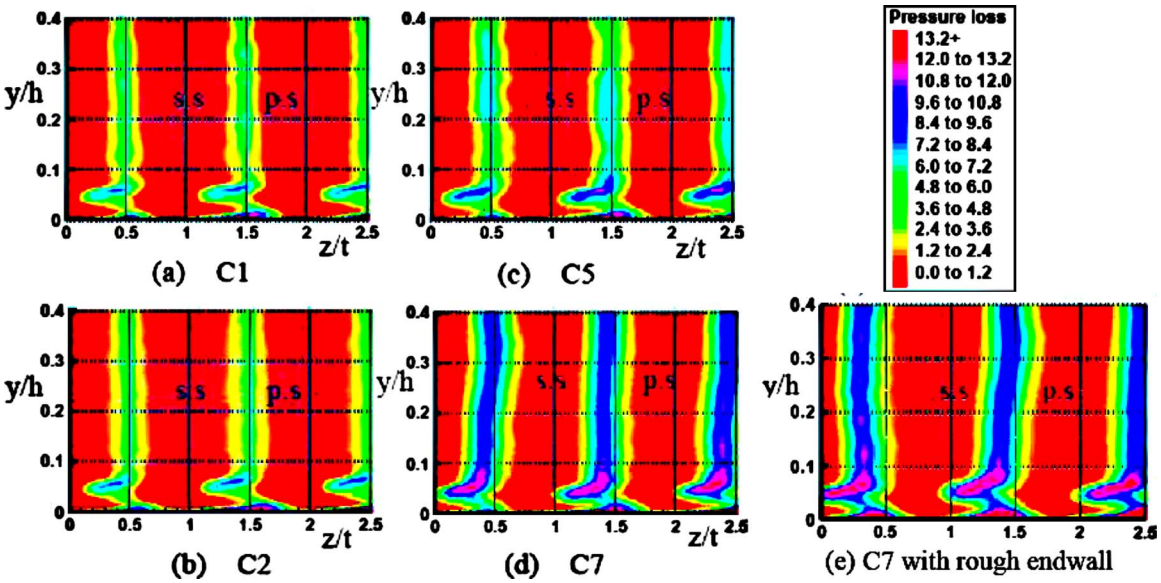

Fig. 12 Turbine vane total pressure loss data from Matsuda et al. [95] for $Re_c=8.7\times10^5$ and Tu=0.5%: ((*a*)–(*d*)) rough vanes with smooth endwall; (*e*) rough C7 vane with rough endwall. ($Re_{cx}\approx0.7\ Re_c$) (Figs. 9 and 15).

geometry modifications. Examples include rotor tip wear [97], leading edge deposit buildup [98], and large surface steps created by TBC spallation [56]. Studies of the impact of these geometry modifications typically neglect the associated surface roughness effects since they are considered to be of secondary importance.

6 Roughness Effects on Film Cooling

Film cooling is employed in high pressure turbine stages to provide a layer of cooler air near the metal surface. The proliferation of film cooling and TBCs has allowed gas turbine firing temperatures to continue rising over the past two decades. Since the highest heat load occurs in the stagnation zone, multiple spanwise rows of compound angle holes are typically used in this region. Additional streamwise-aligned film cooling rows are often found on the pressure surface and near the leading edge on the suction surface as well. Film holes can either be cylindrical or fan-shaped at the exit. The fan shape provides for additional diffusion of the coolant and thus better surface coverage over a wide range of coolant flowrates. Film cooling performance is evaluated using the film cooling effectiveness parameter $\eta=(T_s-T_\infty)/(T_c-T_\infty)$, which is generally spanwise or area-averaged in the region downstream of the film holes. Figure 13 shows the effect of roughness on film cooling effectiveness as reported by Rutledge et al. [99]. For their study, Rutledge et al. used a distributed array of conical roughness elements ($k_s/c\approx8.4\times10^{-4}$) on the surface of a film-cooled HP turbine vane in a low-speed linear cascade ($Re_{cx}\approx5\times10^5$). The trends in the data of Fig. 13 are typical of the results obtained by others [51,100–102]. At low blowing ratios ($M=\rho_c U_c/\rho_\infty U_\infty$), roughness reduces the film effectiveness while at high blowing ratios, roughness can actually improve film effectiveness by limiting jet lift-off from the surface. Surface roughness degrades performance at low blowing ratios through two mechanisms. First, rough surfaces produce thicker boundary layers and thus lower near-wall velocities compared with smooth surfaces. This produces a higher "effective" blowing ratio for the roughness-thickened boundary layer, which can lead to jet lift-off at lower values of M. Second, roughness generates significant near wall turbulence that dissipates coolant more rapidly. Cardwell et al. [103] measured a 30% decrease in endwall film cooling effectiveness due to a combination of these two roughness-induced effects using a vane cascade identical to Rutledge et al. [99]. Their cascade endwall was roughened with 32-grit sandpaper ($Ra=0.23$ mm and $k_s\approx0.64$ mm) while the vane surface was smooth. Film cooling effectiveness alone does not capture the full effect of roughness on film cooling since roughness also enhances surface heat transfer. When the combined effects of film cooling effectiveness and heat transfer are properly accounted for, the result can be a 30–70% increase in surface heat flux with roughness [99] (compared with a smooth surface). Considerable attention has also been given to the damaging effect of flowpath obstructions on film effectiveness, either from deposits [104,105] or TBC residual [106].

7 Roughness Modeling for CFD

Although the focus of this article is the experimental measurements of roughness effects, a brief summary of roughness modeling is included here for completeness. For more detail, the reader can consult any of the excellent references listed in this section. In order to accurately predict the effect of roughness on turbomachinery aerodynamics and heat transfer, models must be developed that account for roughness effects on boundary layer development and transition. Three different modeling strategies have been employed to this end: (1) adding a roughness sensitivity to the turbulent eddy viscosity near the wall; (2) accounting for

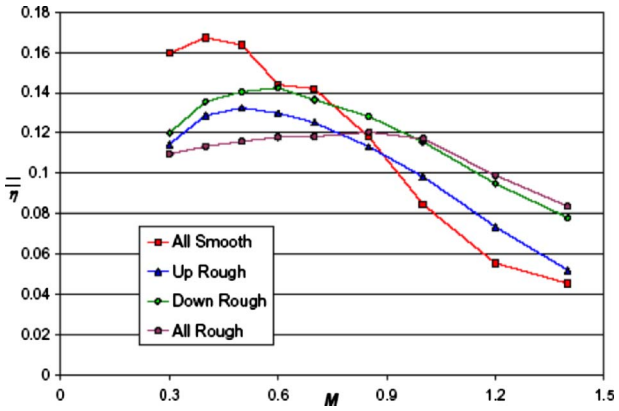

Fig. 13 Area-averaged film effectiveness versus blowing ratio for roughness elements upstream, downstream, or both upstream and downstream ("all") of film holes on vane cascade. $Re_c=1\times10^6$ ($Re_{cx}\approx0.5\ Re_c$) and Tu=6% (Fig. 5 from Rutledge et al. [99]).

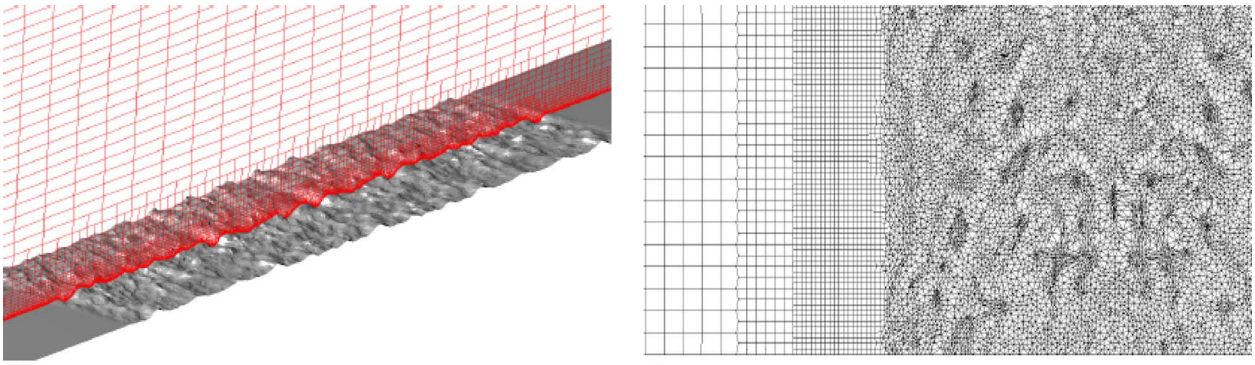

(*a*) (*b*)

Fig. 14 (*a*) Cutting plane showing the viscous adaptive Cartesian grid for a 240×60 mm² patch of erosion roughness. (*b*) Surface grid on the erosion surface showing grid refinement near leading edge. From Bons et al. [119].

roughness blockage, heat transfer, and obstruction drag through a "discrete-element model" (DEM); and (3) fully discretizing the roughness features.

The majority of turbulence models in use today incorporate the turbulent eddy viscosity (μ_t) somehow in their formulation. Accordingly, the most common method of accounting for roughness is to make μ_t a function of roughness height. For example, Boyle [50,107] incorporated Cebeci and Chang's [108] roughness model into a 2D Navier–Stokes solver used for turbine heat transfer predictions by modifying a version of the Baldwin–Lomax turbulent eddy viscosity model. For a rough surface, the turbulent length-scale (and thus μ_t) in this zero-equation model increases with the equivalent roughness height (k_s^+), effectively eroding the effect of viscous damping near the wall (e.g., van Driest damping). Similar implementations have been employed by others [37,69]. Alternative strategies incorporate roughness into the wall boundary condition for μ_t [62,109,110] or ω (in k-ω turbulence model [43,65]) or through modified wall functions [53,111]. Using the Cebeci and Chang model, Boyle and Senyitko reported reasonably accurate predictions for vane profile loss [43] but not for vane heat transfer [112]. This result was only achieved with fine-tuning of both a k_s/Rq correlation and a roughness-induced transition model. The fundamental weakness of these models is their reliance on k_s to characterize the roughness. Even if some consensus could be reached as to the proper conversion from "real" roughness to "equivalent sand" roughness (see discussion above), the roughness "equivalence" (as proposed originally by Schlichting) was only for skin friction (c_f). Therefore, the use of the same k_s for predictions of heat transfer or boundary layer transition in addition to c_f is fundamentally flawed. An excellent review of this issue is given by Aupoix and Spallart [109] and Stripf et al. [74]. In essence, extrapolating from roughness effects on c_f to St is problematic since Reynolds analogy ($2\mathrm{St}/c_f \cong \mathrm{const}$) is inappropriate for rough surfaces [59] and gas turbine flows in general [113].

A popular alternative to k_s-based roughness models is the "discrete-element" approach. This method accounts for the roughness by extra terms in the governing equations, which represent the flow blockage due to the roughnesses and the drag and heat flux on roughness elements [74,92,114–116]. As such, it is not dependent on the appropriateness of Reynolds analogy and does not require a sand-roughness equivalent. Although originally developed for ordered roughness elements (e.g., spheres and cones), this method has been successfully applied to real randomly rough surfaces as well [117,118]. In its current form, the discrete-element method is not formulated for three-dimensional unsteady flowfields and thus has seen limited application to turbomachinery flowfields.

Theoretically, the reliance on roughness models could be eliminated if the roughness is fully resolved with the computational grid. Bons et al. [119] presented a comparison of c_f and St predictions for a 3D Reynolds-averaged Navier–Stokes (RANS) solver and a 2D discrete-element model. The 3D RANS solver (with Spalart–Allmaras turbulence model) required over 1×10^6 cells to adequately resolve the surface features on a 240 $\times$60 mm² patch of scaled turbine roughness (Fig. 14). Figure 15 shows a comparison of the predicted percent increase in c_f and St for the 3D RANS versus the DEM versus an experimental measurement. The results show only marginal differences between the two models, although the 3D high spatial fidelity RANS simulation requires two to three orders of magnitude more computational time for this flat plate turbulent boundary layer test case. Clearly, fully resolving surface roughness features in complex turbomachinery flowfields is beyond current computational resources. Even if the surface roughness is eventually accommodated by the computational grid, there will remain the issue of boundary layer transition. Many of the roughness model implementations cited above fail to provide accurate predictions for c_f and St because they do not adequately model the effect of roughness on transition. Recently, several transition models have been proposed with roughness sensitivity [43,72,74,120]. Stripf et al. [73] combined a discrete-element roughness formulation with a two-layer model of turbulence and a roughness-sensitive transition model to obtain very good agreement with suction surface heat transfer coefficient distributions in a linear turbine vane cascade (Fig. 16).

8 Engineered Roughness for Improved Performance

Because of the beneficial effect of surface roughness in overcoming laminar boundary layer separation at low Reynolds numbers by inducing early transition, roughness has been explored as a form of passive flow control in many turbomachinery applications. Ishida et al. [121] applied a 40-grit sandpaper to the hub-side only of a vaneless diffuser for a centrifugal blower and reported increased stall margin (up to 42%) due to the suppression of three-dimensional separation at low flow rates. The additional pressure drop due to the locally rough wall was less than 1% of the entire pressure rise for the blower. Boese and Fottner [122] studied the application of spanwise aligned v-groove type riblets to a highly loaded compressor cascade and found similar success controlling separation on the suction surface. Their optimal v-groove configuration reduced the total pressure loss coefficient up to a maximum of 5% within the range $1.5\times10^5<\mathrm{Re}_c<11\times10^5$. Riblet heights in excess of 210 μm ($k/c=1.2\times10^{-3}$ and $k^+=21$) caused turbulent boundary layer separation thus increasing profile losses. Optimal performance was for a rib with a height of $k^+=9$ and a spacing of $s^+=18$. Several passive flow control studies have been conducted on low pressure turbine cascades using various roughness elements including trip wires [123,124], roughness [75], spanwise ribs [75], scallops [125], v-grooves

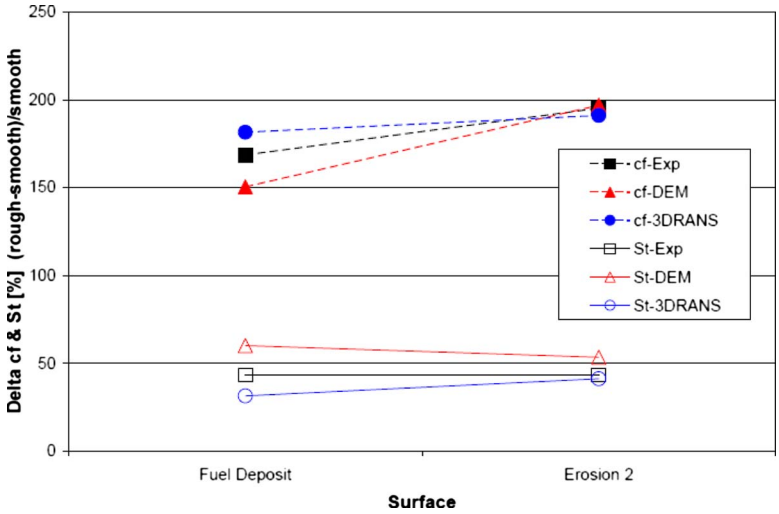

Fig. 15 Comparison of percent change in c_f and St from experiment and computation (3D RANS and DEM). Two different roughness surfaces: fuel deposit and erosion. Zero pressure gradient turbulent boundary layer with Re=1×10^6. From Bons et al. [119].

[126], and dimples [126]. All have shown reasonable success at low Reynolds numbers as expected, although the results are sometimes obscured with the addition of upstream wakes. For rotor tip flow control, Rao et al. [127] artificially roughened the outer rotor casing in their single-stage HP turbine facility and found a significant reduction in leakage mass flow rate and a reduction in momentum deficit for the core of the tip vortex. They speculated that the observed change was due to the roughness-induced increases in the casing boundary layer thickness, thus allowing less mass and momentum flux through the tip gap. Although in many of these cases the same level of roughness could arise due to the natural degradation processes, it is unlikely to occur in precisely the magnitude and location desired by the designer. Thus, strategically engineered roughness may become more commonplace in gas turbines of the future. Although unrelated to the topic of this study, engineered roughness elements in the form of cross stream and angled ribs are routinely used to augment heat transfer in internal turbine cooling passages as well.

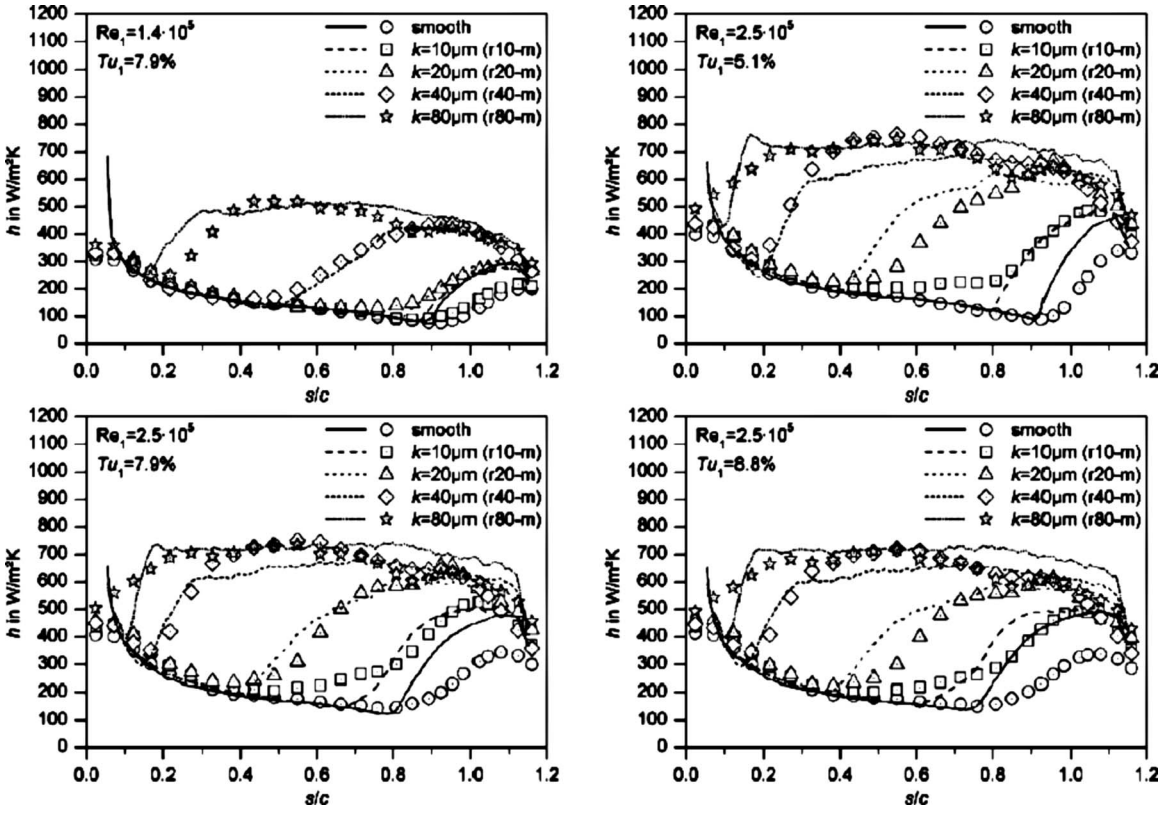

Fig. 16 Comparison of predicted and measured suction side heat transfer coefficient on a linear vane cascade for various roughness heights (k), turbulence levels (Tu_1), and Re_1. (1.6 $Re_1 \approx Re_{cx}$) (Fig. 6 from Stripf et al. [73]).

9 Summary and Conclusions

The adverse effects of surface roughness caused by natural degradation processes in gas turbines have been studied for over half a century. Both compressors and turbines are affected by this phenomenon. While there is some consensus as to the general trends, accurate models for predicting roughness effects on profile losses and surface heat transfer are still beyond our present capability. This is largely due to the rich parameter space required to adequately characterize roughness (e.g., size, shape, spacing, and blade location). The broad use of the equivalent sandgrain roughness characterization (k_s) has hampered modeling since it does not account for different roughness effects on skin friction, heat transfer, and boundary layer transition. Discrete-element and high resolution CFD models are making significant progress to overcoming this shortcoming. Yet, there is still significant work to be done in the area of roughness modeling. The proper accounting of roughness effects on boundary layer transition is a critical aspect of this modeling conundrum. Finally, current roughness models are universally validated with experimental data from ordered roughness elements. Thus, the proper application of these models to the more random roughness characterizations typical of serviced gas turbine hardware is a topic worthy of considerable attention.

Nomenclature

B = log law constant
M = Mach number film cooling blowing ratio, $\rho_c U_c / \rho_\infty U_\infty$
Nu = Nusselt number
Ra = centerline average roughness
Re_c = Reynolds number based on true chord and inlet or exit conditions (for compressor or turbine respectively), unless otherwise noted
Re_{cx} = Reynolds number based on axial chord and inlet or exit conditions (for compressor or turbine respectively), unless otherwise noted
Re_k = roughness Reynolds number ($k_s U_\infty / \nu$)
Re_x = Reynolds number based on streamwise distance (x)
Rq = rms roughness
Rz = average peak to valley roughness
St = Stanton number ($h / \rho c_p U_\infty$)
T = temperature
Tu = freestream turbulence level (%)
U = velocity
b_2 = centrifugal impeller discharge height
c = vane or blade true chord
c_f = skin friction coefficient
c_p = specific heat at constant pressure
c_x = vane or blade axial chord
d_h = hydraulic diameter
h = heat transfer coefficient
k = roughness height
k^+ = dimensionless roughness parameter ($k_s u_\tau / \nu$)
k_s = sand roughness or equivalent sand-roughness height
$k_{s,\mathrm{adm}}$ = admissible sand roughness
t = roughness spacing
u = velocity
u^+ = dimensionless velocity (u / u_τ)
u_τ = shear or friction velocity $(\tau / \rho)^{1/2}$
x = streamwise distance
y^+ = dimensionless wall distance ($y u_\tau / \nu$)
α_f = mean forward facing angle roughness parameter from Bons [59]
δ = boundary layer thickness
κ = von Karman constant (0.41)
Λ_s = roughness shape density parameter from Sigal and Danberg [49]
λ = roughness shape density parameter from Kind et al. [34]
π_c = compressor pressure rise
ρ = fluid density
η = efficiency
η_{film} = film cooling effectiveness $(T_s - T_\infty)/(T_c - T_\infty)$
θ = boundary layer momentum thickness
μ = viscosity
μ_t = turbulent eddy viscosity
ν = kinematic viscosity
ω = total pressure loss coefficient

Subscripts

c = compressor or coolant
ex = exit conditions
in = inlet conditions
s = surface
tr = boundary layer transition
∞ = freestream conditions
1 = inlet conditions
2 = exit conditions

References

[1] Diakunchak, I. S., 1992, "Performance Deterioration in Industrial Gas Turbines," ASME J. Eng. Gas Turbines Power, **114**, pp. 161–168.
[2] Kurz, R., and Brun, K., 2001, "Degradation in Gas Turbine Systems," ASME J. Eng. Gas Turbines Power, **123**, pp. 70–77.
[3] Kacprynski, G. J., Gumina, M., and Roemer, M. J., 2001, "A Prognostic Modeling Approach for Predicting Recurring Maintenance for Shipboard Propulsion Systems," ASME Paper No. 2001-GT-0218.
[4] Caguiat, D. E., Zipkin, D. M., and Patterson, J. S., 2002, "Compressor Fouling Testing on Rolls Royce/Allison 501-K17 and General Electric LM2500 Gas Turbine Engines," ASME Paper No. GT-2002-30262.
[5] Fielder, J., 2003,"Evaluation of Zero Compressor Wash Routine in RN Service," ASME Paper No. GT2003-38887.
[6] Syverud, E., Brekke, O., and Bakken, L. E., 2007, "Axial Compressor Deterioration Caused by Saltwater Ingestion," ASME J. Turbomach., **129**, pp. 119–126.
[7] Ghenaiet, A., Tan, S. C., and Elder, R. L., 2001, "Particles Trajectories Through an Axial Fan and Performance Degradation Due to Sand Ingestion," ASME Paper No. 2001-GT-0497.
[8] Hamed, A. A., Tabakoff, W., Das, K., Rivir, R. B., and Arora, P., 2005, "Turbine Blade Surface Deterioration by Erosion," ASME J. Turbomach., **127**, pp. 445–452.
[9] Haq, I. U., and Bu-Hazza, A. I., 2001, "Modeling and Computation of Fouling of a 36 MW Multistage Centrifugal Compressor Train Operating in a Cracker Gas Environment," ASME Paper No. 2001-GT-0229.
[10] Dunn, M. G., Baran, A. J., and Miatech, J., 1996, "Operation of Gas Turbine Engines in Volcanic Ash Clouds," ASME J. Eng. Gas Turbines Power, **118**, pp. 724–731.
[11] Hefazi, H., Kaups, K., and Murry, R., 1996, "Ice Accretion on a Radial Inflow Turbine Blade," ASME J. Turbomach., **118**, pp. 606–612.
[12] Basler, B., and Marx, D., 2001, "Heavy Fuel Operation at Limay Bataan Power Station," ASME Paper No. 2001-GT-0213.
[13] Basendwah, A. A., Pilidis, P., and Li, Y. G., 2006, "Turbine Off-Line Water Wash Optimization Approach for Power Generation," ASME Paper No. GT2006-90244.
[14] Tarada, F., and Suzuki, M., 1993, "External Heat Transfer Enhancement to Turbine Blading Due to Surface Roughness," ASME Paper No. 93-GT-74.
[15] Taylor, R. P., 1990, "Surface Roughness Measurements on Gas Turbine Blades," ASME J. Turbomach., **112**, pp. 175–180.
[16] Bogard, D. G., Schmidt, D., and Tabbita, M., 1998, "Characterization and Laboratory Simulation of Turbine Airfoil Surface Roughness and Associated Heat Transfer," ASME J. Turbomach., **120**(2), pp. 337–342.
[17] Bons, J. P., Taylor, R. P., McClain, S. T., and Rivir, R. B., 2001, "The Many Faces of Turbine Surface Roughness," ASME J. Turbomach., **123**, pp. 739–748.
[18] Walsh, W. S., Thole, K. A., and Joe, C., 2006, "Effects of Sand Ingestion on the Blockage of Film-Cooling Holes," ASME Paper No. GT2006-90067.
[19] Ghenaiet, A., Tan, S. C., and Elder, R. L., 2002, "Numerical Simulation of the Axial Fan Performance Degradation Due to Sand Ingestion," ASME Paper No. GT-2002-30644.
[20] Ghenaiet, A., Tan, S. C., and Elder, R. L., 2004, "Study of Erosion Effects on an Axial Fan Global Range of Operation," ASME Paper No. GT2004-54169.
[21] Levine, P., and Angello, L., 2005, "Axial Compressor Performance Maintenance," ASME Paper No. GT2005-68014.
[22] Syverud, E., and Bakken, L. E., 2006, "The Impact of Surface Roughness on

Axial Compressor Performance Deterioration," ASME Paper No. GT2006-90004.
[23] Stalder, J.-P., 2001, "Gas Turbine Compressor Washing State of the Art: Field Experiences," ASME J. Eng. Gas Turbines Power, **123**, pp. 363–370.
[24] Veer, T., Haglerod, K. K., and Bolland, O., 2004, "Measured Data Correction for Improved Fouling and Degradation Analysis of Offshore Gas Turbines," ASME Paper No. GT2004-53760.
[25] Zwebek, A., and Plidis, P., 2003, "Degradation Effects on Combined Cycle Power Plant Performance, Part 1: Gas Turbine Cycle Component Degradation Effects," ASME J. Eng. Gas Turbines Power, **125**, pp. 651–657.
[26] Zwebek, A., and Plidis, P., 2003, "Degradation Effects on Combined Cycle Power Plant Performance, Part 2: Steam Turbine Cycle Component Degradation Effects," ASME J. Eng. Gas Turbines Power, **125**, pp. 658–663.
[27] Zwebek, A., and Plidis, P., 2004, "Degradation Effects on Combined Cycle Power Plant Performance, Part 3: Gas and Steam Turbine Degradation Effects," ASME J. Eng. Gas Turbines Power, **126**, pp. 306–315.
[28] Millsaps, K. T., Baker, Lt. J., and Patterson, J. S., 2004, "Detection and Localization of Fouling in a Gas Turbine Compressor From Aerothermodynamic Measurements," ASME Paper No. GT2004-54173.
[29] Tabakoff, W., Lakshminarasimha, A. N., and Pasin, M., 1990, "Simulation of Compressor Performance Deterioration Due to Erosion," ASME J. Turbomach., **112**, pp. 78–83.
[30] Bammert, K., and Milsch, R., 1972, "Boundary Layers on Rough Compressor Blades," ASME Paper No. 72-GT-48.
[31] Wiesner, F. J., 1979, "A New Appraisal of Reynolds Number Effects on Centrifugal Compressor Performance," ASME J. Eng. Power, **101**, pp. 384–396.
[32] Koch, C. C., and Smith, L. H., Jr., 1976, "Loss Sources and Magnitudes in Axial-Flow Compressors," ASME J. Eng. Power, **98**, pp. 411–424.
[33] Simon, H., and Bülskämper, A., 1984, "On the Evaluation of Reynolds Number and Relative Surface Roughness Effects on Centrifugal Compressor Performance Based on Systematic Experimental Investigations," ASME J. Eng. Gas Turbines Power, **106**, pp. 489–501.
[34] Kind, R. J., Serjak, P. J., and Abbott, M. W. P., 1998, "Measurements and Prediction of the Effects of Surface Roughness on Profile Losses and Deviation in a Turbine Cascade," ASME J. Turbomach., **120**, pp. 20–27.
[35] Nikuradse, J., 1933, "Laws for Flows in Rough Pipes," VDI-Forchungsheft 361, Series B, Vol. 4 (English translation NACA TM 1292, 1950).
[36] White, F. M., 1991, *Viscous Fluid Flow*, 2nd ed., McGraw-Hill, New York.
[37] Gbadebo, S. A., Hynes, T. P., and Cumpsty, N. A., 2004, "Influence of Surface on Three-Dimensional Separation in Axial Compressors," ASME Paper No. GT2004–53619.
[38] Schlichting, H., 1936, "Experimentelle Untersuchungen zum Rauhigkeitsproblem," Ingenieur-Archiv, **7**, pp. 1–34.
[39] Schlichting, H., 1979, *Boundary Layer Theory*, 7th ed., McGraw-Hill, New York.
[40] Coleman, H. W., Hodge, B. K., and Taylor, R. P., 1984, "A Re-Evaluation of Schlichting's Surface Roughness Experiment," ASME J. Fluids Eng., **106**, pp. 60–65.
[41] Mills, A. F., 1992, *Heat Transfer*, 1st ed., Irwin, Illinois.
[42] Kays, W. M., and Crawford, M. E., 1993, *Convective Heat and Mass Transfer*, 3rd ed., McGraw-Hill, New York.
[43] Boyle, R. J., and Senyitko, R. G., 2003, "Measurements and Predictions of Surface Roughness Effects on Turbine Vane Aerodynamics," ASME Paper No. GT2003-38580.
[44] Braslow, A.L., 1960, "Review of the Effect of Distributed Surface Roughness on Boundary-Layer Transition," AGARD Report No. 254.
[45] Speidel, L., 1962, "Determination of the Necessary Surface Quality and Possible Losses Due to Roughness in Steam Turbines," Elektrizitätswirtschaft, **61**(21), pp. 799–804.
[46] Forster, V. T., 1966, "Performance Loss of Modern Steam Turbine Plant Due to Surface Roughness," Proc. Instrn. Mech Engrs, **181**(1), pp. 391–405.
[47] Bammert, K., and Sandstede, H., 1976, "Influences of Manufacturing Tolerances and Surface Roughness of Blades on the Performance of Turbines," ASME J. Eng. Power, **98**, pp. 29–36.
[48] Schäffler, A., 1980, "Experimental and Analytical Investigation of the Effects of Reynolds Number and Blade Surface Roughness on Multistage Axial Flow Compressors," ASME J. Eng. Power, **102**, pp. 5–13.
[49] Sigal, A., and Danberg, J., 1990, "New Correlation of Roughness Density Effect on the Turbulent Boundary Layer," AIAA J., **28**(3), pp. 554–556.
[50] Boyle, R. J., and Civinskas, K. C., 1991, "Two-Dimensional Navier–Stokes Heat Transfer Analysis for Rough Turbine Blades," AIAA Paper No. 91-2129.
[51] Barlow, D. N., and Kim, Y. W., 1995, "Effect of Surface Roughness on Local Heat Transfer and Film Cooling Effectiveness," ASME Paper No. 95-GT-14.
[52] Hoffs, A., Drost, U., and Boics, A., 1996, "Heat Transfer Measurements on a Turbine Airfoil at Various Reynolds Numbers and Turbulence Intensities Including Effects of Surface Roughness," ASME Paper No. 96-GT-169.
[53] Guo, S. M., Jones, T. V., Lock, G. D., and Dancer, S. N., 1998, "Computational Prediction of Heat Transfer to Gas Turbine Nozzle Guide Vanes With Roughened Surfaces," ASME J. Turbomach., **120**, pp. 343–350.
[54] Abuaf, N., Bunker, R. S., and Lee, C. P., 1998, "Effects of Surface Roughness on Heat Transfer and Aerodynamic Performance of Turbine Airfoils," ASME J. Turbomach., **120**, pp. 522–529.
[55] Boyle, R. J., Spuckler, C. M., Lucci, B. L., and Camperchioli, W. P., 2001, "Infrared Low-Temperature Turbine Vane Rough Surface Heat Transfer Measurements," ASME J. Turbomach., **123**, pp. 168–177.
[56] Bunker, R. S., 2003, "The Effects of Thermal Barrier Coating Roughness Magnitude on Heat Transfer With and Without Flowpath Surface Steps," ASME Paper No. IMECE2003-41073.
[57] Shabbir, A., and Turner, M. G., 2004, "A Wall Function for Calculating the Skin Friction With Surface Roughness," ASME Paper No. GT2004-53908.
[58] Zhang, Q., and Ligrani, P. M., 2006, "Aerodynamic Losses of a Cambered Turbine Vane: Influences of Surface Roughness and Freestream Turbulence Intensity," ASME J. Turbomach., **128**, pp. 536–546.
[59] Bons, J., 2005, "A Critical Assessment of Reynolds Analogy for Turbine Flows," ASME J. Heat Transfer, **127**, pp. 472–485.
[60] Stripf, M., Schulz, A., and Wittig, S., 2005, "Surface Roughness Effects on External Heat Transfer of a HP Turbine Vane," ASME J. Turbomach., **127**, pp. 200–208.
[61] Hummel, F., Lotzerich, M., Cardamone, P., and Fottner, L., 2005, "Surface Roughness Effects on Turbine Blade Aerodynamics," ASME J. Turbomach., **127**, pp. 453–461.
[62] Yuan, L. Q., and Kind, R. J., 2006, "Measurements and Computations of Compressible Flow Through a Turbine Cascade With Surface Roughness," ASME Paper No. GT2006-90018.
[63] Traupel, W., 1988, *Thermische Turbomaschinen*, Vol. 1, 3rd ed., Springer, Berlin.
[64] Bons, J. P., 2002, "St and c_f Augmentation for Real Turbine Roughness With Elevated Freestream Turbulence," ASME J. Turbomach., **124**, pp. 632–644.
[65] Elmstrom, M. E., Millsaps, K. T., Hobson, G. V., Patterson, J. S., 2005, "Impact of Non-Uniform Leading Edge Coatings on the Aerodynamic Performance of Compression Airfoils," ASME Paper No. GT2005-68091.
[66] Harbeche, U. G., Riess, W., and Seume, J. R., 2002, "The Effect of Milling Process Induced Coarse Surface Texture on Aerodynamic Turbine Profile Losses," ASME Paper No. GT-2002-30333.
[67] Roberts, W. B., Prahst, P. S., Thorp, S., Stazisar, A. J., 2005, "The Effect of Ultrapolish on a Transonic Axial Rotor," ASME Paper No. GT2005-69132.
[68] McIlroy, H. M., Budwig, R. S., and McEligot, D. M., 2003, "Scaling of Turbine Blade Roughness for Model Studies," ASME Paper No. IMECE2003-42167.
[69] Blair, M. F., 1994, "An Experimental Study of Heat Transfer in a Large-Scale Turbine Rotor Passage," ASME J. Turbomach., **116**, pp. 1–13.
[70] Leipold, R., Boese, M., and Fottner, L., 2000, "The Influence of Technical Surface Roughness Caused by Precision Forging on the Flow Around a Highly Loaded Compressor Cascade," ASME J. Turbomach., **122**, pp. 416–425.
[71] Feindt, E. G., 1956, "Untersuchungen uber die Abhangigkeit des Umschlages laminar-turbulent von der Oberflachenrauhigkeit und der Druckverteilung," Diss. Braunschweig, Jb. 1956 Schiffbautechn. Gessellschaft 50, pp. 180–203.
[72] Roberts, S. K., and Yaras, M. I., 2004, "Boundary Layer Transition in Separation Bubbles Over Rough Surfaces," ASME Paper GT2004-53667.
[73] Stripf, M., Schulz, A., Bauer, H. J., 2005, "Surface Roughness and Secondary Flow Effects on External Heat Transfer of a HP Turbine Vane," 17th International Symposium on Air Breathing Engines, ISABE Paper No. 2005-1116.
[74] Stripf, M., Schulz, A., and Bauer, H. J., 2008, "Modeling of Rough Wall Boundary Layer Transition and Heat Transfer on Turbine Airfoils," ASME J. Turbomach., **130**, p. 021003.
[75] Vera, M., Zhang, X. F., Hodson, H., and Harvey, N., 2007, "Separation and Transition Control on an Aft-Loaded Ultra-High-Lift LP Turbine Blade at Low Reynolds Numbers: High-Speed Validation," ASME J. Turbomach., **129**, pp. 340–347.
[76] Pinson, M. W., and Wang, T., 2000, "Effect of Two-Scale Roughness on Boundary Layer Transition Over a Heated Flat Plate: Part 1—Surface Heat Transfer," ASME J. Turbomach., **122**, pp. 301–307.
[77] Bammert, K., and Woelk, G. V., 1980, "The Influence of the Blading Surface Roughness on the Aerodynamic Behavior and Characteristics of an Axial Compressor," ASME J. Eng. Power, 102.
[78] Elrod, R., and King, P. I., 1990, ASME Paper No. 90-GT-208.
[79] Schreiber, H., Steinert, W., and Küsters, B., 2002, "Effects of Reynolds Number and Free-Stream Turbulence on Boundary Layer Transition in a Compressor Cascade," ASME J. Turbomach., **124**, pp. 1–9.
[80] Suder, K. L., Chima, R. V., Strazisar, A. J., and Roberts, W. B., 1995, "The Effect of Adding Roughness and Thickness to a Transonic Axial Compressor Rotor," ASME J. Turbomach., **117**, pp. 491–505.
[81] Roberts, W. B., Armin, A., Kassaseya, G., Suder, K. L., Thorp, S. A., and Strazisar, A. J., 2002, "The Effect of Variable Chord Length on Transonic Axial Rotor Performance," ASME J. Turbomach., **124**, pp. 351–357.
[82] Benra, F., Klapdor, V., Schulten, M., 2006, "Sensitivity Study on the Impact of Surface Roughness Due to Milling on the Efficiency of Shrouded Centrifugal Compressor Impellers," ASME Paper No. GT2006-90499.
[83] Kim, J., Dunn, M. G., Baran, A. J., Wade, D. P., and Tremba, E. L., 1993, "Deposition of Volcanic Materials in the Hot Sections of Two Gas Turbine Engines," ASME J. Eng. Gas Turbines Power, **115**, pp. 641–651.
[84] Wenglarz, R. A., 1992, "An Approach for Evaluation of Gas Turbine Deposition," ASME J. Eng. Gas Turbines Power, **114**, pp. 230–234.
[85] Wenglarz, R. A., and Fox, R. G., Jr., 1990, "Physical Aspects of Deposition From Coal-Water Fuels Under Gas Turbine Conditions," ASME J. Eng. Gas Turbines Power, **112**, pp. 9–14.
[86] Borom, M. P., Johnson, C. A., and Peluso, L. A., 1996, "Role of Environmental Deposits and Operating Surface Temperature in Spallation of Air Plasma Sprayed Thermal Barrier Coatings," Surf. Coat. Technol., **86–87**, pp. 116–126.
[87] Bunker, R. S., 1997, "Effect of Discrete Surface Disturbances on Vane External Heat Transfer," International Gas Turbine and Aeroengine Congress & Exhibition, June.

[88] Bammert, K., and Sandstede, H., 1972, "Measurements Concerning the Influence of Surface Roughness and Profile Changes on the Performance of Gas Turbines," ASME J. Eng. Power, **122**, pp. 207–213.
[89] Yun, Y. I., Park, I. Y., and Song, S. J., 2005, "Performance Degradation Due to Blade Surface Roughness in a Single-Stage Axial Turbine," ASME J. Turbomach., **127**, pp. 137–143.
[90] Boynton, J. L., Tabibzadeh, R., and Hudson, S. T., 1993, "Investigation of Rotor Blade Roughness Effects on Turbine Performance," ASME J. Turbomach., **115**, pp. 614–620.
[91] Dunn, M. G., Kim, J., Civinskas, K. C., and Boyle, R. J., 1994, "Time-Averaged Heat Transfer and Pressure Measurements and Comparison With Prediction for a Two-Stage Turbine," ASME J. Turbomach., **116**, pp. 14–22.
[92] Taylor, R. P., Taylor, J. K., Hosni, H. H., and Coleman, H. W., 1992, "Heat Transfer in the Turbulent Boundary Layer With a Step Change in Surface Roughness," ASME J. Turbomach., **114**, pp. 788.
[93] Bunker, R. S., 1997, "Separate and Combined Effects of Surface Roughness and Turbulence Intensity on Vane Heat Transfer," International Gas Turbine and Aeroengine Congress & Exhibition, June.
[94] Zhang, Q., Goodro, M., Ligrani, P. M., Trindade, R., and Sreekanth, S., 2006, "Influence of Surface Roughness on the Aerodynamic Losses of a Turbine Vane," ASME J. Turbomach., **128**, pp. 568–578.
[95] Matsuda, H., Otomo, F., Kawagishi, H., Inomata, A., Niizeki, Y., and Sasaki, T., 2006, "Influence of Surface Roughness on Turbine Nozzle Profile Loss and Secondary Loss," ASME Paper No. GT2006-90828.
[96] Waigh, D. R., and Kind, R. J., 1998, "Improved Aerodynamic Characterization of Regular Three-Dimensional Roughness," AIAA J., **36**(6), pp. 1117–1119.
[97] Bunker, R. S., and Bailey, J. C., 2001, "Effect of Squealer Cavity Depth and Oxidation on Turbine Blade Tip Heat Transfer," ASME Paper No. 2000-GT-0155.
[98] El-Batsh, H., and Haselbacher, H., 2002, "Numerical Investigation of the Effect of Ash Particle Deposition on the Flow Field Through Turbine Cascades," ASME Paper No. GT-2002–30600.
[99] Rutledge, J. L., Robertson, D., and Bogard, D. G., 2006, "Degradation of Film Cooling Performance On a Turbine Vane Suction Side Due To Surface Roughness," ASME J. Turbomach., **128**, pp. 547–554.
[100] Goldstein, R. J., Eckert, E. R. G., Chiang, H. D., and Elovic, E., 1985, "Effect of Surface Roughness on Film Cooling Performance," ASME J. Eng. Gas Turbines Power, **107**, pp. 111–116.
[101] Bogard, D., Snook, D., and Kohli, A., 2003, "Rough Surface Effects on Film Cooling of the Suction Side Surface of a Turbine Vane," ASME Paper No. 2003-42061.
[102] Schmidt, D.L., Sen, B., Bogard, D.G., "Effects of Surface Roughness on Film Cooling," ASME Paper No. 96-GT-299.
[103] Cardwell, N. D., Sundaram, N., and Thole, K. A., 2006, "Effects of Mid-Passage Gap, Endwall Misalignment and Roughness on Endwall Film-Cooling," ASME J. Turbomach., **128**, pp. 62–70.
[104] Demling, P., and Bogard, D. G., 2006, "The Effects of Obstructions on Film Cooling Effectiveness on the Suction Side of a Gas Turbine Vane," ASME Paper No. GT2006-90577.
[105] Sundaram, N. and Thole, K. A., 2006, "Effects of Surface Deposition, Hole Blockage, and TBC Spallation on Vane Endwall Film-Cooling," ASME Paper No. GT2006-90379.
[106] Bunker, R. S., 2000, "Effect of Partial Coating Blockage on Film Cooling Effectiveness," ASME Paper No. 2000-GT-0244.
[107] Boyle, R. J., 1994, "Prediction of Surface Roughness and Incidence Effects on Turbine Performance," ASME J. Turbomach., **116**, pp. 745–751.
[108] Cebeci, T., and Chang, K. C., 1978, "Calculation of Incompressible Rough-Wall Boundary Layer Flows," AIAA J., **16**(7), pp. 730–735.
[109] Aupoix, B., and Spalart, P.R., 2003, "Extensions of the Spalart–Allmaras Turbulence Model to Account for Wall Roughness," Int. J. Heat Fluid Flow, **24**(4), pp. 454–462.
[110] Lee, J., and Paynter, G.C., 1996, "Modified Spalart–Allmaras One Equation Turbulence Model for Rough Wall Boundary Layers," J. Propul. Power, **12**(4), pp. 809–812.
[111] Kang, Y. S., Yoo, J. C., and Kang, S. H., 2004, "Numerical Study of Roughness Effects on a Turbine Stage Performance," ASME Paper No. GT2004-53750.
[112] Boyle, R. J., and Senyitko, R. G., 2005, "Effects of Surface Roughness on Turbine Vane Heat Transfer," ASME Paper No. GT2005-68133.
[113] Holley, B.M., and Langston, L.S., 2006, "Surface Shear Stress and Pressure Measurements in a Turbine Cascade," ASME Paper No. GT2006-90580.
[114] Tarada, F. H. A., 1987, "Heat Transfer to Rough Turbine Blading," Ph.D. thesis, University of Sussex, Brighton.
[115] Tolpadi, A. K., and Crawford, M. E., 1998, "Predictions of the Effect of Roughness on Heat Transfer From Turbine Airfoils," ASME Paper No. 98-GT-87.
[116] Aupoix, B., 1994, "Modelling of Boundary Layers over Rough Surfaces," *Advances in Turbulence V*, Fifth European Turbulence Conference, Sienna, R. Benzi, ed., Kluwer, Dordrecht, pp. 16–20.
[117] Bons, J. P., and McClain, S. T., 2004, "The Effect of Real Turbine Roughness with Pressure Gradient on Heat Transfer," ASME J. Turbomach., **126**, pp. 385–394.
[118] McClain, S. T., Hodge, B. K., and Bons, J. P., 2004, "Predicting Skin Friction and Heat Transfer for Turbulent Flow Over Real Gas-Turbine Surface Roughness Using the Discrete-Element Method," ASME J. Turbomach., **126**, pp. 259–267.
[119] Bons, J. P., McClain, S. T., Wang, Z. J., Chi, X., and Shih, T. I., 2008, "A Comparison of Approximate vs. Exact Geometrical Representations of Roughness for CFD Calculations of cf and St," ASME J. Turbomach., **130**, p. 021024.
[120] Roberts, S. K., and Yaras, M. I., 2003, "Modeling of Boundary Layer Transition," ASME Paper No. GT2004-53664.
[121] Ishida, M., Sakaguchi, D., and Ueki, H., 2001, "Suppression of Rotating Stall by Wall Roughness Control in Vaneless Diffusers of Centrifugal Blowers," ASME J. Turbomach., **123**, pp. 64–72.
[122] Boese, M., and Fottner, L., 2002, "Effects of Riblets on the Loss Behavior of a Highly Loaded Compressor Cascade," ASME Paper No. GT-2002-30438.
[123] Vera, M., Hodson, H. P., and Vazquez, R., 2005, "The Effects of a Trip Wire and Unsteadiness on a High Speed Highly Loaded Low-Pressure Turbine Blade," ASME J. Turbomach., **127**, pp. 747–754.
[124] Volino, R. J., 2003, "Passive Flow Control on Low-Pressure Turbine Airfoils," ASME J. Turbomach., **125**, pp. 754–764.
[125] Pacciani, R., and Spano, E., 2006, "Numerical Investigation of the Effect of Roughness and Passing Wakes on LP Turbine Blades Performance," ASME Paper No. GT2006-90021.
[126] Lake, J. P., King, P. I., and Rivir, R. B., "Low Reynolds Number Loss Reduction on Turbine Blades with Dimples and V-Grooves," AIAA Paper No. 00-738.
[127] Rao, N. M., Gumusel, B., Kavurmacioglu, L., and Camcl, C., 2006, "Influence of Casing Roughness on the Aerodynamic Structure of Tip Vortices in an Axel Flow Turbine," ASME Paper No. GT2006-91011.

Predictions of Turbulent Flow for the Impeller of a NASA Low-Speed Centrifugal Compressor

K. M. Guleren[1]
Department of Mechanical Engineering,
Faculty of Engineering,
Cumhuriyet University,
Sivas, 58140, Turkey
e-mail: melihguleren@cumhuriyet.edu.tr

I. Afgan
Institute of Avionics and Aeronautical Engineering,
Air University,
Sector E-9,
Islamabad, 44200, Pakistan

A. Turan
School of MACE,
University of Manchester,
George Begg Building,
Sackville Street, P.O. Box 88,
Manchester, M60 1QD, UK

The turbulent flow inside a low-speed centrifugal compressor at design condition is investigated using large-eddy simulation (LES) comprising of up to 26×10^6 computational volume cells. Unlike in the past, the current study's special emphasis is placed on the turbulence field evolution inside the impeller. LES predictions suggest that the Boussinesq hypothesis does not seem to be valid, especially near the exit of the impeller where the blade unloading takes place. Reynolds stress variations show a tendency toward an "axisymmetric expansion" type of turbulence after the impeller exit for which the subgrid-scale stress contribution shows a monotonic decrease. Probability density function analysis for the leakage flow show that instantaneous velocities in the wake region are less intermittent as compared with those in the jet. Time spectra analysis display also another feature that the energy cascade proceeds at a higher rate and lasts longer in the wake region than in the tip jet region. [DOI: 10.1115/1.3140824]

Keywords: LES, centrifugal compressor, tip leakage, turbulence

1 Introduction

The centrifugal compressor is a pressure raising turbomachinery component in which the fluid flow is subjected to strong centrifugal and Coriolis forces. Centrifugal compressors produce higher operating flatter efficiency than axial compressors over a wide range of rotational speeds. However, the efficiency and the performance can be severely affected by the nonuniformities and the unsteadiness of the flow caused by the geometrical characteristics of the centrifugal compressor.

Numerous experimental and numerical studies provided insights into the understanding of the basic flow physics in centrifugal turbomachinery. The "jet-wake" flow phenomenon was first revealed by Dean and Senoo [1] and was later confirmed by Eckardt [2]. The origin and development of the wake region can be strongly altered by the tip clearance flow in unshrouded centrifugal compressors. Hah and Krain [3] showed that the swirling flow and the vortex motion inside the unshrouded impeller are greatly influenced by the relative motion between the rotating impeller and the stationary shroud and, hence, they suggested that the tip clearance should be properly modeled. Hathaway et al. [4] and Zhang et al. [5] simulated the flow in an unshrouded compressor and failed to predict accurately both the size and the original location of the wake region. Byskov et al. [6] presented the earliest large-eddy simulation (LES) predictions for the complex flow in a centrifugal pump. Later, Kato et al. [7] produced typical aeroacoustics studies for a centrifugal pump.

In spite of these studies, there is still a lack of understanding regarding the turbulence field evolution inside the centrifugal turbomachinery. Therefore, this study is dedicated to show the turbulence behavior based on a well resolved LES.

2 Numerical Aspects

2.1 LES and the Numerical Solver. In direct numerical simulation (DNS), all turbulent scales have to be resolved. In large-eddy simulation, on the other hand, only the larger scales are resolved and the smaller ones are modeled via a subgrid-scale (SGS) model. In order to rigorously account for the large scale behavior in the presence of modeled small scales, a filtering operation is performed. The filtered continuity and Navier–Stokes equations read as

$$\frac{\partial \bar{u}_i}{\partial x_i} = 0 \tag{1}$$

and

$$\frac{\partial \bar{u}_i}{\partial t} + \frac{\partial (\bar{u}_i \bar{u}_j)}{\partial x_j} + 2 \in_{ijk} \Omega_j \bar{u}_k = -\frac{1}{\rho}\frac{\partial \bar{p}}{\partial x_i} + \frac{\partial}{\partial x_j}\left(\upsilon \frac{\partial \bar{u}_i}{\partial x_j}\right) - \frac{\partial \tau_{ij}^{\mathrm{SGS}}}{\partial x_j} \tag{2}$$

respectively. The third term on the left hand side of Eq. (2) is the Coriolis force contribution. As is customary, the centrifugal force is combined with the pressure gradient since it is conservative. The last term of Eq. (2) represents the contribution of the SGS stresses that are modeled using the wall-adapting local eddy-viscosity (WALE) model [8]. The WALE model is based on the square of the velocity gradient tensor and represents the near-wall behavior better than the classical Smagorinsky model [9]. In the WALE model, the SGS viscosity becomes

$$\nu_t = (C_w \Delta)^2 \frac{(S_{ij}^d S_{ij}^d)^{3/2}}{(\bar{S}_{ij}\bar{S}_{ij})^{5/2} + (S_{ij}^d S_{ij}^d)^{5/4}} \tag{3}$$

where $C_w = 0.1$ is the model coefficient, Δ is the filler width, $S_{ij}^d = \frac{1}{2}(\bar{g}_{ij}^2 + \bar{g}_{ji}^2) - \frac{1}{3}\delta_{ij}\bar{g}_{kk}^2$, and $\bar{g}_{ij} = \partial \bar{u}_i / \partial x_j$. Since $S_{ij}^d S_{ij}^d$ behaves like $O(y^{+2})$ near the wall, $(S_{ij}^d S_{ij}^d)^{3/2}$ becomes $O(y^{+3})$. The denominator of Eq. (3) is $O(1)$ since S_{ij} is $O(1)$. In order to avoid ill conditioning, $(S_{ij}^d S_{ij}^d)^{5/4}$ is added in to the denominator. $(S_{ij}^d S_{ij}^d)^{5/4}$ is $O(y^{+5/2})$ and negligible near the wall. With this form, Eq. (3) becomes $O(y^{+3})$. In the Smagorisnky model [9], on the other hand, the SGS viscosity reads as $\upsilon_t = (C_s \Delta)^2 |\bar{S}|$, where C_s is the

[1]Corresponding author.

Contributed by the Turbomachinery Division of ASME for publication in the JOURNAL OF TURBOMACHINERY. Manuscript received June 19, 2007; final manuscript received February 6, 2008; published online January 11, 2010. Review conducted by Nick Cumpsty.

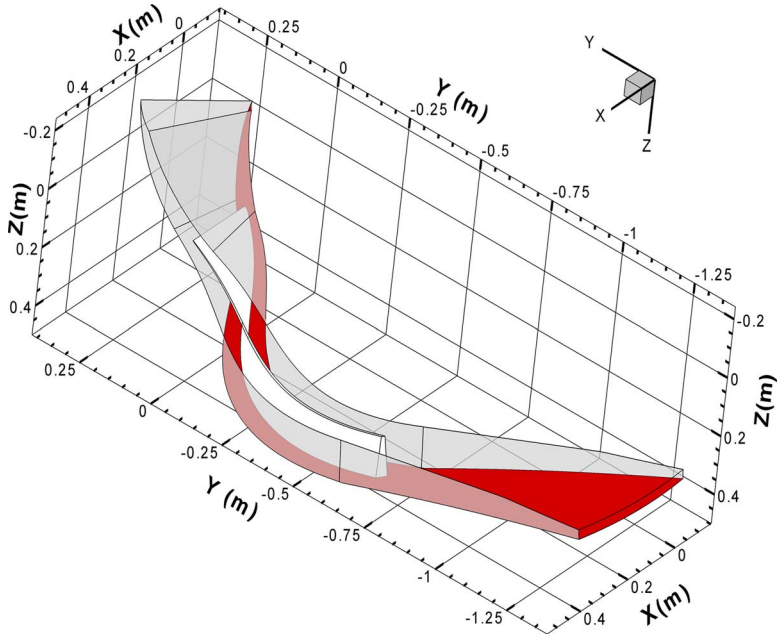

Fig. 1 Three-dimensional view of the LSCC blade passage

model coefficient and $|\bar{S}| = \sqrt{2\bar{S}_{ij}\bar{S}_{ij}}$. The SGS has the incorrect wall behavior of $O(1)$ since S_{ij} is $O(1)$.

The governing differential equations for Eqs. (1) and (2) are solved via a finite volume technique based on the projection method [10]. For all calculations, a bounded central differencing scheme is used. A full second-order implicit scheme is applied for the temporal discretization. The pressure-implicit with splitting of operators (PISO) algorithm and pressure staggering option (PRESTO) scheme are adopted for the velocity-pressure coupling and the pressure interpolation, respectively. The set of linearized equations are solved by the Gauss–Seidel method, which is coupled with an algebraic multigrid method to accelerate convergence.

2.2 Case Model and Flow Conditions. In this paper, LES results for the NASA low-speed centrifugal compressor (LSCC) [4] are presented for the first time in the open literature. Low-speed centrifugal compressors are more suitable for the current established LES methodologies than their high-speed counterparts considering the Reynolds number and the compressibility effects. The variation in density throughout the compressor is negligible, as shown by Moore and Moore [11] for the NASA LSCC. This results in justifying the use of an incompressible flow assumption which further eliminates the concerns regarding the subgrid-scale modeling and the boundary condition implementation accompanying the case of compressible LES.

The LSCC was designed to duplicate the essential flow physics in a high-speed subsonic centrifugal compressor. In fact, Hathaway et al. [4] showed that the LSCC results are similar to the results presented for the high-speed centrifugal compressor [12,13] and concluded that the NASA LSCC is also representative of the prevalent flow features in a typical high-speed unshrouded centrifugal compressor. Therefore, to validate the current numerical predictions, we used the experimental data of Hathaway et al. [4].

The NASA LSCC is composed of two parts: a backswept impeller and a vaneless diffuser. The impeller has 20 full blades with a 55 deg backsweep angle. The design tip speed, U_e, is 153 m/s according to the experimental measurements. Inlet and exit diameters of the impeller are 87 cm and 152.4 cm, respectively. Heights of the impeller blades at the inlet and the exit are 21.8 cm and 14.1 cm, respectively. This corresponds to a tip clearance percentage of 1.165 and 1.8 at the inlet and the exit, respectively. For the LSCC, the design mass flow rate is 30 kg/s and the rotational speed is 1862 rpm.

A three-dimensional view of the LSCC blade passage is shown in Fig. 1. The shroud is removed for the sake of clarity. Semitransparent periodic boundaries provide a better view of the impeller blade (colored white) and the hub (colored black). Upstream and downstream regions of the impeller follow the inlet and the exit of the blade angles, respectively.

2.3 Grid Distribution. Meridional cross-sectional stations are divided into five subregions for ease of a structured grid layout. In the simulated geometry, there are 13 impeller stations (12 sections) accounting for 60 computational blocks created to geometrically outline the impeller. Including 5 blocks in the upstream and 40 blocks downstream of the impeller passages; this number increases to 105. Three grid topologies, namely, the coarse mesh (CM), the medium mesh (MM), and the fine mesh (FM), are adopted in this study to delineate the grid dependency. For all grid topologies, the mesh is refined near the hub and at the tip of the blade. Along the pitchwise direction and in the tip clearance region, uniform grid spacing is utilized. A structured grid is also adopted along the meridional direction. Near the leading edge of the impeller blade, the grid is refined as dictated by the high curvature regions of the leading edge. In order to avoid highly skewed cells, the grid is "body-fitted" near the high curvature regions. The meridional and the cross-sectional views of the grid distribution are depicted in Fig. 2. The entire grid distribution for the centrifugal compressor, including upstream and downstream of the impeller regions are tabulated in Table 1. More information about the grid distribution can be found in Ref. [14].

2.4 Boundary Conditions and Rotation Model. In the current study, the multiple reference frame (MRF) model [15] is adopted for the flow rotation in a centrifugal impeller. The MRF model requires a specification of the rotation rate for each subdomain. Zero rotation, therefore, represents a stationary flow. The flow in the impeller $(0 < m_i/m < 1)$ is assumed to be rotating with the same rotational speed as that of the impeller (1862 rpm). Therefore, the impeller blades and the attached hub surfaces are also rotating at 1862 rpm. No-slip boundary conditions are applied at the shroud walls. Upstream $(m_i/m < 0)$ and downstream

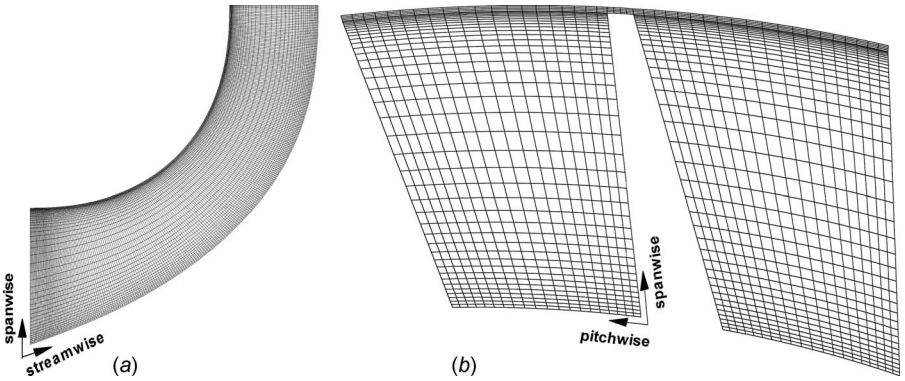

Fig. 2 Coarse grid distribution on the meridional plane (*a*) and on the cross-sectional plane (*b*)

($m_i/m>1$) impeller zones are assumed to be stationary and hence no-slip boundary conditions are also applied for the hub and shroud walls in these regions. As shown by the semitransparent surface in Fig. 1, periodic boundaries are located at the midpitch. These periodic boundaries are extended upstream and downstream of the impeller by following the blade inlet and exit angles, respectively. Available experimental data of velocity components at the inlet station ($m_i/m=-0.38$) are interpolated to the computational grid and used as the velocity inlet boundary condition. The two-dimensional random vortex method [16] is utilized to perturb the inlet flow field. At the outlet, the velocity variables are extrapolated from within the domain and have no effect on the upstream flow. The extrapolation procedure results in a reasonable pressure gradient not only from the pressure side (PS) to the suction side (SS), but also provides a realistic variation in pressure variation from the hub to shroud sides. Therefore, a consistent blade loading in agreement with the experimental measurements is achieved with the current outflow condition.

2.5 Temporal and Spatial Resolution. The time step is chosen in such a way that one blade passing is completed in 100 time steps. This corresponds to 2000 time steps to complete one full impeller revolution. LES calculations are performed 10,000 time steps (five full impeller revolutions) to reach the statistically stationary state. Another 30,000 time steps (15 full impeller revolutions) are performed to collect the flow statistics. Since the impeller rotational speed is 1862.4 rpm, one revolution is completed in 3.2×10^{-2} s and, hence, one blade passing lasts 1.6×10^{-3} s. Therefore, the time step (t) becomes 1.6×10^{-5} s. To find out whether the adopted time scale is adequate enough to capture the small scales, the time scales associated with larger scales ($T=k/\varepsilon$), the Taylor time scales ($\lambda_t=15\nu/\varepsilon)^{1/2}$ and the smallest time scales (the Kolmogorov time scales, $\tau=(\nu/\varepsilon)^{1/2}$) are calculated as area-averaged values on the meridional stations and compared with the physical time step size chosen for the LES cases. As shown in Fig. 3(*a*), the adopted numerical time step is even smaller than the Kolmogorov time scale for the meridional stations.

The estimation of the spatial (grid) resolution is based on the same calculation principles as that of the temporal resolution. In this case, the larger length scales ($L=k^{1.5}/\varepsilon$), the Taylor length scales ($\lambda=(10\ \nu k/\varepsilon)^{1/2}$), and the Kolmogorov length scales ($\eta=(\nu^3/\varepsilon)^{1/4}$) are calculated and compared with the filter length ($\Delta=V^{1/3}$) of the three different grid topologies. Figure 3(*b*) shows the location of the adopted grid topologies among these length scales. Generally, the CM lies between the larger length (L) and the Taylor (λ) length scales. In the context of LES, the CM seems to be acceptable according to Fig. 3(*b*). However, since the aim of the current study is to reveal refined flow physics, then at least a Taylor scale resolution is required. This is achieved with the MM everywhere in the computational domain apart from the blade wake region ($1<m_i/m<1.1$). The FM case provides much better resolution, since it is even smaller than Taylor scales without any exceptions.

3 Results and Discussion

3.1 Grid Dependency. Figure 4 shows the meridional velocity distribution from the impeller inlet to the impeller exit at midpitch for two spanwise locations. The flow accelerates gradually starting from the impeller inlet till $m_i/m=0.3$ for 50% span and $m_i/m=0.25$ for 90% span then decelerates continuously. The deceleration of the flow is often referred to as diffusion (pressure conversion) of the flow. The diffusion rate of the flow is higher at 90% span due to the effect of the wake region, which will be discussed later in detail. The MM results are consistent with the FM results. The CM results, on the other hand, display marked differences compared with the FM results, especially at 90% span. To summarize, the grid sensitivity test shows that mean flow results of the MM and FM cases coincide, suggesting that at least for the meridional velocity field grid dependency is reasonably achieved. Due to the space limitation, y^+ distributions are not shown. However, detailed information about y^+ distributions is available in Ref. [14].

3.2 The Reverse Flow Mechanism. The flow reversal is thought to be an undesirable feature in centrifugal compressors, as for many turbomachinery applications. At the design flow rate, it is attributed to the extremely complex flow field existing therein. There is little understanding of this complex flow phenomenon,

Table 1 Grid distribution for the centrifugal compressor

	Streamwise			Spanwise			
	Upstream	Impeller	Diffuser	Tip	Blade	Pitchwise	Total (10^6)
CM	50	284	123	4	40	40	0.9
MM	100	512	144	8	80	80	7
FM	120	791	200	16	120	150	26

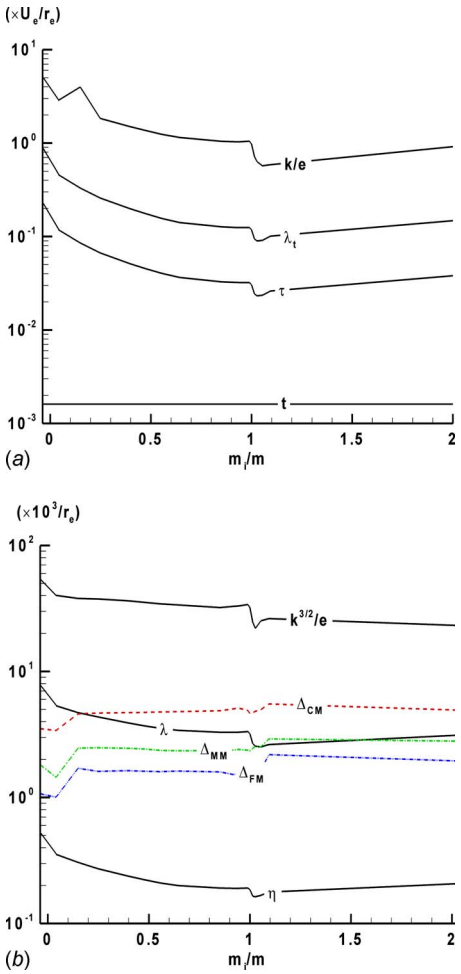

Fig. 3 Time (*a*) and grid resolution (*b*) of LES study for LSCC

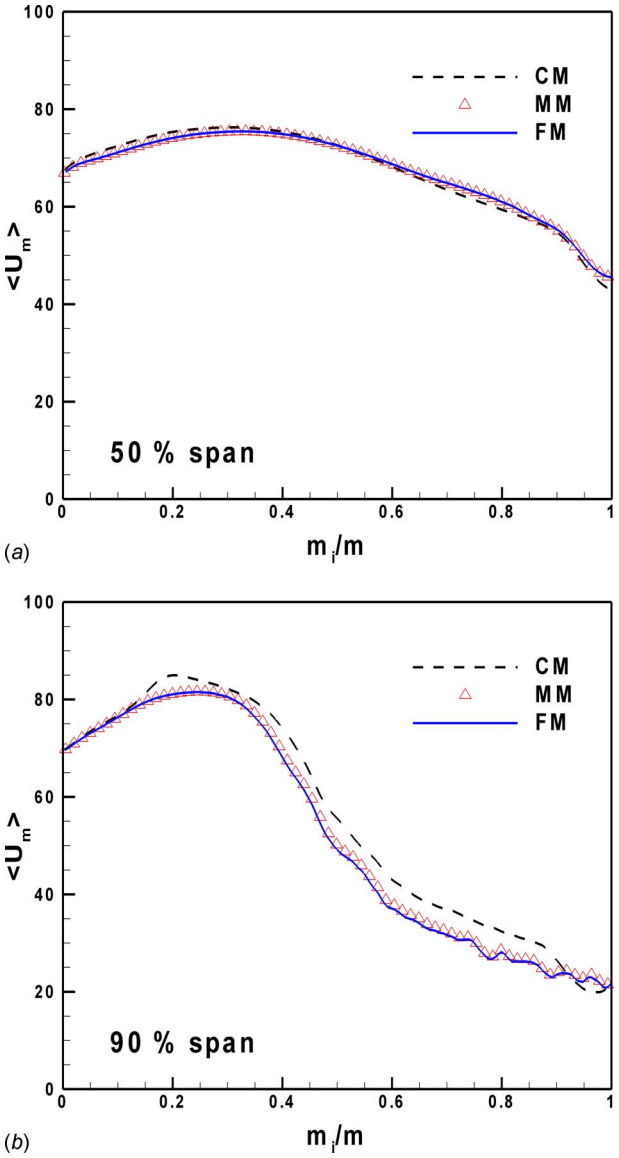

Fig. 4 Meridional velocity comparisons for LES cases at 50% (*a*) and at 90% (*b*) span form the hub

which consequently affects design strategies adopted for advanced compressor designs. In order to find out whether this feature also exists in this particular configuration, the best way would be to investigate the meridional velocity and the flow streamlines along the meridional plane. The previous discussion on the meridional velocity was limited to a 90% span. In this section, the meridional variation is demonstrated close to the casing.

Meridional velocity contours close to the impeller exit at 30% and 50% pitch from the PS are displayed in Figs. 5(*a*) and 5(*b*), respectively. The flow is found to be more susceptible to separation at the impeller exit along the midpitch location due to the strong deceleration. In fact, a closer view near the impeller exit shows the existence of reverse flow. The flow detaches from the shroud just before the impeller exit but soon after attaches in the diffuser region. A vortex bubble is formed within the separation region. At midpitch, it is seen that the vortex has a meridional length of around 3.5 cm and a spanwise length of 0.9 cm. Whereas the vortex size is significantly reduced along the 30% pitch.

3.3 Turbulence Mechanism in the LSCC. Information about the turbulence behavior in a centrifugal compressor is very limited and is not very well known. In this section, the LES predicted turbulence field evolution is investigated in detail by examining attributes from the turbulent kinetic energy, the production of turbulence, the contribution of the SGS viscosity, the Reynolds stress anisotropy, the probability distribution function (PDF), and the power spectral density (PSD) analyses.

The normalized kinetic energy distributions ($100\times\sqrt{k}/U_e$, where k is the turbulent kinetic energy and U_e is the tip velocity) at selected meridional cross sections (perpendicular to streamwise direction) are shown in Fig. 6. At $m_i/m=0.149$, turbulence is initially created near the suction side/hub corner. The tip jet, which originates due the pressure difference between the pressure and suction sides, moves in the opposite direction of the compressor rotation, convecting turbulence into the passage. At $m_i/m=0.475$, corresponding to the enlargement of the wake, turbulence is diffused toward the pressure side. Near the SS, a turbulent region is formed due to the increase in the boundary layer. The same level of turbulence is not seen near the PS. At $m_i/m=0.644$, turbulence is diffused further corresponding to the enlargement of the wake. Turbulence near the blade root on the SS is higher in comparison to the previous station, which is due to the interaction of the boundary layer with the tip jet. At $m_i/m=0.921$, the maximum turbulence level is reduced, but the extent of the region subjected to significant turbulence is increased.

The production of turbulence $P_{ii}=-2\langle u_i u_k\rangle \partial U_i/\partial x_k$, which is discussed here only in terms of streamwise components, is proportional to the velocity gradients and the Reynolds stresses. All the turbulent quantities are normalized with the tip velocity, U_e and the exit radius of the impeller, r_e. Figure 7(*a*) shows the

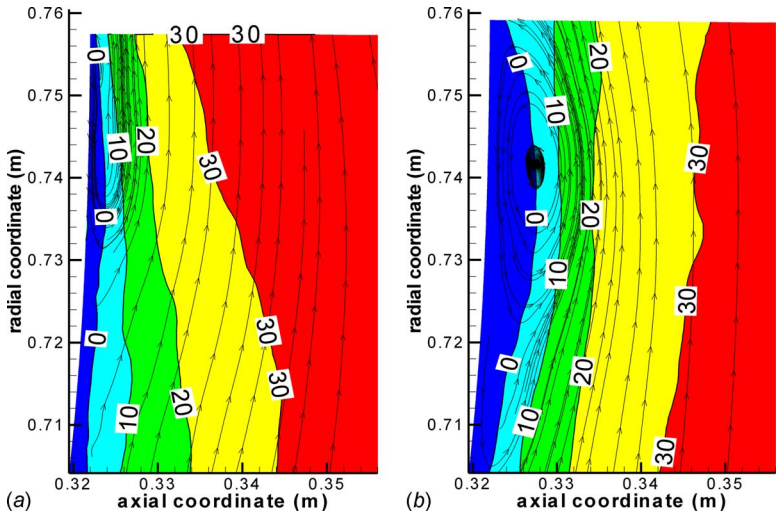

Fig. 5 Meridional velocity variation and reverse flow mechanism near the impeller exit: (*a*) 30% pitch from PS and (*b*) 50% pitch from the PS

gradient of meridional velocity at mid pitch. The primary flow accelerates until $m_i/m \approx 0.35$. The tip clearance flow, on the other hand, decelerates at a high rate. After the onset of the wake around $m_i/m \approx 0.40$, the primary flow decelerates but at a low rate. The deceleration of the flow in the wake region is hence reduced, and the meridional velocity gradient becomes positive near the exit due to the blade unloading. The Reynolds normal stresses in the meridional direction at midpitch are shown in Fig. 7(*b*). The variation in the meridional normal stress is in accordance with the variation in the turbulent kinetic energy. This stress is mostly produced in the wake region. Highest stresses are observed as soon as the wake develops. Stresses decrease after $m_i/m=0.55$, since the effect of curvature decreases. Figure 7(*c*) shows the production of the turbulence. The sign of the turbulence production is dictated by the velocity gradients. Near the shroud, low values of turbulence production are located for $m_i/m<0.35$ and close to the impeller exit. On the other hand, high values of turbulence production are located where the meridional normal stresses are high. One can also observe from the same figure that turbulence production is reduced in conjunction with a decrease in meridional normal stress. If only the wake is considered, one notices that a limited qualitative agreement exists between the meridional normal stress and the meridional velocity gradients. The highest stress level regions are where the highest velocity gradients occur, whereas the stresses are reduced in response to a decrease in velocity gradients. However, the blade unloading effect is not actually seen by the stresses and the negative meridional velocity gradients from the inlet of the impeller do not start till around $m_i/m=0.35$.

Figure 8 shows the correlation between the turbulent intensity

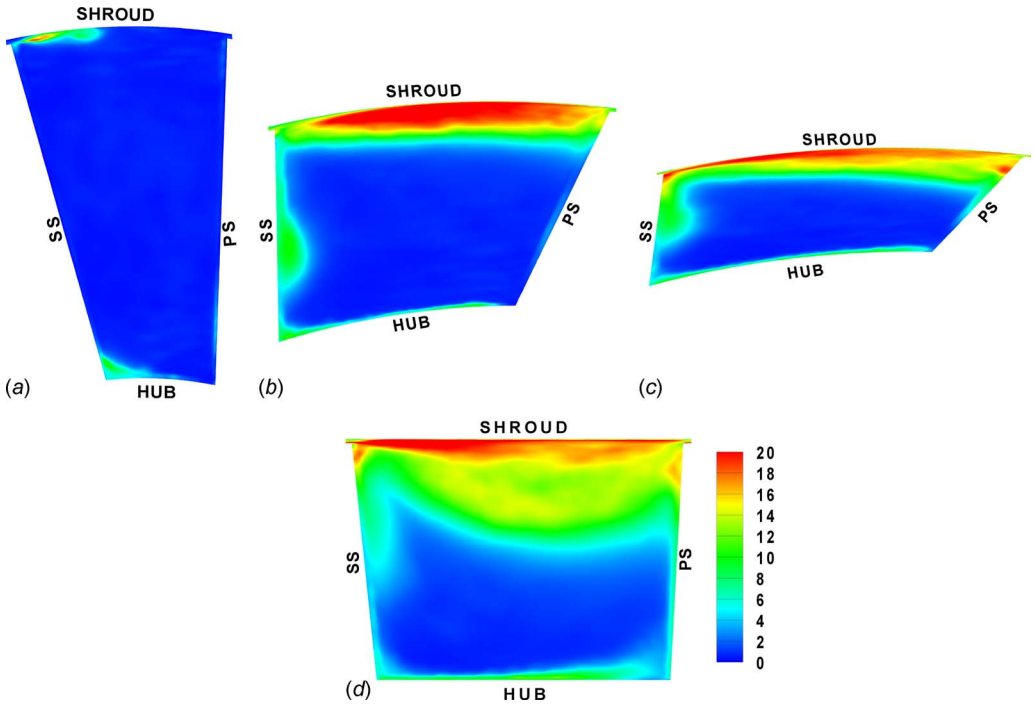

Fig. 6 Normalized turbulent kinetic energy distribution at cross-sectional planes: $m_i/m=0.149$ (*a*), $m_i/m=0.475$ (*b*), $m_i/m=0.644$ (*c*), and $m_i/m=0.921$ (*d*)

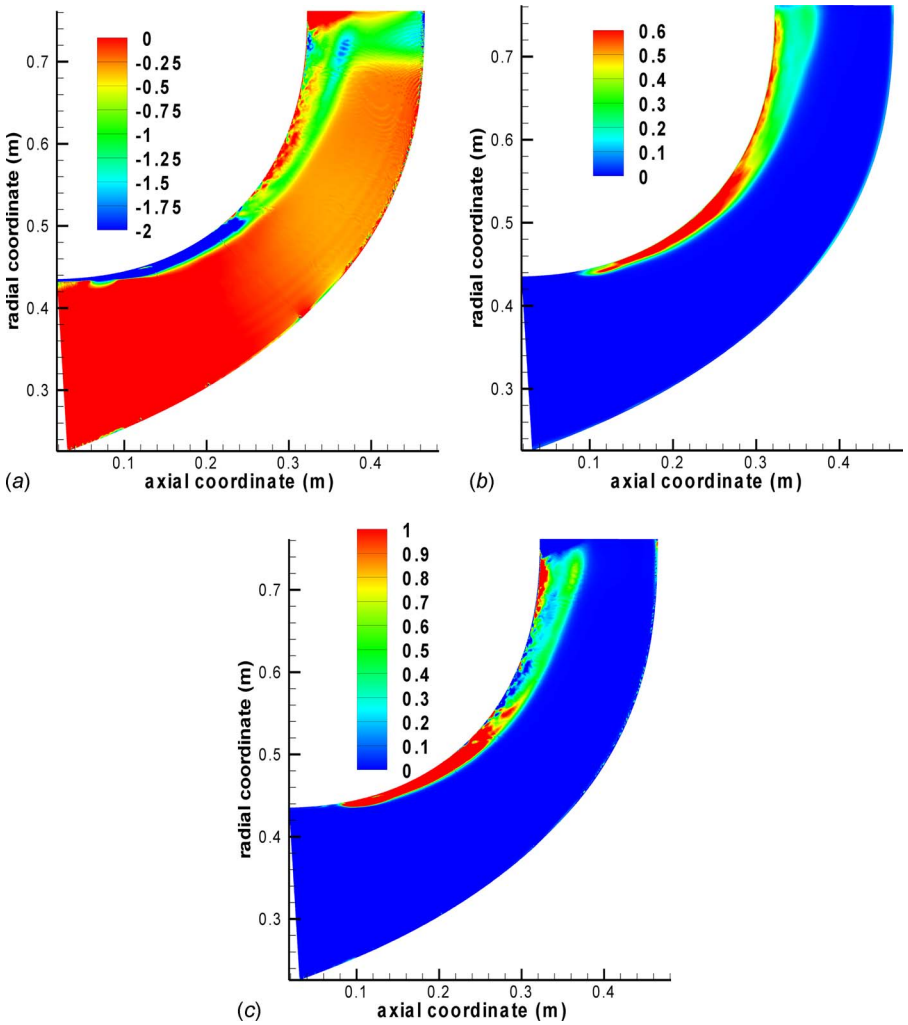

Fig. 7 Meridional velocity gradient (*a*), meridional normal stresses (*b*), and production of turbulence (*c*) at midpitch

and the SGS viscosity. One notices from this figure that both the turbulent intensity and SGS viscosity continuously increase till the exit of the impeller. However, when the blade wake is formed, there is a sharp rise in the turbulent intensity. The response of the SGS viscosity, on the other hand, is slightly delayed. In the diffuser section, the trend is slightly different, where the turbulent intensity stays approximately constant at around 17% and the SGS viscosity gradually decreases. Thus one can safely conclude that in the impeller section, turbulence is strongly correlated with the SGS viscosity.

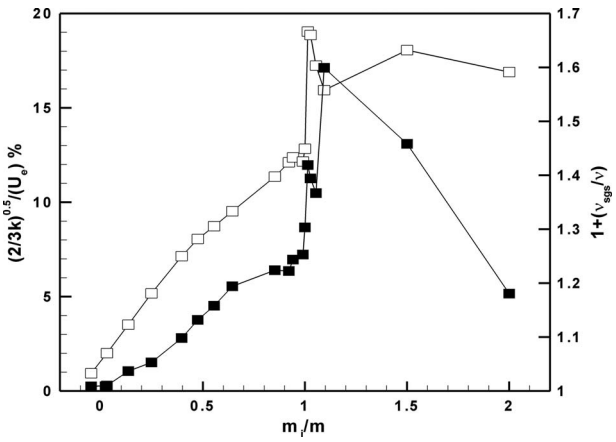

Fig. 8 Turbulence intensity variation (left *y*-axis) shown with open symbols and contribution of SGS viscosity (right *y*-axis) shown with filled symbols

The cross-sectional average values of the Reynolds stress anisotropy b_{ii} ($=a_{ij}/2k$, where $a_{ij}=\langle u_i u_j\rangle - 2/3k\delta_{ij}$) are demonstrated in Fig. 9. The diagonal terms of the Reynolds stress anisotropy are defined in terms of radial (b_{rr}), tangential (b_{tt}), and axial (b_{ww}) values. The radial component, b_{rr}, is seen to be negligible in the impeller. Tangential and axial components are, however, seen to correlate inversely in the impeller. In the diffuser section in terms of direction and level the axial and radial components follow the previously stated trend. However, the evolution of the tangential component is such that its magnitude is equal to the sum of the other two components. This anisotropy in Reynolds stress variation shows a tendency toward an axisymmetric expansion type of turbulence. This is attributed to the decrease in curvature effects.

In the context of the turbulence, the temporal history of the instantaneous velocity field is also extremely important. At station $m_i/m=0.644$, seven equidistant points ("b," "d," "e," "f," "g," "h," and "i") were predefined in the tip clearance region. The distance between each of these points was set to approximately 15% of the pitch. Instantaneous radial velocities were monitored at each of these points for at least 30 blade passing periods. In

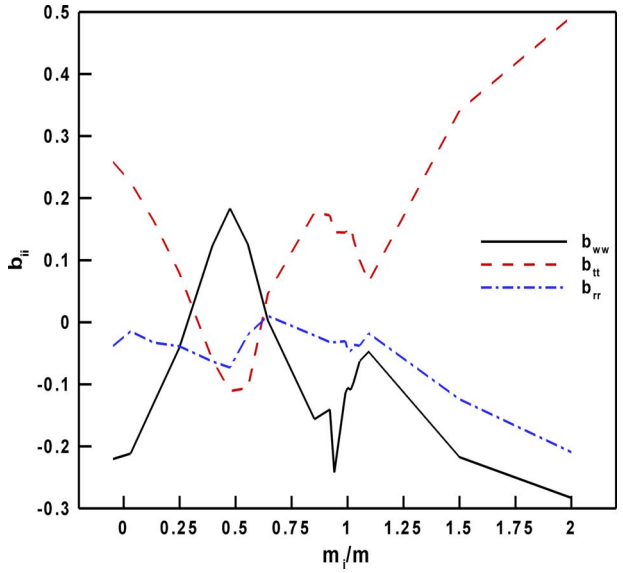

Fig. 9 Reynolds stress anisotropy variation

addition to the points in the tip clearance region, two more monitoring locations were predefined at 90% span, one being close to SS labeled as "a" and the other being close to the PS labeled as "c."

As tabulated in Table 2, it is found that the point a, which is near the SS, has a negative skewness and the point c, which is near the PS, has a positive skewness. The point b, which is located in the tip clearance gap between the points a and c, has almost zero skewness and therefore its probability density function closely approximates a Gaussian distribution. At these locations (points a, b, and c), instantaneous velocity values seem to display less intermittency than the other points. The intermittency rate of a signal determines the level of flatness (or kurtosis) of the PDF. As seen in Table 2, the points a, b, and c have higher flatness values. Starting from the point a (around 15% pitch), the intermittency (or flatness) increases, and the PDF profiles become flatter. This tendency continues till the point f (around 45% pitch). At points g, h, and i, peak values of the PDF gradually increase without a significant change in skewness. To conclude, the PDF profiles suggest that instantaneous velocity values in the wake and around the blade tip are less intermittent (i.e., more peaky), whereas they are highly intermittent (i.e., flatter) within around 50% pitch from the SS. It is also noted that the skewness of the PDF profiles is low in the wake region and slightly positive within around 50% pitch from the SS.

The energy spectrum is calculated via a fast Fourier transform (FFT) algorithm incorporating a Hamming window. The inertial subrange region for the energy spectrum for points a, b, and c have a slope higher than $-5/3$, as shown in Table 3. It is noted that the slope and the extent of the inertial region are maximum for the point b. At point a, the slope and the extent is less than the corresponding values at point b. At point c, they are reduced even further as compared with point a. At point e (30% of the pitch), there is a significant deviation from the Kolmorogov's $-5/3$ slope. In fact, the energy containing region and the dissipation regions of the energy spectrum seem to lie very close to each other. The point f and onwards, both the slope and the range of the inertial region increases till the PS side. To conclude, the spectrum analysis shows that the energy transfer rate from the larger scales to the smaller scales and the frequency range where the inertial region is deemed valid increase as one approaches the wake from the SS.

4 Conclusion

In this study, LES predictions are presented for a low-speed centrifugal compressor. Quantitative mean velocity and pressure predictions show that grid convergence is achieved. The leakage flow emanating across the tip clearance gap between the blade and the shroud causes a strong secondary flow, which is directed from the SS to PS. This alters the mean flow and the turbulence in the blade passage significantly. As emphasized numerous times, the mean flow comprises a jet region and a corresponding wake region located near the SS and PS, respectively. Time-averaged meridional contours indicate that a significant reverse flow exists near the shroud surface, which is believed to have an adverse impact on the isentropic efficiency and the performance of the compressor.

Unlike the past studies, this study has undertaken a detailed mapping of the turbulence behavior in the LSCC. The tip clearance produces a noticeably high turbulence region, which is constrained by the hub surface region. The Boussinesq stress-strain relation frequently employed by turbulence modelers is seen to be incorrect, especially near the exit of the impeller where the blade unloading takes place. The anisotropy of the Reynolds stresses is found to be correlated with the reducing effect of curvature. PDF profiles suggest that the instantaneous velocity values in the tip

Table 2 Skewness and flatness of the instantaneous data at some particular points

	a	b	c	d	e	f	g	h	i
Skewness	−0.45	0.07	0.56	0.12	0.18	0.13	−0.08	0.03	0.06
Flatness	3.24	3.06	3.00	2.69	2.55	2.63	2.56	2.84	2.88

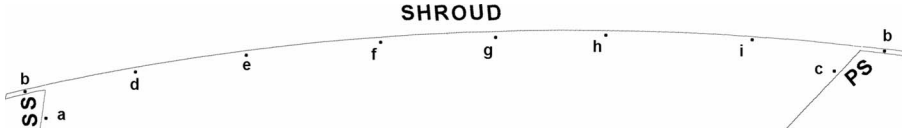

Table 3 The range and rate of the energy transfer process associated with the time spectra of the instantaneous data at some particular points

	a	b	c	d	e	f	g	h	i
Min. freq. (10^3)	1.5	2.8	0.5	0.7	3.4	2.1	1.3	1.8	1.0
Max. freq. (10^3)	5.5	8.5	2.5	6.6	7.4	6.3	5.7	6.5	6.0
Difference (10^3)	4.0	5.7	2	4.9	4.0	4.2	4.4	4.7	5.0
Slope	−3.4	−4.6	−2.3	−1.6	−1.2	−2.0	−2.7	−3.8	−3.1

wake are less intermittent as compared with the values in the tip jet. Energy spectra profiles also highlight unambiguously the local nature of the energy cascade process, i.e., it proceeds at a higher rate and lasts longer in the wake region than in the tip jet region.

Acknowledgment

The authors would like to thank to Dr. Michael D. Hathaway from NASA for providing the experimental data for the centrifugal compressor.

References

[1] Dean, R. C., Jr., and Senoo, Y., 1960, "Rotating Wakes in Vaneless Diffusers," ASME J. Basic Eng., **82**, pp. 563–574.
[2] Eckardt, D., 1975, "Instantaneous Measurements in Jet-Wake Discharge Flow of a Centrifugal Compressor Impeller," ASME J. Eng. Power, **97**(3), pp. 337–346.
[3] Hah, C., and Krain, H., 1990, "Secondary Flows and Vortex Motion in a High-Efficiency Backswept Impeller at Design and Off-Design Conditions," ASME J. Turbomach., **112**(1), pp. 7–13.
[4] Hathaway, M. D., Chriss, R. M., Wood, J. R., and Strazisar, A. J., 1993, "Experimental and Computational Investigation of the NASA Low-Speed Centrifugal Compressor Flow Field," ASME J. Turbomach., **115**, pp. 527–541.
[5] Zhang, M., Pomfret, M. J., and Wong, C. M., 1996, "Three-Dimensional Viscous Flow Simulation in a Backswept Centrifugal Impeller at the Design Point," Comput. Fluids, **25**(5), pp. 497–507.
[6] Byskov, R. K., Jacobsen, C. B., and Pedersen, N., 2003, "Flow in a Centrifugal Pump Impeller at Design and Off-Design Conditions—Part II: Large Eddy Simulations," ASME J. Fluids Eng., **125**(1), pp. 73–83.
[7] Kato, C., Yamade, Y., Wang, H., Miyazawa, M., Takaishi, T., Yoshimura, S., and Takano, Y., 2007, "Numerical Prediction of Sound Generated From Flows With a Low Mach Number," Comput. Fluids, **36**, pp. 53–68.
[8] Nicoud, F., and Ducros, F., 1999, "Subgrid-Scale Stress Modelling Based on the Square of Velocity Gradient Tensor," Flow, Turbul. Combust., **62**, pp. 183–200.
[9] Smagorinsky, J., 1963, "General Circulation Experiments With Primitive Equations. I. The Basic Experiment," Mon. Weather Rev., **91**, pp. 99–164.
[10] Fluent Inc., 2001, FLUENT 6.2 User Guide, Lebanon, NH.
[11] Moore, J., and Moore, J. G., 1990, "A Prediction of 3-D Viscous Flow and Performance of the NASA Low-Speed Centrifugal Compressor," ASME Paper No. 90-GT-234.
[12] Krain, H. and Hoffman, W., 1989, "Verification of an Impeller Design by Laser Measurements and 3D-Viscous Flow Calculations," ASME Paper No. 89-GT-159.
[13] Krain, H., and Hoffman, W., 1990, "Centrifugal Impeller Geometry and Its Influence on Secondary Flows," AGARD Secondary Flows in Turbomachines.
[14] Guleren, K. M., 1990, "Large-Eddy Simulation of Wall-Bounded Flows Subjected to Curvature and Rotation," Ph.D. thesis, The University of Manchester, UK; http://www.cumhuriyet.edu.tr/melihguleren/PhDthesis.pdf.
[15] Luo, J. Y., Issa, R. I., and Gosman, A. D., 1994, "Prediction of Impeller-Induced Flows in Mixing Vessels Using Multiple Frames of Reference," Inst. Chem. Eng. Symp. Ser., **136**, pp. 549–556.
[16] Sergent, E., 2002, "Vers une methodologie de couplage entre la Simulation des Grandes Echelles et les modeles statistiques," Ph.D. thesis, L'Ecole Centrale de Lyon, Lyon, France.

Aerothermal Impact of Stator-Rim Purge Flow and Rotor-Platform Film Cooling on a Transonic Turbine Stage

M. Pau

G. Paniagua

D. Delhaye

A. de la Loma

Department of Turbomachinery and Propulsion,
von Karman Institute for Fluid Dynamics,
1640 Rhode Saint Genèse, Belgium

P. Ginibre
Department of Turbine Aerodynamics,
Snecma-Groupe Safran,
77550 Moissy Cramayel, France

The sealing of the stator-rotor gap and rotor-platform cooling are vital to the safe operation of the high-pressure turbine. Contrary to the experience in subsonic turbines, this paper demonstrates the potential to improve the efficiency in transonic turbines at certain rim seal rates. Two types of cooling techniques were investigated: purge gas ejected out of the cavity between the stator rim and the rotor disk, and cooling at the rotor-platform. The tests were carried out in a full annular stage fed by a compression tube at $M_{2is} = 1.1$, $Re = 1.1 \times 10^6$, *and at temperature ratios reproducing engine conditions. The stator outlet was instrumented to allow the aerothermal characterization of the purge flow. The rotor blade was heavily instrumented with fast-response pressure sensors and double-layer thin film gauges. The tests are coupled with numerical calculations performed using the ONERA's code ELSA. The results indicate that the stator-rotor interaction is significantly affected by the stator-rim seal, both in terms of heat transfer and pressure fluctuations. The flow exchange between the rotor disk cavity and the mainstream passage is mainly governed by the vane trailing edge shock patterns. The purge flow leads to the appearance of a large coherent vortex structure on the suction side of the blade, which enhances the overall heat transfer coefficient due to the blockage effect created. The impact of the platform cooling is observed to be restricted to the platform, with negligible effects on the blade suction side. The platform cooling results in a clear attenuation of pressure pulsations at some specific locations. The experimental and computational fluid dynamics results show an increase in the turbine performance compared with the no rim seal case. A detailed loss breakdown analysis helped to identify the shock loss as the major loss source. The presented results should help designers improve the protection of the rotor platform while minimizing the amount of coolant used.*
[DOI: 10.1115/1.3142859]

1 Introduction

Ensuring an adequate blade life at the temperatures reached in today's advanced engines requires efficient cooling methods. In high-pressure turbine stages, cold air is ejected from the cavity, which exists between the stator rim and the rotor disk, to avoid hot gas ingress into the wheelspace interface. Recent publications [1,2] demonstrated that the cold cavity flow is mostly sucked into the rotor hub vortex, leaving the rear platform directly exposed to the hot gas. The consequent high thermal stress leads to a critical mechanical stress buildup at the hub platform. Active platform cooling is therefore applied to ensure appropriate thermal insulation of the blade root and to avoid platform cracking. Additionally, the ejection of coolant from the rear part of the rotating platform protects the hub trailing edge (TE) region.

According to McLean et al. [3], turbine designers should consider three important parameters when designing a high-pressure turbine stage with active wheelspace cooling. First, the coolant temperature in the wheelspace should be below the critical material temperature. Second, the rim seal flow rate should be adjusted to minimize (a) the aerodynamic losses due to mixing with the mainstream flow and (b) the windage losses due to the rotational drag within the same wheelspace cavity. Finally, purge flow effects on the rotor endwall heat transfer should be taken into account. The complex flowfield inside the wheelspace cavity has been described by various researches on simplified rotating cavities [4–6], neglecting the interaction between the purge flow and the mainstream flow. The cavity-mainstream interaction with the leakage flow being extracted from the mainstream has been documented by several authors [7–10]. Several research groups have been investigating the effects of rotating and stationary pressure asymmetries for the past decade [11–15]. At engine conditions, circumferential pressure asymmetries are the primary cause of partial ingestion [3]. The mass flow exchange between the turbine mainstream and the rotor disk cavities is driven by vane trailing edge shock systems, rotor-stator potential interactions, vane wakes, and secondary flow. According to Roy et al. [16,17], the main factors are the vane/blade geometry, axial spacing, configuration of the seals, main and purge air flow rates, and rotor speed. Marini and Girgis [18] investigated the efficiency sensitivity to cavity flows using computational fluid dynamics (CFD) with two platform shapes. Montomoli et al. [19] studied numerically the interaction of the wheelspace coolant and main flow in an aeroderivative low pressure turbine. All the aforementioned authors concluded that purge flow affects significantly the main gas stream.

Platform film cooling investigations have been predominantly conducted on linear cascades. One of the earliest studies on platform film cooling was carried out by Blair [20] using an upstream slot in a large-scale turbine vane passage. Harasgama and Burton [21] conducted heat transfer and aerodynamic measurements in an annular cascade fitted with vanes under engine-representative flow conditions. Their results show that film cooling reduced the Nus-

Contributed by the International Gas Turbine Institute of ASME for publication in the JOURNAL OF TURBOMACHINERY. Manuscript received May 2, 2008; final manuscript received February 14, 2009; published online January 11, 2010. Review conducted by David Wisler. Paper presented at the ASME Turbo Expo 2008: Land, Sea and Air (GT2008), Berlin, Germany, June 9–13, 2008.

selt number on the suction side (SS) by about 50%, suggesting that the coolant was convected toward that region by the passage vortex. Friedrichs et al. [22] described in detail the aerodynamic aspects of platform film cooling using the ammonia and diazo technique. Based on the cooling effectiveness distributions measured in a large scale low-speed turbine cascade, it was concluded that the film cooling traces moved toward the suction side. The coolant film was found to be eroded by the secondary flows, being pushed toward the suction side, thus leading to an increase in aerodynamic losses due to the mixing process.

Experimental studies on film cooling and heat transfer performed on a rotating turbine are scarce in the open literature, primarily due to the difficulties in instrumenting rotating parts. Dring et al. [23] investigated film cooling performance in a low-speed rotating facility and showed that the film coolant experienced only a small radial displacement on the suction side, similar to flat plate results. On the pressure side (PS), the film coolant trace followed an important radial displacement toward the blade tip. Heat transfer effectiveness distributions along the blade span for rotating turbine blades were obtained by Takeishi et al. [24] and Abhari and Epstein [25] using, respectively, gas chromatography and thin film heat flux gauges. Blair [26] also studied the heat transfer on the pressure and suction sides, as well as on the hub platform for a rotating turbine model. Enhanced heat transfer was observed on the platform due to the effect of the secondary flows. Recently, Ahn et al. [27] investigated film cooling effectiveness on the leading edge (LE) of a rotating blade using pressure sensitive paint (PSP). The rotational speed was found to alter significantly the film coolant traces on the blade leading edge. Suryanarayanan et al. [28,29] measured film cooling effectiveness on a rotating turbine blade platform using PSP in a two-stage subsonic turbine. Furthermore stator rim purge flow was investigated, providing information on the optimum purge flow rate.

The present work aims to quantify and understand the influence of stator-rim purge flow and of rotor-platform film cooling on the aerothermal flowfield in a transonic high-pressure turbine. This research in transonic turbines is, to the authors' knowledge, reported for the first time in the open literature. The acquired data will help to validate advanced CFD models, and the result analysis will contribute to understand the flow interactions occurring in cooled transonic turbines.

The tests were carried out in a full stage under engine-representative conditions. The von Karman Institute compression tube multipurpose turbine research facility was equipped with new blades and modified to accommodate the present film cooling research.

In the present paper, the turbine test rig, coolant supply system, advanced instrumentation, and CFD tools are first described. The results of the study are then shown and explained. The purge flow interaction with the mainstream is analyzed from measurements at the vane exit rotor leading edge and rotor blade platform, along 7.5% and 15% of the rotor blade height. Numerical computations calibrated with the experimental results complement this study and allow deeper insight into the flow phenomena. Finally, a turbine efficiency analysis is carried out to compare measured data and CFD results. Kacker and Okapuu's detailed loss breakdown correlations are used to identify the different loss component contributions.

2 Turbine Description and Test Conditions

The tests were performed in a full high-pressure transonic turbine stage operating at engine-representative conditions. Figure 1 represents the current turbine stage, together with a meridional cut showing the path of the coolant to the wheelspace cavity and the rotor platform. The nozzle guide vane is composed of 43 front-loaded vanes, designed to operate in the transonic regime [30]. The vane to vane channel is therefore convergent with a flat rear suction side. The rotor is made up of 64 highly loaded transonic rotor blades. The highly loaded blades are designed with an inlet

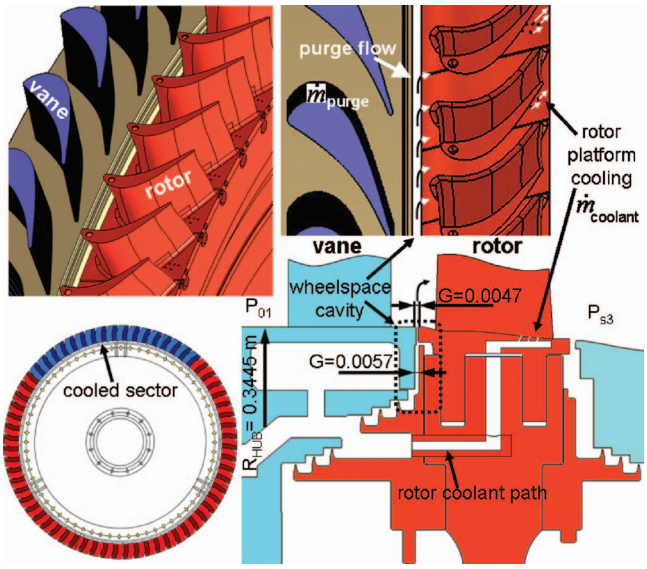

Fig. 1 Turbine stage and rotor-platform coolant path

metal angle of about 45 deg and a turning of about 105 deg to contain the secondary flows. Negative blade lean further reduces secondary flows in the tip region.

The platform cooling is applied to a sector of 17 contiguous blades. The coolant comes out of the platform through five cylindrical holes inclined at 30 deg and located in the platform region close to the rotor blade rear suction side. The stator-rim purge flow coolant is injected radially toward the main channel, as shown in Fig. 1

The inlet total pressure and inlet total temperature are kept constant for all test conditions, respectively, at 1.59 bars and 442.3 K (at midspan), resulting in a vane outlet Reynolds number (based on the true chord) of $\mathrm{Re}=1.1\times10^6$.

Table 1 summarizes the four coolant ejection conditions tested: mass flows, pressure ratios, and nondimensional mechanical speed. The wheelspace and coolant mass flow rates are expressed as a percentage of the mainstream mass flow rate. They were devised to allow differentiation of the respective effects of the purge flow and the platform film cooling, as well as the effect of the rotational speed. Henceforth, the different test conditions are named with reference to the coolant mass flow ingested (negative values) or ejected (positive rim seal) from the wheelspace cavity. The baseline test, i.e., no active cooling, performed at the design speed (6500 rpm), is characterized by net hot gas ingestion into the wheelspace cavity chamber (0.128 m^3) initially at vacuum, thus called *ingestion* −1%.

The main parameters of the rim seal and rotor-platform cooling are listed in Table 2. Regarding the purge flow, the nondimensional cooling mass flow rate and rotational Reynolds numbers are similar to real engine conditions. Concerning the rotor platform, the operating conditions were selected to have a blowing ratio below 1.35.

Table 1 Test conditions (mass flow, pressure ratios, and nondimensional mechanical speed) and uncertainty

Condition	$\dot{m}_{purge}$ (%)	$\dot{m}_{coolant}$ (%)	P_{01}/P_{s3}	$N/\sqrt{T}$
Ingestion −1%	−1.00	0.020	3.13	301.3
Ejection +0.3%	0.28	0.043	3.14	301.2
Ejection +0.8%	0.76	0.040	3.10	300.7
Low-rpm	0.15	0.038	3.14	212.4
Uncertainty	±0.04	±0.004	±0.016	±0.05

Table 2 Main nondimensional parameters of the rim seal and rotor-platform cooling

	Rim seal		Rotor platform cooling		
Condition	C_w	Re_θ ($\times 10^5$)	Blowing ratio	Density ratio	Momentum ratio
Ingestion −1%	−16747	2.61	0.59	1.14	1.14
Ejection +0.3%	4886	4.26	1.35	1.38	1.38
Ejection +0.8%	13110	4.13	1.16	1.34	1.34
Low-rpm	2638	3.12	1.01	1.33	1.33

3 Experimental Apparatus

3.1 Test Rig. Measurements were performed in the compression tube turbine test rig CT3 at the von Karman Institute [31], illustrated in Fig. 2(*a*). The sudden release (0.4 s) of hot gas on to the cold turbine airfoils reproduces the heat transfer process of a real engine. Such operation allows preserving the temperature ratios at identical Reynolds and Mach numbers. The operation cycle of the rig is fully described by Dénos and Paniagua [32].

3.2 Measurement Techniques. Advanced instrumentation is required to adequately capture the aerothermal impact of film cooling and interstage purge flow ejection on turbine efficiency under real engine conditions. The radial aerothermal profile is obtained at the turbine inlet and outlet (planes 1 and 3 in Fig. 2(*b*)) using Kiel probes, static pressure taps, and miniaturized type K thermocouples. The static pressure at the vane exit (plane 2, $0.035 \times C_{S,\mathrm{ax}}$ downstream of the vane trailing edge) is measured at five locations along the hub endwall, covering one stator pitch. The wheelspace cavity is instrumented on the stator rim (at $R/R_0=0.944$) with five pneumatic taps and five subsurface mounted fast-response transducers. The rotor blade static pressure is measured on the platform surface with six high frequency response pressure sensors. The stagnation pressure at the rotor leading edge (at 15%, 50%, and 85% of the height) is obtained with recessed Pitot probes, as depicted in Fig. 2(*c*). The heat transfer is measured along the blade airfoil at 7.5% and 15% span with thin film gauge resistors mounted on an insulating substrate. On the cooled rotor platform, foil thermocouples are mounted underneath the thin film gauges to retrieve the heat flux, as shown in Fig. 2(*d*). Two independent measurement systems monitor the rpm, using photodiodes.

Table 3 gives the typical absolute measurement uncertainties.

3.3 Heat Transfer Data Processing. At the present flow regimes, the adiabatic wall temperature (T_{aw}) is frequently assumed as the temperature driving the heat flux process. This choice allows the determination of the heat transfer coefficient independently from the actual thermal boundary conditions [33]. The heat transfer coefficient thus becomes a function of the geometry, flow field, and fluid properties:

$$h_{\mathrm{aw}} = \frac{q}{(T_{\mathrm{aw}} - T_{\mathrm{wall}})} \tag{1}$$

The adiabatic wall temperature may be obtained by plotting the experimental wall temperature in function of the heat flux. The wall temperature extrapolated at zero heat flux rate corresponds to the adiabatic wall temperature. However, temperature oscillations experienced in the current short testing facility prevent an accurate fit. A close approximation to the adiabatic wall temperature is the recovery temperature, which can be calculated as follows:

$$T_{\mathrm{recovery}} = T_s + r(T_0 - T_s) \tag{2}$$

$$T_0 = \left(1 + \frac{\gamma - 1}{2} \cdot \mathrm{M}^2\right) \cdot T_s \tag{3}$$

where the isentropic Mach number M is based on the measured upstream total pressure and the measured static pressure on the rotor blade. A turbulent recovery factor $\mathrm{Pr}^{1/3}=0.89$ was assumed [34]. This choice of the recovery temperature ensures that h and Nu are reasonably independent of the thermal boundary condition. This approach has been extensively used in the literature as found in Ref. [35].

The Nusselt number presented in all the plots is a scaled heat flux, defined in terms of the airfoil axial chord, total inlet temperature minus the local wall temperature, and thermal conductivity based on the local temperature. 2D heat conduction computations have been performed to obtain the initial heat flux due to the heating caused by the viscous drag dissipated during the spinning up of the rotor. The experimental wall temperature time evolution prior to the blowdown test was used as a boundary condition. Two dimensional effects are seen to be significant at the leading and trailing edges. It is proven that the actual heat flux during a test can be calculated by superposition of the initial preheating heat flux and the actual flux during the blowdown [36].

3.4 Measurement of the Rim Seal and Platform Cooling. During the blowdown, a heat exchanger cools down the coolant flow. Figure 3(*a*) depicts the path followed by the coolant stream. At the elbow pipes exit, the flow is vented through three possible outlets:

- the internal chamber
- the rotor-platform film cooling
- injection into the wheelspace

The total supply mass flow to the test section is adjusted using choked orifices (P_{elbow}). The flow rate entering the inner chamber is computed based on the volume of the chamber. The pressure (P_{chamber}) and temperature in the chamber are monitored by pneumatic taps and microthermocouples. The mass flow fed into the rotor blade is evaluated from the total pressure (P_{coolant}) and temperature measured in rotation inside the coolant channel, plus the static pressure field distribution on the platform (obtained by the CFD). Finally, the mass flow into the wheelspace cavity is computed by performing a mass balance.

Figure 3(*b*) shows pressure traces at different locations in the coolant path together with the evolution of the stage total inlet pressure P_{01} during the actual testing time (~0.4 s). The coolant injection starts at 0.35 s before the actual blowdown to allow the coolant flow to reach steady state. Once the desired blowing ratios are established, the high pressure and temperature mainstream gas is blown into the stage, producing the sudden increase in P_{01}. The pressure rise in the mainstream channel pressurizes all the inner cavities, remaining constant afterwards during the blowdown time. At *ejection* +0.8%, 1.99% mass flow is pumped through the elbow pipes and 1.19% flows into the inner chamber. The remain-

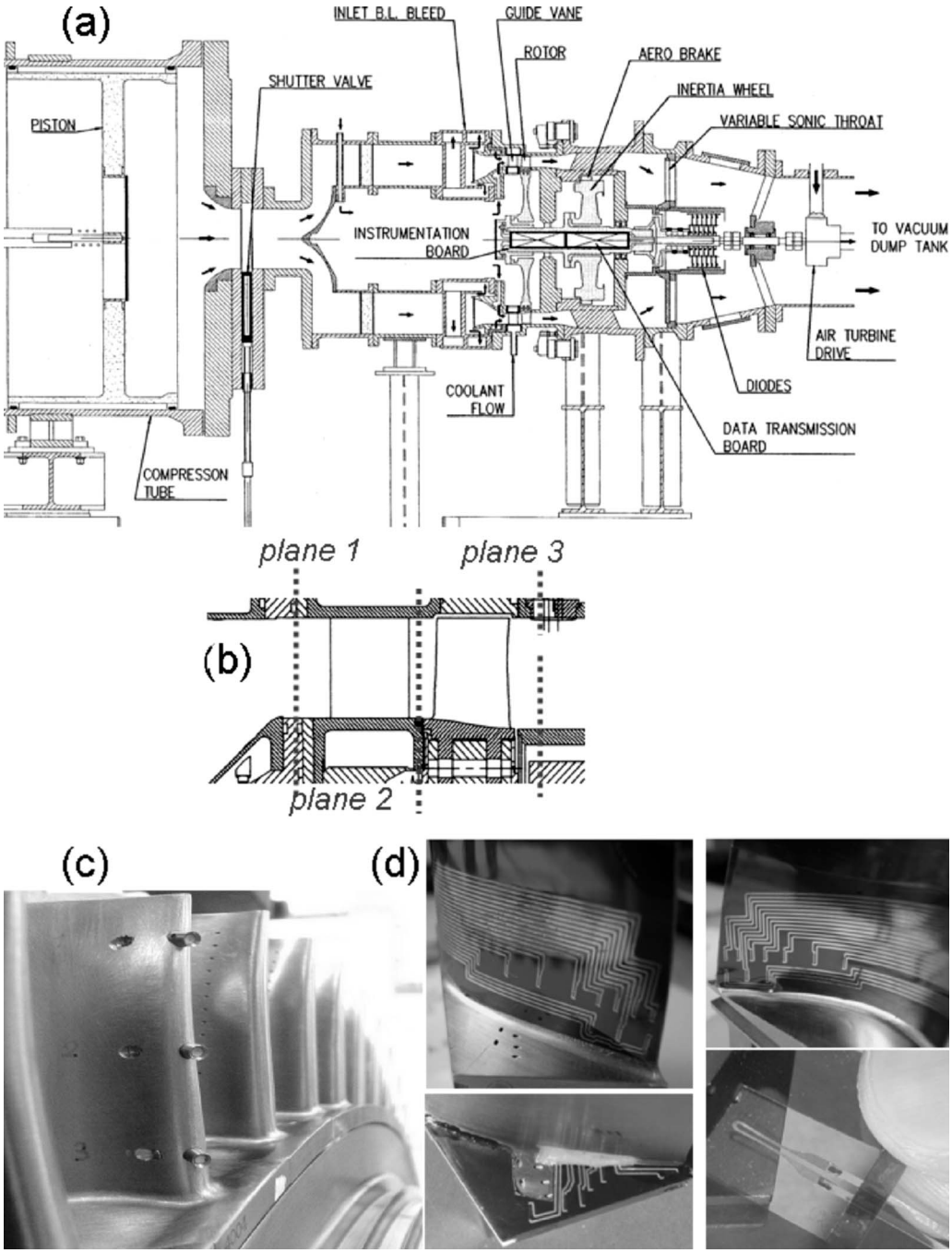

Fig. 2 (*a*) **Meridional view of the turbine rig,** (*b*) **turbine measurement planes,** (*c*) **total pressure sensors located at the rotor leading edge, and** (*d*) **Heat transfer instrumentation at 15% span, 7.5% span, and on the rotor platform**

ing coolant is split into 0.04% to cool the rotor and 0.76% to eject into the warm turbine mainstream.

3.5 Turbine Mass Flow Evaluation. Due to the complexity and size of the facility, it is difficult to install a standard metering system such as venturi or orifice plates. Monitoring the location of the piston, the total pressure, and the total temperature, it is possible to know the mass of air downstream of the piston at any time and hence the mass flow:

$$\dot{m} = \frac{d\rho \cdot V}{dt} = \frac{P_{0\text{tube}}}{\Re \cdot T_{0\text{tube}}} \frac{dV}{dt} = \frac{P_{0\text{tube}}}{\Re \cdot T_{0\text{tube}}} \frac{dV}{dt} \frac{\pi D^2}{4} \frac{dx}{dt} \tag{4}$$

To estimate all the quantities, a model performs balances of mass flow and energy as a function of time in the different volumes of the rig, i.e., the upstream tube, the settling chamber, and the downstream dump tank [37]. This procedure requires the measurement of the upstream total pressure P_{01}, total temperature T_{01}, the estimation of the sonic throat area A, and the discharge coefficient

Table 3 Typical uncertainty levels of the measurements

P_{steady}	P_{unsteady}	T_{steady}	Nu	rpm
±8 mbars	±10 mbars	±2 K	5%	±0.22

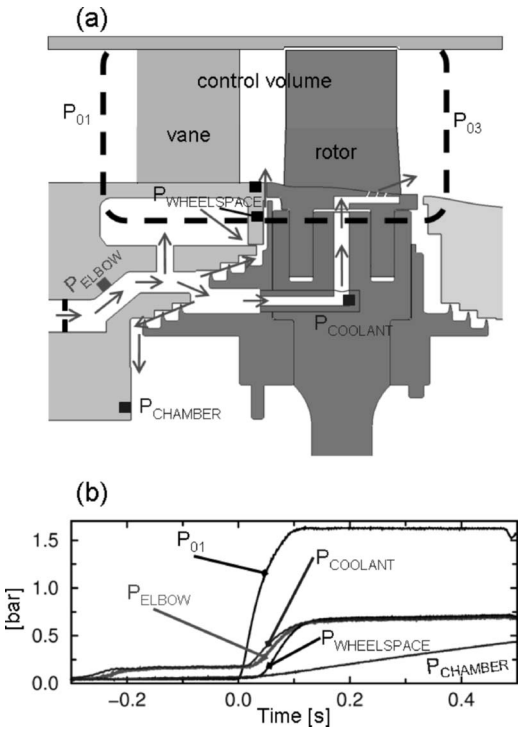

Fig. 3 (*a*) Coolant flow paths and (*b*) pressure signals along the coolant path during a typical test

C_d. The turbine is assimilated to a sonic orifice; hence the mass flow can be computed according to [38]

$$m = C_d \frac{P_{01}}{\sqrt{C_p T_{01}}} A \frac{\gamma}{\sqrt{\gamma - 1}} \left[\frac{\gamma + 1}{2} \right]^{-(\gamma+1)/2(\gamma-1)} \quad (5)$$

Once the model is fitted to an ensemble of tests, a virtual test is run under perfectly constant conditions. The mass flow conservation between the tube exit and the stage inlet can be applied and the coefficients can be determined.

Table 4 summarizes the inlet mass flows evaluated according to this procedure. The outlet mass flows are obtained adding or subtracting the purge flow and rotor-platform coolant. Negligible differences are appreciated on the turbine inlet mass flow, the dispersion remains within the random error estimated by statistical analysis to be ± 0.1 kg/s.

4 Numerical Simulations

In order to better understand the flow features, numerical computations have been conducted utilizing the ELSA flow solver developed at ONERA [39]. The CFD code ELSA solves the 3D–Reynolds Averaged Navier-Stokes (3D-RANS) equations with a finite volume method and multidomain approach on structured grids. The Jameson centered scheme is implemented for spatial integration, whereas the time integration is performed using the backward Euler scheme. An iterative implicit phase and a local time stepping are performed in order to accelerate convergence to steady state. The turbulent closure is performed with Wilcox's k-ω turbulence model.

Table 4 Turbine inlet and outlet mass flow measured

Condition	$\dot{m}_{\text{inlet}}$ (kg/s)	$\dot{m}_{\text{outlet}}$ (kg/s)	$\pm 1.96\sigma$
Ingestion −1%	9.94	9.84	0.073
Ejection +0.3%	9.91	9.94	0.109
Ejection +0.8%	9.88	9.96	0.104
Low-rpm	9.88	9.90	0.103

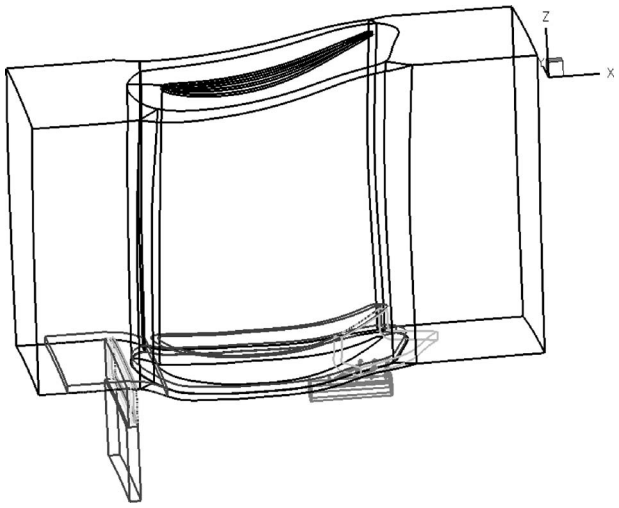

Fig. 4 Structure of the blocks used to mesh the rotor

The complex geometry is handled by the Chimera technique with overlapping blocks, as well as refining blocks near the injection areas. Figure 4 outlines the grid blocks of the rotor. The main flow path of the rotor blade is meshed with seven conformal blocks including an O block around the blade, with 1.9×10^6 points. When overlapped by a finer mesh block, coarse grids are blanked in order to avoid unnecessary computations and to ensure accuracy of the flow solution in this region. Overlapping boundaries are taken into account with interpolations. All the technological features (rotor fillet, rotor hub disk leakage channels, platform cooling channels, and cooling holes) are meshed using simple topologies thanks to the Chimera technique. The stage configuration comprises in a total of 5.25×10^6 points. The resulting $y+$ values at the wall are below 1 except in the rotor tip clearance region.

Steady state simulations were performed using a mixing plane approach. The mixing plane, where all quantities are pitchwise averaged, was located upstream of the cavity. Therefore, vane trailing edge shocks are not transferred downstream, but this approach serves to investigate the cavity-rotor interactions. Two different stage configurations were thoroughly studied:

- no wheelspace cavity, no platform film cooling
- wheelspace cavity and platform cooling

The stage inlet boundary conditions (radial profiles) were imposed based on the experimental values. The outlet profiles were obtained from the measured static pressure at the hub and the radial equilibrium equations. Walls are treated applying a no-slip condition associated with a uniform temperature distribution ($T_{\text{wall}} = 289$ K). The boundary conditions to the cavity (at constant radius) comprise the measured total temperature, the mass flow, and the radial inlet flow in the absolute frame.

5 Aerothermal Results and Discussion

5.1 Inner Cavity Purge Flow. The core of the wheelspace cavity flow is governed by the radial pressure gradient. The supersonic vane outlet conditions create large pitchwise asymmetries. Close to the rotor disk, the high shear transfers momentum to the gas, which is then pumped out of the cavity by centrifugation. The outer part of the wheelspace cavity region resembles the well studied *lid-driven cavity flow* [40]. Regardless of the mainstream nonuniformities, Fig. 5(*a*) shows how the pressure gradient in the pitch-wise direction attenuates very rapidly along the depth

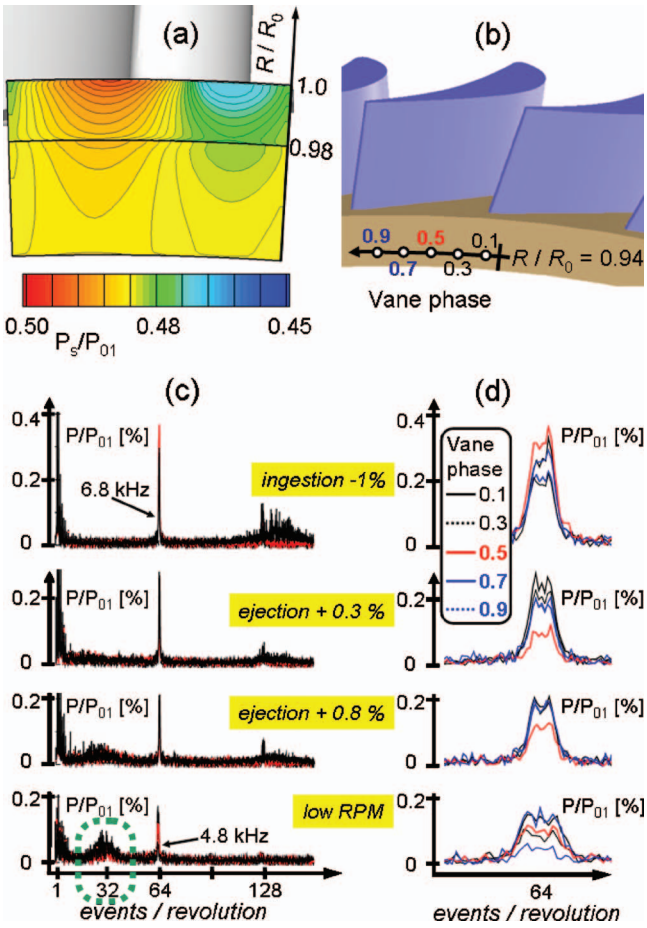

Fig. 5 (*a*) **CFD static pressure distribution on the stator-rim cavity,** (*b*) **measurement locations on the stator rim at** R/R_0 **=0.944,** (*c*) **experimental pulsations of static pressure for all the conditions, and** (*d*) **enlarged detail of the unsteady static pressure amplitudes at the blade passing frequency**

of the cavity (reducing R/R_0).

The pressure fluctuations on the stator rim were measured with five subsurface piezoresistive sensors at R/R_0=0.944. Figure 5(*b*) displays the measurement locations. Each sensor is labeled according to the vane pitch location (0 when aligned with the vane leading edge). Figure 5(*c*) shows the frequency spectrum of the unsteady pressure measurements in the stator rim. Overall the maximum fluctuations are around $\pm 0.4\%$ of P_{01} for the ingestion case. In the subsonic turbine investigated by Cao et al. [15], the maximum pressure fluctuations measured in the cavity were around $\pm 0.5\%$ of P_{01}. In all cases the dominant frequency of the fluctuations occurs at 64 events per revolution (around 6.8 kHz at -1% and 4.8 kHz for the *low-rpm*). Interestingly when flow is purged through the cavity, a resonance frequency appears associated to the passage of two blades (half of the blade passing events) while the amplitude of the fluctuations is reduced. The resonance frequency is particularly clear at the low-rpm condition.

Figure 5(*d*) illustrates a zoom of the fluctuations close to the fundamental frequency. It is important to observe that the sensor located at vane phase 0.5 experiences a larger reduction in the pressure oscillations than the other gauges; this indicates that the impact of the vane shocks reaches inside the cavity.

5.2 Interaction of the Cavity and the Mainstream Flow. The rim seal should be ejected while minimizing the aerodynamic impact on the mainstream flow. Moreover, since the cooling gas is usually extracted from the compressor, the coolant flow rate needs

Table 5 Pressure ratio, Mach number, and degree of reaction at the hub cavity downstream of the stator

Condition	P_{01}/P_{s2h}	$M_{2is,h}$	r_{hub}
Ingestion -1%	2.33	1.16	0.236
Ejection +0.3%	2.27	1.15	0.251
Ejection +0.8%	2.17	1.12	0.278
Low-rpm	2.38	1.19	0.209

to be diminished. This ensures that the gas turbine cycle efficiency is preserved. Therefore, the study of the interaction between the purged cavity flows and the mainstream is of vital importance.

Table 5 shows the statistics on the pressure ratio, the Mach number downstream of the stator, and the degree of reaction. By increasing the ejection rate, the purge cavity blockage is enhanced, leading to a lower Mach number downstream of the stator and a smaller pressure ratio across the vane hub. As a consequence, the rotor inlet Mach number decreases locally, modifying the incidence in the relative frame and increasing the degree of reaction at the hub.

The measurement of the static pressure, both at the hub vane exit and in the wheelspace cavity (along the pitch), allows identifying the ingestion and ejection zones of gas in the stationary frame. The static pressure distribution within the wheelspace cavity and at the stator hub endwall (plane 2) is shown in Fig. 6 for three conditions: -1%, +0.3%, and +0.8%. The static pressure gradients decay very rapidly inside the wheelspace cavity (Fig. 5(*a*)), resulting in a constant level of pressure (at a given radius) along the vane pitch. By contrast, P_{s2} (the static pressure at the vane exit hub endwall) varies by $\sim 19\%$ around its mean level due to the vane trailing edge shock pattern. The comparison of the different conditions reveals that ejecting rim seal flow leads to a higher increase in the static pressure in the cavity than at the vane outlet. For each condition, the coolant ejection and ingestion zones are clearly identified analyzing the different pressure levels. A higher local pressure in the cavity than in the mainstream flow leads to ejection of air out of the cavity, while the opposite situation leads to ingestion. Looking at Fig. 6, the mainstream gas

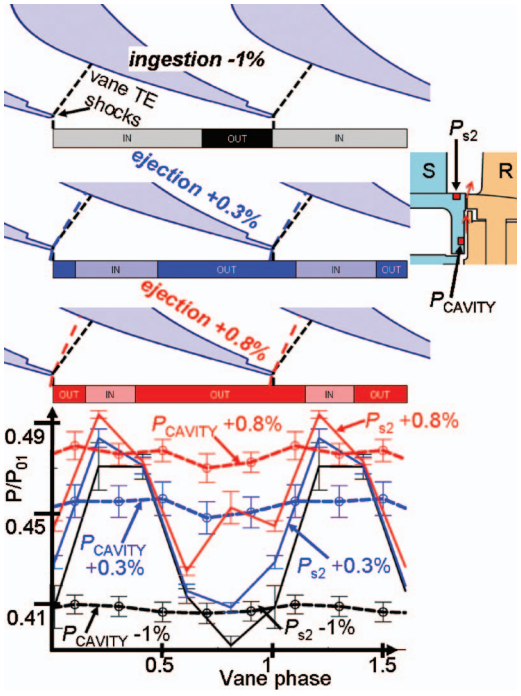

Fig. 6 Pitchwise static pressure variation at the stator rim

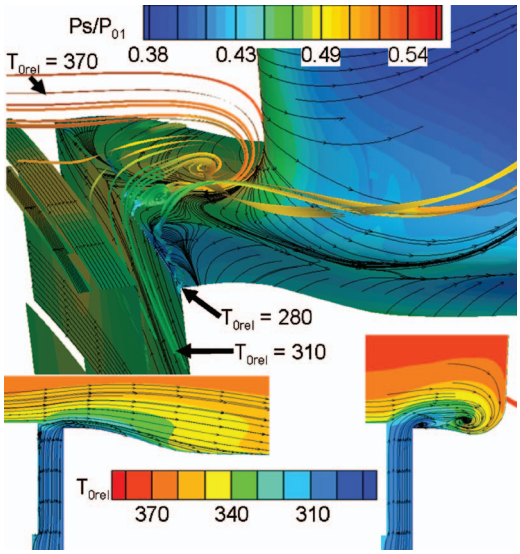

Fig. 7 Interaction of the hot mainstream flow with the cold purge flow: (*a*) stream traces of the cold rim seal and hot mainstream flow on the 3D rotor static pressure field, (*b*) isotemperature contours at blade midpitch, and (*c*) isotemperature contours in an axial plane aligned with the rotor leading edge

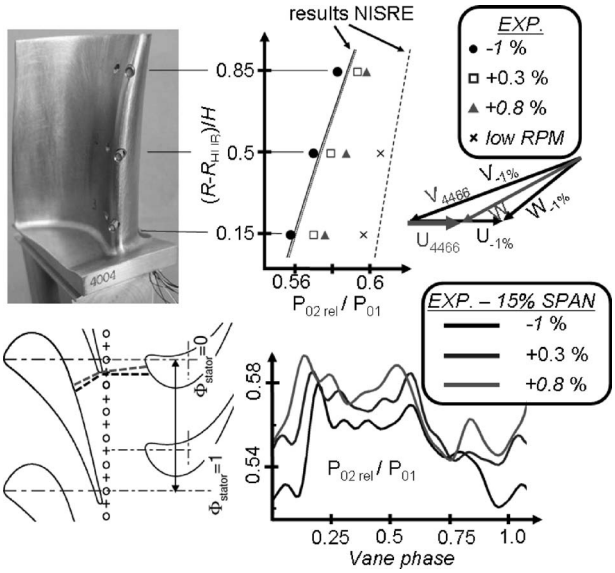

Fig. 8 (*a*) Time-averaged total pressure in the relative frame on the rotor leading edge and (*b*) time-resolved total relative pressure at 15% span

enters the cavity over 68% of the pitch in the ingestion −1% case. The ratio is reversed for ejection +0.3%: air enters the cavity over 38% of the pitch, although there is a net coolant rate ejected to the mainstream of 0.3% of the mainstream flow. Finally, for the ejection +0.8% condition, air is ejected across 78% of the pitch and the flow is ingested into the cavity due to the high static pressure only close to the left running shock. Thus, the unsteady interactions between the purge flow ejected from the wheel space cavity and the mainstream flow is dictated by the shock structures downstream of the stator. However, the effects of the stator potential flow field and secondary flow effects could not be detected.

Figure 7 presents the interaction of the cavity flow with the rotor, neglecting the pitchwise nonuniformities generated by the transonic vane. Figure 7(*a*) shows the purge flow being collected by the horseshoe vortex, which rolls up in front of the blade leading edge (Fig. 7(*c*)). The cold flow gradually mixes inside the vortex structure, lowering its core temperature. Due to the radial injection into the mainstream, a separation region is detected close to the cavity edge, in front of the rotor blade leading edge. Hub disk leakage streamlines show that the coolant flow is also collected by the hub passage vortex, which develops along the blade passage. Effects of the hub disk leakage interaction on the rotor flow field can be analyzed on the rotor blade leading edge where the total relative pressure has been measured, as described in Sec. 5.3.

5.3 Rotor Blade Leading Edge. The effect of the purge flow on the total relative pressure distribution at the leading edge of the rotor blades is illustrated in Fig. 8(*a*). The effect of the ejected air on the channel blockage is perceived in all three measuring locations at 15%, 50%, and 85% of the span. Compared with ingestion −1%, for which no blockage of the purge flow exists (even the vane endwall boundary layer is aspirated), the pressures are 1.9% and 3.0% higher, respectively, for ejection +0.3% and ejection +0.8%. The blockage effect is highest at the hub where the pressures are, respectively, 2.2% and 3.3% higher than for the baseline. When the rpm is lowered, the relative flow velocity at the rotor inlet increases and the total pressure increases on average by 7%. Considering the uncertainty on the Kulite transducers, the through-flow solver prediction for the baseline condition agrees quite well with the measurements with a maximum difference of about 10 mbars. The through-flow solver is based on radial equilibrium of the flow at the exit of each row, the conservation of mass flow across the rows, and loss and deviation correlations.

The phase-locked averaged evolution of the pressure over 1 1/2 pitch is shown in Fig. 8(*b*) for the three coolant rates. The shift in vane phase of the total pressure reveals a gradual change in the intensity and incidence angle of the vane trailing edge shocks with the purged flow rate. The amplitudes of the pressure variation are 0.09% for the baseline condition and 0.075% for ejection +0.3% and ejection +0.8%. The blowing condition at the stator-rotor interface seems therefore to have a limited impact on the unsteady variation of the total pressure amplitude. A transition to an earlier phase of the impingement of the shock on the rotor blades occurs as the coolant mass flow rate is increased. Compared with the baseline, the phase of the shock is shifted by 0.022φ and 0.06φ, respectively, for ejection +0.3% and ejection +0.8%. Figure 8(*b*) shows that the decrease in Mach number associated with the blockage causes the shock lines to become more normal to the flow and indeed impinge on the rotor at an earlier phase.

5.4 Purge Flow Impact Along 15% and 7.5%. Figure 9 depicts the Nusselt number distributions at 15% and 7.5% of the span. The Nusselt distribution is similar for all conditions, albeit with smaller heat flux rates for the baseline. This is related to the blockage created by the purge flow affecting the heat transfer distribution. The low-rpm presents the highest Nusselt levels. At 15% (Fig. 9(*a*)) in the rear suction side, ejection +0.8% shows an increase in heat transfer levels. However, the apparent beneficial effect is of the same order of magnitude as the repeatability. At 7.5% (Fig. 9(*b*)), there is no clear effect of the rotor-platform cooling at the rear suction side (differences between the baseline and ejection +0.8% remain within the experimental repeatability). At 15% (Fig. 9(*a*)), in the case of ingestion −1%, at $S/S_{max}=0.44$ there is a zone of relatively low heat flux that could be due to the vicinity of secondary flows. At ejection +0.8%, the region with low Nusselt is displaced upstream, at $S/S_{max}=0.33$, which could be due to more intense secondary flows rolling up earlier.

5.5 Effects on the Rotor Platform. Figure 10 shows static pressure contours and streamlines at the rotor platform for the baseline condition and for the ejection +0.8%. For the baseline condition, it is possible to detect clearly the saddle point in front of the blade leading edge, the suction and pressure side leg of the

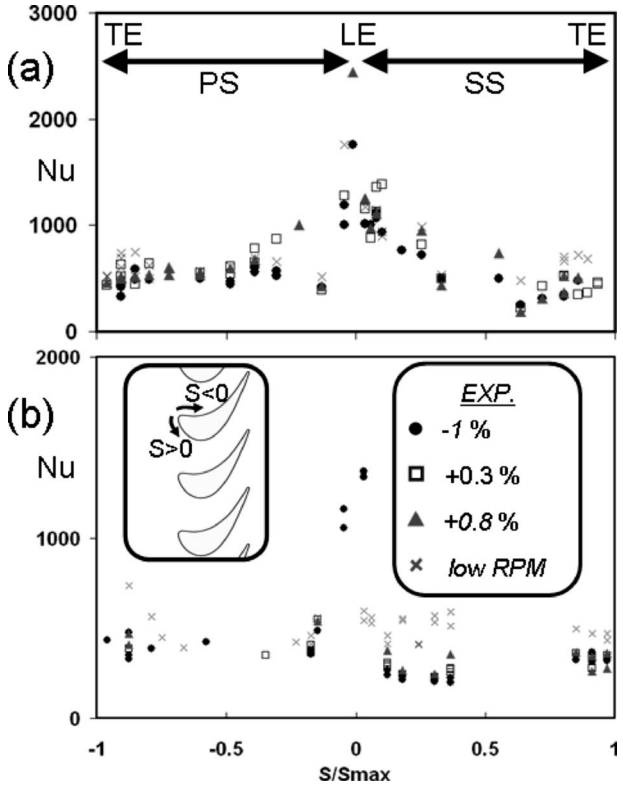

Fig. 9 Nusselt number distribution along the rotor airfoil: (top) at 15% span and (bottom) at 7.5% span

horseshoe vortex, and the pressure side corner vortex. The purge flow ejection from the wheelspace cavity modifies completely the flow field upstream of the rotor blade row. The saddle point moves upstream toward the cavity, due to the purge flow swallowed by the horseshoe vortex in front of the rotor blade leading edge, and a separation line appears close to the cavity. This separation line runs along the blade passage close to the blade suction side, and finally it is pushed by the rotor-platform cooling ejection toward the blade suction surface close to the trailing edge. The purge flow re-enters the mainstream with a smaller swirl angle than the main channel flow.

Considering a Lagrangian reference, the purge flow generates a streamwise vorticity component, which combines with the one generated by the secondary flow, contributing to increase the passage vortex intensity. Regarding the normal component to the streamwise vorticity (in the blade to blade plane), the purge flow

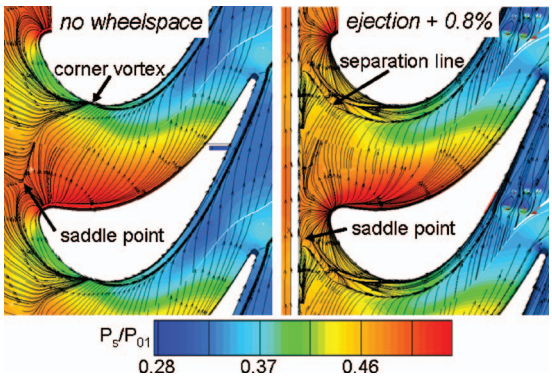

Fig. 10 Static pressure field on the rotor platform without cavity flow and for ejection +0.8% (streamlines through the blade passage do not line-up due to the computational-domain)

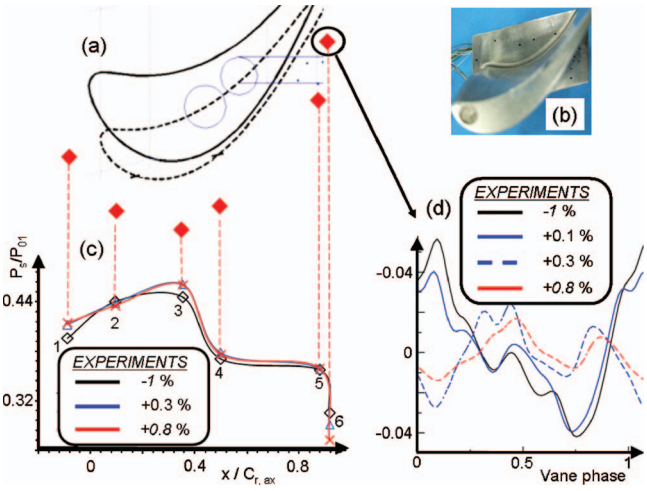

Fig. 11 (*a*) Pressure measurement locations on the rotor platform, (*b*) photograph of the instrumented blade, (*c*) time-averaged static pressure on the rotor platform, and (*d*) time-resolved static pressure downstream of the coolant holes

tends to push the streamlines in the direction opposite to the hub passage vortex. Hence, the purge flow contributes to strengthen the vortex structures which counter-rotate with the passage vortex. Therefore the separation line shown in Fig. 10 is representative of a vortex entity, which counter-rotates with respect to the passage vortex and is fed directly by the purge flow. The purge flow leaves the wheelspace mainly from a circumferential position close to the blade suction side, aspirated by the rotor blade pressure field at the platform.

Figures 11(*a*) and 11(*b*) show the location of the pressure sensors on the rotor platform and a picture of the instrumented blade. Figure 11(*c*) illustrates the time-averaged measured static pressure along the rotor midpitch. Figure 11(*d*) presents the time-resolved component of the unsteady pressure on the rotor platform for gauge 6, downstream of the rotor-platform film cooling. "Ingestion −1%" exhibits a single pressure fluctuation at the fundamental vane blades passing frequency. This could be caused by a pressure wave emanating from upstream convected through the rotor channel. On the other hand, ejection +0.3% and ejection +0.8% show a phenomenon that is occurring at twice the vane blade passing frequency, with a lower intensity. This might be caused by an unsteady interaction between the platform coolant and the gas convected from the hub disk region.

On the platform, the Nusselt is around 600, which is similar to the levels on the rotor pressure side measured at 7.5% of the blade span. Overall, the baseline configuration presents the lowest values. Figure 12 shows the gauge directly exposed to the coolant ejection. This gauge experiences a 20% reduction in heat transfer coefficient of 20% at ejection +0.8%.

5.6 Turbine Exit Flow Field. Figure 13 shows radial traverses of measured and computed total pressure and total temperature downstream of the stage. The pressure is nondimension-

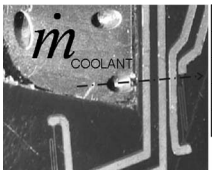

Condition	Nu
Ingestion -1%	490.1
Ejection +0.3%	418.5
Ejection +0.8%	462.9
Low rpm	488.3

Fig. 12 (Left) Detailed view of the heat transfer sensor located downstream of the cooling holes and (right) Nusselt number at the same sensor

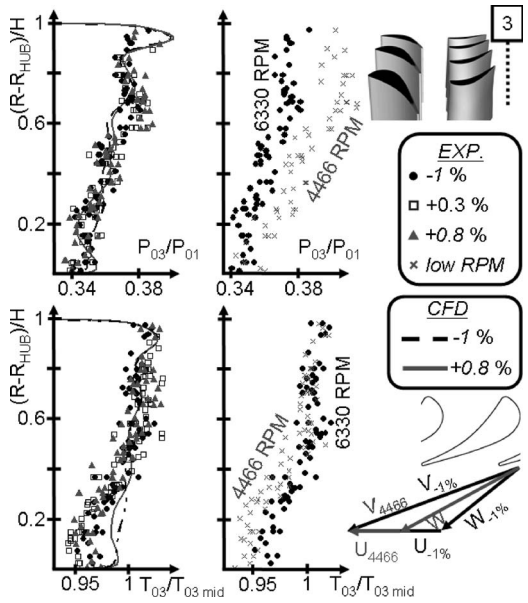

Fig. 13 Turbine exit flow field, experiments, and CFD

alized by the total pressure at turbine inlet, while the total temperature is nondimensionalized by the total temperature at midspan downstream of the rotor. The 3D Navier–Stokes computations show the same features than the experimental data. The high-pressure region at about 90% of the span can be related to the rotor tip leakage flow.

Effects of the rotor hub passage vortex can be detected up to 20% of the blade height measured from the platform. Ejecting cold flow increases the rotor hub secondary flow and the loss core can be identified at about 20% of the span, where a total pressure reduction is observed. Small differences can be noticed between computation and experiments at about 60% of the span probably due to the vane tip passage vortex not modeled by the CFD (due to the mixing plane). Concerning the total temperature distributions, the CFD overpredicts by 2% the total temperature at the hub. Close to 20% of the span, a reduction in temperature is observed in the case of coolant ejection, due to the coolant entrained in the hub passage vortex. When lowering the coolant flow rate, cooling effects become visible close to the hub, at 10% of the span, since the coolant remains closer to the endwall.

Reducing the rotational speed increases the incidence on the rotor blade. The flow then experiences a higher turning and secondary flows are intensified with a decrease in efficiency. As a consequence of the reduction in extracted work, the total temperature at midspan is higher for low-rpm than for the baseline. The total temperature radial traverse shows that the hub main vortex core for the baseline (ingestion −1%) is located at about 15%. At low-rpm a local minimum seems to be located at ~20% of the span, indicating an increase in the penetration height of the hub vortex in line with previously observed studies [18]. Unfortunately, the low resolution in the total pressure traverses prevents an accurate estimation of the penetration heights for all the operating conditions.

6 Turbine Efficiency Analysis

The efficiency was evaluated through a mechanical approach, in which the real power is retrieved from the measurement of the shaft power, based on the measurement of the inertia [41] and mechanical losses [37]. The power can thus be expressed as

$$p_{\text{real}} = p_{\text{shaft}} + p_{\text{losses}} = I\omega\frac{\partial\omega}{\partial t} + p_{\text{loss}} \tag{6}$$

where P_{loss} accounts for the mechanical losses. The control volume used to evaluate efficiency is shown in Fig. 3(*a*). The inlet and outlet planes of the control volume coincides with the measurements planes. The purge flow temperature and pressure were monitored with a thermocouple and a pressure transducer on the rotor disk coolant path. This allows gathering the total temperature and pressure levels of the coolant injected. Hence the isentropic power can be expressed as follows:

$$p_{\text{is}} = \dot{m}_{\text{inlet}}C_pT_{01}\left[1-\left(\frac{P_{03}}{P_{01}}\right)^{\gamma-1/\gamma}\right] + \dot{m}_{\text{coolant}}C_pT_{0\text{coolant}}\left[1-\left(\frac{P_{03}}{P_{0\text{coolant}}}\right)^{\gamma-1/\gamma}\right] \tag{7}$$

Due to the variation of inlet and total pressure variables along the span, the efficiency formulation makes use of mass flow average quantities, so that the efficiency can finally be expressed as the ratio between the real and isentropic powers.

$$\eta = \frac{I\omega\dfrac{\partial\omega}{\partial t} + P_{\text{loss}}}{(\dot{m}_{\text{inlet}} - \dot{m}_{\text{leakage}})C_p\bar{T}_{01}\left[1-\left(\dfrac{\bar{P}_{03}}{\bar{P}_{01}}\right)^{\gamma-1/\gamma}\right] + \dot{m}_{\text{coolant}}C_pT_{0\text{coolant}}\left[1-\left(\dfrac{\bar{P}_{03}}{P_{0\text{coolant}}}\right)^{\gamma-1/\gamma}\right]} \tag{8}$$

The leakage mass flow refers to hot gas ingestion from the main channel into the wheelspace cavity and therefore appears only in the baseline condition. The coolant mass flow is the cold flow purged from the wheelspace and rotor platform. The random uncertainty is 0.68%, and the systematic uncertainty is 1.21%. The level of dispersion in the measured efficiency is 1.9% ($\pm 1.96\sigma$) due to the dispersion in the pressure ratio of the experiments. Windage losses have been computed separately according to the Traupel formulation [41]. With respect to the baseline condition, efficiency penalties of 0.19% and 0.26% have been predicted, respectively, for ejection +0.3% and ejection +0.8%. Decreasing the rotational speed reduces the windage loss 0.17%. Figure 14 summarizes the measured turbine efficiency variations for the different test conditions evaluated, considering the baseline (ingestion −1%) as reference. At ejection +0.3%, the efficiency is +1.11% higher but when the mass flow is further raised to ejection +0.8%, the efficiency is +1.04% above the baseline. The CFD also predicts a rise in the efficiency of 0.9% compared with the baseline. Lowering the turbine speed low-rpm results in a decreased efficiency of about 9.8%.

To get deeper insight into the efficiency sensitivity, measured values have been used to calculate loss correlations [42]. The

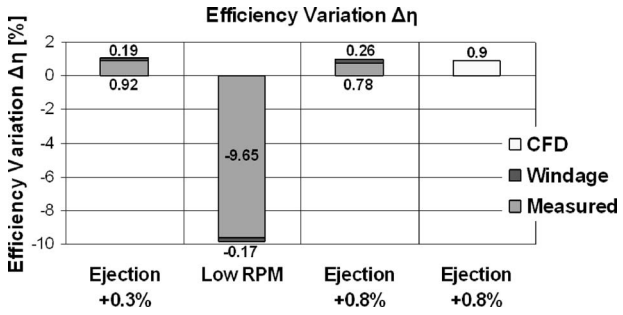

Fig. 14 Measured turbine efficiency and windage effects compared with the ingestion −1%

turbine aerodynamic losses are evaluated using the correlations of Kacker and Okapuu [43]. Previous studies have proven the applicability of Kacker and Okapuu at off-design conditions [44]. The ξ_{AMDC} is the Ainley–Mathieson/Dunham–Came boundary layer loss, which remains nearly constant for all the investigated configurations. When the inlet Mach number at hub is higher than 0.4, a "shock loss" correction is introduced:

$$\xi_{\text{shock loss}} = 0.75 \cdot (M_{1,\text{hub}} - 0.4)^{1.75} \cdot \left(\frac{R_{\text{hub}}}{R_{\text{tip}}}\right) \cdot \left(\frac{P_{s1}}{P_{s2}}\right) \cdot \frac{1 - \left(1 + \frac{\gamma - 1}{2} \cdot \mathrm{M}_1^2\right)^{\gamma - 1/\gamma}}{1 - \left(1 + \frac{\gamma - 1}{2} \cdot \mathrm{M}_2^2\right)^{\gamma - 1/\gamma}} \tag{9}$$

This is particularly useful for the conditions tested in this work, since the purge flow ingestion/ejection modify the vane outlet Mach number. The "channel flow acceleration" term is computed with the following expression:

$$K_P = 1 - (\mathrm{M}_1/\mathrm{M}_2)^2 \cdot 1.25 \cdot (\mathrm{M}_2 - 0.2) \tag{10}$$

The "supersonic drag rise" includes the term proposed by Dunham and Came [45] as follows:

$$\xi_{\text{supersonic drag rise}} = 1 + 60 \cdot (\mathrm{M}_2 - 1)^2 \tag{11}$$

$$\xi_{\text{profile}} = 0.914\left(\frac{2}{3}\xi_{\mathrm{AMDC}} \cdot K_P + \xi_{\text{shock loss}}\right) \cdot \xi_{\text{supersonic drag rise}} \tag{12}$$

Results obtained from the correlations are illustrated in Fig. 15, showing the different contributions of the vane and rotor losses. The loss prediction follows the trend shown by the experiments, but the predictions are conservative. The coefficients computed using Kacker and Okapuu's correlation [34] are summarized in Table 6. Considering the small discrepancies in efficiency due to

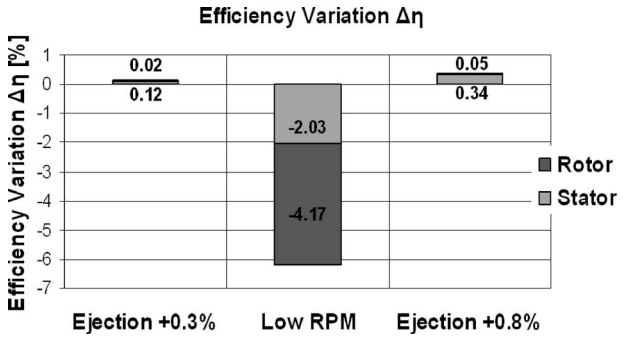

Fig. 15 Turbine efficiency predicted using Kacker and Okapuu [43] correlations, with reference to the ingestion −1%

Table 6 Efficiency variation for different test condition

Condition	Loss coefficients		
	ξ_{AMDC}	$\xi_{\text{supersonic drag rise}}$	$\xi_{\text{shock loss}}$
	Vane/rotor	Vane	Rotor
Ingestion −1%	0.042/0.030	1.421	0.0060
Ejection +0.3%	0.042/0.029	1.333	0.0057
Ejection +0.8%	0.042/0.029	1.124	0.0046
Low-rpm	0.041/0.031	1.750	0.0738

the coolant ejection rate, the main effect can be attributed to the trailing edge shock losses generated by the stator. Differences on the rotor losses are negligible. Ejecting coolant fluid from the hub disk cavity leads to a performance improvement. This raise in efficiency could be explained by the modification on the shock system downstream of the stator, as shown in Fig. 6.

Coolant flow injection through the wheelspace cavity causes a blockage effect, which decreases the Mach number downstream of the stator forcing the shock to move backward inside the nozzle guide vane. This limits the flow acceleration close to the stator trailing edge, thus reducing the trailing edge shock losses. Lowering the rotational speed leads to a slight increase in the vane outlet Mach number. This effect combined with the reduction in peripheral speed results in a high increase in positive incidence in the rotor. The loss calculation predicts a reduction of 6.2% in the performance ($\Delta\eta_{\text{total}}$) by decreasing the rotational speed from nominal to low-rpm. When the rotational speed decreases, the losses related to the shock loss ($\Delta\eta_{\text{rotor}}$) tend to increase more than the vane trailing edge shock (supersonic drag rise) losses ($\Delta\eta_{\text{stator}}$). Low-rpm shows a difference between correlations and experiments of almost 3.3%. Lowering the rotational speed increases the tip clearance from 1% to 1.4% of the blade height, therefore providing an extra loss contribution.

7 Conclusions

A complete aerothermal experimental and computational investigation on the purge and platform film cooling has been carried out on a transonic turbine stage. The turbine stage, operating at engine-representative conditions, has been studied at various cooling rates in order to isolate the individual impact of purge flows from the platform cooling.

Within the wheelspace cavity, the ejection of purge flow reduces the amount of pressure fluctuations by 50%. The unsteady interaction between the purge flow and the mainstream was found to be mainly dictated by the vane trailing edge shocks. Conversely, the hub disk leakage has an impact on the stator shock system over the whole blade height. By contrast, no clear effects of the stator potential flow field and secondary flow effects were detected. The purge flow directly feeds the rotor hub passage vortex and enhances the effect of the counter-rotating pressure side corner vortex.

Rotor blade leading edge relative pressure stagnation measurements showed an impact in terms of blockage of the purge flow over the whole blade span. Effects in reducing the rotor inlet Mach number have been detected. Larger coolant flow rates lead to a decrease in incidence in the relative rotor frame, thus increasing the degree of reaction at the hub.

The investigated conditions resulted in higher heat flux rates than the ingestion −1%. This is linked to the blockage created by the purge flow affecting the heat transfer distribution. The purge flow distorts the flow, enhancing the heat transfer coefficient on the platform. The low-rpm presents the highest Nusselt levels. Increasing the coolant rate also tends to decrease the importance of the unsteady phenomena at the platform.

The effect of platform cooling is almost entirely restricted to the platform, with minimal effects on the suction side or trailing edge.

Measurements, CFD, and correlations show the same trend: Ejecting purge flow leads to an increase in efficiency, mainly due to the modification of the shock system downstream of the stator and to a reduction of the stator trailing edge shock losses.

Acknowledgment

The authors would like to thank Bertrand Haguenauer and Tolga Yasa for their assistance in the testing and data processing. The authors would also like to acknowledge the financial support of the European Commission and Industrial Partners involved in TATEF2 "Turbine Aero-Thermal External Flows 2."

Nomenclature

A = area (m^2)
C_d = discharge coefficient
C_P = specific heat at constant pressure (J/kg K)
C_{rotor} = rotor chord (m)
C_{stator} = stator chord (m)
$C_w = \dot{m}_{coolant}/\mu \cdot R_0$ = nondimensional cooling flow rate
$G = s/R_{HUB}$ = cavity gap ratio
H = blade height (m)
h = heat transfer coefficient (W/m^2 K)
I = moment of inertia (kg m^2)
k_g = thermal conductivity (W/m K)
$\underline{kp}$ = loss coefficient
$M = v/\sqrt{\gamma \Re T}$ = Mach number
$\dot{m}$ = mass flow rate (kg/s)
N = rotational speed (rpm)

$$Nu = \frac{q \cdot C_{rotor}}{k_{gas} \cdot (T_{gas} - T_{wall})}$$ = rotor Nusselt number

p = power (W)
P = pressure (bar)
q = heat flux (W/m^2)
r = recovery factor

$$r = 1 - \frac{1 - (P_{s2}/P_{01})^{\gamma - 1/\gamma}}{1 - (P_{s3}/P_{01})^{\gamma - 1/\gamma}}$$ = degree of reaction

$\Re$ = gas constant (J/kg K)
R = radius (m)
R_0 = cavity outer radius (m)
R_{hub} = vane hub radius (m)
$Re_2 = \rho \cdot v_2 \cdot C_{stator}/\mu$ = mainstream Reynolds number
$Re_\theta = \rho \cdot w \cdot R_0^2/\mu$ = disk rotational Reynolds number
s = cavity axial clearance (m)
S = curvilinear abscissa (m)
T = temperature (K)
t = time (s)
$u = R \cdot N \cdot 2\pi/60$ = peripheral speed (m/s)
v = velocity in the absolute frame (m/s)
V = volume (m^3)
w = velocity in the relative frame (m/s)
x = distance along the turbine axis (m)

Greek

ρ = density (kg/m^3)
μ = dynamic viscosity (kg/m s)
η = efficiency (%)
γ = specific heat ratio
Φ = phase in sense of rotation, relative to the rotor/stator
ξ = pressure loss coefficient (%)

Subscripts

0 = total conditions
1 = stator inlet
2 = stator outlet, rotor inlet
3 = rotor outlet
aw = adiabatic wall condition
ax = axial direction, aligned with the machine axis
is = isentropic conditions
r = frame of reference relative to rotor
s = static conditions

References

[1] Paniagua, G., Denos, R., and Almeida, S., 2004, "Effect of the Hub Endwall Cavity Flow on the Flow Field of a Transonic High-Pressure Turbine," ASME J. Turbomach., **126**, pp. 578–586.
[2] Ong, J. H. P., Miller, R. J., and Uchida, S., 2006, "The Effect of Coolant Injection on the Endwall Flow of High-Pressure Turbine," ASME Paper No. GT2006-91060.
[3] McLean, C., Camci, G., and Glezer, B., 2001, "Mainstream Aerodynamic Effects Due to Wheelspace Coolant Injection in a High Pressure Turbine Stage," ASME J. Turbomach., **123**, pp. 687–703.
[4] Phadke, U. P., and Owen, J. M., 1988, "Aerodynamic Aspects of the Sealing of Gas-Turbine Rotor-Stator Systems," Int. J. Heat Fluid Flow, **9**, pp. 98–117.
[5] Ko, S. H., and Rhode, D. L., 1992, "Thermal Details in a Rotor-Stator Cavity at Engine Conditions With a Mainstream," ASME J. Turbomach., **114**, pp. 446–453.
[6] Laroche, E., Desportes de la Fosse, S., Djaoui, M., Debuchy, R., and Pate, L., 1999, "A Combined Experimental and Numerical Investigation of the Flow in a Heated Rotor/Stator Cavity With a Centripetal Injection," ASME Paper No. 99-GT-170.
[7] Pfau, A., Treiber, M., Sell, M., and Gyarmathy, G., 2001, "Flow Interaction From the Exit Cavity of an Axial Turbine Blade Row Labyrinth Seal," ASME J. Turbomach., **123**, pp. 342–352.
[8] Anker, J. E., and Mayer, J. F., 2002, "Simulation of the Interaction of Labyrinth Seal Leakage Flow and Main Flow in an Axial Turbine," ASME Paper No. 2002-GT-30348.
[9] Hunter, S. D., and Manwaring, S. R., 2000, "Endwall Cavity Flow Effects on Gas Path Aerodynamics in an Axial Flow Turbine," ASME Paper No. 2000-GT-651.
[10] Rosic, B., and Denton, J.D., 2006, "The Control of Shroud Leakage Loss by Reducing Circumferential Mixing," ASME Paper No. GT2006-90946.
[11] Bohn, D., Deuker, E., Emunds, R., and Gorzelitz, V., 1995, "Experimental and Theoretical Investigations of Heat Transfer in Closed Gas-Filled Rotating Annuli," ASME J. Turbomach., **117**, pp. 175–183.
[12] Bohn, D., Rudzinski, B. E., Surken, N., and Gartner, W., 2000, "Experimental and Numerical Investigations of the Influence of Rotor Blades on Hot Gas Ingestion Into the Upstream Cavity of an Axial Turbine Stage," ASME Paper No. 2000-GT-284.
[13] Roy, R. P., Xu, G., Feng, J., and Kang, S., 2001, "Pressure Field and Main-Stream Gas Ingestion in a Rotor-Stator Disk Cavity," ASME Paper No. 2001-GT-0564.
[14] Gentilhomme, O., Hills, N. J., Turner, A. B., and Chew, J. W., 2003, "Measurement and Analysis of Ingestion Through a Turbine Rim Seal," ASME J. Turbomach., **125**, pp. 505–512.
[15] Cao, C., Chew, J. W., Millington, P. R., and Hogg, S. I., 2003, "Interaction of Rim Seal and Annulus Flows in an Axial Flow Turbine," ASME Paper No. 2003-GT-38368.
[16] Roy, R. P., Feng, J., Narzary, D., Saurabh, P., and Paolillo, R. E., 2004, "Experiments on Gas Ingestion Through Axial-Flow Turbine Rim Seals," ASME Paper No. 2004-GT-53394.
[17] Roy, R.P., Zhou, D.W., Ganesan, S., Johnson, B.V., Wang, C. -Z, and Paolillo, R.E., 2007, "The Flow Field and Main Gas Ingestion in a Rotor-Stator Cavity," ASME Paper No. GT2007-27671.
[18] Marini, R., and Girgis, S., 2007, "The Effect of Blade Leading Edge Platform Shape on Upstream Disk Cavity to Mainstream Flow Interaction of a High-Pressure Turbine Stage," ASME Paper No. GT2007-27429.
[19] Montomoli, F., Massini, M., Maceli, N., Cirri, M., Lombardi, L., Ciani, A., D'Ercole, M., and de Prosperis, R., 2006, "Interaction of Wheelspace Coolant and Main Flow in a New Aeroderivative LPT," ASME Paper No. GT2006-90877.
[20] Blair, M. F., 1974, "An Experimental Study of Heat Transfer and Film Cooling on Large-Scale Turbine Endwalls," ASME J. Heat Transfer, **96**, pp. 524–529.
[21] Harasgama, S. P., and Burton, C. D., 1992, "Film Cooling Research on the Endwall of a Turbine Nozzle Guide Vane in a Short Duration Annular Cascade: Experimental Technique and Results," ASME J. Turbomach., **114**, pp.

734–740.
[22] Friedrichs, S., Hodson, H. P., and Dawes, W. N., 1996, "Distribution of Film-Cooling Effectiveness on a Turbine Endwall Measured Using Ammonia and Diazo Technique," ASME J. Turbomach., **118**, pp. 613–621.
[23] Dring, R. P., Blair, M. F., and Hoslyn, H. D., 1980, "An Experimental Investigation of Film Cooling on a Turbine Rotor Blade," ASME J. Eng. Power, **102**, pp. 81–87.
[24] Takeishi, M., Aoki, S., Sato, T., and Tsukagoshi, K., 1992, "Film Cooling on a Gas Turbine Rotor Blade," ASME J. Turbomach., **114**, pp. 828–834.
[25] Abhari, R. S., and Epstein, A. H., 1994, "An Experimental Study of Film Cooling in a Rotating Transonic Turbine," ASME J. Turbomach., **116**, pp. 63–70.
[26] Blair, M. F., 1994, "An Experimental Study of Heat Transfer in a Large-Scale Turbine Rotor Passage," ASME J. Turbomach., **116**, pp. 1–13.
[27] Ahn, J., Schobeiri, M.T., Han, J.C., and Moon, H.K., 2004, "Film Cooling Effectiveness on the Leading Edge of a Rotating Turbine Blade," IMECE Paper No. 2004-59852.
[28] Suryanarayanan, A., Mhetras, S. P., Schobeiri, M. T., and Han, J.C., 2009, "Film-Cooling Effectiveness on a Rotating Blade Platform," ASME J. Turbomach. **131**, p. 011014.
[29] Suryanarayanan, A., Ozturk, B., Schobeiri, M. T., and Han, J.C., 2007, "Film Cooling Effectiveness on a Rotating Turbine Platform Using Pressure Sensitive Paint Technique," ASME Paper No. GT2007-27122.
[30] Sieverding, C. H., Arts, T., Dénos, R., and Martelli, F., 1996, "Investigation of the Flow Field Downstream of a Turbine Trailing Edge Cooled Nozzle Guide Vane," ASME J. Turbomach., **118**, pp. 291–300.
[31] Sieverding, C. H., and Arts, T., 1992, "The VKI Compression Tube Annular Cascade Facility CT3," ASME Paper. 92-GT-336.
[32] Dénos, R., and Paniagua, G., 2005, "Rotor/Stator Interaction in Transonic HP Turbines," *Effects of Aerodynamic Unsteadiness in Axial Turbomachines*, R. Denos and G. Paniagua, eds., von Karman Institute Lecture Series, Rhode Saint Genèse, Belgium.
[33] Popp, O., Smith, D., Bubb, J., Grabowski, H., and Diller, T., 1999, "Steady and Unsteady Heat Transfer in a Transonic Film Cooled Turbine Cascade," ASME Paper No. 99-GT-259.
[34] Schlichting, H., 1968, *Boundary Layer Theory*, 6th ed., Springer, Berlin.
[35] Thorpe, J., Yoshino, S., Ainsworth, R., and Harvey, N., 2004, "Improved Fast Response Instrumentation for Short-Duration Wind Tunnels," Meas. Sci. Technol., **15**, pp. 1897–1909.
[36] Solano, J.P., Paniagua, G., and de la Loma, A., 2008, "Novel 2D Transient Heat Conduction Calculation in a Cooled Rotor: Ventilation Preheating—Blowdown Flux," ASME Paper No. GT2008-51308.
[37] Dénos, R., Paniagua, G., Yasa, T., and Fortugno, E., 2006, "Determination of the Efficiency of a Cooled HP Turbine in a Blowdown Facility," ASME Paper No. GT2006-90460.
[38] Ames Research Staff, 1953, "Equations, Tables and Charts for Compressible Flow," NACA Report No. 1135.
[39] Cambier, L, and Gazaix, M., 2002, "elsA: An Efficient Object-Oriented Solution to CFD Computations," AIAA Paper No. 2002-0108
[40] Ghia, U., Ghia, K. N., and Shin, C. T., 1982, "High-Re Solutions for Incompressible Flow Using the Navier-Stokes Equations and a Multigrid Method," J. Comput. Phys., **48**, pp. 387–411.
[41] Paniagua, G., and Yasa, T., 2007, "Accurate Turbine Inertia Measurement," J. Experimental Mechanics, **47**, pp. 693–700.
[42] Yasa, T., Paniagua, G., and Bussolin, A., 2007, "Performance Analysis of a Transonic High Pressure Turbine," Proc. Inst. Mech. Eng., Part A, **221**, pp. 769–778.
[43] Kacker, S. C., and Okapuu, U., 1982, "A Mean Line Prediction Method for Axial Flow Turbine Efficiency," ASME J. Eng. Power, **104**, pp. 111–119.
[44] Woinowsky-Krieger, M., Lavoie, J. P., Vlasic, E. P., and Moustapha, S. H., 1999, "Off-Design Performance of a Single-Stage Transonic Turbine," ASME J. Turbomach., **121**, pp. 177–183.
[45] Dunham, J., and Came, P. M., 1970, "Improvements to the Ainley-Mathieson Method of Turbine Performance Prediction," ASME J. Eng. Power, **92**, pp. 252–256.

Improving Efficiency of a High Work Turbine Using Nonaxisymmetric Endwalls—Part I: Endwall Design and Performance

T. Germain
e-mail: thomas.germain@muc.mtu.de

M. Nagel

I. Raab

MTU Aero Engines GmbH,
Dachauer Strasse 665,
80995 München, Germany

P. Schüpbach

R. S. Abhari

Department of Mechanical and Process Engineering,
LEC, Laboratory of Energy Conversion,
ETH Zurich,
8092 Zurich, Switzerland

M. Rose
Institute of Aeronautical Propulsion,
University of Stuttgart,
70569 Stuttgart, Germany

This paper is the first part of a two part paper reporting the improvement of efficiency of a one-and-half stage high work axial flow turbine by nonaxisymmetric endwall contouring. In this first paper the design of the endwall contours is described, and the computational fluid dynamics (CFD) flow predictions are compared with five-hole-probe measurements. The endwalls have been designed using automatic numerical optimization by means of a sequential quadratic programming algorithm, the flow being computed with the 3D Reynolds averaged Navier-Stokes (RANS) solver TRACE. *The aim of the design was to reduce the secondary kinetic energy and secondary losses. The experimental results confirm the improvement of turbine efficiency, showing a stage efficiency benefit of 1% ± 0.4%, revealing that the improvement is underestimated by CFD. The secondary flow and loss have been significantly reduced in the vane, but improvement of the midspan flow is also observed. Mainly this loss reduction in the first row and the more homogeneous flow is responsible for the overall improvement. Numerical investigations indicate that the transition modeling on the airfoil strongly influences the secondary loss predictions. The results confirm that nonaxisymmetric endwall profiling is an effective method to improve turbine efficiency but that further modeling work is needed to achieve a good predictability.* [DOI: 10.1115/1.3106706]

1 Introduction

Endwall losses in turbines contribute significantly to the overall losses, especially when cost and weight reasons induce the reduction in stage number and airfoil count, resulting in increased stage loading and airfoil lift. Hence it becomes more and more necessary to understand the secondary loss production mechanisms as well as to establish design methods to reduce them. The continuously growing computational power makes it nowadays possible to simulate the complex three-dimensional viscous flows and to make intensive use of numerical optimization algorithms, but the accuracy of the predictions is still a key issue and the results of computational fluid dynamics (CFD) simulations should be taken with some circumspection.

Nevertheless for the past decade impressive progress has been made in understanding secondary flow phenomena, and several promising methods have been proposed and validated for the reduction in secondary loss. Most of them may also have strong consequences on the whole flow field and not only on the endwall regions, particularly in low aspect ratio passages.

2 Secondary Flows in Turbines

2.1 Flow Phenomena. Secondary flow in a blade row originates in the incoming endwall boundary layer, as depicted in Fig. 1. The first phenomena will be the rolling up of the layer in front of the leading edge, resulting in the horseshoe vortex that separates in two legs along pressure and suction side. The turning of the inlet vorticity will introduce streamwise vorticity and thus build up the passage vortex, the low momentum fluid in the endwall layer being driven by the freestream transverse pressure gradient to cross the passage from pressure to suction side. In the corner between airfoil and endwall, so called corner vortices may form under the action of the horseshoe or the passage vortex. A comprehensive description of secondary flows was provided by Sieverding [1] and later by Langston [2].

Additional features are the trailing filament and trailing shed vorticity described by Hawthorne [3], the former being related to the deformation of an inlet vortex filament and usually acting in the neighborhood of the passage vortex, and the latter phenomenon being the consequence of nonuniform lift over the span. Their importance for turbine design was underlined more recently by Pullan et al. [4] and Schlienger et al. [5].

2.2 Reduction in Secondary Loss. Different methods have been proposed and experimentally investigated, especially airfoil and endwall redesign. Gier et al. [6] provided a detailed literature review on this topic.

Three-dimensional airfoil modifications include leaning and bowing, as suggested by Dejc and Zarjankin [7], Harrison [8], or Kawagishi and Kawasaki [9]. The latter concluded that bowing resulted in radial loss redistribution rather than loss reduction. Airfoil thickening was addressed by Eymann et al. [10] in combination with endwall contouring, but the reduction in secondary loss was partially balanced by an increased profile loss. Leading edge modifications lead also to loss reductions as reported by Sauer and Wolf [11]. Investigations by Becz et al. [12] revealed the importance of the fillet radii, which could also result in efficiency improvements.

Axisymmetric endwall contouring was introduced by Dejc and Zarjankin [7], and several authors proved it to be an efficient method.

Contributed by the International Gas Turbine Institute of ASME for publication in the JOURNAL OF TURBOMACHINERY. Manuscript received January 26, 2009; final manuscript received February 10, 2009; published online January 12, 2010. Review conducted by David Wisler. Paper presented at the ASME Turbo Expo 2008: Land, Sea and Air (GT2008), Berlin, Germany, June 9–13, 2008.

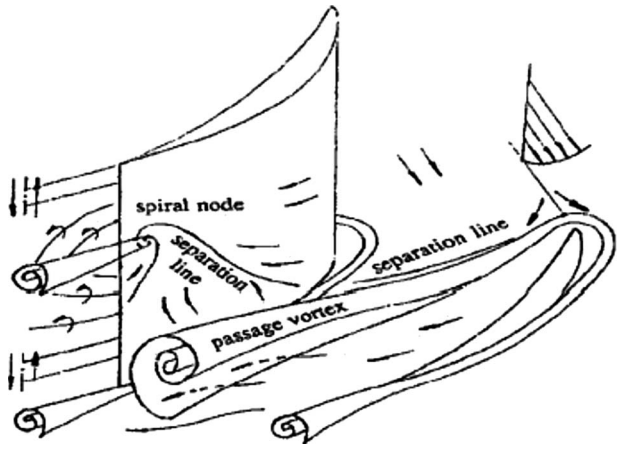

Fig. 1 Schematic view of secondary flow structures in a turbine, after Langston [2]

Nonaxisymmetric endwall contouring was initially proposed by Rose [13] in order to equalize the endwall pressure field with the aim to reduce purge flow requirements. With two nonaxisymmetric endwalls for the Durham cascade, Hartland et al. [14] and Gregory-Smith et al. [15] demonstrated that significant loss reduction is achievable. Using experiences from the Durham cascade investigation, Brennan et al. [16] and Rose et al. [17] redesigned the endwalls of a high pressure (HP) turbine model rig and improved the turbine efficiency by about 0.6%.

Combining airfoil profiling and nonaxisymmetric endwall contouring in full three-dimensional design optimization, Nagel et al. [18] achieved a loss reduction by 22% in an experimentally validated cascade.

2.3 CFD Predictions. The only industrially practical loss predictions for the highly complex secondary flow phenomena are obtained from three-dimensional Reynolds averaged Navier-Stokes (RANS) simulations. Though improvements have been made in the past years in the field of turbulence and transition modeling, supported by increasing computational power, usual CFD codes still have difficulties in predicting secondary losses accurately.

Hartland et al. [14] and Gregory-Smith et al. [15] reported poor loss predictions based on CFD for their cascade experiments, but they noticed that the secondary kinetic energy (SKE) was well predicted and correlated with the experimentally determined secondary loss. The high pressure turbine redesign by Rose et al. [17] was based on these correlations and successfully validated the approach. However, Ingram et al. [19] continued cascade investigations using the same methodology, but the predicted and validated SKE reductions did not correspond to any experimental loss reduction.

The loss predictions made by Nagel et al. [18] matched the experimental data, and more recently Praisner et al. [20] reported the successful optimization of nonaxisymmetric endwalls in a high-lift airfoil cascade, while the design was based on CFD loss.

Obviously the loss mechanisms of secondary flows are not fully understood and the achievement of optimal designs is still challenging. In order to help the understanding of the flow features, Germain et al. [21] presented some visualization techniques for CFD results, aiming to identify the vortical regions responsible for loss generation. A modified definition of SKE was provided for the evaluation of pitchwise and spanwise nonhomogeneities of the flow as well as a criterion based on flow field topology for the identification of vortical structure (the "vortex strength").

Table 1 Characteristics of the LISA turbine at design operating point

Turbine	
Rotor speed (rpm)	2700
Pressure ratio (1.5-stage, total-to-static)	1.60
Turbine entry temperature (°C)	55
Total inlet pressure (bar abs norm)	1.4
Shaft power (kW)	292
Hub/tip diameter (mm)	660/800
First stage	
Pressure ratio (first stage, total-to-total)	1.35
Degree of reaction (−)	0.39
Loading coefficient $\psi=\Delta h/u2$ (−)	2.36
Flow coefficient $\varphi=cx/u$ (−) (based on cx at the R1 exit)	0.65

3 Endwall Design

The research turbine "LISA" of the Turbomachinery Laboratory at the Swiss Federal Institute of Technology, originally a two-stage shrouded turbine [22], has been recently redesigned as a one-and-half stage unshrouded turbine so that it is representative of a high work, cooled turbine [23]. Tables 1 and 2 show the main characteristics of the turbine, as reported by Behr et al. [23]. The turbine cross section is shown in Fig. 2.

For the present investigation this one-and-half stage configuration has been modified using nonaxisymmetric endwalls while the airfoil profiles remained unchanged. Both hub and tip endwalls of the first stator as well as the hub endwall of the rotor have been optimized with the aim at reducing secondary flow.

Fillet radii modify the shape of a nonaxisymmetric endwall in the region close to the airfoils and thus may have a strong impact on the action of the contour. This makes it necessary to take them into account during the endwall design. Their effect on the flow structures is demonstrated in Sec. 5.2. The fillets have a radius of 2 mm in the stators and 3 mm in the rotor.

Table 2 Characteristic geometry and performance parameters of the 1.5-stage turbine configuration

	S1	R1	S2
No. of blades	36	54	36
Inlet flow angle (midspan) (deg)	0	54	−42
Exit flow angle (midspan) (deg)	73	−67	64
Solidity (chord/pitch)	1.3	1.4	1.3
Mean stagger angle (deg)	52.8	39.4	34.5
Aspect ratio (span/chord)	0.87	1.17	0.82
Profile stacking	LE	CoG	LE
Blade row relative exit Mach numbers (average) (−)	0.54	0.5	0.48
Reynolds number based on true chord and blade row relative exit velocity (−)	710,000	380,000	510,000

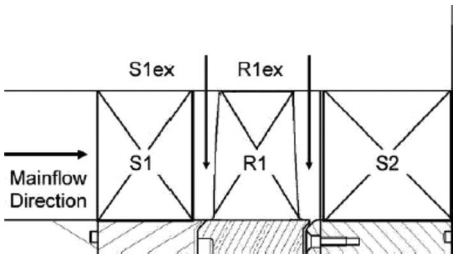

Fig. 2 Cross section of the LISA turbine

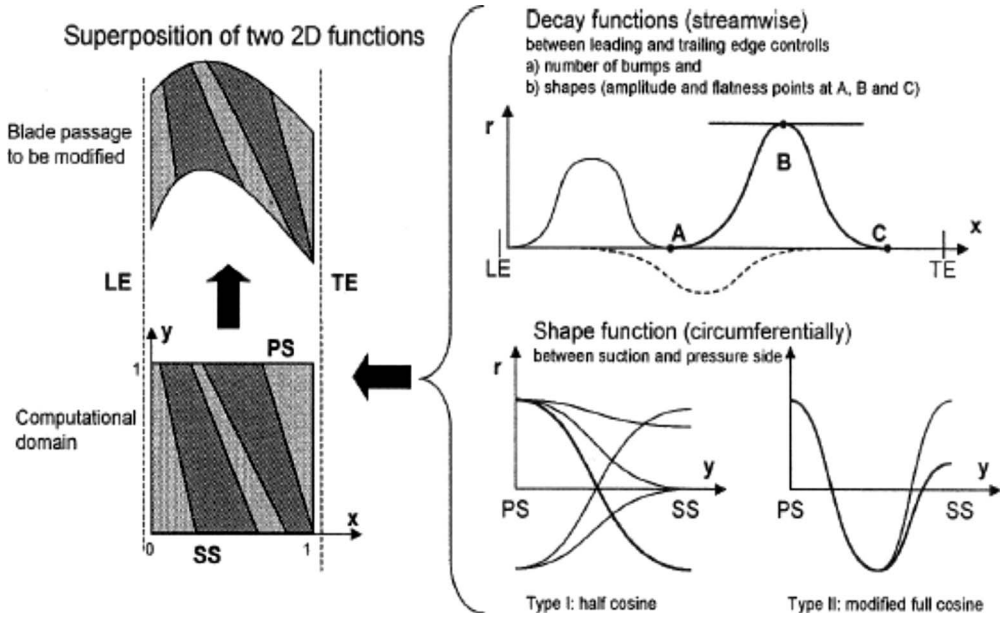

Fig. 3 Parametrization of the nonaxisymmetric endwalls

3.1 Endwall Parametrization. The parametrization of the endwalls is "object oriented" in the sense that various "bumps," elevations, and depressions can be placed on the wall, as shown in Fig. 3. They can be superposed and their amplitude, position, and shape can be individually adjusted. Each of these objects is described by an axial decay function and a circumferential shape function, which represents approximately 15 parameters per object. This parametrization allows influencing flow structures, in particular, by adding a contouring object in a specific endwall region. This approach turns out to be very effective since each turbine blade shows different flow structures and needs a customized endwall topology. Furthermore the transfer of an optimal endwall contour from one platform to another is easily accomplished. This parametrization was first introduced by Nagel et al. [18], but the underlying mathematical functions have been modified in order to allow more complex and easier adjustable endwall shapes. The axial decay function comprises a polynomial of sinusoidal functions. In the present design, one contouring object per endwall was used.

3.2 Surface Generation and Meshing. In order to ensure a high quality of the whole production chain from aerodynamics design to manufacturing, the initial airfoil and endwall geometry definition including fillet radii occurs on computer aided design (CAD) basis. The computational mesh is then projected on the parametrized CAD surfaces.

CFD Norway's G3DMESH [24] has been used to generate the multiblock grid, allowing the exact representation of the fillets as found in the real turbine (Fig. 4). The nondimensionalized wall distance on the airfoils and the endwalls is around $y+=1$. The resulting number of nodes is about 1.5×10^6 per turbine row. The tip clearance gap was fully discretized using 17 points radially.

3.3 Flow Solver. The CFD simulations are performed using the unsteady Reynolds averaged Navier-Stokes (URANS) code TRACE developed at DLR and MTU, which has been especially designed for the simulation of steady and unsteady turbomachinery flows. The turbulence is modeled by the Wilkox k-ω two-equation model in a low-Reynolds version with compressibility extension. The boundary layers are computed following the low-Reynolds approach. A transition model is used on the airfoil suction side and pressure side based on the modified correlations of Abu-Ghannam and Shaw [25]. The model can be activated on the airfoil, while the endwall boundary layers are assumed to be of turbulent nature. For more information about the numerical implementation of the solver and the transition model, see Ref. [26].

3.4 Optimization. The endwalls have been designed using automatic numerical optimization by means of the sequential quadratic programming algorithm DONLP2 developed by Spellucci [27], which allows nonlinear constrained optimization.

A combination of total pressure losses and SKE was used as the objective function, while the averaged exit yaw angle of each row was allowed to vary only within a small range in order to conserve the capacity of the baseline turbine. The raw result of the stator S1 optimization still showed a deviation in capacity compared with the axisymmetric baseline, and thus the airfoil was staggered by 0.55 deg without changing its profile. The definition of the SKE used in the design is given by Germain et al. [21]: The construction of the reference flow—which is the base of any SKE definition—involves two successive averaging in the radial and pitchwise directions, the first averaging defining a first reference flow and a first secondary flow field, which is used itself for the

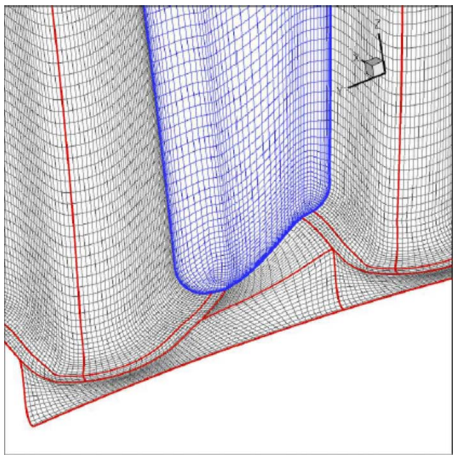

Fig. 4 Meshing of the fillet radius

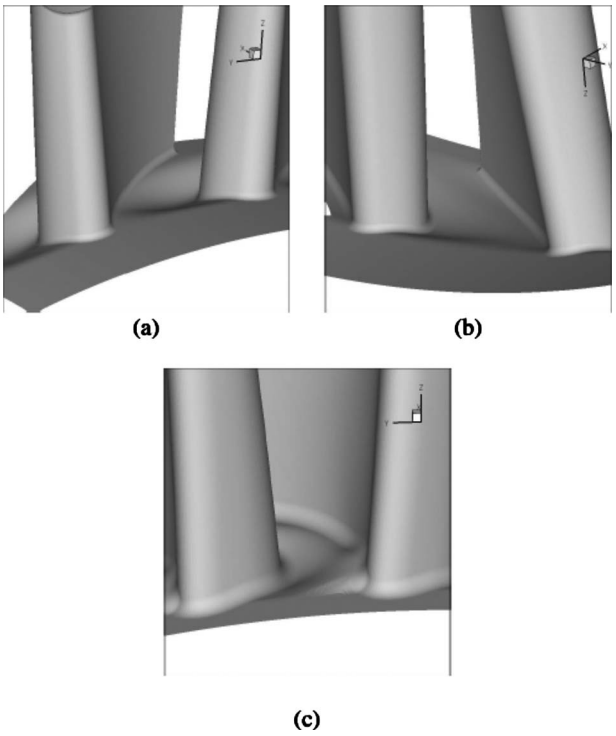

Fig. 5 Nonaxisymmetric endwall shapes of (*a*) stator 1 hub, (*b*) stator 1 tip, and (*c*) rotor 1 hub

second averaging. The purpose of this new definition was to account also for radial nonhomogeneities in the flow like the over- and underturning. For the exact formula refer to Ref. [21].

The optimization results are shown in Fig. 5. In the stator the endwall contour is mainly characterized by a depression along the suction side, the amplitudes at the hub being larger than at the tip (respectively, −9% and −4% chord lengths). In the rotor a similar depression is completed by an elevation close to the leading edge (±5% chord length). The nonaxisymmetric modulation is axially restricted to the passage between leading and trailing edges.

4 Experimental Technique

The air-loop of the facility is quasiclosed and includes a radial compressor, a two-stage water to air heat exchanger, and a calibrated Venturi nozzle for massflow measurements. Upstream of the turbine section is a 3 m flow conditioning stretch to ensure a homogeneous flow field. Additionally the flow undergoes an acceleration ahead of the turbine section in order to reduce the significance of remaining flow uniformities from upstream. At the exit of the turbine section the air loop opens to atmosphere. A dc generator absorbs the turbine power and controls the rotational speed with an indicated accuracy of ±0.02% (±0.5 rpm). A heat exchanger controls the inlet total temperature $T_{t,\text{in}}$ to an accuracy of ±0.3%. A torque meter measures the torque on the rotor shaft. With a compressor ratio limited to $P_{c,\max}=1.5$ it is necessary to add a tandem deswirl vane arrangement to recover the static pressure at the exit of the second stator back to the ambient level in order to reach the intended turbine pressure ratio of $P_{1.5\text{-stage}}=1.65$. The turbine is unshrouded with a nominal tip gap of 1% of the span. The variation in the tip gap between builds is less than 1% of the tip gap, which ensures good repeatability. At the exit of the first nozzle guide vane row the flow is subsonic but compressible with an exit Mach number of 0.53.

The experimental investigation of the steady flow field includes the traversing of four planes using a miniature cobrahead five-hole probe with a tip diameter of 0.9 mm: at the inlet of the turbine and at the outlet of each row. The first plane was only measured for the axisymmetric baseline, while the two intermediate and the turbine outlet planes were measured for both the baseline and the contoured turbine. Each plane was measured at 41 circumferential and 40 radial positions. Additionally static pressure tappings were used on the endwall of the contoured turbine at 12 axial and 8 circumferential positions.

5 Results and Discussion

5.1 Performance. Rig operation parameters, such as torque of the turbine stage and massflow, were measured, allowing the calculation of mechanical efficiency. It is defined as the ratio of specific shaft power over the enthalpy difference in the isentropic expansion

$$\eta_m = \left(\frac{\omega \cdot M}{\dot{m}}\right) \Big/ \left(c_p T_{\text{in}} \left(1 - \left(\frac{p_{t,\text{out}}}{p_{t,\text{in}}}\right)^{(\kappa-1)/\kappa}\right)\right)$$

The efficiency of the turbine has been significantly improved due to the nonaxisymmetric endwalls. The total-to-total stage efficiency rises by 1.0% ± 0.4% at design operating point, while the capacity remains within a range of ±0.1% (the turbine being run at the same pressure ratio, rotation speed, and inlet temperature).

The benefit due to the endwall contouring was predicted to be +0.2%, which underestimates the real loss reduction. The predicted SKE was lowered by about 30%, which has been confirmed in the experiment.

This result confirms partly previous publications concerning the difficulty of CFD to provide accurate loss predictions for the design of nonaxisymmetric endwalls. Nevertheless the origin of the discrepancy is described in the accompanying paper [29] in more detail since the reduction in secondary flow turns out to be only a part of the efficiency improvement.

5.2 Flow Structures. The radial distributions of pitchwise massflow averaged total pressure loss at the stator exit give useful information on the origins of loss reduction. Figure 6 shows the experimental loss coefficient and yaw angle distribution as well as the CFD predictions as part of the design with a standard numerical setup.

Secondary loss has been reduced at the stator hub as indicated by the lower loss peak at 10% span. The range of this secondary loss region remains approximately the same as in the baseline, whereby the loss maximum has slightly moved toward midspan. The yaw angle distribution in Fig. 6 confirms the reduction in hub secondary flow since the underturning became smaller in the contoured turbine.

At the tip the secondary flow intensity has not been reduced as much as at the hub, but a reduction in the extent of the secondary flow has been achieved.

A surprising and not expected feature is the large reduction in midspan loss. Profile losses have been reduced over the entire span. Especially the region extending from the tip secondary flow to about 40% of the span has been improved. This effect was not predicted by CFD to occur over the whole primary flow region, but just close to the endwalls and between 60% and 80% spans. The average yaw angle seems not to have been influenced as much in the mid region.

The radial distribution of SKE in Fig. 6 confirms the large reduction in secondary flow intensity as does the total pressure loss distribution and also indicates a more homogeneous flow in the spanwise direction over a large region extending from about 15% to 70% span. This is certainly in relation with the midspan loss reduction.

Figure 7 shows the 2D total pressure field in the same traverse at the stator 1 exit. The reduction in loss core at the hub is clearly visible as well as the wake modification over the entire span with a reduction in intensity and width.

While this reduction in profile loss is difficult to interpret, the static pressure data gained from the endwall tappings in Fig. 8 give some explanations for the secondary loss reduction. The

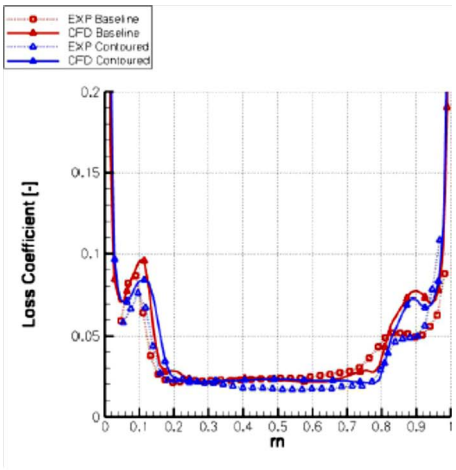

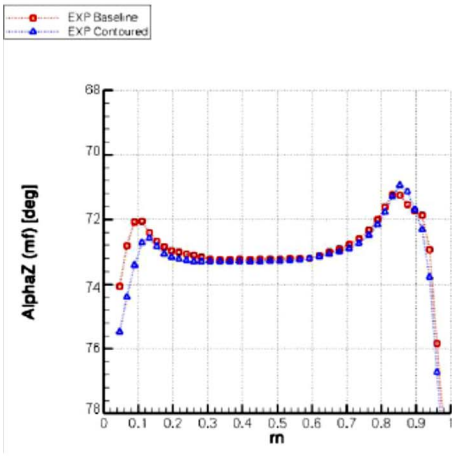

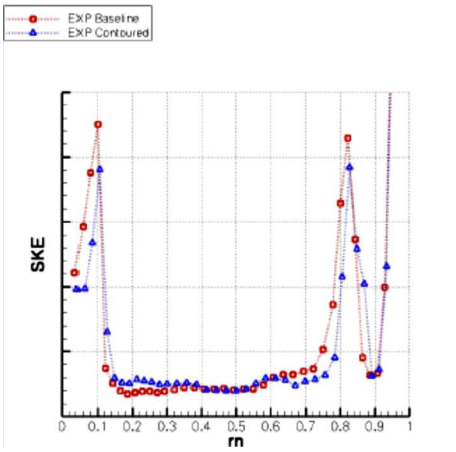

Fig. 6 Pitchwise averaged loss, yaw angle, and SKE at the stator 1 exit

cross pressure gradient has been significantly reduced over the main part of the stator passage, especially in the central part, explaining the modifications of the secondary flow behavior. The pressure isolines are almost perpendicular to the contoured case in the throat area region and thus the force driving the crossflow from pressure to suction side is almost completely eliminated. However, this change has been achieved at the expense of the pressure distribution in the front part of the passage. The CFD simulation produces a very realistic picture of the static pressure distribution. The contoured endwall at the tip produces a similar but weaker cross pressure gradient reduction and is not shown here.

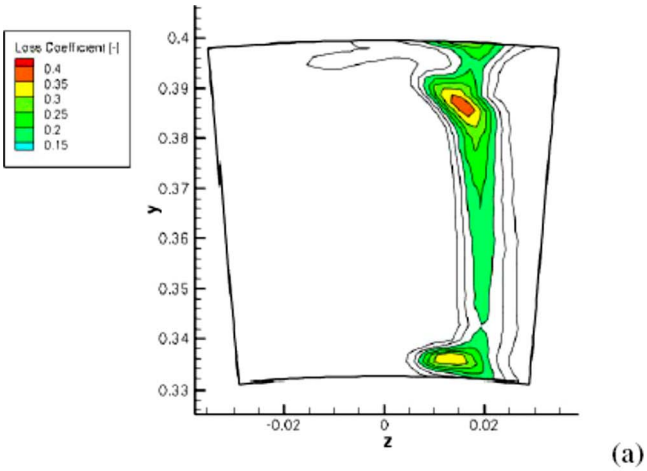

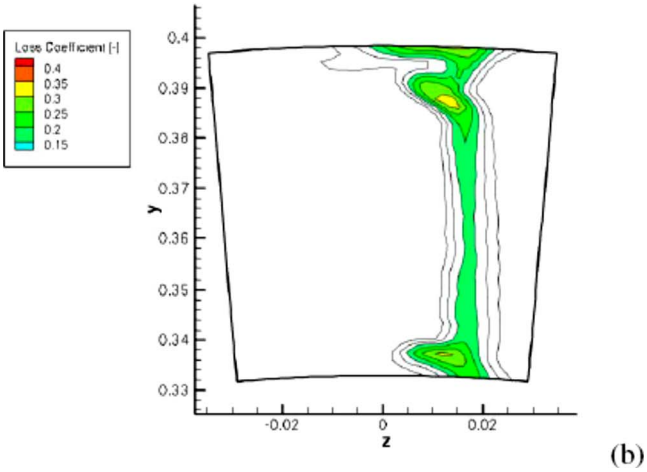

Fig. 7 2D Loss distribution at the stator 1 exit: (*a*) baseline and (*b*) contoured

The rotor exit flow field is documented in Fig. 9, showing again pitchwise averaged distributions of the relative total pressure and yaw angle. The effect of endwall contouring there is very small. The predictions show good agreement with the experimental data.

The efficiency improvement seems to rely mostly on the loss reduction in the stator. The reduction in secondary loss can be explained by the transverse pressure gradient, but the reason for the enlargement of the secondary flow region is not clear. Results of previous publications on nonaxisymmetric endwalls usually report that the contours shifted the loss core toward the endwall. A much more unexpected feature is the benefit at the midspan. Section 6.3 is dedicated to the analysis of these phenomena and will focus on the flow modifications in the stator, where the largest flow modifications occur.

5.3 Numerical Analysis

5.3.1 Hub Endwall Flow. First the hub endwall flow is analyzed in more detail. Figure 10 shows four successive planes normal to the machine axis within the stator passage in the baseline on the left and the contoured case on the right. Portions of the suction side and of the hub are visible, an adjacent airfoil having been omitted for more clarity. The view is taken downstream of the trailing edge in the upstream direction. The plane cutting through the flow is visible on the upper left corner and moves

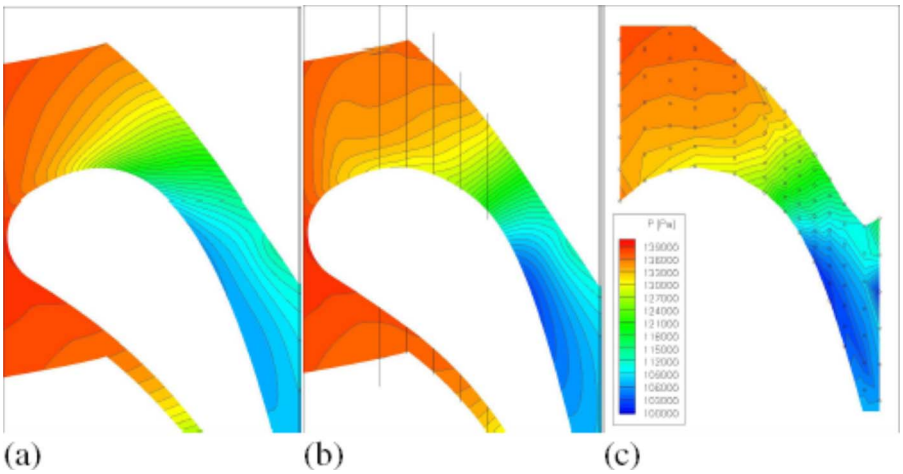

Fig. 8 Endwall pressure on the S1 hub: (*a*) CFD baseline, (*b*) CFD contoured, and (*c*) experimental contoured

toward the observer. Contours of the static pressure are plotted on the walls of the total pressure in the cutting plane as well as vortex strength isolines. The plane positions are indicated in Fig. 8.

On view (a), the suction side leg horseshoe vortex is identified close to the airfoil and also a small corner vortex. View (b) indicates the beginning migration of some endwall boundary layer fluids toward the suction side in the contoured case driven by the stronger normal pressure gradient, as seen in Fig. 8, forming what can be called a corner-passage vortex, whereas in the baseline there is no indication for this feature. Total pressure loss contours confirm the vortical structure. View (c) depicts the progress of the vortices along the passage, and additionally the formation of a small vortex in the baseline under the action of the cross pressure gradient, while the corner-passage vortex in the contoured case already starts to move along the suction side toward the midspan. Finally view (d) gives evidence that at the point where the largest pressure gradient reduction occurs in the contoured case, the endwall boundary layer flow climbs up the suction side earlier than in the baseline. This explains the slightly enlarged secondary flow region, whereas the loss intensity is globally reduced since the cross pressure gradients move less low momentum fluid toward the suction side.

5.3.2 Profile Loss Reduction. A few general considerations are necessary at this point. Nonaxisymmetric endwall profiling has different effects on the flow field, which can all be used to achieve some efficiency improvement. First the contouring introduces some additional curvatures on the endwall, thus influencing the pressure field, for the reduction in crossflow, for example. This effect is local and occurs at or close to the endwall. Another mechanism is the change in cross sections, which will influence the whole flow field over the span. A third effect will be the modification of blockage, in particular, through the use of steep bumps in the leading edge region.

Obviously the second mechanism has a strong influence in this contoured LISA turbine. Thus not only secondary flow but the entire airfoil flow can be improved by endwall shaping.

Figure 11 shows static pressure distributions on stator 1 for three sections at 5%, 50%, and 95% spans. The loading of the airfoil has been significantly modified: The profile has become significantly aft loaded, while the overall loading was reduced in each section. One reason for this is the increase in the suction side surface due to the contouring, while the augmentation of the throat area was adjusted by rotating the airfoil during the design to keep capacity and work constant.

These characteristics explain again the reduction in the secondary flow, but the reason for the midspan loss reduction is still not obvious. Two effects are thought to be responsible for this, which actually cannot be fully separated. The first is the off-loading of the pressure distribution even at the midspan, leading to smaller Mach number level and reduced diffusion for the suction side flow. Both effects will reduce the profile loss in a strictly 2D flow regime. The second effect can be seen in Fig. 12. The flow pattern on the suction side is not purely two dimensional even at the midspan and changes to some extent in the contoured case. The streamlines show a flow structure, which is close to a separation bubble. Due to the radial pressure gradient the slow flow in this almost separated flow structure migrates from the tip to the hub. The developing transition then closes this structure and realigns the boundary layer flow with the main flow. In the contoured case this effect is weaker due to the changed pressure distribution. This will reduce the mixing losses in this case. Since the CFD only predicts part of the loss change in the core flow (see Fig. 6) despite the use of a transition model, this flow structure change may still be underpredicted by the CFD.

5.3.3 Influence of Fillets and Transition. The next series of figures shows different geometrical and numerical setups for CFD analysis and is intended to show the importance of an exact geometry representation and of transition modeling on the airfoil for the prediction of the secondary flow.

A fully turbulent suction side prediction for the baseline is compared in Fig. 13 with the standard transition model used at MTU. The midspan loss level is very well matched by the transition model. The figure also reveals the importance of representing real fillet geometry since the CFD simulation that utilized a mesh without fillet shows a nonrealistic drop of loss at about 75% span. This underlines the importance of taking into account the fillets when contouring the endwalls.

The secondary losses, however, are quite well predicted at the hub, but in the tip region CFD overpredicts the secondary loss. As shown by the following numerical analysis, the secondary flow structures in this turbine are very sensitive to transitional effects on the airfoil.

The used numerical setting for the transition modeling assumes that a portion of the airfoil boundary layer is turbulent near the endwalls. The effect of reducing this region has an important effect on the secondary flow, as shown in Fig. 14. It results in a better matching of the predictions in the region extending from 70% to 85% span. Above 85% the simulation has still deficiencies. At the hub, however, the initial setup shows much better agreement than the modified one.

The inlet turbulence intensity was then increased in order to evaluate the sensitivity of the transition model and the secondary

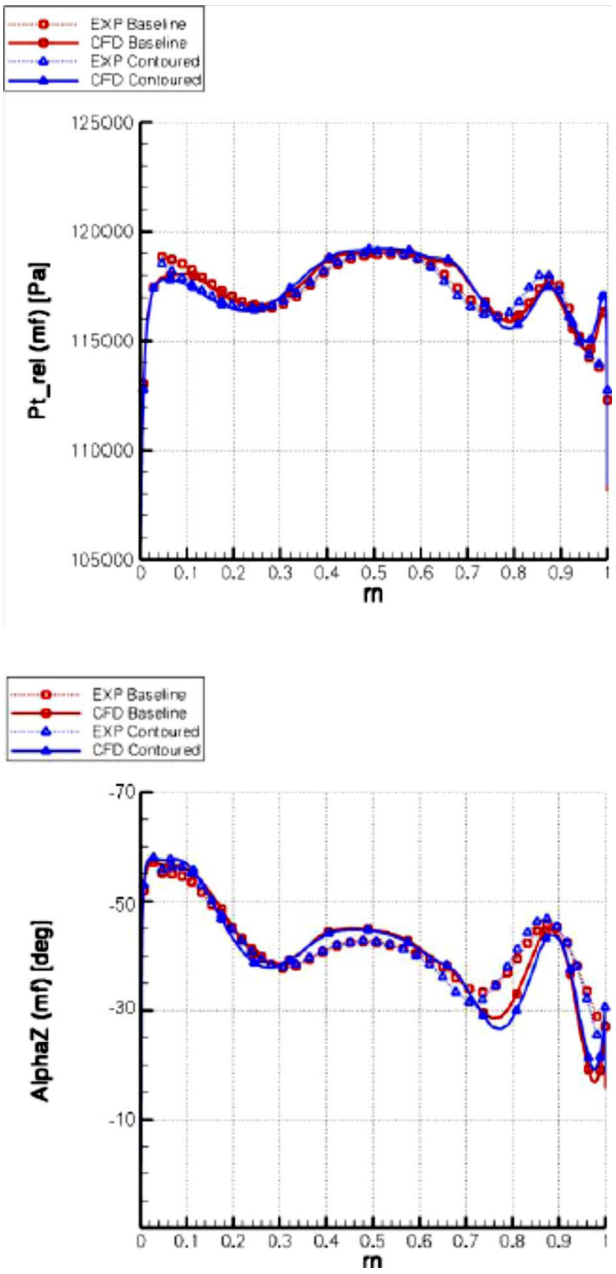

Fig. 9 Pitchwise averaged relative total pressure and yaw angle at the rotor R exit

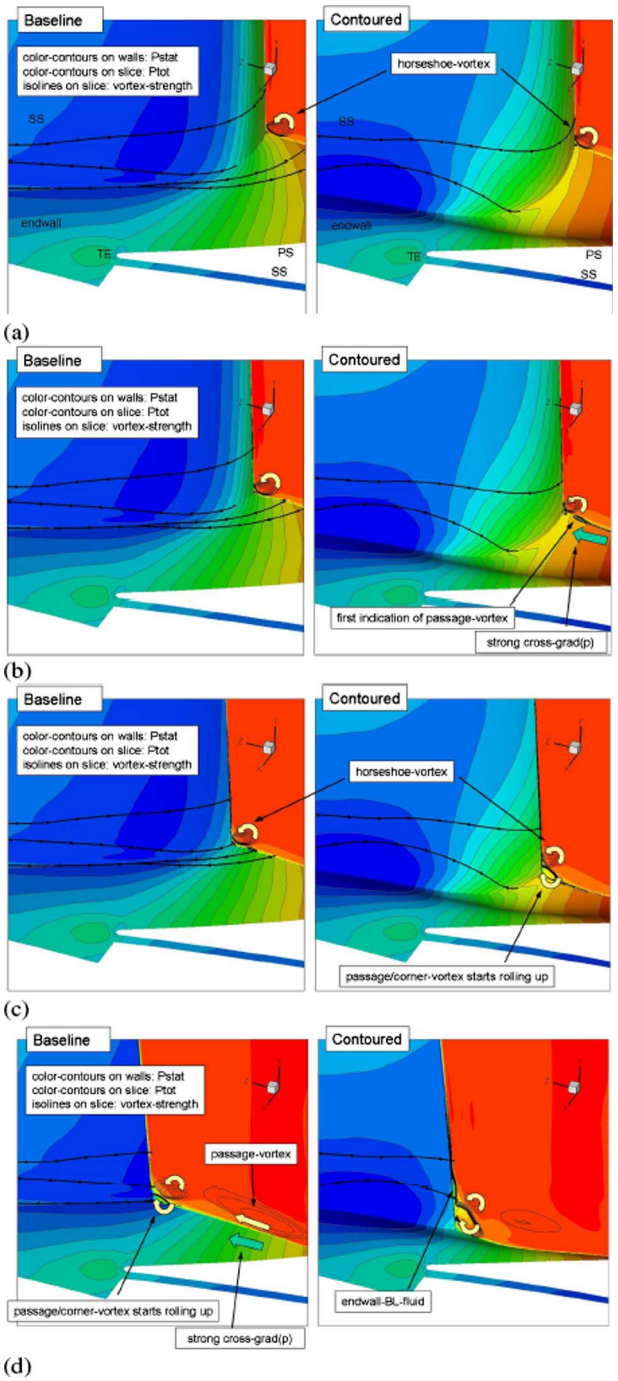

Fig. 10 Wall p, flow p_t, and vortex strength on four different planes within the passage

flow in this particular case (Fig. 15). The region from 20% to 85% is very well predicted in the baseline and shows a slight loss ramp from the hub to the tip as does the experimental data.

Obviously the secondary flow is triggered by strong transitional effects. It is also very probable that the endwall boundary layers themselves behave in a transitional manner, as it has been revealed recently by Vera et al. [28] in an experimental study. Thus transition prediction is crucial not only for two-dimensional profile losses but also for the three-dimensional secondary flow structures.

One possible explanation for the weaker wake of the contoured case is addressed in Paper II by Schüpbach et al. [29] using the unsteady experimental data, which cannot yet be confirmed numerically.

6 Conclusions

Efficiency has been significantly improved in a high work one-and-half stage turbine using nonaxisymmetric contouring. This was not only achieved by the reduction in the secondary loss but also by a strong weakening of the midspan losses.

The mechanism of the passage vortex formation has been numerically analyzed, giving an explanation for the flow modification at the stator hub exit.

CFD investigations revealed that the modeling of the real fillet radii in the computational mesh has an important effect on the quality of the predictions. The flow improvement in the primary flow region was not fully predicted by CFD, but the role of transition on the airfoil for the prediction of the secondary flow has been shown to be fundamental.

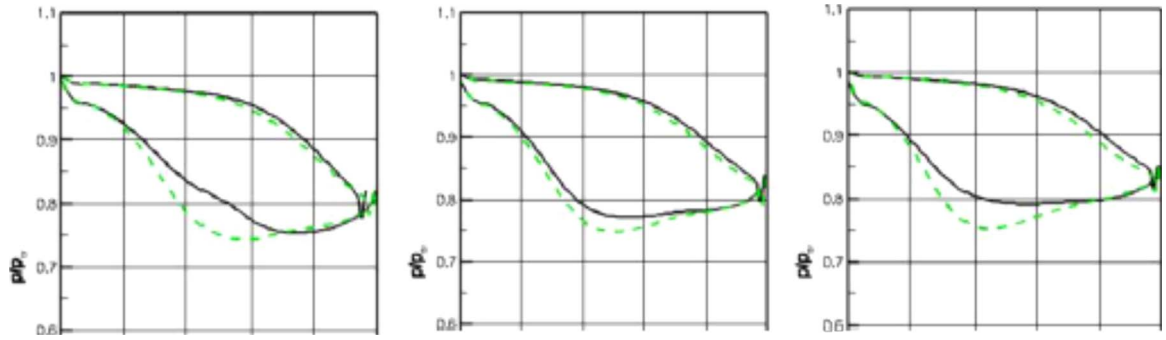

Fig. 11 S1 airfoil static pressure prediction at 5%, 50%, and 95% spans: _ _ baseline and __ contoured

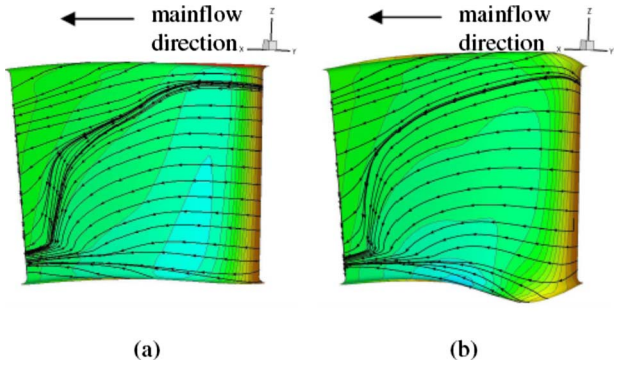

Fig. 12 Predicted S1 suction side wall streamline patterns with pressure contours for (*a*) the baseline and (*b*) the contoured case

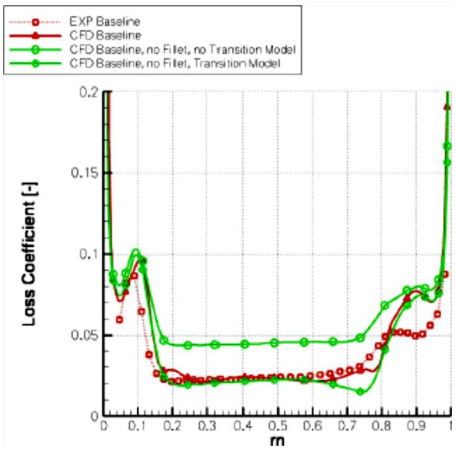

Fig. 13 Pitchwise averaged loss, experimental, and CFD for different fillet configurations

Further analysis will include detailed studies of the transitional behavior of the axisymmetric and nonaxisymmetric turbines, especially on the endwalls.

Acknowledgment

The authors would like to thank MTU Aero Engines in Munich for permitting the publication of this paper and for its support to the project. This work was performed within a joint industrial and academic research program that is part of the "Luftfahrtforschungsprogramm LuFo3" supported by the German Federal Ministry of Economics and Technology.

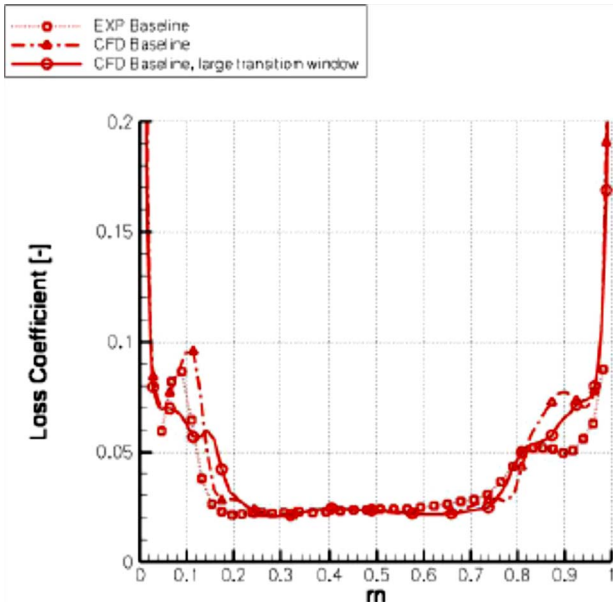

Fig. 14 Pitchwise averaged loss, experimental, and CFD for different transition model setups

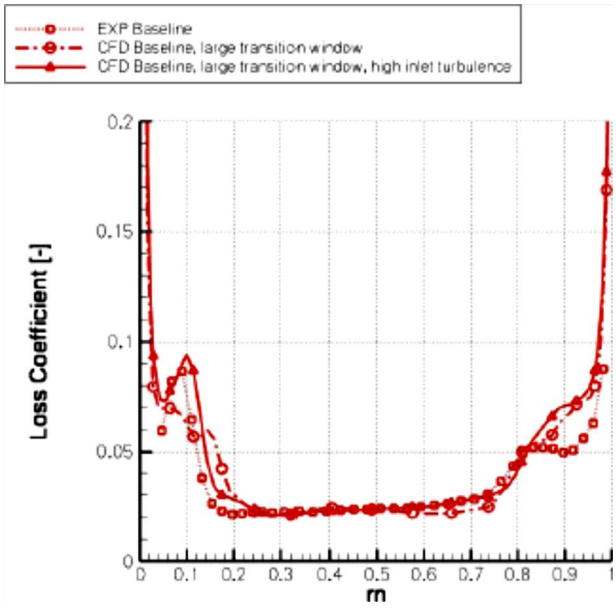

Fig. 15 Pitchwise averaged loss, experimental, and CFD for different inlet turbulence levels

Nomenclature

CAD = computer aided design
CFD = computational fluid dynamics
c_p = specific heat capacity at constant pressure
c_p = specific heat capacity at constant pressure
HP = high pressure
$\dot{m}$ = massflow
M = torque
p = static pressure
p_t = total pressure
RANS = Reynolds averaged Navier-Stokes
T = temperature
T_t = total temperature
URANS = unsteady Reynolds averaged Navier-Stokes
α_z = yaw angle
ζ = loss coefficient $(p_{t,\mathrm{in}}-p_{t,\mathrm{out}}/p_{t,\mathrm{in}}-p_{\mathrm{out}})$
κ = isentropic coefficient $(\kappa=c_p/c_v)$
ω = rotational velocity

Abbreviations

R1 = rotor
S1 = stator 1
S2 = stator 2

References

[1] Sieverding C. H., 1984, "Recent Progress in the Understanding of Basic Aspects of Secondary Flow in Turbine Blade Passages," ASME Paper No. 84-GT-78.
[2] Langston, L. S., 2001, "Secondary Flows in Axial Turbines—A Review," Ann. N.Y. Acad. Sci., **934**, pp. 11–26.
[3] Hawthorne, W. R., 1955, "Rotational Flow Through Cascades—Part 1. The Components of Vorticity," Q. J. Mech. Appl. Math., **8**, pp. 266–279.
[4] Pullan, G., Denton, J., and Dunkley, M., 2002, "An Experimental and Computational Study of the Formation of a Streamwise Shed Vortex in a Turbine Stage," ASME Paper No. GT-2002-30331.
[5] Schlienger, J., Kalfas, A. I., and Abhari, R. S., 2005, "Vortex-Wake-Blade Interaction in a Shrouded Axial Turbine," ASME J. Turbomach., **127**(4), pp. 699–707.
[6] Gier, J., Ardey, S., Eymann, S., Reinmöller, U., and Niehuis, R., 2002, "Improving 3D Flow Characteristics in a Multistage LP Turbine by Means of Endwall Contouring and Airfoil Design Modification—Part 2: Numerical Simulation and Analysis," ASME Paper No. GT-2002-30353.
[7] Dejc, M. E., and Zarjankin, A. E., 1960, "Methods of Increasing the Efficiency of Turbine Stages," Teploenergetika (Moscow, Russ. Fed.), **2**, pp. 18–24.
[8] Harrison, S., 1992, "The Influence of Blade Lean on Turbine Losses," ASME J. Turbomach., **114**, pp. 184–190.
[9] Kawagishi, H., and Kawasaki, S., 1991, "The Effect of Nozzle Lean on Turbine Efficiency," ASME Paper No. H00652.
[10] Eymann, S., Reinmöller, U., Niehuis, R., Förster, W., Bewersdorf, M., and Gier, J., 2002, "Improving 3D Flow Characteristics in a Multistage LP Turbine by Means of Endwall Contouring and Airfoil Design Modification—Part 1: Design and Experimental Investigation," ASME Paper No. GT-2002-30352.
[11] Sauer, H., and Wolf, H., 1997, "Influencing the Secondary Flow in Turbine Cascades by the Modification of the Blade Leading Edge," Second European Conference on Turbomachinery, Antwerp.
[12] Becz, S., Majewski, M. S., and Langston, L. S., 2004, "An Experimental Investigation of Contoured Leading Edges for Secondary Flow Loss Reduction," ASME Paper No. GT2004-53964.
[13] Rose, M. G., 1994, "Non-Axisymmetric Endwall Profiling in the HP NGV's of an Axial Flow Gas Turbine," ASME Paper No. 249-GT-94.
[14] Hartland, J., Gregory-Smith, D., Harvey, N., and Rose, M., 2000, "Nonaxisymmetric Turbine End Wall Design: Part II—Experimental Validation," ASME J. Turbomach., **122**(2), pp. 286–293.
[15] Gregory-Smith, D., Ingram, G., Jayaraman, P., Harvey, N., and Rose, M., 2001, "Non-Axisymmetric Turbine End Wall Profiling," *Proceedings of the Fourth European Conference on Turbo-Machinery*.
[16] Brennan, G., Harvey, N., Rose, M., Fomison, N., and Taylor, M., 2003, "Improving the Efficiency of the Trent 500-HP Turbine Using Nonaxisymmetric End Walls—Part 1: Turbine Design," ASME J. Turbomach., **125**(3), pp. 497–504.
[17] Rose, M., Harvey, N., Seaman, P., Newman, D., and McManus, D., 2001, "Improving the Efficiency of the Trent 500 HP Turbine Using Non-Axisymmetric End Walls. Part II: Experimental Validation," ASME Paper No. 2001-GT-0505.
[18] Nagel, M., Fottner, L., and Baier, R.-D., 2001, "Optimization of Three Dimensionally Designed Turbines Blades and Side Walls," ISABE Paper No. 2001-1058.
[19] Ingram, D., Rose, M., and Harvey, N., 2002, "The Effect of End-Wall Profiling on Secondary Flow and Loss Development in a Turbine Cascade," ASME Paper No. GT-2002-30339.
[20] Praisner, T. J., Allen-Bradley, E., Grover, E. A., Knezevici, D. C., and Sjolander, S. A., 2007, "Application of Non-Axisymmetric Endwall Contouring to Conventional and High-Lift Turbine Airfoils," ASME Paper No. GT2007-27579.
[21] Germain, T., Nagel, M., and Baier, R.-D., 2007, "Visualisation and Quantification of Secondary Flows: Application to Turbine Bladings With 3D-Endwalls," *Proceedings of the Eighth ISAIF*, Lyon.
[22] Sell, M., Schlienger, J., Pfau, A., Treiber, M., and Abhari, R. S., 2001, "The 2-Stage Axial Turbine Test Facility LISA," ASME Paper No. 2001-GT-0492.
[23] Behr, T., Kalfas, A. I., and Abhari, R. S., 2007, "Unsteady Flow Physics and Performance of0020a One-and-1/2-Stage Unshrouded High Work Turbine," ASME J. Turbomach., **129**, pp. 348–359.
[24] Weber, A., 2004, "3D Structured Grids for Multistage Turbomachinery Applications Based on G3DMESH, 1st revision ed.," Institute of Propulsion Technology, German Aerospace Centre, DLR No. IB-325-05-04.
[25] Abu-Ghannam, B. J., and Shaw, R., 1980, "Natural Transition of Boundary Layers—The Effect of Turbulence, Pressure Gradient and Flow History," J. Mech. Eng. Sci., **22**(5), pp. 213–228.
[26] Gier, J., Engel, K., Stubert, B., and Wittmaack, R., 2006, "Modeling and Analysis of Main Flow—Shroud Leakage Flow Interaction in LP Turbines," ASME Paper No. GT2006-90773.
[27] Spellucci, P., 1995, DONLP2, User's Guide, Technical University Darmstadt, FB4, AG8.
[28] Vera, M., de la Rosa Blanco, E., Hodson, H., and Vazquez, R., 2007, "Endwall Boundary Layer Development in an Engine Representative Four-Stage Low Pressure Turbine Rig," ASME Paper No. GT-2007-27842.
[29] Schüpbach, P., Abhari, R. S., Rose, M. G., Germain, T., Raab, I., and Gier, J., 2010, "Improving Efficiency of a High Work Turbine Using Nonaxisymmetric Endwalls—Part II: Time-Resolved Flow Physics," ASME J. Turbomach., **132**, p. 021008.

Improving Efficiency of a High Work Turbine Using Nonaxisymmetric Endwalls—Part II: Time-Resolved Flow Physics

P. Schüpbach[1]
e-mail: schuepbach@lec.mavt.ethz.ch

R. S. Abhari

Department of Mechanical and Process Engineering,
LEC, Laboratory of Energy Conversion,
ETH Zurich,
8092 Zurich, Switzerland

M. G. Rose
Institute of Aeronautical Propulsion,
University of Stuttgart,
70569 Stuttgart, Germany

T. Germain

I. Raab

J. Gier

MTU Aero Engines GmbH,
Dachauer Strasse 665,
80995 München, Germany

This paper is the second part of a two part paper that reports on the improvement of efficiency of a one and a half stage high work axial flow turbine. The first part covered the design of the endwall profiling, as well as a comparison with steady probe data; this part covers the analysis of the time-resolved flow physics. The focus is on the time-resolved flow physics that leads to a total-to-total stage efficiency improvement of 1.0%±0.4%. The investigated geometry is a model of a high work ($\Delta h/U^2=2.36$), axial shroudless HP turbine. The time-resolved measurements have been acquired upstream and downstream of the rotor using a fast response aerodynamic probe (FRAP). This paper contains a detailed analysis of the secondary flow field that is changed between the axisymmetric and the nonaxisymmetric endwall profiling cases. The flowfield at the exit of the first stator is improved considerably due to the nonaxisymmetric endwall profiling and results in reduced secondary flow and a reduction in loss at both hub and tip, as well as a reduced trailing shed vorticity. The rotor has reduced losses and a reduction in secondary flows mainly at the hub. At the rotor exit, the flow field with nonaxisymmetric endwalls is more homogenous due to the reduction in secondary flows in the two rows upstream of the measurement plane. This confirms that nonaxisymmetric endwall profiling is an effective tool for reducing secondary losses in axial turbines. Using a frozen flow assumption, the time-resolved data are used to estimate the axial velocity gradients, which are then used to evaluate the streamwise vorticity and dissipation. The nonaxisymmetric endwall profiling of the first nozzle guide vane show reductions in dissipation and streamwise vorticity due to the reduced trailing shed vorticity. This smaller vorticity explains the reduction in loss at midspan, which is shown in the first part of the two part paper. This leads to the conclusion that nonaxisymmetric endwall profiling also has the potential of reducing trailing shed vorticity. [DOI: 10.1115/1.3103926]

1 Introduction

In order to improve efficiency and reduce costs, turbine designers strive to reduce the number of stages and blades per row. Therefore, both stage loading and lift coefficients are being continuously pushed up. With increasing stage loading, the secondary loss rises and can be up to half of the total loss generated [1]. In low aspect ratio turbines such as that investigated here (NGV1: 0.87, Rotor: 1.17, and NGV2: 0.82), the losses are even more pronounced as the hub and tip secondary flows interact closely with each other. A detailed review of secondary flows in cascades can be found in Refs. [2,3]. The losses are generated in part from dissipation of the kinetic energy of rotation of the vortices, little of which is recovered in the following blade rows. Schlienger et al. [4] gave a detailed analysis of secondary flows in a shrouded axial turbine (Fig. 1).

In the past a variety of methods have been developed to reduce secondary flows. One approach is the active methods such as boundary layer blowing investigated by Sturm et al. [5] and Biesinger [6], which showed reductions in loss.

However, many studies of passive methods have also been reported. The most frequently used are blade leaning, and axisymmetric and nonaxisymmetric endwall profiling. Harrison [7] investigated in detail the effect of blade leaning. He reported that there is no loss reduction within the row in which blade leaning is applied. The performance increase comes rather from an improved flowfield into the subsequent blade rows.

The concept of axisymmetric endwall profiling was introduced by Dejc et al. [8] as a contraction of the annulus from the leading edge to the trailing edge. A loss reduction of up to 20 % was verified in linear cascade tests by Morris et al. [9]. The most promising endwall geometry incorporated a strong contraction early in the passage (often known as the "Russian kink") that results in a thinner boundary layer. Atkins [10] investigated different endwall contours in a linear cascade. He showed that the losses near the endwall can be influenced by its shape and the resulting pressure field. Sauer et al. [11] described a loss reduction by leading edge modifications.

During the past decade, emerging computational fluid dynamics (CFD) capabilities have made it possible to design more complex three-dimensional nonaxisymmetric endwalls. Nonaxisymmetric profiling using such capabilities was first introduced by Rose [12]. His goal was to have a more homogenous pressure field at the exit platform, which would reduce the turbine disk coolant massflow. Later Hartland [13] and Ingram [14] investigated nonaxisymmetric endwall profiling in the Durham linear cascade and showed that secondary loss reductions of 24% could be attained. Brennan [15] et al. and Rose et al. [16] demonstrated an increase in stage efficiency of 0.4% from computations and 0.59%±0.25% from measurements. Duden et al. [17] and Eymann et al. [18] investigated the combined effects of endwall contouring and blade thickening.

[1]Corresponding author.

Contributed by the International Gas Turbine Institute of ASME for publication in the JOURNAL OF TURBOMACHINERY. Manuscript received July 9, 2008; final manuscript received January 27, 2009; published online January 12, 2010. Review conducted by David Wisler. Paper presented at the ASME Turbo Expo 2008: Land, Sea and Air (GT2008), Berlin, Germany, June 9–13, 2008.

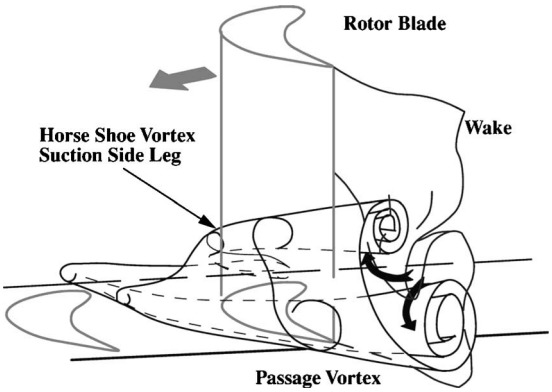

Fig. 1 Secondary flow model by Schlienger [4]

The work presented here improves our understanding of the time-resolved flow physics that lead to an improved stage efficiency. Furthermore, the work shows the potential of reducing both the endwall secondary losses and the losses at midheight in low aspect ratio turbines by reducing the trailing shed vorticity.

2 Experimental Method

The experimental investigation was performed in the research turbine "LISA" in the Laboratory of Energy Conversion at the Swiss Federal Institute of Technology. Recently the existing two-stage, shrouded turbine configuration [19] was redesigned as a one and a half unshrouded turbine that it is representative of a high work, cooled turbine. Further details of the new design are presented by Behr et al. [20] but its salient features are described below.

2.1 Experimental Turbine Facility. The air loop of the facility is quasiclosed and includes a radial compressor, a two-stage water to air heat exchanger, and a calibrated venturi nozzle for mass flow measurements. Upstream of the turbine section is a 3 m flow conditioning stretch to ensure a homogenous flowfield. Additionally the flow undergoes an acceleration ahead of the turbine section in order to reduce the significance of remaining flow uniformities from upstream. At the exit of the turbine section, the air loop opens to atmosphere. A dc generator absorbs the turbine power and controls the rotational speed with an indicated accuracy of $\pm 0.02\%$ (± 0.5 rpm). A heat exchanger controls the inlet total temperature $T_{t,\text{in}}$ to an accuracy of $\pm 0.3\%$. A torquemeter measures the torque on the rotor shaft. With the compressor ratio limited to $\Pi_{c,\max}=1.5$, it is necessary to add a tandem deswirl vane arrangement to recover the static pressure at the exit of the second stator back to the ambient level, in order to reach the intended turbine pressure ratio of $\Pi_{1.5}=1.65$. The turbine is unshrouded with a nominal tip gap of 1% of the span. The variation in the tip gap between builds is less than 1% of the tip gap, which ensures good repeatability. At the exit of the first nozzle guide vane row, the flow is compressible with an exit Mach number of 0.53.

2.2 Measurement Technology. The unsteady flow field is measured with a fast response aerodynamic probe (FRAP), which was developed at the LEC [21,22]. The probe is capable of capturing unsteady flow features up to frequencies of 48 kHz based on measurements including the total and static pressures, flow yaw and pitch angles, and Mach number. The frequency bandwidth of the temperature is limited to a frequency of 10 Hz. However, the influence of the measured temperature on the velocity is very modest. The FRAP probe has a 1.8 mm tip diameter and is equipped with two sensors. The probe is operated in a virtual-four-sensor mode to measure three-dimensional, time-resolved flow properties. The data are acquired at a sampling rate of 200 kHz over a period of 2 s. The postprocessing is done for three consecutive rotor pitches. The sampling rate resolves 82 points in the relative frame of reference. Table 1 gives the typical measurement uncertainties of the FRAP probe.

Table 1 Uncertainty bandwidth of FRAP probe

Yaw angle	Pitch angle	$p_t/(p_t-p_s)$	$p_s/(p_t-p_s)$
0.24 deg	0.36 deg	1%	1.2%

2.3 Measurement Plane. The spatial resolution of the measurement grid consisted of 39 radial and 40 circumferential points (covering one stator pitch) with a radial clustering near the endwalls. The data are acquired at a sampling rate of 200 kHz over a period of 2 s. The postprocessing is done for three consecutive rotor pitches. The temporal resolution is 82 points per blade passing period.

3 Results and Discussion

In Sec. 3.2 and 3.3, the time-resolved flowfield data are presented. The analysis focuses on the changes of the secondary flow features. The data case has axisymmetric endwalls, while the profiled case has nonaxisymmetric hub and tip endwalls in stator 1 and a nonaxisymmetric rotor hub endwall.

3.1 Operating Conditions. During the measurements, the turbine 1.5 stage total-to-static pressure ratio is kept constant at $\Pi_{1.5}=1.65$. The constant entry temperature is kept constant to permit an accurate comparison between measurements made on different days. To account for the change in ambient pressure on different measurement days, the pressures are nondimensionalized by the respective inlet total pressure. Table 2 gives the operating conditions as well as the characteristic geometrical parameters.

Figure 2 shows the geometry and the relative positions of stators 1 and 2, as well as the relative position of the traverse planes S1ex and R1ex.

3.2 First Stator Exit Flow Field. Figure 3 shows the total pressure field at the exit of stator 1. The plots show a downstream view of one stator pitch at the same relative blade position. Although it is generally considered sufficient to look at steady data to evaluate the flow field of a stationary row, the current result illustrates that there is already a strong unsteady signature at the exit of stator 1 due to the downstream rotor. This unsteady signature results from the unsteady work done by the rotor upstream potential field, also termed as the bow wave.

One can identify clearly the stator secondary flows and the wake as low total pressure regions. The core of the hub passage vortex (HPV) extends from about 5–15% span, while the tip passage vortex core lies between 80% and 90% spans. The high total pressure zone to the left of the pitch centerline is the signature of

Table 2 Operating conditions and characteristics of geometry

$\Pi_{1.5}$	$1.65 \pm 0.4\%$	
$T_{t,\text{in}}$	328 ± 0.2	K
$\frac{\dot{m}\sqrt{T_{t,\text{in}}}}{p_{t,\text{in}}}$	$152 \pm 0.2\%$	kg $K^{1/2}$/s bar
$\frac{N}{\sqrt{T_{t,\text{in}}}}$	2.48 ± 0.05	rps/$K^{1/2}$
Aspect ratio (S1/R1/S2)	0.87/1.17/0.82	
Mach number (S1/R1/S2)	0.54/0.26/0.46	
Reynolds number (S1/R1/S2) ($\times 10^5$)	7.1/3.8/5.1	
Blade count (S1/R1/S2)	36/54/36	

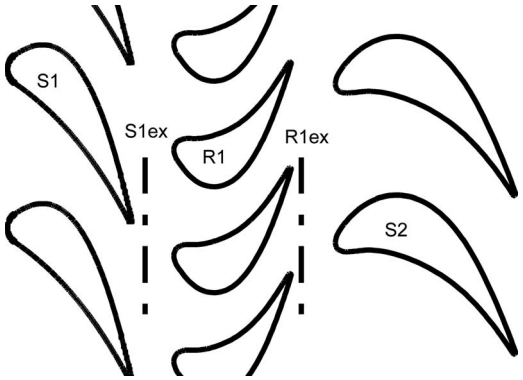

Fig. 2 Illustration of geometrical relations

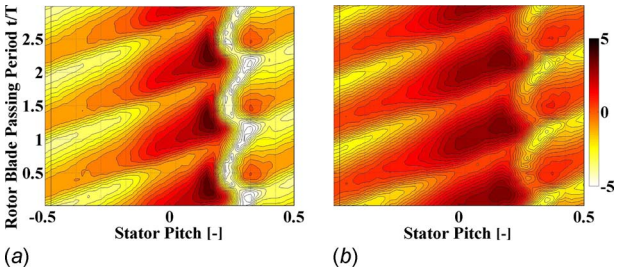

Fig. 4 Time-space diagram: pitch angle at traverse plane S1ex

the rotor bow wave. The low total pressure cores at hub and tip, as well as in the wake region, are more pronounced in the axisymmetric case.

Figure 4 shows the pitch angle variation in the time-space format at midheight, which is shown as line *Y* in Fig. 3. Inside the wake, there is a much stronger inward pitch angle in the axisymmetric case identified as the white region, as well as a strong outward pitch angle shown as the dark color regions. This results in a stronger circumferential pitch angle gradient than for the profiled case. This stronger gradient is the signature of stronger trailing edge vorticity due to the variation in lift up the span. Therefore, there is more streamwise vorticity, as well as higher dissipation within the wake. As a result there is more loss at midheight in the datum case.

In order to better understand the unsteady rotor-stator interaction, time-space diagrams at three radial heights corresponding to the lines *X*, *Y*, and *Z* in Fig. 3 are presented in Fig. 5. The first cut at $Z=10\%$ span goes through the hub passage vortex, the second cut at midheight *Y* shows the wake interaction, and the third cut at $X=82\%$ details the tip passage vortex. Vertically oriented features in the stationary frame space-time diagrams can be attributed to the stator flowfield, while rotor flow features show up as inclined parallel structures. The inclined highest total pressure regions in Fig. 5 are the rotor bow waves. The low total pressure region at 0.3 pitch is either the stator secondary flow or the wake depending on the radial height. When this region interacts with the rotor leading edge, its total pressure increases close to the freestream level. One can also see the wake that moves circumferentially as it interacts with the rotor leading edge. At the hub of the baseline case, the rotor-stator interaction is stronger. The endwall profiling shows beneficial changes at all three heights. The low total pressure regions are smaller and less profound in the profiled case. However, the effect at midheight is strongest because of the reduced shed vorticity in the profiled case. This effect was not anticipated in the design phase.

Figure 5 shows that endwall profiling in low aspect ratio turbines reduces the losses both in the endwall region and also at midheight. At height *Z* the profiled case seems to be more homogenous in the freestream region compared with the baseline measurement.

Figure 6 shows the relative total pressure at midheight. The circumferential coordinate given as a fractional of stator pitch is plotted against time. One can see an underlying variation in the stator pitch direction due to the potential field of the vane. This creates work lines in the relative frame. It can be seen as much larger regions of low relative total pressure in the data case. In the freestream the relative total pressure varies over time. This is the result of a time variation of the rotor lift and indicates unsteady flow in the rotor frame of reference.

3.3 Rotor Exit Flow Field. *Time resolved*. The unsteady interaction of stator 1 flow features and the rotor flow features are next examined. A good indicator of flow features are the root mean square (rms) values of the random part of the total pressure signal. Regions of high rms are indicative of eddy shedding or regions of high turbulence. Using the triple decomposition of the time-resolved pressure signal, as shown in Eq. (1), the random part $p'(t)$ can be evaluated as the difference between the raw pressure $p(t)$ signal of the FRAP probe and the phase-locked averaged pressure $\bar{p}+\tilde{p}(t)$. The same approach was used by Porreca et al. [23] to derive turbulent quantities.

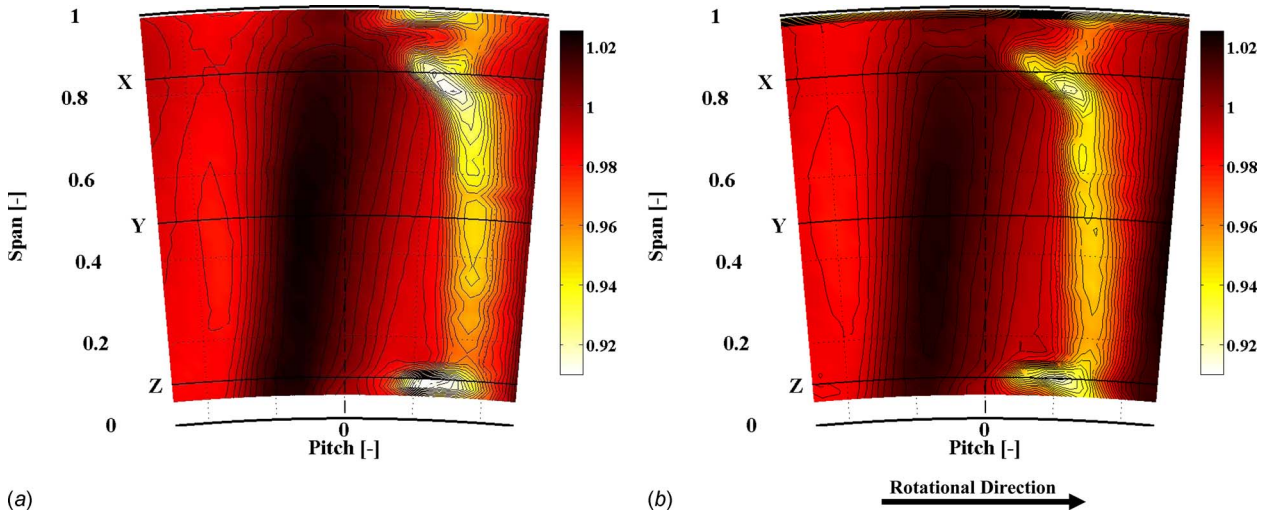

Fig. 3 Total pressure at traverse plane S1ex

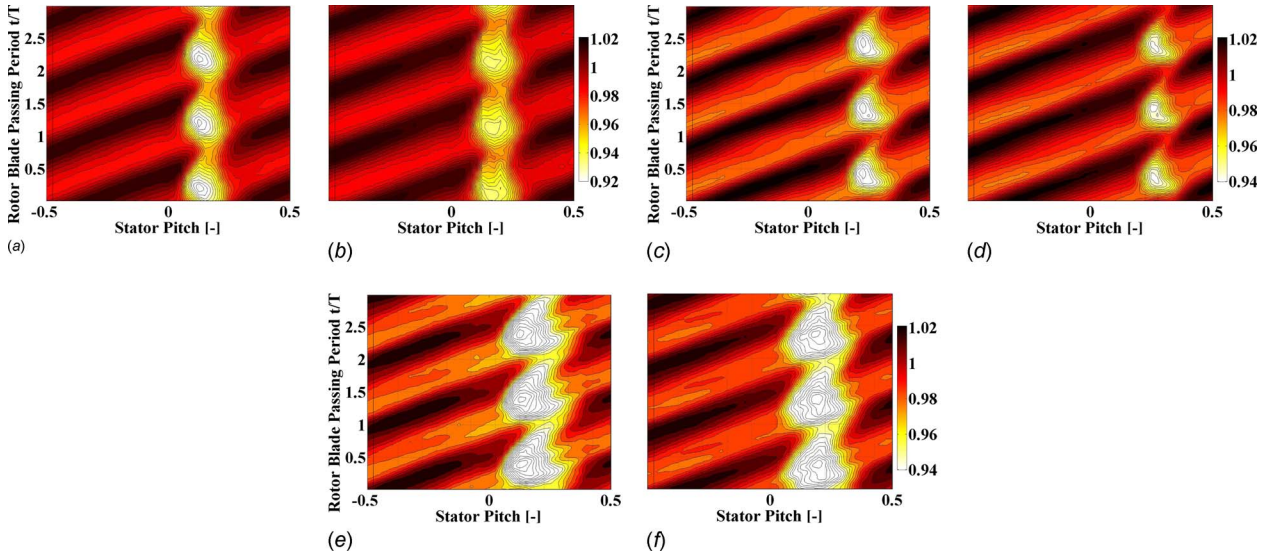

Fig. 5 Time-space diagram: total pressure at traverse plane S1ex

$$p(t) = \bar{p} + \tilde{p}(t) + p'(t) \tag{1}$$

Figure 7 shows the downstream view of the relative total pressure field of two stator pitches at one instant in time. One can see the secondary flow features of the three blades as three low relative total pressure zones. From 90% span to the tip, one can identify the loss core of the tip leakage vortex labeled as 1 in between 60% and 80% spans the loss core of the rotor tip passage vortex 2 and finally between 15% and 35% spans the loss core of the rotor hub passage vortex 3.

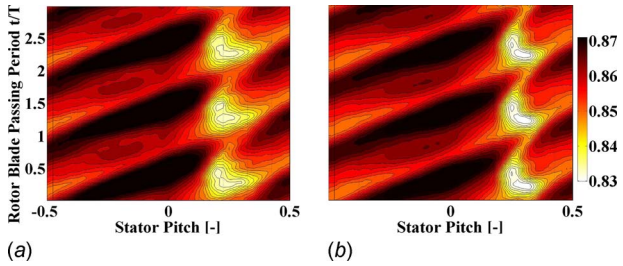

Fig. 6 Time-space diagram: relative total pressure at traverse plane S1ex

The two passage vortices are connected by the rotor wake. The shape of the loss cores of the secondary flow features changes between different zones of interaction (A–C).

Figures 8 and 9 show the normalized relative total pressure and rms in space-time diagrams. The diagonal bands of low relative total pressure and high rms are associated with the rotor wake. One sees only minor differences between the data and profiled cases. At 0% pitch the upstream potential effect of the second stator is seen as a high relative total pressure zone. Furthermore, there is a horizontal feature of high relative total pressure and high rms labeled 1. This zone shows the remains of the stator 1 wake. The data case shows a much larger zone of high relative total pressure, which also contains higher unsteadiness in terms of rms. The wake of stator 1 shows a 4% increase of relative total pressure of the stage total pressure drop over the rotor in both cases. This indicates that work is done on the wake in the relative frame, which is consistent with the results presented in Ref. [24].

The more extended high relative total pressure zone in the data case results in greater mixing loss and lower efficiency. Based on the stationary flow field, one can differentiate between the three interaction zones. The traverses, marked as A–C in Figs. 7–9 are

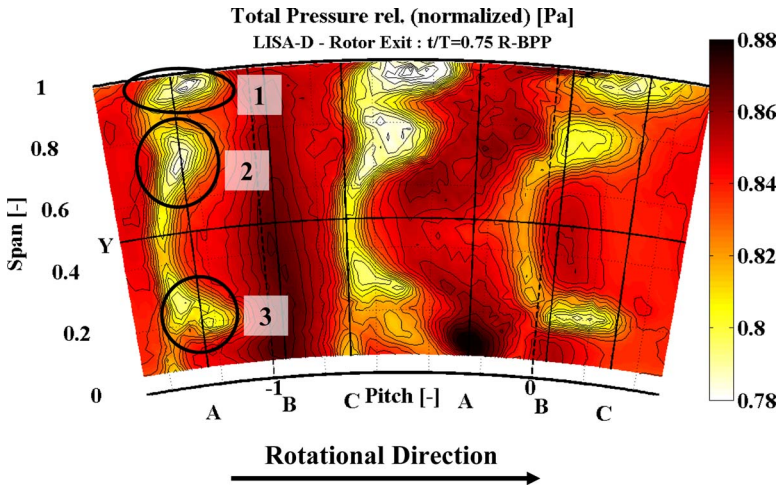

Fig. 7 Relative total pressure at traverse plane R1ex

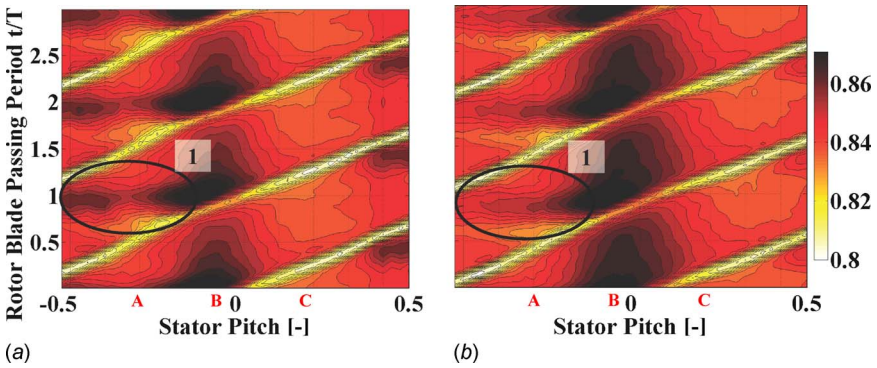

Fig. 8 Time-space diagram: relative total pressure at traverse plane R1ex

representatives of these three interaction zones. In zone A, the rotor flow features interact with flow features coming from the upstream vane characterized by a region of high rms between the two rotor wakes. Traverse B shows the interaction of the rotor secondary flows with the leading edge of the downstream stator, seen as a high relative total pressure zone in Fig. 8. Finally, along traverse C there are no significant rotor-stator interactions characterized by low rms values in the freestream region between the two rotor wakes.

In order to further analyze the interactions, the three radial traverses at A–C are plotted against time, seen in Figs. 10 and 11. Figure 10 shows the radial-time diagram of the root mean square values of the random part of the total pressure signal. One can differentiate between different levels of unsteadiness in the three cases. The regions of high rms are indicative of a potential source of loss that subsequently dissipates and causes a rise in entropy.

Figures 10(*e*) and 10(*f*) representing traverse C show only minimal rotor-stator interactions characterized by the lowest integral rms values. The rotor flow features identified in Fig. 7 can be seen as high rms regions. From 90% span to the tip, one can identify

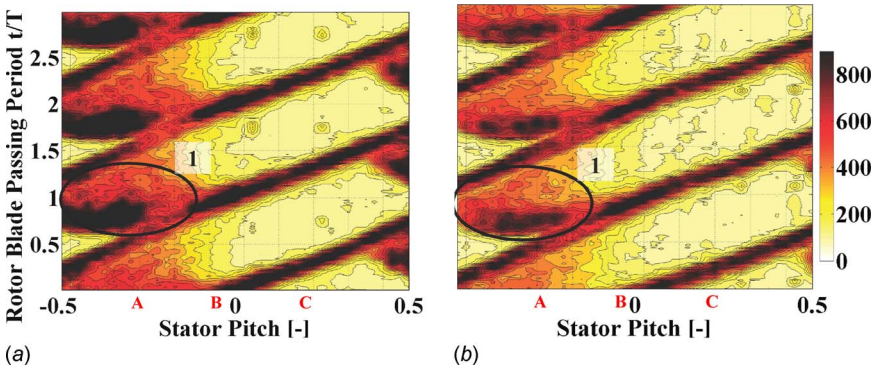

Fig. 9 Time-space diagram: rms of the total pressure random part at traverse plane R1ex (Pa)

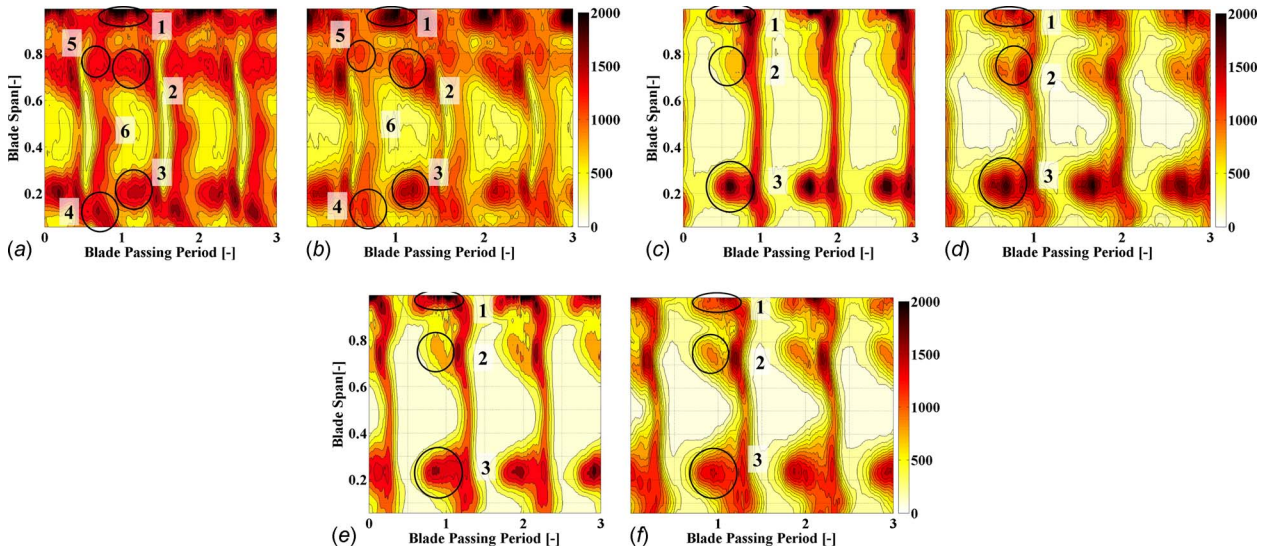

Fig. 10 rms of the total pressure random part at traverse plane R1ex (Pa)

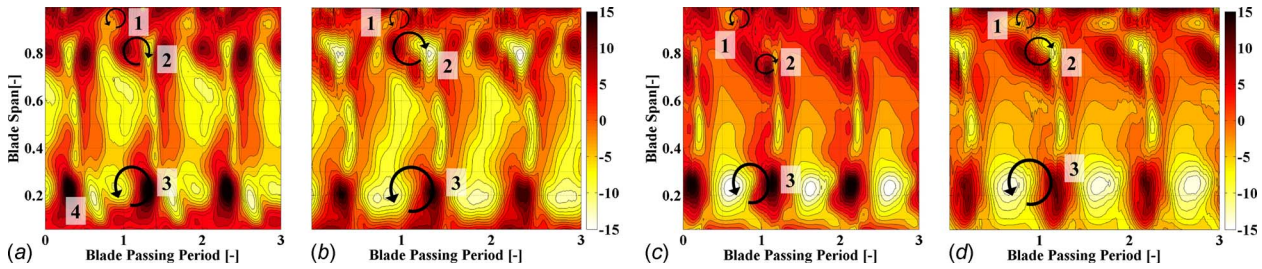

Fig. 11 Pitch angle at traverse plane R1ex

the tip leakage vortex labeled with 1 in between 60% and 80% spans the rotor tip passage vortex 2 and finally between 15% and 35% spans the rotor hub passage vortex 3. With endwall profiling, the unsteadiness of the hub passage was reduced. The tip passage vortex is almost unaltered, while the tip leakage vortex was reduced with endwall profiling.

In traverse B, the unsteadiness in the rotor hub passage vortex rises due to the interaction with the downstream stator leading edge. In the profiled case, the rotor hub passage vortex seems to be larger but less intense in terms of the unsteadiness.

Along traverse A the integral rms values rise once more as additional high rms zones occur. These zones show the remains of the upstream vane flow features. There is a high rms zone at the hub labeled 4 associated with the upstream vane hub passage vortex. With endwall profiling this region has reduced in size and intensity. The high rms zone at 70% span labeled 5 can be associated with the vane tip passage vortex. Also, this zone has reduced in size and intensity in the profiled case. Finally, there is the high rms zone labeled 6, which can be identified as the residual signature of the upstream stator wake. Also the rms values in this region have reduced with endwall profiling. In traverse A, the unsteadiness has decreased profoundly with endwall profiling. This is mainly a consequence of improvements in stator 1.

Figure 11 shows the radial-time diagram for the pitch angle of the radial traverses A and C. If streamwise vorticity is present in a flowfield, one will find circumferential gradients of pitch angle. As the rotor vortices travel circumferentially through the radial traverse, time gradients seen in Fig. 11 are related to circumferential pitch angle gradients in the rotor frame of reference.

Figures 11(*c*) and 11(*d*) show the pitch angle distribution of traverse C. Between 15% and 35% spans, there is a positive timewise pitch angle gradient associated with the rotor hub passage 3. With endwall profiling, this gradient has reduced by $\Delta\gamma = 10.2$ deg per blade passing period from $\gamma = 65$ deg per blade passing period in the baseline case. At around 80% span, there is a pitch angle gradient of opposite sign, which is induced by the tip passage vortex 2. The region of negative pitch in the profiled case is much more pronounced. The minimum pitch at 80% is 6 deg lower in the profiled case. Around 90% span, there is another pitch angle gradient, which is associated with the tip leakage vortex 1. The gradient is modest in both cases leading to the conclusion that the tip leakage flow is only of modest vortical nature.

Figures 11(*a*) and 11(*b*) shows the radial-time diagram of traverse A. In the data case, there is a strong negative pitch angle zone labeled 4 that is coincident with the high rms zone associated with the vane hub passage vortex. In the profiled case, this zone has merged with the low pitch angle region of the rotor hub passage vortex leading to a reduction in pitch angle gradients near the hub.

Figure 12 shows the radial-time diagram of the total pressure for traverse A. The rotor loss features are seen as low total pressure zones. However, the hub loss features that originate from the upstream vane, which are seen as regions of high rms in Fig. 10 and of low pitch angle in Fig. 11, have a higher total pressure level compared with the freestream region 4. In the profiled case, the region labeled 4 is more homogenous. The inhomogeneities in the data case will mix out and result in higher losses.

Using the rms plots, the vane and rotor loss cores at the exit of the rotor can be identified and the associated rotor exit total pressure values of the stator 1 wake and hub passage vortex can be also determined. The freestream total pressure value at rotor exit is defined as the total pressure value coincident with the lowest rms region in traverse A. The rotor inlet freestream total pressure is defined as the time-averaged midspan value at -0.2 pitch. The stator 1 wake total pressure value at rotor inlet is defined as the minimum value at midspan. The upstream vane hub passage vortex total pressure at rotor inlet is defined as the minimum value at height Z. Using these values, the total pressure drop of the stator 1 wake and hub passage vortex fluid, as well as the total pressure drop in the freestream, can be calculated. Table 3 gives the total pressure drop of the freestream and the upstream vane wake and hub passage vortex. The pressure drop is nondimensionalized by the average stage total pressure drop. There is a 20% less total pressure drop of the stator 1 loss regions compared with the freestream. The loss features of the profiled case show 3.8% and 2.5% higher total pressure drops in the wake and hub passage vortex, respectively. This means that there is a higher work extraction in the profiled case, which contributes to the higher effi-

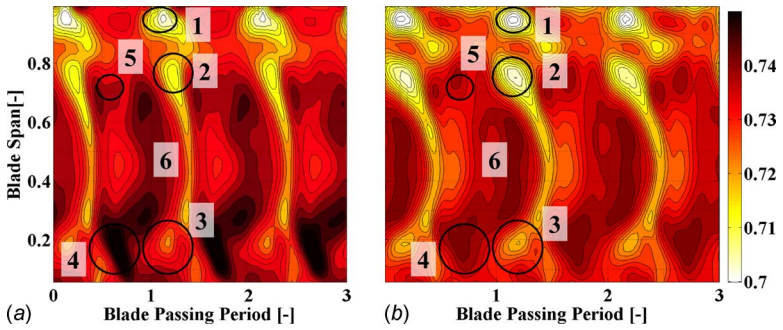

Fig. 12 Total pressure at traverse plane R1ex

Table 3 Nondimensional total pressure drop

	Data	Profiled	Δ%
Freestream	1.0	1.0	
S1 Wake	0.78	0.81	3.8%
S1 HPV	0.80	0.82	2.5%

ciency. These results show that the upstream nozzle guide vane wake and vortices do less work on the rotor than the freestream, a conclusion that is consistent with the ideas presented in Ref. [24].

3.4 Streamwise Vorticity. The time-averaged streamwise vorticity and the dissipation function are next examined. The streamwise vorticity is the scalar product of the vorticity, whose components are given in Eqs. (2)–(4) and the primary flow vector. The streamwise vorticity is related to secondary flows as it introduces flow perpendicular to the primary flow direction, defined as the circumferentially mass-averaged velocity profile. Therefore, a reduction in streamwise vorticity normally leads to a reduction in secondary loss. To calculate the three-dimensional vorticity vector, the axial gradients of the radial and circumferential velocity components are needed. In a single axial plane traverse, it is not possible to calculate these axial gradients.

$$\Omega_x = \frac{1}{r}\left(\frac{\partial}{\partial r}(ru_\theta) - \frac{\partial u_r}{\partial \theta}\right) \tag{2}$$

$$\Omega_r = \frac{1}{r}\frac{\partial u_x}{\partial \theta} - \frac{\partial u_\theta}{\partial x} \tag{3}$$

$$\Omega_\theta = \frac{\partial u_r}{\partial x} - \frac{\partial u_x}{\partial r} \tag{4}$$

Therefore, the axial gradients are estimated using the time-resolved data, with the assumption that the flow structures are frozen over one timestep. Multiplane measurements performed subsequent to this paper verify that this assumption is valid; these measurements will be presented in a future publication. For example, the following approximation for the axial derivative of the radial velocity can be used:

$$\frac{\partial u_r}{\partial x} \approx \frac{\partial u_r}{u_x \cdot \partial t} \tag{5}$$

This approach is only correct if the flow direction is within a very small range such as ±10 deg, with respect to the axial direction. For a larger range, it is necessary to interpolate in the circumferential direction using the circumferential displacement $d\theta$ of a fluid particle over one timestep t. So if the fluid particle is traveling in positive circumferential direction, it is displaced by $-d\theta$ relative to the traverse Tr in the preceding timestep. Therefore, an interpolation within the measurement grid consisting of the radial traverses Tr is required to determine the velocity at the same circumferential position. Equation (5) is then rewritten as Eq. (6) and illustrated in Fig. 13.

$$\frac{\partial u_r}{\partial x} \approx \frac{u_r(t,\theta) - u_r(t+1,\theta+d\theta)}{u_x \cdot dt} \tag{6}$$

Figure 14 shows the streamwise vorticity at stator exit time averaged in the stationary frame of reference. At 85% span, there is a region of positive streamwise vorticity 3, which is associated with the tip passage vortex. Zone 1 shows the vorticity of the opposite sign that represents the tip trailing shed vortex. Zone 2 shows the negative streamwise vorticity of the hub passage vortex. Zone 4 shows the positive vorticity that represents the hub trailing shed vortex. Between 15% and 75% spans, there is a band of positive vorticity that is associated with trailing shed vorticity 5. This trailing shed vorticity has been reduced by a factor of 2 with nonaxisymmetric endwall contouring.

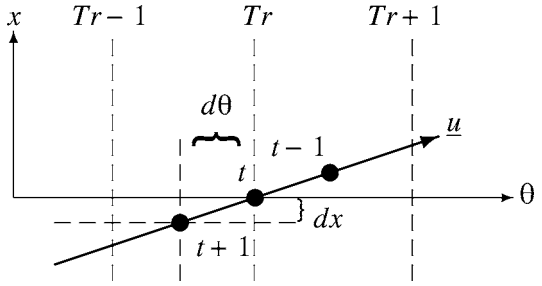

Fig. 13 Illustration for circumferential interpolation

Figure 15 shows the streamwise vorticity at rotor exit time averaged in the rotating frame of reference. The positive streamwise vorticity at 20% span is due to the rotor hub passage vortex labeled 3. It is therefore evident that the nonaxisymmetric rotor hub endwall reduces the vorticity of the hub passage vortex as was the design intent. Zone 5 shows the negative streamwise vorticity of the hub trailing edge shed vortex. It is therefore evident that the nonaxisymmetric rotor hub endwall also reduces the strength of the hub trailing shed vortex. At 75% there is a region of negative streamwise vorticity 2. This region is associated with the tip passage vortex. Zone 4 shows the tip trailing shed vortex. Along the casing the positive vorticity signature of the tip leakage vortex is seen in zone 1. As the turbine has an unshrouded rotor, no endwall contouring at the tip is possible. The tip gap size is only changed by 1% of gap size. Therefore, the observed changes in the outer part of the annulus come from the different stator 1 exit flow field. One sees an increase in vorticity in the tip passage vortex region as well as a reduction in the tip leakage region with endwall profiling.

3.5 Dissipation. The rate of irreversible heat generation by doing work against the viscous forces is given in Eq. (7) given in Ref. [25]. The viscosity in Eq. (7) is the molecular or laminar viscosity. In order to evaluate the dissipation correctly, one would need a fine spatial resolution. The instantaneous velocity vector with its deterministic and turbulent fluctuations is also needed. In practice, the spatial resolution is limited by the traverse grid size and the temporal resolution is only deterministic. For these reasons, the calculated dissipation must be regarded with some care as the modest spatial resolution and the deterministic time signature will result in an underestimate of the dissipation.

$$dQ_F = dt \cdot \Delta V \cdot \mu \cdot \Phi \tag{7}$$

Φ, the viscous dissipation function, is given in cylindrical coordinates in Eq. (8). The required axial gradients are approximated in the same manner as for the streamwise vorticity shown in Fig. 13 and given in Eq. (6).

$$\Phi = 2\left[\left(\frac{\partial u_r}{\partial r}\right)^2 + \left(\frac{1}{r}\frac{\partial u_\theta}{\partial \theta} + \frac{u_r}{r}\right)^2 + \left(\frac{\partial u_x}{\partial x}\right)^2\right] + \left[r\frac{\partial}{\partial r}\left(\frac{u_\theta}{r}\right) + \frac{1}{r}\frac{\partial u_r}{\partial \theta}\right]^2 + \left[\frac{1}{r}\frac{\partial u_x}{\partial \theta} + \frac{\partial u_\theta}{\partial x}\right]^2 + \left[\frac{\partial u_r}{\partial x} + \frac{\partial u_x}{\partial r}\right]^2 - \frac{2}{3}(\nabla \cdot \underline{u})^2 \tag{8}$$

In order to better quantify the dissipation function, it is normalized by the flux of kinetic energy given in

$$\dot{m} \cdot \frac{u^2}{2} = \rho \cdot u_x \cdot A_x \cdot \frac{u^2}{2} \tag{9}$$

where

$$u^2 = u_x^2 + u_r^2 + u_\theta^2 \tag{10}$$

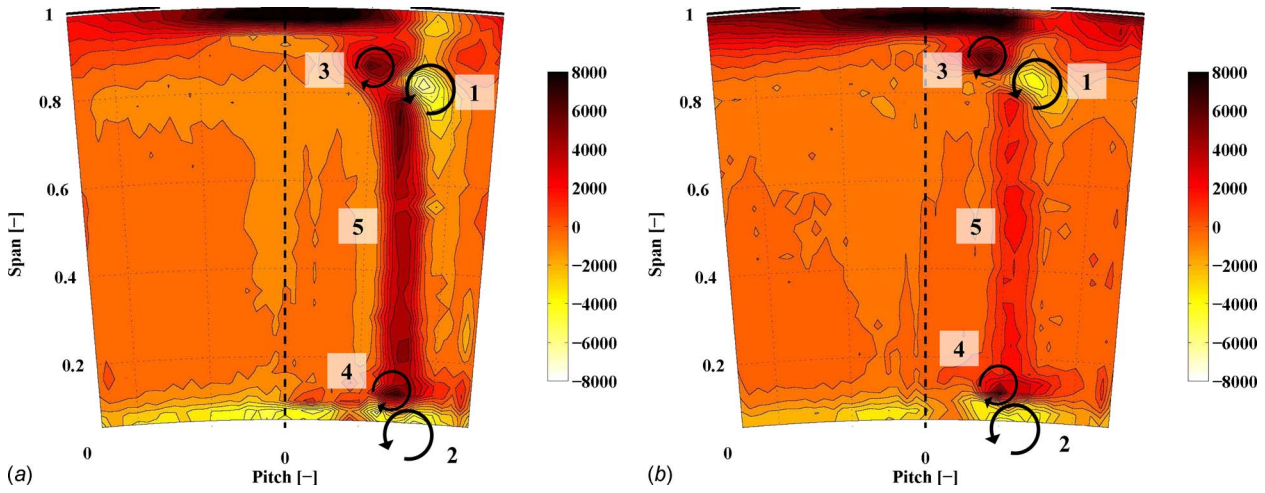

Fig. 14 Time-averaged streamwise vorticity in the stator frame of reference at traverse plane S1ex (1/s)

Thus we have the modified dissipation function D given in

$$D = \frac{\mu \cdot \Phi}{\rho \cdot \frac{u^2}{2}} \tag{11}$$

Figure 16 shows the time-averaged dissipation function at the stator exit in the stationary frame of reference. For purposes of scaling, we present contours of the D parameter. D can be interpreted as the percentage rate at which kinetic energy is converted into heat per second. It should be noted that Fig. 16 shows the

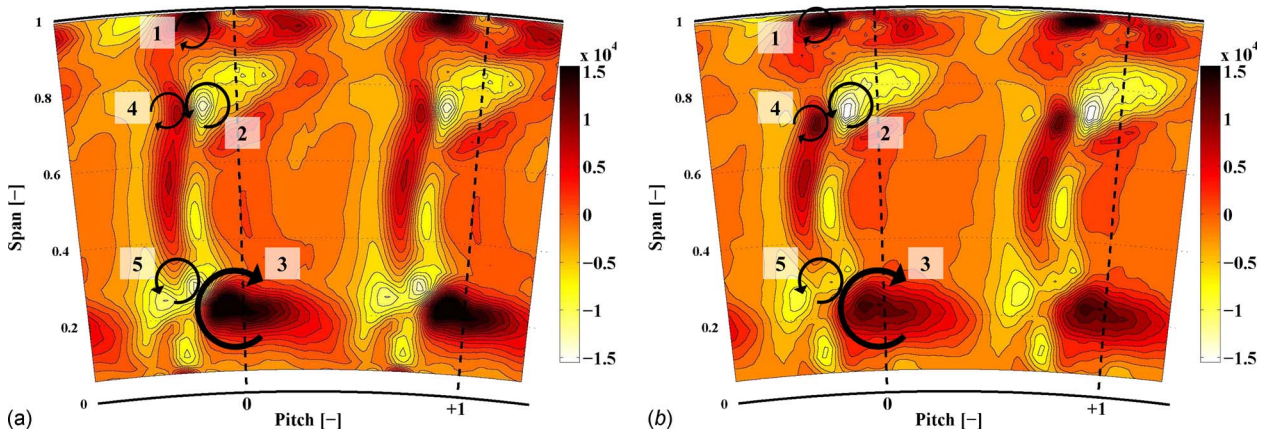

Fig. 15 Time-averaged streamwise vorticity in the rotor frame of reference at traverse plane R1ex (1/s)

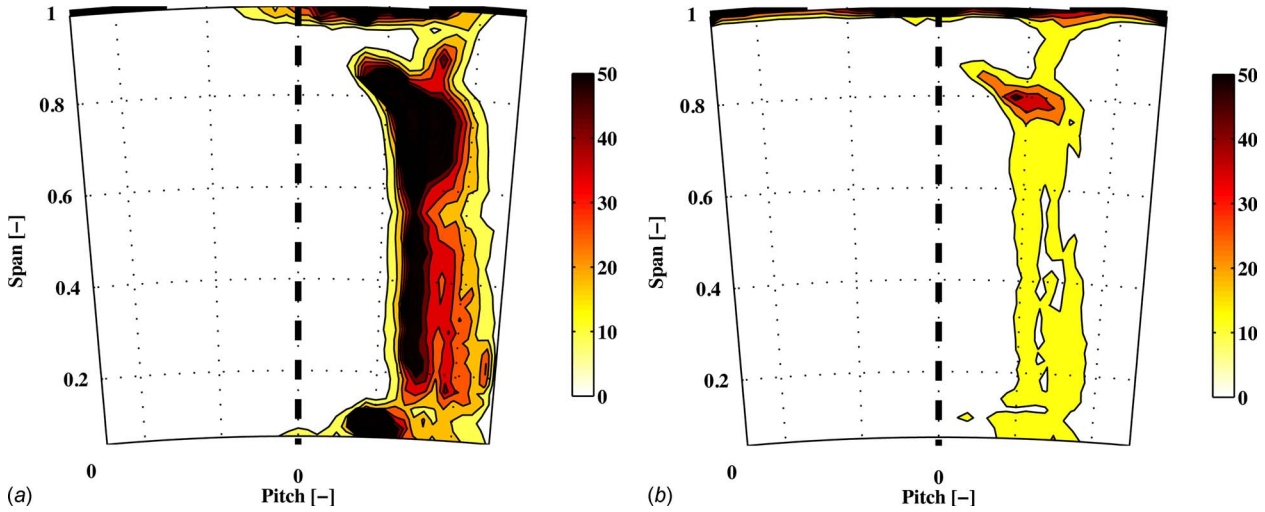

Fig. 16 Time-averaged *D* parameter in the stator frame of reference at traverse plane S1ex (%/s)

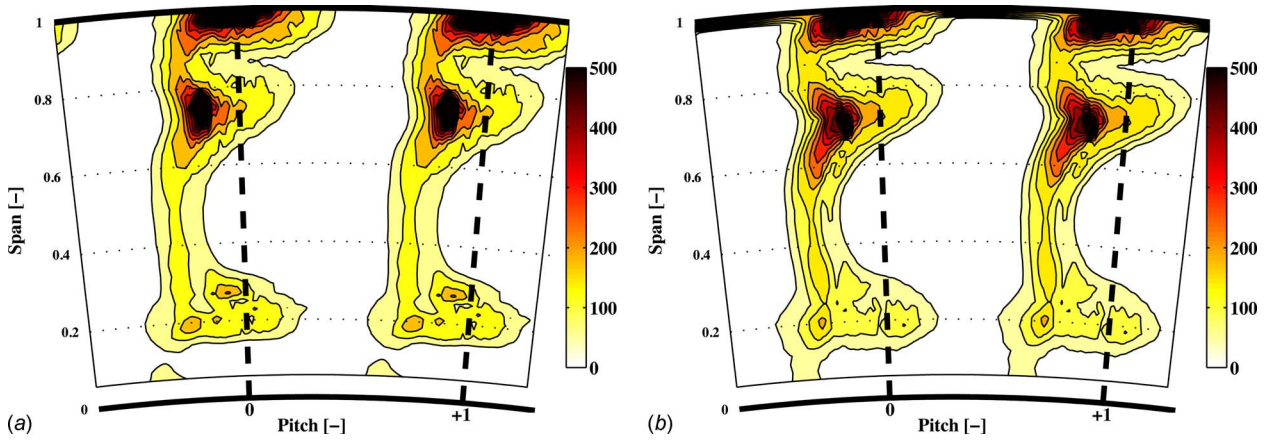

Fig. 17 Time-averaged *D* parameter in the rotor frame of reference at traverse plane R1ex (%/s)

dissipation over only one single traverse plane. In order to relate the dissipation to loss, one would need to integrate over the whole volume. Nevertheless the nonaxisymmetric profiling considerably reduces the D parameter over the whole span. This is a good indication of the observed loss reduction. At the casing the high dissipation region in the nonaxisymmetric case is confined to the endwall, whereas it is accumulated in the baseline case. The dissipation in the wake of the axisymmetric case is four to five times higher. At the hub the zone of high dissipation is no longer visible in the nonaxisymmetric case.

Figure 17 shows the time-averaged D parameter at rotor exit in the rotating frame of reference. In Fig. 17 the dissipation is much stronger than at the exit of the upstream nozzle guide vane, as shown in Fig. 16. The scale is an order of magnitude greater. The highest values are measured both in the tip leakage region and in the interaction zone of the trailing edge shed vortex and the tip passage vortex. The dissipation at the hub is much less pronounced and reduced with endwall profiling. At 75% span, the integrated dissipation is about the same. However, the axisymmetric case shows a more intense core, while the core is diffused over a larger area in the nonaxisymmetric case.

4 Conclusions

The results shown in this paper provide detailed explanations for the improved efficiency of about $\Delta\eta_{tt}=1.0\%$. In this particular design, most of the improvement can be found in the first vane row. With a new approach using time derivatives, the streamwise vorticity could be calculated from a single plane traverse. Doing this it became evident that the endwall profiling has suppressed the streamwise vorticity of the secondary flow in stator 1 and the rotor hub as intended in the design. However, it was found that the main reductions in streamwise vorticity with profiling, more than 50%, were achieved in the nozzle wake due to the reduced trailing shed vorticity. The dissipation function in the wake at nozzle guide vane exit is reduced by a factor of 5 with nonaxisymmetric endwall profiling. The reduction in streamwise vorticity and dissipation are mainly responsible for the stator 1 loss reduction of 12% reported in the first part of this two part paper.

The rotor hub endwall profile contributed to the total efficiency increase by reducing the streamwise vorticity of the hub passage vortex. The less distorted stator flowfield of the profiled case, which enters the rotor leads potentially to a larger work extraction, as well as to a more homogenous rotor exit field. With a more homogenous rotor exit flowfield, the mixing losses are reduced. At rotor exit it was possible to identify the wake and loss cores of the upstream vane via their rms signature. The variation in pitch angle and relative total pressure in the zone of rotor and upstream vane interaction seem to have reduced with endwall profiling.

Achnowledgement

The work reported here was carried out within the joint industrial and academic research program that is part of the "Luftfahrtforschungsprogramm LuFo3" supported by the German Federal Ministry of Economics and Technology.

Nomenclature

A = area (m^2)
D = dissipation function (%/s)
h = enthalpy (J/kg)
$\dot{m}$ = massflow (kg/s)
N = rotational speed (rps)
p = pressure (Pa)
$\bar{p}$ = time mean part of pressure signal (Pa)
$\tilde{p}$ = periodic part of pressure signal (Pa)
p' = random part of pressure signal(Pa)
Q = amount of heat (J)
r = radial coordinate (m)
T = temperature (K)
T = blade period (s)
t = time (s)
U = mean height blade speed (m/s)
u = velocity (m/s)
V = volume (m^3)
x = axial coordinate (m)

Greek

η = efficiency
θ = circumferential coordinate (m)
μ = viscosity (kg/ms)
Π = pressure ratio
ρ = density (kg/m^3)
Φ = dissipation function ($1/s^2$)
Ω = vorticity (1/s)

Subscripts

c,max = compressor
F = frictional
in = turbine inlet
r = radial coordinate
t = stagnation flow quantity
tt = total-to-total
x = axial coordinate
θ = circumferential coordinate
1.5 = total-to-static 1.5 stages

Abbreviations

FRAP = fast response aerodynamic probe

HPV = hub passage vortex
NGV1 = first nozzle guide vane
NGV2 = second nozzle guide vane
rms = root mean square
R1ex = rotor 1 exit
R1 = rotor 1
R1ex = rotor 1 exit
S1ex = stator 1 exit
S1 = stator 1
S2 = stator 2
Tr = traverse number

References

[1] Dunham, J., 1970, "A Review of Cascade Data on Secondary Losses in Turbines," J. Mech. Eng. Sci., **12**(1), pp. 48–59.
[2] Sieverding, C. H., 1985, "Recent Progress in the Understanding of Basic Aspects of Secondary Flows in Turbine Blade Passages," Trans. ASME: J. Eng. Gas Turbines Power, **107**(2), pp. 248–257.
[3] Langston, L. S., Nice, M. L., and Hooper, R. M., 1977, "3-Dimensional Flow Within a Turbine Cascade Passage," ASME J. Eng. Power, **99**(1), pp. 21–28.
[4] Schlienger, J., Kalfas, A. I., and Abhari, R. S., 2005, "Vortex-Wake-Blade Interaction in a Shrouded Axial Turbine," ASME J. Turbomach., **127**(4), pp. 699–707.
[5] Sturm, W., Scheugenpflug, H., and Fottner, L., 1992, "Performance Improvements of Compressor Cascades by Controlling the Profile and Sidewall Boundary-Layers," ASME J. Turbomach., **114**(3), pp. 477–486.
[6] Biesinger, Th. E., 1993, "Secondary Flow Reduction Techniques in Linear Turbine Cascades," Ph.D. thesis, University of Durham, Durham, UK.
[7] Harrison, S., 1992, "The Influence of Blade Lean on Turbine Losses," ASME J. Turbomach., **114**(1), pp. 184–190.
[8] Dejc, M. E., and Zarjankin, A. E., 1960, "Methods of Increasing the Efficiency of Turbine Stages," Teploenergetika (Moscow, Russ. Fed.), **2**, pp. 18–24.
[9] Morris, A. W. H., and Hoare, R. G., 1975, "Secondary Loss Measurements in a Cascade of Turbine Blades With Meridional Wall Profiling," ASME Paper No. 75-WA/GT-13.
[10] Atkins, M. J., 1987, "Secondary Losses and End-Wall Profiling in a Turbine Cascade," *Proceedings of IMechE Turbo Conference*, C255(87), pp. 29–42.
[11] Sauer, H., Muller, R., and Vogeler, K., 2001, "Reduction of Secondary Flow Losses in Turbine Cascades by Leading Edge Modifications at the Endwall," ASME J. Turbomach., **123**(2), pp. 207–213.
[12] Rose, M. G., 1994, "Non-Axisymmetric Endwall Profiling in the HP NGVs of an Axial Flow Gas Turbine," ASME Paper No. 94-GT-249.
[13] Hartland, J. C., Gregory-Smith, D. G., Harvey, N. W., and Rose, M. G., 2000, "Nonaxisymmetric Turbine End Wall Design: Part II—Experimental Validation," ASME J. Turbomach., **122**(2), pp. 286–293.
[14] Ingram, G. L., Gregory-Smith, D. G., Rose, M. G., Harvey, N. W., and Brennan, G., 2002, "The Effect of End-Wall Profiling on Secondary Flow and Loss Development in a Turbine Cascade," ASME Paper No. GT-2002–30339.
[15] Brennan, G., Harvey, N. W., Rose, M. G., Fomison, N., and Taylor, M. D., 2001, "Improving the Efficiency of the Trent 500 HP Turbine Using Non-Axisymetric End Walls: Part I: Turbine Design," ASME Paper No. 2001-GT-0444.
[16] Rose, M. G., Harvey, N. W., Seaman, P., Newman, D. A., and McManus, D., 2001, "Improving the Efficiency of the Trent 500 HP Turbine Using Non–Axisymetric End Walls: Part II: Experimental Validation," ASME Paper No. 2001-GT-0505.
[17] Duden, A., Raab, I., and Fottner, L., 1998, "Controlling the Secondary Flow in a Turbine Cascade by 3D Airfoil Design and Endwall Contouring," ASME Paper No. 98-GT-072.
[18] Eymann, S., Foerster, W., Beversdorf, M., Reinmoeller, U., Niehuis, R., and Gier, J., 2002, "Improving 3D Flow Characteristics in a Multistage LP Turbine by Means of Endwall Contouring and Airfoil Design Modification: Part I: Design and Experimental Investigation," ASME Paper No. GT-2002–30352.
[19] Sell, M., Schlienger, J., Pfau, A., Treiber, M., and Abhari, R. S., 2001, "The 2-Stage Axial Turbine Test Facility LISA," ASME Paper No. 2001-GT-0492.
[20] Behr, T., Kalfas, A. I., and Abhari, R. S., 2007, "Unsteady Flow Physics and Performance of a One-and-1/2-Stage Unshrouded High Work Turbine," ASME J. Turbomach., **129**(2), pp. 348–359.
[21] Kupferschmied, P., Kopperl, O., Gizzi, W. P., and Gyarmathy, G., 2000, "Time Resolved Flow Measurements With Fast Aerodynamic Probes in Turbomachinery," Meas. Sci. Technol., **11**, pp. 1036–1054.
[22] Pfau, A., Schlienger, J., Kalfas, A. I., and Abhari, R. S., 2003, "Unsteady 3-Dimensional Flow Measurement Using a Miniature Virtual 4 Sensor Fast Response Aerodynamic Probe (FRAP)," ASME Paper No. GT2003–38128.
[23] Schlichting, H., 1951, *Grenzschicht-Theorie*, G. Braun, Karlsruhe, Germany.
[24] Porreca, L., Hollenstein, M., Kalfas, A. I., and Abhari, R. S., 2007, "Turbulence Measurements and Analysis in a Multistage Axial Turbine," J. Propul. Power, **23**(1), pp. 227–234.
[25] Rose, M. G., and Harvey, N. W., 2000, "Turbomachinery Wakes: Differential Work and Mixing Losses," ASME J. Turbomach., **122**(1), pp. 68–77.

Effects of Compact Radial-Vaned Air Separators on Stalling Characteristics of an Axial-Flow Fan

Nobuyuki Yamaguchi

Masayuki Ogata

Meisei University,
2-1-1 Hodokubo,
Hino-shi,
Tokyo 191-8506, Japan

Yohei Kato

Japan Filter Technology, Ltd.,
I-1-1 Aza Sugise,
Tsuhata-machi, Kawakita-gun,
Ishikawa Prefecture 929-0454, Japan

The stall-prevention effect of air separators incorporating radial vanes in place of the existing axial vanes was investigated on a low-speed, single-stage, lightly loaded axial-flow fan for effective and compact air separators of a simplified structure. From the survey, paying attention to several geometrical dimensions of the device, the following conclusions are obtained: (1) Simplified radial vanes made of flat plates could show strong stall-prevention effect comparable to those of the curved-vane type one. The most favorable ones showed no stall up to the fan shut-off conditions. (2) Radial heights of the recirculation passage within the air separator showed significant influences on the stall improvement. It should be larger than some critical size experimentally given in the study. (3) The axial length of the device should be larger than some critical size given experimentally in the study. Too much reduced axial length could give rise to an abrupt loss in the effect. (4) The optimum axial locations of the rotor-tip blade leading edge within the device inlet opening were found to lie near the center of the width of the inlet opening from both aspects of stall improvement and fan efficiency. [DOI: 10.1115/1.3104613]

Keywords: fluid machinery, fluid mechanics, axial-flow fan, fan stalling, antistall device, air separator

1 Introduction

Improved performance efficiency of turbomachines, such as gas turbines, jet engines, compressors, and fans, is desired in the fields of electric power generation, prime movers, and industrial plants from the point of view of not only the economy of operation but also the problems of global climate changes and energy security. The authors, aiming to raise both working efficiencies and operational safety of axial-flow compressors and fans, have strived for the improvement of stall and surge characteristics of the machines.

To improve stall characteristics of axial-flow fans and compressor stages, a variety of devices have hitherto been attempted, such as casing treatment, suction bypass, blade separator, and air separator, by many researchers and institutes (for example, see Refs. [1,2]). Among them, the present authors have paid attention to the air separator, especially the radial-vaned air separator, which was proposed by one of the authors [3,4]. The preceding study [5] has made clear that the radial-vaned air separator, Type A, has a significantly favorable and stable effect on stall prevention. In addition to that, experimental data on effects of several parameters on the stall-prevention effects and on the optimum relative dimensions and locations of the air separators of Type A were obtained.

In this report, as a continuation of the preceding study [5], the results of the experimental study toward simplification and compact sizing of the radial-vaned air separators will be described. The results, together with the preceding ones [5], will form a body of useful information and guidelines for practical application of the devices.

Contributed by the Turbomachinery Division of ASME for publication in the JOURNAL OF TURBOMACHINERY. Manuscript received September 5, 2008; final manuscript received November 27, 2008; published online January 12, 2010. Review conducted by Aspi Wadia.

2 Axial Fan for Test

The experimental fan is a single stage one of axial inlet type consisted of a rotor and exit guide vanes. The fan casing near the rotor tip was modified for mounting an air separator device. Table 1 gives main numerical figures about the fan. Table 2 gives blade geometrical data as measured for the rotor blades at the tip and the root. Each rotor blade is made of a twisted metal plate formed in circular-arc sectional shapes of 2 mm thickness. The rotor-tip clearance is 2 mm in radius.

With respect to the fan performances, fan flow rates Q were evaluated from the pressure difference of a Venturi tube located downstream of the fan for test. Fan rotor static-pressure rise Δp_S was evaluated from a difference in static pressures at an upstream suction duct wall and at the casing wall immediately downstream of the rotor blades. Fan power input P from the electric power input to the fan motor (after the inverter). Fan efficiency includes motor efficiency. The fan speed was set at 2600 rpm. The fan working conditions were regulated by throttling the exit valve of the fan test ducting. The details of the test facility are given in Yamaguchi et al. [5]. Fan stalling was judged to occur at the zero-slope point of the fan rotor total-pressure coefficient.

For flow coefficient φ_t below 0.20 in the stalled zone of the solid wall condition, reversal of strong swirling flow up to the suction duct inlet was observed [5]. Since the swirling flow reversal affected the accuracy in measurement of the fan pressure rise, the solid wall condition characteristics for flow coefficient above 0.2 is employed here for a basis for comparison. The fan Reynolds number based on the blade chord length and the blade tip speed was around 4×10^5. The uncertainty in pressure measurements is evaluated to be 1.5% [5].

3 Air Separator Devices

The terms "air separator" and "solid wall" are abbreviated AS and SW, respectively, hereafter in this report. Figure 1 shows symbols of variables that are inevitable in the process of optimizing

Table 1 Numerical data about the experimental fan

Casing diameter D_t	394 mm
Tip diameter	390 mm
Hub diameter D_h	194 mm
Tip clearance	2 mm
Fan speed	2600 rpm
Nominal motor power	1.5 kW
Nominal fan pressure rise	0.20 kPa
Nominal fan flow rate	100 m^3/min

the AS geometry. S and C are the respective widths of the inlet opening and the exit opening of the AS device, b is the width of the inner ring, W is the height of the internal passage, g and h are distances, respectively, from the upstream edge and the downstream edge of the AS inlet opening to the leading edge of the rotor-tip blade section, H is the fan annulus height, and Za is the axial chord of the rotor blade at its tip. Prototypical values of the present experimental machine are as follows:

$$H = 100 \text{ mm} \quad \text{and} \quad Za = 35 \text{ mm}$$

$$W = 33 \text{ mm}, \quad C = 43 \text{ mm}, \quad S = 37.5 \text{ mm}, \quad b = 25 \text{ mm}$$

In the course of the investigation, various dimensions were changed and adjusted.

The AS devices studied here are Types A, B, C, and D and Types 10 and 5. Type A is the one studied in the preceding study [5]. Types B, C, and D and Types 10 and 5 are discussed in Secs. 5 and 6, respectively.

4 Nondimensional Parameters

Performance results are normalized with respect to the blade tip speed u_t,

$$\text{Flow coefficient} \quad \phi_t = V_a/u_t \tag{1}$$

Table 2 Conditions of the rotor blades as measured

	Tip	Root
Number of rotor blades	6	
Chord length l (mm)	115	130
Blade spacing t (mm)	190	117.5
Pitch-chord ratio t/l	1.65	0.90
Stagger angle ξ	71 deg	43 deg
Camber angle θ	31.7 deg	43.5 deg

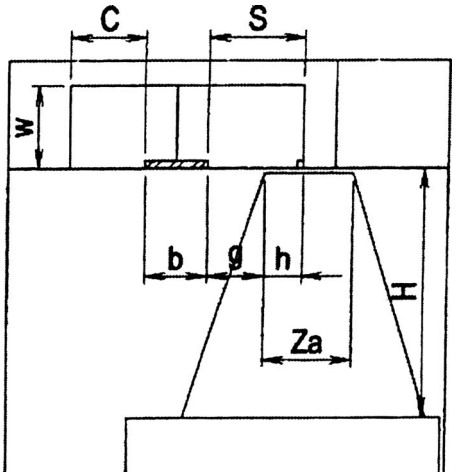

Fig. 1 Dimensions of the studied air separator and the fan

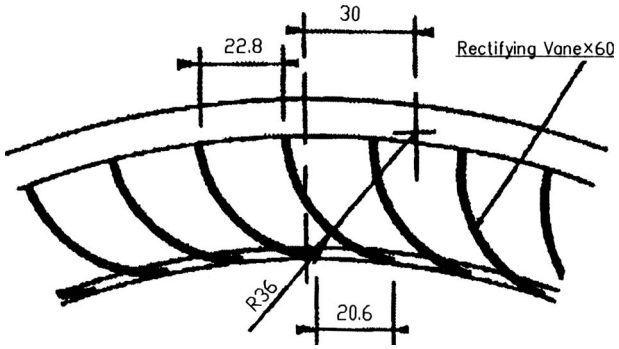

Fig. 2 Configuration of radial vanes for air separator Type A (W=33 mm)

$$\text{Rotor total-pressure coefficient} \quad \psi_t = \Delta p_T/\tfrac{1}{2}\rho u_t^2 \tag{2}$$

$$\text{Fan efficiency} \quad \eta_T = Q\Delta p_T/P \tag{3}$$

Here, Q is the fan flow rate (m^3/s), P is the motor power input (W), u_t is the fan rotor-tip speed (m/s), V_a is the annulus-average axial velocity (m/s), ρ is the air density (kg/m^3), Δp_S is the fan rotor static-pressure rise (Pa) between the suction duct wall pressure and the fan casing-wall pressure downstream of the rotor tip, and Δp_T is the fan rotor total-pressure rise (Pa),

$$V_a = Q/\left[\frac{\pi}{4}(D_t^2 - D_h^2)\right] \tag{4}$$

$$\Delta p_T = \Delta p_S + \tfrac{1}{2}\rho V_a^2[1 - (1 - \nu^2)^2] \tag{5}$$

Here, D_t and D_h, diameters of the fan casing and hub, respectively (m), and ν is the hub-to-tip radius ratio,

$$\nu = D_h/D_t \tag{6}$$

5 Trials of Simplified Radial-Vaned Air Separator

The preceding investigation [5] studied about the effects of AS Type A, about which the results are summarized as follows. Type A has radial vanes having a circular-arc sectional form, shown in Fig. 2, and numerical dimensions of W, C, S, and b listed in Sec. 3. The relative location of the leading edges of the rotor-tip blade section to the AS inlet opening that showed favorable results in the stall-prevention effect and the fan efficiency was for g/S of around 0.2–0.7. The characteristics of g/S of 0.4 is shown in Fig. 6 as AS-Aψ_t and AS-Aη_T. The effects of the relative location of the leading edges of the tip blade section on the stall flow coefficient ϕ_{tS} and the fan peak efficiency η_{TP} are shown in Fig. 9 as AS-Aϕ_{tS} and AS-Aη_{TP}.

In the continuation of the study [5], the authors have wished to make the AS devices simpler and more compact for easier practical applications. So, as the next stage, the following three types of simplified radial-vaned AS devices were tried. The sectional shapes of the radial vanes are changed to straight-plate ones in place of the circular-arc shape of Type A.

- Type B (Fig. 3): Radial vanes are simplified to inclined straight plates. The setting angle is 15 deg. W=33 mm.
- Type C (Fig. 4): Radial vanes are simplified to inclined straight plates. The setting angle is 45 deg. W=33 mm.
- Type D (Fig. 5): Radial vanes are simplified to inclined straight plates. The setting angle is 45 deg. W=11 mm, a third of those of Types A, B, and C.

Their axial dimensions C, S, and b are the same as those of Type A listed in Sec. 3. The relative radial heights of the AS passages are as follows:

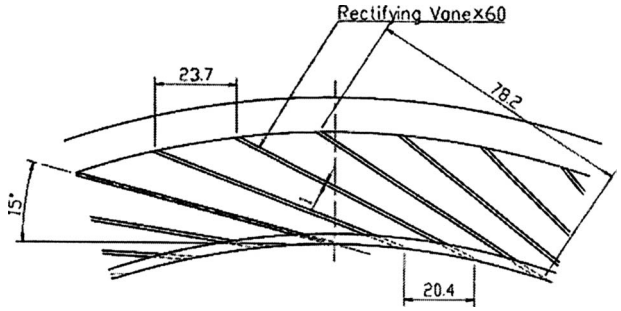

Fig. 3 Configuration of radial vanes for air separator Type B (*W*=33 mm)

$$W/H = 0.33(\text{Types A,B,C}), 0.11(\text{Type D})$$

$$W/Za = 0.94(\text{Types A,B,C}), 0.31(\text{Type D})$$

Figures 6 compares the performances effected by AS devices Types A, B, C, and D and the SW condition. Respective conditions are expressed as AS-A, AS-B, AS-C, AS-D, and SW in the figure. The relative locations of the leading edges of the rotor-tip blade sections to the AS inlet opening were kept the same as the optimum one for Type A, i.e., $g/S=0.4$ [5].

Both Types A and C eliminate the stall region over the entire flow coefficient. Type C shows a higher pressure coefficient at the shut-off condition. Types B and D prevent stalling over a very wide flow range but show a peak pressure coefficient around ϕ_t of 0.05 immediately before the shut-off condition, yielding a narrow positive-slope region.

With respect to the fan efficiency, all four AS devices show no steep drops in efficiency in the SW stalling zone. Type A keeps favorable efficiency comparable with the SW one in the SW sound condition and shows better level in the SW stalled zone. Types B and C show similar efficiency behaviors, in which the efficiency is lower by 1–2% than the SW one and is close to that of Type A in the SW stalled region. Type D shows an efficiency curve lower by 2–3% than those of SW and AS Type A over the whole flow range.

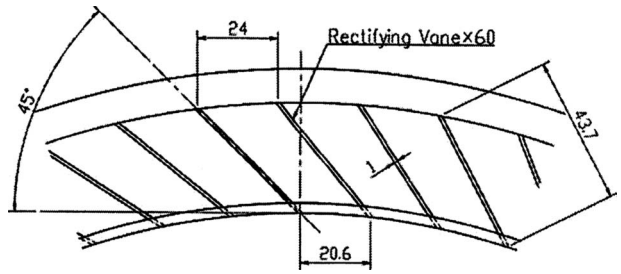

Fig. 4 Configuration of radial vanes for air separator Type C (*W*=33 mm)

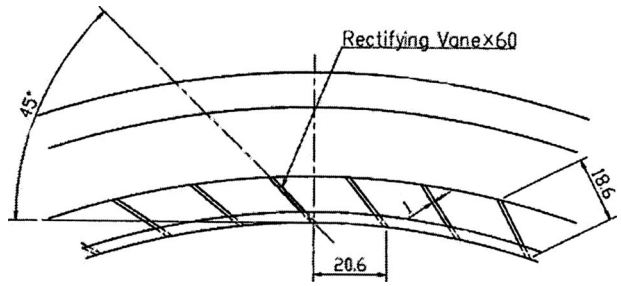

Fig. 5 Configuration of radial vanes for air separator Type D (*W*=11 mm)

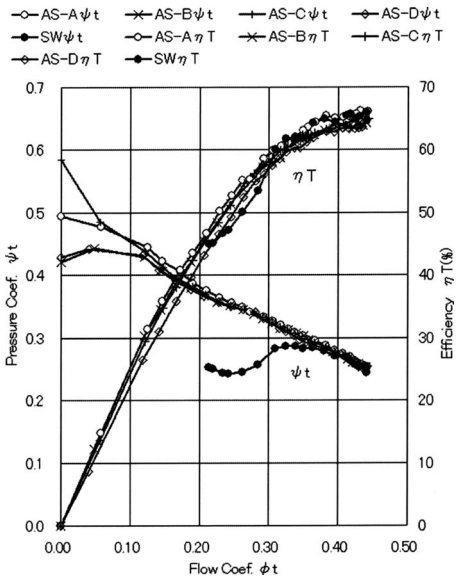

Fig. 6 Comparison of the effects of air separators of Types A–D together with the solid wall conditions on the fan characteristics

The following are summarized from the above observation.

(1) AS Type A is the best of the four from both viewpoints of stall prevention and fan efficiency level.
(2) The simplified configurations of the radial vanes are able to provide a large stall-prevention effect. However, some drops in the fan efficiency appear accompanied. The fan efficiency levels of Types B and C are comparable. Type C, which has a setting angle of 45 deg relative to the circumference, appears advantageous in suppressing stalling down to the shut-off condition.
(3) From the results on Type D, a reduction in the radial height of the AS passage is possible but tends to accompany some drops in the fan efficiency.

Related to the above item (2), the higher effectiveness in stall prevention up to the shut-off condition achieved by Type C compared with Type B could be explained very tentatively as follows. According to Tanaka and Murata [6] on a fan applied with a blade separator device, the meridional flow in the stall-improved region contains a large-scale recirculation flow forming an annular vortex ring, encasing the rotor blade tips, and extending toward the upstream of the separator and the rotor blade row. The recirculation flow is stabilized by flowing through the separator passage; thus the fan flow condition might be stabilized as a whole. The AS situation here could be similar to the above blade-separator one. So, it is supposed, though tentatively, that the flow rate through the AS passage might be relatively large near the shut-off condition, where the fan flow rate itself appears very small; thus, the higher setting angle of the radial vanes of Type C would be advantageous to treat with the large recirculation flow rate.

6 Effect of Height Reduction of the Radial-Vaned Air Separator

In order to put the AS devices to practical use, it is necessary to reduce the size for easier embeddability into casing walls of fans and compressors. From the aspect, the following two AS devices were made on the basis of the above results and some experiences of the authors for survey on the stall-prevention effects.

(1) AS Type 10: The radial height of the internal passage *W* is 10 mm. The vane configuration is shown in Fig. 7. Each vane is made of two pieces of straight plates: a main

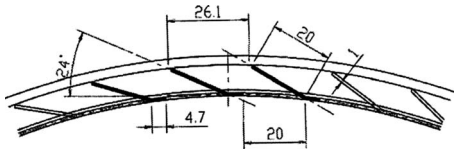

Fig. 7 Configuration of radial vanes for Type 10 air separator (*W*=10 mm)

straight plate of a length of 20 mm inclined at an angle of 24 deg to the casing circumference and a short front piece of a length of 4.7 mm attached circumferentially to the front edge of the main plate. Widths of the inlet opening and the exit one are $S=30$ mm and $C=45.5$ mm.

(2) AS Type 5: The radial height of the internal passage W is 5 mm. The vane configuration is shown in Fig. 8. Each vane is made of two pieces of straight plates: a main plate of a length of 12.4 mm inclined at an angle of 27.5 deg to the casing circumference and a front piece of a length of 4.8 mm attached circumferentially to the front edge of the main plate. Widths of the inlet opening and the exit one are $S=28$ mm and $C=43.5$ mm.

The short front plate attached to the main plate has two aims. The first is to approximate the vane configuration to a circular-arc one, as is seen for Type A. It could enhance the scooping action and will tend to reduce possible backflow reflected out of the AS passage into the fan main flow, which were often experienced in other types of AS devices. It has also an effect of increasing the row solidity. The second aim is, from a manufacturing point of view, to cut the whole row of the vanes out of only one long band of sheet metal or other materials. It could save the cost required for manufacturing or assembling the device out of many pieces.

6.1 Effects of Locations of the AS Devices Relative to the Rotor-Tip Blades. Effects of locations of the AS devices relative to the rotor-tip blade section on the stall prevention were surveyed by varying the dimensions g and h in Fig. 1, with the other dimensions kept the same as before. Figure 9 summarizes the behaviors of stall flow coefficients and peak efficiencies affected by the relative location g/S, including the results on AS Type A obtained in the preceding study [5]. In Fig. 9, symbol notes AS_A, AS_10, AS_5, and SW mean conditions of AS Type A, Type 10, Type 5, and SW, respectively. φ_{tS} and η_{TP} are the stalling flow coefficient and peak total efficiency, respectively. The behavior of the stall flow coefficients φ_{tS} in Fig. 9 shows that there exist favorable zones of relative location g/S for the maximum stall-prevention effect. For the smaller AS passage height W, the favorable zones are the narrower and the stall-prevention effects are the less. Type 5 shows a drastic reduction in both the zone width and its effectiveness in stall prevention in contrast to the very wide range of Type A that has achieved the complete unstalling down to the shut-off condition $\varphi_{tS}=0$. Nevertheless, Type 5 has a stalling flow coefficient of $\phi_{tS}=0.20$ in contrast to $\phi_{tS}=0.32$ for the SW condition.

As seen in Fig. 9, the stall-prevention effect disappears drastically at the upper limiting end of the optimum zone of g/S for all the AS types tested, which could be ascribed to a situation similar

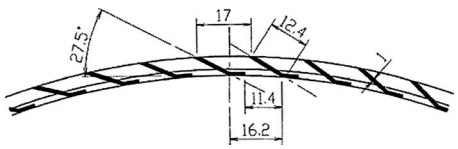

Fig. 8 Configuration of radial vanes for Type 5 air separator (*W*=5 mm)

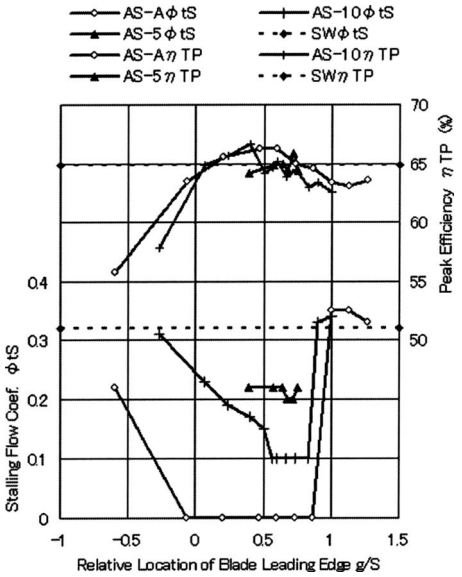

Fig. 9 Effects of relative locations of air separators Type A, Type 10, and Type 5 on the stalling flow coefficients and the peak efficiencies

to the deteriorated stall-prevention effect caused by retracted leading edges mentioned in the preceding study [5]. In the AS devices having a shorter passage height, the phenomenon appears even for the condition of the blade leading edges intruding into the axial width of the AS inlet opening. On the other hand, reduction in the effectiveness in the stall prevention toward the smaller g/S is seen rather gradually in Fig. 9, which could be related partly to the situation of the deteriorated stall-prevention effect caused by protruded leading edges described in the preceding study [5].

For the shorter-height AS devices, the peak-efficiency levels, whose accuracy is rather low and tentative, tend to be lower, and the favorable range becomes narrower compared with those of Type A condition.

6.2 Effects of the Widths of the Openings *S* and *C* of the AS Inlet and Exit. The effects of widths of the AS inlet and exit openings, S and C, were surveyed on the stall prevention, with the relative location g/S kept at respective optimum values selected from the above results. The employed values of g/S were 0.4 for Type A, 0.70 for Type 10, and 0.68 for Type 5. The inlet opening widths S were set by extending the width b of the AS inner ring by sticking adhesive tapes of a constant width on the radial-vane leading edges, and the exit openings C were set by inserting annular spacer rings with different thicknesses.

Figure 10 shows some typical behaviors of performance characteristics when the width C of the AS exit opening was changed with the width S of the inlet opening kept constant at 20 mm. In the symbol notes ($SxxCyy$) in Fig. 10, xx and yy mean the values of S and C in millimeters, respectively. It is seen that large stall-prevention effects are obtained for C larger than 10 mm. For the closed exit, i.e., $C=0$ mm, a certain degree of effect is seen to remain.

Figure 11 shows some typical behaviors of performance characteristics when the width S of the AS inlet opening was changed, with the width C of the exit opening kept constant at 20 mm. The symbol notes are expressed in quite the same manner as in Fig. 10. Stall-prevention effects by the AS devices are seen to be large but slightly changeable depending on the values of S and C.

6.3 Stall-Prevention Effect Affected by the Widths of the Openings of the AS Inlet and Exit. Since the stall-prevention effects are seen to vary depending on the combinations of the values of S and C, the variations in the effectiveness in functions

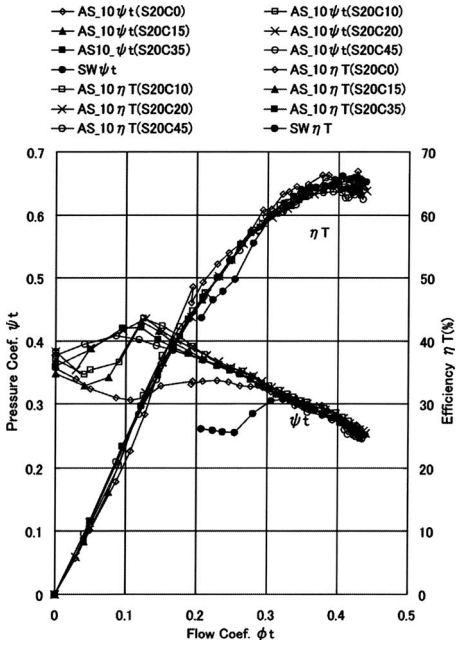

Fig. 10 Fan characteristics affected by the application of air separators Type 10 for *S*=20 mm and variable sizes of *C*

of S and C are summarized below. As a measure of stall-prevention effect, the following index B_s is employed:

$$B_S = [1 - (Q_S^*/Q_S)] \times 100(\%) \tag{7}$$

Here, fan flow rates at the stall point are expressed as Qs for the SW condition and Qs^* for the AS condition. For the case of no stall down to the shut-off condition, $Bs=100$, and in the case of no effect, $Bs=0$.

Figures 12 and 13 show contour maps for index B_S for AS devices Type 10 and Type 5, respectively, against of S and C. The iso-B_S lines are interpolated from data measured at "X" points on the maps.

The largest values of achieved B_S are 72.7 for Type 10, 39.4 for Type 5, and 100 for Type A [5], which are attained at the top-right points of the respective figures.

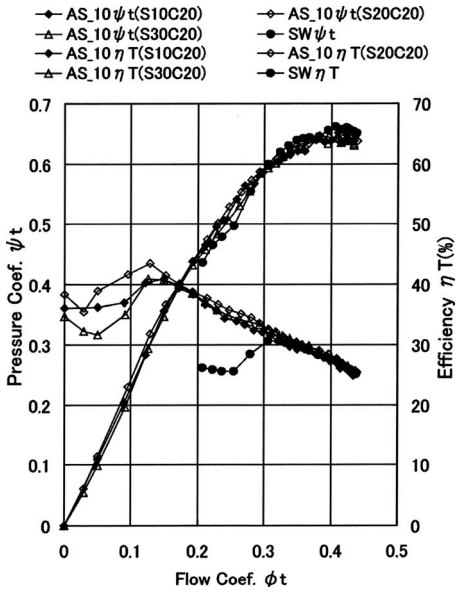

Fig. 11 Fan characteristics affected by the application of air separators Type 10 for *C*=20 mm and variable sizes of *S*

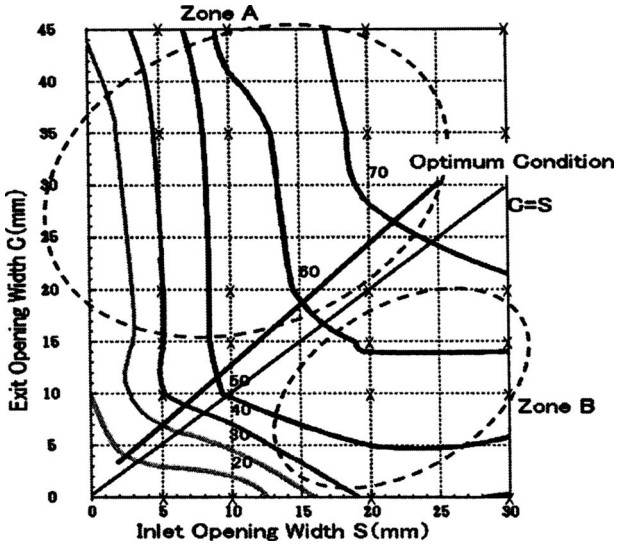

Fig. 12 Effects of opening widths of the inlet and the exit of air separator Type 10 on the stall improvement index *Bs*

Figures 12 and 13 show tendencies similar to those for Type A given in the preceding study [5]. There exist Zones A and B, where the iso-B_S lines are determined mostly by the inlet opening width S in the former and by the exit opening width C in the latter, respectively. Zone B for Type 5 in Fig. 13 is seen to be influenced by both S and C.

AS dimensions determined in such a manner as to minimize the additive value $(S+C)$ on each iso-Bs contour could minimize the axial size of the device for the Bs value. Such a condition is drawn as an optimum line, though very roughly, in Figs. 12 and 13. Line $C=S$, meaning the condition of equal widths of the inlet opening and the exit opening, is inserted for reference in the figures.

7 Summary and Considerations

7.1 Influence of Reduced Passage Height *W*. As seen in the decreasing order of the maximum Bs of AS devices Types A, 10, and 5, the reduction in the AS passage height W causes a signifi-

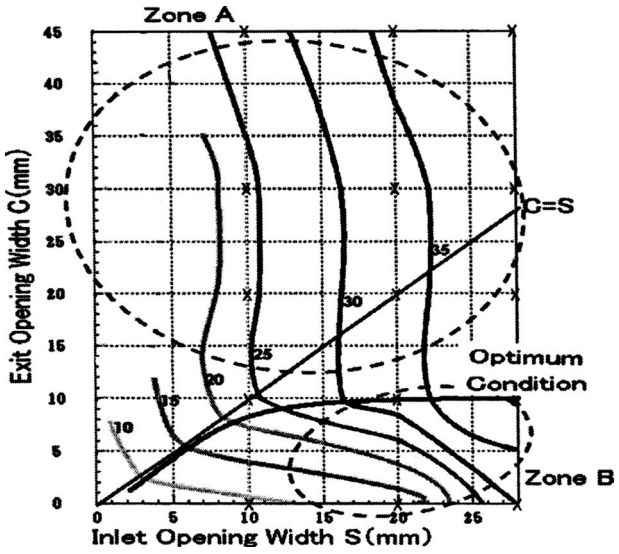

Fig. 13 Effects of opening widths of the inlet and the exit of air separator Type 5 on the stall improvement index *Bs*

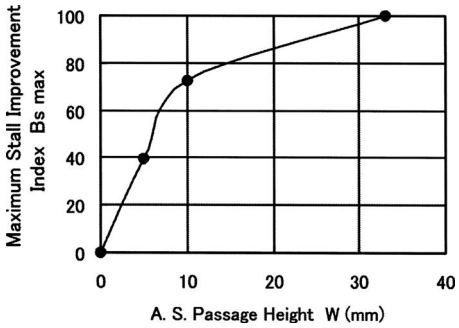

Fig. 14 Achieved maximum stall improvement indices *Bs* max for air separator passage height *W*

cant drop in the effectiveness of stall prevention. Figure 14 shows the tendency in the maximum *Bs* values affected by the passage height *W* of the respective AS devices, though including possibly some influences owing to the differences in the vane configurations. As seen in Fig. 14, devices smaller than Type 10 ($W=10$ mm) could have a steeply reduced *Bs* max value. As a measure, *W* larger than 10 mm for this particular fan is recommended. Or, in a relative form defined with the axial chord of the rotor-tip blade section *Za* as the reference length, W/Za larger than around 0.3 could be recommended.

The reduced effectiveness could be ascribed to the lowered capacity of the AS passage because of the insufficient passage height, i.e., reduction in the scooped flow rate in the inlet opening and incomplete discharge from the exit opening of the scooped flow.

7.2 Influence of the Axial Length of the AS Devices. Maximum values of stall improvement index *Bs* achievable by a given axial length of AS devices $(C+S)$ are plotted in Fig. 15, whose data are read from Figs. 12 and 13 in the present report and from Fig. 12 in the preceding report [5]. The right edge points of the curves are the respective maximum *Bs* max values shown in Fig. 14. It is seen that the highest magnitude of achievable *Bs* is determined mainly by the AS passage height *W* and that, with a decrease in the axial length $(C+S)$, the achievable *Bs* lowers. For further decrease in $(C+S)$, *Bs* tends toward 0. In order to obtain a level near *Bs* max, $(C+S)$ larger than roughly 45 mm for this particular fan or $(C+S)/Za$ larger than 1.3 in a relative form

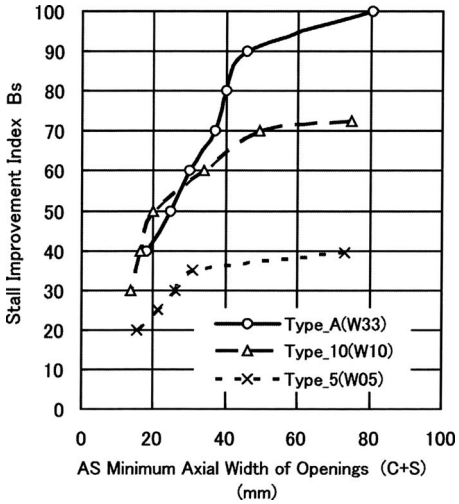

Fig. 15 Tendency of stall improvement indices *Bs* achievable for given axial widths of air separator openings *(C+S)*

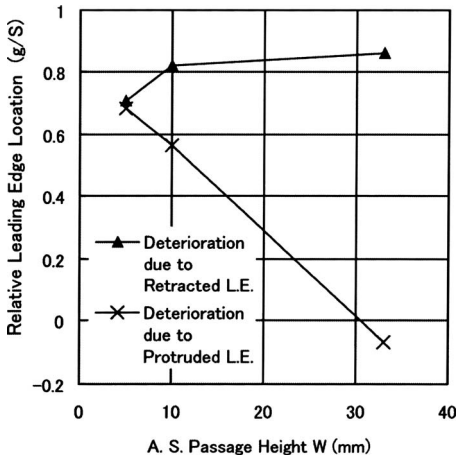

Fig. 16 Favorable range of *g/S* for stall improvement affected by the air separator passage height *W* for respective maximum widths of inlet and exit openings

would be necessary.

With respect to the respective lengths *S* and *C*, the optimum lines given in Figs. 12 and 13 in the present report and in Fig. 12 in the preceding report [5] could be referred to.

7.3 Favorable Relative Locations of the AS Devices. As shown in Fig. 9, with reducing AS passage height *W*, the favorable ranges of g/S become narrower, and at the same time the optimum location moves. The tendency is shown in Fig. 16 for the condition of the maximum widths of the AS openings. While the deterioration due to retracted leading edges is seen to occur roughly above g/S of around 0.8 common for the three types, the deterioration due to protruded leading edges and exposed blade tips are seen to occur earlier, with decreasing height of the devices. Accordingly, the optimum location moves from g/S of around 0.4 for Type A to around 0.7 for Types 10 and 5. For the smaller *W*, the deterioration due to protruded leading edges appears, with the leading edges located halfway in the axial width of the AS inlet opening, which suggests a more complicated situation than that supposed for Type A. As a possible situation in the relatively wide AS inlet openings, in addition to the above deterioration, a considerable part of the flow pushed into the inlet opening might have reflected back into free space in front of the blade tips in vain, only giving more disturbances to the main flow, thus reducing the probable stall-prevention effect.

7.4 Influence of Closed Exit Opening. Condition $C=0$ mm in Figs. 12 and 13 means a completely closed exit opening of the AS devices. For the condition, the rate of throughflow within the AS passage is zero. Even at this condition, a certain extent of the stall-prevention effect is seen to remain.

The authors suppose that, in the condition, the effect is helped by a mechanism similar to the casing treatment effect. The term "casing treatment" is abbreviated as CT hereafter. The stall-prevention effect by the CT (for example, see Ref. [7]) is considered as follows; while rotor-tip blade sections sweep the treated surface, the pressure-side high pressure of a blade pushes the air into the internal volume of the CT, and the pushed-in and compressed air blows back into the lower pressure region of the blade suction-side, blowing away the low-energy flow and making the tip environment cleaner.

As to AS Type 5 with the closed exit opening ($C=0$ mm), it is considered that the above phenomenon could have occurred and improved somewhat the stalling environment. In addition to that, as seen in Fig. 13, an increase in the width of the AS exit opening above *C* of around 10 mm does not cause further stall-prevention effects. It is conjectured that even when *C* is sufficiently large,

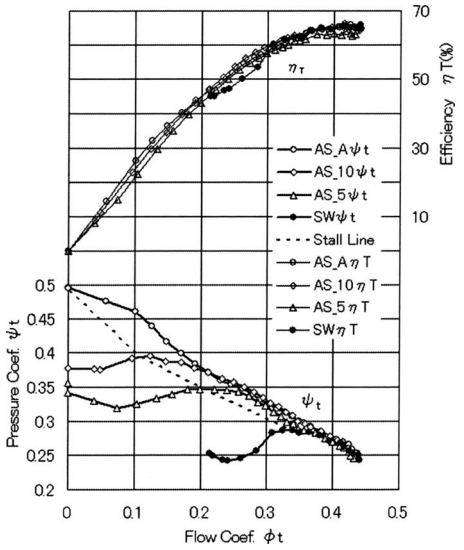

Fig. 17 Comparison of overall performances optimally improved by the applied air separators

Type 5 could not discharge all the scooped flow out of the exit opening, and a significant portion of the scooped flow might be reflected back at the inlet opening in a similar manner to the CT action.

In contrast to the above, the essential feature of the AS is to rectify all the scooped flow and discharge them out of the exit opening, which could be more effective if the conditions are well prepared. The situation of Type 10 seems to be halfway between those of Types A and 5.

7.5 Comparison of the Stall-Prevention Effects With Those of Casing Treatments. The order of magnitude of the stall-prevention index B_S in the CT application has been reported by Fujita and Takata [8] to be 20 in maximum and by Yamaguchi et al. [9] to be as large as 38 in maximum. The maximum *Bs* values of order of 40 obtained by Type 5 in this study are considered to be comparable to the highest possible level of those by CTs.

In consideration of the structural complexity of the AS devices compared with the simplicity of the CT structure, by far the more effective AS devices are desired for the practical application. For the purpose, an AS device with passage height W larger than 10 mm, which is equivalent to Type 10, is recommended for the particular fan condition. Or, in a relative form, W/Za greater than around 0.3 could be recommended as a measure.

7.6 Influence of the Thinner AS Devices on the Overall Performances. Figure 17 compares the best overall performances for the AS devices Types A, 10, and 5 and for the SW condition. It will be useful to predict the performance achieved by intermediate AS height conditions.

The stall points on the curves are seen lying on a dotted line nearly parallel to the pressure curve of Type A. It demonstrates the reduction in the stall-prevention effects with the reduction in the AS passage height. It suggests that the maximum recirculation flow rate allowable in the respective AS passages might have influences on the effectiveness.

According to Lee [10] on stall-improving effects by suction or injection through treated casing walls near the blade tips, the amount of the stall improvement depends greatly on the flow rate of the suction or injection. In the AS conditions, the recirculation flow rate will be determined in a self-balanced way, depending on several quantities, such as centrifuging forces of the flow, pressure losses within the AS passage, and wall pressure difference in the main flow between at the ASAS passage inlet and exit, many of which are intimately tied with the geometrical layout of the device and the relative arrangement of the blade tip and the AS device. In the smaller AS device, a sophisticated structure will be the key for success since the recirculation flow rate would naturally be smaller and the stall-prevention effects would be lower.

The efficiency curves show similar behaviors for the AS applied conditions. Peak efficiencies are the best for the conditions of SW and AS Type A. Type 5 shows some drop in the peak efficiency compared with the two. In the SW stalled region, all the AS applied conditions show improved efficiencies compared with the SW one.

8 Conclusion

The experimental study aimed to simplify the structure and reduce the sizes of radial-vaned air separators was conducted in the continuation of the preceding study [5]. By use of the AS devices equipped with simplified radial vanes made of inclined flat plates, the effects of the passage height W and the widths of the inlet opening and the exit opening, S and C, respectively, on the stall prevention were surveyed.

The following conclusions have been obtained, which are considered to be applicable to fans having conditions similar to the lightly loaded one tested here.

(1) AS devices equipped with radial vanes made of an inclined straight plate, when having a sufficiently large AS passage height (W), achieved favorable stall-prevention effects comparable to those of radial vanes having a circular-arc sectional shape (Type A [5]).
(2) AS passage height W exerted a significant influence on the stall-prevention effect. The height satisfying the condition $W/Za > 0.3$ is recommended if Za could be selected as an appropriate measure for the purpose. Below the level, drastic drops in the stall-prevention effects and the efficiencies could occur.
(3) Favorable relative locations g/S of the AS inlet opening relative to the leading edges of the rotor-tip blade section range roughly from 0.4 for large W to 0.7 for small W.
(4) A possible minimum axial length of the AS devices for a given stall-prevention index *Bs* could be determined as a condition for the minimum values of $(S+C)$ for the *Bs* value. As to the axial length, the value of $(S+C)/Za > 1.3$ is recommended.
(5) The stall-prevention effect by the smallest AS device, Type 5, with the exit opening closed ($C=0$), is comparable to the possible maximum effects achieved by casing treatments.
(6) Although AS devices are considered to have naturally a greater potential for stall prevention than that by CTs, the structures tend to be more complicated than those of CTs. Therefore, for practical use of the AS devices taking full advantages of the excellent potential, an AS size greater than Type 10 for the particular fan conditions or a relative passage height $W/Za > 0.3$ is recommended.

The authors consider that the above results have provided important basic data both from the practical point of view of developing more effective stall-prevention devices and from the phenomenological point of view of considering the mechanism of the AS effects. For highly loaded fans and compressor stages, further investigations are necessary, but the above results could be suggestive also in the study process.

Acknowledgment

The authors would like to express their deep thanks to the following graduate students of the Mechanical Department of Meisei University, Tokyo, Japan, who have devoted their efforts to the research: Mr. Mutsuhiro Ujihara, Mr. Kazuhiro Omichi, and Mr. Kazutaka Kumagai.

Nomenclature

b = axial length of the inner ring of the air separator (m)
Bs = index of improvement of stalling flow (%)
C = axial width of the exit opening of the air separator (m)
D_h = hub diameter of the fan (m)
D_t = casing-wall diameter of the fan (m)
g = distance between the leading edge of the rotor tip and the upstream edge of the inlet opening of the air separator (m)
h = distance between the leading edge of the rotor tip and the downstream edge of the inlet opening of the air separator (m)
H = annulus height of the fan (m)
l = chord length of the rotor bade (m)
P = power input to the driving motor (W)
Q = fan flow rate (m^3/s)
Q_S = stalling flow rate of the solid-wall fan flow rate (m^3/s)
Q_S^* = stalling flow rate of the fan with the air separator (m^3/s)
S = axial width of the inlet opening of the air separator (m)
t = spacing of neighboring blades (m)
u_t = peripheral speed of the rotor tip (m/s)
V_a = axial velocity (m/s)
W = height of the internal passage of the air separator (m)
Za = axial width of the rotor blade tip (m)
Δp_S = fan rotor static-pressure rise (Pa)
Δp_T = fan rotor total-pressure rise (Pa)
η_S = fan static efficiency
η_T = fan total efficiency
ρ = air density (kg/m^3)
θ = camber angle of the rotor blade (deg)
φ_t = fan flow coefficient
ψ_t = fan rotor total-pressure coefficient
ξ = stagger angle of the rotor blade (deg)

Indices

P = fan peak-efficiency point
t = normalized with reference to the rotor-tip speed
T = total pressure
S = static pressure or Stalling point
* = stalling point in the presence of the air separator

References

[1] Yamaguchi, N., 2005, "Stall and Surge of Axial Flow Compressors," Journal of Turbomachinery Society of Japan, **33**(8), pp. 490–502.
[2] Yamaguchi, N., 2005, "Stall Prevention by Means of Suction Rings and Casing Treatments, (1) Suction Rings and Casing Treatments," Journal of Turbomachinery Society of Japan, **33**(10), pp. 637–640.
[3] Yamaguchi, N., Takami, I., and Arimura, H., 1991, "Improvement of Air Separators of Axial Blowers," 250th Symposium of the Kansai Chapter of Japan Society of Mechanical Engineers, pp. 176–178.
[4] Yamaguchi, N., Owaki, T., Goto, M., Itaka, H., and Arimura, H., 1994, "Development of Mitsubishi General-Purpose Axial Fan (WIDEMAX Fan)," Tech. Rev.-Mitsubishi Heavy Ind., **31**(3), pp. 201–204.
[5] Yamaguchi, N., Ogata, M., and Kato, Y., 2008, "Improvement of Stalling Characteristics of an Axial Fan by Radial-Vaned Air Separator, Part I: Effects of Radial-Vaned Air Separators," Trans. Jpn. Soc. Mech. Eng., Ser. B, **074**(746), pp. 2163–2172.
[6] Tanaka, S., and Murata, S., 1975, "Post-Stall Characteristics and Rotating Stalls in an Axial Flow Fan, The Third Report: Stall Improvement Devices and Stalling Characteristics," Trans. Jpn. Soc. Mech. Eng., **41**(343), pp. 863–873.
[7] Takata, H., 1977, "Casing Treatment," The Fourth Seminar by Gas Turbine Society of Japan.
[8] Fujita, H., and Takata, H., 1981,"Study on the Effect of Casing Treatment Configuration in an Axial Flow Compressor," Jpn. Soc. Mech. Eng., preprint, No. 810-15, pp. 229–231.
[9] Yamaguchi, N., Otsukla, T., Higaki, K., Murakami, T., Goto, M., and Midori, M., 1983, "Development of Axial-Type Primary Air Fans for Coal-Fired Boilers: Development of Casing-Treated Adjustable Moving Blade Axial Fans," Tech. Rev.-Mitsubishi Heavy Ind., **20**(3), pp. 229–236.
[10] Lee, N. K. W., 1988, "Effects of Compressor Endwall Suction and Blowing on Stability Enhancement," MIT, GTL Report No. 192.

Particle Image Velocity Investigation of a High Speed Centrifugal Compressor Diffuser: Spanwise and Loading Variations

Beni Cukurel
Patrick B. Lawless
Sanford Fleeter

Purdue University,
West Lafayette, IN 47907-2040

An efficient diffuser is essential to a modern compressor stage due to its significance in stage performance, durability, and operability. To address the need for data that describe the complex, unsteady flow field in a vaned diffuser, particle image velocity is utilized to characterize the spanwise and circumferential variations in the flow features in the vaned diffuser passage of a transonic centrifugal compressor. The spanwise variation in the diffuser flow field is further investigated by the comparison of three different operating conditions representative of low, nominal, and high loading. These data demonstrate that not only the diffuser flow field is highly dependent on the operation conditions, e.g., hub-to-shroud variation increases with loading, but also the circumferential periodicity, created by the highly three dimensional impeller discharge flow, generates a larger unsteadiness toward the hub region of the vaned diffuser. [DOI: 10.1115/1.3104616]

1 Introduction

Future small gas turbines rely on higher efficiency and pressure ratio centrifugal compressors to achieve lower specific fuel consumption, higher specific power, and higher power to weight ratio. An efficient diffuser is essential to a modern compressor stage due to its significance in stage performance, durability, and operability.

Even though investigations of low speed compressor flow fields have been used to develop a knowledge base for design and generating flow models, they are not true representations of transonic centrifugal compressors. Hathaway et al. [1] conducted an investigation for identifying the feasibility of using a low speed compressor to capture the flow physics and as a starting point for experimentally validating codes that would later be used for designing high speed machines. It was concluded that the secondary flows, which are significant in centrifugal compressors, are strongly affected by the impeller speed, and for high speed applications, empirical data from nonscaled models are crucial.

Also, often data on the exit flows of impellers with vaneless diffusers have been used for design models that included vaned diffusers, i.e., making use of an isolated impeller approximation. Though this approach might be a starting point for advanced designs, it is very limited in its accuracy [2]. For example, Inoue and Cumpsty [3] reported that the presence of diffuser vanes considerably increases the pressure at the exit of the impeller, thus coupling the vane inlet and impeller exit flow fields [4,5]. Consequently, matching a vaned diffuser to an impeller is a nontrivial task due to the complicated flow mechanics involved [6].

Another approximation in the design process is that most compressors are designed for steady relative flows, but the actual flow is unsteady with a high degree of interaction between the impeller and diffuser. The effects of the diffuser geometry on the compressor stage are difficult to predict due to the existence of this coupling between the impeller and diffuser. The potential field generated by the diffuser and imposed on the impeller exit is not only driven by its geometry but also dependent on the unsteady diffuser loading. This loading is in turn a function of the rotating impeller potential field and the highly three dimensional velocity field produced by the impeller.

Unfortunately, adequate steady and unsteady data, representative of today's advanced high speed compressors, are limited in the open literature. From a high cycle fatigue (HCF) perspective, El-Aini et al. [7], in a review of the limitations in predicting and designing for HCF, outlined that the current prediction tools fall short for forced response analysis of today's machines. The necessary development areas were indicated as high Mach number unsteady flows, strong fluctuations in incidence angle, unsteady separated flows, and cases of high incidence. Specific needs were identified to be not only prediction techniques but also experimental data for validation.

HCF is a key issue especially in the impeller trailing edge region due to the unsteady pressure fluctuations caused by the diffuser potential field, which is also a function of the flow structures present at the vane throat. In radial flow turbo pumps, it has been shown that these cyclic pressure variations imposed on the impeller trailing edge can be larger than the steady pressure rise across the machine [8,9]. Less information is available on the interaction in high speed air compressors. Characterization of this type of impeller-diffuser interaction is not only important from a HCF perspective but increased coupling could lead to larger tip leakage losses characterized by considerably larger entropy production at the impeller [6], and thus affecting the stage efficiency. One of the most important parameters in unsteady impeller-diffuser interaction is the ratio of the diffuser inlet radius to impeller exit radius, i.e., the radial gap. Ziegler et al. [4,5] acquired steady and unsteady (laser-to-focus) measurements at the impeller exit and diffuser throat regions while changing this parameter. These experiments thus worked to characterize the effect of impeller-diffuser coupling on efficiency, impeller flow structures, and unsteady diffuser loading.

In an impeller passage there are high and low momentum regions that are often referred to as the jet and wake, respectively. The intensity of these zones not only varies in the circumferential direction but also along the span [10]. As the flow emerges from the impeller, the blade forces are lost and the jet and wake undergo a rapid mixing process in the vaneless space. Even though some early models have assumed uniform flow due to this mixing in the circumferential directions downstream of the vaneless

Contributed by the International Gas Turbine Institute of ASME for publication in the JOURNAL OF TURBOMACHINERY. Manuscript received October 1, 2008; final manuscript received November 25, 2008; published online January 12, 2010. Review conducted by David Wisler. Paper presented at the ASME Turbo Expo 2008: Land, Sea and Air (GT2008), Berlin, Germany, June 9–13, 2008.

space, it has been shown by Gallier et al. [11] and Gallier [12] that the mixing process is not sufficient to produce a homogeneous flow region. On the contrary, the flow imposed on the vaned diffuser inlet is highly irregular and three dimensional. There are other results supporting this observed flow complexity in the vaneless space. Krain [13,14] used laser-to-focus measurements to show large unsteady vane inlet flow angle variations in both the spanwise and circumferential directions.

This diffuser inlet flow unsteadiness was shown to propagate far into the diffuser passage. The delayed mixing in the spanwise direction and the circumferential propagation of low momentum fluid from the impeller resulted in a highly three dimensional flow field throughout the diffuser [15]. The vaned diffusers are highly sensitive to the mean and unsteady incidence. The single most important parameter governing the channel diffuser recovery is the boundary layer blockage at the throat [16], and this is known to be a nearly linear function of the vane leading edge incidence [17].

From an operability aspect, often the flow range of a centrifugal compressor is limited by stall or choke of the vaned diffuser, and the most important portion of the diffuser is the semivaneless space between the leading edge and the throat of the diffuser vanes [18]. The blockage factor at the throat, which is based on the diffusion from the leading edge of the blade to the throat and the inlet condition of the diffuser channel, is determined by this part of the diffuser. The complexity of the inlet flow, specifically the periodic variations in the flow angle, has adverse affects on the performance and operability, if not managed well. It is also known that the mean and unsteady incidence relative to the vane suction surface is the significant parameter for diffuser performance and stall [18]. If the flow field in the diffuser is well understood, this creates potential for radial machines to have higher efficiencies and wider operation ranges.

Overall, the flow field through the impeller exit and vaned diffuser is three dimensional, coupled, and characterized by high levels of deterministic unsteadiness. The vane flow features include shocks [19], boundary layer/shock interactions [18], partial separation zones (concentrated in the hub leading edge) [15], varying inlet flow momentum, and incidence regions imposed on the diffuser vanes [13–15]. In addition, there is a high degree of interaction between the impeller and diffuser that prevents accurate analysis as isolated components [3,5]. To address the need for experimental characterization of this complex flow field, presented herein are the results from the particle image velocimetry (PIV) measurements in the diffuser passage of the Purdue high speed centrifugal compressor. This high-efficiency compressor features an impeller that produces a diffuser entry flow field typical of modern transonic compressors. The flow characteristics are analyzed from hub-to-shroud at several relative impeller-diffuser positions for operating conditions at low (on the choke line), nominal, and prestall loading.

2 Technical Approach

2.1 Experimental Facility. The Purdue high speed centrifugal compressor facility consists of an Allison 250-C30G turboshaft engine that drives the research compressor through a slave gearbox. The centrifugal test compressor includes an advanced design 50 deg back-sweep impeller that consists of 15 full and splitter blade pairs upstream of 22 wedge-type diffuser vanes. The ratio of the diffuser inlet radius to the impeller exit radius is 1.094. The nominal operating speed of the compressor is 48,450 rpm. The design and nominal performance parameters of the research compressor are noted in Table 1.

The facility is instrumented with various steady temperature, pressure, and optical probes to measure rotational speed, mass flow rate, pressure ratio, and efficiencies. To change the speed of the test compressor, the C-30 engine output shaft speed is changed. The compressor is throttled with a butterfly valve at the exit of the outflow duct. The mass flow rate is calculated from the total and static pressures and the inlet total temperature measured with two rakes upstream of the test section. The pressure ratio (PR) is determined by the ratio of the mass averaged inlet total pressure and the mass averaged exit total pressure calculated from the measurements of four three-headed total pressure rakes distributed in four separate diffuser passages. Also, the exit gas temperature is measured at the exit plenum. From these measurements, the compressor's flow-pressure characteristic can be defined by the corrected speed and corrected mass flow rate.

Table 1 Research compressor parameters

Impeller	
Tip diameter	21.65 cm
Inlet diameter	14.2 cm
No. of blades	15 full and splitter pairs
Backsweep angle	50 deg
Design speed	48,450 rpm (CW seen from inlet)
Diffuser	
Inlet diameter	23.67 cm
Exit diameter	34.50 cm
Axial passage width	1.384 cm
No. of vanes	22
Radial gap	1.094
Diffuser inlet vane angle	79.4 deg
Wedge diffuser opening angle	7.85 deg

2.2 PIV Velocity Measurements. PIV is an optical imaging technique that allows velocities in a flow field to be measured. The flow is seeded with particles that track the fluid, and a planar laser light sheet is pulsed to illuminate these particles. An image of the particles is captured by a charge-coupled device (CCD) camera perpendicular to the plane of the light sheet. A second laser pulse and exposure is made after a short time delay to extract a second image of the flow field. During analysis, both of these images are then divided into smaller sectors, called interrogation regions, and an average velocity within each interrogation region is determined by advanced cross correlation methods.

The PIV configuration for these experiments consists of a Solo PIV Nd:YAG laser of 532 nm wavelength, a Hi-sense MKII CCD camera, and Nikon Nikkor 35 mm focal length camera lens. To synchronize the laser and the camera, Dantec DYNAMICS FLOW MANAGER, Version 4.71, software was used. This software also provided the necessary routines to process the PIV images. A BNC Model 555 pulse delay generator is used to generate a phase lag to a once-per-revolution trigger signal digitally generated by TTI LT-850 laser tachometer. This allows data acquisition of different relative impeller-diffuser positions.

The seeding was introduced by a Topas Model ATM 210/H aerosol generator using diethyl hexyl sebacate (DEHS) seeding fluid. The DEHS seeding fluid particles have a mean diameter of 0.25 μm. A detailed analysis by Gallier [12] showed that they are small enough to track flow features as small as 0.5 mm with error limited to 1.09% of the true velocity in regions bounded by the sonic velocity in the diffuser region. Clearly, for shock structures where the length scale is small (a few mean free paths), the error is considerably larger. Based on the above analysis, the "smearing" of the shock interface to a more finite length scale in the range of 10^{-4} m is thus expected.

An iterative multigrid cross correlation routine with window offsetting was used to extract the velocity information. In the current analysis, raw images are subjected to an adaptive correlation routine with initial and final interrogation areas of 128 $\times$ 128 pixels and 16 $\times$ 16 pixels, respectively, with a 50% overlap applied among different regions at each four refinement steps.

Assuming an adiabatic process from the diffuser to the plenum, the total temperature throughout the diffuser is taken as that measured in the discharge plenum, and this with the measured velocity determines the local static temperature, local acoustic speed, and

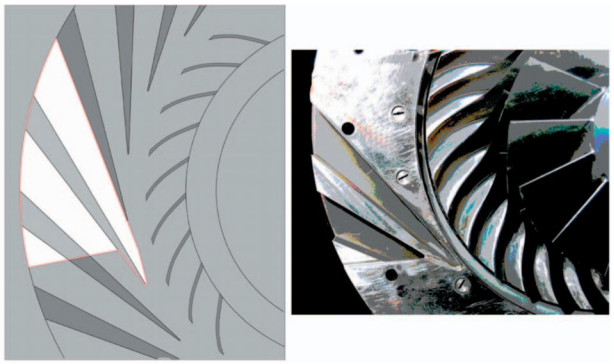

Fig. 1 Diffuser access window

thus the Mach number, M. The flow angles presented are measured from the centerline of the diffuser passage and taken positive in the clockwise direction.

2.3 Error Analysis. The PIV measured velocity $V=S\Delta p/\Delta t$, where Δp, S, and Δt are particle pixel displacement, optical magnification, and the time delay between the two consecutive images, respectively. Westerweel et al. [20] reported that the average measurement error for an interrogation analysis through cross correlation with window offset was approximately 0.04 pixels. Assuming the maximum particle displacement of 4 pixels (one-fourth of the diameter of a 16×16 pixel interrogation window), this would imply a relative measurement error of $\delta(\Delta p)/\Delta p=1\%$. In this setup, the scale factor, S, is 12.108 pixels/mm. It is established by comparing the images of a high precision Max Levy DA039 line grid ruler with the distances indicated by the grid. Considering the magnification factor, the grid lines appear 0.92 pixels wide through the CCD camera; thus the scale is known to be within a pixel. Using this information, the uncertainty due to optical magnification is $\delta(S)/S=0.41\%$. In this experiment, the time delay between the two consecutive images of the CCD camera is the minimum allowed by the hardware limitations, $\Delta t=10^{-6}$ s. The architecture of integrated circuits, such as those found on a computer board, may introduce fluctuations in the time delay, on the order of 1 ns. Thus the uncertainty associated with the time delay can be calculated as $\delta(\Delta t)/\Delta t=0.1\%$. For the above considerations, the uncertainty in the velocity measurements based on the experimental setup is given by

$$\delta(V)/V = \pm[(\delta(S)/S)^2+(\delta(\Delta p)/\Delta p)^2+(\delta(\Delta t)/\Delta t))^2]^{1/2} \quad (1)$$

using the formula outlined by Kline and McClintock [21] for a three-parameter model, which in this case is equal to 1.08%.

2.4 Experiment Conditions. In these experiments, the diffuser flow field in the Purdue centrifugal compressor is investigated utilizing PIV. Experiments are conducted in the vaned diffuser at three spanwise locations: 25%, 50%, and 75% spans, referred to as the hub, mid, and shroud planes. At all spanwise locations, five relative diffuser-impeller locations are considered, with the impeller full-splitter blade passage pair divided into five equally spaced phase delays, referred to as Delay 0, Delay 1, Delay 2, Delay 3, and Delay 4. The data presented are ensemble averaged with 200 images with a local minimum of 25 valid time instances for each vector flow field map. The window over the diffuser section where data are acquired is shown in Fig. 1.

Experiments are conducted at three operating conditions representative of low, nominal, and prestall loading conditions [22]. The corresponding corrected speeds (N_{cor}), corrected mass flow rates (m_{cor}), and total-to-total stage PRs are given in Table 2.

Table 2 Testing conditions

Loading	N_{cor}	m_{cor} (kg/s)	PR
Low	$101.87\%\pm0.06\%$	2.326 ± 0.009	4.0452 ± 0.004
Nominal	$101.23\%\pm0.06\%$	2.296 ± 0.009	4.2414 ± 0.004
Prestall	$101.08\%\pm0.06\%$	2.023 ± 0.008	4.5556 ± 0.004

3 Results

3.1 Vaneless Space: Diffuser Inlet Flow. Prior to analyzing the diffuser results from this study, it is useful to characterize the relationship between structures in the impeller exit flow and those in the diffuser flow field. The impeller discharge flow, as described by Dean [16], consists of two main regions characterized by high and low relative momentum fluids referred to as the jet and wake. Although later authors have refined the details of this model, this basic description of the exit flow of the impeller is both accurate and useful. The wake region, accumulating at the corner formed by the suction surface and the shroud, is a low velocity region in the impeller frame of reference. Due to the high tangential component created by the wheel speed in the fixed frame of reference, the wake is identified as a high velocity region with a flow angle mainly in the tangential direction. The jet region is a high velocity region in the relative frame but similarly is observed as a low momentum region in the fixed reference frame.

PIV experiments conducted by Gallier [12] for the 90% speed line describe the flow in the vaneless space of the Purdue Centrifugal Research Facility. Gallier's results show a jet and wake structure persisting from the hub to the shroud at the impeller exit, with the extent of the wake fluid increasing toward the shroud, with the mean incidence on the vanes varied by 11.1 deg from hub to shroud. There were also significant circumferential variations in velocity and flow angle due to the jet/wake passing.

To visualize the relationship between the flow in the vaneless space and that measured in the diffuser, Mach contours reported by Gallier are matched with exemplary diffuser data gathered in this investigation at 100% speed for a single relative impeller-diffuser position (Fig. 2). Even though Gallier's investigation was conducted at lower speed, this illustration provides a qualitative interpretation of the flow features imposed on the diffuser. For illustrative purposes, local flow vectors, shown as black arrows superimposed on the contour plot, are drawn to be representative of the flow direction and are scaled to the local Mach numbers. The suction and pressure surfaces of the vanes and blades are indicated with an s or p, respectively.

With all data in the fixed frame, Vector A indicates the impeller jet flow imposed on the diffuser suction side wall, with less swirl and lower momentum than the wake fluid. Vector B shows the approach of the impeller wake toward the diffuser suction side wall. For the given impeller-diffuser geometry, with 30 full and splitter blades and 22 vanes, there are 1.35 blade passages imposed on the diffuser inlet at any given time. For the delay shown, there is impingement of yet another impeller jet on the semivaneless space region just before the diffuser throat, Vector D. In the prethroat region E, the flow coming from the upstream portion of the vane with higher momentum, Vectors B and C, interacts with the low momentum region of the impeller jet (Region D). As the fluid enters the throat, it accelerates due to area reduction. Downstream of the throat, Vector F, the flow transitions supersonic to subsonic. Further downstream, there is a more uniform diffusion region, represented by Vector G.

3.2 Diffuser Flow Field-Nominal Loading. Figures 3 and 4 present the diffuser flow field at the hub measurement plane for five time delays at nominal loading. Figure 3 is the phase locked ensemble averaged Mach number, and Fig. 4 is the corresponding flow angle; the flow angles presented are measured from the cen-

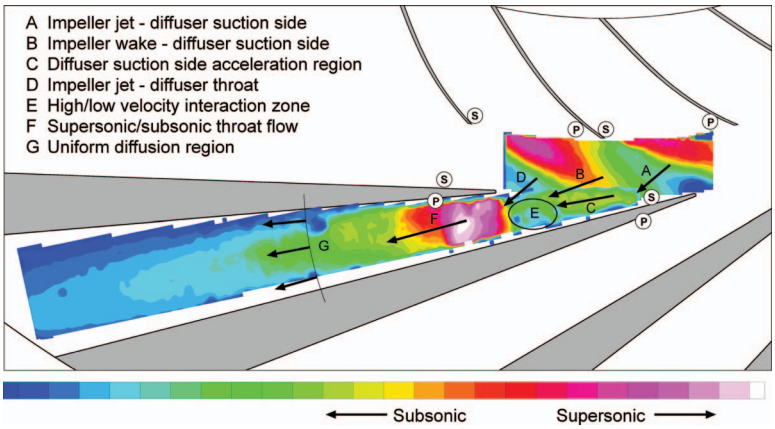

Fig. 2 Impeller flow interaction with the diffuser, Mach number distribution, and typical delay

terline of the diffuser passage and taken positive in the clockwise direction (i.e., with impeller rotation). In this coordinate system, increasing flow angles (more positive) indicate flow in a more tangential direction.

There is a Mach number increase just downstream of the leading edge of the vane suction surface, in what is termed the semivaneless space. The semivaneless space consists of the triangular region restricted by the suction side leading edge, pressure side leading edge, and the diffuser throat. The Mach number is approximately 0.9 in this region, consistent from the design criteria outlined by Pampreen [23] that suggest that designers avoid supersonic flows in this region, thereby avoiding prethroat shock structures and their adverse effects on boundary layer growth. This region is consistent with a blockage-driven acceleration of the flow about the suction side of the diffuser and is seen in all time instances. As shown in Fig. 4, circumferential flow angle variation across the entry to the semivaneless space is on the order of 12 deg.

In Fig. 4, the more negative (i.e., more radial) flow angle data reflect the passage of the jet flow structure into the diffuser. As explained in Fig. 2, due to the blade-to-vane ratio of 1.35, two impeller jet regions are seen to be imposed on the semivaneless space, most visible in Delay 3. Immediately after the acceleration at the start of the semivaneless space, the flow decelerates again, most clearly seen at Delays 0 and 3 in Fig. 3 where the Mach number changes from 0.8 to 0.7 before the throat is reached. The

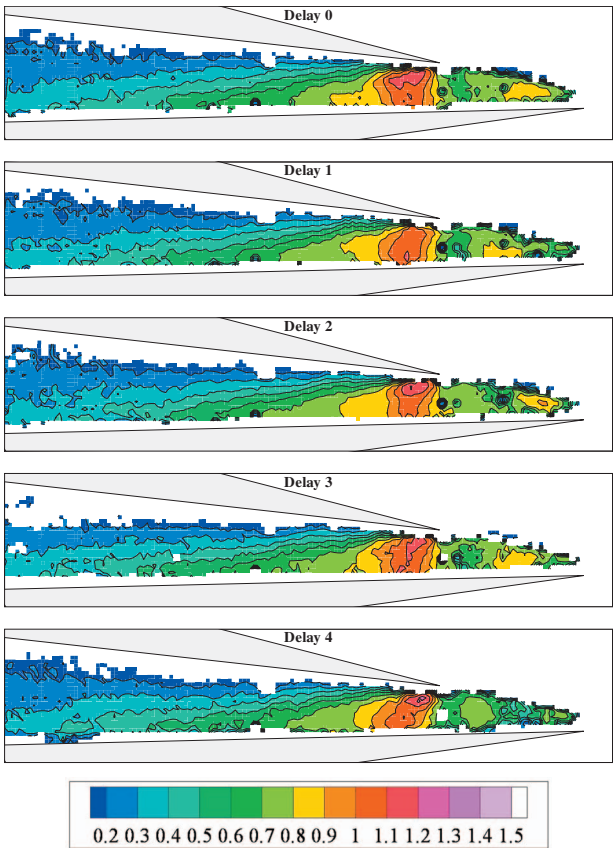

Fig. 3 Nominal loading, hub plane, Mach number

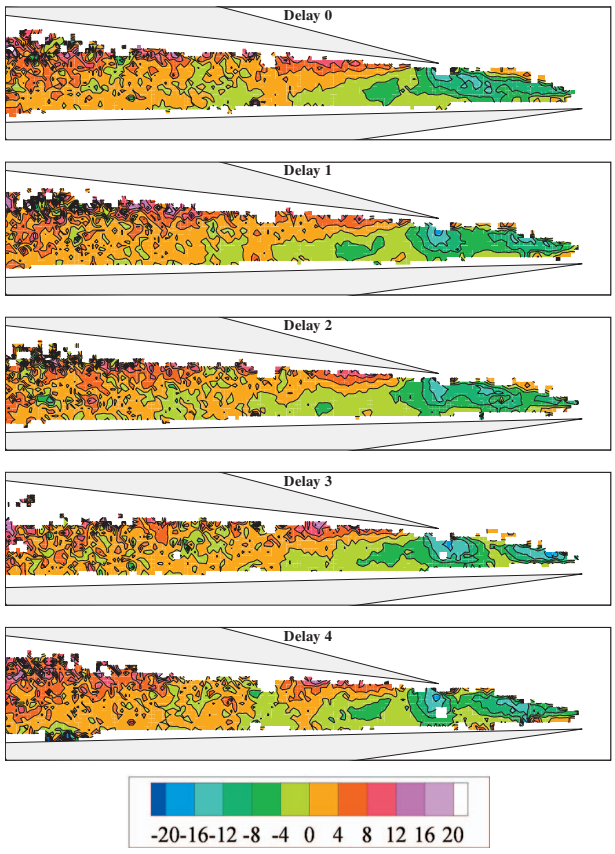

Fig. 4 Nominal loading, hub plane, flow angle α°

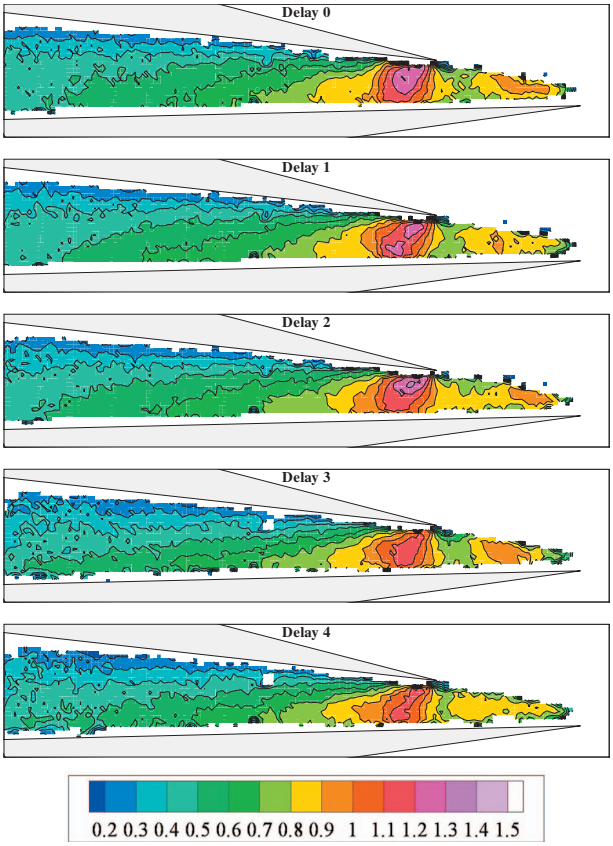

Fig. 5 Nominal loading, midplane, Mach number

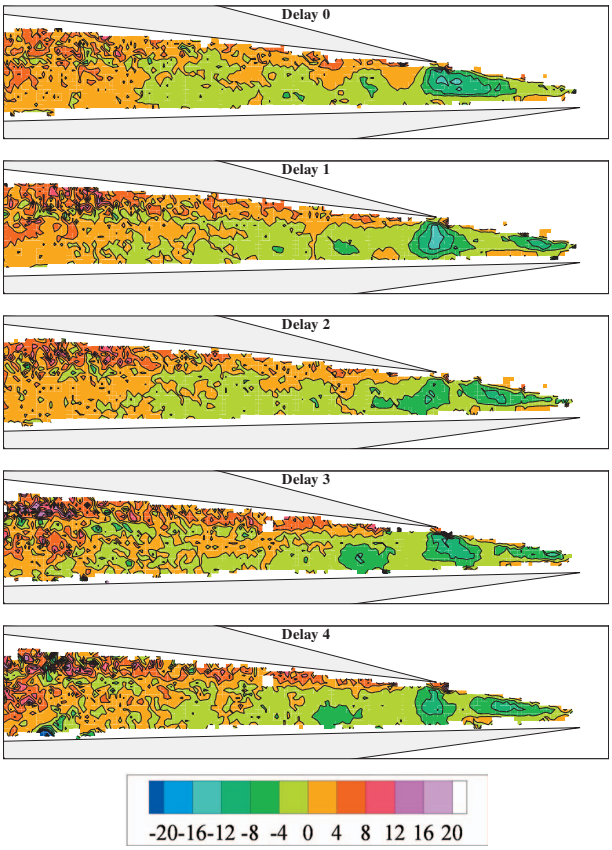

Fig. 6 Nominal loading, midplane, flow angle α°

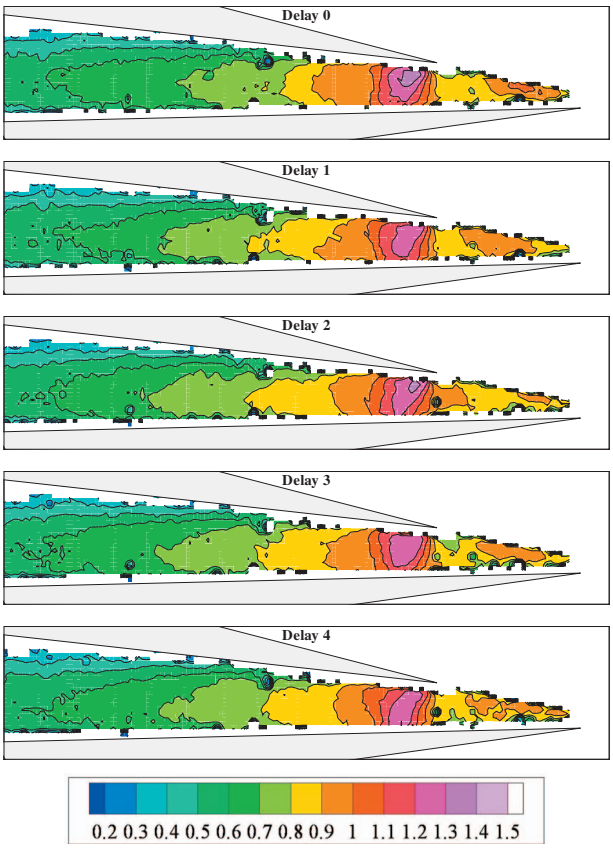

Fig. 7 Nominal loading, shroud plane, Mach number

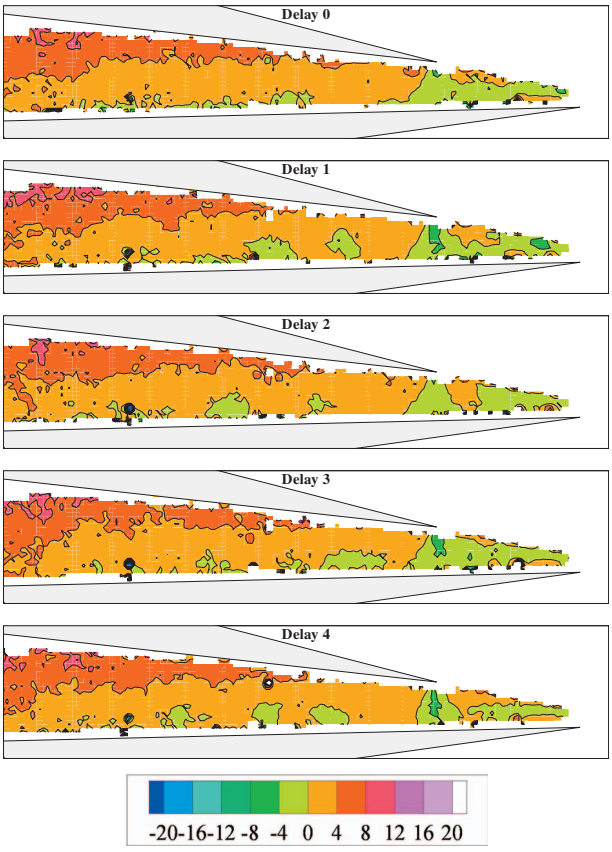

Fig. 8 Nominal loading, shroud plane, flow angle α°

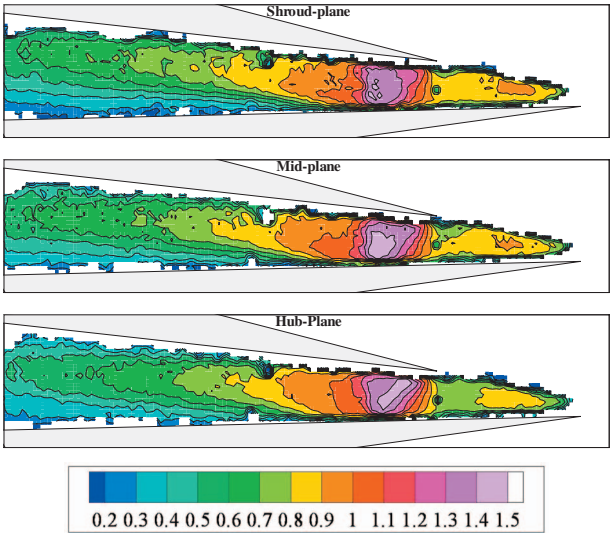

Fig. 9 Choke loading, mean Mach number

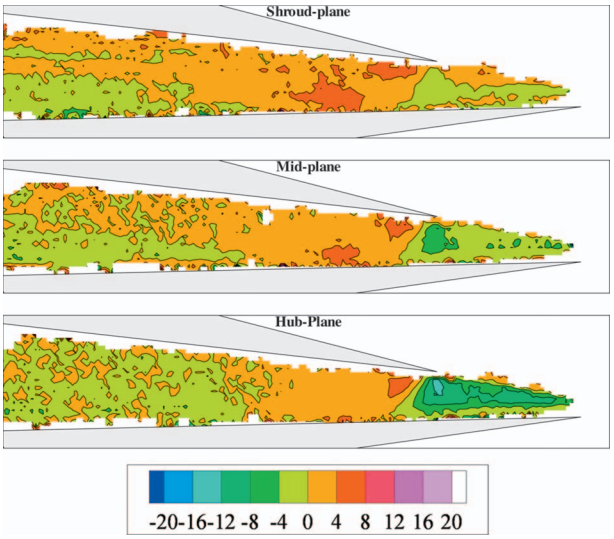

Fig. 10 Choke loading, mean flow angle $\alpha°$

behavior of the flow in this region is partly a function of the area increase with increased radius, as it is seen at all time instances to some extent. But the main cause is believed to be due to the jet flow, characterized by a large negative flow angle region by the diffuser throat (Fig. 4) interacting with the suction side acceleration region, identified by a locally higher Mach number in the semivaneless space (Fig. 3). This interaction creates a zone of rapid adjustment, where these two flow fields interact, identified by the locally lower Mach number region upstream of the throat.

The flow downstream of the throat seems to be fairly unaffected by the circumferential variations after M=0.8 is reached (Fig. 3). In contrast, near the throat, the flow is significantly affected by the impeller position. The flow reaches a supersonic Mach number, then shocks down to a subsonic flow, with the location of this shock transition and the maximum Mach number a function of the vane-impeller relative position.

Figures 5 and 6 present the flow Mach number and angles for the midplane region at nominal loading. Similar features to that of the hub plane are observed in the flow field. In Fig. 6, at the start of the semivaneless space the minimum flow angle has become more tangential, resulting in a maximum circumferential flow angle variation of approximately 8 deg. Also, comparing Figs. 3 and 5, the Mach numbers in the semivaneless space and the throat are elevated, consistent with the higher momentum levels expected at midspan. These results are consistent with an increasing fraction of the flow being wake fluid compared with the hub plane. The Mach numbers for the region downstream of the throat at the midspan are also elevated, approximately by 0.25 compared with the near hub measurement plane, expected by the higher inlet momentum flow. In the throat region, the Mach number variations with delay time are also larger when compared with the hub measurement location. At the hub plane, the flow downstream of the throat seems to be fairly unaffected by the circumferential variations after M=0.8 is reached.

Focusing on the near-shroud plane at nominal loading (Fig. 7), the trend of an increase in the overall Mach numbers as the shroud is approached continues. This is especially noticeable in the extension of the semivaneless space acceleration region as well as downstream of the throat. This feature is consistent with an increasing fraction of wake fluid. Comparing the flow angle data (Fig. 8) with other spanwise locations (Figs. 4 and 6), the flow is more in the tangential direction, and the circumferential variation across the entry to the semivaneless space has been further reduced to 4 deg. Also, the flow downstream of the throat appears to be much more uniform when compared with other spanwise locations (Figs. 4 and 6). This is mainly due to the fact that at this spanwise plane the effects of the jet flow are minimized.

3.3 Diffuser Flow Field-Loading Effects. Overall at nominal loading, there is a large inhomogeneity in the diffuser flow field dependent on not only spanwise measurement location but also on the impeller-vane relative position. To compare the effects of loading change on the spanwise variation in the diffuser flow, mean flow Mach number and mean flow angles are reported for loading conditions representing low loading on the choke line and the flow characteristics of near stall loading conditions. The mean reported data are acquired by the averaging of phase-resolved PIV data, and thus contain only the delay-independent information.

When the lower loading condition along the 100% speed line is considered (Figs. 9 and 10), higher velocities are observed when compared with the nominal loading case as expected with the increased mass flow rate. The velocity increase seems mainly in the hub and midplane, reducing the overall variation that is seen from the hub to the tip in the nominal loading case. Downstream, it can be seen that the role of the upper and lower surfaces of the vanes as suction and pressure side has reversed with the changing incidence on the vane (Fig. 10). Figure 10 also shows that the flow angles entering the semivaneless space are similar to those seen at nominal loading expected from the relatively small excursion in mean impeller exit flow angle ($\sim$1 deg) expected in this case.

At nominal loading, maximum average Mach numbers in the throat region were M=1.2 at the shroud plane, with M=1.1 typical of the mid and hub measurement planes. This region is followed by a mild supersonic deceleration and finally by a normal shock that brings the flow down to subsonic velocities (Fig. 11). At choke loading, Mach numbers greater than 1.2 are now observed at all spanwise planes, with the highest throat Mach numbers now found in the hub plane. There is a clear supersonic acceleration region associated with the expansion fan that originates from the upper vane leading edge. The turning in this region is also indicative of these principle flow features (Fig. 12). Downstream of the expansion fan, the flow is decelerated down to a lower Mach number by an oblique shock and through a normal shock terminates to subsonic flow.

Figures 13 and 14 present the mean Mach number and flow angle data for the case where the compressor is throttled to a point just prior to stall/surge. At this condition, the flow in the throat is now subsonic at all spanwise planes. Starting with the hub flow, the maximum Mach number observed at the hub is only approximately 0.7 and that is located in the semivaneless space acceleration region (Fig. 13). Focusing on the hub plane in Fig. 14, when

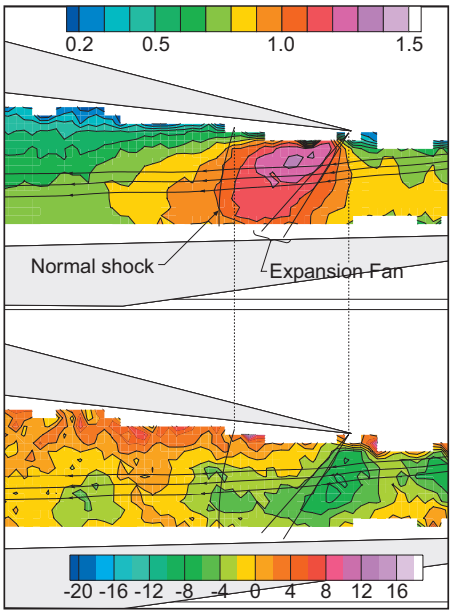

Fig. 11 Nominal loading, midplane, typical delay, throat shock structures, Mach number (top), and flow angle α° (bottom)

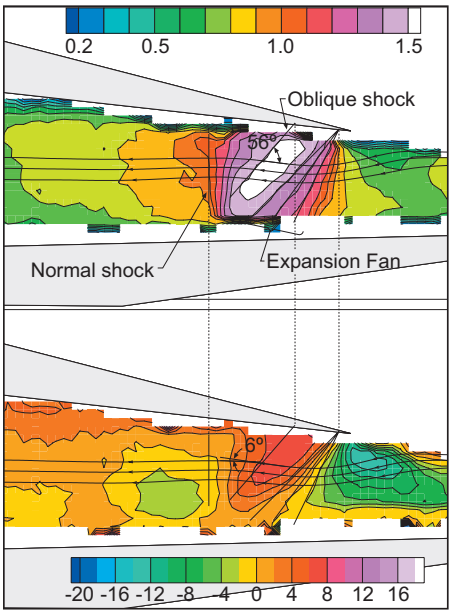

Fig. 12 Choke loading, midplane, typical delay, throat shock structures, Mach number (top), and flow angle α° (bottom)

compared with the previous loading conditions studied, in the aft sections of the diffuser passage more spatial flow angle variations are observed. At midplane, the trend of higher velocities toward the shroud seen at nominal loading is again observed. Also, for the midplane and shroud plane spanwise locations, the variation in flow angle downstream of the throat observed for the hub plane is significantly reduced, indicating less random unsteadiness. Comparing the choke, nominal, and prestall loading cases at the hub, the increasing nondeterministic unsteadiness is likely indicative of a hub flow breakdown as the stall is approached. From the velocity data at nominal and prestall loading, there is also evidence for a hub-pressure side unsteady separation, taking the form of a separation bubble at the leading edge similar to that described by Justen et al. [19] and Dawes [2]. Although the separation zone was not resolved sufficiently to directly characterize it from velocity measurements in the core, the flow in the leading edge region still provides evidence of its existence. It was shown by Dawes that an unsteady separation bubble at the pressure-side hub region is not necessarily phase locked to the impeller. Thus, a separation of this type would result in a higher variance calculated from the ensemble averaged vector maps.

For the nominal loading case, the variance in the ensemble about the throat region for all three spanwise locations can be seen in Fig. 15. The variance is calculated separately for the radial component, U, and transverse component, V, of the velocities and summed linearly. Notice the high variance zone at the hub leading edge around the pressure side. This occurs in a region of the flow field otherwise characterized by a low value of variance, and likely is a result of the mean flow deflecting due to a transient leading edge bubble. A similar region can also be seen for the midplane with reduced magnitude, which supports the idea that the separation region at the vane leading edge is more concentrated at the hub. Focusing on the shroud plane, the high variance region as seen in the other spanwise locations does not exist, indicating that the unsteadiness in this plane is mostly impeller

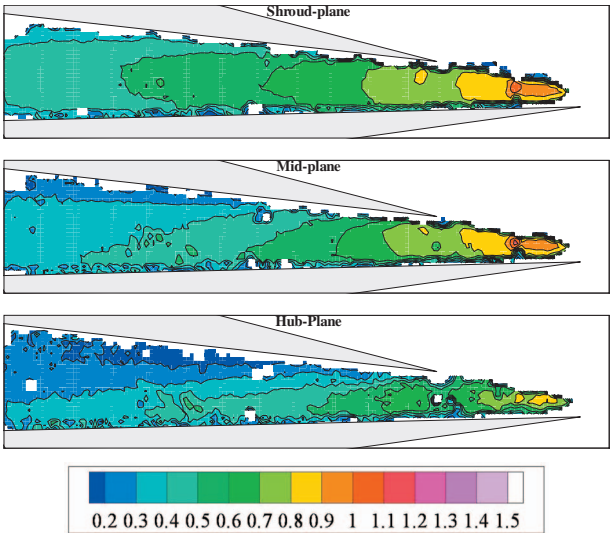

Fig. 13 Prestall loading, mean Mach number

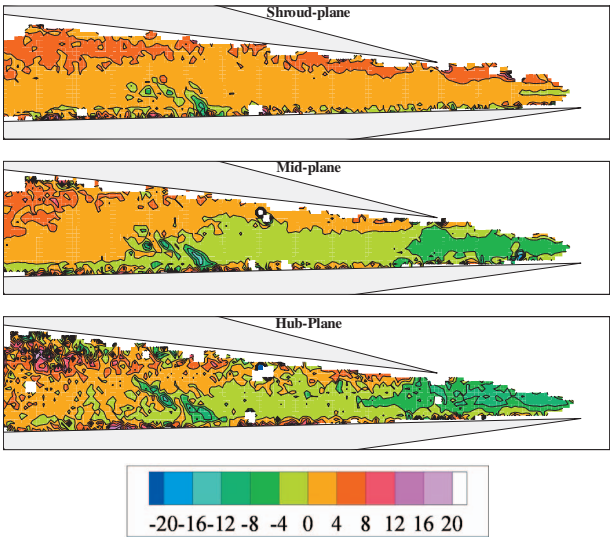

Fig. 14 Prestall loading, mean flow angle α°

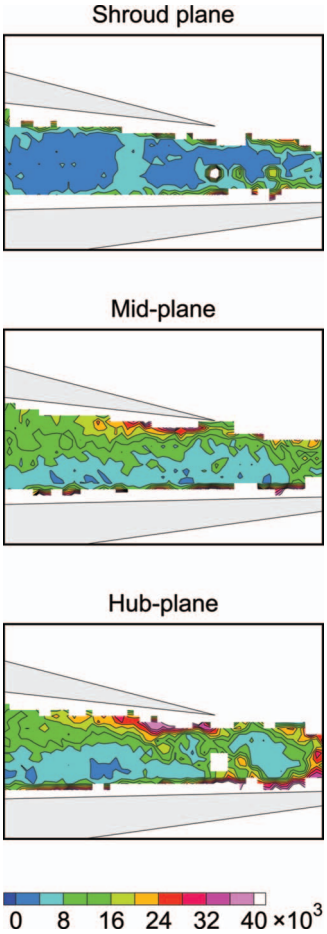

Fig. 15 Nominal loading, sum of variances (m^2/s^2)

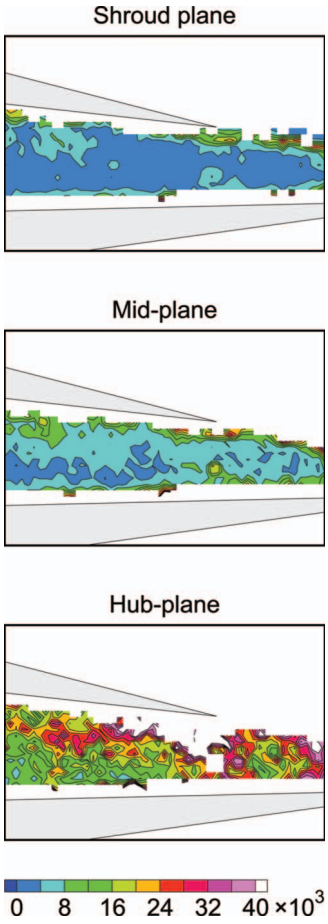

Fig. 16 Prestall loading, sum of variances (m^2/s^2)

phase locked.

When a similar variance analysis is conducted for the prestall operating point, the shroud plane variance is similar to the prior lower loading condition (Fig. 16). In the hub region, there is a large high variance zone supportive of the hub flow breakdown previously suggested in Figs. 13 and 14. Interestingly, in the midplane the variance near the leading edge is reduced, possibly due to some incidence alleviation from the hub flow blockage. However, the ensemble average velocity data in this region do not provide sufficient resolution to confirm this.

4 Summary and Conclusions

This study has provided detailed phase-resolved velocity information in the vaned diffuser of the Purdue centrifugal compressor through a PIV technique. The data at all loading conditions demonstrated that the flow field in the diffuser is, as expected, characterized by a much more complicated structure than that which would be associated with steady, uniform diffusion. Although mixing clearly occurs in the vaneless space, these data demonstrate that strong momentum variations still exist in both the spanwise and the circumferential directions in the diffuser.

The nominal loading case indicated that the circumferential variations, driven by the jet/wake flow structure exiting the impeller, are highest for the hub plane. At the midspan, the flow features are similar to the hub plane, but the variation is reduced. In the shroud region, the circumferential variations are of lesser magnitude, dominated by the large extent of the impeller wake in that region. In all cases, circumferential variations are dominant in the prethroat region, and much reduced after the throat. Hub to shroud variations in the diffuser passage velocities are increased as the compressor is throttled back from the choke line, with the hub flow gradually being starved for flow until, just prior to compressor stall, the hub flow begins to break down.

Diffuser throat structures were shown to vary significantly with loading at all spanwise locations. Near the choke line, the throat Mach numbers are supersonic at all planes. The flow then adjusts to the downstream subsonic flow through an oblique and then a normal shock. Further increase in loading results in a more mildly supersonic condition and an adjustment to subsonic flow through a normal shock. As the mass flow is further decreased, the entire diffuser flow field becomes subsonic.

Acknowledgment

This research was funded in part by the Rolls-Royce Corporation. This support is most gratefully acknowledged.

Nomenclature

α = flow angle measured from diffuser passage centerline (+CW)
$\delta(\ )$ = absolute uncertainty
Δp = particle pixel displacement
Δt = time lag between consecutive images
M = Mach number
m_{cor} = corrected flow rate
N_{cor} = corrected speed
S = optical magnification factor
V = local velocity

References

[1] Hathaway, M. D., Chriss, R. M., Wood, J. R., and Stazisar, A. J., 1993, "Ex-

perimental and Computational Investigation of the NASA Low-Speed Centrifugal Compressor Flow Field," ASME J. Turbomach., **115**, pp. 527–542.
[2] Dawes, W. N., 1994, "A Simulation of the Unsteady Interaction of a Centrifugal Impeller With Its Vaned Diffuser," ASME Paper No. 94-GT-105.
[3] Inoue, M., and Cumpsty, N. A., 1984, "Experimental Study of Centrifugal Impeller Discharge Flow in Vaneless and Vaned Diffusers," ASME J. Eng. Gas Turbines Power, **106**, pp. 455–467.
[4] Ziegler, K. U., Gallus, H. E., and Niehuis, R., 2003, "A Study on Impeller-Diffuser Interaction—Part I: Influence on the Performance," ASME J. Turbomach., **125**(1), pp. 173–182.
[5] Ziegler, K. U., Gallus, H. E., and Niehuis, R., 2003, "A Study on Impeller-Diffuser Interaction—Part II: Detailed Flow Analysis," ASME J. Turbomach., **125**(1), pp. 183–192.
[6] Shum, Y. K. P., Tan, C. S., and Cumpsty, N. A., 2000, "Impeller Diffuser Interaction in a Centrifugal Compressor," ASME J. Turbomach., **122**, pp. 777–786.
[7] El-Aini, Y., deLaneuville, R., Stoner, A., and Capece, V., 1997, "High Cycle Fatigue of Turbomachinery Components—Industry Perspective," AIAA Paper No. 97-3365.
[8] Arndt, N., Acosta, A. J., Brennen, C. E., and Caughey, T. K., 1990, "Experimental Investigation of Rotor-Stator Interaction in a Centrifugal Pump With Several Vaned Diffusers," ASME J. Turbomach., **112**(1), pp. 98–108.
[9] Arndt, N., Acosta, A. J., Brennen, C. E., and Caughey, T. K., 1989, "Rotor-Stator Interaction in a Diffuser Pump," ASME J. Turbomach., **111**(3), pp. 213–221.
[10] Chen, Y. N., Seidel, U., Haupt, U., and Rautenberg, M., 1996, "Jet, Wake and Intrinsic Motion in Impellers of Centrifugal Compressors," ASME Paper No. 96-GT-261.
[11] Gallier, K., Lawless, P. B., and Fleeter, S., 2007, "PIV Characterization of High Speed Centrifugal Compressor Impeller-Diffuser Interaction," 43rd AIAA/ASME/SAE/ASEE Joint Propulsion Conference, pp. 153–160.
[12] Gallier, K., 2005, "Experimental Characterization of High Speed Centrifugal Compressor Aerodynamic Forcing Functions," Ph.D. thesis, Purdue University, West Lafayette, IN.
[13] Krain, H., 1999, "High Pressure Ratio Centrifugal Compressor With Transonic Flow," ASME Paper No. FEDSM99-7801.
[14] Krain, H., 2002, "Unsteady Diffuser Flow in a Transonic Centrifugal Compressor," Int. J. Rotating Mach., **8**(3), pp. 223–231.
[15] Ibaraki, S., Matsuo, T., and Yokoyama, T., 2007, "Investigation of Unsteady Flow in a Vaned Diffuser of a Transonic Centrifugal Compressor," ASME J. Turbomach., **129**, pp. 686–693.
[16] Dean, R. C., 1974, "The Fluid Dynamic Design of Advanced Centrifugal Compressors," VKI Lecture Series 66.
[17] Connor, W. A., 1987, "Design and Off-Design Performance Prediction of High Pressure Ratio Centrifugal Compressors," VKI Lecture Series 1987-01.
[18] Senoo, Y., 1984, "Vaned Diffusers," *Flow in Centrifugal Compressors*, Von Karman Institute for Fluid Dynamics.
[19] Justen, F., Ziegler, K. U., and Gallus, H. E., 1999, "Experimental Investigation of Unsteady Flow Phenomena in a Centrifugal Compressor Vaned Diffuser of Variable Geometry," ASME J. Turbomach., **121**, pp. 763–771.
[20] Westerweel, J., Dabiri, D., and Gharib, M., 1997, "The Effect of a Discrete Window Offset on Accuracy of Cross-Correlation Analysis of Digital PIV Recordings," Exp. Fluids, **23**, pp. 20–28.
[21] Kline, S. J., and McClintock, F. A., 1953, "Describing Uncertainties in Single-Sample Experiments," Mech. Eng., **75**(1), pp. 3–8.
[22] Carnell, W. F., 2002, "Aerodynamic Performance and Forcing Function Measurements in a High-Speed Centrifugal Compressor," MSME thesis, Purdue University, West Lafayette, IN.
[23] Pampreen, R. C., 1972, "The Use of Cascade Technology in Centrifugal Compressor Vaned Diffuser Design," ASME Paper No. 72-GT-39.

Adjoint Aerodynamic Design Optimization for Blades in Multistage Turbomachines—Part I: Methodology and Verification

D. X. Wang
School of Engineering,
Durham University,
Durham DH1 3LE, UK

L. He
Department of Engineering Science,
Oxford University,
Parks Road,
Oxford OX1 3PJ, UK

The adjoint method for blade design optimization will be described in this two-part paper. The main objective is to develop the capability of carrying out aerodynamic blading shape design optimization in a multistage turbomachinery environment. To this end, an adjoint mixing-plane treatment has been proposed. In the first part, the numerical elements pertinent to the present approach will be described. Attention is paid to the exactly opposite propagation of the adjoint characteristics against the physical flow characteristics, providing a simple and consistent guidance in the adjoint method development and applications. The adjoint mixing-plane treatment is formulated to have the two fundamental features of its counterpart in the physical flow domain: conservation and nonreflectiveness across the interface. The adjoint solver is verified by comparing gradient results with a direct finite difference method and through a 2D inverse design. The adjoint mixing-plane treatment is verified by comparing gradient results against those by the finite difference method for a 2D compressor stage. The redesign of the 2D compressor stage further demonstrates the validity of the adjoint mixing-plane treatment and the benefit of using it in a multi-bladerow environment. [DOI: 10.1115/1.3072498]

1 Introduction

With the advance in computational fluid dynamics (CFD) and computing power, modern turbomachinery aerodynamic design relies almost completely on CFD to develop three dimensional blade sections [1]. There are many different approaches that are used to explore three dimensional features of turbomachinery blades. All these approaches can be generally classified into two categories: inverse design methods and direct design methods.

The conventional inverse design offers better designs with low and affordable computational time cost [2,3]. The major disadvantage of this method is that it requires the specification of target flow field in terms of pressure or velocity distributions on a blade surface; hence its success depends largely on a designer's experience and insight. Apart from that, it is usually difficult to apply constraints in the inverse design [4].

The direct design methods can be further classified into gradient-based methods and stochastic methods. Stochastic methods, such as the genetic algorithm and the simulated annealing, do not need gradients of an objective function but values of an objective function only. In principle, these methods are able to find the global optimum in a design space and have long been researched in turbomachinery aerodynamic design optimization [4–6]. But their applications in routine designs are normally restricted due to their huge time costs. The response surface method [7] and the evolutionary method with approximate models [8] have been gaining a lot of attention over the past several years mainly due to their easy implementation and affordable time cost with a few design variables.

The gradient-based methods, according to the way in which gradients are calculated, include the finite difference method, the linearized method, and the adjoint method. The finite difference method suffers from step size dependence and is not recommended. The main drawback is that the time cost of evaluating objective function derivatives using both the finite difference method and the linearized method is usually proportional to the number of design variables; hence they are not preferred for situations where there are a large number of design variables. The adjoint method does not have the well-known disadvantage of the finite difference method and offers a means to calculate derivatives of an objective function with respect to design variables with low time cost independent of the number of design variables. However the adjoint method is complex and counterintuitive, which has been curbing its popularity.

The application of the adjoint method in aerodynamic design optimization based on CFD was pioneered by Jameson [9]. Based on the way in which a final discrete adjoint system is formed, there are two variations: the continuous adjoint method and the discrete adjoint method. In the continuous adjoint method, the nonlinear flow equations in a partial differential equation form are linearized first with respect to a design variable. Then an adjoint system will be derived from the linearized flow equations, followed by discretization. In the discrete adjoint method, the flow equations in a partial differential equation form are discretized first, followed by the linearization and adjoint formulation.

The discrete adjoint method can produce the exact gradient of an objective function with respect to the variables in a discretized flow system, which will ensure that a design process converges quickly and fully. However it is very difficult to develop discrete adjoint codes, particularly by hand and with high-order upwind schemes and sophisticated turbulence models implemented in a flow solver. It is worthwhile to note that automatic differentiation (AD) can be exploited to generate discrete adjoint codes, and data structures of a flow solver can be exploited to improve the runtime performance of AD generated adjoint codes. However the discrete adjoint codes usually require more memory and CPU time compared with its continuous counterpart [10]. In particular, the discrete adjoint codes obtained with the state of the art AD technologies would typically consume three times of CPU time compared with that by a flow solver [11,12] (the time cost of a continuous adjoint solver is usually the same as that of its flow solver). In the

Contributed by the International Gas Turbine Institute of ASME for publication in the JOURNAL OF TURBOMACHINERY. Manuscript received August 31, 2008; final manuscript received October 7, 2008; published online January 13, 2010. Review conducted by David Wisler. Paper presented at the ASME Turbo Expo 2008: Land, Sea and Air (GT2008), Berlin, Germany, June 9–13, 2008.

continuous adjoint method, one is free to discretize the adjoint equations in any consistent way, although it is always better to consult the flow solver schemes. The gradients from a continuous adjoint solver are subject to two levels of discretization errors for both the flow equations and the adjoint equations, which vanish with mesh refinement. More details about the advantages and disadvantages of the two approaches can be found in Refs. [10,13].

In the context of a CFD-based design optimization, the adjoint method (both the continuous one and the discrete one) first gained attention in applications to external flows (e.g., for aerofoil designs). This might be due to the fact that the adjoint method was first introduced to the external flow community. Jameson and coworkers [9,10,14,15] investigated both the continuous adjoint method and the discrete one for designs ranging from aerofoils and wings to aircrafts. Kim and Nakahashi [16] and Nielsen and Anderson [17] developed hand-coded discrete adjoint solvers based on flow solvers using unstructured meshes for the ONERA M6 wing design optimization. Recently the adjoint method has been extended to aerofoil designs with an unsteady flow field involved using the unsteady time-domain flow equations [18] and frequency domain flow equations [12,19] to control the time-averaged aerodynamic performance, unsteady aerodynamics, or aeroelasticity.

The applications of the adjoint method in design optimization to internal flows have been lagging far behind. The status might be indicated by the fact that an adjoint solution with the 2D Euler flow equations for turbomachinery blading aerodynamics was still a research topic very recently (see, e.g., Refs. [20,21]). There have been increasing efforts made in the applications of the adjoint method in turbomachinery blading aerodynamics. Yang et al. [22] and Wu et al. [23] applied the continuous adjoint method to 2D turbomachinery blading aerodynamic design optimization. Wu et al. [24] and Papadimitriou and Giannakoglou [25] developed continuous adjoint solvers for 3D turbomachinery blading aerodynamic design optimization. Corral and Gisbert [26] developed a hand-coded discrete adjoint solver for turbine end-wall profiling to reduce the secondary flow losses. The AD tool TAPENADE was exploited by Duta et al. [11] to generate discrete adjoint solvers to save human effort in coding development for turbomachinery aerodynamic design optimization. Florea and Hall [27] developed a discrete adjoint solver based on the time-linearized method for sensitivity analysis of an unsteady inviscid flow through turbomachinery cascades. Thomas et al. [12] used the AD tool TAF to develop adjoint codes to model unsteady aerodynamic design sensitivities. The adjoint method was also used for an efficient blade forced response minimization by Duta et al. [28].

It is noted that all the reported design optimizations of turbomachinery blades by using the adjoint method have been carried out in a single blade row computational domain. For multistage turbomachines, the matching between adjacent blade rows has important effects. There are different levels of computational analysis tools for including these blade row matching/interaction effects ranging from a fully time-domain unsteady Reynolds averaged Navier-Stokes (RANS) to a relatively simple circumferentially mixing-out steady flow treatment (the mixing-plane treatment first proposed by Denton [29]). The mixing-plane multistage steady flow analysis has become a standard industrial tool used in a design environment. Given the importance of the multistage matching, it seems natural to argue that an aerodynamic design optimization should be carried out in a multistage environment in order to make an effective impact on practical design processes. Recognizing this need and the current status of the multistage analysis in practical blading designs, the present work is aimed at developing an adjoint mixing-plane method for aerodynamic design optimization of blades in a multistage environment using the adjoint method.

2 Flow Equations and Boundary Conditions

The flow solver was developed at Durham University [30]. It has been under extensive development for steady and unsteady flow field calculations and has been validated against experimental data, analytic solution or benchmark results for its capability of producing quality steady and unsteady flow field [31–33]. As we all know, turbomachinery involves rotary components, and the time-averaged flow field inside turbomachinery exhibits a periodicity in the circumferential direction. Therefore, it is convenient to adopt a cylindrical coordinate system, which will facilitate an easy implementation of the periodic boundary condition and the use of a single blade passage domain. The 3D Reynolds averaged steady flow Navier-Stokes equations in a cylindrical coordinate system are given by

$$\frac{\partial (F - V_x)}{\partial x} + \frac{\partial (G - U v_g - V_\theta)}{r\,\partial \theta} + \frac{\partial r (H - V_r)}{r\,\partial r} = S \tag{1}$$

where

$$U = (\rho, \rho u, \rho v r, \rho w, \rho E)^T$$

$$F = (\rho u, \rho u^2 + p, \rho v r u, \rho w u, \rho H u)^T$$

$$G = (\rho v, \rho u v, (\rho v^2 + p) r, \rho w v, \rho H v)^T$$

$$H = (\rho w, \rho u w, \rho v r w, \rho w^2 + p, \rho H w)^T$$

$$S = (0, 0, 0, (\rho v^2 + p)/r, 0)^T$$

$$V_x = (0, \tau_{xx}, r\tau_{\theta x}, \tau_{rx}, u\tau_{xx} + v\tau_{\theta x} + w\tau_{rx} + q_x)^T$$

$$V_\theta = (0, \tau_{x\theta}, r\tau_{\theta\theta}, \tau_{r\theta}, u\tau_{x\theta} + v\tau_{\theta\theta} + w\tau_{r\theta} + q_\theta)^T$$

$$V_r = (0, \tau_{xr}, r\tau_{\theta r}, \tau_{rr}, u\tau_{xr} + v\tau_{\theta r} + w\tau_{rr} + q_r)^T$$

v_g is the grid velocity at the circumferential direction.

Four sets of boundary conditions are used in the computations. They are the subsonic inlet boundary condition, the subsonic exit boundary condition, the viscous solid wall boundary condition, and the periodic boundary condition. At a subsonic inlet boundary, total pressure, total temperature, and flow angles are specified. At a subsonic exit boundary, static pressure is prescribed at the hub or tip, with the pressure radial distribution subject to the simple radial equilibrium. Along a viscous solid wall boundary, a slip boundary condition together with a wall function (log-law), as used by Denton [29], is adopted to reduce the mesh density near the solid wall region to save computational time. The periodic boundary condition is the simplest one among the four to be implemented and requires flow variables in dummy cells along a periodic boundary to be equal to flow variables in corresponding repeating cells.

In a multistage computation, the circumferentially averaged and characteristic-based mixing-plane treatment [34] is used at an interface between adjacent rows to enable the communication in the flow solution between adjacent rows. The flow mixing-plane treatment will ensure the conservation in mass, momentum, and energy across an interface at each radial section. This circumferential mixing-out of the flow nonuniformity will inevitably generate the mixing loss across the interface. In addition, the mixing-out would consequently mean that the unsteady interaction between adjacent rows cannot be included in this treatment.

The flow governing equations are spatially discretized in a cell-centered finite volume method framework with inviscid fluxes calculated using the central difference scheme coupled with a blended second- and fourth-order numerical dissipation. Time integration is achieved by using the four-stage Runge–Kutta method. The turbulent viscosity (μ_t) is obtained by the one equation Spalart–Allmaras turbulence model. The multigrid and local time-stepping techniques are employed to speed up the convergence of the solution process.

3 Adjoint Equations and Boundary Conditions

The continuous adjoint method has been adopted in our research due to its lower memory requirement, lower CPU time cost, and easier implementation (compared with the discrete one). The derivation of the adjoint equations based on the above flow governing equations follows the same way given in Refs. [13,14]. Turbulent viscosity is frozen in our adjoint formulation for simplicity. Thus for each design cycle, the gradient calculations are conducted at a frozen turbulent viscosity, while it will be updated in the direct flow solution once in every design cycle.

3.1 Adjoint Principle. The principle of the adjoint formulation will be first illustrated concisely here. The objective function I (a scalar) in an aerodynamic design optimization is a function of the flow variable vector U and a design variable α expressed as follows:

$$I = I(U, \alpha) \tag{2}$$

The relation between the flow variable and the design variable is determined through the nonlinear flow equation (a vector equation),

$$R(U, \alpha) = 0 \tag{3}$$

In a gradient-based design optimization, the gradient of the objective function to design variables is an essential element. Once the gradients are obtained, the steepest descent method or the conjugate gradient method can be applied directly for an optimization. The gradient of the objective function to a design variable can be given by

$$\frac{dI}{d\alpha} = \frac{\partial I}{\partial \alpha} + \frac{\partial I}{\partial U}\frac{\partial U}{\partial \alpha} \tag{4}$$

In the above gradient expression, $\partial I/\partial \alpha$ and $\partial I/\partial U$ can be calculated analytically or by the complex variable method [35], and no iteration will be involved. The calculation of the flow variable sensitivity $\partial U/\partial \alpha$ will have to involve solving equations (the nonlinear flow equations or the linearized flow equations). This can be done either directly by taking a difference between a perturbed flow field solution and the original (i.e., the finite difference method) or by solving the linearized flow equation,

$$\frac{\partial R}{\partial \alpha} + \frac{\partial R}{\partial U}\frac{\partial U}{\partial \alpha} = 0 \tag{5}$$

The linearized flow Eq. (5) again will need to be solved in an iterative process, accounting for the main time cost in the gradient evaluation. This linearized equation also depends on a design variable, implying that each design variable requires the linearized flow equation to be solved once. Hence both the direct finite difference and the linearized methods prohibit the use of a large number of design variables. The situations with a large number of design variables are exactly what the adjoint method is devised to deal with. The key is to find a way to decouple the influence of different design variables on an objective function through the flow variable sensitivity, and this can be achieved by eliminating the explicit dependency of the objective function sensitivity on the flow variable sensitivity $\partial U/\partial \alpha$ in Eq. (4).

Multiplying the right hand side of the linearized flow equation (5) with the adjoint variable vector (also called Lagrange multiplier) λ of the same dimension of U and subtracting the product from the gradient expression in Eq. (4) yields

$$\frac{dI}{d\alpha} = \frac{\partial I}{\partial \alpha} + \frac{\partial I}{\partial U}\frac{\partial U}{\partial \alpha} - \lambda^T\left[\frac{\partial R}{\partial \alpha} + \frac{\partial R}{\partial U}\frac{\partial U}{\partial \alpha}\right] \tag{6a}$$

We regroup the above in the following way:

$$\frac{dI}{d\alpha} = \frac{\partial I}{\partial \alpha} - \lambda^T\frac{\partial R}{\partial \alpha} + \left[\frac{\partial I}{\partial U} - \lambda^T\frac{\partial R}{\partial U}\right]\frac{\partial U}{\partial \alpha} \tag{6b}$$

If the adjoint variable is chosen to satisfy the following equation:

$$\frac{\partial I}{\partial U} - \lambda^T\frac{\partial R}{\partial U} = 0 \tag{7}$$

then the gradient expression is reduced as follows:

$$\frac{dI}{d\alpha} = \frac{\partial I}{\partial \alpha} - \lambda^T\frac{\partial R}{\partial \alpha} \tag{8}$$

This new gradient expression (8) does not depend on the flow variable sensitivity anymore. Furthermore, the adjoint equation (7) does not depend on any design variable. This implies that the gradient of a scalar objective function to all the design variables can be obtained by solving only two sets of equations: the flow equation (Eq. (3)) and the adjoint equation (Eq. (7)). Once the flow and adjoint solution is obtained, it can be substituted into the new gradient expression (8) to calculate the gradients very efficiently.

3.2 Adjoint Equations. The illustration in the preceding section is presented in an algebraic way. As mentioned in Sec. 1, the continuous adjoint method works on the flow equations in a partial differential equation form. Instead of regrouping in expression (6*b*), integration by parts needs to be used to derive the corresponding adjoint equations in a partial differential equation form. This section presents the detailed derivation of the adjoint equations from the flow equations in a partial differential equation form.

The derivation of the adjoint equations based on the Reynolds averaged Navier–Stokes Eqs. (1) is given in Appendix A1. The following derivation is based on the Euler flow equations, aimed at a simpler illustration of the principal procedure of a continuous adjoint formulation.

In the present research work, the objective function is a weighted sum of mass flow rate, pressure ratio and entropy generation rate, which can be expressed as a boundary integral in the following general form:

$$I = \int_{\partial D} M ds \tag{9}$$

where M is a function of flow variables and design variables. The gradient of the objective function to a design variable takes the following formulation:

$$\frac{dI}{d\alpha} = \int_{\partial D}\left[\frac{\partial M}{\partial U}\tilde{U} + \frac{\partial M}{\partial \alpha}\right]ds + \int_{\partial D} M\widetilde{ds} \tag{10}$$

where $\tilde{U} = \partial U/\partial \alpha$ is the flow variable sensitivity. $\partial M/\partial \alpha$ can be obtained in an analytic way or by the complex variable method [35] with little effort. However, the flow variable sensitivity is determined through the linearized flow equations,

$$\frac{\partial(A\tilde{U})}{\partial x} + \frac{\partial(B\tilde{U} - \tilde{U}v_g)}{r\,\partial\theta} + \frac{\partial r(C\tilde{U})}{r\,\partial r} - D\tilde{U} = f \tag{11}$$

where $A = \partial F/\partial U$, $B = \partial G/\partial U$, $C = \partial H/\partial U$, and $D = \partial S/\partial U$ are Jacobian matrices. f contains the linearization of geometric terms in the flow equations to a design variable α corresponding to $-\partial R/\partial \alpha$ in Eq. (5).

In order to avoid solving Eq. (11) n times for n design variables, we resort to the adjoint method, which offers a means to calculate the objective function sensitivity at a low time cost independent of the number of design variables.

Multiplying two sides of Eq. (11) with the adjoint variable λ and rearranging yields

$$\lambda^T\left[\frac{\partial(A\tilde{U})}{\partial x} + \frac{\partial(B\tilde{U} - \tilde{U}v_g)}{r\,\partial\theta} + \frac{\partial r(C\tilde{U})}{r\,\partial r} - D\tilde{U} - f\right] = 0 \tag{12a}$$

where $\lambda = (\lambda_1, \lambda_2, \lambda_3, \lambda_4, \lambda_5)^T$. λ_1, λ_2, λ_3, λ_4, and λ_5 correspond to the continuity equation, the axial momentum equation, the mo-

ment of momentum equation, the radial momentum equation, and the energy equation, respectively. Equation (12*a*) is a scalar equation and is valid everywhere in a computational domain, no matter what value the adjoint variable will take. Integrating the left hand side of the above equation over the whole computational domain, one has

$$\int_D \lambda^T \left[\frac{\partial(A\tilde{U})}{\partial x} + \frac{\partial(B\tilde{U} - \tilde{U}v_g)}{r\,\partial\,\theta} + \frac{\partial r(C\tilde{U})}{r\,\partial\,r} - D\tilde{U} - f \right] dv \tag{12b}$$

Performing integration by parts once yields

$$\int_{\partial D} [\lambda^T A n_x + \lambda^T (B - v_g I) n_\theta + \lambda^T C n_r] \tilde{U} ds - \int_D \left[\frac{\partial \lambda^T}{\partial x} A + \frac{\partial \lambda^T}{r\,\partial\,\theta}(B - v_g I) + \frac{\partial \lambda^T}{\partial r} C + \lambda^T D \right] \tilde{U} dv - \int_D \lambda^T f dv \tag{12c}$$

where I is a 5×5 identity matrix. Expression (12*c*) is zero. Subtracting expression (12*c*) from Eq. (10) does not change the gradient in Eq. (10), namely,

$$\frac{dI}{d\alpha} = \int_{\partial D} \left[\frac{\partial M}{\partial U}\tilde{U} + \frac{\partial M}{\partial \alpha} \right] ds + \int_{\partial D} M\widetilde{ds} - \int_{\partial D} [\lambda^T A n_x + \lambda^T (B - v_g I) n_\theta + \lambda^T C n_r] \tilde{U} ds + \int_D \left[\frac{\partial \lambda^T}{\partial x} A + \frac{\partial \lambda^T}{r\,\partial\,\theta}(B - v_g I) + \frac{\partial \lambda^T}{\partial r} C + \lambda^T D \right] \tilde{U} dv + \int_D \lambda^T f dv \tag{13a}$$

Collecting the domain integral terms with $\tilde{U}$ and boundary integral terms with $\tilde{U}$ separately, one has

$$\frac{dI}{d\alpha} = \int_D \left[\frac{\partial \lambda^T}{\partial x} A + \frac{\partial \lambda^T}{r\,\partial\,\theta}(B - v_g I) + \frac{\partial \lambda^T}{\partial r} C + \lambda^T D \right] \tilde{U} dv - \int_{\partial D} \left[\lambda^T A n_x + \lambda^T (B - I) n_\theta + \lambda^T C n_r - \frac{\partial M}{\partial U} \right] \tilde{U} ds + \int_{\partial D} \frac{\partial M}{\partial \alpha} ds + \int_{\partial D} M\widetilde{ds} + \int_D \lambda^T f dv \tag{13b}$$

Returning to the original objective of developing the adjoint method, the gradient for n design variables can be efficiently evaluated if we do not have to solve the flow equations n times. This can be achieved if the explicit dependence of the objective function gradient on the flow variable sensitivity can be eliminated. In order to eliminate the dependence of the gradient on the flow variable sensitivity $\tilde{U}$, the first two integral terms on the right hand side of expression (13*b*) must vanish. Inside a computational domain, at every point, components of $\tilde{U}$ are independent and cannot always be zero; then the term multiplying $\tilde{U}$ in the domain integral term needs to vanish, leading to the adjoint Euler equations,

$$\frac{\partial \lambda^T}{\partial x} A + \frac{\partial \lambda^T}{r\,\partial\,\theta}(B - v_g I) + \frac{\partial \lambda^T}{\partial r} C + \lambda^T D = 0 \tag{14}$$

Along the boundary of a computational domain, components of $\tilde{U}$ are not always independent and can always be zero somewhere; e.g., on a viscous solid wall, the convective fluxes are always zero. Therefore the term multiplying $\tilde{U}$ in the boundary integral does not need to be zero all the time. The flow boundary conditions need to be incorporated to eliminate the dependence of the boundary integral term multiplying $\tilde{U}$ in expression (13*b*) on the flow variable sensitivity $\tilde{U}$, leading to the adjoint boundary conditions. These boundary conditions will be detailed in the following adjoint boundary condition section. The remaining terms including both the domain integral terms and boundary integral terms in Eq. (13*b*) are independent of the flow variable sensitivity $\tilde{U}$. These terms give the final expression of the gradient in an intended form, independent of the flow variable sensitivity,

$$\frac{dI}{d\alpha} = \int_{\partial D} \frac{\partial M}{\partial \alpha} ds + \int_{\partial D} M\widetilde{ds} + \int_D \lambda^T f dv \tag{15}$$

The values of the adjoint variables are determined through a solution to the adjoint equations. No matter how many design variables are there, there are now only two sets of equations to be solved: the nonlinear flow equations and the linear adjoint equations. The time cost of solving the adjoint equations is equivalent to that for the baseline flow equations. Once the adjoint solution is obtained, it can be substituted into the above gradient expression to calculate gradients very efficiently.

3.3 Adjoint Boundary Conditions. It can be seen from the previous section (e.g., Eqs. (13*b*) and (14)) that the adjoint field equation is obtained by eliminating the dependence on the flow variable sensitivity in the *field* integration. Accordingly, the starting point of the adjoint boundary condition treatment is to eliminate the dependence on the flow variable sensitivity in the *boundary* integration, i.e., to ensure at a boundary,

$$\left[\lambda^T A n_x + \lambda^T (B - I) n_\theta + \lambda^T C n_r - \frac{\partial M}{\partial U} \right] \tilde{U} = 0 \tag{16}$$

Corresponding to the flow boundary conditions, there are also four sets of adjoint boundary conditions: the subsonic inlet boundary condition, the subsonic exit boundary condition, the viscous solid wall boundary condition, and the periodic boundary condition.

Another important element in the boundary condition treatment is the equation and its characteristics. Equation (14) is usually solved in a time-marching manner with a pseudo-time-derivative term added to the equation to form a hyperbolic system (Eq. (21)). For a hyperbolic system, the specification of boundary conditions is based on the propagation of characteristic information. The basic compatibility requirement is that the number of boundary conditions specified must be equal to the number of the characteristics running into the computational domain. Hence the directions of the characteristics matter. As Giles and Pierce [36] pointed out, the sign of each adjoint characteristic velocity is opposite to that of each corresponding flow characteristic velocity. Overall it is useful to note that in a simple but consistent sense, the adjoint information propagates in exactly the opposite way to the physical information. This "antiphysics" path of information propagation in fact governs all the boundary condition treatments for the adjoint equations, described in this section and in Sec. 4. This will also be illustrated further in the numerical examples, to be presented later.

At a subsonic inlet boundary for the flow equations, there are four incoming characteristics and one outgoing characteristic. Typically the static pressure at the boundary is extrapolated from the interior domain, and other flow variables are determined through the isentropic relation and specified quantities. Thus at the inlet boundary, pressure is the only independent flow variable. The flux perturbation can be expressed as the derivative of the flux to the pressure times the pressure perturbation. The corresponding adjoint boundary condition is applied to eliminate the dependence of the boundary integral term along an inlet boundary on the flow variable sensitivity,

$$\lambda^T \cdot \partial F/\partial p \cdot n_x = \partial M/\partial p \tag{17}$$

in which an inlet plane is assumed to be normal to the x axis, resulting in the x-directional flux only through the boundary. Equation (17) is a scalar equation. This is consistent with one incoming and four outgoing characteristics for the adjoint equations at a subsonic inlet boundary. The adjoint variables $\lambda_{1,2,3,4}$ are extrapolated from the interior domain, while λ_5 is worked out through Eq. (17). The derivative of the flux vector to the pressure $(\partial F/\partial p)$ can be obtained efficiently via the complex variable method [35].

At a subsonic exit boundary, there is one incoming and four outgoing characteristics for the flow equations. In the present flow solver, the density and three velocity components are extrapolated from the interior domain, and static pressure is determined through the value specified at the hub or tip and the simple radial equilibrium distribution. This means that at a flow exit, density and velocity components are independent flow variables. The flux perturbation at the boundary can be expressed as follows:

$$\tilde{F} = \partial F/\partial \rho \cdot \tilde{\rho} + \partial F/\partial u \cdot \tilde{u} + \partial F/\partial v \cdot \tilde{v} + \partial F/\partial w \cdot \tilde{w} \tag{18}$$

The corresponding adjoint boundary condition takes the following form:

$$\lambda^T \partial F/\partial q \cdot n_x = \partial M/\partial q, \quad q = \rho, u, v, w \tag{19}$$

where again an exit plane is assumed to be normal to the x axis. Equation (19) represents four equations. This is in line with the four incoming and one outgoing adjoint characteristics at a subsonic exit boundary. The adjoint variable λ_5 is extrapolated from the interior domain; other four adjoint variables are determined through Eq. (19).

Corresponding to a slip boundary condition with the log-law at a viscous solid wall boundary, the adjoint boundary condition is formulated as follows:

$$\lambda_2 \cdot n_x + \lambda_3 \cdot n_\theta \cdot r + \lambda_4 \cdot n_r + \lambda_5 \cdot n_\theta \cdot v_g = \partial M/\partial p$$

$$\sigma_x = \tau_w/W \cdot \lambda_2$$

$$\sigma_\theta = \tau_w/W \cdot (\lambda_3 + \Omega \cdot \lambda_5)$$

$$\sigma_r = \tau_w/W \cdot \lambda_4$$

$$\frac{\partial \lambda_5}{\partial n} = 0 \quad \text{for an adiabatic wall}$$

$$\lambda_5 = 0 \quad \text{for a nonadiabatic wall (temperature specified)} \tag{20}$$

Ω is the angular speed of the rotating mesh associated with a blade. τ_w is the wall shear stress calculated by the log-law. W is the magnitude of the velocity along the slip wall.

The implementation of the adjoint periodic boundary condition is identical to the flow periodic boundary and simply equals the adjoint variables at corresponding periodic boundaries. The adjoint mixing-plane treatment will be illustrated in the next section in detail.

In order to solve the adjoint Eq. (14) in a finite volume framework, it is first written in a strong conservative form with extra terms taken as source terms. Then a pseudo-time-derivative term is added to the adjoint equations as follows to make use of the Runge–Kutta time integration method:

$$\frac{\partial \lambda}{\partial \tau} - \frac{\partial A^T \lambda}{\partial x} - \frac{\partial (B - v_g I)^T \lambda}{r\,\partial \theta} - \frac{\partial C^T \lambda}{\partial r} = \left[\frac{\partial A^T}{\partial x} + \frac{\partial (B - v_g I)^T}{r\,\partial \theta} + \frac{\partial C^T}{\partial r} - D^T \right] \lambda \tag{21}$$

As can be seen from the above, compared with Eq. (14), all terms change their signs into their opposite ones when the pseudo-time-derivative term is added. This is again in line with the property of adjoint characteristics (Giles and Pierce [36]) propagating in exactly the opposite way to the flow characteristics.

The spatial discretization and time integration of the adjoint equations are implemented in the same way as for the flow governing equations. The multigrid and local time-stepping techniques are also used to speed up solving the adjoint equations. Subroutines in the flow solver, such as those for time-marching, multigrid, and metrics calculation, can be reused in developing the adjoint solver without any major modification. As for the initialization of the adjoint solution, our practice shows that the adjoint solution can be initialized with zeros or real numbers of small magnitudes.

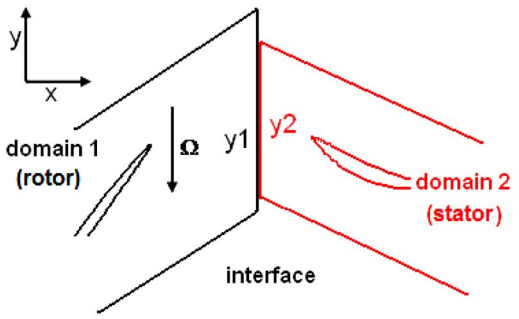

Fig. 1 An interface between a rotor and a stator configuration

4 Adjoint Mixing Plane

The main objective of the present work is to enable the adjoint-method-based design optimization to be carried out in a multistage environment. The basis of the present development is the mixing-plane treatment for flow solutions after Denton [29]. There are two basic features in the mixing-plane approach. The first is to satisfy the conservation of the total mass, momentum, and energy, which is fundamentally required. The second is to be nonreflective, which is highly desirable. The present adjoint mixing-plane treatment is also aimed at having these two features.

In the flow mixing-plane treatment, the circumferentially averaged fluxes of mass, momentum, and energy are conserved across an interface, as schematically shown in Fig. 1. In the adjoint mixing-plane treatment, the adjoint variable weighted and circumferentially averaged fluxes are conserved across an interface (see Appendix A2 for details),

$$\frac{1}{Y_1}\int_{y1} \lambda_1 \rho u dy = \frac{1}{Y_2}\int_{y2} \lambda_1 \rho u dy \tag{22a}$$

$$\frac{1}{Y_1}\int_{y1} \lambda_2 (\rho u^2 + p) dy = \frac{1}{Y_2}\int_{y2} \lambda_2 (\rho u^2 + p) dy \tag{22b}$$

$$\frac{1}{Y_1}\int_{y1} \lambda_3 (\rho v u) dy = \frac{1}{Y_2}\int_{y2} \lambda_3 (\rho v u) dy \tag{22c}$$

$$\frac{1}{Y_1}\int_{y1} \lambda_4 (\rho w u) dy = \frac{1}{Y_2}\int_{y2} \lambda_4 (\rho w u) dy \tag{22d}$$

$$\frac{1}{Y_1}\int_{y1} \lambda_5 (\rho H u) dy = \frac{1}{Y_2}\int_{y2} \lambda_5 (\rho H u) dy \tag{22e}$$

where Y_1 and Y_2 are the pitch lengths of two adjacent domains. $y1$ and $y2$ are the exit of domain 1 and the inlet of domain 2, respectively. This conservation ensures that the two boundary integral terms in Eq. (A9) cancel out each other, leading to the indepen-

dence of Eq. (A9) on the flow variable sensitivity.

The conservation of these adjoint variable weighted fluxes can be achieved through the nonreflective implementation following the nonreflective boundary conditions for solving the flow equations [34]. Applying the mean value theorem for integration to either side of the equalities (22*a*)–(22*e*), the following mixed-out variables can be obtained:

$$\widehat{\lambda_{1,i}} = \frac{\int_{yi} \lambda_1 \rho u dy}{\int_{yi} \rho u dy} \tag{23a}$$

$$\widehat{\lambda_{2,i}} = \frac{\int_{yi} \lambda_2 (\rho u^2 + p) dy}{\int_{yi} (\rho u^2 + p) dy} \tag{23b}$$

$$\widehat{(\lambda_3 v)_i} = \frac{\int_{yi} \lambda_3 (\rho v u) dy}{\int_{yi} (\rho u) dy} \tag{23c}$$

$$\widehat{(\lambda_4 w)_i} = \frac{\int_{yi} \lambda_4 (\rho w u) dy}{\int_{yi} (\rho u) dy} \tag{23d}$$

$$\widehat{\lambda_{5,i}} = \frac{\int_{yi} \lambda_5 \rho H u dy}{\int_{yi} \rho H u dy} \tag{23e}$$

In expressions (23*c*) and (23*d*), the mass flux is used in the denominator instead of corresponding momentum fluxes. This is because the circumferential and radial momentum fluxes may change their signs along an interface, which violates the premise of the mean value theorem for integration. However the mass flux, axial momentum flux, and energy flux usually do not change their signs along an interface (no reverse flow). According to the conservation in equalities (22*a*)–(22*e*), the mixed-out variables in Eqs. (23*a*)–(23*e*) should also be equal across an interface. Once there is a difference in these mixed-out variables across the interface, this difference is taken as a characteristic jump disturbance. The present implementation will pass the disturbance to the two sides of the interface. The local adjoint variables will be corrected according to the adjoint characteristic propagation to drive the difference to zero.

The adjoint characteristic variables in term of the variable perturbation are expressed as follows:

$$\tilde{\lambda}^c = S^T \tilde{\lambda} \tag{24}$$

where S is the matrix diagonalizing the Jacobian matrix $A = \partial F / \partial U = S \Lambda S^{-1}$, with Λ being a diagonal matrix of which diagonal elements are eigenvalues of the matrix A. Expanding the vector form of Eq. (24) gives

$$\tilde{\lambda}_1^c = \tilde{\lambda}_1 + (u - c)\tilde{\lambda}_2 + v r \tilde{\lambda}_3 + w \tilde{\lambda}_4 + (H - uc)\tilde{\lambda}_5 \tag{25a}$$

$$\tilde{\lambda}_2^c = \tilde{\lambda}_1 + (u + c)\tilde{\lambda}_2 + v r \tilde{\lambda}_3 + w \tilde{\lambda}_4 + (H + uc)\tilde{\lambda}_5 \tag{25b}$$

$$\tilde{\lambda}_3^c = \tilde{\lambda}_3 + \frac{v}{r}\tilde{\lambda}_5 \tag{25c}$$

$$\tilde{\lambda}_4^c = \tilde{\lambda}_4 + w \tilde{\lambda}_5 \tag{25d}$$

$$\tilde{\lambda}_5^c = \frac{\tilde{\lambda}_1}{u} + \tilde{\lambda}_2 + \left(u - \frac{W^2}{2u}\right)\tilde{\lambda}_5 \tag{25e}$$

where c is the speed of sound, $W^2 = u^2 + v^2 + w^2$, and r is the radial coordinate.

The information represented by $\tilde{\lambda}_1^c$ propagates at the speed of $-u+c$. The information represented by $\tilde{\lambda}_2^c$ propagates at the speed of $-u-c$. And the information represented by the other three adjoint characteristic variables all propagates at the same speed of $-u$. For both incoming and outgoing adjoint characteristic variables, flow variables in the adjoint characteristic expressions take their local values. For incoming adjoint characteristic variables, the primitive adjoint variable perturbations take values through the difference in the mixed-out variables across the interface, e.g.,

$$\tilde{\lambda}_1 = \widehat{\lambda_{1,2}} - \widehat{\lambda_{1,1}} \tag{26a}$$

$$\tilde{\lambda}_2 = \widehat{\lambda_{2,2}} - \widehat{\lambda_{2,1}} \tag{26b}$$

$$\tilde{\lambda}_3 = \frac{\widehat{(\lambda_3 v)_2} - \widehat{(\lambda_3 v)_1}}{v} \tag{26c}$$

$$\tilde{\lambda}_4 = \frac{\widehat{(\lambda_4 v)_2} - \widehat{(\lambda_4 v)_1}}{w} \tag{26d}$$

$$\tilde{\lambda}_5 = \widehat{\lambda_{5,2}} - \widehat{\lambda_{5,1}} \tag{26e}$$

For outgoing adjoint characteristic variables, the primitive adjoint variable perturbations take the local values.

In Fig. 1, the interface separates two boundaries, an exit for domain 1 and an inlet for domain 2. The exit of domain 1 has four incoming adjoint characteristics $(\tilde{\lambda}_2^c, \tilde{\lambda}_3^c, \tilde{\lambda}_4^c, \tilde{\lambda}_5^c)$, which will be calculated through expressions (25) and (26). The inlet of domain 2 has one incoming adjoint characteristic $\tilde{\lambda}_1^c$, which will be also obtained through expressions (25) and (26).

Once all the adjoint characteristic variables are obtained for each side of an interface, they can be converted to primitive adjoint variable perturbations via the following formulation. The primitive adjoint variable perturbations can then be directly used to update the local adjoint solution,

$$\tilde{\lambda} = (S^T)^{-1} \tilde{\lambda}^c \tag{27}$$

The scalar form of the above is given by

$$\tilde{\lambda}_5 = \frac{k-1}{c^2}\left(\frac{\tilde{\lambda}_1^c}{2} + \frac{\tilde{\lambda}_2^c}{2} - u\tilde{\lambda}_3^c - v r \tilde{\lambda}_4^c - w\tilde{\lambda}_5^c\right) \tag{28a}$$

$$\tilde{\lambda}_4 = -w\tilde{\lambda}_5 + \tilde{\lambda}_5^c \tag{28b}$$

$$\tilde{\lambda}_3 = -\frac{v}{r}\tilde{\lambda}_5 + \tilde{\lambda}_4^c \tag{28c}$$

$$\tilde{\lambda}_2 = -u\tilde{\lambda}_5 + \frac{1}{2c}(-\tilde{\lambda}_1^c + \tilde{\lambda}_2^c) \tag{28d}$$

$$\tilde{\lambda}_1 = \frac{W^2}{2}\tilde{\lambda}_5 + \frac{u}{2c}(\tilde{\lambda}_1^c - \tilde{\lambda}_2^c + 2c\tilde{\lambda}_3^c) \tag{28e}$$

5 Gradient Calculation

The gradient expression (15) is in terms of the adjoint variable and geometric gradient. The term f is related to the perturbation of the steady flow residual R to a design variable, expressed in the following way:

$$f = -\frac{\partial R}{\partial \alpha}$$

The calculation of f requires perturbing the mesh followed by calculating the flow residual perturbation due to this mesh perturbation.

For n design variables, n times of mesh perturbation are required. For thousands of design variables, the time cost for all the mesh perturbation is not negligible, but the time cost does not usually exceed that of a steady flow/adjoint solution. For example, the mesh needs to be perturbed once for each design variable to calculate the corresponding flow residual perturbation. Such a residual perturbation calculation has a cost that is more or less one-fourth of one full four-stage Runge–Kutta iteration. With a complex variable implementation, the cost of flow residual perturbation is doubled. Therefore for 100 design variables, the time cost will be 50 full four-stage Runge–Kutta iterations, which is only a fraction of thousands of iterations required to solve either the flow equations or the adjoint equations.

Though there are ways to avoid perturbing the mesh by converting the domain integral in Eq. (15) into a boundary integral [25,14], it usually involves calculation of spatial derivatives of flow variables along the boundary of a computational domain, which is not easy to obtain with desirable accuracy. Therefore, the gradient calculation here adopts the mesh perturbing approach.

In addition, in our computations, this residual sensitivity is obtained using the complex variable method [35]. The complex variable method is an alternative to the finite difference method but does not share the well-known disadvantage of subtraction cancellation of the finite difference method when a perturbation size becomes very small. According to the above gradient expression, boundary conditions applied when solving the flow equations should be applied in a gradient calculation.

6 Results and Discussion

6.1 Lift Coefficient Gradient. The adjoint solution provides information with which gradients of an objective function to a large number of design variables can be obtained efficiently. Thus the adjoint solution can be validated by comparing gradients using the adjoint solution with those calculated by other well established methods.

A simple means to obtain gradients of an objective function to design variables is the finite difference method. However it should be recalled that this approach suffers from step size dependence. A big step size may lead to unreliable gradient results if the relation between an objective function and design variables is highly nonlinear. The complex variable method or linearized method is a better alternative to the finite difference method. However its implementation in a large-scale nonlinear flow solver requires a lot of extra work.

As we know, within a certain range of angle of attack, the lift coefficient of an aerofoil has a linear relationship with its angle of attack. This provides a good case to calculate the gradient of the lift coefficient of an aerofoil to its angle of attack by the finite difference method by choosing a step size that is big enough to avoid significant subtraction cancellation errors.

The lift coefficient of NACA0012 with a chord length of 0.15 m is calculated for angles of attack between 0 deg and 2 deg at a Mach number of 0.62 in the far field. The computational domain is extended about ten times chord away from the aerofoil surface and is divided into four blocks with about 15,000 mesh points. Figure 2 shows the mesh around NACA0012, Fig. 3 shows the Mach number distribution, and Fig. 4 shows the adjoint solution

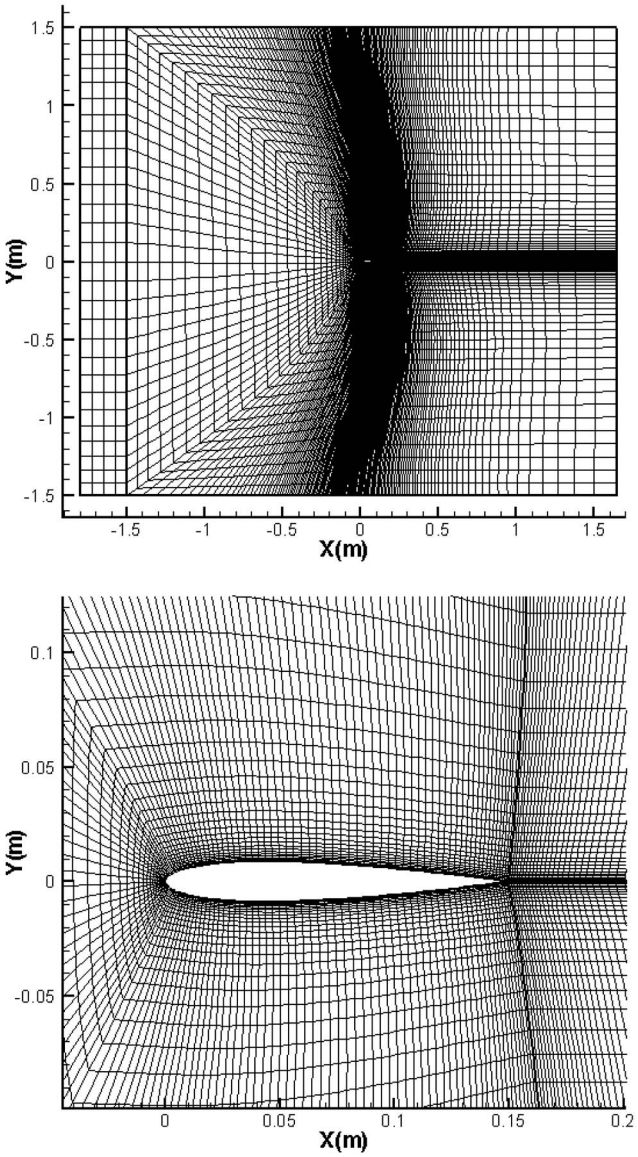

Fig. 2 Overview (upper) and close-up (lower) of the mesh around a NACA0012 aerofoil

(the adjoint variable corresponding to the continuity equation) distribution at zero angle of attack. Comparing the adjoint solution contours and those of Mach number, one can see that the upstream of the flow field corresponds to the downstream of the adjoint field, and vice versa. This is consistent with the property of the adjoint characteristics, which have an opposite direction to the flow characteristics.

The linear relationship between the lift coefficient of NACA0012 and its angle of attack is presented in Fig. 5. The gradient by the finite difference method and that by the adjoint method are in very good agreement at different angles of attack (Fig. 5). The biggest relative difference between the gradients by the two methods is within 5%.

6.2 Inverse Design. Inverse design is a popular case for adjoint method researchers to demonstrate their proper implementation of the adjoint method [22]. As a conventional inverse design, it may require the specification of a target pressure distribution on a blade surface. The pressure distribution on the surface of NACA0015 with a chord length of 0.15 m is obtained by the present flow solver at a flow condition, which is identical to that

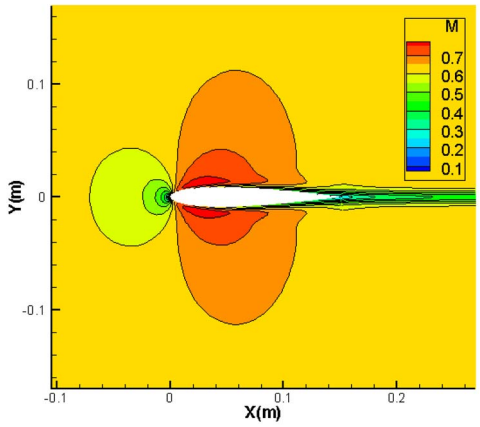

Fig. 3 Mach number contours around NACA0012 at zero angle of attack

for the previous NACA0012 case. This is taken as the target pressure distribution. The NACA0012 profile is taken as the initial aerofoil by the design system to approach the target pressure distribution. The objective function for this inverse design is given by

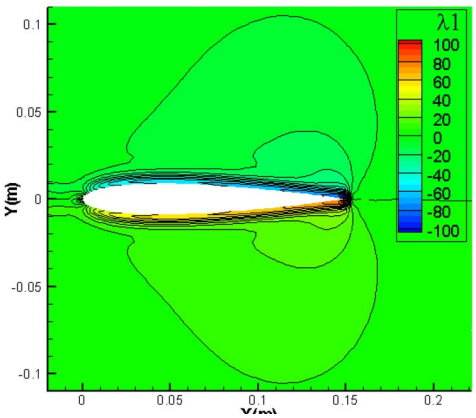

Fig. 4 Adjoint field (λ_1) around NACA0012 at zero angle of attack

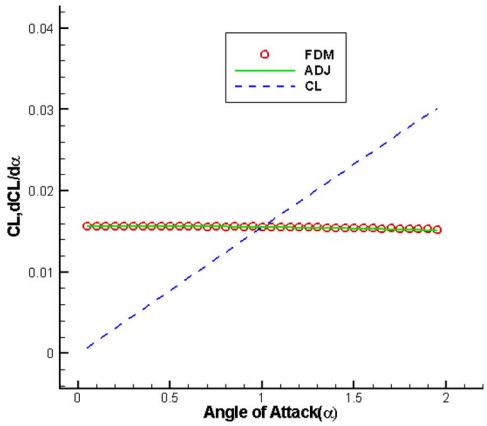

Fig. 5 Lift coefficient/gradient versus angle of attack for NACA0012 (FDM: finite difference method, ADJ: adjoint method, and CL: calculated lift coefficient)

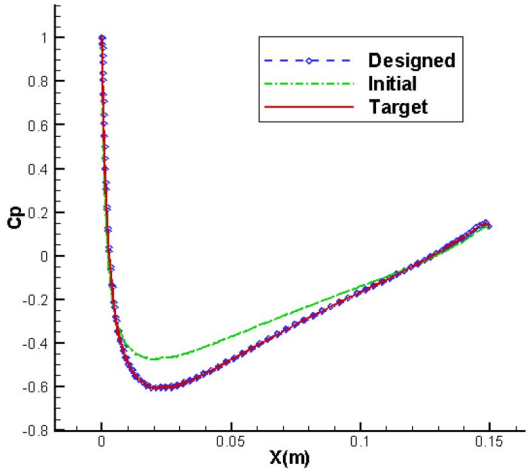

Fig. 6 Pressure coefficient distributions over the initial, target, and designed aerofoils' surface for the inverse design

$$I = \frac{\int_{BS} (p - p_t)^2 ds}{\int_{BS} (p_0 - p_t)^2 ds}$$

where "BS" denotes the blade surface, p_t is the target pressure distribution, and p_0 is the pressure distribution on the NACA0012 blade surface. During the design process, the chord length of the NACA0012 aerofoil is fixed by fixing the leading and trailing points. The Hicks–Henne function as used by Yang et al. [22] is used to parametrize perturbations of y coordinates of all mesh points (except for the leading and trailing edge points) on the blade surface, resulting in 155 design variables. With the adjoint method, only two sets of equations (the flow equation and the adjoint equation) are solved with some postprocessing at each design cycle to enable the gradients of the objective function to all design variables to be calculated. However the finite different method requires the flow equation to be solved at least 156 times at each design cycle. The great time saving by the adjoint method over the finite difference method is apparent.

The initial, target, and designed pressure coefficient distributions are compared in Fig. 6. The target pressure is achieved with good accuracy in the inverse design. As Fig. 7 reveals, the target aerofoil profile is recovered. Figure 8 depicts the change in the objective function with design cycles. The objective function in terms of the pressure difference is reduced by three orders of magnitude from its initial value.

6.3 Validation of Adjoint Mixing-Plane Treatment. For the verification of the adjoint mixing-plane treatment, the Euler equations are solved and the adjoint equations are based on the Euler flow solution to avoid complexity introduced by the viscous effects and freezing the turbulent viscosity. The verification case uses a span section of a 3D compressor stage—a transonic DLR (German Aerospace Center) compressor stage [37]. The section is put on a cylindrical surface at a constant radius. Figure 9 shows the mesh with a mesh density of 110×37 for the rotor domain and 90×37 for the stator domain.

The Mach number distribution is shown in Fig. 10. Figure 11 shows the contour of the adjoint variable corresponding to the continuity equation when the objective function is the tangential force on the stator blade. Figure 12 shows the contour of the adjoint variable corresponding to the moment of the momentum equation when the objective function is the mass flow rate calculated at the exit of the stator. The two adjoint solution contours

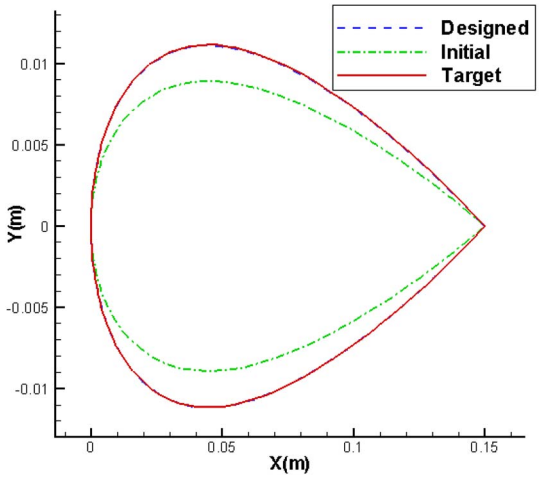

Fig. 7 Comparison between initial, target, and designed aerofoil profiles for the inverse design

consistently depict that the adjoint solution information propagates in a direction opposite to that of the physical flow disturbances. The flow upstream region becomes the downstream region of the adjoint solution, and the flow downstream region becomes the upstream region of the adjoint solution. Figure 13 compares the gradient results of the tangential force on the stator blade to design variables parametrizing the stator blade shape. The gradients by the adjoint method are very close to those by the finite difference method. The appropriate implementation of the adjoint mixing-plane treatment is further demonstrated in the good comparison of the gradient results of the mass flow rate to design variables parametrizing the rotor blade shape (Fig. 14). The mass flow rate is calculated at the exit of the stator exit (stage exit). According to the subsonic inlet boundary condition (Eq. (17)), $\partial M / \partial p$ is zero at the inlet of the stage. This means that the objective function information is applied at the stage exit only. Apart from that, the mass flow rate gradient calculation requires the rotor computational domain alone to be perturbed. Therefore the adjoint mixing-plane treatment plays a vitally important role in passing the objective function information correctly through the interface of the 2D rotor-stator configuration. Figures 11 and 12 also show that along the interface, there is a clear cut of contour lines right on both sides of the interface, which indicates clearly that the adjoint mixing-plane treatment is nonreflective.

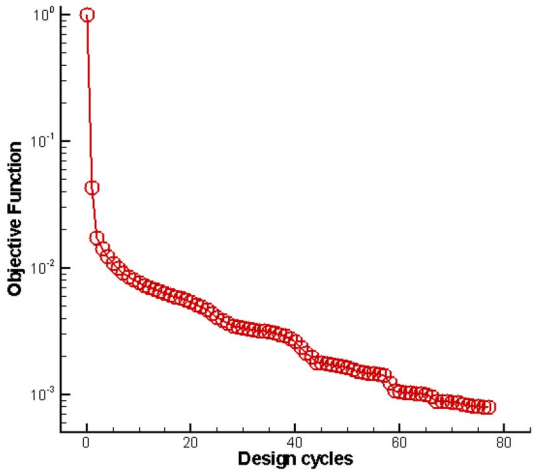

Fig. 8 History of the objective function for the inverse design

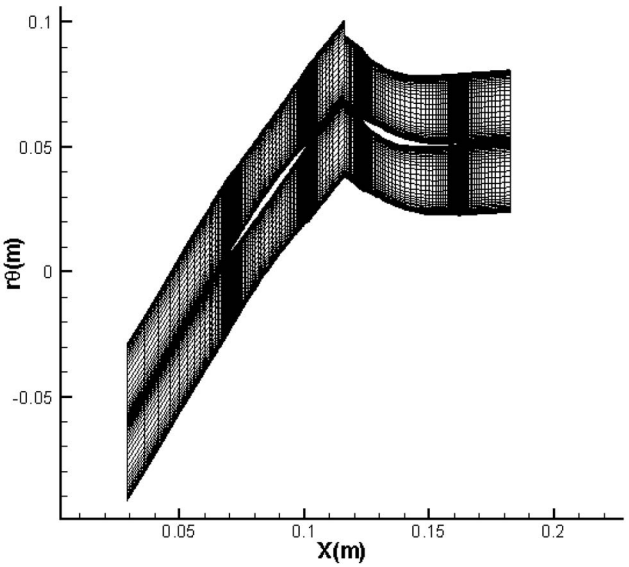

Fig. 9 Computational mesh of the 2D compressor stage

6.4 Redesign of Compressor Stage. The 2D section of the compressor stage used in Sec. 6.3 is optimized to increase the isentropic efficiency while maintaining its mass flow rate and pressure ratio. The objective function is a weighted sum of the entropy generation rate and the two constraints of mass flow rate and stagnation pressure ratio (for further details see Ref. [38]).

In this case, the RANS equations are solved. Ten design variables are used to parametrize perturbation to the rotor blade shape and eight design variables to the stator blade shape. The isentropic efficiency of the stage is increased from 84.91% to 88.00% with negligible changes in mass flow rate and pressure ratio. It should be pointed out the baseline flow state is not a very efficient one and is chosen here mainly for demonstrating the adjoint mixing-plane method. Figure 15 shows the difference of the optimized rotor blade from the original one. The optimized blade is curved toward its suction side between the leading edge and the mid-chord, leading to a weaker shock in the passage (Fig. 16). The trailing edge region is curved in an opposite direction toward the pressure side, better matched with the stator. Figure 17 shows the geometry change of the stator blade; the stator camber is increased to reduce the flow separation around the stator trailing edge

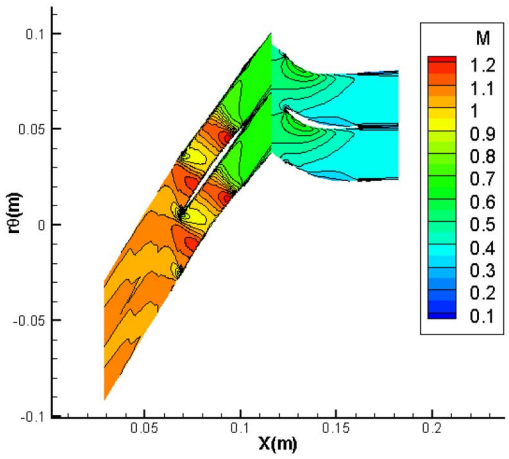

Fig. 10 Relative Mach number contours (2D configuration of the compressor stage)

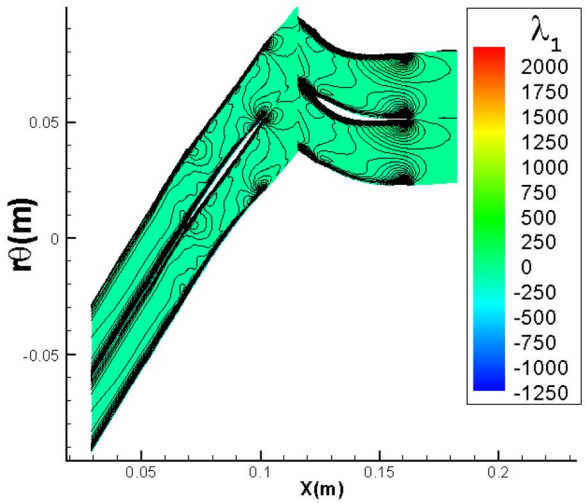

Fig. 11 Adjoint field (λ_1) with the tangential force on the stator blade as the objective function

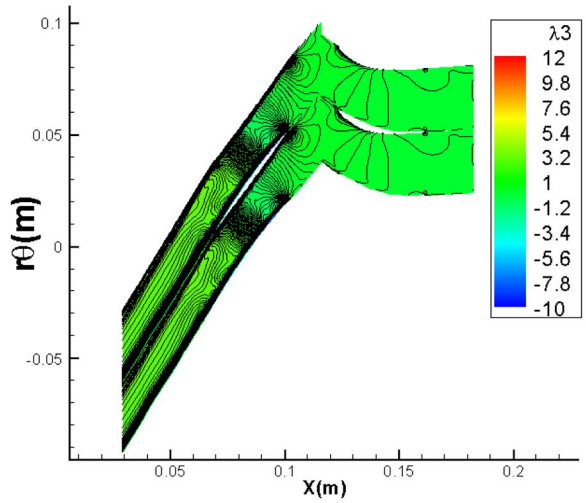

Fig. 12 Adjoint field (λ_3) with mass flow rate as the objective function

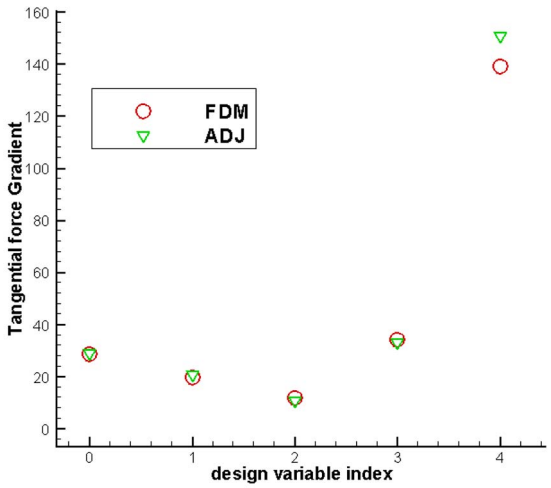

Fig. 13 Gradients of the tangential force on the stator blade (FDM: finite difference method and ADJ: adjoint method)

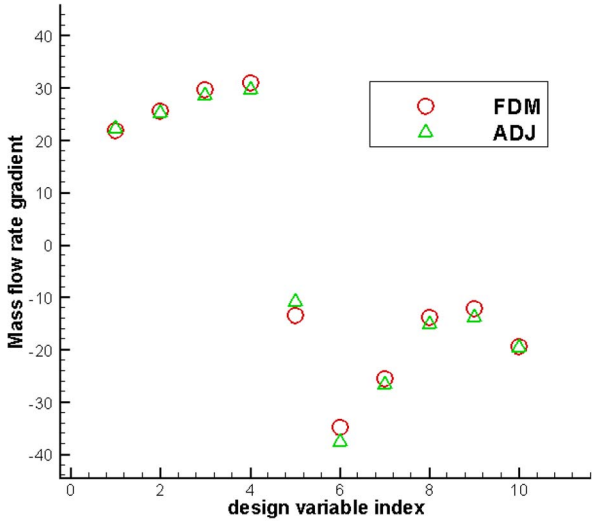

Fig. 14 Gradients of stage mass flow rate (FDM: finite difference method and ADJ: adjoint method)

(Fig. 16).

This case provides an illustration of the validity and advantage of the present adjoint mixing-plane treatment. Clearly it is far more effective to optimize both the rotor and stator at the same time than to deal with them separately and iteratively.

7 Concluding Remarks

The adjoint method for turbomachinery blading aerodynamic design optimization with the emphasis on the adjoint mixing-plane treatment is presented. It is believed that development and application of an adjoint method can benefit considerably from a clear appreciation of the antiphysics adjoint information propagation, as demonstrated in the computational results. The good agreement of the lift coefficient gradient by the adjoint method

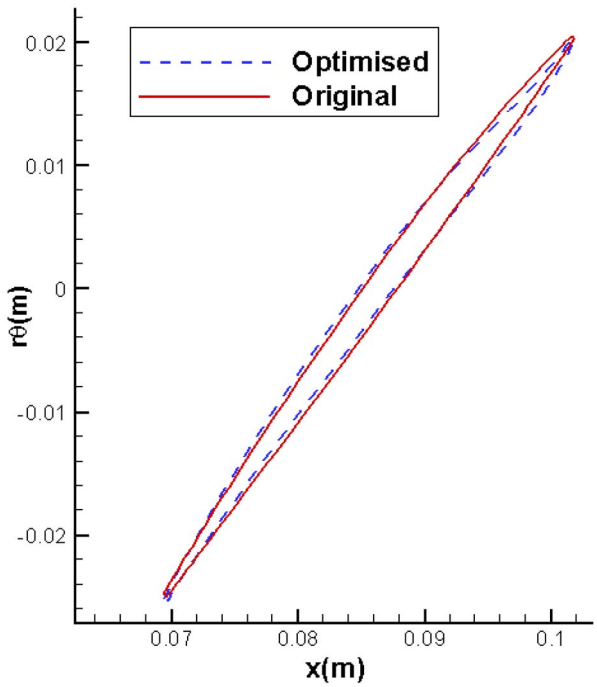

Fig. 15 Comparison of the original rotor blade and the optimized rotor blade

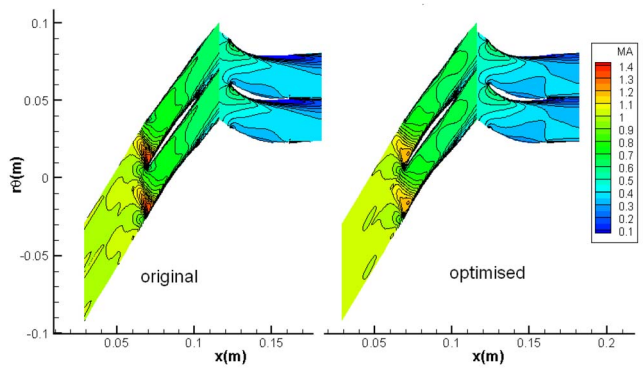

Fig. 16 Relative Mach contours of the original blade passage and the optimized blade passage

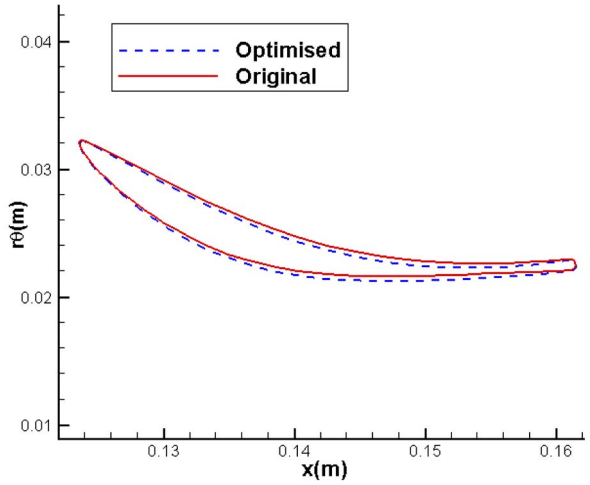

Fig. 17 Comparison of the original stator blade and the optimized stator blade

with that by the finite difference method demonstrates the validity of the adjoint method in the gradient calculation and its appropriate implementation. These are further confirmed by the inverse design well recovering the target pressure coefficient distribution and the target aerofoil profile. The close agreement of the gradient results by the adjoint method with those by the finite difference method for a 2D rotor-stator configuration case demonstrates the appropriate formulation and implementation of the adjoint mixing-plane treatment. The characteristic-based adjoint mixing-plane treatment is also shown to be nonreflective. The validity and advantage of the adjoint mixing-plane treatment is further confirmed by the optimization of the 2D compressor stage. Further validations and applications of the present approach to realistic 3D configurations in a multirow environment are presented in the companion paper [38].

Acknowledgment

The authors would like to thank Siemens Industrial Turbomachinery Ltd. for funding this work and allowing its publication. Discussions with Dr. Y.S. Li, R.G. Wells, and Dr. T. Chen at Siemens are much appreciated. The authors also would like to thank Dr. H.D. Li for his help during the early stage of the work.

Nomenclature

F,G,H = axial, circumferential, and radial flux vectors
u,v,w = axial, circumferential, and radial velocity components
S = source term of the flow equations
U = conservative flow variable vector
U_v = viscous flow variable vector
$V_{x,\theta,r}$ = axial, circumferential, and radial viscous flux vectors
ρ = fluid density
Ω = angular velocity
E = specific total energy
H = specific total enthalpy
p = pressure
τ_{ij} = $i,j=x,\theta,r$ shear stress
q_i = $i,j=x,\theta,r$ heat flux
λ = adjoint variable vector
A,B,C,D = Jacobian matrices of inviscid flux vectors and the source term to the conservative flow variable vector
A_v,B_v,C_v = Jacobian matrices of viscous flux vectors to the conservative flow variable vector
$D_{x,\theta,r}$ = adjoint viscous terms
σ_{ij} = adjoint viscous stress terms

Appendix

1 Derivation of Viscous Adjoint Equations. Linearizing the flow equations (1) with respect to a design variable, one has

$$\frac{\partial(A\tilde{U}-A_v\tilde{U}-D_{xx}\tilde{U}_x-D_{x\theta}\tilde{U}_\theta-D_{xr}\tilde{U}_r)}{\partial x}+\frac{\partial(B\tilde{U}-\tilde{U}v_g-B_v\tilde{U}-D_{\theta x}\tilde{U}_x-D_{\theta\theta}\tilde{U}_\theta-D_{\theta r}\tilde{U}_r)}{r\,\partial\theta}+\frac{\partial r(C\tilde{U}-C_v\tilde{U}-D_{rx}\tilde{U}_x-D_{r\theta}\tilde{U}_\theta-D_{rr}\tilde{U}_r)}{r\,\partial r}-D\tilde{U}=f \tag{A1}$$

where A, B, C, and D are as defined before in Eq. (11), and

$$A_v=\partial V_x/\partial U,\quad B_v=\partial V_\theta/\partial U,\quad C_v=\partial V_r/\partial U$$

$$\tilde{U}_x=\partial\tilde{U}/\partial x,\quad \tilde{U}_\theta=\partial\tilde{U}/(r\,\partial\theta),\quad \tilde{U}_r=\partial(r\tilde{U})/(r\,\partial r)$$

$$D_{ij}=\partial V_i/\partial U_j,\quad i,j=x,\theta,r$$

Multiplying Eq. (A1) with the adjoint variable and rearranging yields

$$\lambda^T\left[\frac{\partial(A\tilde{U}-A_v\tilde{U}-D_{xx}\tilde{U}_x-D_{x\theta}\tilde{U}_\theta-D_{xr}\tilde{U}_r)}{\partial x}+\frac{\partial(B\tilde{U}-\tilde{U}v_g-B_v\tilde{U}-D_{\theta x}\tilde{U}_x-D_{\theta\theta}\tilde{U}_\theta-D_{\theta r}\tilde{U}_r)}{r\,\partial\theta}+\frac{\partial r(C\tilde{U}-C_v\tilde{U}-D_{rx}\tilde{U}_x-D_{r\theta}\tilde{U}_\theta-D_{rr}\tilde{U}_r)}{r\,\partial r}-D\tilde{U}-f\right]=0 \tag{A2}$$

The linearized flow equations (Eq. (A1)) hold no matter what value the adjoint variable will take. Integrating the left hand side of the above equation over the whole computational domain, one has

$$\int_D \lambda^T \left[\frac{\partial(A\tilde{U} - A_v\tilde{U} - D_{xx}\tilde{U}_x - D_{x\theta}\tilde{U}_\theta - D_{xr}\tilde{U}_r)}{\partial x} + \frac{\partial(B\tilde{U} - \tilde{U}v_g - B_v\tilde{U} - D_{\theta x}\tilde{U}_x - D_{\theta\theta}\tilde{U}_\theta - D_{\theta r}\tilde{U}_r)}{r\,\partial\,\theta} + \frac{\partial r(C\tilde{U} - C_v\tilde{U} - D_{rx}\tilde{U}_x - D_{r\theta}\tilde{U}_\theta - D_{rr}\tilde{U}_r)}{r\,\partial\,r} - D\tilde{U} - f \right] dv = 0 \tag{A3}$$

Performing integration by parts once gives

$$\int_{\partial D} [\lambda^T(\tilde{F} - \tilde{V}_x)n_x + \lambda^T(\tilde{G} - \tilde{U}v_g - \tilde{V}_\theta)n_\theta + \lambda^T(\tilde{H} - \tilde{V}_r)n_r]ds - \int_D \left[\frac{\partial\lambda^T}{\partial x}(A - A_v) + \frac{\partial\lambda^T}{r\,\partial\,\theta}(B - v_gI - B_v) + \frac{\partial\lambda^T}{\partial r}(C - C_v) + \lambda^T D \right] \tilde{U} dv + \int_D \left[\frac{\partial\lambda^T}{\partial x}(D_{xx}\tilde{U}_x + D_{x\theta}\tilde{U}_\theta + D_{xr}\tilde{U}_r) + \frac{\partial\lambda^T}{r\,\partial\,\theta}(D_{\theta x}\tilde{U}_x + D_{\theta\theta}\tilde{U}_\theta + D_{\theta r}\tilde{U}_r) + \frac{\partial\lambda^T}{\partial r}(D_{rx}\tilde{U}_x + D_{r\theta}\tilde{U}_\theta + D_{rr}\tilde{U}_r) \right] dv - \int_D \lambda^T f dv = 0 \tag{A4}$$

Rearranging the last second domain integral in the above by collecting like terms with $\tilde{U}_x$, $\tilde{U}_\theta$, and $\tilde{U}_r$ yields

$$\int_D \left[\left(\frac{\partial\lambda^T}{\partial x}D_{xx} + \frac{\partial\lambda^T}{r\,\partial\,\theta}D_{\theta x} + \frac{\partial\lambda^T}{\partial r}D_{rx} \right)\tilde{U}_x + \left(\frac{\partial\lambda^T}{\partial x}D_{x\theta} + \frac{\partial\lambda^T}{r\,\partial\,\theta}D_{\theta\theta} + \frac{\partial\lambda^T}{\partial r}D_{r\theta} \right)\tilde{U}_\theta + \left(\frac{\partial\lambda^T}{\partial x}D_{xr} + \frac{\partial\lambda^T}{r\,\partial\,\theta}D_{\theta r} + \frac{\partial\lambda^T}{\partial r}D_{rr} \right)\tilde{U}_r \right] dv \tag{A5}$$

Performing integration by parts to the above once gives

$$\int_{\partial D} \left[\left(\frac{\partial\lambda^T}{\partial x}D_{xx} + \frac{\partial\lambda^T}{r\,\partial\,\theta}D_{\theta x} + \frac{\partial\lambda^T}{\partial r}D_{rx} \right)\tilde{U}\cdot n_x + \left(\frac{\partial\lambda^T}{\partial x}D_{x\theta} + \frac{\partial\lambda^T}{r\,\partial\,\theta}D_{\theta\theta} + \frac{\partial\lambda^T}{\partial r}D_{r\theta} \right)\tilde{U}\cdot n_\theta + \left(\frac{\partial\lambda^T}{\partial x}D_{xr} + \frac{\partial\lambda^T}{r\,\partial\,\theta}D_{\theta r} + \frac{\partial\lambda^T}{\partial r}D_{rr} \right)\tilde{U}\cdot n_r \right] ds - \int_D \left[\frac{\partial}{\partial x}\left(\frac{\partial\lambda^T}{\partial x}D_{xx} + \frac{\partial\lambda^T}{r\,\partial\,\theta}D_{\theta x} + \frac{\partial\lambda^T}{\partial r}D_{rx} \right) + \frac{\partial}{r\,\partial\,\theta}\left(\frac{\partial\lambda^T}{\partial x}D_{x\theta} + \frac{\partial\lambda^T}{r\,\partial\,\theta}D_{\theta\theta} + \frac{\partial\lambda^T}{\partial r}D_{r\theta} \right) + \frac{\partial}{\partial r}\left(\frac{\partial\lambda^T}{\partial x}D_{xr} + \frac{\partial\lambda^T}{r\,\partial\,\theta}D_{\theta r} + \frac{\partial\lambda^T}{\partial r}D_{rr} \right) \right] \tilde{U} dv \tag{A6}$$

Substituting Eq. (A6) into Eq. (A4) and collecting like terms yields

$$\int_{\partial D} \left[\lambda^T(\tilde{F} - \tilde{V}_x)n_x + \lambda^T(\tilde{G} - \tilde{U}v_g - \tilde{V}_\theta)n_\theta + \lambda^T(\tilde{H} - \tilde{V}_r)n_r + \left(\frac{\partial\lambda^T}{\partial x}D_{xx} + \frac{\partial\lambda^T}{r\,\partial\,\theta}D_{\theta x} + \frac{\partial\lambda^T}{\partial r}D_{rx} \right)\tilde{U}\cdot n_x + \left(\frac{\partial\lambda^T}{\partial x}D_{x\theta} + \frac{\partial\lambda^T}{r\,\partial\,\theta}D_{\theta\theta} + \frac{\partial\lambda^T}{\partial r}D_{r\theta} \right)\tilde{U}\cdot n_\theta + \left(\frac{\partial\lambda^T}{\partial x}D_{xr} + \frac{\partial\lambda^T}{r\,\partial\,\theta}D_{\theta r} + \frac{\partial\lambda^T}{\partial r}D_{rr} \right)\tilde{U}\cdot n_r \right] ds - \int_D \left[\frac{\partial\lambda^T}{\partial x}(A - A_v) + \frac{\partial\lambda^T}{r\,\partial\,\theta}(B - v_gI - B_v) + \frac{\partial\lambda^T}{\partial r}(C - C_v) + \lambda^T D + \frac{\partial}{\partial x}\left(\frac{\partial\lambda^T}{\partial x}D_{xx} + \frac{\partial\lambda^T}{r\,\partial\,\theta}D_{\theta x} + \frac{\partial\lambda^T}{\partial r}D_{rx} \right) + \frac{\partial}{r\,\partial\,\theta}\left(\frac{\partial\lambda^T}{\partial x}D_{x\theta} + \frac{\partial\lambda^T}{r\,\partial\,\theta}D_{\theta\theta} + \frac{\partial\lambda^T}{\partial r}D_{r\theta} \right) + \frac{\partial}{\partial r}\left(\frac{\partial\lambda^T}{\partial x}D_{xr} + \frac{\partial\lambda^T}{r\,\partial\,\theta}D_{\theta r} + \frac{\partial\lambda^T}{\partial r}D_{rr} \right) \right] \tilde{U} dv - \int_D \lambda^T f dv \tag{A7}$$

Adding Eq. (A7) to the gradient expression in Eq. (10) and collecting the domain integral terms with $\tilde{U}$, one has

$$-\int_D \left[\frac{\partial\lambda^T}{\partial x}(A - A_v) + \frac{\partial\lambda^T}{r\,\partial\,\theta}(B - v_gI - B_v) + \frac{\partial\lambda^T}{\partial r}(C - C_v) + \lambda^T D + \frac{\partial}{\partial x}\left(\frac{\partial\lambda^T}{\partial x}D_{xx} + \frac{\partial\lambda^T}{r\,\partial\,\theta}D_{\theta x} + \frac{\partial\lambda^T}{\partial r}D_{rx} \right) + \frac{\partial}{r\,\partial\,\theta}\left(\frac{\partial\lambda^T}{\partial x}D_{x\theta} + \frac{\partial\lambda^T}{r\,\partial\,\theta}D_{\theta\theta} + \frac{\partial\lambda^T}{\partial r}D_{r\theta} \right) + \frac{\partial}{\partial r}\left(\frac{\partial\lambda^T}{\partial x}D_{xr} + \frac{\partial\lambda^T}{r\,\partial\,\theta}D_{\theta r} + \frac{\partial\lambda^T}{\partial r}D_{rr} \right) \right] \tilde{U} dv$$

Choose the value of the adjoint variable in such a way so that the above domain integral vanishes, leading to the viscous adjoint equations,

$$\frac{\partial\lambda^T}{\partial x}(A - A_v) + \frac{\partial\lambda^T}{r\,\partial\,\theta}(B - v_gI - B_v) + \frac{\partial\lambda^T}{\partial r}(C - C_v) + \lambda^T D + \frac{\partial}{\partial x}\left(\frac{\partial\lambda^T}{\partial x}D_{xx} + \frac{\partial\lambda^T}{r\,\partial\,\theta}D_{\theta x} + \frac{\partial\lambda^T}{\partial r}D_{rx} \right) + \frac{\partial}{r\,\partial\,\theta}\left(\frac{\partial\lambda^T}{\partial x}D_{x\theta} + \frac{\partial\lambda^T}{r\,\partial\,\theta}D_{\theta\theta} + \frac{\partial\lambda^T}{\partial r}D_{r\theta} \right) + \frac{\partial}{\partial r}\left(\frac{\partial\lambda^T}{\partial x}D_{xr} + \frac{\partial\lambda^T}{r\,\partial\,\theta}D_{\theta r} + \frac{\partial\lambda^T}{\partial r}D_{rr} \right) = 0 \tag{A8a}$$

The above equation can be rearranged as follows:

$$(A - A_v)^T\frac{\partial\lambda}{\partial x} + (B - v_gI - B_v)^T\frac{\partial\lambda}{r\,\partial\,\theta} + (C - C_v)^T\frac{\partial\lambda}{\partial r} + P^T\left(\frac{\partial D_x}{\partial x} + \frac{\partial D_\theta}{r\,\partial\,\theta} + \frac{\partial D_r}{\partial r} \right) + D^T\lambda = 0$$

$$P = \frac{\partial U}{\partial U_v}, \quad U_v = (p,u,v,w,T)^T$$

$$D_x = (0,\sigma_{xx},\sigma_{\theta x}/r,\sigma_{rx},\phi_x)^T$$

$$D_\theta = (0,\sigma_{x\theta},\sigma_{\theta\theta}/r,\sigma_{r\theta},\phi_\theta)^T$$

$$D_r = (0,\sigma_{xr},\sigma_{\theta r}/r,\sigma_{rr},\phi_r)^T$$

$$\sigma_{xx} = \frac{2}{3}\mu\left[2\left(\frac{\partial\lambda_2}{\partial x} + u\frac{\partial\lambda_5}{\partial x} \right) - \left(\frac{\partial\lambda_3}{\partial\theta} + v\frac{\partial\lambda_5}{r\,\partial\,\theta} \right) - \left(\frac{\partial\lambda_4}{\partial r} + w\frac{\partial\lambda_5}{\partial r} \right) \right]$$

$$\sigma_{\theta\theta} = \frac{2}{3}\mu\left[2\left(\frac{\partial\lambda_3}{\partial\theta} + v\frac{\partial\lambda_5}{r\,\partial\,\theta} \right) - \left(\frac{\partial\lambda_2}{\partial x} + u\frac{\partial\lambda_5}{\partial x} \right) - \left(\frac{\partial\lambda_4}{\partial r} + w\frac{\partial\lambda_5}{\partial r} \right) \right]$$

$$\sigma_{rr} = \frac{2}{3}\mu\left[2\left(\frac{\partial\lambda_4}{\partial r} + w\frac{\partial\lambda_5}{\partial r} \right) - \left(\frac{\partial\lambda_3}{\partial\theta} + v\frac{\partial\lambda_5}{\partial\theta} \right) - \left(\frac{\partial\lambda_2}{\partial x} + u\frac{\partial\lambda_5}{\partial x} \right) \right]$$

$$\sigma_{x\theta} = \sigma_{\theta x} = \mu\left[\left(\frac{\partial\lambda_2}{r\,\partial\,\theta} + u\frac{\partial\lambda_5}{r\,\partial\,\theta} \right) + \left(r\frac{\partial\lambda_3}{\partial x} + v\frac{\partial\lambda_5}{\partial x} \right) \right]$$

$$\sigma_{xr} = \sigma_{rx} = \mu\left[\left(\frac{\partial\lambda_2}{\partial r} + u\frac{\partial\lambda_5}{\partial r} \right) + \left(\frac{\partial\lambda_4}{\partial x} + w\frac{\partial\lambda_5}{\partial x} \right) \right]$$

$$\sigma_{r\theta} = \sigma_{\theta r} = \mu\left[\left(\frac{\partial\lambda_4}{r\,\partial\,\theta} + w\frac{\partial\lambda_5}{r\,\partial\,\theta} \right) + \left(r\frac{\partial\lambda_3}{\partial r} + v\frac{\partial\lambda_5}{\partial r} \right) \right]$$

$$\phi_x = k\frac{\partial \lambda_5}{\partial x}, \quad \phi_\theta = k\frac{\partial \lambda_5}{r\,\partial\,\theta}, \quad \phi_r = k\frac{\partial \lambda_5}{\partial r} \tag{A8b}$$

2 Conservation of Adjoint Variable Weighted Fluxes. According to expression (13*b*), for two adjacent computational domains separated by an interface, each has a boundary integral term depending on the flow variable sensitivity $\tilde{U}$ along the interface. As Fig. 1 shows, if an interface is perpendicular to the x direction, then the boundary integral terms can be reduced as follows:

$$\frac{1}{Y_1}\int_{y1} \lambda^T A\tilde{U}dy - \frac{1}{Y_2}\int_{y2} \lambda^T A\tilde{U}dy \tag{A9}$$

The appearance of the pitch length accounts for the whole annulus effect. Expression (A9) depends on the flow variable sensitivity $\tilde{U}$. The adjoint method requires these two terms to vanish, namely,

$$\frac{1}{Y_1}\int_{y1} \lambda^T A\tilde{U}dy - \frac{1}{Y_2}\int_{y2} \lambda^T A\tilde{U}dy = 0 \tag{A10a}$$

This can be achieved in two ways. One is to make each of them vanish. This requires setting $\lambda^T A = 0$ at every point along an interface, as the flow variable sensitivity $\tilde{U}$ is not always zero along an interface. Because the Jacobian matrix A usually has a full rank, setting $\lambda^T A = 0$ is equivalent to setting $\lambda = 0$, which is sufficient but too much to satisfy Eq. (A10*a*). The other way is to satisfy Eq. (A10*a*) as a whole across the interface. This means that each of the two terms from the two sides of the interface may not be zero, but they equal each other and hence cancel out.

Equation (A10*a*) can be written in the following equivalent form:

$$\frac{1}{Y_1}\int_{y1} \lambda^T \tilde{F}dy - \frac{1}{Y_2}\int_{y2} \lambda^T \tilde{F}dy = 0 \tag{A10b}$$

The adjoint variable vector is independent of a design variable; therefore, one has

$$\lambda^T \tilde{F} = \widetilde{\lambda^T F}$$

Substituting the above into Eq. (A10*b*) yields

$$\frac{1}{Y_1}\int_{y1} \widetilde{\lambda^T F}dy - \frac{1}{Y_2}\int_{y2} \widetilde{\lambda^T F}dy = 0 \tag{A10c}$$

The interface geometry can be kept intact when a design variable is perturbed. Hence the differentiation operation and integration operation can exchange their sequences, resulting in the following equivalent equation:

$$\widetilde{\frac{1}{Y_1}\int_{y1} \lambda^T F dy} - \widetilde{\frac{1}{Y_2}\int_{y2} \lambda^T F dy} = 0 \tag{A10d}$$

The above equation can be further rearranged as follows by removing the differentiation operation:

$$\frac{1}{Y_1}\int_{y1} \lambda^T F dy - \frac{1}{Y_2}\int_{y2} \lambda^T F dy = 0 \tag{A11}$$

This is a scalar equation. It is satisfied by balancing all the corresponding terms across the interface, leading to the following five equations, with each one corresponding to one adjoint variable:

$$\frac{1}{Y_1}\int_{y1} \lambda_1(\rho u)dy - \frac{1}{Y_2}\int_{y2} \lambda_1(\rho u)dy = 0$$

$$\frac{1}{Y_1}\int_{y1} \lambda_2(\rho u^2 + p)dy - \frac{1}{Y_2}\int_{y2} \lambda_2(\rho u^2 + p)dy = 0$$

$$\frac{1}{Y_1}\int_{y1} \lambda_3(\rho uv)dy - \frac{1}{Y_2}\int_{y2} \lambda_3(\rho uv)dy = 0$$

$$\frac{1}{Y_1}\int_{y1} \lambda_4(\rho uw)dy - \frac{1}{Y_2}\int_{y2} \lambda_4(\rho uw)dy = 0$$

$$\frac{1}{Y_1}\int_{y1} \lambda_5(\rho Hu)dy - \frac{1}{Y_2}\int_{y2} \lambda_5(\rho Hu)dy = 0 \tag{A12}$$

The five equations in Eq. (A12) state that the adjoint variable weighted and circumferentially averaged fluxes of mass, momentum, and energy are conserved across an interface.

References

[1] Horlock, J. H., and Denton, J. D., 2005, "A Review of Some Early Design Practice Using Computational Fluid Dynamics and a Current Perspective," ASME J. Turbomach., **127**, pp. 5–13.

[2] de Vito, L., Van den Braembussche, R. A., and Deconinck, H., 2003, "A Novel Two-Dimensional Viscous Inverse Design Method for Turbomachinery Blading," ASME J. Turbomach., **125**, pp. 310–316.

[3] van Rooij, M. P. C., Dang, T. Q., and Larosiliere, L. M., 2007, "Improving Aerodynamic Matching of Axial Compressor Blading Using a Three-Dimensional Multistage Inverse Design Method," ASME J. Turbomach., **129**, pp. 108–118.

[4] Büche, D., Guidati, G., and Stoll, P., 2003, "Automated Design Optimization of Compressor Blades for Stationary, Large Scale Turbomachinery," ASME Paper No. GT2003-38421.

[5] Oyama, A., and Liou, M. S., 2004, "Transonic Axial-Flow Blade Optimization: Evolutionary Algorithms/Three-Dimensional Navier-Stokes Solver," J. Propul. Power, **20**(4), pp. 612–619.

[6] Keskin, A., Dutta, A. K., and Bestle, D., 2006, "Modern Compressor Aerodynamic Blading Process Using Multi-Objective Optimization," ASME Paper No. GT2006-90206.

[7] Yi, W., Huang, H., and Han, W., 2006, "Design Optimization of Transonic Compressor Rotor Using CFD and Genetic Algorithm," ASME Paper No. GT2006-90155.

[8] Lian, Y., and Liou, M. S., 2005, "Multi-Objective Optimization of Transonic Compressor Blade Using Evolutionary Algorithm," J. Propul. Power, **21**(6), pp. 979–987.

[9] Jameson, A., 1988, "Aerodynamic Design Via Control Theory," J. Sci. Comput., **3**(3), pp. 233–260.

[10] Nadarajah, S. K., and Jameson, A., 2000, "A Comparison of the Continuous and Discrete Adjoint Approach to Automatic Aerodynamic Optimization," AIAA Paper No. 00-0667.

[11] Duta, M. C., Shahpar, S., and Giles, M. B., 2007, "Turbomachinery Design Optimization Using Automatic Differentiated Adjoint Code," ASME Paper No. GT2007-28329.

[12] Thomas, J. P., Hall, K. C., and Dowell, E. H., 2003, "A Discrete Adjoint Approach for Modelling Unsteady Aerodynamic Design Sensitivities," AIAA Paper No. 03-0041.

[13] Giles, M. B., and Pierce, N. A., 2000, "An Introduction to the Adjoint Approach to Design," Flow, Turbul. Combust., **65**(3/4), pp. 393–415.

[14] Jameson, A., 2003, "Aerodynamic Shape Optimization Using the Adjoint Method," Lectures at the Von Karman Institute, Brussels.

[15] Reuther, J., Jameson, A., Farmer, J., Martinelli, L., and Saunders, D., 1996, "Aerodynamic Shape Optimization of Complex Aircraft Configurations via an Adjoint Formulation," AIAA Paper No. 96-0094.

[16] Kim, H. J., and Nakahashi, K., 2005, "Discrete Adjoint Method for Unstructured Navier-Stokes Solver," AIAA Paper No. 05-449.

[17] Nielsen, E. J., and Anderson, W. K., 1999, "Aerodynamic Design Optimization on Unstructured Meshes Using the Navier-Stokes Equations," AIAA J., **37**(11), pp. 1411–1419.

[18] Nadarajah, S. K., and Jameson, A., 2002, "Optimal Control of Unsteady Flows Using a Time Accurate Method," AIAA Paper No. 02-5436.

[19] Nadarajah, S. K., and Jameson, A., 2006, "Optimum Shape Design for Unsteady Three Dimensional Viscous Flows Using a Nonlinear Frequency Domain Method," AIAA Paper No. 06-3455.

[20] Arens, K., Rentrop, P., Stoll, S. O., and Wever, U., 2005, "An Adjoint Approach to Optimal Design of Turbine Blades," Appl. Numer. Math., **53**, pp. 93–105.

[21] Li, Y., Yang, D., and Feng, Z., 2006, "Inverse Problem in Aerodynamic Shape Design of Turbomachinery Blades," ASME Paper No. GT2006-91135.

[22] Yang, S., Wu, H., Liu, F., and Tsai, H., 2003, "Aerodynamic Design of Cascades by Using an Adjoint Equation Method," AIAA Paper No. 03-1068.

[23] Wu, H., Yang, S., and Liu, F., 2003, "Comparison of Three Geometric Repre-

sentation of Airfoils for Aerodynamic Optimization," AIAA Paper No. 2003-4095.
[24] Wu, H., Liu, F., and Tsai, H., 2005, "Aerodynamic Design of Turbine Blades Using an Adjoint Equation Method," AIAA Paper No. 05-1006.
[25] Papadimitriou, D. I., and Giannakoglou, K. C., 2006, "Compressor Blade Optimization Using a Continuous Adjoint Formulation," ASME Paper No. GT2006-90466.
[26] Corral, R., and Gisbert, F., 2006, "Profiled End-Wall Design Using an Adjoint Navier-Stokes Solver," ASME Paper No. GT2006-90650.
[27] Florea, R., and Hall, K. C., 2001, "Sensitivity Analysis of Unsteady Inviscid Flow Through Turbomachinery Cascades," AIAA J., **39**(6), pp. 1047–1056.
[28] Duta, M. C., Giles, M. B., and Campobasso, M. S., 2002, "The Harmonic Adjoint Approach to Unsteady Turbomachinery Design," Int. J. Numer. Methods Fluids, **40**, pp. 323–332.
[29] Denton, J. D., 1992, "The Calculation of Three-Dimensional Viscous Flow Through Multistage Turbomachines," ASME J. Turbomach., **114**, pp. 18–26.
[30] He, L., and Denton, J. D., 1994, "Three-Dimensional Time-Marching Inviscid and Viscous Solutions for Unsteady Flows Around Vibrating Blades," ASME J. Turbomach., **116**, pp. 469–476.
[31] He, L., Chen, T., Wells, R. G., Li, Y. S., and Ning, W., 2002, "Analysis of Rotor-Rotor and Stator-Stator Interferences in Multi-Stage Turbomachines," ASME J. Turbomach., **124**, pp. 564–571.
[32] He, L., and Ning, W., 1998, "An Efficient Approach for Analysis of Unsteady Viscous Flows in Turbomachines," AIAA J., **36**(11), pp. 2005–2012.
[33] Moffatt, S., Ning, W., Li, Y. S., Wells, R. G., and He, L., 2005, "Blade Forced Response Prediction for Industrial Gas Turbines," J. Propul. Power, **21**(4), pp. 707–714.
[34] Saxer, A. P., 1992, "A Numerical Analysis of 3D Inviscid Stator/Rotor Interactions Using Non-Reflecting Boundary Conditions," Gas Turbine Laboratory, Massachusetts Institute of Technology, Technical Report.
[35] Vatsa, V. N., 2000, "Computation of Sensitivity Derivatives of Navier-Stokes Equations Using Complex Variables," Adv. Eng. Software, **31**(8–9), pp. 655–659.
[36] Giles, M. B., and Pierce, N. A., 1998, "On the Properties of Solutions of the Adjoint Euler Equations," Sixth ICFD Conference on Numerical Methods for Fluid Dynamics, Oxford, UK.
[37] Dunker, R., Rechter, H., Starken, H., and Weyer, H., 1984, "Redesign and Performance Analysis of a Transonic Axial Compressor Stator and Equivalent Plane Cascades With Subsonic Controlled Diffusion Blades," ASME J. Eng. Gas Turbines Power, **106**, pp. 279–287.
[38] Wang, D. X., He, L., Li, Y. S., and Wells, R. G., 2010, "Adjoint Aerodynamic Design Optimization for Blades in Multistage Turbomachines—Part II: Validation and Application," ASME J. Turbomach. **132**(2), p. 021012.

Adjoint Aerodynamic Design Optimization for Blades in Multistage Turbomachines—Part II: Validation and Application

D. X. Wang
School of Engineering,
Durham University,
Durham DH1 3LE, UK

L. He
Department of Engineering Science,
Oxford University,
Parks Road,
Oxford OX1 3PJ, UK

Y. S. Li

R. G. Wells

Siemens Industrial Turbomachinery Ltd.,
Ruston House,
P.O. Box 1, Waterside South,
Lincoln LN5 7FD, UK

This is the second part of a two-part paper. First, the design-optimization system based on the adjoint gradient solution approach as described in Part I is introduced. Several test cases are studied for further validation and demonstration of the methodology and implementation. The base-line adjoint method as applied to realistic 3D configurations is demonstrated in the redesign of the NASA rotor 67 at a near-choke condition, leading to a 1.77% efficiency gain. The proposed adjoint mixing plane is applied to the redesign of a transonic compressor stage (DLR compressor stage) and an IGV-rotor-stator configuration of a Siemens industrial compressor at a single-operating point, both producing measurably positive efficiency gains. An examination on the choice of the operating mass flow condition as the basis for the performance optimization, however, highlights the limitation of the single-point approach for practical applications. For the three-row compressor configuration, a near peak-efficiency point based redesign leads to a measurable reduction in the choke mass flow, while a near-choke point based redesign leads to a significant performance drop in other flow conditions. Subsequently, a parallel multipoint approach is implemented. The results show that a two-point design optimization can produce a consistently better performance over a whole range of mass flow conditions compared with the original design. In the final case, the effectiveness of the present method and system is demonstrated by a redesign applied to a seven-row industrial compressor at the design point, leading to a remarkable 2.4% efficiency gain.
[DOI: 10.1115/1.3103928]

1 Introduction

Most turbomachines are of a multistage configuration. Nowadays, it is also a common practice to analyze flow field in multistage turbomachines with the aid of the flow mixing-plane approach, following Denton [1]. This provides an opportunity to perform design optimization for turbomachine blades in a multistage environment, preventing mismatch between adjacent rows that can occur when each blade row is redesigned in isolation.

In the past decade, the adjoint method has been established as an efficient method for gradient calculations for design optimization with a very large number of design variables for a very small number of objective functions [2]. However, the applications of the adjoint method in turbomachinery design optimization have been to date restricted to single blade row designs. The first part of the two-part paper [3] describes the development of a proposed adjoint mixing-plane treatment. This treatment enables the adjoint equations to be solved in a multibladerow environment, making it possible to perform turbomachinery blading design optimization in a multistage environment based on an adjoint method. Some preliminary verifications and validations of the adjoint method are presented in Part I [3]. Here, in the second part of the paper, the main aspects of the design system are described, followed by presentations of several validation and application case studies.

2 Objective Function

For the case studies to be presented, the design target is to increase the blade isentropic efficiency while applying constraints to the mass flow rate and stagnation pressure ratio. The constraints are set to limit the mass flow rate and the stagnation pressure ratio changes to less than 0.5%. Although the design target is to increase isentropic efficiency, this is achieved by minimizing the entropy generation rate. The entropy generation rate, as used by Oyama and Liou [4], has a much simpler expression than that of isentropic efficiency. This reduces complexity in deriving objective function related terms for solving the corresponding adjoint equations. The objective function for design optimization is a weighted sum of the two aforementioned constraints and the entropy generation rate, taking the following formulation

$$I = \frac{s}{s_0} + \sigma_1\left(\frac{\dot{m}}{\dot{m}_0} - 1\right)^2 + \sigma_2\left(\frac{\pi}{\pi_0} - 1\right)^2 \tag{1}$$

The definition for the entropy generation rate s in the above is given by

$$s = \frac{\int_e \rho u \frac{p}{\rho^r} ds_x}{\int_e \rho u ds_x} - \frac{\int_i \rho u \frac{p}{\rho^r} ds_x}{\int_i \rho u ds_x}$$

where e denotes the exit plane of a computational domain, and i denotes the inlet plane of a computational domain. The mass flow rate is the arithmetic average of the mass flow rate integrated at the exit and inlet of a computational domain. The stagnation pressure ratio is defined as the ratio of the mass averaged stagnation pressure at the exit to that at the inlet. The subscript "0" denotes the initial values. σ_1 and σ_2 are the weighting factors taking following values for the cases studied

$$\sigma_1 = \sigma_2 = 100 \quad \text{for NASA rotor 67}$$

Contributed by the International Gas Turbine Institute of ASME for publication in the JOURNAL OF TURBOMACHINERY. Manuscript received July 17, 2008; final manuscript received: February 9, 2009; published online January 13, 2010. Review conducted by David Wisler. Paper presented at the ASME Turbo Expo 2008: Land, Sea and Air (GT2008), Berlin, Germany, June 9–13, 2008.

$$\sigma_1 = \sigma_2 = 50 \quad \text{for DLR stage}$$

$$\sigma_1 = \sigma_2 = 500 \quad \text{for Siemens compressor}$$

Different values of σ_1 and σ_2 will usually lead to different designs as also indicated in Ref. [5]. A good choice of these values usually needs some trial and error.

3 Shape Parametrization

Shape parametrization plays a very important role in turbomachinery blade aerodynamic design optimization [6], and it can be a separate research topic [7,8]. With many different approaches for blade shape parametrization appearing in the open literature, what is the best way to parametrize turbomachinery blades remains an open question. Bezier polynomials were used by Arens et al. [9], Büche et al. [10], Benini [11], Sieverding [12], and Lotfi et al. [13]; B splines were adopted by Anderson and Venkatakrishnan [14] and Oyama and Liou [4]. Aerodynamic modes such as sweep and lean [15–17] are a popular choice to reduce the number of design variables.

Instead of parametrizing a blade shape itself, the Hicks–Henne functions were used by Yang et al. [18] to parametrize perturbations to a blade shape. This shape perturbation parametrization approach has been adopted in this research work using the Hicks–Henne function and its variants. Two sets of hump functions are used to parametrize perturbations to tangential coordinates of mesh points on a blade surface: one is the 2D Hicks–Henne functions expressed in Eq. (2), which is a variant of those used in Ref. [18], and the other is given in Eq. (3). The Hicks–Henne functions (2) are applied to mesh points, which are not leading edge or trailing edge or casing section or hub section mesh points, while the other ones (3) are used for those mesh points where (the leading edge, trailing edge, casing section, and hub section mesh points) Hicks–Henne functions fail (x_d or r_d cannot be one or zero in Eq. (2)). The hump functions (2) and (3) determine the amount of perturbation to coordinates of other mesh points when the tangential coordinate of a design mesh point is perturbed

$$\delta_{r\theta} = a \sin^{b_r}(\pi r^{\ln 0.5/\ln r_d}) \cdot \sin^{b_x}(\pi x^{\ln 0.5/\ln x_d}) \tag{2}$$

$$\delta_{r\theta} = a \cdot \sin^{b_r}\left[\frac{\pi}{2}(1 - |r_d - r|)\right] \cdot \sin^{b_x}\left[\frac{\pi}{2}(1 - |x_d - x|)\right] \tag{3}$$

where x is the reduced axial coordinate of a mesh point along an axially running grid line on which the mesh point resides, and r is the reduced radial coordinate of a mesh point along a radially running grid line on which the mesh point resides. The values of x are 0 and 1 at the leading edge and trailing edge, respectively. The value of r is 0 and 1 at the hub and casing section, respectively. x_d and r_d are the reduced axial and radial coordinates of a design mesh point. b_x and b_r control the influence of perturbation to coordinates of a design mesh point on other mesh points. The bigger the value of b, the more local the hump functions will be. a is a design variable and determines the amount of perturbation to the tangential coordinate of a design mesh point. On a blade surface, if it is densely populated with design mesh points, then each hump function can be very local by choosing a big value of b. Otherwise, the hump functions need a small value of b to be more globally smooth. In addition, the blade tangential thickness is kept constant during a design process to avoid producing unrealistically thin blades. The mesh points on a blade span section are also allowed to move along axially running grid lines to accommodate blade sweep effect. When one radial mesh section is perturbed in the axial direction along an axially running grid line, the perturbations to other radial sections are determined according to the following Hicks–Henne function

$$\delta_x = a \sin^{b_r}(\pi r^{\ln 0.5/\ln r_d}) \tag{4}$$

The resultant perturbation to radial coordinates of mesh points is determined through ensuring that the perturbed blade span section moves along the axially running grid line on which this span section resides. Finally, if a blade has a circle fitted around its leading edge, mesh points on the leading edge circle are not allowed to be taken as design mesh points. However, the coordinates of these mesh points will still be changed due to the perturbation to other mesh points to preserve the blade round leading edge shape.

4 Design-Optimization Procedure

The search procedure used in this work is the steepest descent method in which a small step is taken in the negative gradient direction. The step size is given by the following empirical rule. Based on the gradient of an objective function to all design variables, an arbitrary step size (usually big enough to avoid excessive rounding errors) is used initially to calculate perturbations to the coordinates of all the mesh points. Then the maximum perturbation is found and all the perturbation will be scaled to such an extent that the maximum perturbation will be equal to a specified value, say, 0.1% of a blade chord. In this way, a big perturbation, which may result in drastic change in a blade profile in one design cycle, will be avoided.

A design-optimization process is broken down into the following procedures and also shown schematically in the flow chart of Fig. 1.

Step 1: Problem setup. This is the starting point of a design optimization. It includes specification of the initial blade geometry, boundary condition, objective functions and constraints, design variables, etc.

Step 2: Mesh generation. A mesh is generated in an algebraic way that is very fast according to the specified blade geometry.

Step 3: Solve flow equation. The flow equation is solved to obtain the flow solution, which is used to evaluate the performance of the current design and provides information for following steps.

Step 4: Solve adjoint equation. Based on the flow solution, the adjoint equation is solved. The adjoint solution together with the flow solution provides information for the evaluation of gradients of the objective function to design variables.

Step 5: Calculate gradient. Gradients of an objective function to design variables can be obtained with the flow and adjoint solutions and mesh perturbation very efficiently (see details in Sec. 5 of Part 1).

Step 6: Perturb geometry and search. The step size determining the amount of change made to a base-line blade geometry is calculated according to the empirical rule described at the beginning of this section. According to the steepest descent method, the blade geometry is changed at the opposite direction of gradients of an objective function to be minimized.

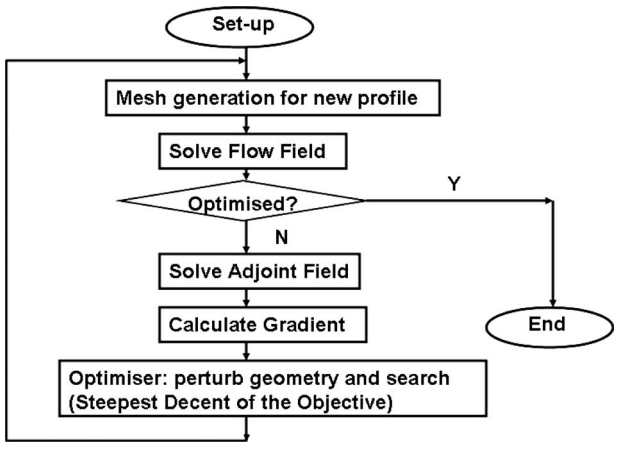

Fig. 1 Flow chart of a single-operating-point design optimization

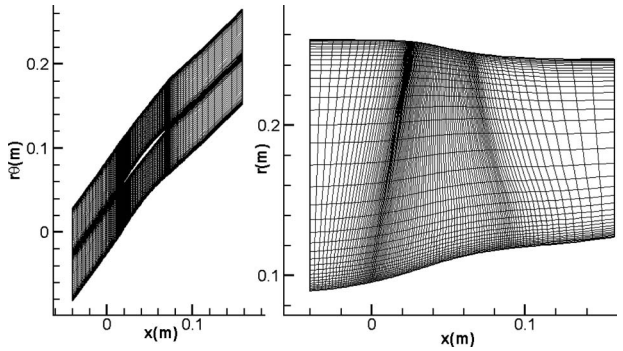

Fig. 2 Meridional view and blade to blade view of the NASA rotor 67 mesh

The above steps 2–6 will repeat until a certain stopping criterion is reached.

5 Results and Discussion

This section presents four design-optimization cases: the redesign of NASA rotor 67 [19], the redesign of the transonic DLR compressor stage [20], and redesigns of the IGV-rotor-stator configuration and a seven-row configuration of a Siemens industrial compressor [21]. For each case, comparisons of the calculated flow results with experimental data are made to demonstrate the quality of the flow field simulation by the present flow solver. The redesign of NASA rotor 67 demonstrates the capability of the design system for its application in a single row environment and lays down the basis for design optimization in a multirow environment. The other three cases demonstrate the capability of the design system for design optimization in a multirow environment.

5.1 Redesign of NASA Rotor 67. NASA rotor 67 is an undampered low-aspect-ratio design and is the first stage rotor of a two-stage fan. The rotor design pressure ratio is 1.63 at a mass flow rate of 33.25 kg/s. The design rotational speed is 16,043 rpm, which yields a tip speed of 429 m/s and an inlet tip relative Mach number of 1.38. The rotor has 22 blades and an aspect ratio of 1.65 (based on average span/root axial chord). The rotor solidity varies from 3.11 at the hub to 1.29 at the tip. The inlet and exit tip diameters are 51.4 cm and 48.5 cm, respectively, and the inlet and exit hub/tip radius ratios are 0.375 and 0.478, respectively. The rotor was experimentally investigated in NASA Lewis Research Center to produce data for validating numerical results [19] and has been a popular test case for design optimization [4,16,22,23].

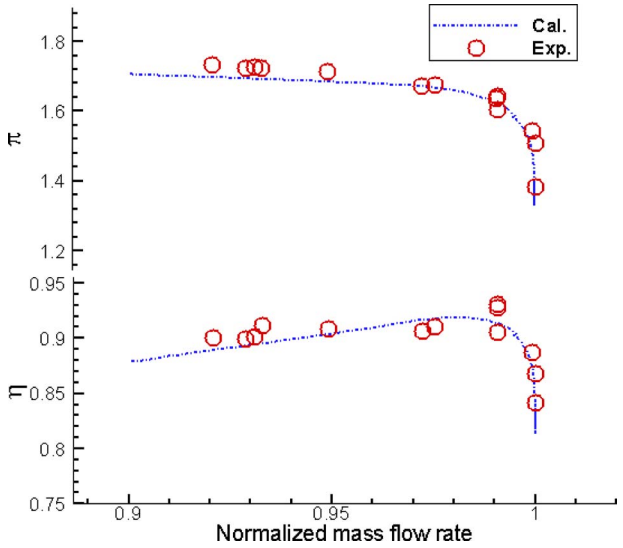

Fig. 3 Performance map comparison of the numerical results with experimental data (NASA rotor 67)

Table 1 Performance comparison between the original and optimized blades for the NASA rotor 67 redesign

	Mass flow rate (kg/s)	Pressure ratio	Isentropic efficiency (%)
Original	34.32	1.6536	90.50
Optimized	34.37	1.6523	92.27
Change	+0.15%	−0.08%	+1.77

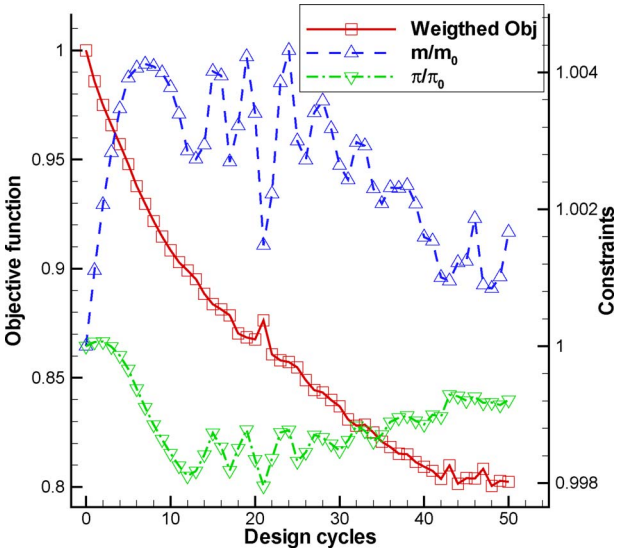

Fig. 4 Evolution of the objective function and two constraints with design cycles (NASA rotor 67 redesign)

A single passage computational domain with a mesh density of $110\times49\times37$ in the axial, pitchwise, and radial directions has been used to model the blade. Figure 2 shows the meridional view and blade to blade view of the mesh.

The calculated performance map of NASA rotor 67 is compared with the experimental data in Fig. 3. The mass flow rate is normalized by its choke mass flow rate as suggested in Ref. [24]. Both the calculated pressure ratio and efficiency show a fair agreement with their experimental values, except that pressure ratio and efficiency are underpredicted for operating points close to stall.

The design optimization is carried out at a near-choke operating point[1] with its performance listed in Table 1. 143 design variables with 13 design variables for each of 11 spanwise sections are used to parametrize the blade shape perturbations. The 11 spanwise mesh sections divide the blade span into 10 approximately equal intervals. 48 design cycles are completed over 63 h.[2] The evolution of the objective function and two constraints with design cycles is depicted in Fig. 4. The objective function is reduced by 19% in total. The overshoot in the objective function curve at the 21st design cycle corresponds to an increase in entropy generation rate and a severe violation of the pressure ratio constraint and a much better satisfaction of the mass flow rate constraint relative to its preceding design cycle, as also revealed by the corresponding spikes in the two constraint curves.

Table 1 compares the performance between the original and optimized blades at the near-choke operating point. The optimized

[1]The normalized mass flow rate at this operating point is 0.995.

[2]All the single-operating point design optimizations were run on a single 2.2 GHz Opteron processor.

blade increases the blade isentropic efficiency by 1.77% point with 0.15% increase in the mass flow rate and 0.08% reduction in the pressure ratio. This can be considered as a fairly good redesign in terms of efficiency gain and the satisfaction of constraints.

Figure 5 depicts the spanwise distribution of the circumferentially averaged isentropic efficiency, stagnation pressure ratio, and stagnation temperature ratio at the rotor exit. The local efficiency is increased over the whole span with greater increase in the tip and hub regions. The local stagnation pressure ratio and stagnation temperature ratio are raised in the hub region and lowered in the tip region shifting blade load from the tip region toward the hub region.

In the original flow field, as Fig. 6 reveals, there is a strong passage shock normal to the casing. However, in the flow field of the optimized blade, on the blade pressure surface, there are two shocks that are much weaker than that in the original flow field. On the blade suction surface (Fig. 7), compared with the original flow field, the optimized flow field has a shock that is slightly weaker and is pushed upstream a little. The reduction in the shock strength accounts for the main efficiency gain.

The blade geometry change against the original design is shown in Fig. 8. In the hub region, the blade section has increased camber, which is in line with the increased blade load in hub region as revealed in Fig. 5. There is also significant geometry change from the midspan to tip regions where the tip sections have been changed from an MCA type into a reverse-cambered type of profile shape. Although the geometric change is small in the midspan region, it is relatively larger in the hub and tip regions and it is much larger than manufacturing tolerance. The geometric change is normally difficult to be achieved using a conventional manual design approach.

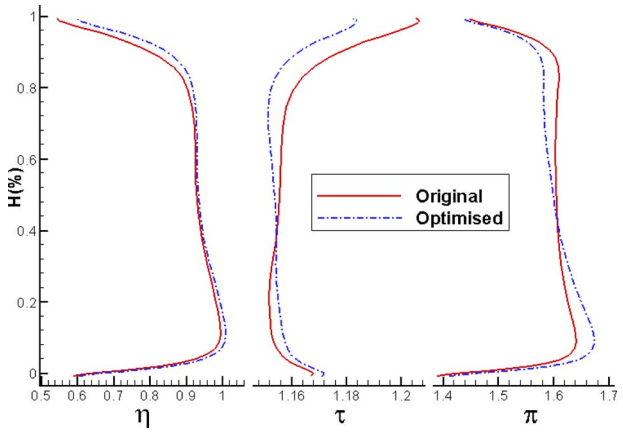

Fig. 5 Spanwise distributions of efficiency, stagnation temperature ratio and stagnation pressure ratio at the blade exit (NASA rotor 67 redesign)

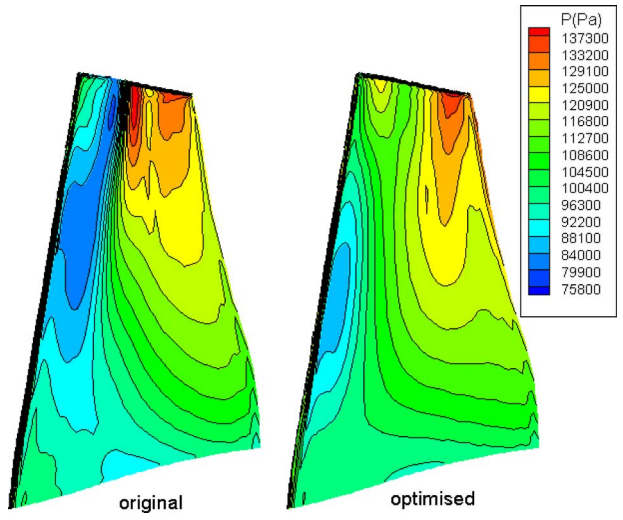

Fig. 6 Pressure contours on the blade pressure surface (NASA rotor 67 redesign)

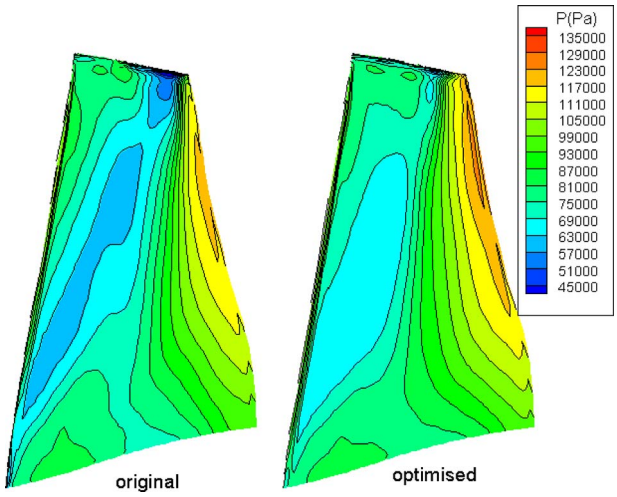

Fig. 7 Pressure contours on the blade suction surface (NASA rotor 67 redesign)

5.2 Redesign of DLR Transonic Stage. The DLR stage [20] is a transonic axial flow compressor stage without inlet guide vanes. The stage was designed for a rotational speed of 20,260 rpm with a stagnation pressure ratio of 1.51 at an equivalent mass flow rate of 17.3 kg/s. The rotor inlet diameter is 39.8 cm with a hub/tip ratio of 0.51. The rotor consists of 28 MCA-profiled blades with a tip chord length of 6.0 cm. The blade solidities vary between 2 and 1.34 from hub to tip. The stator has 31 controlled diffusion blades with solidity varying from 1.68 at the hub to 1.05 at the tip.

The single passage H mesh consists of two rows with a mesh density of $110\times37\times39$ for the rotor and $90\times35\times39$ for the stator in the axial, circumferential, and radial directions, respectively. The tip and hub clearances are treated by the simple pinched-up approach and three cells are used to accommodate a gap. The meridional view and blade to blade view of the mesh are

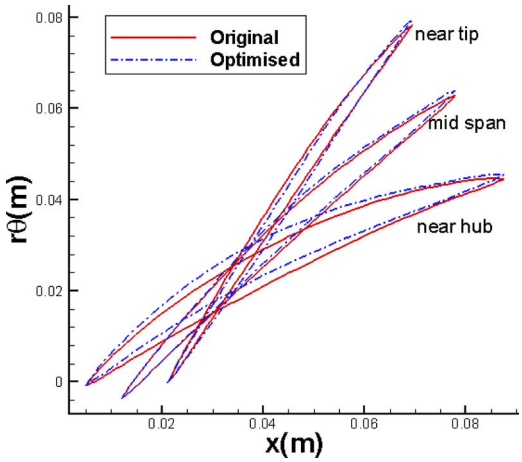

Fig. 8 Comparison of blade geometry between NASA rotor 67 and the optimized blade

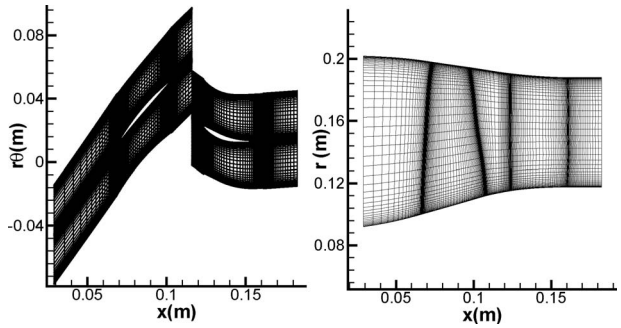

Fig. 9 Blade-to-blade and meridional view of the DLR stage mesh

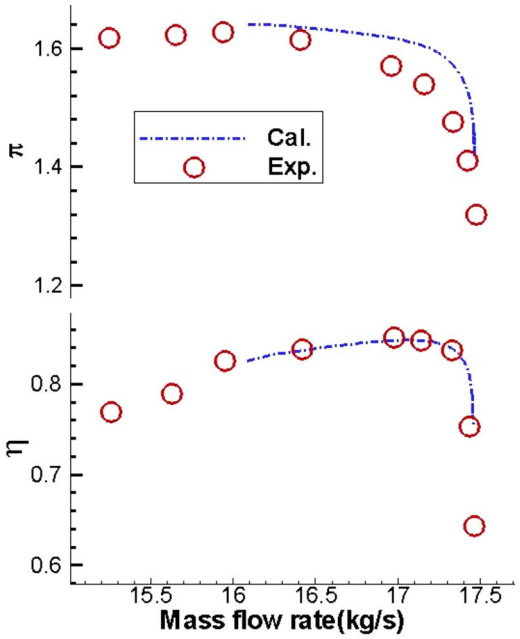

Fig. 10 Performance map comparison of the numerical results with experimental data for the DLR stage

shown in Fig. 9.

Figure 10 compares the calculated and experimental performance maps. As can be seen, the calculated flow range is smaller than the experimental one. From the experimental pressure ratio curve, one can see that the pressure ratio decreases with the reduction in mass flow rate, which indicates the occurrence of large scale flow separation in the tested compressor. Convergence in this flow range with a negative slope of pressure ratio characteristics is usually difficult with the current flow solver using a single passage computational domain due to a numerical surge. Except for that, the calculated efficiency and pressure ratio versus mass flow rate curves agree reasonably well with the experimental data. The calculated choke mass flow rate is very close to the experimental value.

Table 2 Performance comparison between original and optimized blades for the DLR stage redesign

	Mass flow rate (kg/s)	Pressure ratio	Isentropic efficiency (%)
Original	17.07	1.5987	85.11
Optimized	17.07	1.5987	85.83
Change	0.0%	0.0%	+0.72

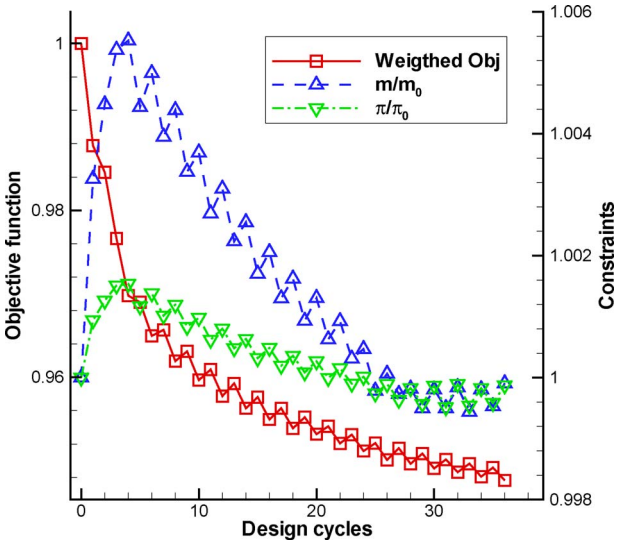

Fig. 11 Evolution of the objective function and two constraints with design cycles (DLR stage redesign)

The redesign is carried out at the stage peak-efficiency operating point of the original design with its performance listed in Table 2. There are 154 design variables with 14 design variables on each of 11 spanwise sections parametrizing perturbations to the rotor blade shape and 121 design variables with 11 design variables on each of 11 spanwise sections to perturb the stator blade shape.

Thirty-six design cycles are finished within 4 days. The evolution of the objective function as well as two constraints with design cycles is depicted in Fig. 11. 80% of the total drop in the objective function is achieved within the first 10 design cycles; the remaining 26 design cycles consume most of the elapsed time with only 20% drop. This is probably due to the shortcoming of the steepest descent method, which converges slowly when the curvature of the design space is quite different in different directions. The constraints are violated significantly for the first few design cycles and are better satisfied when the design process converges.

The performance of the original blade and the optimized design is compared in Table 2. The optimized design has an efficiency that is 0.72% higher than its original counterpart, while it has the

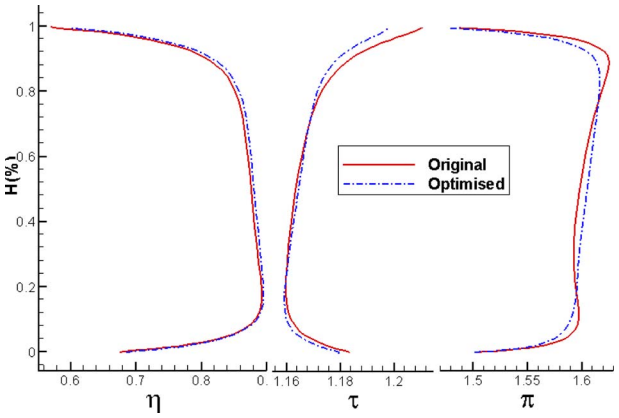

Fig. 12 Spanwise distributions of circumferentially averaged efficiency, stagnation temperature, and pressure ratios at the compressor's exit (DLR stage redesign)

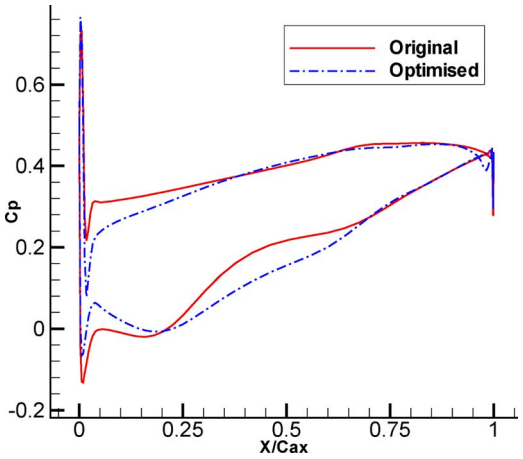

Fig. 13 Pressure coefficient distributions at 25% span of the original and optimized DLR rotors

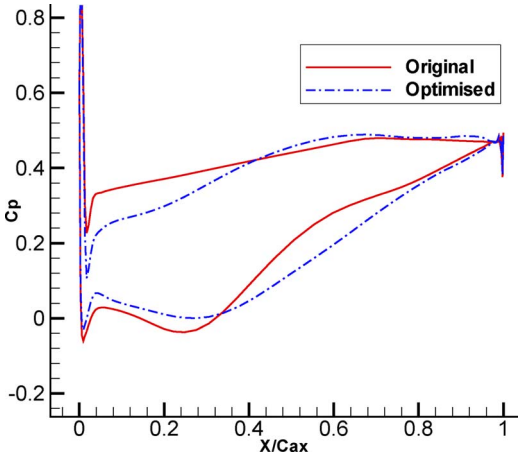

Fig. 14 Pressure coefficient distributions at 50% span of the original and optimized DLR rotors

same mass flow rate and pressure ratio as the original values.

It is shown in Fig. 12 where for the optimized blades there is an increase in isentropic efficiency over the whole span at the stage exit. The pressure ratio and temperature ratio are decreased in both the hub and tip regions and increased in the midspan region suggesting spanwise shift of load toward the midspan region from both endwall regions.

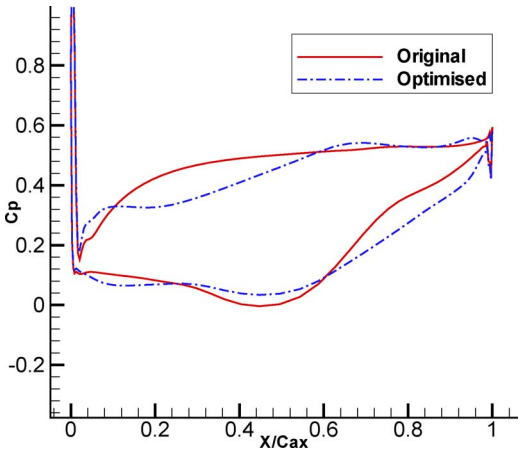

Fig. 15 Pressure coefficient distributions at 85% span of the original and optimized DLR rotors

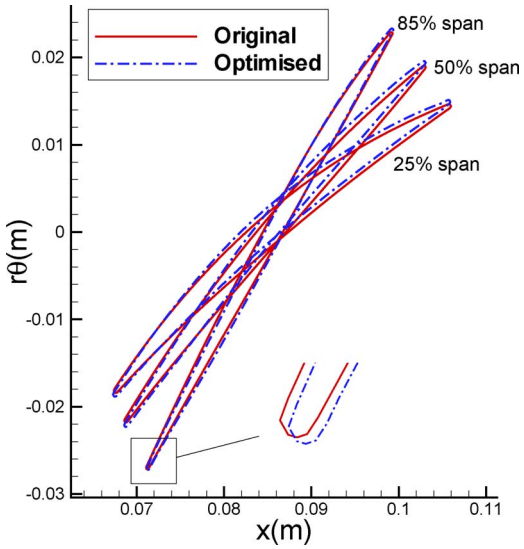

Fig. 16 Comparison of blade geometry between the DLR rotor and the optimized rotor

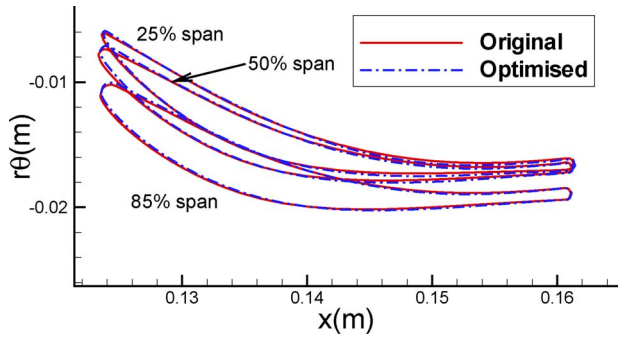

Fig. 17 Comparison of blade geometry between the DLR stator and the optimized stator

Examination of the pressure coefficient distributions on the three span locations of the rotor (Figs. 13–15) suggests that there is also a chordwise load shift from the leading edge toward the trailing edge. As Figs. 13 and 14 suggest, near the hub and midspan regions, blade load is shifted mainly from the leading edge region to the midchord region. While in the tip region, the load shift is from the blade leading edge region to the trailing edge region. The achievement of the efficiency increase in this case is believed to be through the reduction in secondary flow near the endwall regions (loading shift from both endwall regions to the midspan region as revealed in the pressure ratio spanwise distribution in Fig. 12).

The geometry of the original rotor and stator is compared with that of the optimized blades at three span locations: 25% span, 50% span, and 85% span (Figs. 16 and 17). The major geometry change is seen to occur in the rotor blade with most change taking place near the rotor blade trailing edge. During the design process, the round rotor leading edge shape (Fig. 16) is well preserved.

5.3 Redesign of the IGV-Rotor-Stator Configuration of an Industrial Compressor. The Siemens three-stage transonic test compressor is a high specific flow and high pressure ratio compressor designed using 3D aerodynamic design methods to achieve high performance [21]. The compressor has a design mass flow of 26.3kg/s at a pressure ratio of 3:1. The compressor has

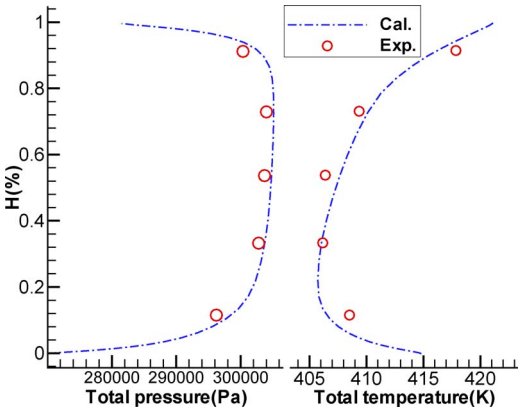

Fig. 18 Spanwise distributions of stagnation pressure and stagnation temperature at the Siemens three-stage compressor exit

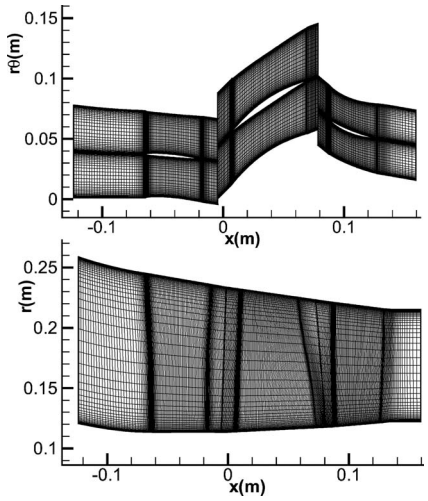

Fig. 20 Blade to blade view (upper) and meridional view (lower) of the IGV-R1-S1 configuration mesh

been extensively tested both aerodynamically and aeromechanically in the rig to evaluate its aerodynamic performance and structural integrity.

For the work reported in this paper, the flow field inside the machine at its design point is simulated. The calculated spanwise distribution of stagnation pressure and temperature at the compressor exit is in close agreement with the experimental data (Fig. 18). The calculated casing static pressure distribution also has a close agreement with the experimental data (Fig. 19).

The first three rows, including the IGV, the first rotor and first stator, are taken out of the seven-row Siemens compressor. The computational domain after the first stator is extended to allow for the application of a subsonic exit boundary condition. Figure 20 shows the blade to blade view and meridional view of the three-row mesh. The mesh has 49 mesh points in the radial direction and 37 mesh points in the circumferential direction for all the three rows. The IGV, rotor 1, and stator 1 have 125, 124, and 117 mesh points in the axial direction. In the design-optimization process, the IGV remains unchanged, 187 design variables are used to parametrize perturbations to the rotor blade shape, and 154 design variables are used for the stator blade shape. These design variables are distributed on 11 radial mesh sections; therefore, each section has 17 and 14 design variables for the rotor and the stator, respectively.

For practical applications, any optimized redesign will need to produce a better performance at a chosen operating point without sacrificing those at other operating point. This issue is highlighted in this case.

In the first instance, the three-row configuration is redesigned at the stage peak-efficiency point to further increase its isentropic efficiency while maintaining its mass flow rate and pressure ratio. As Figs. 21 and 22 show, although the optimized design delivers an efficiency gain of about 1.0% point at the stage peak-efficiency point, this design has noticeable lower choke mass flow rate. It is expected to get a redesign, which can not only deliver higher efficiency at the original stage peak-efficiency operating point but also maintain the choke mass flow rate. It is then conjectured that this kind of design might be obtained by performing the design optimization at a near-choke operating point. The redesign at the near-choke point deteriorates its performance dramatically with decreasing mass flow rate from the near-choke value, although it increases the efficiency and the choke mass flow rate (Figs. 21 and 22).

The above observations lead to the consideration of introducing a parallel multipoint implementation of the base-line optimization

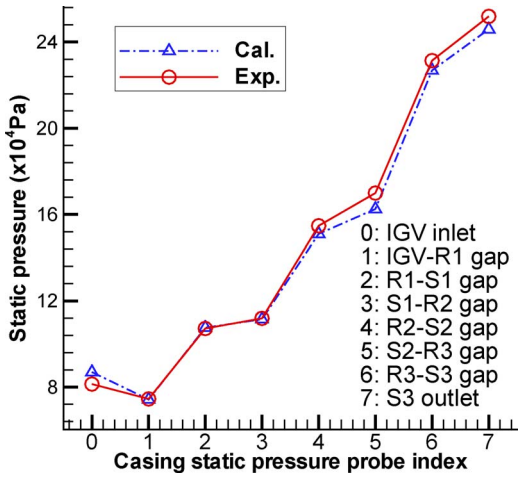

Fig. 19 Casing static pressure distributions inside the Siemens three-stage compressor

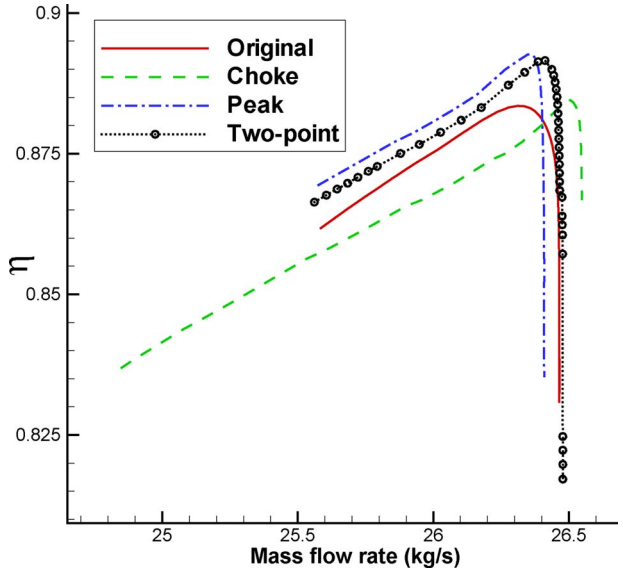

Fig. 21 Efficiency versus mass flow of different designs (IGV-R1-S1 configuration redesign)

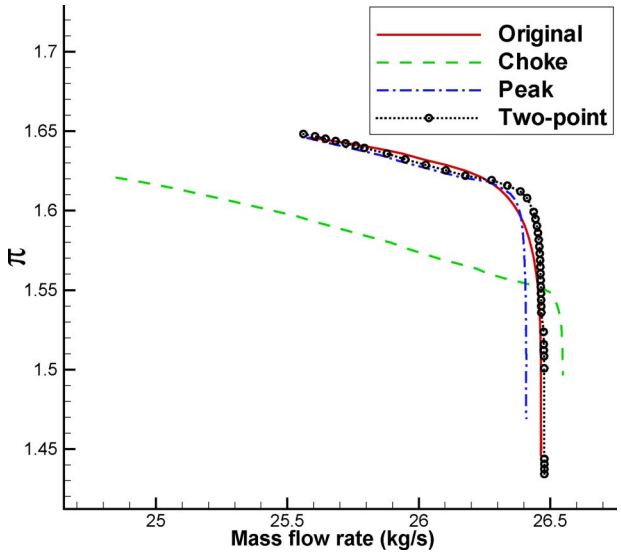

Fig. 22 Pressure ratio versus mass flow of different designs (IGV-R1-S1 configuration redesign)

procedure. In the first instance, it is of interest to examine the impact of simultaneous design optimization of just the two points at the peak-efficiency operating point and at the near-choke operating point.

For this two-operating-point design optimization, the total objective function is simply a linear combination of the objective functions (1) at the two operating points of interest.

$$I = \sigma_{\text{peak}} \cdot I_{\text{peak}} + \sigma_{\text{choke}} \cdot I_{\text{choke}} \tag{5}$$

The aim of this redesign is to increase the efficiency at the stage peak-efficiency point of the original design while the choke mass flow rate is maintained. This is to suggest that more priority should be put at the peak-efficiency point; therefore, σ_{peak} is assigned a value of 0.8 and $\sigma_{\text{choke}}=0.2$. The gradient of the total objective function to a design variable is expressed by

$$\frac{dI}{d\alpha} = \sigma_{\text{peak}} \cdot \frac{dI_{\text{peak}}}{d\alpha} + \sigma_{\text{choke}} \cdot \frac{dI_{\text{choke}}}{d\alpha} \tag{6}$$

$dI_{\text{peak}}/d\alpha$ can be calculated from the flow solution and the adjoint solution at the peak-efficiency point only, and $dI_{\text{choke}}/d\alpha$ can be determined from the flow solution and the adjoint solution at the near-choke point only. This means the two gradients can be calculated separately and then combined linearly to form the gradient of the total objective function. This gives rise to the parallelization of the code, which is easy to implement and can result in considerable real time saving. Therefore, the original serial code for single-operating point design optimization is parallelized using the message passing interface (MPI) standard to enable multiple operating points design optimization to be carried out (Fig. 23). Though only two operating points are considered in this demonstration case, the parallelized code can handle as many operating points as one likes. In practice, two or three operating points might be normally enough to be considered in a design optimization guaranteeing a design of a better performance map.

From Figs. 21 and 22, by comparing the two-operating-point design with the single-point design and the original one at the stage peak-efficiency point, one can see clearly that the performance curves of the two-point design are shifted toward higher mass flow rate and the original design choke margin is maintained as a result of the design constraint on the choke mass flow rate. The peak-efficiency point of the two-point design has also been shifted toward higher mass flow and it differs from the original stage peak-efficiency point. The mass flow versus pressure ratio characteristic of the two-point design is steeper than the original design. The maximum efficiency gain seems to be achieved between the two chosen operating points. The peak efficiency has been improved by 1.0% point. Overall, the two-point design optimization is a better design than any of the two single-point designs.

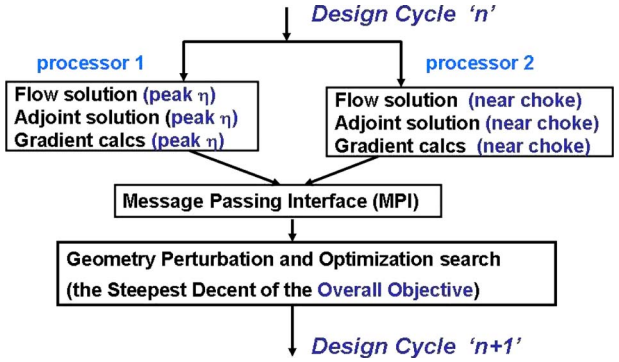

Fig. 23 Flow chart of a parallel two-operating-point design optimization

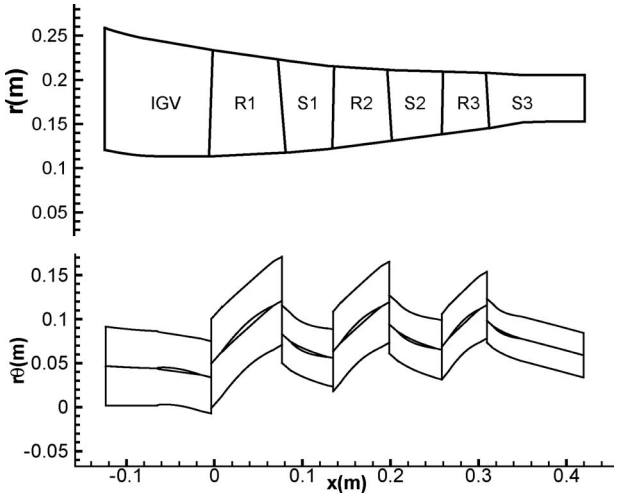

Fig. 24 Meridional view and blade to blade view of the Siemens three-stage compressor computational domain

5.4 Redesign of Siemens Three-Stage Compressor. In this case, the computational domain consists of seven rows and its blade to blade view of a midspan section and meridional view are shown in Fig. 24. Each row has 45 mesh points in the circumfer-

Table 3 Number of axial mesh points and design variables for each row of the Siemens three-stage compressor

	IGV	R1	S1	R2	S2	R3	S3
Number of axial mesh points	125	124	102	107	117	111	124
Number of design variables	0	187	154	165	187	165	165

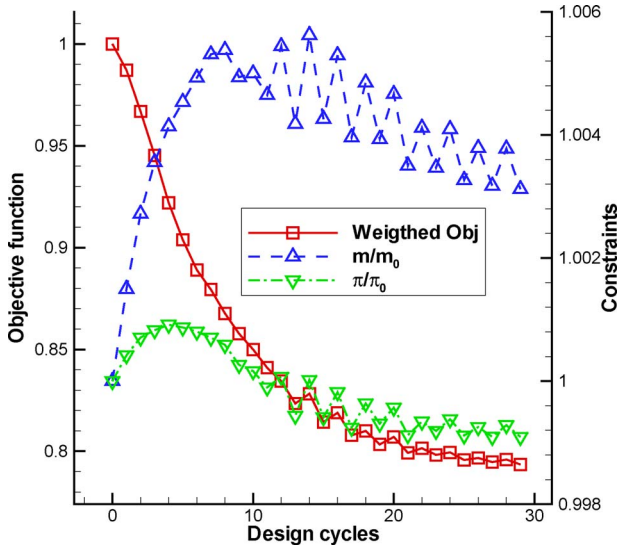

Fig. 25 Evolution of the objective function and two constraints with design cycles (Siemens three-stage compressor redesign)

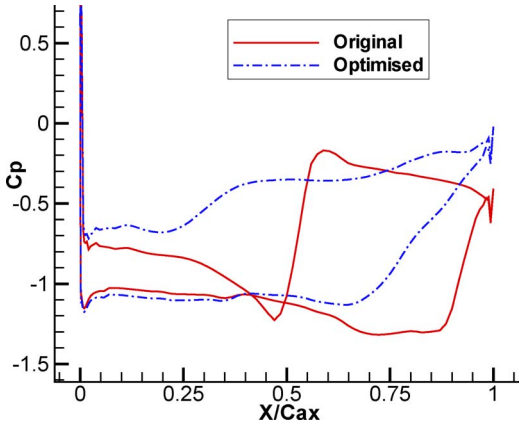

Fig. 27 Pressure coefficient distributions at 85% span of Rotor 1 (Siemens three-stage compressor redesign)

Table 4 Performance comparison between original and optimized blades for the Siemens three-stage compressor redesign

	Mass flow rate (kg/s)	Pressure ratio	Isentropic efficiency (%)
Original	26.46	2.9885	86.81
Optimized	26.55	2.9860	89.28
Change	+0.34%	−0.08%	+2.47

ential direction and 37 in the radial direction. The number of mesh points in the axial direction varies for different rows and listed in Table 3. Due to the large number mesh points, the computational mesh is not shown here.

In the design optimization, the IGV remains unchanged as for the three-row design optimization, while the other six rows are allowed to be changed, with the number of design variables for each row also listed in Table 3, resulting in 1023 design variables in total. For each blade row, the design variables are distributed on 11 spanwise sections with the same number of design variables for each section. A single-point design optimization is carried out at the original design point of the compressor. Twenty-nine design cycles are completed over 11 days. The history of the objective function and the two constraints with design cycles is shown in Fig. 25, where a 20% reduction in the objective function is obtained. The behavior of the two constraints with design cycles is qualitatively the same to the other case studies: there is more violation at the beginning and the constraints are much better met when the objective function converges.

The performance comparison between the original compressor and the optimized one at the chosen operating point is presented in Table 4. The optimized design has an efficiency that is 2.47% point higher than the original one with 0.34% increase in the mass flow rate and 0.08% decrease in the pressure ratio.

Figure 26 compares the spanwise distribution of circumferentially averaged efficiency, stagnation temperature ratio, and stagnation pressure ratio at the compressor exit. The optimized design has higher efficiency than the original design over the whole span. The stagnation temperature ratio in the optimized design is lower

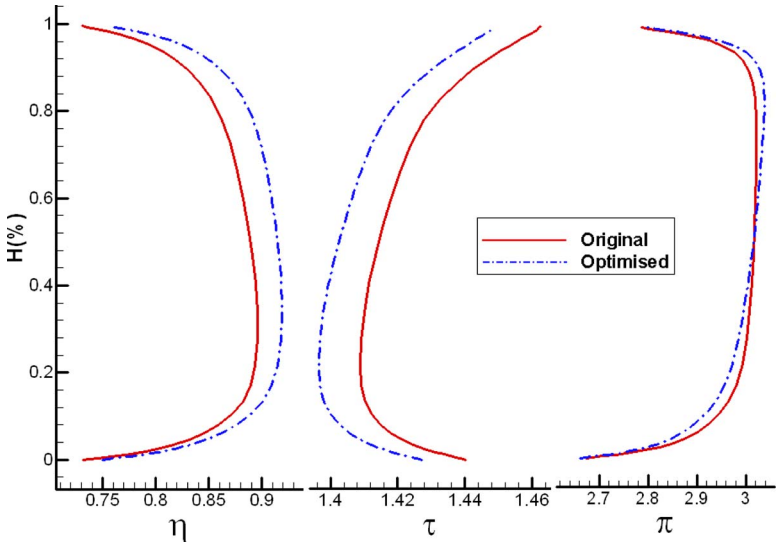

Fig. 26 Spanwise distributions of circumferentially averaged efficiency, stagnation temperature ratio and stagnation pressure ratio at the compressor exit (Siemens three-stage compressor redesign)

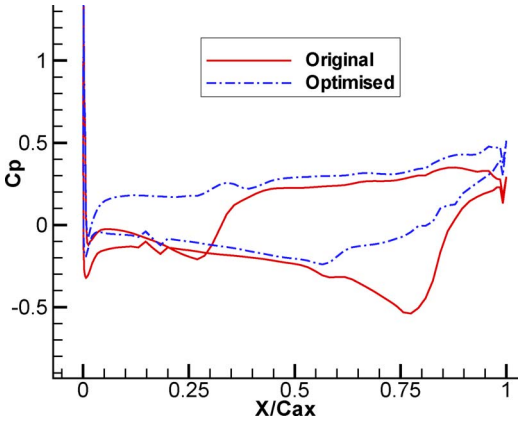

Fig. 28 Pressure coefficient distributions at 85% span of Rotor 2 (Siemens three-stage compressor redesign)

than the original design over the whole span. The stagnation pressure ratio in the optimized design is increased in the tip region and decreased in the hub region.

An examination on the pressure coefficient distributions on different spanwise locations of the first and second rotors shows that the optimized design shifts blade load of the first two rotors upstream relative to their original designs (see Figs. 27 and 28). The strength of passage shocks inside the first and second rotors is significantly reduced resulting in the efficiency increase in the optimized design. With design constraints on the mass flow rate and overall stagnation pressure ratio, the design optimization has driven the redesign of the three transonic stages to different matching conditions.

The change of blade geometry is revealed in Figs. 29–31. Figures 29 and 30 compare the original blade geometry to the optimized blade geometry of the first rotor and stator. The first rotor blade profile has been changed significantly in the leading edge region, particularly near the hub. There is also a considerable change in the tip region of the rotor blade geometry where the original MCA type of profile has been replaced by a reverse-cambered type of profile. The first stator is decambered with increased turning in the front part of the airfoil and reduced turning toward the trailing edge. During the design process, the round leading edge shape is well preserved (Fig. 29). Figure 31 shows

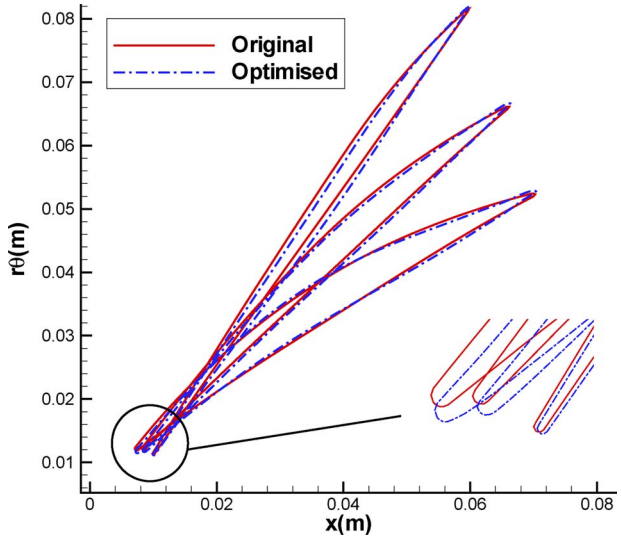

Fig. 29 Comparison of blade geometry for Rotor 1 (Siemens three-stage compressor redesign)

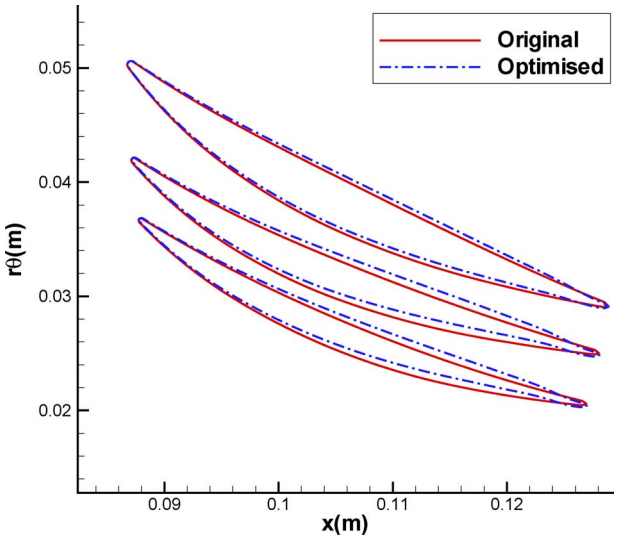

Fig. 30 Comparison of blade geometry for Stator 1 (Siemens three-stage compressor redesign)

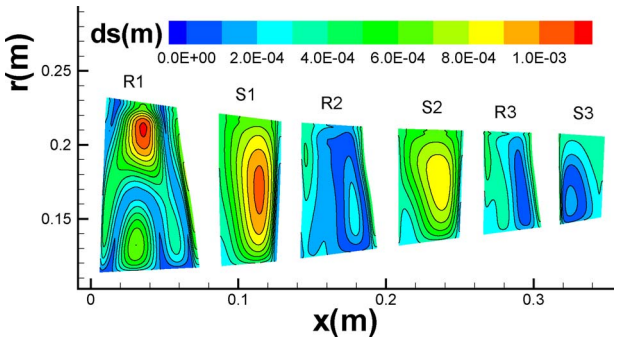

Fig. 31 Geometry changes on blade surfaces of the Siemens three-stage compressor

the contours of the circumferential geometry displacement on one side of the blades. Due to the nature of the shape perturbation parametrization in this research work, corresponding mesh points on both sides of the blades have the same distance change (except for the leading edge region) during the design-optimization process; hence the geometry displacement on one side of the blades is shown only. The first rotor, the first stator, and the second stator have the major geometry change with the maximum change up to 1.1 mm (1.4 % of chord for rotor 1 and 2.6% chord for stator 1).

6 Concluding Remarks

Four redesigns have been carried out, producing encouraging improvements. The redesign of NASA rotor 67 delivers 1.77% point increase in efficiency while maintaining the mass flow rate and stagnation pressure ratio at values close to those specified for the original design. The optimized DLR stage has an increase in stage efficiency of 0.72% point at the same stagnation pressure ratio and mass flow rate. The limitation of a single-point optimization is highlighted in the three-row configuration. Consequently, a multipoint parallel procedure is introduced. It is shown that a two-point parallel optimization behaves qualitatively differently from a single-point one, and can produce a design with a higher peak efficiency while *satisfying* performances at other operating conditions. The Siemens seven-row compressor is optimized to achieve 2.47% point efficiency increase while maintaining the original design point stagnation pressure ratio and mass flow rate. The multirow design cases, particularly the redesign of Siemens

seven-row compressor, have consistently demonstrated the validity and implementation of the proposed adjoint mixing-plane treatment and the capability of the design system in aerodynamic design optimization for multistage turbomachines.

Acknowledgment

The authors would like to acknowledge Siemens Industrial Turbomachinery Ltd. for funding this work and allowing this publication.

Nomenclature

I = objective function
σ = weighting factor
s = entropy generation rate
$\dot{m}$ = mass flow rate
π = stagnation pressure ratio
η = isentropic efficiency
τ = stagnation temperature ratio
$\delta_{r\theta}$ = perturbation to the $r\theta$ coordinate of a mesh point
δ_x = perturbation to the x coordinate of a mesh point
p = static pressure
ρ = fluid density
ds_x = differential area element projected in the x direction
Cp = pressure coefficient
DLR = German Aerospace Centre

References

[1] Denton, J. D., 1992, "The Calculation of Three-Dimensional Viscous Flow Through Multistage Turbinemachines," ASME J. Turbomach., **114**, pp. 18–26.
[2] Giles, M. B., and Pierce, N. A., 2000, "An Introduction to the Adjoint Approach to Design," Flow, Turbul. Combust., **65**(3/4), pp. 393–415.
[3] Wang, D. X., and He, L., 2010, "Adjoint Aerodynamic Design Optimization for Blades in Multistage Turbomachines—Part I: Methodology and Verification," ASME J. Turbomach., **132**(2), p. 021011.
[4] Oyama, A., and Liou, M. S., 2004, "Transonic Axial-Flow Blade Optimization: Evolutionary Algorithms/Three-Dimensional Navier–Stokes Solver," J. Propul. Power, **20**(4), pp. 612–619.
[5] Wu, H., Liu, F., and Tsai, H., 2005, "Aerodynamic Design of Turbine Blades Using an Adjoint Equation Method," AIAA Paper No. 05-1006.
[6] Wu, H., Yang, S., and Liu, F., 2003, "Comparison of Three Geometric Representation of Airfoils for Aerodynamic Optimization," AIAA Paper No. 2003-4095.
[7] Miller, P. L., IV, Oliver, J. H., Miller, D. P., and Tweedt, D. L., 1996, "Blade CAD: An Interactive Geometric Design Tool for Turbomachinery Blades," NASA Technical Report No. 107262.
[8] Samareh, J.A., 1999, "A Novel Shape Parameterization Approach," NASA Technical Report No. TM-1999-209116.
[9] Arens, K., Rentrop, P., Stoll, S. O., and Wever, U., 2005, "An Adjoint Approach to Optimal Design of Turbine Blades," Appl. Numer. Math., **53**, pp. 93–105.
[10] Büche, D., Guidati, G., and Stoll, P., 2003, "Automated Design Optimization of Compressor Blades for Stationary, Large Scale Turbomachinery," ASME Paper No. GT2003-38421.
[11] Benini, E., 2004, "Three-Dimensional Multi-Objective Design Optimization of a Transonic Compressor Rotor," J. Propul. Power, **20**, pp. 559–565.
[12] Sieverding, F., Ribi, B., Casey, M., and Meyer, M., 2004, "Design of Industrial Axial Compressor Blade Sections for Optimal Range and Performance," ASME J. Turbomach., **126**, pp. 323–331.
[13] Lotfi, O., Teixeira, J. A., Ivey, P. C., Kinghorn, I. R., and Sheard, A.G., 2006, "Shape Optimization of Axial Fan Turbines Using Genetic Algorithm and a 3D Navier–Stokes Solver," ASME Paper No. GT2006-90659.
[14] Anderson, W. K., and Venkatakrishnan, V., 1997, "Aerodynamic Design Optimization On Unstructured Grids With a Continuous Adjoint Formulation," AIAA Paper No. 97-0643.
[15] Jang, C. M., Samad, A., and Kim, K. Y., 2006, "Optimal Design of Swept, Leaned and Skewed Blades in a Transonic Axial Compressor," ASME Paper No. GT2006-90384.
[16] Li, H. D., He, L., Li, Y. S., and Wells, R. G., 2006, "Blading Aerodynamics Design Optimization With Mechanical and Aeromechanical Constraints," ASME Paper No. GT2006-90503.
[17] Yi, W., Huang, H., and Han, W., 2006, "Design Optimization of Transonic Compressor Rotor Using CFD and Genetic Algorithm," ASME Paper No. GT2006-90155.
[18] Yang, S., Wu, H., Liu, F., and Tsai, H., 2003, "Aerodynamic Design of Cascades by Using an Adjoint Equation Method," AIAA Paper No. 03-1068.
[19] Strazisar, A. J., Wood, J. R., Hathaway, M. D., and Suder, K. L., 1989, "Laser Anemometer Measurements in a Transonic Axial-Flow Fan Rotor," NASA Technical Report No. 2879.
[20] Dunker, R., Rechter, H., Starken, H., and Weyer, H., 1984, "Redesign and Performance Analysis of a Transonic Axial Compressor Stator and Equivalent Plane Cascades With Subsonic Controlled Diffusion Blades," ASME J. Eng. Gas Turbines Power, **106**, pp. 279–287.
[21] Li, Y. S., and Wells, R. G., 1999, "The Three Dimensional Aerodynamic Design and Test of a Three-Stage Transonic Compressor," ASME Paper No. GT-99-68.
[22] Lian, Y., and Liou, M. S., 2005, "Multi-Objective Optimization of Transonic Compressor Blade Using Evolutionary Algorithm," J. Propul. Power, **21**(6), pp. 979–987.
[23] Pierret, S., 2005, "Multi-Objective and Multi-Disciplinary Optimization of Three Dimensional Turbomachinery Blades," Sixth World Congress of Structural and Multidisciplinary Optimization, Rio de Janeiro, Brazil, May 30–Jun. 3.
[24] Arnone, A., 1993, "Viscous Analysis of Three-Dimensional Rotor Flow Using a Multigrid Method," NASA Technical Report No. TM106266.

Design and Optimization of the Internal Cooling Channels of a High Pressure Turbine Blade—Part I: Methodology

Sergio Amaral[1]
Department of Aerospace Engineering,
Pennsylvania State University,
229 Hammond Building,
University Park, PA 16802
e-mail: sergio.amaral@ge.com

Tom Verstraete
e-mail: tom.verstraete@vki.ac.be

René Van den Braembussche
e-mail: vdb@vki.ac.be

Tony Arts
e-mail: arts@vki.ac.be

Department of Turbomachinery and Propulsion,
von Kármán Institute for Fluid Dynamics,
Waterloosesteenweg 72,
640 Sint-Genesius-Rode, Belgium

This first paper describes the conjugate heat transfer (CHT) method and its application to the performance and lifetime prediction of a high pressure turbine blade operating at a very high inlet temperature. It is the analysis tool for the aerothermal optimization described in a second paper. The CHT method uses three separate solvers: a Navier–Stokes solver to predict the nonadiabatic external flow and heat flux, a finite element analysis (FEA) to compute the heat conduction and stress within the solid, and a 1D aerothermal model based on friction and heat transfer correlations for smooth and rib-roughened cooling channels. Special attention is given to the boundary conditions linking these solvers and to the stability of the complete CHT calculation procedure. The Larson–Miller parameter model is used to determine the creep-to-rupture failure lifetime of the blade. This model requires both the temperature and thermal stress inside the blade, calculated by the CHT and FEA. The CHT method is validated on two test cases: a gas turbine rotor blade without cooling and one with five cooling channels evenly distributed along the camber line. The metal temperature and thermal stress distribution in both blades are presented and the impact of the cooling channel geometry on lifetime is discussed. [DOI: 10.1115/1.3104614]

1 Introduction

Gas turbines have become a major equipment for power generation by electric utilities and independent power producers. Improvements in the design concept, structural materials, and coating of the gas turbine hot section components enable an increase in the turbine inlet temperature and have resulted in considerable efficiency gains. However, higher temperatures accelerate the degradation of the blades and inevitably lead to severe damage of the superalloy substrate. Countermeasures currently applied to the hot gas path components include film cooling, internal cooling, impingement flow, thermal barrier coating, or a combination of all.

The interaction between the temperature and thermal stress and its impact on the lifetime is difficult to estimate and emphasizes the need for a computer aided technique to maximize the lifetime of the blade.

A traditional gas turbine blade development starts with an aerodynamic design and a layout of the cooling geometry. This phase is followed by a thermal and structural analysis to verify the maximum stresses and lifetime. If mechanical limitations are exceeded, the designer will need to remodel the blade within a given design space until it complies with the mechanical constraints. More advanced design systems incorporate multidisciplinary numerical optimization techniques to reduce the design cost and time, and to increase the overall efficiency and lifetime of the machine.

The present paper describes a CHT method that allows a detailed prediction of the temperature and thermal stress distribution inside the solid. These are the inputs for the gas turbine rotor blade lifetime prediction model also described in this paper. Both methods provide the input for the multidisciplinary optimization of the cooling channel geometry, presented in the second paper [1].

Two test cases are analyzed: a gas turbine rotor blade without cooling and one with straight cooling channels evenly distributed along the camber line. The metal temperature and thermal stress distribution for both blades are presented and the impact of the cooling channel geometry on lifetime is discussed.

2 Conjugate Heat Transfer Method

A literature survey [2–12] reveals that two main strategies are used for solving the CHT problem, depending on how the continuity of temperature and heat flux at the interface are imposed.

One approach integrates the entire set of equations in the fluid and solid as one single system and implicitly guarantees the continuity of the temperature and heat flux. This approach, referred to in the literature as the *conjugate method*, is computationally efficient and requires only one solver. Interpolation at the interface between the solid and fluid can be avoided if the grids are continuous. However, this results in a more difficult mesh generation process and meshes that may not be optimal for both solvers. No commercial codes are available to compute the thermal stresses from the resulting temperature field inside the solid finite volume mesh. Hence the results need to be interpolated to the mesh of a FEA solver for further analysis. Consequently, the solid needs to be meshed twice.

A second approach calculates separately the flow and the thermal field of the solid. The solid and fluid flow solvers alternate with an exchange of boundary conditions at their interface. The solid domain is solved directly in steady state by the FEA solver, which is an attractive feature in terms of computational cost. However, the drawback of this approach, known as the *coupled method*, is the need for sequential iterations between the two platforms and an interpolation of the boundary conditions from one grid to the other. The main advantage of the coupled approach is that one can make use of standard grid generators and Navier–Strokes (NS) and FEA solvers. Those codes have been extensively

[1]Present address: GE Infra Energy, Greenville, SC.

Contributed by the International Gas Turbine Institute of ASME for publication in the JOURNAL OF TURBOMACHINERY. Manuscript received September 30, 2008; final manuscript received November 19, 2008; published online January 13, 2010. Review conducted by David Wisler. Paper presented at the ASME Turbo Expo 2008: Land, Sea and Air (GT2008), Berlin, Germany, June 9–13, 2008.

validated and their limitations and capabilities are well known. A FEA calculation is anyway needed for stress and vibration analysis.

Moreover, the CHT method predicts the temperature in each node of the solid mesh, allowing a straightforward computation of the thermal stresses. Temperature dependent material laws can be used to compute the stress resulting from centrifugal and pressure forces. The interpolation algorithm that transfers the temperature and heat flux at the interface can also be used to transfer the pressure forces from the NS analysis to the FEA stress prediction. The thermal stresses and dilatation of the blade, the centrifugal and pressure stresses, the deformations, and the natural blade frequencies can be computed without additional complexity. This makes the coupled method not only a competitive tool for the conjugate heat transfer computations but also a framework for a multidisciplinary analysis of turbomachinery components.

Another advantage of the coupled method is the simple coupling of full 3D models with 2D axisymmetric ones at the interfaces between rotating and fixed components. The same interpolation algorithm as for the 3D-3D interaction can be used, with an additional circumferential averaging of the full 3D model.

2.1 Coupled Method. The advantages of a coupled method in the framework of a multidisciplinary design tool has been the main argument for using it in the present study. Three different methods exist, based on the way the quantities are transferred at the interface.

A first coupled method is the flux forward temperature back (FFTB) [4] method in which the wall temperature distribution is imposed on the fluid solver. The corresponding heat flux distribution, predicted by the fluid computation, is imposed as a boundary condition for the solid conduction solver. The latter one predicts an updated temperature distribution at the fluid solver solid boundaries. This loop is repeated until convergence, i.e., until the temperature and heat flux distribution do not change with further iterations. It can be proven [13] that the FFTB method is stable only for problems with a Biot number below 1.

Alternatively, one can impose the heat flux distribution as a boundary condition for the fluid computation and the resulting wall temperature to the solid conduction solver. The updated heat flux is then returned as a boundary condition to the fluid solver. This method is known as the temperature forward flux back (TFFB) method, and has been successfully applied by Heidmann [5]. It can be proven that the TFFB method is stable for problems with a Biot number above 1 [13].

The method used in the present paper uses the convective boundary condition (Eq. (1)) to update the boundary conditions of the solid conduction calculation [3,4,14]. It is therefore called the convective boundary condition method, or abbreviated the *h-method*.

$$q_{\text{wall}} = h \cdot (T_{\text{wall}} - T_{\text{fluid}}) \tag{1}$$

The method starts with an initial temperature distribution T_{wall} at the solid boundary of the flow solver. The results of the NS computation are used to estimate the heat convection coefficient h and fluid temperature T_{fluid}. Substituting these in Eq. (1) provides an implicit relation between T_{wall} and q_{wall} that can be used as a boundary condition for the solid conduction computation. The advantage of using Eq. (1) as boundary condition is an automatic adjustment of q_{wall} as a function of T_{wall} in the FEA. The latter one is then returned to the fluid solver and the loop is repeated until convergence.

The remaining problem is the definition of h and T_{fluid} from the NS solution. They also need to satisfy Eq. (1) in which T_{wall} is the imposed boundary condition and q_{wall} is the solution of the fluid solver. However, there is only one equation for two unknowns. One possibility is to make an extra fluid flow calculation with a different wall temperature [4] or even an adiabatic wall ($q_{\text{wall}} = 0$) [3]. Substituting the two solutions of q_{wall} in Eq. (1) and assuming that h and T_{fluid} remain unchanged results in Eq. (2) defining h.

$$h = \frac{q^2_{\text{wall}} - q^1_{\text{wall}}}{T^2_{\text{wall}} - T^1_{\text{wall}}} \tag{2}$$

T_{fluid} can then be calculated by Eq. (1) as a function of the imposed T_{wall} and corresponding q_{wall}.

A simpler and more stable approach is by imposing a constant positive value of h. This is allowed because the value of h influences only the convergence rate and not the final result [11]. A smaller value of h results in a larger change of the wall temperature between two successive iterations, for a given flux difference. This accelerates the convergence but can lead to divergence of the method. It can be shown [13] that a sufficient but not necessary condition for this method to converge is an h value larger than $h_{\max}/2$ with $h_{\max}$ the highest convection coefficient at the interface. This method has been validated by comparing the results with those obtained by the two other methods [12].

The initial guess of the wall temperature at the common boundary can be a uniform temperature or the local fluid temperature of an adiabatic NS computation. This initial solution is used as a first guess for the first flow computation of the coupled method. Each subsequent NS computation starts from the flow field of the previous computation.

2.2 Cooling Channel Model. The flow in each of the five cylindrical cooling channel is predicted by a one-dimensional (1D) flow model taking into account the heat transfer and friction coefficients corrected for turbulators and Coriolis forces. The geometry of the ribbed cooling channel is simplified to a smooth one and the convection and friction coefficients are set as the average over one inter-rib passage. This approach is believed to be the most cost effective because it is very fast and incorporates well established experimental correlations to characterize the heat convection. A Reynolds averaged Navier–Stokes (RANS) computation of the cooling channel flow at each conjugate heat transfer iteration would substantially increase the computational effort, without a significant increase of accuracy. The use of a large eddy simulation (LES), as recommended in Ref. [15], for a more accurate prediction of the heat transfer in turbulated cooling channels is prohibitive within an optimization procedure.

The 1D flow model is coupled to the FEA by a fluid temperature and heat convection coefficient forward and heat flux backward approach, as shown in Eqs. (3), (4), and (5).

$$T^{\text{FEA}^i}_{\text{fluid}} = T^{\text{1D}^i}_{\text{fluid}} \tag{3}$$

$$h^{\text{FEA}^i}_{\text{wall}} = h^{\text{1D}^i}_{\text{wall}} \tag{4}$$

$$q^{\text{1D}^{i+1}}_{\text{wall}} = q^{\text{FEA}^i}_{\text{wall}} \tag{5}$$

The 1D solver imposes conservation of mass, momentum, and energy when marching from the blade root to the tip. Boundary conditions are the cooling channel total pressure and temperature at the inlet as well as the static pressure at the outlet. The heat flux at the circular boundary is the result of the previous heat transfer computation in the solid (Eq. (5)).

The Nusselt number and friction factor of the smooth cooling channels are based on experimental correlations (Eq. (6) and (7)) [16–18]. Their values are a function of the cooling channel diameter. The latter will be a free optimization parameter in the second paper [1].

$$\text{Nu} = \frac{h \cdot D_H}{\lambda} = 0.023 \ \text{Re}_D^{0.8} \ \text{Pr}^{0.4} \tag{6}$$

$$f = 0.184 \ \text{Re}_D^{-0.2} \tag{7}$$

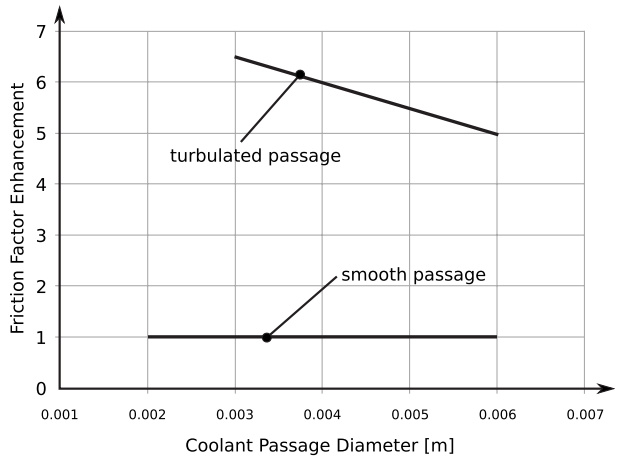

Fig. 1 Cooling channel friction enhancement factor

Heat transfer and friction enhancement factors, based on experimental correlations [19–21], account for the turbulators and Coriolis forces acting on the flow inside the cooling channels (Figs. 1 and 2). Turbulators are used only if the diameter is large enough to accept them (>3 mm). The Coriolis force pushes the flow toward the pressure side of the cooling channel and increases the heat transfer at that location (upper dashed curve in Fig. 2). The heat transfer near the suction side of turbulated channels is decreased (lower dashed curve in Fig. 2).

The 1D model computations are repeated every time the external flow field is updated. They provide the distribution of the fluid temperature and heat convection coefficient required by the convective boundary condition (Eq. (1)) of the FEA. The main stream fluid temperature and cooling channel heat flux distribution are passed back and forth until the solution has converged, i.e., until the wall temperature and heat flux at the boundaries do not change anymore between iterations. All calculations converge simultaneously.

3 Lifetime Prediction

Upon completion of the CHT analysis, the solid temperature is known at each node of the FEA grid, which allows a straightforward calculation of the thermal stress. The stresses due to the centrifugal forces and blade bending, resulting from the pressure difference between pressure and suction side, can be computed on the same grid with a temperature dependent material model. Assuming linearity, the total stresses are the sum of thermal, centrifugal, and pressure stresses. Knowing the temperature and stress in each node of the FEA grid allows a computation of the blade lifetime.

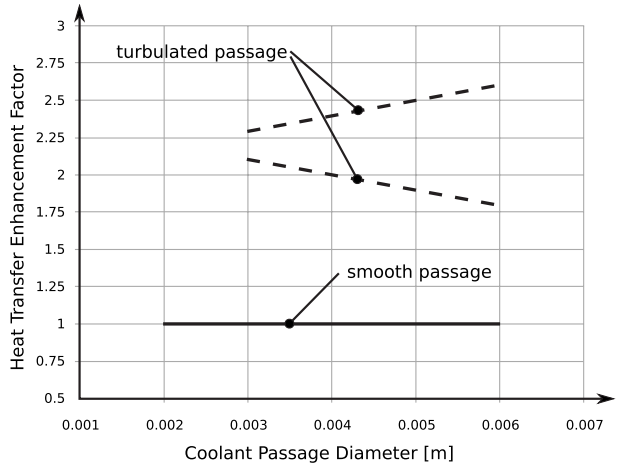

Fig. 2 Cooling channel heat transfer enhancement factor

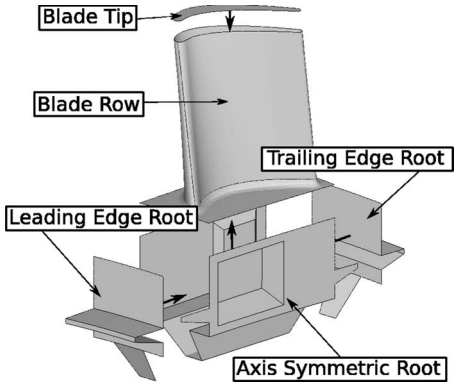

Fig. 3 Exposed view on rotor blade model

The lifetime of the blade is assumed to depend on the creep-to-rupture failure. This assumption is made because no information regarding low-cycle and high-cycle fatigues is known at this stage of the design. Fracture-to-rupture failure requires a rotor-stator interaction analysis over the entire operating range and is beyond the scope of present work.

The creep-to-rupture lifetime is based on Hill's anisotropic equation (Eq. (8)) obtained from Ref. [22]. The equivalent stress γ ranges from 0 to 1. The material is considered to fail when $\gamma=1$.

$$\gamma = H(\sigma_{xx}-\sigma_{yy})^2 + F(\sigma_{yy}-\sigma_{zz})^2 + G(\sigma_{zz}-\sigma_{xx})^2 + 2N(\tau_{xy})^2 + 2L(\tau_{yz})^2 + 2M(\tau_{zx})^2 \quad (8)$$

H, F, G, N, L, and M in Eq. (8) are the material properties that depend on the Larson–Miller parameters (LMPs) in the longitudinal and transverse directions. They are specified by Eq. (9). The parameters for the directionally solidified nickel superalloy material GTD-111 are used for the present analysis [23].

$$\mathrm{LMP} = T \cdot [\log_{10}(l) + 23] \quad (9)$$

An iterative approach is used to determine the lifetime of the blade. The algorithm starts with a first guess of l and computes the Larson–Miller parameter (Eq. (9)) in each node of the solid grid. These parameters are inputted for the calculation of the material properties (H, F, G, N, L, and M). The material failure is checked in each node (Eq. (8)). Depending on the result, a new estimation of l is made, i.e., l is lowered if the maximum value of γ is larger than 1, or vice versa. This computation is repeated until a value of l is found for which the largest γ equals 1, plus or minus a tolerance.

4 Geometry and Boundary Condition

The test case is the rotor blade shown in Fig. 3. The blade shape is a VKI design with optimized external aerodynamic performance. The operating conditions are given in Table 1. The geometry specifications are listed in Table 2.

TRAF3D [24] is used as NS solver and the commercial code SAMCEF [25] for the computation of the heat transfer in the solid

Table 1 Stage operating conditions

Inlet total pressure	7×10^5 Pa
Inlet total temperature	1350 K
Inlet Mach number	0.3
Outlet static pressure	3.5×10^5 Pa
Outlet Mach number	0.8
Mass flow rate	400 kg/s

Table 2 Blade geometry specifications

Blade height	0.200m
Number of blades	90
Hub axial length	0.130m
Hub pitch to chord ratio	0.667

and the stress required for the lifetime determination. The convection coefficient h, required for the NS-FEA coupling (Eq. (1)), is fixed at 3000 W/m^2 K. A distance-weighted interpolation, based on Shepard's method [26], is used in both transfers of boundary conditions (NS to FEA and FEA to NS).

The computational FEA grid consists of 100,000 nodes and 70,000 quadratic tetrahedral elements for the blade without cooling channels. 243,000 nodes and 160,000 quadratic elements are used for the case with cooling channels.

The NS grid is structured and consists of $172 \times 64 \times 64$ or 700,000 finite volumes. A 1D grid containing 250 cells in the longitudinal direction is constructed for each cooling channel. The Reynolds number based on the cooling channel diameter is between 30,000 and 60,000. Turbulators start 2.5 cm above the hub surface and end 2.5 cm below the tip surface. The ribs are normal to the coolant flow direction and have a pitch to height ratio of approximately ten.

The tip clearance flow is not included in the NS calculations. The solid boundary conditions (Eq. (1)) are applied at the blade tip with a fluid temperature of 1200 K and a convection coefficient of 750 W/m^2 K. The latter is based on experimental results conducted at the von Karman Institute for Fluid Dynamics [27].

The blade has five cylindrical cooling channels in order to control the temperature and maintain the mechanical integrity. The cooling channel inlet boundary conditions are given in Table 3. A uniform tip static pressure is prescribed in each of the five patches specified in Fig. 4.

The computational model further assumes no leakage flow through the hub surface. The heat transfer from one blade root to the neighboring one is minimal since they are in contact on both sides and the lateral root surfaces are considered adiabatic. A convective boundary condition, based on rotor-stator aerothermodynamic correlations [28], is applied to the leading and trailing edge root surfaces. The convective boundary conditions are given in Table 4.

Table 3 Cooling channel inlet boundary conditions

Cooling channels	1–2	3–5
Total pressure (Pa)	8×10^5	5×10^5
Total temperature (K)	600	600

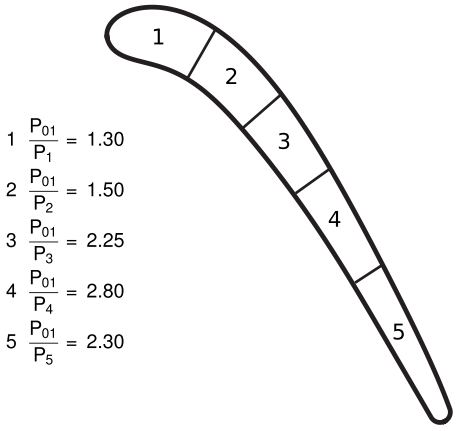

Fig. 4 Blade tip pressure distribution

Table 4 Root leading and trailing edge boundary conditions

	Root leading edge	Root trailing edge
h	1000 W/m^2	1000 W/m^2
T_{fluid}	700 K	600 K

5 Results

The impact of the cooling channels is assessed by comparing the results of a blade without cooling with the ones of a blade where the cooling channels are evenly distributed along the camber line. The computation converges after 15 CHT iterations, with 100 NS time steps per CHT iteration. The temperature distribution on the blade surface without cooling channels is shown in Fig. 5. The only cooling is through the flow captured in the cavity between the rotor and stator. The maximum material temperature is observed at the trailing edge tip and equals 1249 K. A large part of the blade has a temperature above 1200 K. The part of the blade in the main flow field acts as a cooling fin with radially increasing temperature away from the cooling source.

Figure 6 shows the temperature distribution for the blade with cooling channels. An important reduction in temperature is observed. The major part of the blade cooling is now performed by the cooling channels and the flow in the root cavities has only a small impact on the cooling. The maximum material temperature, again observed at the trailing edge tip, is reduced to 1222 K and only a small part of the blade has a temperature above 1200 K. 14.075 g/s of coolant flow is needed for each blade, which, for 90 blades, results in a total coolant flow of 0.3% of the mass flow of the first stage.

Thermal stresses for the blade without cooling channels are shown in Fig. 7. As could be expected, the highest values are observed at the junction between blade and hub, where the highest temperature gradients occur. The maximum is located at the hub trailing edge and equals 263 MPa.

The thermal stresses for the blade with cooling channels are shown in Fig. 8. They have increased and the maximum value (369 MPa) now appears at the hub leading edge. The variation in the stresses, observed between the midspan and the blade tip, are due to the large temperature gradients induced by the cooling channels. The position of the latter can be recognized by the chordwise variation in the thermal stresses.

The computation of the creep-to-rupture lifetime based only on the thermal stresses results in a lifetime of 161 h for the case without cooling channels and increases to only 220 h when cooling channels are introduced. This small increase in lifetime is due to an inappropriate location of the cooling holes and emphasizes the need for an optimization of the cooling hole geometry and location.

Figures 9 and 10 show the corresponding normal effective stress at rupture. This is the γ distribution (Eq. (8)) at the blade lifetime l and shows the location where the blade will fail ($\gamma = 1$). The uncooled blade fails near the hub trailing edge. Note that although the highest stress is found at the hub leading edge, the cooled blade also fails at the trailing edge. The lower temperature at which these higher stresses occur results in an increased lifetime.

Previous computations of the lifetime are based only on the thermal stresses and are therefore too optimistic. A more realistic prediction requires that also the centrifugal and pressure stresses are considered. Table 5 summarizes the results for both geometries. The pressure difference between suction and pressure side results in rather low bending stresses because of the relatively small blade height and can be neglected. The stresses resulting

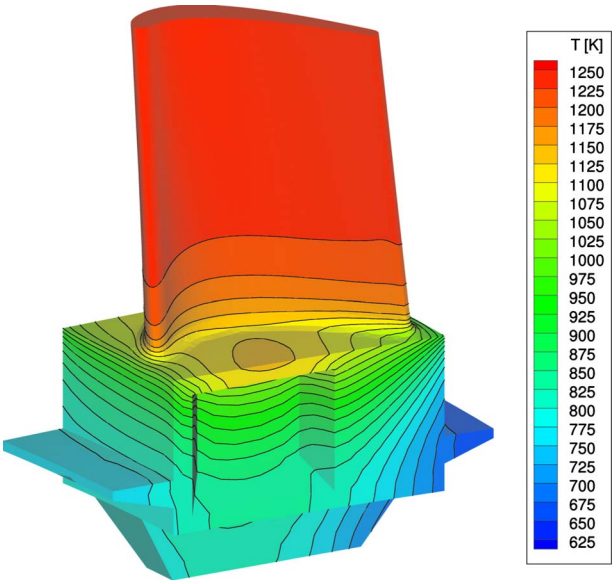

Fig. 5 Temperature distribution for the blade without cooling channels

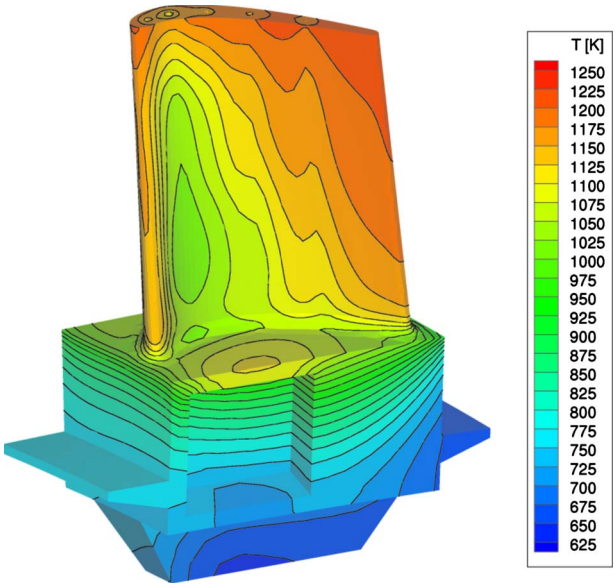

Fig. 6 Temperature distribution for the blade with cooling channels

from the centrifugal forces are of the same order of magnitude as the thermal stresses. Figures 11 and 12 show the blade effective stresses at failure when accounting for all three stresses. In both cases, the centrifugal stresses result in an extended zone of material damage near the hub trailing edge. The lifetime has reduced to, respectively, 9.8 h and 17.7 h for the blade without and with cooling channels. The extremely low lifetime of both blades is a consequence of the very high inlet temperatures, the limited cooling, and the absence of any thermal barrier coating. Additional cooling holes or film cooling will be needed before such severe conditions allow realistic lifetimes. The harsh operating environment is intentionally chosen by the authors to evaluate the possible improvements by means of the optimization system presented in Ref. [1].

It is obvious that the centrifugal stresses have a negative impact on the lifetime of the blade. However, they are most likely oriented in the spanwise direction and only weakly depend on the position of the cooling channels. Neglecting them during the optimization process will have a small impact on the optimum. The optimization of the cooling channel position requires only the change in stresses and the temperatures for the lifetime ranking of the geometries. As shown in present test cases, an increase in lifetime based only on the thermal stresses also leads to an increased lifetime based on the total stresses. The model no longer predicts the real lifetime to failure but is computationally less expensive. A lifetime evaluation of the final optimized geometry based on the total stresses is still required.

6 Conclusions

An automated coupled method for conjugate heat transfer calculations and its application for the aerothermal analysis of an internally cooled turbine blade is presented. A combination of an accurate 3D Navier–Stokes solver, a finite element analysis

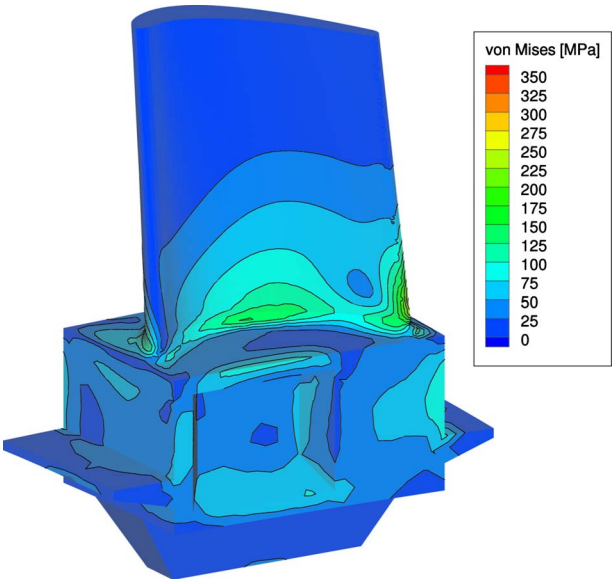

Fig. 7 von Mises stress distribution for the blade without cooling channels

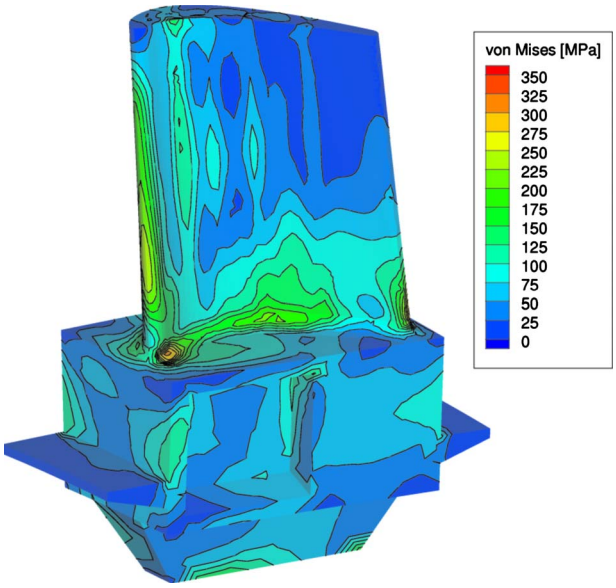

Fig. 8 von Mises stress distribution for the blade with cooling channels

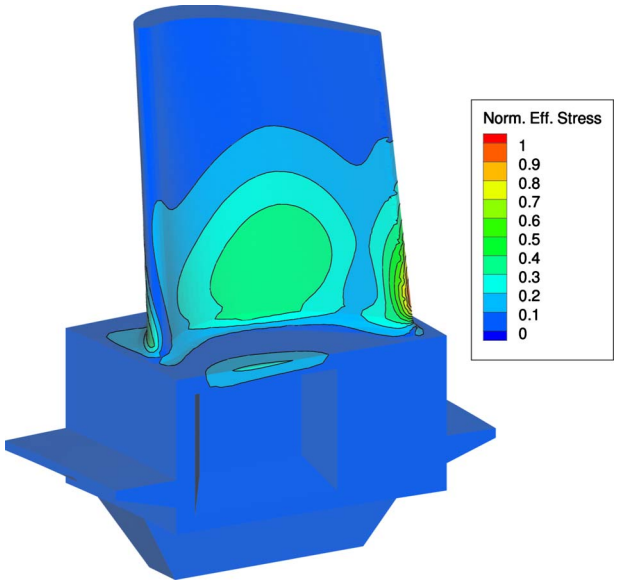

Fig. 9 Effective stress distribution at rupture (l=161 h) for the blade without cooling channels

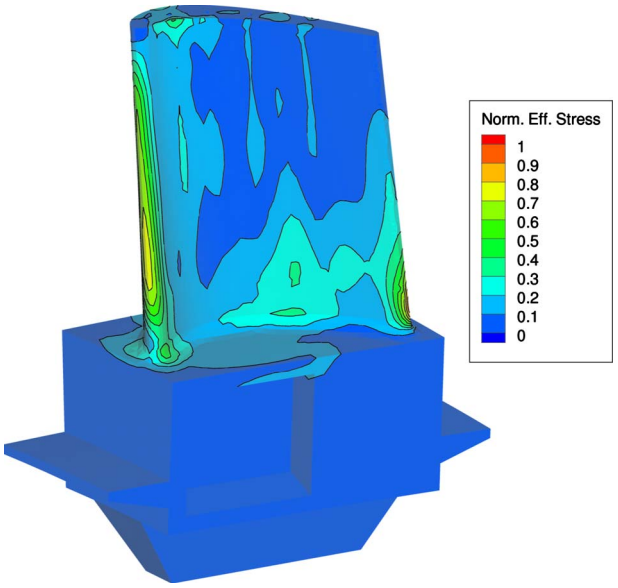

Fig. 10 Effective stress distribution at rupture (l=220 h) for the blade with cooling channels

method, and a 1D model based on experimental correlations for the cooling channels is used as a trade-off between accuracy and numerical cost. The detailed distribution of the thermal stresses and temperatures are computed and used for lifetime predictions.

Table 5 Results for different models. stresses shown are von Mises stresses

	Without cc	With cc
Maximum temperature (K)	1249	1222
Maximum thermal stress (MPa)	263	369
Lifetime only therm. stress (h)	161	220
Maximum centrifugal stress (MPa)	355	323
Maximum pressure stress (MPa)	31.1	30.9
Maximum total stress (MPa)	445	474
Lifetime (h)	9.8	17.7

Two main analyses are presented. The results for an uncooled blade are compared with the ones of a blade with internal cooling channels. Although the cooling resulted in a substantial temperature decrease, only a relatively small increase in lifetime is obtained. This limited improvement is due to an inappropriate position of the cooling holes. The complex relation between temperature and thermal stress on lifetime emphasizes the need for an optimization of the cooling hole geometry and location, described in the second paper.

The impact of centrifugal and pressure stresses on the lifetime is discussed. Although the total stress is required for an accurate prediction of the lifetime, it is shown that the lifetime based only on the thermal stresses can be used for the optimization of cooling configurations.

The multidisciplinary analysis tool for the prediction of the life-

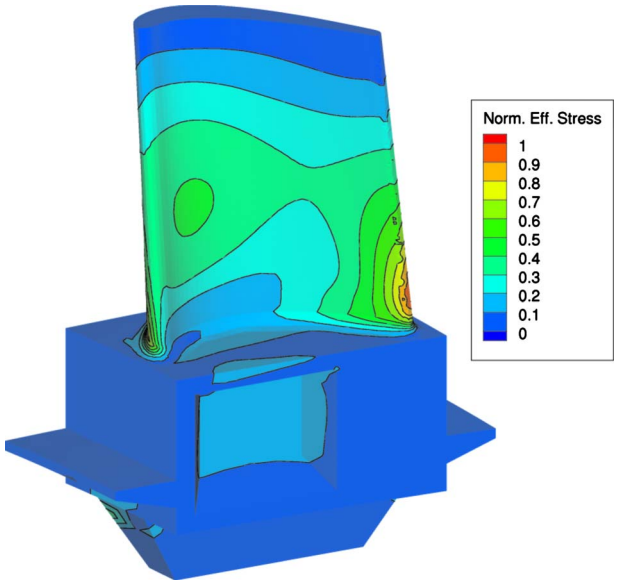

Fig. 11 Effective stress distribution at rupture (l=9.8 h), computed with total stress for the blade without cooling channels

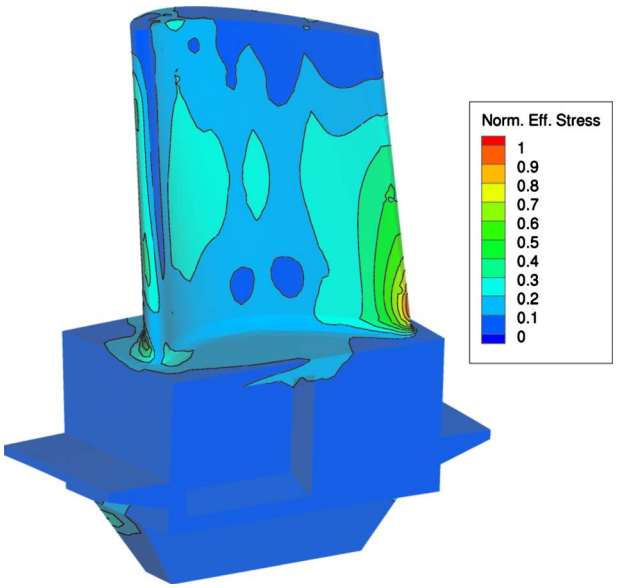

Fig. 12 Effective stress distribution at rupture (l=17.7 h), computed with total stress for the blade with cooling channels

time of the blade, presented in this first paper, is fully automated and opens the road toward a multidisciplinary optimization, presented in the second paper [1].

Acknowledgment

The financial support by Laborelec for the development of this method is gratefully acknowledged. Special thanks to Jean-Pierre Keustermans, Sébastien Grégoire, and Bea Ghys for their stimulating discussions.

Nomenclature

- cc = cooling channel
- D_H = hydraulic diameter
- f = friction factor
- h = convection coefficient (W/m^2 K)
- l = lifetime (h)
- Nu = Nusselt number
- q = heat flux (W/m^2)
- Re_D = Reynolds number based on diameter
- T = temperature (K)
- γ = normalized equivalent stress
- λ = conductivity of the fluid (W/mK)
- σ = normal stress
- τ = shear stress

References

[1] Verstraete, T., Amaral, S., Van den Braembussche, R., and Arts, T., 2010, "Design and Optimization of the Internal Cooling Channels of a High Pressure Turbine Blade—Part II: Optimization," ASME J. Turbomach., **132**(2), p. 021014.
[2] Han, Z. X., Dennis, B. H., and Dulikravich, G. S., 2000, "Simultaneous Prediction of External Flow-Field and Temperature in Internally Cooled 3-D Turbine Blade Material," ASME Paper No. 2000-GT-253.
[3] Montenay, A., Paté, L., and Duboué, J., 2000, "Conjugate Heat Transfer Analysis of an Engine Internal Cavity," ASME. Paper No. 2000-GT-282.
[4] Verdicchio, J. A., Chew, J. W., and Hills, N. J., 2001, "Coupled Fluid/Solid Heat Transfer Computation for Turbine Discs," ASME. Paper No. 2001-GT-0205.
[5] Heidmann, J. D., Kassab, A. J., Divo, E. A., Rodriguez, F., and Steinthorsson, E., 2003, "Conjugate Heat Transfer Effects on a Realistic Film-cooled Turbine Vane," ASME, Paper No. GT2003-38553.
[6] York, W. D., and Leylek, J. H., 2003, "Three-Dimensional Conjugate Heat Transfer Simulation of an Internally-Cooled Gas Turbine Vane," ASME Paper No. GT2003-38551.
[7] Bohn, D., Heuer, T., and Kusterer, K., 2003, "Conjugate Flow and Heat Transfer Investigation of a Turbo Charger—Part I: Numerical Results," ASME Paper No. GT2003-3844.
[8] Bohn, D., Bonhoff, B., and Schonenborn, H., 1995. "Combined Aerodynamic and Thermal Analysis of a Turbine Nozzle Guide Vane," International Gas Turbine Congress, Paper No. 95-108.
[9] Garg, V. K., 2002, "Heat Transfer Research on Gas Turbine Airfoils at NASA GRC," Int. J. Heat Fluid Flow, **23**, pp. 109–136.
[10] Lassaux, G., Daux, S., and Descamps, L., 2004. "Conjugate Heat Transfer Analysis of a Tri-Dimensional Turbine Blade Internal Cavity," 24th ICAS.
[11] Verstraete, T., Alsalihi, Z., and Van den Braembussche, R. A., 2007, "Numerical Study of the Heat Transfer in Micro Gas Turbines," ASME J. Turbomach., **129**(4), pp. 835–841.
[12] Verstraete, T., Alsalihi, Z., and Van den Braembussche, R. A., 2007, "A Comparison of Conjugate Heat Transfer Methods Applied to an Axial Helium Turbine," Proc. Inst. Mech. Eng., Part A J. Power Energy, **221**, pp. 981–989.
[13] Verstraete, T., 2008, "Multi-Disciplinary Turbomachinery Component Optimization Considering Performance, Stress and Internal Heat Transfer," Ph.D. thesis, Universiteit Gent/von Karman Institute for Fluid Dynamics.
[14] Heselhaus, A., 1998, "A Hybrid Coupling Scheme and Stability Analysis for Coupled Solid/Fluid Turbine Blade Temperature Calculations," ASME. Paper No. 98-GT-88.
[15] Vass, P., Rambaud, P., Arts, T., and Benocci, C., 2007, "Numerical Investigation of Flow and Heat Transfer in a Ribbed Square Duct Applying LES," *Proceedings of the Seventh European Conference on Turbomachinery*, pp. 1051–1061.
[16] Dittus, F. W., and Bölter, M. L. K., 1930, *Heat Transfer in Automobile Radiators of the Tubular Type*, Vol. 2, University of California Publications on Engineering, Berkeley, CA, p. 443.
[17] Bejan, A., ed., 1995, *Convective Heat Transfer*, Wiley, New York.
[18] Incropera, F., and DeWitt, D., 2002, *Fundamentals of Heat and Mass Transfer*, Wiley, New York.
[19] Cakan, M., 2000, "Aero-Thermal Investigation of Fixed Rib-Roughened Internal Cooling Passages," Ph.D. thesis, Universit Catholique de Louvain/von Karman Institute for Fluid Dynamics.
[20] Viswanathan, A. K., and Tafti, D. K., 2006, "Detached Eddy Simulation of Flow and Heat Transfer in Fully Developed Rotating Internal Cooling Channel With Normal Ribs," Int. J. Heat Fluid Flow, **27**, pp. 351–370.
[21] Kai, L. C., Hongwu, D., Zhi, T., Shuiting, D., and Xuguoqiang, 2006, "Prediction of Turbulent Flow and Heat Transfer Within Rotating U-Shaped Passages," Heat Transfer Asian Research, **35**, pp. 410–420.
[22] Dowling, N., 2007, *Mechanical Behaviors of Materials*, Prentice-Hall, Englewood Cliffs, NJ.
[23] Ibanez, A. R., Srinivasan, V. S., and Saxena, A., 2006, "Creep Deformation and Rupture Behavior of Directionally Solidified GTD 111 Superalloy," Fatigue Fract. Eng. Mater. Struct., **29**, pp. 1010–1020.
[24] Arnone, A., 1994, "Viscous Analysis of Three-Dimensional Rotor Flow Using a Multigrid Method," ASME J. Turbomach., **116**(3), pp. 435–445.
[25] Samtech Group, 2006, SAMCEF FEA code www.samcef.com.
[26] Shepard, D., 1968. "A Two-Dimensional Interpolation Function for Irregularly Spaced Data," *Proceedings of the 23rd ACM National Conference*, pp. 517–524.
[27] Key, N., and Arts, T., 2006, "Comparison of Turbine Tip Leakage Flow for Flat Tip and Squealer Tip Geometries at High-Speed Conditions," ASME J. Turbomach., **128**(2), pp. 213–220.
[28] Roy, R., Xu, G., and Feng, J., 2001, "A Study of Convective Heat Transfer in a Model Rotor-Stator Disk Cavity," ASME J. Turbomach., **123**, pp. 621–632.

Tom Verstraete
Department of Turbomachinery and Propulsion,
von Kármán Institute for Fluid Dynamics,
Waterloosesteenweg 72,
640 Sint-Genesius-Rode, Belgium
e-mail: tom.verstraete@vki.ac.be

Sergio Amaral[1]
Department of Aerospace Engineering,
Pennsylvania State University,
229 Hammond Building,
University Park, PA 16802
e-mail: sergio.amaral@ge.com

René Van den Braembussche
e-mail: vdb@vki.ac.be

Tony Arts
e-mail: arts@vki.ac.be

Department of Turbomachinery and Propulsion,
von Kármán Institute for Fluid Dynamics,
Waterloosesteenweg 72,
640 Sint-Genesius-Rode, Belgium

Design and Optimization of the Internal Cooling Channels of a High Pressure Turbine Blade—Part II: Optimization

This second paper presents the aerothermal optimization of the first stage rotor blade of an axial high pressure (HP) turbine by means of the conjugate heat transfer (CHT) method and lifetime model described in Paper I. The optimization system defines the position and diameter of the cooling channels leading to the maximum lifetime of the blade while limiting the amount of cooling flow. It is driven by the results of a CHT and subsequent stress analysis of each newly designed geometry. Both temperature and stress distributions are the input for the Larson–Miller material model to predict the lifetime of the blade. The optimization procedure makes use of a genetic algorithm (GA) and requires the aerothermal analysis of a large number of geometries. Because of the large computational cost of each CHT analysis, this results in a prohibitive computational effort. The latter has been remediated by using a more elaborate optimization system, in which a large part of the CHT analyzes is replaced by approximated predictions by means of a metamodel. Two metamodels, an artificial neural network and a radial basis function network, have been tested and their merits have been discussed. It is shown how this optimization procedure based on CHT calculations, a GA, and a metamodel can lead to a considerable extension of the blade lifetime without an increase in the amount of cooling flow or the complexity of the cooling geometry. [DOI: 10.1115/1.3104615]

1 Introduction

The optimization of the coolant scheme of a high pressure (HP) gas turbine rotor blade aims to minimize the amount of coolant flow needed to achieve the required lifetime. The conjugate heat transfer (CHT) method used to perform the aerothermal analysis and the required boundary conditions have been presented in Paper I [1]. The calculation procedure and the results of the CHT analysis of a gas turbine rotor blade, with and without cooling channels, are also discussed in Ref. [1].

The present paper reports on the use of this aerothermal analysis method for the design of the cooling channel geometry by means of a multidisciplinary optimization system. The latter is based on a concurrent approach that searches for a global optimum by considering simultaneously the lifetime and the cooling mass flow constraints.

A multidisciplinary optimization technique offers numerous benefits over traditional design techniques, such as an improved performance, a shortening of the design time, and a reduction in the human effort thanks to a fully automated scheme and the concurrent performance analysis with different disciplines. Moreover, the designer can learn from the decisions proposed by the optimizer and gain a better insight into the design problem. Optimal solutions with unexpected new features may be found.

A literature survey on cooling system optimization, summarized in Ref. [2], describes only cooling systems in which the CHT analysis is substituted by applying convective boundary conditions to the blade exterior wall and the internal cooling channels. Moreover, the optimization objective for all reported papers is a reduction in the maximum temperature [3] or both temperature and thermal stress [2,4,5]. This does not necessarily increase the lifetime since the reduction in temperature can be at places of low thermal stresses.

Aerothermal optimizations require a large number of performance evaluations by means of CHT computations. However, each CHT computation requires approximately 10 h of CPU time on a modern PC, which results in prohibitive computational efforts. The use of a multiprocessor cluster alleviates the problem but the computational cost remains a true challenge as more than 1000 evaluations may be required by the optimization scheme [2–5]. The following describes a powerful optimization scheme that limits the number of CHT analyses to less than 100.

2 Optimization Strategy

The optimization method is an extension of the aerodynamic optimization tool for axial and radial impellers and stators developed at the von Karman Institute [6–8]. The system (Fig. 1) makes use of a genetic algorithm (GA), a database, a CHT analysis tool, and a metamodel for the CHT tool. The basic idea of this system is a two level optimization. A first one uses a rapid but less accurate analysis by the metamodel to evaluate the large number of geometries generated by the GA. The optimum geometry, according to the metamodel predictions, is then analyzed by a more accurate but computationally much more expensive CHT calculation to verify the accuracy of the metamodel predictions. The outcome of such an optimization cycle is added to the database, which is used to train the metamodel. It is expected that, after a new training of the metamodel on the extended database, it will be more accurate because it is based on more information. This feedback of the more accurate CHT predictions into the metamodel makes the system self-learning and is the key feature of the optimization method. The learning cycle is repeated until the CHT results confirm the accuracy of the metamodel predictions, i.e., until the GA optimization has been made with an accurate prediction tool.

[1]Present address: GE Infra Energy, Greenville, SC.

Contributed by the International Gas Turbine Institute of ASME for publication in the JOURNAL OF TURBOMACHINERY. Manuscript received September 30, 2008; final manuscript received November 19, 2008; published online January 13, 2010. Review conducted by David Wisler. Paper presented at the ASME Turbo Expo 2008: Land, Sea and Air (GT2008), Berlin, Germany, June 9–13, 2008.

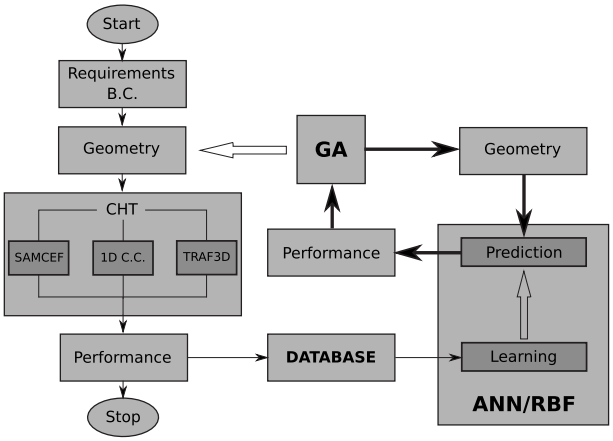

Fig. 1 Schematic overview of the optimization algorithm

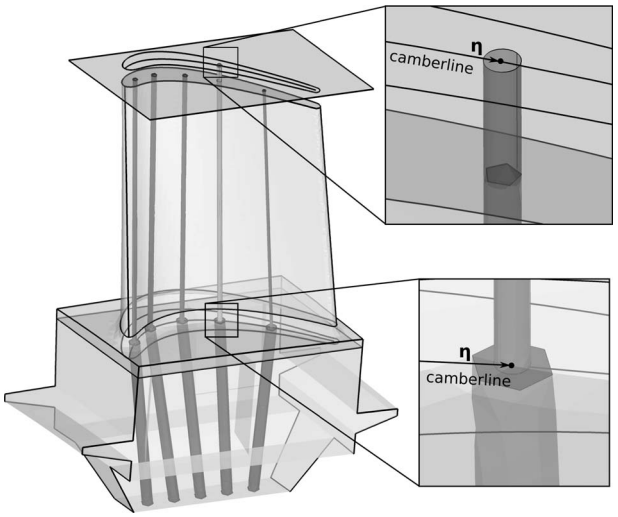

Fig. 3 Definition of the fourth cooling channel with $\varepsilon=0$

The components of the optimization algorithm are discussed in more detail in the following. The use of an artificial neural network (ANN) and a radial basis function (RBF) network as a metamodel is evaluated, and the results are compared in Sec. 3.

2.1 Parametrization of the Cooling Channels. The five cooling channels are straight cylinders defined by the position of their center at hub and shroud and by their diameter. The centers are defined by the local curvilinear (η,ε) coordinates instead of the Cartesian (x,y) coordinates. The $\eta\in[0,1]$ coordinate represents the length along the camber line, while $\varepsilon\in[-1,1]$ defines the position perpendicular to the camber line, as shown in Fig. 2. The maximum value of ε (±1) corresponds to half the blade thickness at each η location. This facilitates the definition of a valid set of design parameters, i.e., for which the cooling channels do not intersect the blade wall.

The local coordinates are the same at hub and shroud in order to reduce the number of design parameters. Figure 3 shows the 3D definition of the fourth cooling channel with $\varepsilon=0$.

Five individual cooling channels, parametrized by three numbers (η, ε, and D), result in 15 design variables. Table 1 shows the individual range for all parameters of each cooling channel.

Limits of ε are smaller than 1. This is a first restriction of the design space to avoid that cooling channels intersect with the suction or pressure side wall. The allowed η-ranges of cooling channels 3–5 are overlapping (see Table 1), which could result in intersecting cooling channels. Additional constraints during the optimization reject those geometries for which the distance between two cooling channels or between the cooling channel and the blade wall is smaller than 2 mm.

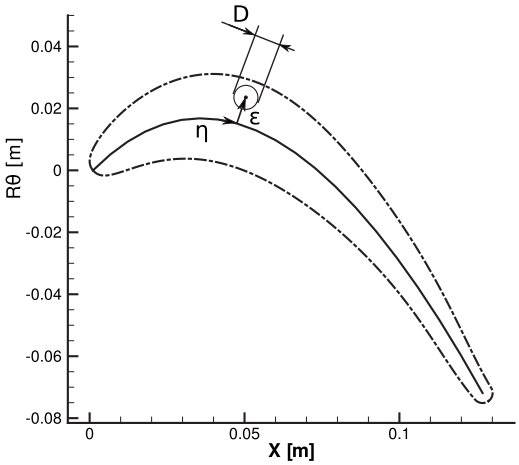

Fig. 2 Parametrization of the location and diameter of the cooling channel

2.2 CHT Analysis. The CHT method and required boundary conditions have been described in detail in Paper I [1]. Upon determination of the 15 free parameters, each pair (η,ε) is transformed back to its absolute coordinates, and an automated GAMBIT [9] journal constructs the finite element analysis (FEA) and 1D cooling channel computational grids. The wall boundary conditions, applied to the cooling channels, depend on the diameter because turbulators are introduced if the diameter is larger than 3 mm. The thermal stresses are computed after the convergence of the CHT analysis, and a lifetime prediction is performed. This entire process is fully automated and does not require any user interaction.

2.3 Performance. The performance of the geometry is assessed after each CHT and thermal stress analysis or after the prediction by the metamodel. In order to achieve the target lifetime with minimum coolant mass flow, a penalty related to an insufficient lifetime and increased coolant mass flow is given to each design. The task of the optimization algorithm thereby consists in finding the parameters that minimize the penalty. The total penalty, also known as the objective function (OF), is a weighted sum of the penalties given by Eq. (1).

$$\mathrm{OF}(\boldsymbol{G}) = w_l \cdot P_l(\boldsymbol{G}) + w_{\dot{m}} \cdot P_{\dot{m}}(\boldsymbol{G}) \tag{1}$$

The penalty on the lifetime (Eq. (2)) is proportional to the difference between the calculated $l(\boldsymbol{G})$ and the target lifetime l_{tar}. The latter is set to 20,000 h, which is very high considering the high inlet temperature. This penalty is zero only if the target lifetime (l_{tar}) is achieved (Fig. 4).

$$P_l(\boldsymbol{G}) = \max(l_{\mathrm{tar}} - l(\boldsymbol{G}), 0) \tag{2}$$

Table 1 Parameter range

	$\eta_{\min}$	$\eta_{\max}$	$\varepsilon_{\min}$	$\varepsilon_{\max}$	$D_{\min}$	$D_{\max}$
cc1	0.050	0.225	−0.65	0.75	0.002	0.005
cc2	0.225	0.375	−0.60	0.75	0.002	0.006
cc3	0.375	0.600	−0.60	0.75	0.002	0.005
cc4	0.550	0.750	−0.60	0.70	0.002	0.005
cc5	0.700	0.950	−0.35	0.40	0.002	0.003

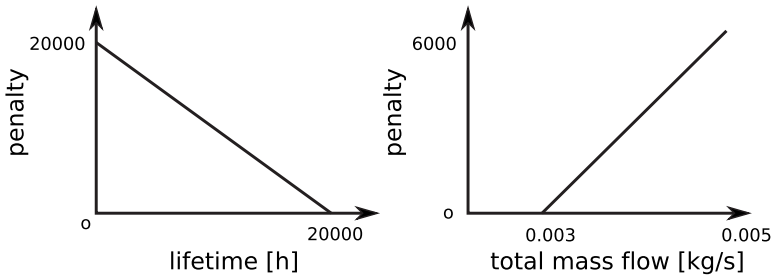

Fig. 4 Lifetime and coolant mass flow versus penalty

An increase in coolant mass flow results in a lower overall cycle efficiency and is penalized (Eq. (3)). The penalty increases when the mass flow is higher than an offset value $\dot{m}_{\text{offset}}=3$ g/s (Fig. 4).

$$P_{\dot{m}}(\boldsymbol{G}) = \max\left(\frac{\dot{m}(\boldsymbol{G}) - \dot{m}_{\text{offset}}}{\dot{m}_{\text{offset}}}, 0\right) \tag{3}$$

Considering that the lifetime penalty is more important than the mass flow penalty, the weight given to the mass flow penalty is 400. This results in a penalty of 133.33 for each g/s exceeding the limit of 3 g/s. The weight given to the lifetime is 1/h.

Note that both objectives—lifetime and mass flow—are grouped into one single objective (Eq. (1)). It is believed that multi-objective optimizations, trying to minimize the individual penalties, as described in, e.g., Refs. [10–12], would be less efficient for present application. Since both targets conflict with each other, no optimal solution may exist for which both penalties are zero. The optimization is likely to result in a Pareto front (Fig. 5) containing the non-dominated geometries, i.e., the geometries $\boldsymbol{G}$ for which one penalty cannot be decreased without increasing the other one. The choice is then left to the designer to select at the end of the optimization one geometry out of the non-dominated ones.

However, in most engineering applications, the relative importance of each objective is known at the start of the design. This allows defining weights for each penalty and the use of a single OF such as Eq. (1). Geometries lying on the dashed lines of Fig. 5 have the same OF and are considered as equal in performance. Changing the relative weights changes the slope of those lines. The smaller the OF, the closer the lines come to the Pareto front. The optimal solution is the one indicated by the black dot in Fig. 5.

By transforming a multi-objective optimization into a single-objective one, important decisions are not postponed until after the optimization. The optimization is well targeted, and less computations will be required to obtain the optimum. Moreover, present optimization uses a metamodel for which the accuracy is not guaranteed during the whole process. This would result in an inaccurate Pareto front and a false optimum unless the predictions are also verified by a CHT calculation. In a single-objective optimization, only the geometries in the neighborhood of the optimum, marked by the dark gray area in Fig. 5, need to be analyzed in detail. This is more cost effective, given the large computational effort for every CHT computation, while the designer still has the possibility to select the region of interest by changing the weights in Eq. (1).

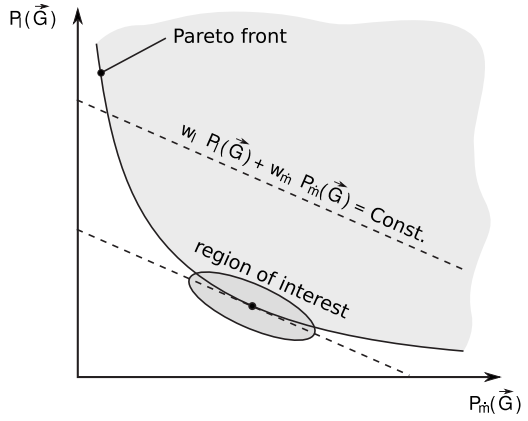

Fig. 5 Pareto front for a two objective optimization versus single-objective optimization

2.4 Database. The convergence to the optimum geometry strongly depends on the accuracy of the approximated predictions, which in turn depends on the information contained in the database. Database samples are needed at the start of the optimization algorithm to train the metamodel. A series of geometries must therefore be analyzed by the CHT method before the optimization can start. The design of experiment (DOE) method is used to define the samples of the initial database. This maximizes the amount of information contained in the database for a given number of computations [13].

The DOE technique considers that each design variable can take two values, fixed at 25% and 75% of the design range. A full factorial design would require a total of 2^{15} experiments, which is unfeasible. A so-called 2^{k-p} fractional factorial design is used where k is the total number of design parameters (15) while p defines the number of lower order parameter combinations that are not analyzed. The latter is fixed at 9, which results in a total of $2^6=64$ samples in the initial database.

One additional geometry for which all parameters are at 50% of their range is also added. It corresponds to the geometry with evenly distributed cooling channels, for which results are presented in Paper I.

2.5 Genetic Algorithm. GAs [14] are widely used in optimization. They are global search algorithms based on the mechanism of natural selection and simulate the survival of the fittest to obtain the optimum. Each design parameter is represented by 8 bits, allowing 256 possible values in between the parameter limits listed in Table 1. With 15 design variables this results in a total of 120 bits per geometry, which can be considered as the DNA of the individual.

The GA starts with an initial population of 50 individuals. The fitness of each geometry is evaluated by the computationally cheap metamodel. A tournament selection mechanism randomly picks two individuals and retains the one with the best performance. A second tournament selects a second individual, and both winning individuals are used as parents for the offspring. Two new individuals are generated based on a cross-over of the binary code of the parents. This procedure is repeated until all 50 new individuals of the next generation are defined. A cross-over with 75% probability and randomly selected cross-over position (out of 119 possibilities) is applied. Mutation probability is 0.8%. Elitism is used, which means that, if the best individual of the previous generation is not present in the new generation, it will replace a

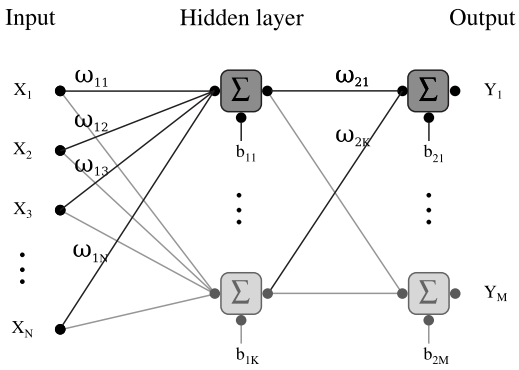

Fig. 6 Artificial neural network topology

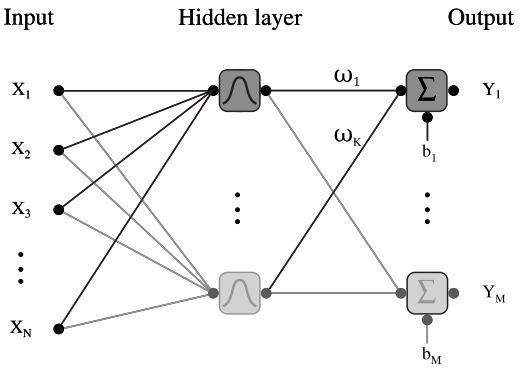

Fig. 7 Radial basis function network topology

randomly selected individual of the new generation. This guarantees that the best individual of the new generation is at least as good as the best from previous generation.

Each GA run consists of 1000 generations. Hence a total of 50,000 function evaluations is performed. This requires less than 1 s of CPU due to the small computational effort needed by the metamodel.

2.6 Metamodels. Metamodels mimic the exact evaluation tools (such as the CHT in the present application) and allow a very fast prediction of the performance of a geometry as function of its parameters. The prediction is based on the relation between input and output of several already evaluated geometries stored in the database. Two distinct steps are required for the use of a metamodel.

The first one is the learning or training of the model. This process defines the parameters of the metamodel that minimize the discrepancy between the model predictions and the results obtained by an accurate performance analysis of existing geometries. Once the metamodel is trained, it can be used to predict the performance of new geometries that are different from the training geometries.

Two different metamodels, an ANN and RBF network, have been used and their performance has been compared. Both have N input values and M output values.

2.6.1 ANN. An ANN, schematically shown in Fig. 6, is composed of several elementary processing units called neurons. These neurons are arranged in layers and joined by connections of different intensity, called connection weights. The network used by the present optimization has three layers: The input layer consists of the 15 design variables ($N=15$) and the hidden layer has $K=10$ neurons. Six individual ANNs are used, each with one single output neuron ($M=1$). Five of them predict the mass flow in the individual cooling channels and one predicts the lifetime.

The input to output relation for each hidden neuron i is given by Eq. (4), where X_j denotes the input, N is the number of input connections to the neuron, ω_j is the weight given to the jth connection, b_i is a bias value, and out_i is the output. A similar relation is used to define the output as function of the hidden layer neurons.

$$\text{out}_i = F\left(\sum_{j=0}^{N} \omega_j \cdot X_j + b_i\right) \tag{4}$$

The non-linear activation function F is a sigmoid (Eq. (5)).

$$F(x) = \frac{1}{1+\exp(-x)} \tag{5}$$

The standard back propagation technique is used to train the ANN, i.e., to determine the values of the weights ω_j and the bias b_i for each neuron i.

The ANN used in the present study is the "SNNS" developed at the Institute for Parallel and Distributed High Performance Systems of the University of Stuttgart [15,16].

2.6.2 RBF. The RBF network is also a three layer network with a non-linear mapping from the input layer to the hidden layer and a linear mapping from the hidden layer to the output layer (Fig. 7). The present application makes use of a Gaussian RBF network. The hidden neurons are associated with the so-called RBF centers, which are points in the N-dimensional space. The output of each hidden neuron is computed by a Gaussian function (Eq. (6)).

$$h_i = \exp\left(-\frac{\|\boldsymbol{x}-\boldsymbol{r_i}\|^2}{2\sigma_i^2}\right) \tag{6}$$

The vector $\boldsymbol{x}$ represents the input to the neuron, the vector $\boldsymbol{r_i}$ is the RBF center, and σ_i is the amplitude of neuron i. The $\|\ \|$ operator computes the Euclidean distance between the input vector $\boldsymbol{x}$ and the RBF center $\boldsymbol{r_i}$. The output of a RBF neuron is thus directly related to the distance between the input and the RBF center. The amplitude σ_i determines the activation range, i.e., the distance for which the neurons become active and have a significant output. The weight factor of a sample decreases with increasing distance from the RBF center.

The weighted sum of all outputs of the hidden neurons is the RBF output

$$Y_j = \sum_{i=1}^{K} \omega_i \cdot h_i + b_j \tag{7}$$

Training of the RBF network consists of finding the RBF centers $\boldsymbol{r_i}$, the amplitude σ_i, and the weight ω_i for each neuron such that the error on the prediction of the samples in the database is minimal. The resilient back propagation (RPROP) [17] applied to 20 RBF centers is used to train the RBF in the present application. Similar to the ANN, six individual RBFs are used to predict, respectively, the mass flow in each cooling channel and the lifetime of the blade. The RBF used in the present study is "RBF++" of Ref. [17].

3 Results

Two distinct optimizations are performed starting from the same initial database. One uses the ANN while the other uses the RBF to predict the same quantities. Both optimizations are run for 30 iterations, after which a synchronization of the databases is made, i.e., all existing samples are put together in one unified database. Additional 20 optimization iterations are performed restarting with this extended database. The purpose of this synchronization is to exchange information between both optimizers and see if they can profit from it.

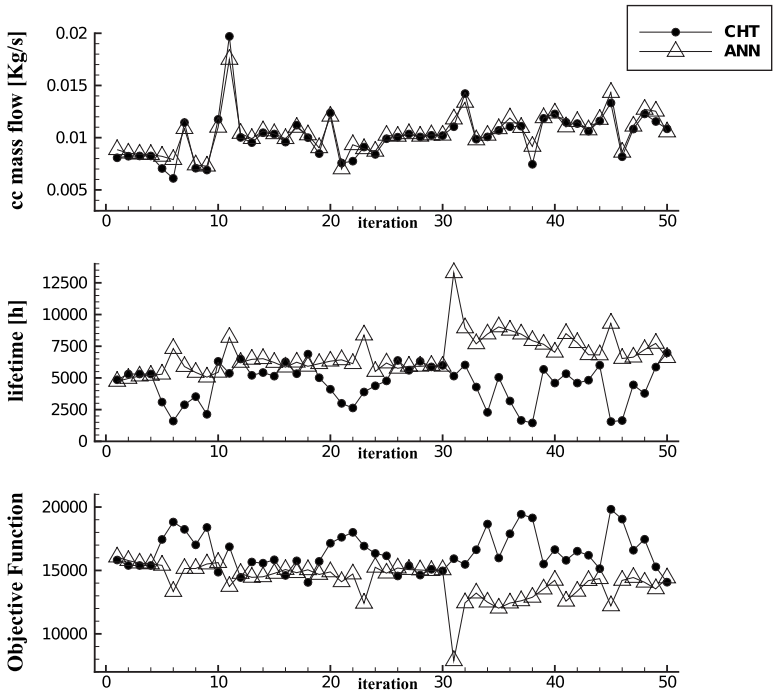

Fig. 8 ANN results

Figure 8 shows the evolution per iteration of the mass flow, lifetime, and OF of the ANN optimization. The metamodel predictions are compared with the results of the CHT and lifetime calculation. The mass flow in the individual cooling channels is immediately well predicted. This is not surprising since an almost direct relation exists between the diameter and the cooling mass flow. However, the lifetime is less accurately predicted. The ANN is too optimistic and predicts in most cases a higher lifetime than the CHT based computation. An even larger discrepancy is observed after the synchronization of the databases at iteration 30.

The convergence of the RBF is shown in a similar way in Fig. 9. The cooling mass flow is reasonably well predicted, however, less accurate than with the ANN. On the other hand, the lifetime is much better predicted until iteration 30. The convergence toward the optimum is rather monotonic except for two stepwise increases in lifetime. They correspond to a new choice by the optimization algorithm based on the newly acquired information. The systematic reduction in the OF observed before iteration 30 has disappeared after the synchronization. Only a small decrease in the OF is obtained. Although the lifetime is no longer accurately

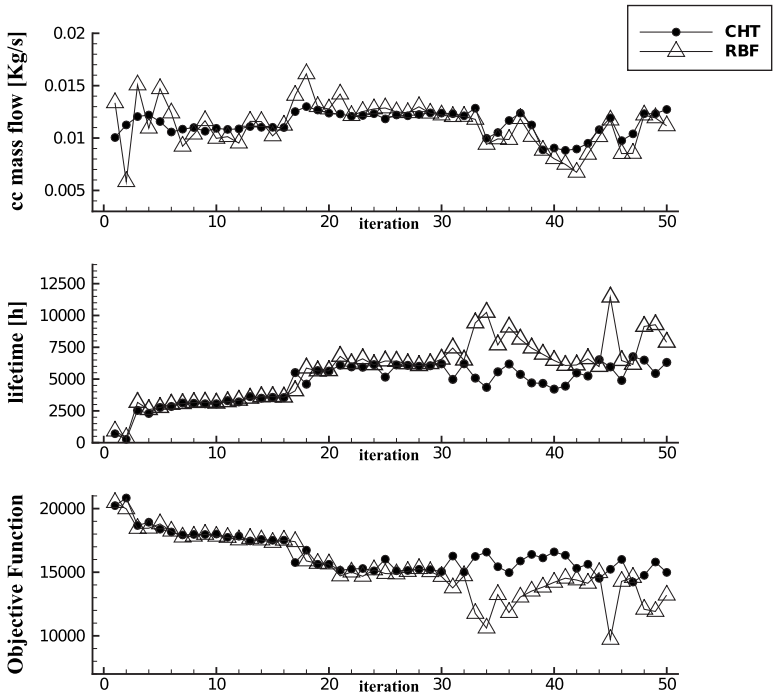

Fig. 9 RBF results

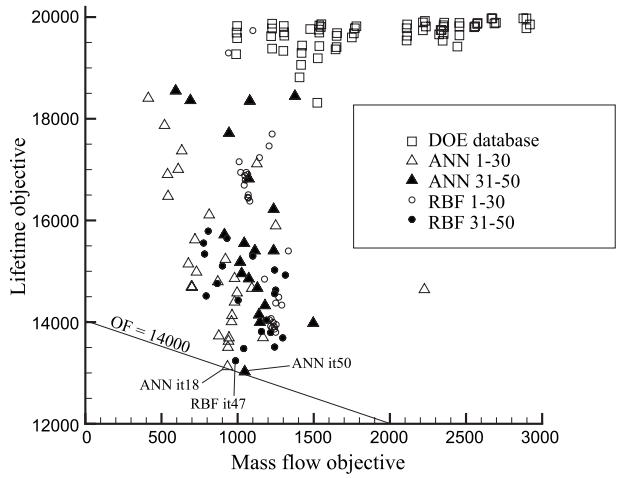

Fig. 10 Pareto front

predicted, the best RBF geometry is found at iteration 47 with a total penalty of 14,227. It has a lifetime of 6758 h for 10.4 g/s cooling flow.

As can be seen in Figs. 8 and 9, the prediction capabilities of both methods decrease after the synchronization. This is probably due to the increased number of training samples, requiring more hidden neurons, respectively, RBF centers to remain accurate.

Figure 10 shows the mass flow penalty versus the lifetime penalty for the initial database samples and both optimizations. It is clear that all geometries created by the optimization system outperform the initial database ones. Whereas the maximum lifetime of the samples contained in the initial database does not exceed 1685 h with an average lifetime of only 300 h, most optimized geometries have a lifetime above 5000 h. This illustrates the capability of the optimization system to rapidly improve the performance starting from only a limited amount of information.

The envelope of all CHT results constitutes a Pareto front. It is a very incomplete one because the optimizer has been targeted toward a particular combination of the two penalty functions (Eq. (1)). A large part of the design space has not been investigated. Results are in agreement with the expectations that increasing the lifetime requires a higher coolant mass flow. None of these optimized geometries achieves the target lifetime. The Pareto front almost exclusively consists of ANN geometries. The RBF optimization has produced geometries with a comparable lifetime but with a larger mass flow and hence a higher OF. After the synchronization of the databases, the RBF based optimization starts searching toward geometries with lower mass flow, indicating some benefit from the ANN acquired information.

The line of minimum OF (OF=14,000) is drawn in Fig. 10. As already discussed for Fig. 5, a number of geometries with almost equal OF are found. The best geometry, according to the present weight factors, is the 18th ANN iteration. This one is considered as the final optimized geometry. It has a total penalty of 14,058 corresponding to a lifetime of 6872 h and a cooling mass flow of 10 g/s. The ANN iteration 50 has a longer lifetime (6900 h) but needs a larger cooling mass flow.

The influence of the fifth cooling channel diameter on mass flow and lifetime is shown in Fig. 11. As can be expected, the mass flow increases almost linearly with diameter. The sudden reduction in mass flow at $D=3$ mm is due to the higher friction losses when the channel is turbulated. Both the ANN and RBF optimizers indicate that, based on the lifetime, the optimal diameter is situated around 2.85 mm.

Figure 12 shows the influence of a variation in the fifth cooling channel η-coordinate between 0.70 and 0.95 on mass flow and lifetime. Both optimizers indicate that it is of interest to put the coolant channel as close as possible to the trailing edge.

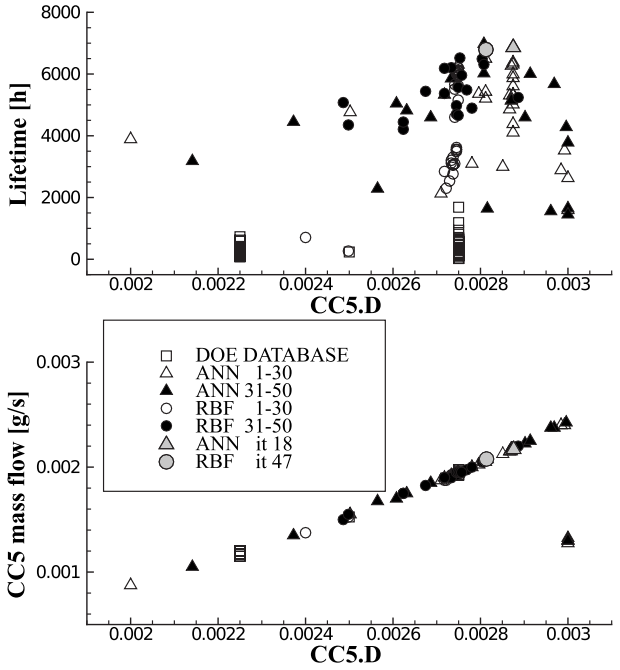

Fig. 11 cc5 diameter versus lifetime and mass flow

Figure 13 shows the influence of the diameter of the fourth channel on lifetime and mass flow. A sudden variation in the mass flow is again observed at 3 mm due to the activation of the turbulators. The longest lifetime is obtained with a turbulated cooling channel of 4.5 mm diameter.

The influence of the η-coordinate of the third channel is shown in Fig. 14. Geometries with a long lifetime are found over the entire range of η positions, indicating that other parameters play a more important role. However, there is a small bias toward geometries with a high η values. Also interesting to note is that the ANN geometries generated during iterations 1–30 cluster around

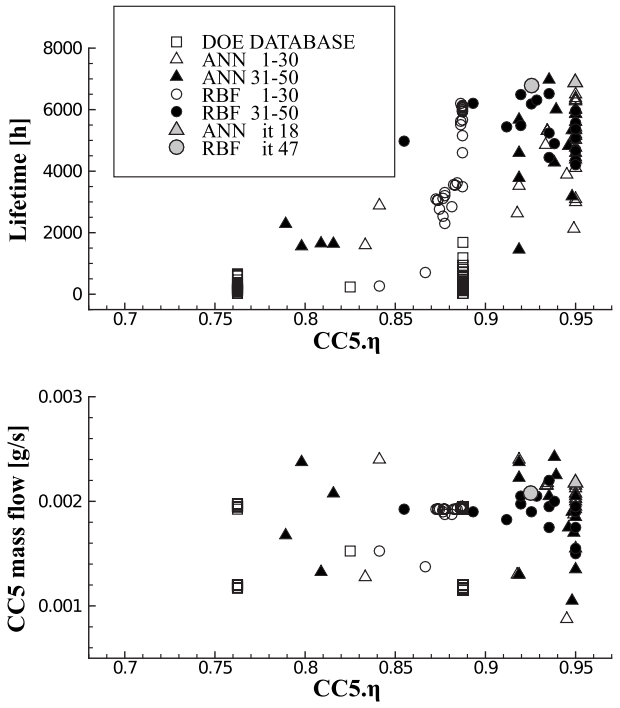

Fig. 12 cc5 η versus lifetime and mass FLOW

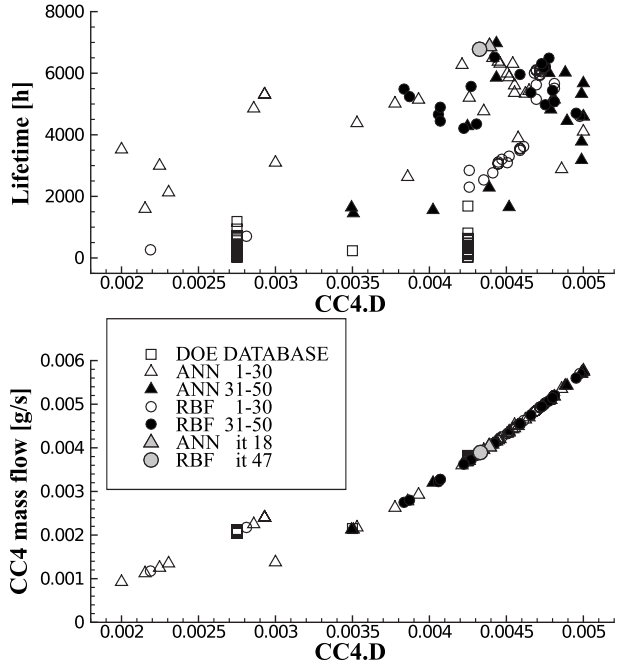

Fig. 13 cc4 diameter versus lifetime and mass flow

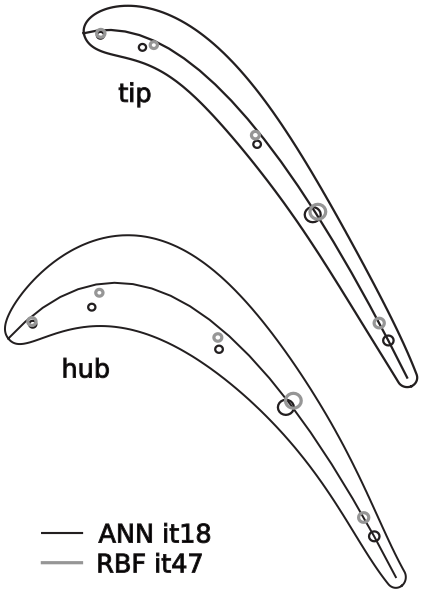

Fig. 15 Comparison of ANN and RBF optimized geometries at hub and shroud

the maximum η value of 0.6, while the RBF geometries of the same iterations cluster around 0.53. After the synchronization of the database, the RBF confirms a higher lifetime for the same diameter as predicted by the ANN. It is concluded that the gradual geometry changes, resulting from the RBF optimization, have converged to a local minimum and that this has been remediated by extending the database with the results of the ANN optimization.

The different behavior of the RBF and ANN optimizations results from the way the design space is explored. The outcome of a RBF prediction is a constant value (b_i) and some local corrections (higher or lower performance) in the activation range around the RBF centers (Eq. (7)). As a consequence, the highest and lowest OFs can only be found in the neighborhood of the database samples. Hence, the GA will never propose a new geometry that is very different from the existing ones.

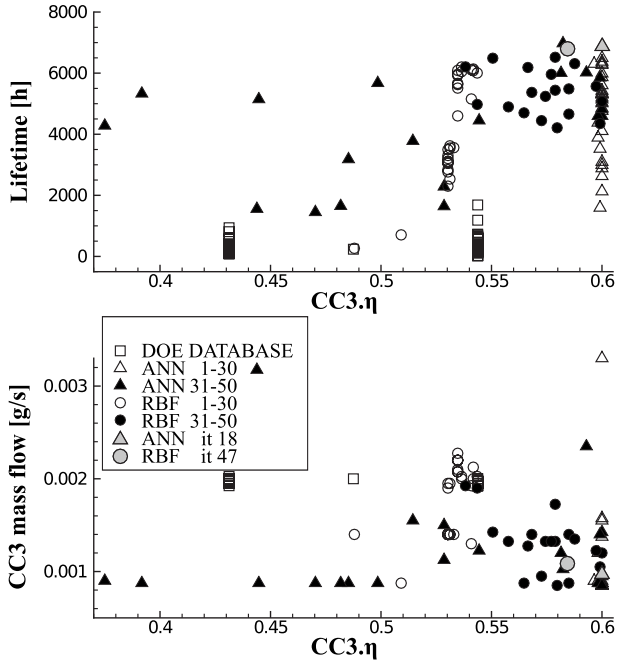

Fig. 14 cc3 η versus lifetime and mass flow

In an ANN prediction, each database sample influences the performance over the entire design space. The best performing geometries are no longer bound to existing designs but can be found everywhere. As a consequence, the predictions are less accurate, and large oscillations in performance between two successive iterations may be observed. It results, however, in a faster convergence to near optimal geometries.

It is likely that an optimization with mixed metamodels could perform even better. A possible combination could be a first scanning of the design space by an ANN metamodel followed by a local search using the RBF once the approximate location of the optimum is found. Another possibility could be to use both optimizers in parallel with one single database. Both optimizers would then benefit from each other's newly gained experience. This would most probably guide the RBF much quicker toward the optimal solution, while the ANN can also benefit from the RBF's more accurate predicted geometries.

Figure 15 compares the optimal solutions found by both optimizations. A tendency toward small non-turbulated cooling channels, near the pressure side of the blade, is observed. The trailing edge cooling channel should be positioned as far downstream as possible (η=0.95).

The temperature distribution for geometry 18 of the ANN optimization is shown in Fig. 16. A lower trailing edge temperature is obtained with respect to the geometry with evenly distributed cooling channels, presented in Part I. A higher temperature is now spotted at the leading edge.

The highest temperature gradient is near the fourth cooling channel and results in a local increase in thermal stresses. The normal effective stress distribution is given in Fig. 17. The optimized blade fails at the tip near cooling channel 4, whereas the blade discussed in Paper I [1] failed at the hub trailing edge. Compared with the blade with evenly distributed cooling channels, larger parts of the blade have a γ close to 1. The lifetime and strength is more uniformly distributed over the blade.

The results suggest that smaller temperature gradients and hence lower stresses would increase the lifetime. This could be possible by using a larger number of smaller cooling channels.

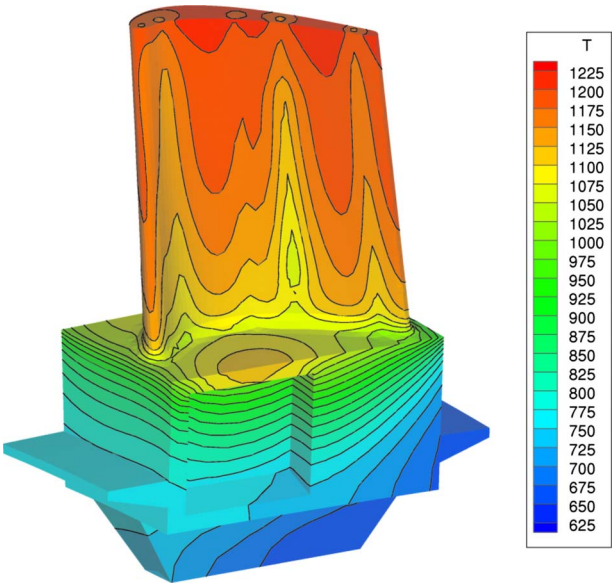

Fig. 16 Wall temperature of ANN iteration 18

However, the number of channels was fixed at 5, and the minimum channel diameter is limited by the manufacturability and by the risk that the cooling channels get contaminated and plugged.

Table 2 compares the results of ANN geometry 18 with those of RBF geometry 47. The real lifetime, based on the total stress (including centrifugal and pressure stresses), reduces to 450 h and 373 h, respectively, for the ANN and RBF optimized blades. This is unacceptably low but 25–30 times longer than for the nonoptimized blade (presented in Ref. [1]). The too low lifetime obtained with these optimizations is a consequence of the very harsh operating conditions, the limited cooling mass flow that has been allowed, and the absence of film cooling and a thermal barrier coating.

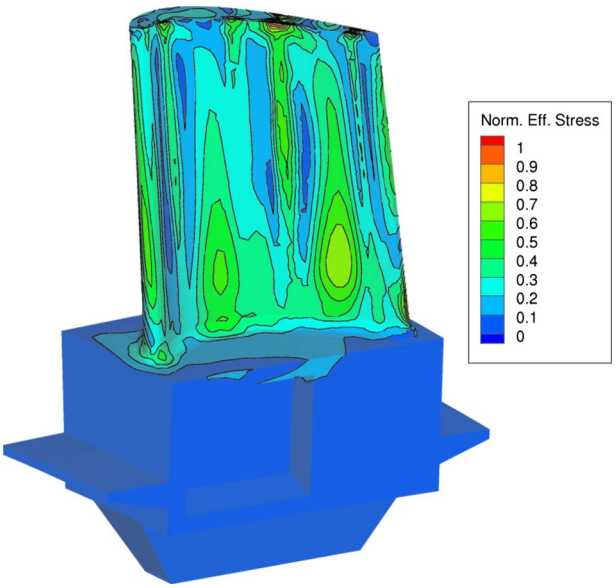

Fig. 17 Effective stress at rupture of ANN iteration 18

Table 2 Results for ANN it18 and RBF it47; stresses shown are von Mises stresses

	ANN it18	RBF it47
Maximum temperature (K)	1217	1217
Maximum thermal stress (MPa)	364	357
Lifetime only therm. stress (h)	6872	6758
Maximum centrifugal stress (MPa)	343	358
Maximum pressure stress (MPa)	32.6	32.0
Maximum total stress (MPa)	392	406
Lifetime (h)	450	373

4 Conclusions

This paper reports on the use of a multidisciplinary optimization algorithm that aims for maximum lifetime of a turbine blade operating at very high inlet temperature while limiting the cooling mass flow. The search is based on the accurate but computationally very expensive information obtained from the flow, stress, and CHT calculation methods described in Part I.

It is shown how the use of a metamodel allows a drastic reduction in the number of computational expensive CHT analyses to only 65 initial database geometries and 30 optimized geometries. Optimizing the geometry and position of the cooling channels resulted in a considerable increase in lifetime. The optimization system has shown to be cost effective and is suited for industrial applications.

The two different metamodels that have been tested show a rather different behavior but converge to a similar optimum. The RBF based optimization shows a slower but systematic approach toward the optimum. It behaves more like a gradient type method and could be trapped in a local minimum. The ANN based optimization makes a more random approach. Optimal solutions can be found over the whole design space, and the system is less sensitive to local minima.

The best geometry is found by the ANN based optimization. It has a lifetime of 6872 h based only on thermal stresses. This is significantly higher than the lifetime of the blade presented in Paper I (220 h) as well as the best sample of the initial database (1685 h). It turns out that the location and size of the cooling holes have a very large impact of the effectiveness in terms of lifetime. The main reason for not reaching the target values are the unrealistic harsh conditions and the very small cooling mass flow.

Acknowledgment

The financial support by Laborelec for the development of this method is gratefully acknowledged. Special thanks to Jean-Pierre Keustermans, Sébastien Grégoire, and Bea Ghys for their stimulating discussions.

Nomenclatrue

D = cooling channel diameter
$\boldsymbol{G}$ = geometry vector
l = lifetime
$\dot{m}$ = mass flow
P = penalty
w = penalty weight
ε = nondimensional position perpendicular to the camber line
η = nondimensional position along the camber line
ω = metamodel connection weight

References

[1] Amaral, S., Verstraete, T., Van den Braembussche, R., and Arts, T., 2010, "Design and Optimization of the Internal Cooling Channels of a High Pressure Turbine Blade—Part I: Methodology," ASME J. Turbomach., **132**(2), p. 021013.
[2] Nowak, G., and Wróblewski, W., 2007, "Thermo-Mechanical Optimization of Cooled Turbine Vane," ASME Paper No. 2007-GT-28196.
[3] Nowak, G., and Wróblewski, W., 2007, "Vane Cooling Optimization," *Proceedings of the Seventh European Conference on Turbomachinery*, pp. 687–697.
[4] Dennis, B. H., Egorov, I. N., Sobieczky, H., Dulikravich, G. S., and Yoshimura, S., 2003, "Parallel Thermoelasticity Optimization of 3-D Serpentine Cooling Passages in Turbine Blades," ASME Paper No. 2003-GT-38180.

[5] Dennis, B. H., Egorov, I. N., Dulikravich, G. S., and Yoshimura, S., 2003, "Optimization of a Large Number of Coolant Passages Located Close to the Surface of a Turbine Blade," ASME Paper No. 2003-GT-38051.
[6] Pierret, S., and Van den Braembussche, R. A., 1999, "Turbomachinery Blade Design Using a Navier Stokes Solver and Artificial Neural Networks," ASME J. Turbomach., **121**, pp. 326–332.
[7] Cosentino, P., Alsalihi, Z., and Van den Braembussche, R. A., 2001, "Expert System for Radial Impeller Optimization," *Proceedings of the Fourth European Conference on Turbomachinery*, pp. 481–490.
[8] Rini, P., Alsalihi, Z., and Van den Braembussche, R. A., 2001, "Evaluation of a Design Method for Radial Impellers Based on Artificial Neural Network and Genetic Algorithm," *Proceedings of the Fifth ISAIF Conference*, pp. 535–543.
[9] GAMBIT mesh code, 2007, http://www.fluent.com/software/gambit/index.htm.
[10] Giotis, A. P., Giannakoglou, K. C., and Périaux, J., 2000, "A Reduced-Cost Multi-Objective Optimization Method Based on the Pareto Front Technique, Neural Networks and PVM," *Proceedings of the ECCOMAS*.
[11] Karakasis, M. K., and Giannakoglou, K. C., 2004, "On the Use of Surrogate Evaluation Models in Multi-Objective Evolutionary Algorithms," *Proceedings of the ECCOMAS*.
[12] Karakasis, M. K., and Giannakoglou, K. C., 2006, "On the Use of Metamodel-Assisted, Multi-Objective Evolutionary Algorithms," Eng. Optimiz., **38**, pp. 941–957.
[13] Montgomery, D., 2006, *Design and Analysis of Experiments*, Wiley, New York.
[14] Goldberg, D. E., 1989, *Genetic Algorithms in Search, Optimization and Machine Learning*, Addison-Wesley, Boston, MA.
[15] University of Stuttgart, 2006, Stuttgart Neural Network Simulator, http://www.nada.kth.se/orre/snns-manual.
[16] Zell, A., Korb, T., Sommer, T., and Bayer, R., 1990, "Applications of Neural Networks," *Conference Proceedings SPIEs Aerospace Sensing International Symposium*, Vol. 1294, pp. 16–20.
[17] Buck, S., 2006, RBF++: A Library for Function Approximation by Means of Radial Basis Functions, http://www9.in.tum.de/people/buck/RBF/.

Improvement of Stalling Characteristics of an Axial-Flow Fan by Radial-Vaned Air-Separators

Nobuyuki Yamaguchi

Masayuki Ogata

Meisei University,
2-1-1 Hodokubo, Hino-shi,
Tokyo 191-8506, Japan

Yohei Kato

Japan Filter Technology, Ltd.,
I-1-1, Aza Sugise,
Tsuhata-machi, Kawakita-gun,
Ishikawa Prefecture 929-0454, Japan

An improved construction of air-separator device, which has radial-vanes embedded within its inlet circumferential opening with their leading-edges facing the moving tips of the fan rotor-blades so as to scoop the tip flow, was investigated with respect to the stall-prevention effect on a low-speed, single-stage, lightly loaded, axial-flow fan. Stall-prevention effects by the separator layout, relative location of the separator to the rotor-blades, and widths of the openings of the air-separator inlet and exit were parametrically surveyed. As far as the particular fan is concerned, the device together with the best relative location has proved to be able to eliminate effectively the stall zone having existed in the original solid-wall characteristics, which has confirmed the promising potential of the device. Guidelines were obtained from the data for optimizing relative locations of the device to the rotor-blades, maximizing the stall-prevention effect of the device, and minimizing the axial size of the device for a required stall-prevention effect, at least for the particular fan and possibly for fans of similar light-load fans. The data suggest the changing internal flow conditions affected by the device conditions.
[DOI: 10.1115/1.3104612]

Keywords: fluid machinery, fluid mechanics, axial-flow fan, fan stalling, antistall device, air-separator

1 Introduction

Improved performance efficiency of turbomachines, such as gas turbines, jet engines, compressors, fans, and so on, is being desired in the fields of electric power generation, prime movers, and industrial plants, from a view not only to the economy of operation but also to the problems of global climate changes and energy security. The authors, aiming for raising both working efficiencies and operational safety of axial-flow compressors and fans, have strived for improvement of stall and surge characteristics of the machines. Improved stall characteristics could widen the working area, enabling us to take full advantage of the peak-efficiency area close to the near-stall zone. It could achieve substantial saving in the whole plant power requirement in addition to the plant operational safety [1,2].

To improve stall characteristics of axial-flow fans and compressor stages, a variety of devices have hitherto been attempted such as casing treatment, suction bypass, blade separator, air-separator, etc., by many researchers and institutes [1,2]. Among them, the present authors have paid attention to the air-separator, which was proposed first by Ivanov et al. [3]. 2 decades ago, Miyake et al. [4,5] conducted a pioneering work on the effects of the air-separators. McKenzie and co-workers [6–8] made researches for application in axial compressors. Investigations on the effect of geometrical dimensions of air-separator devices on the stall prevention were reported by Ziabasharhagh et al. [7]. Yamaguchi et al. [9,10] made developmental investigation on the practical application of the air-separator device to industrial fans. A practical application and the effect of a similar device on a low-pressure axial fan were reported by Bard [11].

The air-separator has a significant advantage in that its construction is completely embedded in the fan casing and no parts of the device are exposed to the incoming flow and the rotor-blades. The advantage is similar to casing treatments. In contrast, blade separators and suction rings having parts exposed to incoming flows and the rotor-blades, tend to injure aerodynamic performances and mechanical safety of the rotor-blades in addition to induced increases in noise level.

The air-separator is hereafter abbreviated AS. The general construction of the conventional AS introduced above has an open circumferential cavity as the AS inlet facing the rotor-blade tips. In the recirculation passage downstream of the inlet cavity, a circumferential row of vanes is provided for rectifying the swirling flow to axial direction. Downstream of the axial-vanes, an open circumferential cavity as the AS exit. So, the AS is named axial-vaned AS here.

A schematic structure of the air-separator device, which the present authors are concerned with here and has been proposed in Ref. [9], is shown in Figs. 4 and 5. A circumferential row of curved radial-vanes shown as a shadowed part are mounted within the circumferential slit of the AS inlet opened to the moving rotor-blade tips in contrast to the conventional axial-vaned AS. The type is named radial-vaned AS hereafter. The radial-vanes are expected to scoop directly a portion of the flow swirling along the casing wall around the blade tip. The vanes eliminate the swirl and turn the flow into axial direction; after that the flow out of the AS exit opening joins the main axial flow smoothly.

The principle of the stall-prevention effect of the radial-vaned AS is expected to be the same as that of the conventional axial-vaned ones. When the stage working condition comes close to stalling, small zones of low-energy fluid tend to appear locally and temporarily in the endwall region near the blade tip, initiating embryos of stall, or disturbances such as local reversed flow, precursor of rotating-stall cells, and so on. The disturbances could interfere with the main inflow and bring about strong disturbances, tending to force the stage into stalling. In the situation, the

Contributed by the Turbomachinery Division of ASME for publication in the JOURNAL OF TURBOMACHINERY. Manuscript received September 5, 2008; final manuscript received November 27, 2008; published online January 13, 2010. Review conducted by Aspi Wadia.

AS device, if equipped, would absorb and rectify the embryos and separate them from the main flow. In the tip flow environment thus kept cleaner [1,2], the blade tip-section could work to the best of the performance. In addition to that, increased flow recirculation through the AS passage would tend to alter the flow structure gradually to an axisymmetric annular one, like an annular vortex ring encasing the blade tips, as was shown for the case of blade separators by Tanaka and Murata [12]. The circumstances would make the meridional streamlines through the rotor bladings more and more inclined radially outward as in mixed flow fans and pumps, toward the lower flow rate. Thus the fan pressure rise would continue to increase toward a lower flow rate. All such situations are expected to make a great improvement in stall prevention.

The embryos of stalls are supposed to tend to swirl more or less accompanied by the rotor-blades; when stalling conditions come closer, the swirl velocity would be larger; thus the centrifugal forces would be stronger than the ambient flow. The embryos would be centrifuged spontaneously into the AS inlet opening, if present. Thus, the effect of the AS could be reasonably considered to be of a nature of passive stall control. The presence of the radial-vanes proposed here would be advantageous for capturing definitely such embryos, scooping them into the AS passage and rectifying them soon.

Yamaguchi et al. [9] showed that the device demonstrated a very strong and stable stall-prevention effect. Nishioka et al. [13] confirmed a similar stall-prevention effect using an AS device having a similar construction. Furthermore, Yamaguchi et al. [10] showed experimentally that an axial-flow fan equipped with both variable-pitch inlet guide-vanes and a radial-vaned AS could achieve favorable performances covering a very wide range of flow rate, which could surpass that of suction-vane-controlled turbo-type centrifugal fans.

In the above situation, the authors have made a more detailed experimental study on the effects of radial-vaned AS devices with a view to both optimization of the stall-prevention effect, related to the AS geometry, and reduction in the device size by use of a single-stage, low-pressure, axial-flow fan [14,19]. The results are summarized below.

The general tendency surveyed from existing data on the stall-prevention effects achieved by the axial-vaned AS and the radial-vaned AS is summarized in Fig. 13 in the Appendix, with attention to the shifts of the stalling points from the solid-wall ones to the improved ones by the ASs on a map of pressure coefficient versus flow coefficient. On the map, the present fan for test is seen to belong to very light-loaded ones, which appear at a first glance to be easy to improve by use of AS devices. Even in the zone, however, general rules or guidelines for the optimum AS devices have not been available as yet. In the situation, the aim of the present investigation is to prepare a part of the database and to establish a line of thinking for stall improvement by means of radial-vaned ASs.

This paper describes the experimental results on a radial-vaned AS having a relatively spacious size that could have achieved an excellent stall-prevention effect. With respect to the reduction in the radial height of the AS device, including simplification of the radial-vane configurations, readers should refer to the following part of this report [15].

2 Experimental Axial Fan

The experimental fan is a commercially available one of single-stage, axial-inlet type consisted of a rotor and exit guide-vanes. The fan casing near the rotor tip was modified for mounting an AS device.

Table 1 gives main numerical figures about the fan. Figure 1 shows a photograph of the fan rotor equipped with a built-in AS device in the fan casing. Table 2 gives blade geometrical data as measured of the rotor at the tip and the root. Each rotor-blade was made of a thin metal plate of thickness 2 mm formed to circular-arc sectional shapes twisted along the height. The rotor-tip clearance is 2 mm in radius.

Table 1 Numerical data of the experimental fan

Casing diameter D_t	394 mm
Tip diameter	390 mm
Hub diameter D_h	194 mm
Tip clearance	2 mm
Fan speed	2600 rpm
Nominal motor power	1.5 kW
Nominal fan pressure rise	0.20 kPa
Nominal fan flow rate	100 m^3/min

Figure 2 shows the exit guide-vanes and the driving electric motor when the fan rotor is removed. As seen in Fig. 2, the exit guide-vanes do not constitute an ordinary regular cascade since the lower part serves as a support of the motor. Although this is an unfavorable situation in the hope of a uniform flow leaving the rotor, the situation could not be changed. So, as a next best, static pressures were measured at four points on the circumference immediately downstream of the rotor-blades and averaged.

Figure 3 shows the fan test facility. Upstream of the fan is a short suction duct of diameter 0.394 m. Fan static-pressure rises Δp_S were evaluated from wall pressures at the upstream tap ($Ps1$) and the tap ($Ps2$) on the fan casing downstream of the rotor and immediately upstream of the exit guide-vanes. Downstream of the fan is connected a delivery duct of length of 3.0 m, including a flow-straightener and a Venturi tube for metering the fan flow rate Q. The fan working condition is regulated by a throttling device of cone-type at the duct exit. The fan power inputs P were measured from the electric power inputs to the fan motor (after the inverter), which includes motor power losses also. The fan speed was set at 2600 rpm. The fan Reynolds number based on the blade-chord length and the blade tip speed was around 4×10^5.

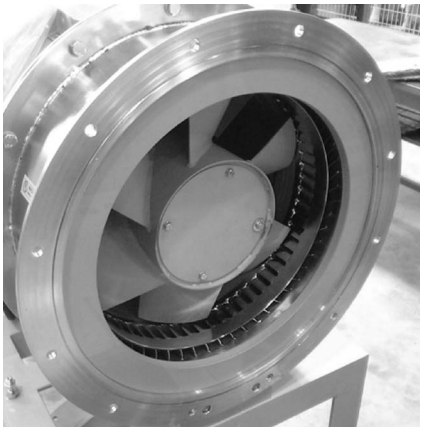

Fig. 1 The rotor mounted together with the air-separator device

Table 2 Conditions of the rotor-blades

	Tip	Root
No. of rotor-blades	6	6
Chord length l (mm)	115	130
Blade spacing t (mm)	190	117.5
Pitch-chord ratio t/l	1.65	0.90
Stagger angle ξ (deg)	71	43
Camber angle θ (deg)	31.7	43.5

Fig. 2 The exit guide-vanes and the driving electric motor

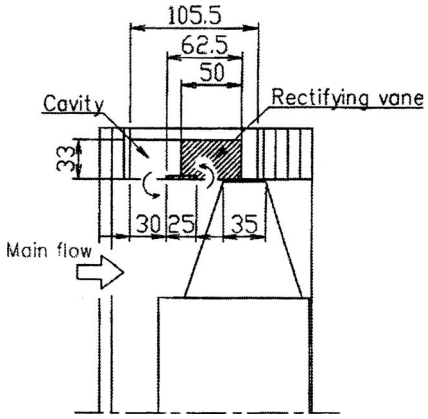

Fig. 4 Original dimensions of the studied fan and the air-separator device

Uncertainty in pressure measurements is about 1.5% mainly because of the diaphragm-type pressure indicators of low pressure-level used for the experiment. Uncertainty in the fan flow rate is therefore evaluated 1.1%. The accuracy of the wattmeter for the motor is 0.5%. The uncertainty in fan efficiency is therefore evaluated 1.9%.

3 Air-Separator Device

The structure and dimensions of the AS device employed in the study, and the location of the AS device relative to the rotor-blades are shown schematically in Fig. 4. The configuration of the radial-vanes embedded in the AS device, which is named Type A, is shown in Fig. 5. The vane is formed in a circular-arc sectional form and the inner leading-edge is extended in flush with the fan casing wall. The vanes are aimed for scooping directly the swirling flow close to the casing wall in the tip blade leading-edge region. The flow is considered, in near-stalling or stalling conditions, to be flowing predominantly in the direction of blade movement accompanied by the blade rotation. In the situation, the radial-vanes are expected to establish effectively a more axisymmetric flow pattern within the AS inlet opening independently of the rotor speed, than conventional axial-vanes, which have been suggested by Yamaguchi et al. [9].

The numerical figures given in Figs. 4 and 5 are prototypical ones for the setup. In the course of the investigation, various dimensions will be changed and adjusted. For example, in Sec. 8, the axial location of the AS device will be changed relative to the rotor-blades by the use of spacer rings with different thicknesses, which makes parametric study easy on the effect of the relative axial locations.

4 Nondimensional Parameters

Performance results are normalized with respect to the blade tip speed u_t.

$$\text{Flow coefficient:} \quad \phi_t = V_a/u_t \tag{1}$$

$$\text{Fan rotor total-pressure coefficient:} \quad \psi_t = \Delta p_t/\tfrac{1}{2}\rho u_t^2 \tag{2}$$

$$\text{Fan rotor static-pressure efficiency:} \quad \eta_S = Q\Delta p_S/P \tag{3}$$

$$\text{Total pressure efficiency:} \quad \eta_T = Q\Delta p_T/P \tag{4}$$

Here, Q is the fan flow rate (m^3/s), P is the motor power input (W), u_t is the fan rotor-tip speed (m/s), V_a is the annulus-average axial velocity (m/s), ρ is the air density (kg/m^3), Δp_S is the fan rotor static-pressure rise between the fan suction duct wall (location $Ps1$ in Fig. 3) and the rotor exit wall just before the exit guide-vanes (location $Ps2$ in Fig. 3) (Pa), and Δp_T is the fan rotor total-pressure rise (Pa).

$$V_a = Q \Big/ \frac{\pi}{4}(D_t^2 - D_h^2) \tag{5}$$

$$\Delta p_T = \Delta p_S + \tfrac{1}{2}\rho V_a^2[1 - (1 - \nu^2)^2] \tag{6}$$

$$\Delta p_S = p_{S2} - p_{S1} \tag{7}$$

Here, D_t and D_h are the diameters of the fan casing and hub, respectively (m), and υ is the hub-to-tip radius ratio.

$$\nu = D_h/D_t \tag{8}$$

5 Performance of the Solid-Wall Fan

The fan performance with the solid-wall casing is shown in Fig. 6 for a basis in comparing the stalling characteristics affected by AS devices. The solid-wall conditions are abbreviated SW hereafter. For the SW condition, the stalling flow coefficient ϕ_{tS} is 0.32, below which pressure coefficient ψ_t and efficiencies η_T and η_S drop and do not recover. Stalling was judged to occur at the zero-slope point of the fan rotor total-pressure coefficient ψ_t.

For flow coefficient φ_t below 0.20 in the stalled SW condition, reversal of strong swirling flow up to the suction duct inlet up-

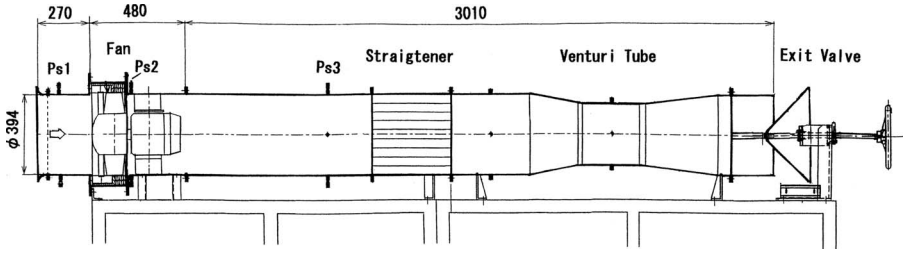

Fig. 3 Test facility of the fan

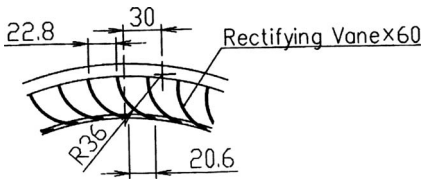

Fig. 5 Rectifying radial-vanes of air-separator Type A

stream of the rotor was observed by visualization of the flow by use of a tuft grid prepared there. The swirling flow reversal was considered to affect the suction wall static pressure; therefore the fan pressure apparently decreases, resulting in the one given by X marks in Fig. 5. When the atmospheric pressure was used as suction standard by altering the suction passage, different pressure-rise characteristics resulted as a more correct performance given by marks ○ for the same range of flow coefficient below 0.20, although for flow coefficient above 0.20 quite the same pressure-flow characteristics were obtained as shown by marks ■ in Fig. 6. In this report, the referential SW characteristics for flow coefficient above 0.2 are employed.

Figure 6 shows some characteristic points of importance in examining the AS effects in the aerodynamic performances of the fan, i.e., stalling-point flow coefficient ϕ_{tS}, stalling-point total-pressure coefficient ψ_{tS}, and peak total efficiency η_{TP}.

6 Effects of Air-Separator Devices

Figure 7 shows one of the best AS performance obtained in this investigation, in comparison with the SW performance. The AS performance, about which details are described in Sec. 7, was obtained for the layout shown in Fig. 4, at the best location of the AS device Type A relative to the rotor-blade tip, $g/Za=0.64$. In the figure, solid marks are for the SW performance and the white marks are for the best AS one. The best AS performance shows no stall over the originally stalled range from the SW stall point of φ_{tS} of 0.32 down to the shut-off condition. The steep drop in the SW efficiency around the SW stall point is seen to have disappeared in the AS condition. For the AS condition was never seen

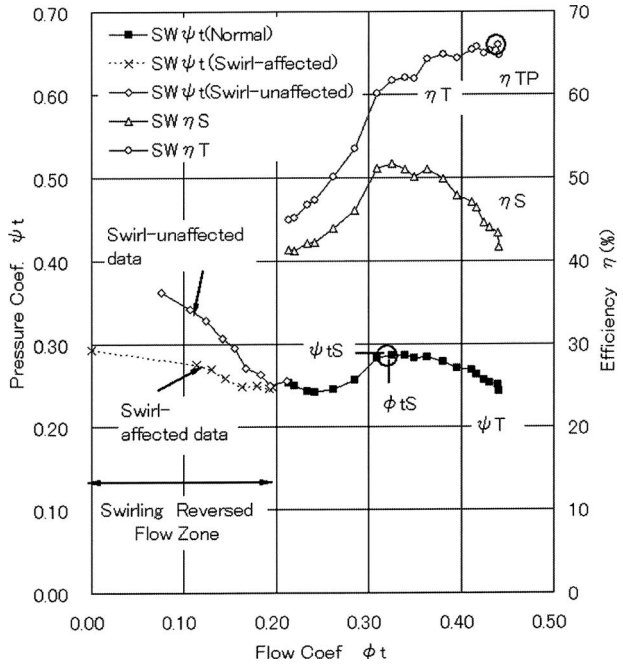

Fig. 6 Fan performance characteristics in the solid-wall condition and reference points

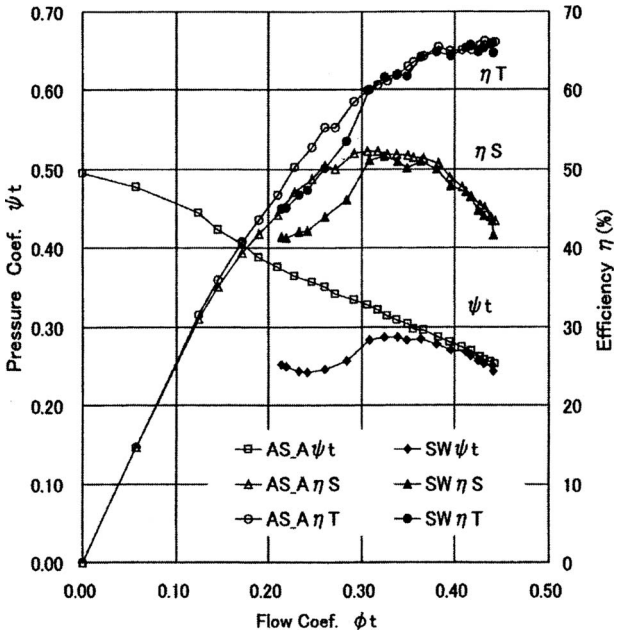

Fig. 7 Comparison of fan performances for conditions with the best air-separator (Type A, *S*=37.5 mm, *C*=30 mm, *W*=33 mm, and *g*=22.4 mm) and for the conditions with the solid wall

the swirling reversed flow up to the fan duct inlet, which had been observed for the SW condition. In addition to that, no deterioration in the fan efficiency is seen in the sound region. In Secs. 7 and 8, details leading to the results will be described.

7 Effects of Air-Separator Locations Relative to the Rotor Tip

Figure 8 shows the symbols of variables that are inevitable in describing the process of optimizing the AS geometry. H is the fan annulus height, and Za is the axial chord of the rotor-tip blade-section. With respect to the AS device, S and C are the widths of the inlet opening and the exit opening of the AS device, respectively, b is the width of the inner ring, W is the height of the internal passage, and g and h are distances to the leading-edge of the rotor-tip blade-section from the upstream edge and the downstream edge, respectively, of the AS inlet opening. All values except H and Za could be variable in this investigation.

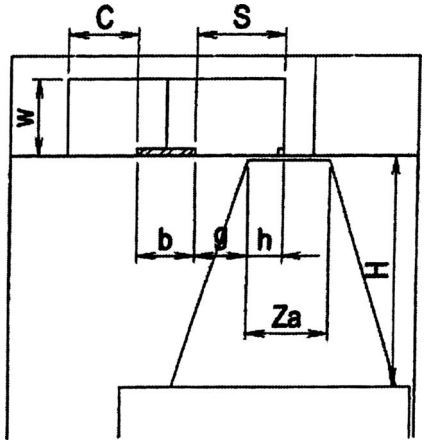

Fig. 8 Variable dimensions of the studied air-separator

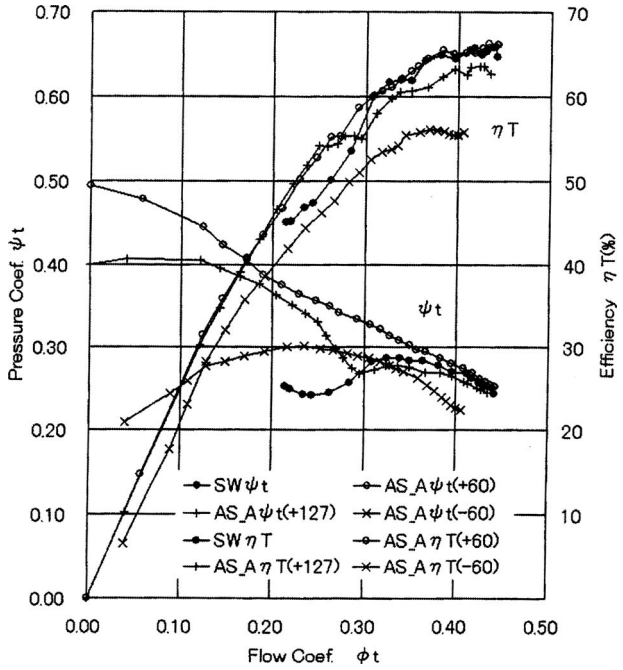

Fig. 9 Comparison of fan performances by air-separator Type A for various relative locations *g/Za* (*S*=37.5 mm, *C*=30 mm, *W*=33 mm, and *b*=25 mm)

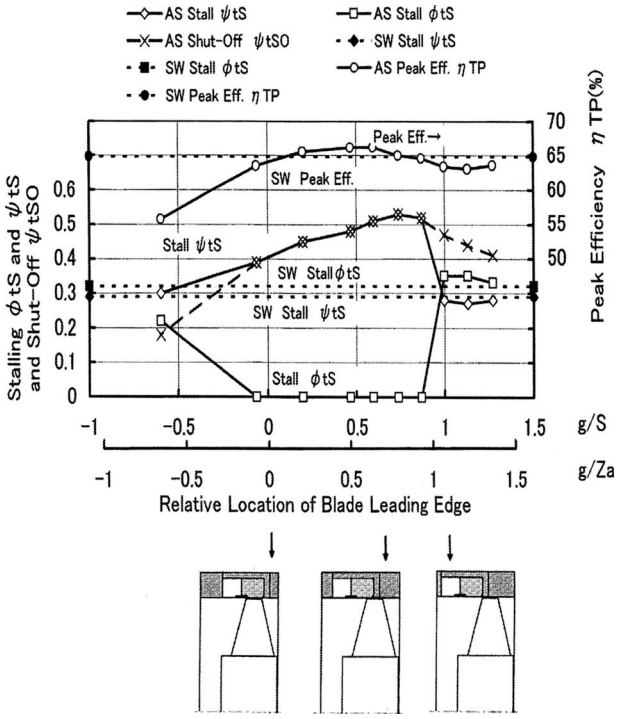

Fig. 10 Effects of relative locations of the air-separator Type A (*S*=37.5 mm, *C*=30 mm, *W*=33 mm, and *b*=25 mm)

The prototypical numerical values of the present device here are given as follows.

(1) Blade data: $H=100$ mm and $Za=35$ mm.
(2) AS data: $W=33$ mm, $C=43$ mm, $S=37.5$ mm, and $b=25$ mm.

The axial width of the radial-vanes of the AS device here is 50 mm throughout the investigation.

In Sec. 7, with numerical values of H, Za, W, b, S, and C kept constant, respectively, as above, g (and accordingly h) were changed to survey the effect of the location of the AS device relative to the blade. In Sec. 8, the effects of the widths of the AS openings were surveyed by changing S and C with other variables kept constant. The effect of the AS passage height W will be reported in the succeeding paper [15] related to this one.

7.1 Effect of the Relative Location on the Characteristic Curves. Figure 9 compares the behaviors of the performance characteristics for different locations of the AS device relative to the leading-edge of the rotor-tip blades. For the purpose, axial locations of the AS device g (and h) were altered by changing annular spacer rings. In Fig. 9, four typical behaviors of fan performance characteristics are shown: (1) the SW condition (tagged as SW in the figure), (2) the AS condition with $g/S=0.60$ (tagged as AS_A(+60)), (3) the AS condition with $g/S=1.27$ (tagged as AS_A(+127)), and (4) the AS condition with $g/S=-0.60$ (tagged as AS_A(−60)). The efficiencies in Fig. 9 are the total ones. AS_A(+60) is the same one as given in Fig. 7, showing no stall zone, i.e., no positive-slope region over the entire flow down to the shut-off condition and improved efficiency in the originally stalled zone for the SW condition.

On the other hand, the other two AS conditions show quite different behaviors. AS_A(−60) shows an improved stalling flow coefficient, but general levels of the pressure coefficient and the efficiency are seen to lower significantly. For AS_A(+127), pressure coefficient lowers below the SW one in the SW sound region, shows a local pressure dent corresponding to stalling, and returns again after the dent to a rising tendency, showing a positive-slope region before the shut-off and reaching at relatively high shut-off pressure coefficient. As a whole, it has nearly a negative-slope tendency, except the local stalling zone and near shut-off region. The efficiency level in the SW sound zone is lower than those for the SW condition and AS_A(+60) condition. After the local pressure dent, the efficiency is close to that of the AS_A(+60) condition.

7.2 Stall-Improved Range for *g/S* . The feature and the cause of the varying performance behaviors observed above will be suggested in Fig. 10, which summarizes the results in terms of stall flow coefficient φ_{tS}, stall pressure coefficient ψ_{tS}, and peak-efficiency η_{TP}. The data were obtained by changing the locations of the AS device relative to the rotor-blade by use of different thicknesses of annular spacer rings. The abscissa of Fig. 10 is the relative AS locations g/S and g/Za. Although the relative axial location of the rotor-blade leading-edge g/S is mainly paid attention to, since it is considered of primary importance, other quantities, such as g/Za, could also have some important influence in a correlated manner. In Fig. 10, the SW data are given by horizontal dotted lines as references.

As shown in Fig. 10, for the condition roughly $0<g/S<1$, the stalling flow coefficient φ_{tS} is zero, namely, it is stall-free over the whole flow range down to the shut-off condition. The favorable results are achieved with the leading-edges of the rotor-tip blade-sections located within the axial width of the AS inlet opening, as shown by the sketches at the bottom of the figure. For the condition $0<g/S<1$, shut-off pressure coefficients ψ_{tSO} agree with stall pressure coefficients ψ_{tS}, reaching at the maximum value at $g/S=0.74$.

The peak total efficiency η_{TP} in the sound region appears improved somewhat in comparison with that of the SW condition for the range $0.2<g/S<0.7$, in which the maximum improvement is seen to be roughly 1% for around $g/S=0.5$. The obtained best performance is shown in Fig. 7. Although, generally speaking, such gain in the efficiency could not be relied on in the situation effected by such stall-improvement devices, repeated tests have

confirmed that this particular fan has the tendency, which should be regarded only as a measure showing an unimpaired flow conditions of the fan there.

7.3 Deterioration of Stall-Improvement Effect Owing to Retracted Blade Leading-Edge. The stall-prevention effect, however, lowers in conditions both for roughly $g/S<0$ and roughly for $g/S>1$. In Fig. 10, around the value of g/S of unity, the stall-prevention effect has been lost completely for a slight increase in g/S where both coefficients of flow and pressure at the stall get suddenly back to the SW ones or even to worse ones.

Around g/S of unity, local depression of fan pressure rise around the stalling point begins to appear on the fan performance curve; with increasing g/S, the depression deepens, and a positive-slope zone appears finally as seen by the performance curve AS_A(+127) in Fig. 9. The apparent drastic deterioration in the stall-improvement effect seen at around g/S of unity in Fig. 10 has resulted from the course of the phenomena.

On the other hand, the shut-off pressure coefficient ψ_{tSO} (shown by mark "X" in Fig. 10) decreases gradually for increasing g/S above around unity. The phenomenon means that, although the fan stalls and the pressure drops once, after that it recovers to a negative-slope tendency. Because of the process, pressure characteristic curves for $g/S>1$ have nearly a negative-slope tendency as a whole, including a local pressure dent.

Geometrically, for condition $g/S>1$, leading-edges of the rotor-tip blade-section are located completely downstream of the AS inlet opening, which is a situation similar to the SW condition. In the situation, it is supposed that embryos of stall could hardly be removed, and therefore stalling would occur in a similar manner to the SW stalling condition. Further flow reduction would make the stalled flow condition worse, causing the flow reversed. At the stage of the flow, the AS passage would start to play a role; the recirculation starts and the fan pressure rise begins to recover and to unstall, as seen in AS_Aψt(+127) in Fig. 9. The situation may be expressed as a "deterioration of the stall-prevention effect caused by retracted leading-edges."

According to Lee [16], having surveyed on stall-improving effects by suction or injection through treated casing walls near the blade tips, the amount of the stall improvement depends greatly on the flow rate of the suction or injection. The above deterioration of the stall-prevention effect could be explained also in terms of possible reduction in the rate of recirculation flow through the AS affected by the relative location of the blade tips and the AS inlet.

7.4 Deterioration of Stall-Improvement Effect Owing to Protruded Blade Leading-Edge. On the other hand, for $g/S<0$, the deterioration takes place gradually and the stalling flow coefficient ψ_{tS} is improved somewhat in comparison with that for the SW condition. The shut-off pressure coefficient ψ_{tSO} is lower than the stall pressure coefficient ψ_{tS}.

In the situation, the leading-edges of the rotor-tip blade-sections are located in front of the upstream edge of the AS inlet opening. Since a significant part of the rotor-tip blade-chord is exposed to the entire width of the AS inlet opening, a part of the flow given work by the blade rows could tend to escape into the AS passage, causing much loss in the pressurized flow. Therefore the fan efficiency drops much, although there remains some stall-prevention effect. The situation may be expressed as a "deterioration of the stall-prevention effect caused by protruded leading-edges and exposed blade tips."

8 Effects of the Width of the Air-Separator Openings

It is concluded from Sec. 7 that the leading-edges of the rotor-tip blade-section should be located within the axial width of the AS inlet opening. With respect to this particular fan, the favorable relative location of the leading-edges g/S lies roughly between 0.2 and 0.7 from the above data. With this ratio kept constant at 0.4 rather conservatively, both the inlet opening width S and the exit opening width C of the AS device shown in Fig. 8 were varied for survey on their effects on stall prevention.

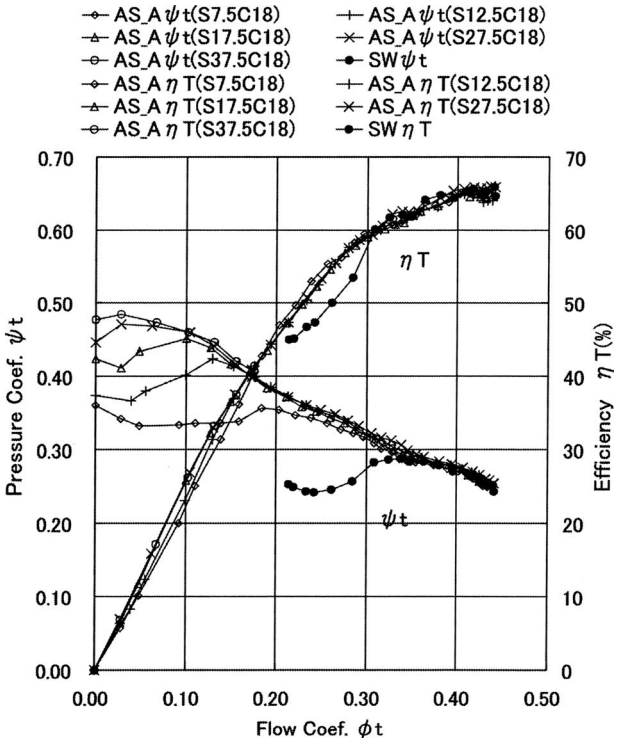

Fig. 11 Fan characteristics affected by inlet opening widths *S* for a constant exit opening width *C*=18 mm for air-separator Type A, *g*/*S*=0.4, *Za*=35 mm, and *W*=33 mm

The widths S of the inlet opening were set by extending the widths b of the AS inner ring by sticking adhesive tapes of a constant width on the radial-vane leading-edges; and the widths C of the exit opening were set by changing the thicknesses of the inserted annular spacer rings. The radial-vanes of the AS device were the original ones having a constant axial width of 50 mm. The width b of the inner ring was changed by the stuck tape, according to the following relation:

$$b(\text{mm}) = 62.5 - S(\text{mm}) \tag{9}$$

Figure 11 shows some typical behaviors of performance characteristics when the width S of the AS inlet opening was changed with the width C of the exit opening kept constant. In the symbol notes (Sxx$C$yy) in Fig. 11, "xx" and "yy" mean the values of S and C in millimeters, respectively. It is seen that increases in S value shift the stall point toward lower flow-coefficient and higher pressure-coefficient.

As a measure of stall-prevention effect, the following index is employed here for clarification of the general trend of the effect and for ease of comparison with other data.

$$B_S = [1 - (Q_S^*/Q_S)] \times 100 \quad (\%) \tag{10}$$

Here, flow rates at stall point are expressed as Q_s and Q_S^* for conditions of the SW and the AS, respectively. As seen in Fig. 13 in the Appendix of this report, stall-prevention effect by AS devices is easily found in changes in the stall flow rate. For the case of no stall down to the shut-off condition, $B_S=100$, and in the case of no effect, $B_S=0$.

Figure 12 shows a contour map for iso-B_S for AS device, Type A. The map was drawn interpolated on the basis of data for pairs of C and S values shown by mark "X" in the figure.

Figure 12 demonstrates the greater stall-prevention effects for the wider widths of both of the openings at the inlet and the exit.

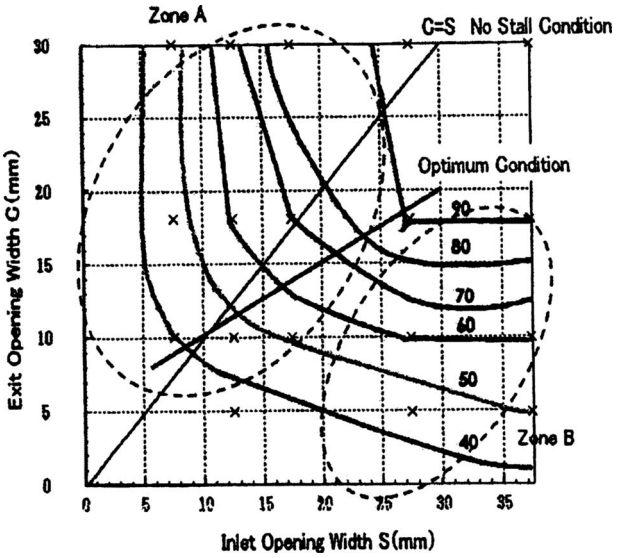

Fig. 12 Effects of opening widths of the inlet and exit of air-separators on the improvement index B_S with respect to stalling flow for $g/S=0.4$, $Za=35$ mm, and $W=33$ mm

The condition at the right top position in the figures, i.e., for the combination of the widest openings in the AS device, achieves $B_S=100$, i.e., stall-free operation over the whole flow range.

When examined further, contour lines are seen to be very characteristic in Zone A for larger C values and Zone B for larger S values, respectively. In Zone A, the lines are roughly parallel to the ordinate axis, showing the stall-prevention effects dominated mainly by the width of the AS inlet opening S, roughly independently of the width of the exit opening C. On the other hand, in Zone B, the lines are roughly parallel to the abscissa axis, showing the stall-prevention effects dominated mainly by the width of the AS exit opening C, rather independently of the width of the inlet opening S. It suggests that the stall-prevention effects are determined mainly by the flow swallowing capacity of the inlet opening in Zone A and by the flow discharging capacity of the exit opening in Zone B, respectively. There is a transition zone between both zones.

In order to minimize the whole axial length of the device, the additive value $(S+C)$ is paid attention to as a main constituent determining the length. Here, the effect of the width b of the inner ring is supposed to be small. The minimum $(S+C)$ points on the respective contour lines are connected as a line as optimum condition in Fig. 12, which gives the condition for the smallest axial length of the AS Type A device. A cross-point of the optimum line and an iso-B_S line will give the minimum axial length condition for the B_S value for AS Type A.

The optimum line suggests a relatively wider inlet opening for the particular AS device, if compared with the line $C=S$ shown as a reference.

9 Comments on the Effectiveness and the Fan Peak-Efficiency

9.1 Effectiveness of the Radial-Vaned Air-Separator. The radial-vaned air-separator proposed here has eliminated stalling of the experimental fan in the best conditions of the size and the relative location. In a research on a high-speed, high-load fan applied with a radial-vaned AS device similar to the present concept conducted by Yamaguchi et al. [9,10], the AS device exhibited a very significant effect, although it could not have reached the stage of complete elimination of stalling. These experiences suggest the strong effectiveness of the AS device of the type. The effect is, however, strongly influenced by several relative dimensions described in the above sections and the AS passage height W. For example, for a height W less than 33 mm, the stall-prevention effect lowered correspondingly, the details of which will be described in the succeeding paper [15] of the present investigation.

Stall-prevention effects in terms of the index B_S achieved so far will be compared with those of the existing AS data and casing treatments ones, the latter of which are the stall-improvement devices of the same nature. With respect to the casing treatment, Fujita and Takata [17] reported a maximum B_s of around 20, and Yamaguchi et al. [18] reported a maximum B_S of 38.

With respect to the conventional axial-vaned AS, Miyake and Inaba [5] reported the highest B_S of 100 for a lightly loaded fan, 70 for a high-load fan, and 82 for the high-load fan with modified axial-vanes. In Fig. 13, all of these fans lie in the region of light-load fans similar to the fan in the present investigation and show a similar tendency. Azimian et al. [6] reported a maximum B_S of 59 for a highly loaded fan.

From a comparison of the order of magnitude of the effects, the stall-prevention effect of the conventional axial-vaned AS is relatively large compared with those of the casing treatment. The stall-prevention effect of the radial-vaned AS proposed here appears to be comparable with those of the axial-vaned AS for fans of similar load level.

Yamaguchi et al. [9] reported that a radial-vaned AS achieved a large and stable stall-prevention effect independently of the fan speed, while an axial-vaned AS showed a great stall-prevention effect for lower fan speeds but the effect lowered very much toward higher fan speeds. The cause has not yet been identified. However, the most probable possibility supposed by the authors is that the inner face of the swirling body of flow within the inlet cavity of the axial-vaned AS would never be a stabilized smooth and axisymmetric one concentric with the fan main flow. To the contrary, the face would be incessantly changing its circularity, concentricity, configuration, smoothness of the face, etc. The tendency would be stronger for the higher swirl speeds. Serious disturbance due to the interference between the main flow and the unsteady inner face of the swirling flow within the AS inlet cavity could cause the above reduction in the high-speed effectiveness for the axial-vaned AS. The authors consider that the above stable effect in the radial-vaned AS could be due to the radial-vanes playing a role of quick deswirling and stabilizing the swirling inflow within the AS inlet opening. With respect to the particular fan used in the present investigation, which is originally a very low-speed one, confirmation of the above phenomena has not been conducted [19].

9.2 Stall Improvement and Flow Rate of Recirculation Through the AS Passage. In Fig. 12, the wider openings of both of the inlet and the exit have achieved the greater stall-improvement effect. The tendency suggests an influence of the magnitude of recirculation rates through the AS passage. As is cited above, Lee [16] showed a great influence of the flow rate of the suction or injection through treated casing wall on the amount of stall improvement. The deterioration of the stall-prevention effect caused by retracted leading-edges cited above could also be explained from the point of view.

The recirculation flow through the AS is determined in a self-balanced way, depending on several quantities, such as flow centrifuging forces, pressure losses in the AS passage, main flow pressure difference between at the openings of AS inlet and exit, and geometrical and aerodynamic layouts of the device relative to the rotor-blades, etc. In addition to the stall-improvement effects, the flow rate is an important factor in view of the fan power loss related to fan efficiency. An AS device that is both effective in the stall prevention and less in the fan power consumption is necessary.

The recirculation flow rate has not been measured in the present study. The authors are planning measurement of internal flow distributions, including the recirculation flow rate through the AS in

the next stage of investigation.

The relative tip clearance is about 2% of both of the rotor-blade height and the rotor-tip chord length, which is rather high compared with conventional axial bladings. From the results obtained here and Figs. 13(*a*) and 13(*b*) in the Appendix including results from a variety of blading conditions, stall-prevention effects by the AS devices appear to be rather insensitive to the blade tip clearances.

9.3 Fan Efficiency. In this study, fan peak-efficiencies in the sound region are seen to be improved slightly by application of the AS device at its optimum relative location. The same tendency has been confirmed by repeated measurements using the same instrumentation. Generally speaking, however, in the presence of stall-improvement devices, occurrences of some slight efficiency drops have usually been experienced. Yamaguchi et al. [10] reported a peak-efficiency drop of about 1% by use of a radial-vaned AS device similar to that in the present investigation. Ziabasharhagh et al. [7] reported peak-efficiency drops of 0–3% on axial-vaned AS devices applied to a high-efficiency stage including cases of no efficiency drop.

Empirically speaking, a low-efficiency fan could happen to be seemingly improved in efficiency by such treatment, which might be the case for the present fan. In addition, in consideration of the rather large uncertainty in the present measurements of the fan performances, it is better to consider that the gain obtained here in the peak-efficiency could not be relied on in a general sense.

10 Conclusion

The radial-vaned air-separator proposed here was applied to a single-stage, lightly loaded fan of axial-inlet type and the following results were obtained.

(1) Performance characteristics and effect of stall prevention with radial-vaned air-separator Type A were surveyed. The data serve for the optimization of the related parameters.
(2) In the optimized condition, the radial-vaned air-separator achieved a stall-free operation of the fan, proving to have a great potential for stall prevention. The potential is comparable with the axial-vaned air-separator applied to a lightly loaded fan.
(3) For achievement of the optimum effect, it is recommended to select the relative leading-edge location of the rotor-tip blades within an experimentally determined beneficial range of the air-separator inlet opening, i.e., $g/S=0.2-0.7$. Under the circumstances, both the stall-prevention effect and fan peak-efficiency are advantageous.
(4) The effects of the widths of the air-separator openings of the inlet and the exit on the stall prevention were surveyed with the ratio g/S kept constant at 0.4. On the basis of the obtained contour map for achievable stall-improvement index B_S, the axially shortest device for a given B_S was derived.

Furthermore, smaller passage height W is indispensable from a viewpoint of the compactness of the air-separator. The reduced height is seen to have a strong adverse effect on the stall prevention, as is described in the succeeding investigation [15].

Acknowledgment

The authors would like to express their deep thanks to the following graduate students of the Mechanical Department of Meisei University, Tokyo, Japan, who have devoted their efforts to the research: Ms. Mariko Hayakawa, Mr. Norihito Sakurai, and Mr. Shuhei Araki.

Nomenclature

b = axial length of the inner ring of the air-separator (m)
B_S = index of improvement of stalling flow (%)
C = axial width of the exit opening of the air-separator (m)
D_h = hub diameter of fan (m)
D_t = casing wall diameter of fan (m)
g = distance between the leading-edge of the rotor tip and the upstream edge of the inlet opening of the air-separator (m)
h = distance between the leading-edge of the rotor tip and the downstream edge of the inlet opening of the air-separator (m)
H = annulus height of fan (m)
l = chord length of the rotor-blade (m)
P = power input to the driving motor (W)
$Ps1$ = wall static pressure at the fan suction duct (Pa)
$Ps2$ = casing wall static pressure downstream of the rotor-blades (Pa)
Q = fan flow rate (m^3/s)
Q_S = stalling flow rate of solid-wall fan flow rate (m^3/s)
Q_S^* = stalling flow rate of fan with air-separator (m^3/s)
S = axial width of inlet opening of the air-separator (m)
t = spacing of neighboring blades of the rotor (m)
u_t = peripheral speed of the rotor tip (m/s)
V_a = axial velocity (m/s)
W = height of the internal passage of air-separator (m)
Za = axial chord length of the rotor-tip blade-section (m)
Δp_S = fan rotor static-pressure rise (Pa)
Δp_T = fan rotor total-pressure rise (Pa)
η_S = fan rotor static efficiency
η_T = fan rotor total efficiency
η_{TP} = fan rotor peak total efficiency
ρ = air density (kg/m^3)
θ = camber angle of the rotor-blade (deg)
ϕ_t = fan flow coefficient
ϕ_{tS} = fan stall flow coefficient
ψ_t = fan rotor total-pressure coefficient
ψ_{tS} = fan rotor stall total-pressure coefficient
ψ_{tSO} = fan rotor shut-off total-pressure coefficient
$\psi_{tT\text{-}S}$ = fan total-to-static pressure coefficient (Appendix)
$\psi_{tT\text{-}T}$ = fan total-to-total pressure coefficient (Appendix)
ξ = stagger angle of the rotor-blade (deg)

Subscripts and Superscripts

P = peak-efficiency point
t = normalized with reference to the rotor-tip speed
T = total pressure
S = static pressure or stalling point
SO = shut-off condition
* = stalling point in the presence of air-separator

Appendix: General Trend of Stall-Prevention Effect by Air-Separator

It has been well known recently that the AS devices have significant effects of stall prevention. However, either summary on the information and data relative to them or general rules applicable to development of the air-separator devices are hardly available in comparison with those on the casing treatments. In the circumstances, even a very simple survey of existing data would

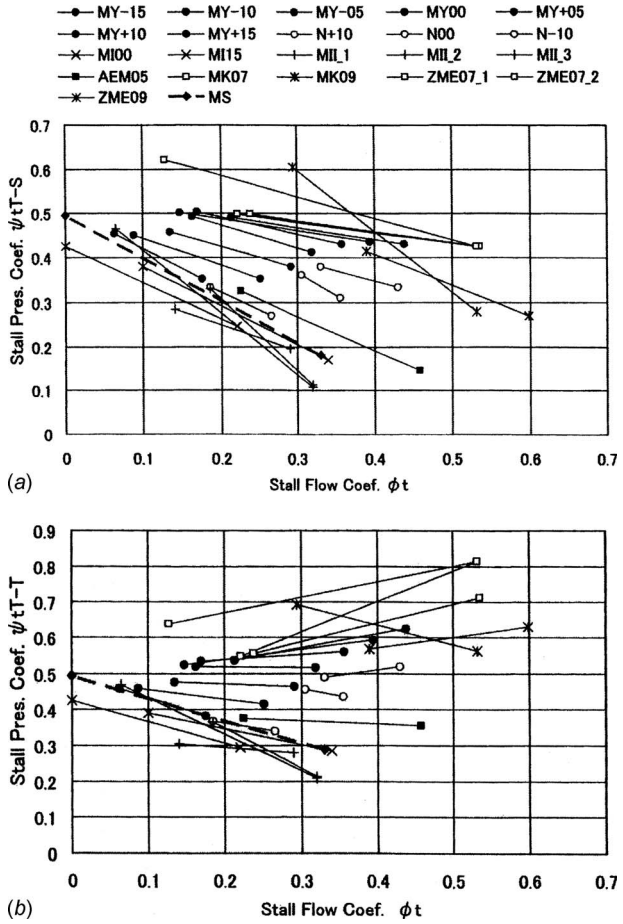

Fig. 13 A survey on tendency in stall improvement from SW stall point to AS stall point achieved by air-separators including axial-vane type and radial-vane type for axial-flow fans of axial-inlet type bladings. (*a*) Total-to-static characteristics. (*b*) Total-to-total characteristics. (Sources) MI and MII: Ref. [5], AEM: Ref. [6], MK: Ref. [8], ZME: Ref. [7], N: (*) Ref. [13], MS: (*) present report or Ref. [19], and MY: (*) Ref. [9]. Together with in-house data of Mitsubishi Heavy Industries, Ltd. Here, (*) attached above shows results for radial-vaned AS, and none (without (*)) for axial-vaned AS.

give a clue to clarification of the status of the study and/or detection of problems in the related fields of research and developments.

Here, we would like to pay attention to stall-prevention data achieved by the conventional axial-vaned AS and the radial-vaned AS, both of which have basically the same working principle of stall prevention. The data having relatively favorable improvement effects are picked up from literature and plotted in Figs. 13(*a*) and 13(*b*). All data are normalized by use of the rotor-tip speed u_t, since the tip condition is supposed to be of primary significance in the air-separator action. Two stalling points of respective fans, of which one is for the SW condition and the other is for the AS condition, are plotted in terms of total-to-static pressure coefficient $\psi_{tT\text{-}S}$ and flow coefficient ϕ_t in Fig. 13(*a*). Each pair of the two points is connected by a short straight line, whose right edge-point is for the SW stall point and the left edge-point is for the AS one. The fans are of the axial-inlet type design, including those of variable-pitch rotor-blades. The sources of the data are noted below the figure, where sources with asterisk (*) are for the radial-vaned AS and one without asterisk are for the axial-vaned AS.

Figure 13(*b*) shows the data in terms of the total-to-total pressure coefficient $\psi_{tT\text{-}T}$ and flow coefficient ϕ_t.

It is seen that the AS device has been attempted on fans covering a wide area of $\psi_{tT\text{-}T}$ versus ϕ_t. The fans included in Fig. 13 are of a variety of blading designs and geometrical dimensions, and the applied AS devices are also various in their constructions, geometrical proportions, dimensions, etc. It is interesting that, in spite of the diversity, they demonstrate some common tendency in the direction of the AS effects. The magnitudes of the effectiveness are, however, seen to be various in the data. From Fig. 13, the following tendency is observed.

(1) The stall-prevention effects by the AS devices are expressed by negative-slope line-segments of total-to-static pressure coefficients $\psi_{tT\text{-}S}$ in Fig. 13(*a*). The tendency is considered to be related to no rotating-stall condition. As a whole, the currently highest improved total-to-static pressure coefficients $\psi_{tT\text{-}S}$ lie around 0.5 but with some exceptions exceeding the value.
(2) When total-to-total pressure coefficient $\psi_{tT\text{-}T}$ is paid attention to in Fig. 13(*b*), fans of low-flow-coefficient and low-pressure-coefficient have negative slopes of improvement tendency; on the other hand, fans of high-flow coefficient and high-pressure-coefficient have positive slopes. Fans having a total-to-total stall pressure coefficient around 0.5 for the SW condition appear to be improved roughly horizontally.
(3) Roughly as a whole, improved stall points tend toward $\psi_{tT\text{-}T}$ of around 0.5 at shut-off condition (ϕ_t=0), irrespective of the SW ones.
(4) As a rough summary, the current state of the maximum pressure-level of AS stall improvement seems to tend to

$$\psi_{tT\text{-}S} = 0.5 \tag{A1}$$

$$\psi_{tT\text{-}T} = 0.5 + \phi_t^2 \tag{A2}$$

Of course, there remains some exceptional data exceeding the above.
(5) When the improvement is considered in terms of the index B_S, meaning the relative improvement in the stall flow defined by Eq. (10), fans of low-flow and low-pressure are advantageous. However, some fans of high-flow and high-pressure do show a very wide improvement in the absolute range in the flow coefficient.

Including the above tentative observations, it can be said that there remains much to study in the clarification of the mechanism and the optimization of the AS devices.

From Fig. 13, the direction of the future study could be listed as follows: (1) clarification of the cause of the significant effectiveness, or the relation between the effects and the internal flow patterns; (2) establishment of conditions for achieving the limiting effect of the AS stall prevention; and (3) further improvement in the limiting effect for high-flow, high-pressure fans or compressor stages. There exist data points, though very few in number, having a value of $\psi_{tT\text{-}S}$ exceeding 0.5 and approaching 0.6, which could be encouraging data suggesting a possibility of achievement of greater effectiveness.

The best result obtained in the present investigation is given by mark ◆ and a dotted line (symbol note: MS) in Fig. 13 in the zone for fans of low flow-coefficient and low pressure-coefficient. Although the data appear to show a very promising tendency, there have been remained many points unplotted because of insufficient effect. Organizing and summarizing the data obtained in the course of the optimization would contribute much to clarification of the improvement mechanism, optimization of the AS device, application of the device to new fans and existing fans, and/or compressor stages.

References

[1] Yamaguchi, N., 2005, "Stall and Surge of Axial Flow Compressors (Serial

Lecture), Chp. 12, Stall Prevention by Means of Suction Rings and Casing Treatments, (1) Suction Rings and Casing Treatments," Journal of Turbomachinery Society of Japan, **33**(8), pp. 490–502.
[2] Yamaguchi, N., 2005, "Stall and Surge of Axial Flow Compressors (Serial Lecture), Chp. 12, Stall Prevention by Means of Suction Rings and Casing Treatments, (1) Suction Rings and Casing Treatments," Journal of Turbomachinery Society of Japan, **33**(10), pp. 637–640.
[3] Ivanov, S. K., Peredery, V. P., and Molchanov, V. N., 1989, "Axial-Flow Fan," U.S. Patent No. 4,871,294.
[4] Miyake, Y., Inaba, T., Nishikawa, Y., Noji, I., and Kato, T., 1984, "Investigation on Air Separators for Axial Flow Fans,"Symposium of Jpn. Soc. Mech. Eng., No. 840-13, pp. 225–232.
[5] Miyake, Y., and Inaba, T., 1985, "Improvement of Axial Flow Fan Characteristics by Means of Separators," Journal of Turbomachinery Society of Japan, **13**(12), pp. 746–752.
[6] Azimian, A. R., Elder, R. L., and McKenzie, A. B., 1989, "Application of Recess Vaned Casing Treatment to Axial Flow Fans," ASME Paper No. 89-GT-68.
[7] Ziabasharhagh, M., McKenzie, A. B., and Elder, R. L., 1992, "Recess Vane Passive Control," ASME Paper No. 92-GT-36.
[8] McKenzie, A. B., 1993, "Passive Stall Control for Fans and Compressors," IMechE seminar on Turbo Compressor and Fan Stability, pp. 7–13.
[9] Yamaguchi, N., Takami, I., and Arimura, H., 1991, "Improvement of Air Separators of Axial Blowers," 250th Symposium of the Kansai Chapter of Japanese Society of Mechanical Engineering, pp. 176–178.
[10] Yamaguchi, N., Owaki, T., Goto, M., Itaka, H., and Arimura, H., 1994, "Development of Mitsubishi General-Purpose Axial Fan (WIDEMAX Fan)," Tech. Rev.-Mitsubishi Heavy Ind., **31**(3), pp. 201–204.
[11] Bard, H., 1984, "The Stabilization of Axial Fan Performance," C120/84, Installation Effects in Ducted Fan Systems, IMechE, pp. 100–106.
[12] Tanaka, S., and Murata, S., 1975, "Post-Stall Characteristics and Rotating Stalls in an Axial Flow Fan, The Third Report: Stall Improvement Devices and Stalling Characteristics," Trans. Jpn. Soc. Mech. Eng., **41**(343), pp. 863–873.
[13] Nishioka, T., Kuroda, S., and Nagano, T., 2004, "Suppression of Rotating Stall by an Air-Separator in an Axial-Flow Fan," Symposium of the Fluid Engineering Division of Japanese Society of Mechanical Engineering.
[14] Kato, Y., Yamaguchi, N., and Ogata, M., 2006, "Improvement of Compressor Stalling Characteristics by Air Separators," 84th Symposium of Fluid Engineering Division of Japanese Society of Mechanical Engineering.
[15] Yamaguchi, N., Ogata, M. and Kato, Y., 2010, "Effects of Compact Radial-Vaned Air Separators on Stalling Characteristics of an Axial-Flow Fan," ASME J. Turbomach., **132**(2), p. 021009
[16] Lee, N. K. W., 1988, "Effects of Compressor Endwall Suction and Blowing on Stability Enhancement," MIT, GTL Report No. 192.
[17] Fujita, H., and Takata, H., 1981, "Study on the Effects of Casing Treatment Configurations in an Axial Flow Compressor," Preprint of Jpn. Soc. Mech. Eng., **810**(15), pp. 229–231.
[18] Yamaguchi, N., Ohwaki, T., and Higaki, T., 1990, "Optimization of the Effect of Casing Treatment in an Axial Fan With Controllable-Pitch Moving Blades," The Third Japan-China Joint Conference on Fluidmachinery, Osaka, Japan, pp. 73–80.
[19] Yamaguchi, N., Ogata, M., and Kato, Y., 2008, "Improvement of Stalling Characteristics of an Axial Fan by Radial-Vaned Air Separators, Part II: Compact Radial-Vaned Air Separator," Trans. Jpn. Soc. Mech. Eng., **74**(746), pp. 2163–2172.

Aerothermal Investigation of Tip Leakage Flow in a Film Cooled Industrial Turbine Rotor

S. K. Krishnababu[1]

H. P. Hodson

Department of Engineering,
University of Cambridge,
Madingley Road, Cambridge CB3 0DS, UK

G. D. Booth[2]
SIEMENS Industrial Turbomachinery Ltd,
Lincoln LN5 7FD, UK

G. D. Lock
Department of Mechanical Engineering,
University of Bath,
Bath BA2 7AY, UK

W. N. Dawes
Department of Engineering,
University of Cambridge

A numerical investigation of the flow and heat transfer characteristics of tip leakage in a typical film cooled industrial gas turbine rotor is presented in this paper. The computations were performed on a rotating domain of a single blade with a clearance gap of 1.28% chord in an engine environment. This standard blade featured two coolant and two dust holes, in a cavity-type tip with a central rib. The computations were performed using CFX 5.6, which was validated for similar flow situations by Krishnababu et al. (2007, "Aero-Thermal Investigation of Tip Leakage Flow in Axial Flow Turbines: Part I—Effect of Tip Geometry," ASME Paper No. 2007-GT-27954). These predictions were further verified by comparing the flow and heat transfer characteristics computed in the absence of coolant ejection with computations previously performed in the company (SIEMENS) using standard in-house codes. Turbulence was modeled using the shear-stress transport (SST) k-ω turbulence model. The comparison of calculations performed with and without coolant ejection has shown that the coolant flow partially blocks the tip gap, resulting in a reduction in the amount of mainstream leakage flow. The calculations identified that the main detrimental heat transfer issues were caused by impingement of the hot leakage flow onto the tip. Hence three different modifications (referred as Cases 1–3) were made to the standard blade tip in an attempt to reduce the tip gap exit mass flow and the associated impingement heat transfer. The improvements and limitations of the modified geometries, in terms of tip gap exit mass flow, total area of the tip affected by the hot flow and the total heat flux to the tip, are discussed. The main feature of the Case 1 geometry is the removal of the rib, and this modification was found to effectively reduce both the total area affected by the hot leakage flow and total heat flux to the tip, while maintaining the same leakage mass flow as the standard blade. Case 2 featured a rearrangement of the dust holes in the tip, which, in terms of aerothermal dynamics, proved to be marginally inferior to Case 1. Case 3, which essentially created a suction-side squealer geometry, was found to be inferior even to the standard cavity-tip blade. It was also found that the hot spots, which occur in the leading edge region of the standard tip, and all modifications contributed significantly to the area affected by the hot tip leakage flow and the total heat flux.
[DOI: 10.1115/1.3144164]

1 Introduction

In unshrouded axial turbines, clearance gaps between the rotor blades and the stationary shroud are necessary to prevent the physical rubbing between them. The pressure difference between the pressure and the suction sides (SSs) of the blade causes an undesirable leakage of fluid through the clearance gap, which adversely affects the stage performance. Typically a clearance of 1%of blade span causes 1–2% of the primary flow to leak over the tip with a corresponding loss of 1–3% on stage efficiency [1].

There are two distinct aspects of tip leakage flows [2]: first, as the flow passes through the tip gap without being properly turned, there is a reduction in work done; and second, due to mixing, there is generation of entropy within the gap, in the blade passage and downstream of the blade row. Furthermore, the rapid acceleration of hot mainstream flow into the tip gap, followed by the separation and reattachment, results in regions of high heat transfer to the metal. This heat flux, together with that to the suction and pressure sides of the blade, must be removed by internal cooling. The compressor supplies this cooling flow, which imposes a further penalty on the engine performance. Hence considerable research has been conducted to understand and quantify the losses and the heat transfer associated with the tip leakage flows.

A review of research quantifying the losses and heat transfer associated with tip clearance flow is provided by Bunker [3]. Much of the early work used idealized models, e.g., Refs. [4,5], and this technique was further pursued more recently by Krishnababu et al. [6]. Much work has been conducted using linear cascades: Bunker et al. [7] measured heat transfer for sharp and radiused-edged blades for different clearance gaps; Kwak and Han [8,9] used the transient liquid crystal technique; and Jin and Goldstein [10] used the naphthalene technique to determine the effects of clearance gap, turbulence intensity, and Reynolds number on the mass/heat transfer from the tip and near-tip surfaces.

In recent years, three-dimensional numerical simulations of flow and heat transfer of tip leakage flow past blades with flat and squealer tip geometries have been reported. Ameri et al. [11] performed a numerical simulation with the k-ω turbulence model of the flow and heat transfer over a turbine blade with a cavity tip. The cavity was found to reduce the mass flow rate through the tip gap by as much as 14% when compared with a flat tip but with only a minor improvement in efficiency. Ameri and Bunker [12] performed a numerical simulation to investigate the distribution of heat transfer coefficient on the tip of flat and radiused-edge blades, with the latter calculation being in better agreement with

[1]Present address: Siemens Industrial Turbomachinery Ltd, Lincoln, UK.
[2]Present address: Doosan Babcock Energy Ltd, Renfrew, UK.

Contributed by the International Gas Turbine Institute of ASME for publication in the JOURNAL OF TURBOMACHINERY. Manuscript received June 19, 2008; final manuscript received: February 22, 2009; published online January 20, 2010. Review conducted by David Wisler. Paper presented at the ASME Turbo Expo 2008: Land, Sea and Air (GT2008), Berlin, Germany, June 9–13, 2008.

their experimental data [7]. This improved agreement was attributed to the absence of flow separation on the tip of the radiused-edge blade.

Yang et al. [13,14] conducted a numerical study of tip leakage flow and heat transfer using a turbine blade with three different cavity-tip gaps, comparing the performance with that of the flat tip. Acharya et al. [15] and Saha et al. [16] investigated the flow and heat transfer characteristics of tip leakage using different tip gap geometries; the lowest leakage flow rates and tip heat transfer coefficients were obtained using a suction-side squealer geometry followed by a cavity geometry.

Mumic et al. [17] studied the aerothermal performance of flat and cavity geometries at three different tip gaps; for both the flat and cavity tip, the overall heat transfer and the leakage mass flow rate increased with increasing tip gap height, with the overall heat transfer to the cavity-tip lower.

Krishnababu et al. [18] investigated the effect of tip geometry on the tip leakage flow and heat transfer characteristics in unshrouded axial flow turbines. A baseline flat tip geometry was compared, in terms of the leakage mass flow and heat transfer to the tip, with a double squealer (i.e., cavity) and suction-side squealer geometries. It was observed that the cavity tip was advantageous both from the aerodynamic and heat transfer perspectives by providing a decrease in the amount of leakage (and hence losses) and in a reduction in the average heat transfer to the tip.

Recent studies (e.g., Refs. [9,19,20]) have investigated the effect of coolant injection on the characteristics of tip leakage flow; all of these studies have been conducted in a cascade, rather than the engine, environment. Very few studies have investigated the effect of relative casing motion on the tip leakage flow. Morphis and Bindon [21] and Yaras and Sjolander [22] showed that the tip leakage mass flow will reduce significantly as a result of such relative motion. Srinivasan and Goldstein [23] revealed a small but definite reduction in heat transfer to the tip due to relative casing motion at small tip gaps; at larger tip gaps this effect was found to be negligible. Rhee and Cho [24,25] also reported a decrease in leakage flow and heat transfer to the tip due to casing motion.

Krishnababu et al. [26] reported the effect of relative casing motion on the performances of flat and squealer geometries (cavity and suction-side squealer) in terms of the leakage mass flow and heat transfer using a tip clearance gap of 1.6% chord. The relative casing motion was found to decrease both the tip leakage mass flow and the average heat transfer to the tip; these effects were due to the decrease in leakage flow velocity caused by the reduction in driving pressure difference. Compared with computations with a stationary casing [18], the average heat transfer to the suction surface of the blade was found to increase for the case of the computations with relative casing motion; this effect was due to the large increase in heat transfer along the footprint of the tip leakage vortex on the SS. Although the relative wall motion considerably increases the realism of such simulations, the flow is still idealized in many aspects. Moreover, the casing motion does not simulate other real engine effects that can lead to radial flows in the blade passage.

The present paper presents a numerical study investigating the flow and heat transfer characteristics of tip leakage flow in a typical, film cooled industrial gas turbine rotor with a clearance gap of 1.28% chord in the engine environment (i.e., in a rotating domain with coolant injection). Three different modifications (referred as Cases 1–3) to a standard blade tip are investigated in an attempt to reduce the tip gap exit mass flow and heat transfer to the blade tip. The improvements and limitations of the modified geometries, in terms of tip gap exit mass flow, total area of the tip affected by the hot flow, and the total heat flux to the tip, are discussed.

2 Computational Details

The simulations reported in this investigation were performed using CFX 5.6, which were validated for similar flow situations by Krishnababu et al. [18], in their investigation using a linear cascade blade. The Navier–Stokes equations were solved using a finite-volume method to discretize the equations. A structured mesh was generated using the commercial mesh generation program ICEM-HEXA. The computations were performed using a single blade (Fig. 1) with periodic boundary conditions imposed along the boundaries in the pitchwise direction.

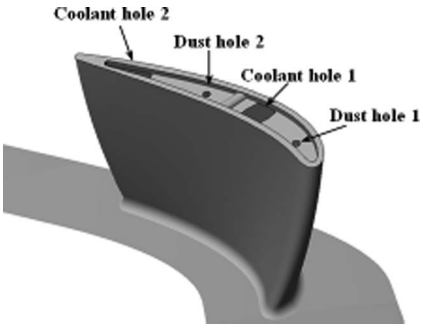

Fig. 1 Computational domain

The imposed boundary conditions were those obtained from previous axisymmetric through-flow calculations performed at SIEMENS using their standard through-flow design code [27]. The inlet boundary condition comprised of the spanwise distribution of the swirl angle, the total pressure, and the total temperature. The outlet boundary condition was defined by specifying a radial variation in static pressure at the exit boundary. These flow conditions correspond to a pressure ratio of 1.95. The domain was set to rotate at 14,100 rpm. The casing was stationary in the absolute frame of reference, simulating the engine environment. No-slip isothermal wall conditions were imposed on the blade and the casing. The temperature of all blade surfaces was specified by averaging the temperatures on the blade surface, measured previously at SIEMENS ($T_w = 78\%\ T_{oin}$).

As seen in Fig. 1, the blade under investigation has a cavity-type tip geometry. The cavity tip, which is separated into two regions by a rib, is cooled by flow from a set of coolant and dust holes.

The grid sensitivity study was performed by using two different meshes, namely, G1 and G2. A typical mesh is shown in Fig. 2. The grids were clustered in the tip gap region and toward the

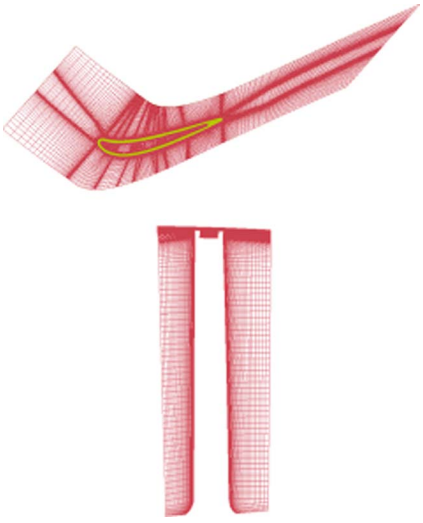

Fig. 2 Typical mesh used in the computations

Table 1 Details of the meshes G1 and G2

Mesh	Y^+ on tip		No. of cells across the tip	Total No. of cells (million)
	Average	Range		
G1	34.3	5–300	25	2.9
G2	22.2	2–146	36	3.3

pressure and suction surfaces of the blade. The average Y^+ values on the tip and the total number of cells across the tip gap for the two meshes considered are given in Table 1.

The computations were performed using the SST k-ω turbulence model with automatic wall functions, which shift gradually between a low Reynolds number formulation and wall functions based on the grid density. The computations were initially performed without coolant injection by blocking the coolant and the dust holes. The contours of heat transfer coefficient on the tip obtained by using the meshes G1 and G2 are shown in Fig. 3(*a*). The differences between the solutions obtained by the two meshes are seen to be minor. Indeed, the area-averaged heat transfer coefficients on tip in the case of the meshes G1 and G2 are 6290 W/m^2 K and 6222 W/m^2 K, respectively. Hence the solution obtained using the smaller mesh G1 was considered to be insensitive to the grid. All further computations were performed using grid G1.

The distribution of computed heat transfer coefficient along the midspan of the blade obtained using mesh G1 is shown in Fig. 3(*b*). The distribution obtained previously by SIEMENS using TEXSTAN [28] is also included for comparison. TEXSTAN is a 2D boundary layer code based on standard k-ε turbulence model [29]. It is seen from Fig. 3(*b*) that the distribution obtained in the present computations is in qualitative agreement with that obtained using TEXSTAN. However, differences in the level of heat transfer coefficient are dramatic in the leading edge stagnation region due to the different turbulence models used. In this region the standard k-ε model is expected to overpredict the levels of heat transfer [18].

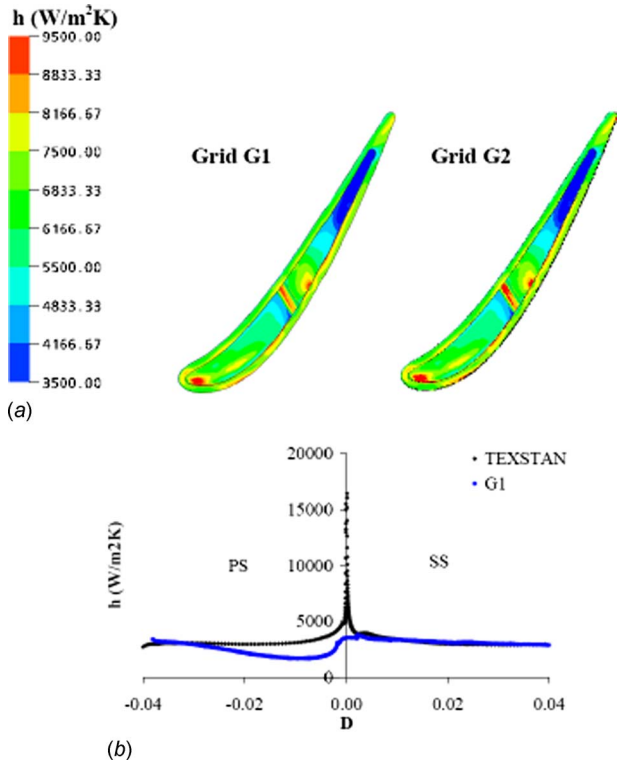

Fig. 3 (*a*) Contours of heat transfer coefficient on the tip and (*b*) Variation in heat transfer coefficient at midspan

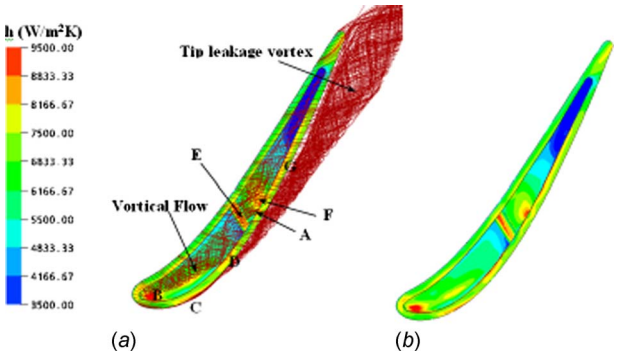

Fig. 4 (*a*) Contours of *h* on tip with streamlines superimposed and (*b*) contours of *h* on tip

3 Investigation of Tip Leakage Flow (Uncooled)

The contours of heat transfer coefficient on the tip along with the streamlines crossing the tip are shown in Fig. 4. The tip leakage vortex, formed by the interaction of the leakage flow with the mainstream flow, is marked in the figure. The flow pattern reveals a vortical structure formed inside the cavity. The flow in this vortical structure moves from the leading edge region toward the trailing edge, from where it exits the tip gap. Blocked by the rib, part of this vortical structure turns and leaves the tip gap in the vicinity of the region marked A and becomes a part of the tip leakage vortex. The remainder of the vortical structure rises and impinges on the top of the rib (marked E) and then onto the cavity floor (marked F). As observed in the case of the low speed blade by Krishnababu et al. [18], high heat transfer coefficients exist in the regions of flow impingement (B–G). It is interesting to note that the high heat transfer regions E and F would not exist if the rib were not present.

4 Tip Leakage Flow With Coolant Flow

In this section the flow and heat transfer characteristics of the tip leakage flow in the presence of coolant injection are investigated. The coolant and the dust holes were unblocked, and the mass flows and stagnation temperatures were specified at the inlet to these holes (Fig. 5). The flow conditions at the entrance to the coolant and the dust holes were determined from a previously performed CFX simulation of flow through the internal coolant passage alone. In Fig. 5 the mass flows and the relative total temperatures at the inlet to the holes are expressed as a percentage of inlet mass flow and the mass averaged inlet relative total temperature, respectively.

In Fig. 6(*a*), the streamlines across the tip are superimposed on the contours of wall heat flux, normalized by maximum magni-

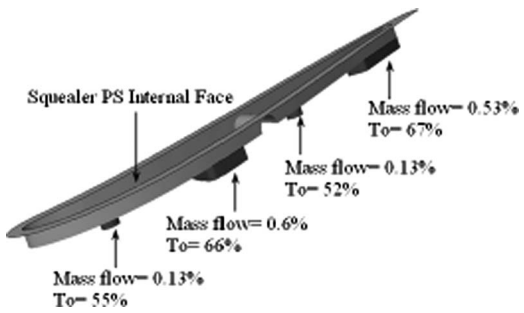

Fig. 5 Flow conditions at inlet to dust and coolant holes

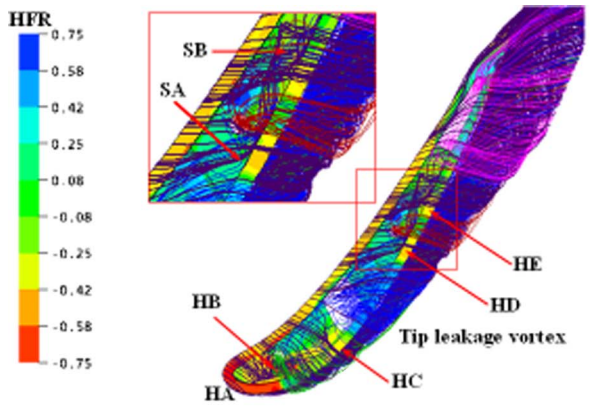

(*a*)

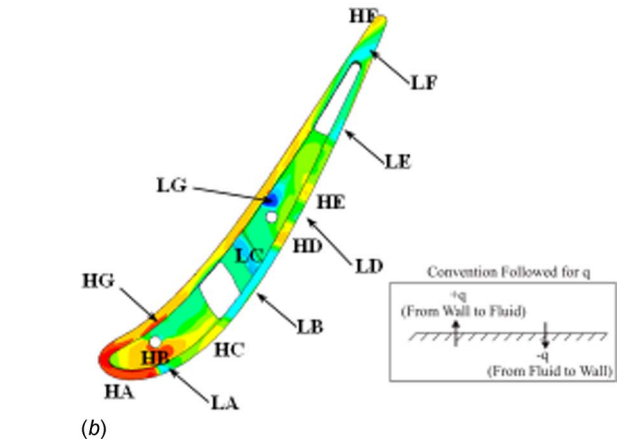

(*b*)

Fig. 6 (*a*) Contours of HFR on tip with streamlines superimposed and (*b*) contours of HFR on tip

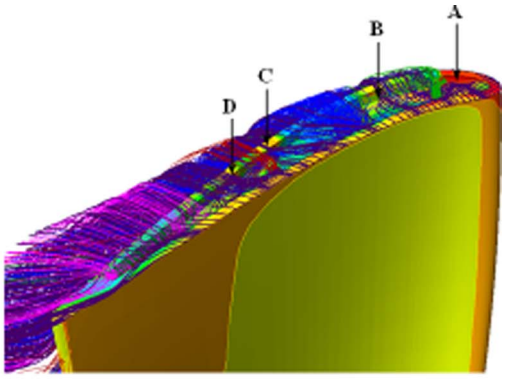

(*a*)

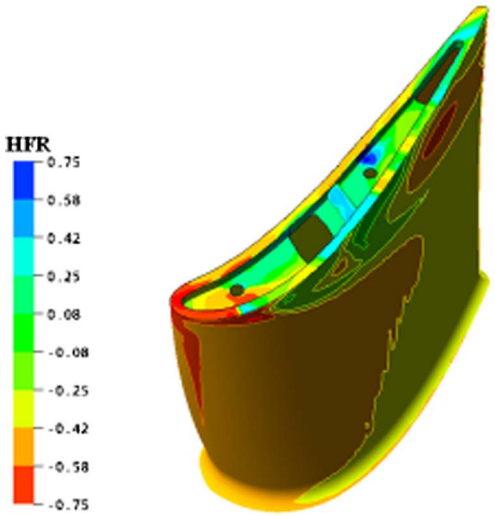

(*b*)

Fig. 7 (*a*) Contours of HFR on blade with streamlines superimposed and (*b*) contours of HFR on blade showing foot print of the tip leakage vortex

tude of the negative wall heat flux, on the tip. For convenience this ratio is henceforth referred to as heat flux ratio (HFR) and is given by $q_{wall}/|\text{maximum negative } q_{wall}|$. According to the standard conventions followed (Fig. 6(*b*)), negative values of wall heat flux implies that the heat is transferred from the hot flow to the blade, and the positive values of wall heat flux implies that the heat is transferred to the flow (essentially the coolant flow) from the blade, which means blade cooling. Hence negative values of HFR refer to the hot regions of the blade, and the positive values of HFR refer to the cold regions of the blade.

In Fig. 6(*a*), the hot mainstream leakage flow and the cold flow emerging from coolant and dust holes are represented by different colors for clarity. This figure reveals that the vortical flow, which was observed in the case of the computation without coolant injection (Fig. 4), is not formed when coolant ejection is present. The hot mainstream leakage, which separates from the pressure-side edge, is blocked by the cold flow emerging from the coolant and dust holes along most of the tip. However, the hot mainstream flow is observed to impinge on the cavity floor (marked HB in Fig. 6(*a*)) and along the top surface of the suction-side squealer (marked HC, HD, and HE in Fig. 6(*a*)).

In Fig. 6(*b*), hot spots are found in the vicinity of the leading edge (marked HA), on the cavity floor (marked HB), on the top of the suction-side squealer (marked HC, HD, and HE), in the vicinity of the trailing edge (marked HF), and along the pressure-side squealer near the leading edge (marked HG). The hot spots marked HB–HE and HG are caused by the impingement of hot leakage flow (see also Fig. 6(*a*)). The hot spot HF is caused by the attached flow of hot leakage fluid near the trailing edge. In Fig. 6(*b*) cold spots are marked as LA–LG. These cold spots are caused either by the impingement of coolant or by attached flow ejecting from the coolant and dust holes. It is interesting to observe that most of the cold flow emerging from the first coolant hole (Coolant hole 1) leaves the tip gap with poor effectiveness, and only part of it remains inside the cavity. The significance of this important observation is discussed in Sec. 5.

The contours of HFR on the aerofoil surfaces of the blade and tip are shown in Figs. 7(*a*) and 7(*b*). Hot spots (marked A–D in Fig. 7(*a*)) are seen on the internal face of the suction-side squealer. Streamlines of hot leakage flow (see SA in Fig. 6(*a*)) enter the cavity and flow chordwise toward the trailing edge, exiting the tip near the position marked SA1. The blockage created by these streamlines diverts the hot leakage flow (marked SB in Fig. 6(*a*)) into the cavity, resulting in impingement on the inner surface of the suction-side squealer. This impingement creates hot spot D in Fig. 7(*a*). Hot spots A, B, and C are also caused by local direct impingement of the hot leakage flow. The footprint of the tip leakage vortex is observed on the suction surface of the blade (Fig. 7(*b*)) as a region of higher HFR.

Table 2 provides a quantitative summary of the tip leakage characteristics of the standard blade. These include the leakage mass flow (including the coolant mass flow) as a percentage of inlet mass flow; the total area affected by the hot leakage flow, i.e., the area with negative HFR as a percentage of the total area of the tip, and the total negative wall heat flux, which is the sum of the heat flux from the hot fluid to the tip. The results obtained in the case of the simulation without the coolant flow is also in-

Table 2 Tip leakage characteristics of the standard blade

Quantity	Cooled	Uncooled
Tip exit mass flow (% inlet mass flow)	2.85	2.48
Area affected (% of total tip area)	52.5	100
Total negative wall heat flux ($\times 10^9$ W/m^2)	6.9	27.1

cluded in Table 2 for comparison. From this table it is seen that, compared with the uncooled case, there is nearly 15% increase in tip exit mass flow. The tip gap inlet mass flow, however, was found to reduce by about 57%. This indicates that the increase in tip exit mass flow is solely caused by the injection of fluid through the coolant and dust holes and the amount of mainstream flow that escapes through the tip gap without doing any useful work on the blade have actually reduced as the coolant flow in effect partially blocks the tip gap, reducing the area available for the flow to pass through from pressure side to the suction side of the blade. Table 2 also shows that there is a 47.5% decrease in the area affected by the hot leakage flow, and the total negative heat flux is about four times less than the uncooled case.

In summary, the observations above identify the impingement of the hot leakage flow as the main cause of hot spots on the blade tip. Hence improved blade tip designs should avoid or limit such impingement. In the following sections attempts are made to reduce heat transfer by modifying the tip geometry and the advantages and limitations of such modifications are presented. The tip geometry investigated in this section, which is currently in use by the company, is henceforth referred to as the "standard blade" with which the characteristics of the modifications attempted in Secs. 5.1–5.3 are compared. The three different modifications attempted are referred to as Case 1, Case 2, and Case 3.

5 Modified Geometries

5.1 Case 1. In the case of the standard blade it was observed (Fig. 6(*a*)) that most of the cold flow ejecting from the first coolant hole (Coolant hole 1) left the tip gap with only a part of it staying inside the cavity and acting effectively. This could be caused by the blockage created by the presence of the rib. The removal of this rib might allow more of the cold fluid to flow downstream toward the trailing edge and hence enhance the cooling performance. Thus the rib was removed and a computation was performed with the same boundary conditions as with the case of the standard blade.

The contours of HFR on the blade tip and the streamlines across the tip are shown in Figs. 8(*a*) and 8(*b*). The hot spots (HA–HG) and cold spots (LA–LG) on the blade are marked in Fig. 8(*a*). As observed in the case of the standard blade, these cold spots are caused by the impingement or by the attached flow (see Fig. 8(*b*)) of the cold fluid emerging from the coolant or dust holes, and the hot spots are caused by the impingement or reattachment of the hot leakage fluid. From Fig. 8(*b*) it is seen that, compared with the case of standard blade (Fig. 6(*a*)), there is no noticeable increase in the amount of cold fluid (from Coolant hole 1) flowing downstream of the coolant hole. However, the streamlines of hot leakage flow (marked SA in Fig. 6(*a*)), which entered the cavity in the case of the standard blade are now diverted by the emerging coolant, thus preventing the entrainment of the kind marked SB in Fig. 6(*a*). As a consequence, hot spot D (which occurred in the case of standard blade, see Fig. 7(*a*)) has been eliminated. Also there is an increase in the amount of cold fluid from Dust hole 2 (red streamlines) being dragged toward the pressure side by the fluid emerging from Coolant hole 1; this increases the extent of the cold region marked LG and may be visualized by the increase in the number of red streamlines being influenced by the blue streamlines (ejecting from Coolant hole 1). Comparing Figs. 6(*b*), 6(*f*), 6(*i*), 6(*g*), and 8(*a*), it is seen that the distribution

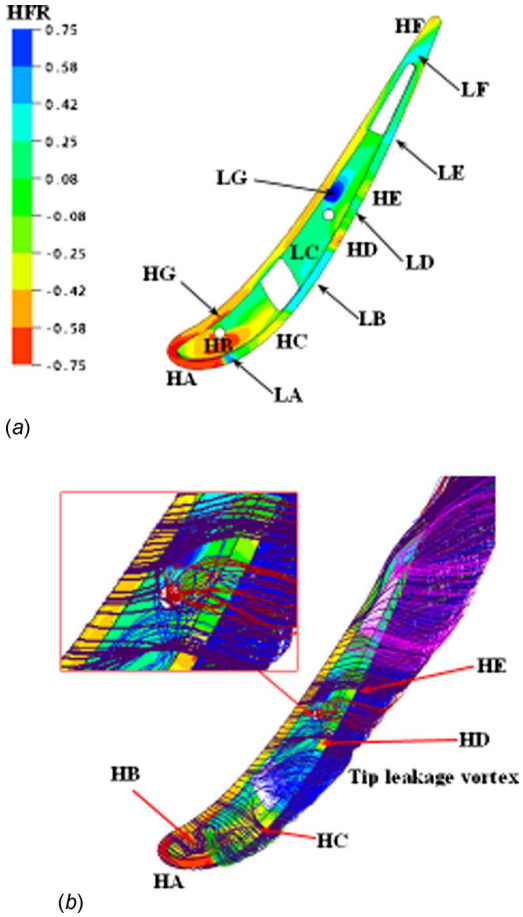

Fig. 8 (*a*) Contours of HFR on tip and (*b*) contours of HFR on tip with streamlines superimposed: Case 1

of HFR on the tip essentially remains the same, except for an increase in the extent of both cold spots LD and LG and a decrease in the extent of hot spot HE.

The tip gap exit mass flow, the area affected as a percentage of the total area of the tip, and the total negative wall heat flux on tip for Case 1 are shown in Table 3. A direct comparison can be made with the standard blade, which is summarized in Table 2: The tip gap exit mass flow remains the same, and there is only a marginal (3%) decrease in the heat flux to the tip; however, there is a considerable (20%) decrease in the area affected by the hot flow. This decrease in area is due to the decrease in extent of hot spot HE and an increase in the extent of the cold spots LD and LG. In conclusion, the removal of the rib proves to be advantageous from a heat transfer perspective.

5.2 Case 2. For both the standard blade and for the Case 1 blade (Figs. 6(*b*) and 8(*a*)), the leading edge region was an area adversely affected by the hot flow. This region accounts for a major contribution of the total heat flux to the tip due to the hot attached flow (see HA in Fig. 6(*a*)) and impingement (see HB in Fig. 6(*a*)). Directing the coolant emerging from Dust hole 1 toward the leading edge might improve this undesirable circum-

Table 3 Tip leakage characteristics of the Case 1 blade

Tip gap exit mass flow (% of inlet mass flow)	2.85
Area affected (% of total tip area)	42.1 (−20%)[a]
Total negative wall heat flux ($\times 10^9$ W/m^2)	6.6 (−3%)[a]

[a]Change in comparison to the standard blade.

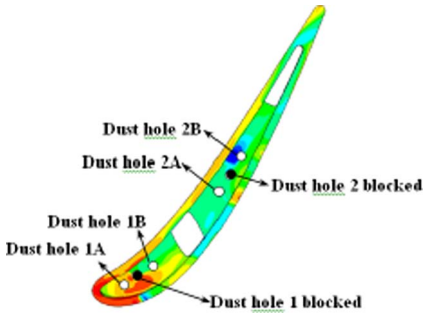

Fig. 9 Schematic of Case 2 tip (derived from Case 1 tip)

stance. Within the limits and constraints governed by the internal coolant passage, Dust hole 1 was moved to a position closer to the leading edge (see Fig. 9). This hole is henceforth referred to as Dust hole 1A. An additional dust hole, referred to as Dust hole 1B, was also created. Dust hole 2 was also blocked and replaced by two dust holes, namely, Dust holes 2A and 2B. It is expected that the Dust holes 2A and 2B would eliminate the hot spots HD and HE that were present in Case 1 (see Figs. 8(*a*) and 8(*b*)). Furthermore, these dust holes were inclined in an attempt to direct the cold flow ejecting from them toward the hotspots. Dust hole 1A was inclined toward the leading edge, and Dust hole 1B was inclined toward the hot spot HG. The inclination of the holes was accomplished without significantly disturbing the internal coolant passage and within the manufacturing constraints specified by SIEMENS. These constraints allowed an inclination angle of 45 deg from the radial axis toward the leading edge in case of Dust hole 1A and an inclination angle of 60 deg toward the hot spot HG for Dust hole 1B. Corresponding modifications were hence made to the internal coolant passage. A CFX computation of flow through the internal coolant passage with these four dust holes were performed to obtain the boundary conditions to be used. The total coolant mass flow is same is that of the previous cases. The results of the computation subsequently performed are presented here.

The contours of HFR on the blade tip and the streamlines across the tip are shown in Figs. 10(*a*) and 10(*b*). The hot spots (HA–HG) and cold spots (LA–LJ) are marked in Fig. 10(*a*). As observed in the previous cases, these cold or hot spots are caused either by the impingement or by attached flow of the cold fluid ejecting from the coolant or dust holes or correspondingly from the hot leakage fluid. The computed distribution can be compared with that for the standard blade (Fig. 6(*b*)). The noticeable differences are a considerable increase in the extent of hot spot HG (resulting in a merger with HA), a decrease in the extent of the hot spot HD, and elimination of hot spot HE. The increase in the size of hot spot HG is due to the impingement (marked I1 and I2 in Fig. 10(*b*)) of hot leakage flow in this region. In addition to the cold spots observed for the standard blade, cold spots marked LA1, LH, LI, and LJ are now present. LI and LJ are caused by the impingement of cold fluid from the dust hole in these regions. Figure 10(*b*) shows that a considerable amount of the cold fluid ejected from the Dust hole 1B surprisingly exits the tip gap on the pressure side and is washed away by the mainstream flow without providing any useful protection to the tip.

The contours of HFR on the blade tip, viewed from the pressure and suction side, respectively, are shown in Figs. 11(*a*) and 11(*b*). Figure 11(*a*) can be compared with Fig. 7(*a*) (Standard blade). The extent of hot spot A has increased and hot spot B, observed previously, has now disappeared. The increased extent of A is due to the impingement of hot leakage flow in this region. Figure 11(*b*) reveals two cold spots (marked IA and IB) near the pressure-side leading edge. These cold spots replaced an area of high heat transfer in Case 1 (the equivalent view of Fig. 11(*b*) for Case 1 is not shown).

Tip gap exit mass flow, the area affected by the hot flow as a

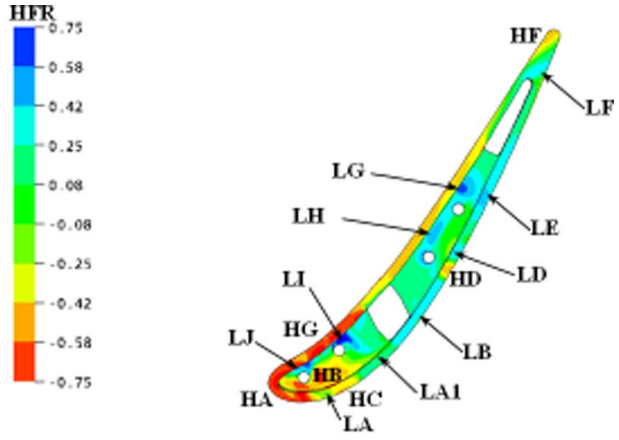

(*a*)

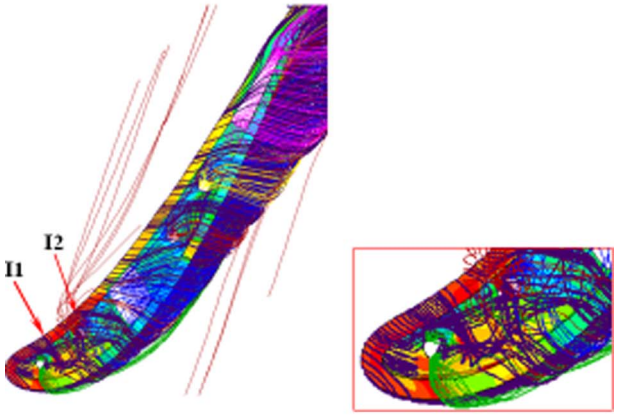

(*b*)

Fig. 10 (*a*) Contours of HFR on tip and (*b*) contours of HFR on tip with streamlines superimposed: Case 2

percentage of the total area of the tip, and the total negative wall heat flux to the tip for Case 2 are shown in Table 4. A direct comparison can be made with the standard blade, which is summarized in Table 2: There is only a marginal change in the tip gap exit mass flow (about 1%) and the total heat flux to the tip; however, there is a considerable (36%) decrease in the area affected by the hot flow. This marginal change in tip gap exit mass flow is caused by a small change (1.5%) in tip gap inlet mass flow, compared with that of Case 1. The decrease in area affected by the hot flow is due to the reduction in hot spot HD, the elimination of the hot spots HE, B, and D (the latter two on the face of the suction-side squealer on the standard blade), and the creation of cold spots IA and IB on the face of the pressure-side squealer. It should be noted that the increase in the intensity of hot spot HG contributes only to an increase in the magnitude of heat flux to the tip and not to the area of the affected by hot flow.

Compared with the Case 1 there is an increase in the total heat flux to the tip by about 8% due mainly to the increase in the intensity of hot region HG, making the Case 2 modification marginally inferior. However, if the cold fluid emerging from Dust hole 1B could be prevented from exiting the tip gap (on the pressure side) and instead be made to impinge onto the squealer, this hot spot, which makes the major contribution to the increase in the total heat flux to the tip, might be eliminated. This might be achieved by changing the angle of inclination, though this modification was not attempted due to time limitations.

5.3 Case 3. The modification for this case was essentially the creation of a suction-side squealer. This geometry used the cavity

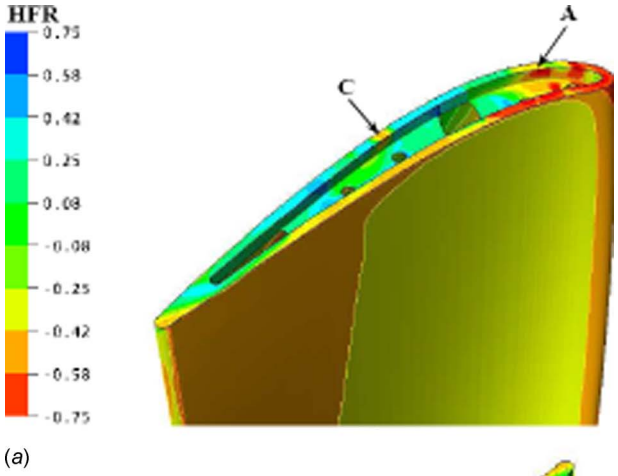

(*a*)

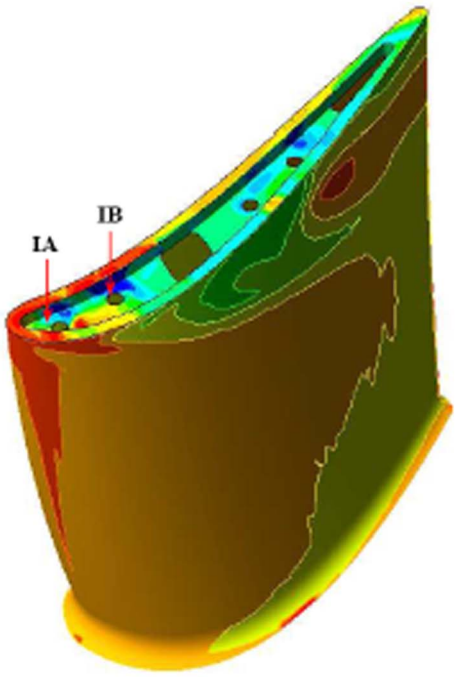

(*b*)

Fig. 11 Contours of HFR on blade (*a*) view from PS and (*b*) view from SS: Case 2

geometry (Case 2) and removed a major part of the pressure-side squealer (see Fig. 12). The dust holes were realigned to the normal. The objective here was to compare the aerothermal performance of the suction-side squealer tip with the cavity tip in the engine environment.

The streamlines across the tip are shown in Fig. 13(*a*). A vortical flow is formed from the leading edge of the squealer, which turns and impinges on the top of the squealer (marked IA) and then leaves the tip gap. The flow exiting the tip gap shears with the mainstream flow and forms the tip leakage vortex. Near the leading edge, the hot leakage flow, which separates from pressure-side edge, is blocked by the presence of the cold flow ejecting from Dust holes 1A and 1B. Part of this flow impinges onto the tip

Table 4 Tip leakage characteristics of the Case 2 blade

Tip gap exit mass flow (% of inlet mass flow)	2.88
Area affected (% of total tip area)	33.2 (−36%)[a]
Total negative wall heat flux ($\times 10^9$ W/m^2)	7.2 (+4%)[a]

[a]Change in comparison to the standard blade.

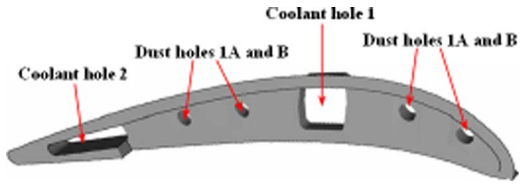

Fig. 12 Suction-side squealer tip (Case 3)

in the vicinity of the dust holes (marked IB) and onto the squealer (marked IC) before exiting the tip gap. The hot leakage flow, which enters the tip gap near Coolant hole 1 is blocked by the emerging cold fluid and hence is diverted toward the trailing edge, staying close to the pressure-side edge. A part of this flow impinges at ID and then exits the tip gap on the pressure side, washed away by the hot mainstream flow. Another part of this flow turns and impinges onto the squealer (marked IE) before leaving the tip gap. In general, the cold fluid ejecting from the coolant and the dust holes impinge onto the squealer and leave the tip gap. The coolant from Dust hole 2B, however, is carried away by the hot leakage flow toward the pressure side (see A in Fig. 13(*a*)).

The contours of HFR on the blade tip are shown in Fig. 13(*b*) with the hot regions (HA–HH) and cold regions (LA–LG) marked. As in the previous cases these cold or hot regions are caused either by the impingement or by the attached flow of cold fluid ejected from the coolant or the dust holes or hot.

The tip gap exit mass flow, the area affected by the hot flow as

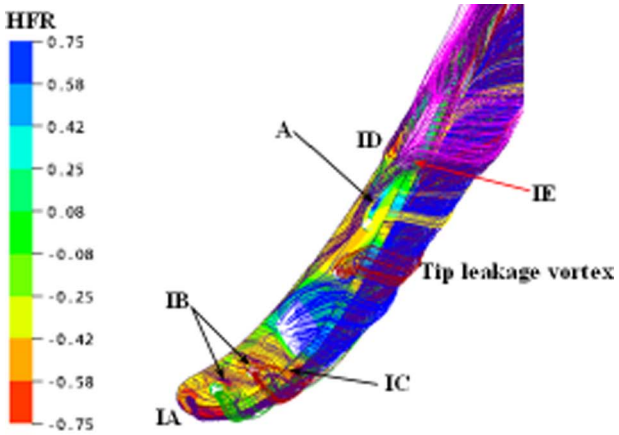

(*a*)

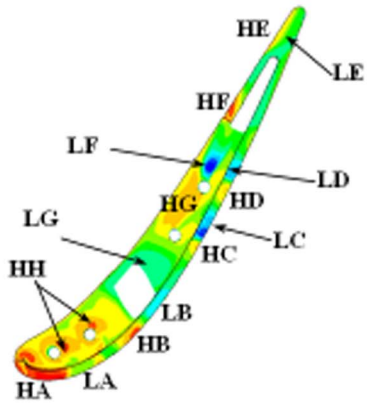

(*b*)

Fig. 13 (*a*) Contours of HFR on tip with streamlines superimposed and (*b*) contours of HFR on tip: Case 3

Table 5 Tip leakage characteristics of the Case 3 blade

Tip gap exit mass flow (% of inlet mass flow)	3.18 (+12%)
Area affected (% of total tip area)	63.5 (+21%)[a]
Total negative wall heat flux ($\times 10^9$ W/m^2)	12.9 (+87%)[a]

[a]Change in comparison to the standard blade.

a percentage of the total area of the tip, and total negative wall heat flux for Case 3 are shown in Table 5. Compared with the standard blade (Table 2), the tip gap exit mass flow has increased by 12%. A similarly poor performance of a suction-side squealer was observed in a previous investigation using a low speed cascade blade [18]. The area affected by the hot flow has increased by 21%, and there is an 87% increase in the total heat flux to the tip. It is interesting to note that the suction-side squealer tip was observed to provide nearly a 40% decrease in tip heat transfer in the previous investigation [18]. The difference between these cases (and others such as Refs. [15,16]) is due to the differences in the flow patterns caused by the cold flow ejected from the coolant and the dust holes.

6 Comparison of the Geometries

The aerothermal performance (in terms of the tip gap exit mass flow, area affected by the hot flow, and total heat flux to the tip) of all modified geometries are compared with those of standard blade in Table 6. There is only a slight change in tip gap exit mass flow for Case 1 and Case 2. However, in the case of the suction-side squealer tip (Case 3), the leakage mass flow increases by 12% thus making it inferior to the other geometries considered.

From the heat transfer perspective, Case 2 is seen to be better in terms of the area affected by the hot flow. However, Case 1 is superior in terms of the total heat flux to the wall, which is the more important criterion. The heat flux for Case 1 is 3% less than for the standard blade and 8% less than for the Case 2 geometry. This reduction in net heat flux is achieved while maintaining the same leakage mass flow across the tip. However, as noted earlier, the Case 2 geometry would be more effective if the cold fluid ejected from Dust hole 1B were to be redirected. The total heat flux for the suction-side squealer tip (Case 3) has increased significantly, indicating a poor design modifications.

7 Conclusions

The flow and heat transfer characteristics of an industrial turbine rotor tip have been investigated. The simulations were performed using CFX 5.6 with the SST k-ω turbulence model. Initial predictions were validated using computations previously performed at SIEMENS using standard codes in the absence of coolant ejection.

The comparison of calculations performed with and without coolant ejection has shown that the coolant flow in effect partially blocks the tip gap reducing the area available for the flow to leak from pressure side to the suction side of the blade, resulting in the reduction in amount of mainstream flow leaking through the tip gap. The tip gap exit mass flow, however, increased by 15%. The coolant flow was identified as the sole contributor to the increase in tip gap exit mass flow.

Three different modifications (referred to as Cases 1–3) were made to a standard blade tip in an attempt to reduce the tip leakage mass flow and heat transfer. The improvements in aerothermal performance and limitations of the modified geometries have been presented. The main feature of the Case 1 geometry was the removal of a rib, and this modification was found to effectively reduce both the total area affected by the hot leakage flow and the total heat flux to the tip while maintaining the same leakage mass flow as the standard blade. Case 2 featured a rearrangement of the dust holes in the tip, which, in terms of aerothermal dynamics, proved to be marginally inferior to Case 1. Case 3, which essentially created a suction-side squealer geometry, was found to be inferior even to the standard cavity-tip blade. It was also revealed that the hot spots, which occur in the leading edge region of the standard tip, and all modifications contributed significantly to the area affected by the hot tip leakage flow and the total heat flux to the tip.

Table 6 Comparison of modified geometries with the standard blade

Reference	Standard	Case 1	Case 2	Case 3
% mass flow	2.85	2.85	2.88	3.18 (+12%)
% area affected	52.55	42.11 (−20%)	33.22 (−36%)	63.53 (+21%)[a]
Total heat flux ($\times 10^9$ W/m^2)	−6.92	−6.65 (−3%)	−7.22 (+4%)	−12.99 (+87%)

[a]Change in comparison to the standard blade.

Acknowledgment

The work presented in this paper was carried out by the first author during his industrial placement at SIEMENS Industrial Turbomachinery Ltd, Lincoln, UK, as a part of a Ph.D. project funded jointly by EPSRC, Alstom Power Ltd, UK, and SIEMENS Industrial Turbomachinery Ltd. Their support is gratefully acknowledged.

Nomenclature

- G1, G2 = mesh used for computations
- h = heat transfer coefficient=$q_w/(T_{oin}-T_w)$
- HFR = $q_{wall}/|$maximum negative $q_{wall}|$
- k = turbulent kinetic energy
- P_{oin} = total pressure at inlet
- p_{exit} = exit static pressure
- q_w = heat flux from air to wall
- T_{oin} = inlet total temperature
- T_w = wall temperature
- ω = turbulence frequency
- ε = rate of dissipation of k

References

[1] Booth, T. C., Dodge, P. R., and Hepworth, H. K., 1982, "Rotor-Tip Leakage: Part 1—Basic Methodology," ASME J. Eng. Power, **104**, pp. 154–161.

[2] Denton, J. D., and Cumpsty, N. A., 1987, "Loss Mechanisms in Turbomachines," *Proc. IMechE Conf., Turbomachinery–Efficiency and Improvement*, Paper No. C260/87.

[3] Bunker, R. S., 2001, "A Review of Turbine Blade Tip Heat Transfer in Gas Turbine Systems," Ann. N.Y. Acad. Sci., **934**, pp. 64–79.

[4] Kim, Y. W., and Metzger, D. E., 1993, "Heat Transfer and Effectiveness on Film Cooled Turbine Blade Tip Models," ASME Paper No. 93-GT-208.

[5] Chen, G., Dawes, W. N., and Hodson, H. P., 1993, "A Numerical and Experimental Investigation of Turbine Tip Gap Flow," *Proceedings of the 29th Joint Propulsion Conference and Exhibit*, AIAA Paper No. 93-2253.

[6] Krishnababu, S. K., Newton, P., Dawes, W. N., Lock, G. D., and Hodson, H. P., 2005, "An Experimental and Numerical Investigation of the Tip Leakage Flow and Heat Transfer Using a Rotor Tip Gap Model," *Proceedings of the Fifth European Turbomachinery Conference*, Lille, France.

[7] Bunker, R. S., Bailey, J. C., and Ameri A. A., 1999, "Heat Transfer and Flow on the First Stage Blade Tip of a Power Generation Gas Turbine: Part I—Experimental Results," ASME Paper No. 99-GT-169.

[8] Kwak, J. S., and Han, J. C., 2002, "Heat Transfer Coefficient and Film-Cooling Effectiveness on a Gas Turbine Blade Tip," ASME Paper No. 2002-GT-30194.

[9] Kwak, J. S., and Han, J. C., 2002, "Heat Transfer Coefficient and Film-Cooling Effectiveness on the Squealer Tip of a Gas Turbine Blade," ASME Paper No. 2002-GT-30555.

[10] Jin, P., and Goldstein, R. J., 2002, "Local Mass/Heat Transfer on Turbine Blade Near-Tip Surfaces," ASME Paper No. 2002-GT-30556.

[11] Ameri, A. A., Steinthorsson, E., and Rigby, D. L., 1998, "Effect of Squealer Tip on Rotor Heat Transfer and Efficiency," ASME J. Turbomach., **120**, pp. 753–759.

[12] Ameri, A. A., and Bunker, R. S., 1999, "Heat Transfer and Flow on the First

Stage Blade Tip of a Power Generation Gas Turbine: Part II—Simulation Results," ASME Paper No. 99-GT-283.
[13] Yang, H., Acharya, S., Ekkad, S. V., Prakash, C., and Bunker, R., 2002, "Flow and Heat Transfer Predictions for a Flat Tip Turbine Blade," ASME Paper No. 2002-GT-30190.
[14] Yang, H., Acharya, S., Ekkad, S. V., Prakash, C., and Bunker, R., 2002, "Numerical Simulation of Flow and Heat Transfer Past a Turbine Blade With a Squealer Tip," ASME Paper No. 2002-GT-30193.
[15] Acharya, S., Yang, H., Prakash, C., and Bunker, R., 2003, "Numerical Study of Flow and Heat Transfer on a Blade Tip With Different Leakage Reduction Strategies," ASME Paper No. 2003-GT-38617.
[16] Saha, A. K., Acharya, S., Prakash, C., and Bunker, R., 2003, "Blade Tip Leakage Flow and Heat Transfer With Pressure Side Winglet," ASME Paper No. 2003-GT-38620.
[17] Mumic, F., Eriksson, D., and Sunden, B., 2004, "On Prediction of Tip Leakage Flow and Heat Transfer in Gas Turbines," ASME Paper No. 2004-GT-53448.
[18] Krishnababu, S. K., Newton, P. J., Lock, G. D., Dawes, W. N., Hodson, H. P., Hannis, J., and Whitney, C., 2007, "Aero-Thermal Investigation of Tip Leakage Flow in Axial Flow Turbines: Part I—Effect of Tip Geometry," ASME Paper No. 2007-GT-27954.
[19] Acharya, S., Yang, H., and Ekkad, S. V., 2002, "Numerical Simulation of Film Cooling on the Tip of a Gas Turbine Blade," ASME Paper No. 2002-GT-30553.
[20] Lock, G. D., Newton, P. J., Krishnababu, S. K., Dawes, W. N., Hodson, H. P., Hannis, J., and Whitney, C., 2007, "Aero-Thermal Investigation of Tip Leakage Flow in Axial Flow Turbines: Part III—Tip Cooling," ASME Paper No. 2007-GT-27368.
[21] Morphis, G., and Bindon, J. P. 1988, "The Effects of Relative Motion, Blade Edge Radius and Gap Size on the Blade Tip Pressures Distribution in an Annular Turbine Cascade With Clearance," ASME Paper No. 88-GT-256.
[22] Yaras, M. I., and Sjolander, S. A., 1992, "Effects of Simulated Rotation on Tip Leakage in a Planar Cascade of Turbine Blades: Part I—Tip Gap Flow," ASME J. Turbomach., **114**, pp. 652–659.
[23] Srinivasan, V., and Goldstein, R. J., 2003, "Effect of Endwall Motion on Blade Tip Heat Transfer," ASME J. Turbomach., **125**, pp. 267–273.
[24] Rhee, D. H., and Cho, H. H., 2006, "Local Heat/Mass Transfer Characteristics on a Rotating Blade With Flat tip in Low-Speed Annular Cascade: Part I—Near Tip Surface," ASME J. Turbomach., **128**, pp. 96–109.
[25] Rhee, D. H., and Cho, H. H., 2006, "Local Heat/Mass Transfer Characteristics on a Rotating Blade With Flat Tip in Low-Speed Annular Cascade: Part II—Tip and Shroud," ASME J. Turbomach., **128**, pp. 110–119.
[26] Krishnababu, S. K., Dawes, W. N., Hodson, H. P., Lock, G. D., Hannis, J., and Whitney, C., 2007, "Aero-Thermal Investigation of Tip Leakage Flow in Axial Flow Turbines: Part II—Effect of Relative Casing Motion," ASME Paper No. 2007-GT-27957.
[27] Wollat, G., 1997, "MW Compressor Turbine-Through-Flow Design," SIEMENS Report No. TDR 97/100.
[28] Gan, X. P., 1998, "TEXSTAN AETC Code Investigation, Modification and Enhancement," Alstom Report No. 21667/1.
[29] Patel, V. C., Rodi, W., and Scheuerer, G., 1985, "Turbulence Models for Near Wall Flows at Low Reynolds Numbers: A Review," AIAA J., **23**, pp. 1308–1318.

Juan Du
Graduate School of Chinese Academy of Sciences,
Beijing 100190, China;
Institute of Engineering Thermophysics,
Chinese Academy of Sciences,
Beijing 100190, China;
Key Laboratory of Advanced Energy and Power,
IET, CAS,
Beijing 100190, China

Feng Lin
Tri-State University,
Angola, IN 46703

Hongwu Zhang

Jingyi Chen

Institute of Engineering Thermophysics,
Chinese Academy of Sciences,
Beijing 100080, China;
Key Laboratory of Advanced Energy and Power,
CAS,
Beijing 100080, China

Numerical Investigation on the Self-Induced Unsteadiness in Tip Leakage Flow for a Transonic Fan Rotor

A numerical investigation on the self-induced unsteadiness in tip leakage flow is presented for a transonic fan rotor. NASA Rotor 67 is chosen as the computational model. It is found that under certain conditions the self-induced unsteadiness can be originated from the interaction of two important driving "forces:" the incoming main flow and the tip leakage flow. Among all the simulated cases, the self-induced unsteadiness exists when the size of the tip clearance is equal to or larger than the design tip clearance. The originating mechanism of the unsteadiness is clarified through time-dependent internal flow patterns in the rotor tip region. It is demonstrated that when strong enough, the tip leakage flow impinges the pressure side of neighboring blade and alters the blade loading significantly. The blade loading in turn changes the strength of the tip leakage flow and results in a flow oscillation with a typical signature frequency. This periodic process is further illustrated by the time-space relation between the driving forces. A correlation based on the momentum ratio of tip leakage flow over the incoming main flow at the tip region is used as an indicator for the onset of the self-induced unsteadiness in tip leakage flow. It is discussed that the interaction between shock wave and tip leakage vortex does not initiate the self-induced unsteadiness, but might be the cause of other types of unsteadiness, such as broad-banded turbulence unsteadiness. [DOI: 10.1115/1.3145103]

1 Introduction

Unsteady flows in the tip region are one of the sources of noise, blade vibration, and flow losses in compressors [1]. In some cases, unsteady tip leakage flow was demonstrated to potentially link to stall inception [2,3]. Although the tip leakage flow has been under extensive studies for many years, its unsteadiness is a recent focus in axial compressor research community [2–11]. Three types of unsteadiness have been reported, which are given as follows.

- *Induced vortex*. In 1999, Mailach [4] reported a phenomenon with oscillatory tip leakage vortex rotating from blade to blade while the compressor still operated in a near stall but stable operating point. This phenomenon is referred to as "rotating instability." A series of papers were then published by Mailach thereafter in regards to rotating instability. In 2001, Marz et al. [5] performed a detailed unsteady casing pressure measurement and a time-accurate numerical simulation for the full annulus of a low-speed axial compressor. The mechanism of rotating instability was attributed to an induced vortex when it travels from suction side to pressure side at roughly half of the rotor speed. Bergner et al. [6] and Hah et al. [7] experimentally and numerically investigated a high-speed transonic compressor stage, respectively. The oscillation in tip leakage flow was also found. This oscillation was attributed to an induced vortex and the shock-vortex interaction.
- *Vortex breakdown*. Furakawa et al. recognized the role of tip leakage vortex breakdown in compressor aerodynamics [8] and further indicated that the breakdown could be one of the sources of unsteadiness in tip leakage flow [9]. The work was extended to a transonic compressor by Yamada et al. [10].
- *Self-induced unsteadiness*. Zhang et al. [11] found a new type of unsteadiness. The tip leakage flow could become unsteady at high loading operating conditions without involving multiblades in a low-speed compressor rotor. Because this type of the unsteadiness is a result of interaction of incoming main flow and tip leakage flow, we call it self-induced unsteadiness. Tong et al. [3] experimentally demonstrated its existence. They also found that spike was initiated at the circumferential location with the strongest unsteadiness.

This paper will extend the study of self-induced unsteadiness to a high-speed compressor. The research questions are the following.

(1) Does the self-induced unsteadiness exist in high-speed rotors? If yes, what are the phenomena?
(2) What is the originating mechanism of the self-induced unsteadiness in high-speed rotors?

This paper is organized as follows. After a brief introduction of NASA Rotor 67 and the computational fluid dynamics (CFD) scheme, the results of CFD are validated with the available experimental results. Having evidenced the location and frequency of the unsteadiness of tip leakage flow, we carefully examine the instantaneous flow fields and clarify the mechanism of the self-induced unsteady tip leakage flow for this rotor. The proposed mechanism is also supported by studying the influence of tip clearance sizes while keeping the incoming main flow unchanged. The results show that the self-induced unsteadiness in tip leakage flow in this high-speed rotor is due to the dynamic interaction of the same two driving "forces" as those in low-speed compressor [11,12]. A correlation based on the momentum ratio of these two driving forces, the tip leakage flow over the incoming main flow at the tip region, is worked out and used as an indicator for the

Contributed by the International Gas Turbine Institute of ASME for publication in the JOURNAL OF TURBOMACHINERY. Manuscript received August 14, 2008; final manuscript received February 23, 2009; published online January 20, 2010. Review conducted by David Wisler. Paper presented at the ASME Turbo Expo 2008: Land, Sea and Air (GT2008), Berlin, Germany, June 9–13, 2008.

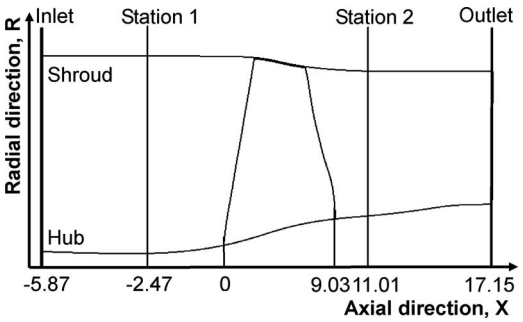

Fig. 1 Measurement location and computation region

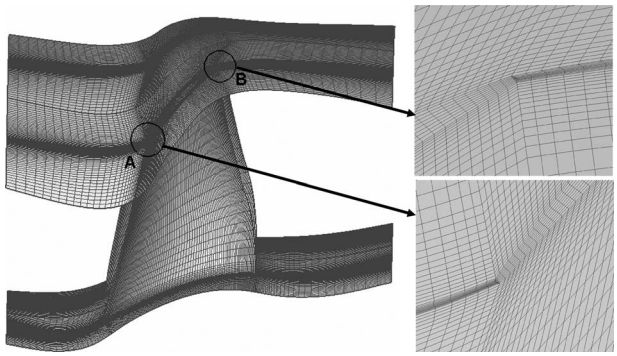

Fig. 2 Computational geometry and grid distribution for Rotor 67

onset of the self-induced unsteadiness. Before concluding the paper, the role of shock wave in regards to the unsteadiness of tip leakage flow and the link of this flow unsteadiness to stall inception are discussed.

2 Rotor 67 and the Numerical Scheme

2.1 Basic Parameters of the Transonic Fan Rotor. NASA Rotor 67, the first stage rotor of a two-stage fan, is a low-aspect-ratio design, which is designed for axial inflow without an inlet guide vane. It had been selected as a computed target to investigate the strong interaction between the tip leakage vortex and the in-passage shock wave by Adamczyk [13]. In this paper, Rotor 67 is used for unsteady investigation of tip leakage flow. The specifications and measurement data of Rotor 67 can be found in Ref. [14].

2.2 Numerical Tool and Computation Scheme. Unsteady flow simulations were performed by solving unsteady three-dimensional, Reynolds-averaged Navier–Stokes equations. A commercial solver package, FLUENT, was utilized for the present work. The solver is a three-dimensional, time-accurate code with implicit second-order scheme. The standard κ-ε turbulence model and standard wall function were used to account for the turbulence flow. Standard and realizable κ-ε turbulence model were compared with improving precision of computation. The comparison between numerical and experimental results demonstrated that the prediction by applying standard κ-ε turbulence model is better. Several numerical researches using this unsteady flow solver have been conducted for low-speed and high-speed compressor rotors [11,12,15], and the computation results matched with experiments well.

It has been shown that in low-speed compressors, the self-induced unsteady tip leakage flow can be simulated using single blade passage computation model [12]. In other words, this kind of unsteadiness can be triggered without invoking cross-blade passage flows, such as leading spillage of tip leakage vortex, reversed flow, and so on. In order to verify this observation in high-speed rotors, self-induced unsteadiness in multipassage environment (five blade passages or 5/22 of the Rotor 67 annulus) is also investigated. The results at the design tip clearance are shown in the Appendix, which clearly demonstrates that the characteristics for all the blade passages are identical while the self-induced unsteadiness is captured. Hence, the computation model in this paper is chosen as a single blade passage model. The computation domain with inlet and outlet axial coordinates is shown in Fig. 1. Total pressure, total temperature, and flow angles were given uniformly at the inlet boundary. Static pressure was specified with simple radial equilibrium law at outlet. Nonslip and adiabatic conditions were imposed on all solid walls.

Figure 2 presents the rotor geometry and grid distribution. The grid resolution for a single blade passage is a structured H-mesh with 160 nodes (80 nodes on the blade) streamwise, 54 nodes pitchwise, and 70 nodes in the spanwise direction. 8, 10, and 16 nodes are applied in the tip clearances of 0.25%, 1.1%, and 2.2% blade tip chords, respectively.

2.3 Validation of Simulation. In order to validate numerical simulation in the present work, the results of simulation are compared with experimental results. The comparison of adiabatic efficiency is depicted in Fig. 3, while that of the total pressure ratio characteristic is presented in Fig. 5. Points I and II are the operating conditions near peak efficiency and near stall, respectively. The numerical results follow the same trend as the experiments, although the discrepancy slightly increases at small normalized mass flow rates. Our discrepancy is of the same order as the discrepancy in other studies. Figure 4 showed the blade-to-blade plots of relative Mach number contours at 90% span from hub for two operating conditions. The Mach number contours, in which the location of the shock waves is clearly displayed, match reasonably well with each other.

Grid independence had also been tested. Although we obtained 0.9% improvement in total pressure ratio prediction, there was no qualitative difference by doubling current numbers of grid cells. Since we will focus on the qualitative unsteady features in the rest of this paper, we decide to use current numbers of grid cells $(160\times54\times70)$ for unsteady simulation for the benefit of shorter simulation time.

3 Results

3.1 The Locations and Frequency of Unsteady TLF. Numerical simulations were carried out for three different tip clearance sizes. Figure 5 depicts the characteristics for each tip clearance. The simulations for this isolated rotor were run at the design rotational speed with various back pressures. All mass flow rates were normalized by the value at choke. Several points are labeled

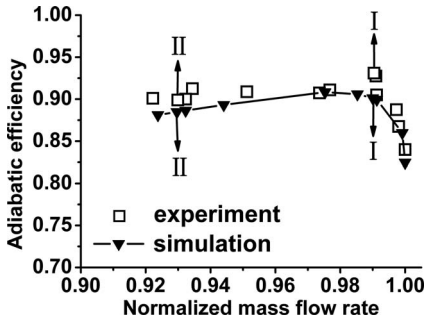

Fig. 3 Computed and measured adiabatic efficiency characteristic for design tip clearance. (*a*) Operating condition near peak efficiency (Point I). (*b*) Operating condition near stall (Point II).

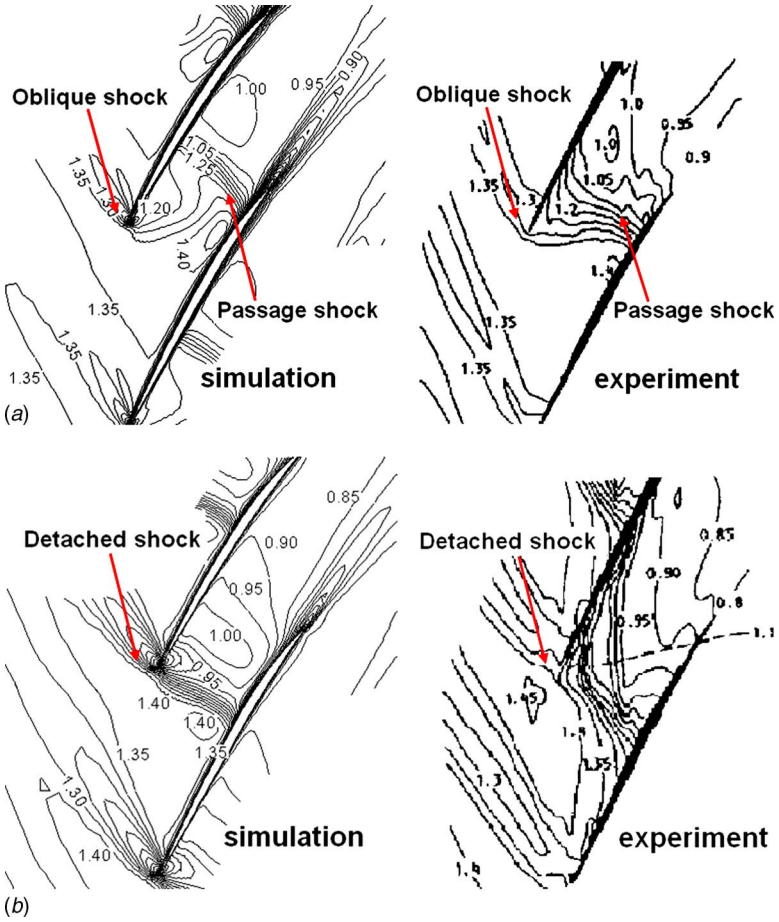

Fig. 4 Comparison of computed and measured relative Mach number at 90% span from hub for design tip clearance

in Fig. 5 for later convenience, among which letters S, U, N, and T are used to represent steady, unsteady, next-to-near-stall, and near-stall operating points, respectively. Subscripts 1, 2, and 3 are for 0.25%, 1.1%, and 2.2% tip chord of tip clearances, respectively. Note that near-stall points are those with highest back pressure before the iterative process diverges. For the design value of 1.1% tip chord, the only unsteady tip leakage flow case happens at the near-stall point. For 0.25% tip chord, unsteady computational results demonstrate that there is no unsteadiness of tip leakage flow. For 2.2% tip chord, unsteadiness is found long before the near-stall point. The first such point is then labeled as U_3 in Fig. 5.

Figure 6 depicts the static pressure root-mean-square (rms) distribution for Rotor 67 at operating point T_2. LE, TE, PS, and SS are abbreviations for leading edge, trailing edge, pressure surface, and suction surface, respectively. The high static pressure rms regions are concentrated on the tip region, and the rms of static pressure at the pressure side is of an order higher than that at the suction side. This result demonstrates that the unsteadiness under investigation is a tip-sensitive phenomenon.

A total of 24 monitoring points are located along the blade surface at 99% span, half of which are set on the pressure side, and half on the suction side. The fast Fourier transform results for the pressure at the points on the pressure side are given in Fig. 7. The magnitude of oscillation on the suction side of blade

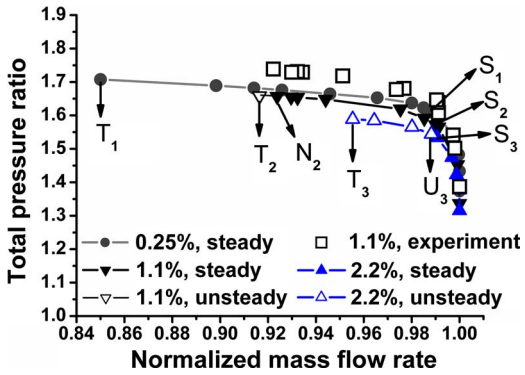

Fig. 5 Computed total pressure ratio characteristic for three tip clearance sizes

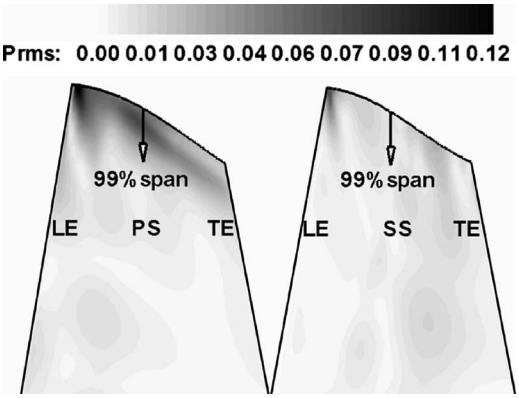

Fig. 6 Static pressure rms distribution for Rotor 67 at T_2

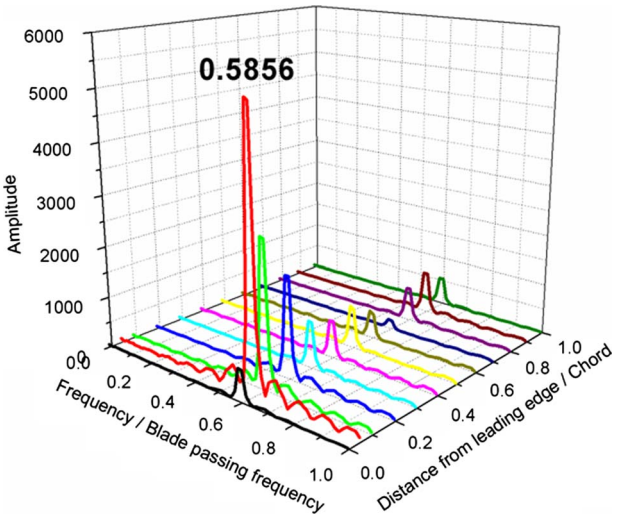

Fig. 7 Frequency and amplitude characteristics in the rotor tip region at 99% span

is too weak to display. The oscillation frequency is 0.5856 blade passing frequency (BPF) for all points, which is fairly close to the results of a low-speed rotor in Ref. [12] and a transonic rotor (Rotor 37) in Ref. [15]. The pressure at 7% tip chord from leading edge fluctuates stronger than any other point.

3.2 The Instantaneous Flow Fields and the Flow Mechanism. The instantaneous flow fields in the rotor tip region are closely examined in order to clarify the originating mechanism of the self-induced unsteadiness. Three types of graphs and curves are used, each of which contains its own information. The contours of static pressure coefficient (C_p) are a classic way used by many researchers to depict the tip leakage vortex trajectory and the shock wave in the flow field. The contour plots of relative total pressure coefficient (C_{rtp}) reveal the influences of low-energy flows because the difference in C_{rtp} along the axial direction is related to the shaft work added onto the flow. The curves of static pressure coefficient distribution along the pressure side are given to clearly display the propagation of low-pressure spot.

Figure 8 lists all three types of graphs and curves side by side for six time instants within one period of fluctuation for the design tip clearance of 1.1% tip chord at near-stall operating condition (Point T_2 in Fig. 5). All of them are taken from the cross section at 99% span (right at the tip of the blade). Note that we have mentioned that the frequency of this unsteadiness is 0.5856 BPF, which corresponds to a period of 1.7 T. Therefore, the last instant, $t=(50/30)T=1.67$ T, is quite close to the first instant.

Before further describing the flow structure in Fig. 8, it is necessary to introduce the interface between the incoming main flow and the tip leakage flow. This interface can be easily identified from the relative total pressure plots (Fig. 8(*b*)). Before the inter-

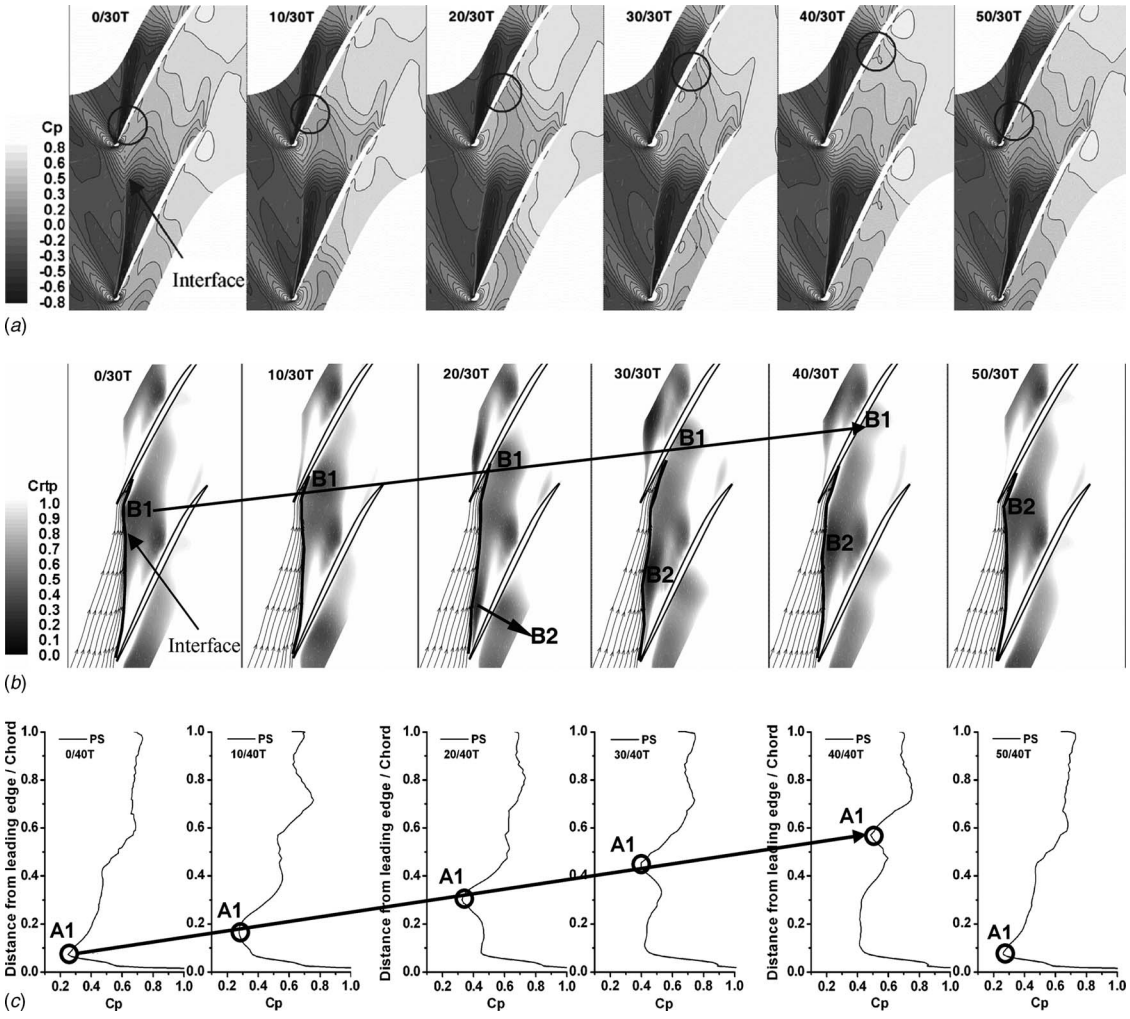

Fig. 8 Instant plots taken from 99% span at T_2 operating condition. (*a*) Static pressure coefficient. (*b*) Relative total pressure coefficient. (*c*) Pressure coefficient distribution on blade pressure surface.

face, it belongs to the incoming flow; after the interface, it is dominated by the tip leakage flow (there may exist some main flows leaking through the boundary layer of the suction side, but they are too weak compared with the tip leakage flow in this region). Since the tip leakage flow does not take any shaft work as energy input (that is why they are called "leakage flow"), their relative total pressure values are low. Therefore, the region influenced by the tip leakage flow can be easily identified in the relative total pressure plot (bounded by the interface lines in Fig. 8(*b*)). Streamlines from incoming main flow are added onto the plots in Fig. 8(*b*), so that one can simultaneously see how incoming flow and the tip leakage flow behave.

The identified interface is then added on the static pressure contours in Fig. 8(*a*) with its one end truncated so that the pressure field near the pressure surface can be seen clearly without interference. The interface is not the trajectory of the vortex, but it follows the tip leakage vortex and extends toward the pressure side of the neighboring blade. If this interface cannot stretch all the way across the blade passage, the incoming main flow can still go through the blade passage and establish a complete circulation around the tip region of the blade. The pressure difference across both sides of the blade is not disturbed, which in turn maintains a steady tip leakage flow. The whole flow field is thus steady.

Once the interface is able to go across the blade passage and reach the pressure side, one of the two possible scenarios may occur. One is that the tip leakage flow is too weak to create a large region of influence. The other is just the opposite: The tip leakage flow behind the interface is strong enough to influence the pressure distribution on the pressure side significantly. For the first scenario, the tip leakage flow is still steady because the incoming main flow dominates. The examples of this scenario can be seen in Figs. 12(*a*), 12(*b*), and 13(*a*) later in this paper. For the second scenario, however, the dynamic interaction between the incoming main flow and the tip leakage flow changes significantly. Figure 8 depicts the second scenario.

Unless otherwise noted, the region of influence by the tip leakage flow can be identified as a low relative total pressure region in Fig. 8(*b*). Due to the facts that the interface goes across the blade passage and that the tip leakage flow behind it is strong, the incoming main flow is blocked by the interface and is directed toward the pressure side of the blade (as seen in Fig. 8(*b*)). The main flow then creates a stagnating high-pressure spot near the leading edge on the pressure side before the interface, followed by the low-pressure spot behind the interface. The low-pressure spot is actually a part of the region of influence by the tip leakage flow, labeled as circle A1 in Fig. 8(*c*). The high-pressure spot pushes the adjacent low-pressure spot downstream (marked by the arrow line) and initiates the unsteadiness. For convenience, the time-dependent process of the low-energy tip leakage flow along the blade pressure surface (B1) and across the blade passage (B2), and the corresponding pressure variation process on the pressure surface (A1), as shown in Fig. 8, is summarized schematically in Fig. 9.

There are two time axes in Fig. 9. The one along the blade chord represents the time instants at which the low-energy spot (B1) and low-pressure spot (A1) propagate along the blade pressure side. The process of the low-energy tip leakage flow (B2) traveling across the blade passage is timed accordingly at the vertical axis. It can be seen that within the same time period, there are two streams of low-energy spots (B1 and B2) and one stream of low-pressure spots (A1). Each low-energy spot on the pressure side (B1) matches with the low-pressure spot (A1) nicely at the same chord location at the same time instant, inferring both are under the influence from the tip leakage flow. Through observing Fig. 9, there are two mechanisms in forming the time-dependent process of the tip leakage flow that need further elaboration. (1) As mentioned above, due to the effect of incoming main flow, the high-pressure spot stretches and pushes the low-pressure spot downstream along the pressure surface. So how will this alter the blade loading and thus create a reaction on the tip leakage flow? (2) How are the two streams of low-energy spots linked with each other and how will the periodicity of tip leakage flow unsteadiness take its place? Figures 10 and 11 in the next two paragraphs will illustrate these two mechanisms.

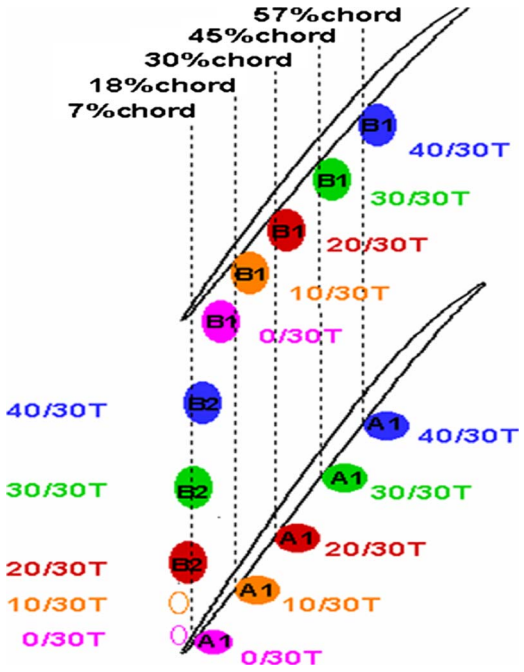

Fig. 9 Schematic of the unsteady process of self-induced tip leakage flow

Figure 10 is a contour plot of time-accurate velocity perturbation of tip leakage flow, which is the difference between the tip leakage flow velocity at each instant during the entire oscillating period and the averaged tip leakage flow velocity over the same period. The philosophy behind this plot is that the low-pressure spot (A1) at the pressure surface can only create pressure perturbation on top of the background pressure, and thus its influence can be clearly seen in velocity perturbation in tip leakage flow. The six dotted lines on the plot indicate the six time instants of Fig. 8. In order to demonstrate the influence of the pressure perturbation (A1), as well as the low-energy spot (B1) on the tip leakage flow, the locations of A1 at the time instants are read from Fig. 8(*c*) and added onto Fig. 10 using black circles. The local minima of velocity perturbation of the tip leakage flow are marked

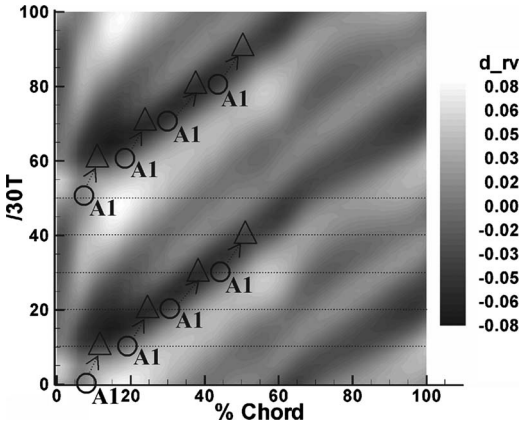

Fig. 10 Contour plot of velocity perturbation of tip leakage flow

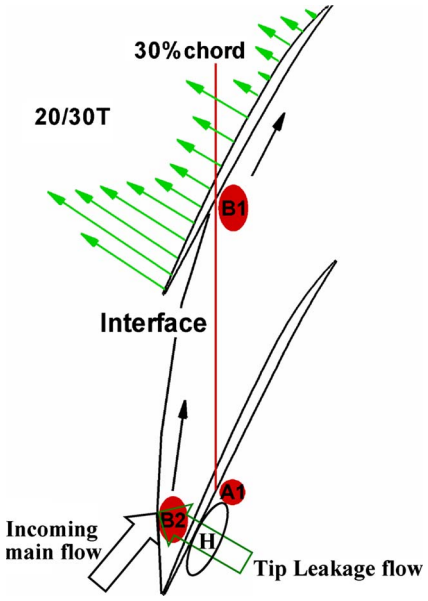

Fig. 11 Schematic of formation of B2 at 20/30 T with an addition of instantaneous velocity of tip leakage flow

as triangles. One can see that as the A1 (and B1) propagates downstream along the pressure surface, it reduces the velocity of tip leakage flow accordingly (but with a time lag as illustrated by the short dotted arrow lines), demonstrating the reaction of blade loading to the tip leakage flow.

The tip leakage flow impinges with the incoming main flow, and thus creates a stream of low-energy spots (B2) that travel across the blade passage. This process can be seen in Fig. 8(*b*) and further illustrated in Fig. 11. Figure 11 takes the snapshot of Fig. 8(*a*) at the time instant of 20/30 T, together with instantaneous velocity vectors of tip leakage flow (marked by the arrows along the blade chord). It can be seen that once the low-pressure spot moves away from the leading edge, the high blade loading due to the high pressure in the first 20% of the chord (copied from Fig. 8(*a*) and marked here as H in the ovals) creates strong tip leakage flow. As illustrated, the low-energy spot (B2) is a result of this strong tip leakage flow interacting with the incoming main flow. The similar interaction repeats at other time instants. Therefore, as shown in Fig. 8 and illustrated in Fig. 9, while the low-pressure spot A1 moves downstream, B2 moves across the blade passage and creates the second stream of the low-energy spots. Once the second stream of low-energy spots (B2) arrives at the pressure surface, the first stream A1 smears with the high-pressure background. The B2 turns itself to B1 seamlessly and a new period of oscillation thus starts. This process is qualitatively the same as what happened in the low-speed compressor in Ref. [12].

From the above description of the unsteady process, one can see that the onset of self-induced unsteadiness depends on whether the low-energy tip leakage flow is strong enough to alter the pressure distribution on the neighboring pressure surface significantly. However, this is closely related to the incoming main flow. If the incoming flow is reduced, the blade loading at the tip region increases, which in turn creates stronger tip leakage flow and thus the unsteadiness is more likely to happen. In other words, the incoming main flow generates the blade loading, which drives the tip leakage flow that then counteracts on the blade loading if its influence is stronger enough. In short, the dynamic interaction between the tip leakage flow and the incoming flow plays a decisive role in the onset of self-induced unsteadiness.

3.3 The Influence of Tip Clearance Sizes. In order to further verify the proposed mechanism that the initiation of the self-induced unsteady tip leakage flow is indeed attributed to the dynamic interaction between two driving forces, the incoming main flow and the tip leakage flow, we test it by varying one of the "forces" while keeping the other unchanged. This is done by comparing the results from different tip clearance sizes at the same incoming flow rate. The relative total pressure coefficient distribution with the same mass flow rate ($0.99m_{\text{choke}}$) for tip clearances of 0.25%, 1.1%, and 2.2% tip blade chords, corresponding with S_1, S_2, and U_3 (unsteady) points in Fig. 5, is shown in Fig. 12. Since larger tip clearance size produces stronger tip leakage flow, with 2.2% tip chord the region of influence by the tip leakage flow not only reaches the pressure side of the neighboring blade, but also penetrates further down along the span of the blade. It is therefore not surprised that only the case with 2.2% tip chord exhibits the unsteadiness at this mass flow rate, while the other two cases are steady.

3.4 Correlation of Onset Conditions. As indicated in Fig. 5, there is a threshold value of mass flow rate for the onset of tip leakage flow unsteadiness for tip clearances of 1.1% and 2.2% of tip chord. Figure 13 provides relative total pressure coefficient distributions at the blade tip right before and after the threshold values for tip clearances of 2.2% tip chord. It can be seen that from steady to unsteady, both the location of the interface between the incoming flow and TLF and the region of influence by TLF vary gradually. This actually is good news from flow control point of view, because it means no hysteresis associated with this change in flow dynamics.

We now propose a means to correlate the onset conditions for the self-induced unsteady tip leakage flow. Since the interface between incoming main flow and tip leakage flow is a consequence of the impact of these two flows in the tip clearance re-

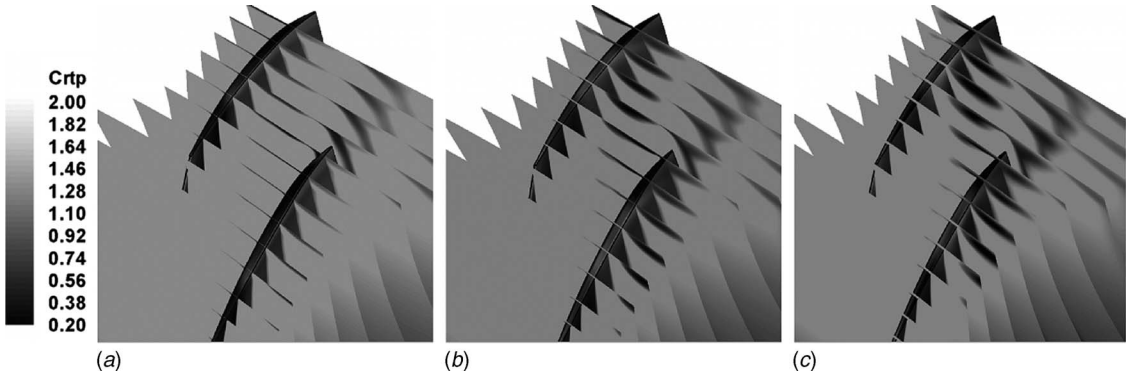

Fig. 12 Relative total pressure coefficient distribution for operating conditions S_1, S_2, and U_3. (*a*) 3D, steady (S_1); (*b*) 3D, steady (S_2); and (*c*) 3D, unsteady (U_3).

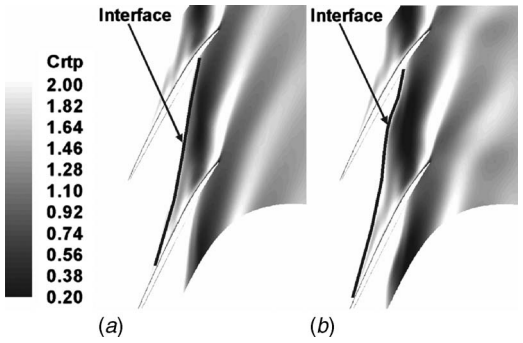

Fig. 13 Relative total pressure coefficient distribution at 98.4% span for tip clearance of 2.2% tip chord. (*a*) Steady (S_3) and (*b*) unsteady (U_3).

gion, we will use the ratio of two momenta as one of the parameters for our correlation. The ratio of M_{Tp} to M_{Is} is

$$R = \frac{M_{Tp}}{M_{Is}} = \frac{M_{Tt}\cos\alpha - M_{Ta}\sin\alpha}{M_{Ia}\cos\alpha + M_{It}\sin\alpha}$$

where subscripts I, T, s, p, t, a, and r are used to represent incoming flow, tip leakage flow, streamwise direction, perpendicular to streamwise direction, tangential direction, axial direction, and radial direction. The other parameter is the dimensionless tip clearance, which is the ratio of tip clearance to the blade height. The available CFD data of two different rotors, NASA Rotor 67 and NASA Rotor 37, are considered. The data for Rotor 37 are taken from Ref. [15]. Figure 14 shows the correlation between the dimensionless tip clearance size and the momentum ratio for onset conditions of unsteady tip leakage flow. The limit curve in this figure can qualitatively predict the occurrence of unsteady TLF. The operating points located at the upper side of the curve are unsteady cases, and those in the lower side of the curve are steady. This figure also indicates that as the tip clearance size increases, the critical momentum ratio decreases. In other words, self-induced unsteadiness with a larger tip clearance size appears earlier as the mass flow rate is throttled.

4 Discussions

4.1 The Role of Shock Wave. Carefully examining Fig. 8(*a*), one can notice that the location of the shock on the suction surface hardly oscillates during the entire period of unsteadiness. Figure 15 depicts the distribution of pressure coefficient on the suction surface for all six time instants used in Fig. 8(*a*). Both the location and the strength of this shock only slightly vary with time. This brings an interesting question on the role of shock wave in the self-induced unsteadiness of tip leakage flow.

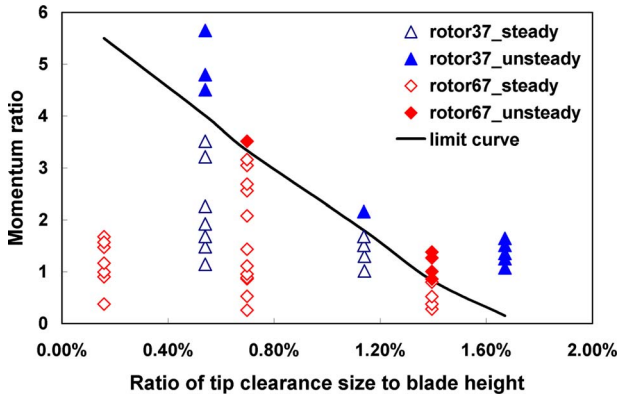

Fig. 14 Correlation for unsteadiness of tip leakage flow

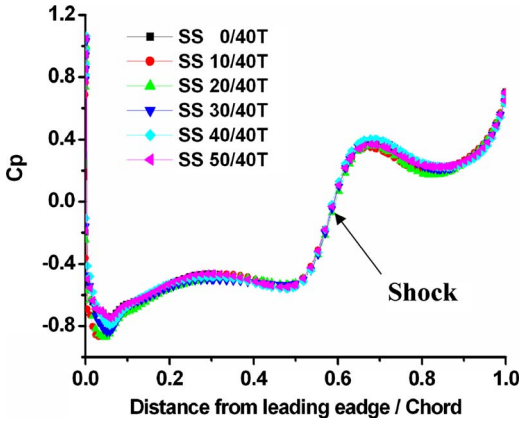

Fig. 15 Pressure coefficient distribution on blade suction surface at six time instants

To further investigate the role of shock wave, the rms distribution across the blade passage is examined. In Fig. 16, the highest unsteadiness is located at A and B, which are the initial position of the tip leakage vortex and the trajectory of the tip leakage vortex, respectively. C is the region for fluctuation of the detached shock wave in front of the leading edge. D is the unsteady region where the tip leakage vortex interacts with the detached shock wave. Obviously, the shock wave oscillates less than the tip leakage vortex.

There are two mechanisms proposed in literatures that concern the role of shock wave in unsteadiness. Yamada et al. [10] found that it is the breakdown of the tip clearance vortex occurring in the Rotor 37 that resulted in self-sustained flow oscillation in the tip leakage flow field. Bergner et al. [6] and Hah et al. [7] argued that the occurrence of unsteady fluctuation is due to the interaction of tip leakage vortex with the shock wave. Both mechanisms are checked carefully against what we found in Rotor 67.

First of all, we realized that Yamada et al. [10] utilized Reynolds-averaged Navier-Stokes (RANS) solver for their study, so do we in the present paper. Hence, when comparing our results with theirs, if there is any qualitative difference in simulation results, it is most likely related to physics of flow, not the computation scheme. Figure 17 depicts the 3D normalized absolute vorticity magnitude (ξ_n) distribution from our simulation and shows

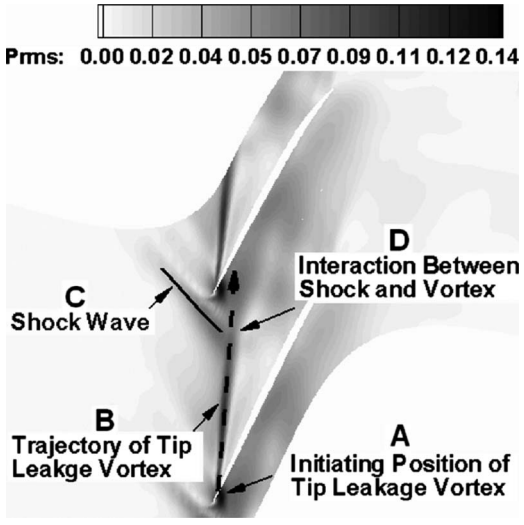

Fig. 16 Static pressure rms distribution for 99% span at T_2 operating condition for 1.1% tip blade chord

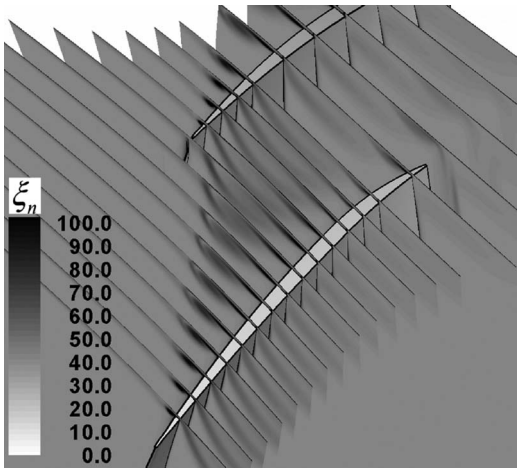

Fig. 17 3D normalized absolute vorticity magnitude distribution at T_2 operating condition

that the vortex does not break down because the magnitude of absolute vorticity does not drop drastically when its trajectory crosses the shock wave. This is fundamentally different from the results in Ref. [10]. Carefully examining Fig. 12 of Ref. [10], we notice that the vortex breakdown caused by the shock behaved randomly; that is, it did not possess any periodic pattern. Yet, it was reported in Ref. [10] that the frequency of unsteadiness was about 60% BPF, amazingly close to what we find in the present paper for Rotor 67. These apparently contradicting phenomena make us believe that the vortex breakdown in Rotor 37 might be responsible for turbulence unsteadiness, which should be random and broadband. The unsteadiness associated with 60% BPF might be due to another mechanism, which could be the same self-induced unsteadiness as what we find in Rotor 67. Both the turbulence unsteadiness and the self-induced unsteadiness might be present in the results of Rotor 37.

In the present study, the region where the vortex and the shock interact (region D in Fig. 16) depicts less rms level than the tip leakage vortex itself. Hah et al. [7] reported that while their RANS solver obtained qualitatively similar result as Fig. 16 for their rotor (see their Fig. 6 in Ref. [6]), the large-eddy-simulation (LES) solver produced rms distribution that matched with experimental results [6] better. But, Hah et al. [7] also reported that "the pressure oscillation from the single passage analysis shown in Fig. 8 is rather random at this operating condition and any distinct frequency could not be clearly identified." This contradicted with the experimental results in Ref. [6], which showed that the vortex trajectory alternated blade by blade, inferring that there was a characteristic frequency at roughly 50% BPF. All these seem pointing to the same direction: Both turbulence unsteadiness and self-induced unsteadiness might coexist in the rotor studied in Refs. [6,7] as well. There is a good chance that such coexistence may also be true for Rotor 67. However, without experiments and LES simulation, we cannot verify it in this paper. Realizing that vortex breakdown is an extreme case of shock/vortex interaction, we tend to believe that shock/vortex interaction produces turbulence unsteadiness and that the coexistence of turbulence unsteadiness and self-induced unsteadiness may be very common in compressors with shocks. Further research is needed.

4.2 Link to Stall Inception. According to Refs. [2,16], the spike disturbance is a result of dynamic interaction of three driving forces: the incoming main flow, the tip leakage flow, and the reversed backflow. The self-induced unsteady tip leakage flow partially shares the same dynamics with the spike disturbance, because as we proposed in Sec. 3, such unsteadiness results from the interaction of incoming flow and the tip leakage flow, two out of the three driving forces for the spike disturbance. This also explains why numerical and experimental data of previous researches [3,15] demonstrated that the suppression of the unsteadiness of tip leakage flow could extend the stability margin of both low-speed and high-speed compressors.

The proposed mechanism offers a new view angle for compressor design such as sweep and dihedral and stability enhancement such as casing treatment. By carefully designing the geometry, the designers should be able to make the dynamic interaction behave in a favorite manner at will, so that the compressor becomes more robust. This is the planned future work for the authors of the present paper.

5 Conclusions

In this paper, unsteady numerical simulation of Rotor 67, a transonic fan rotor, is performed. The goal is to investigate the originating mechanism of the self-induced unsteadiness in tip leakage flows in a transonic environment. The findings can be summarized as follows.

1. The self-induced unsteadiness of the tip leakage flow in this high-speed fan rotor is a result of dynamic interaction of two driving forces: the incoming main flow and the tip leakage flow. These two flows impinge with each other at the tip region and form an interface that separates the two flows. On one hand, behind the interface, if the tip leakage flow is stronger enough to cast a low-energy spot on the pressure side of the neighboring blade, the unsteadiness would be initiated as the low-energy spots move downstream, which in turn cause the time variation of blade loading. On the other hand, the changing blade loading makes the tip leakage flow velocity oscillating, which interacts with the incoming main flow to create the second low-energy spots across the blade passage. When the second stream of low-energy spots arrives at the pressure surface, the first stream smears with the high-pressure background and a new period of oscillation thus starts.
2. The proposed originating mechanism of the self-induced unsteady tip leakage flow is tested by varying the tip clearance sizes while keeping the incoming main flow the same.
3. A correlation based on momentum ratio between the main flow and the tip leakage flow is proposed. It indicates that the momentum ratio can be one of the factors that dominate the self-induced unsteadiness of the tip region.

Acknowledgment

This work was supported by the National Basic Research Program of China Grant No. 2007CB210104 and the National Science Foundation of China Grant No. 50736007. These supports are gratefully acknowledged. F.L. also appreciates the support of Tri-State University through Lilly Faculty Development Grant.

Nomenclature

P = static pressure (Pa)
$\bar{P}$ = time-averaged static pressure (Pa)
P_{rt} = relative total pressure (Pa)
P_{ref} = reference pressure (Pa)
C_p = static pressure coefficient, $C_p=(P-P_{ref})/(0.5\rho U_m^2)$
C_{rtp} = relative total pressure coefficient, $C_{rtp}=(P_{rt}-P_{ref})/(0.5\rho U_m^2)$
P_{rms} = static pressure root-mean-square, $P_{rms}=\sqrt{1/N\sum_{i=0}^{N-1}(P(t)-\bar{P})^2}/0.5\rho U_m^2$
ΔC_p = static pressure coefficient difference
U_m = blade speed at the mean rotor diameter (m/s)
T = rotor blade passing period (s)
M = momentum (N/s)

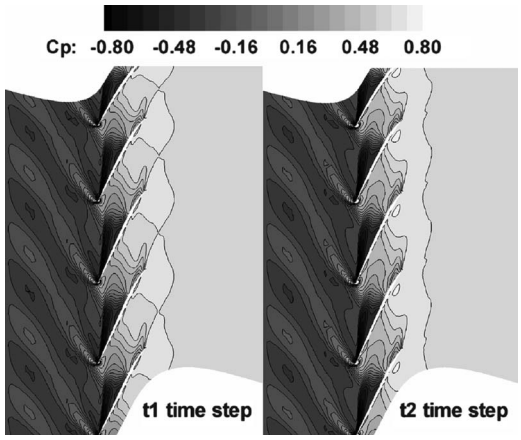

Fig. 18 Instant static pressure coefficient contours taken from 99% span at T2 operating condition in multiblade passages

m_{choke} = mass flow rate at choke point (kg/s)

Greek Symbols

α = angle between streamwise and axial directions
ξ = absolute vorticity magnitude (rad/s)
ω = rotor angular velocity (rad/s)
ξ_n = normalized absolute vorticity magnitude, $\xi_n = |\xi|/2\omega$
ρ = r density (kg/m^3)
τ = ratio of tip clearance size to tip blade chord

Abbreviations

TLF = tip leakage flow

Appendix

One case of self-induced unsteady tip leakage flow in multiblade passages is investigated to demonstrate that it is sufficient to use single blade passage model in this research. One quarter of the annulus of Rotor 67 is chosen. The operating condition and the tip clearance are the same as those in Fig. 8. The unsteady flow fields for the entire oscillating period are captured, and two of them at two different time instants are depicted in Fig. 18. By comparison among the blade passages, one can see that the flow field in each blade passage is identical at every time instants. This indicates that the self-induced unsteadiness does not involve cross-passage dynamics. Single blade passage model is sufficient when investigating the characteristics of self-induced unsteady tip leakage flow.

References

[1] Wisler, D. C., 1985, "Loss Reduction in Axial-Flow Compressor Through Low-Speed Model Testing," ASME J. Turbomach., **107**, pp. 354–363.
[2] Lin, F., Zhang, J. X., Chen, J. Y., and Nie, C. Q., 2008, "Flow Structure of Short Length Scale Disturbance in an Axial Flow Compressor," J. Propul. Power, **24**(6), pp. 1301–1308.
[3] Tong, Z. T., Lin, F., Chen, J. Y., and Nie, C. Q., 2007, "The Self-Induced Unsteadiness of Tip Leakage Vortex and Its Effect on Compressor Stall Inception," ASME Paper No. GT2007-27010.
[4] Mailach, R., 1999, "Experimental Investigation of Rotating Instability in a Low-Speed Research Compressor," Third European Conference on Turbomachinery-Fluid Dynamics and Thermodynamics, London, GB, Mar. 2–5.
[5] Marz, J., Hah, C., and Neise, W., 2001, "An Experimental and Numerical Investigation Into the Mechanisms of Rotating Instability," ASME Paper No. 2001-GT-0536.
[6] Bergner, J., Kinzel, M., Schiffer, H., and Hah, C., 2006, "Short Length-Scale Rotating Inception in a Transonic Axial Compressor-Experimental Investigation," ASME Paper No. GT2006-90209.
[7] Hah, C., Bergner, J., and Schiffer, H., 2006, "Short Length-Scale Rotating Stall Inception in a Transonic Axial Compressor—Criteria and Mechanisms," ASME Paper No. GT2006-90045.
[8] Furukawa, M., Inoue, M., Saiki, K., and Yamada, K., 1999, "The Role of Tip Leakage Vortex Breakdown in Compressor Rotor Aerodynamics," ASME J. Turbomach., **121**, pp. 469–480.
[9] Furukawa, M., Saiki, K., Yamada, K., and Inoue, M., 2000, "Unsteady Flow Behavior Due to Breakdown of Tip Leakage Vortex in an Axial Compressor Rotor at Near-Stall Condition," ASME Paper No. 2000-GT-666.
[10] Yamada, K., Furukawa, M., Inoue, M., and Funazaki, K., 2004, "Unsteady Three-Dimensional Flow Phenomena Due to Breakdown of Tip Leakage Vortex in a Transonic Axial Compressor Rotor," ASME Paper No. GT2004-53745.
[11] Zhang, H. W., Deng, X. Y., Lin, F., Chen, J. Y., and Huang, W. G., 2005, "Unsteady Tip Leakage Flow in an Isolated Axial Compressor Rotor," J. Therm. Sci., **14**(3), pp. 211–219.
[12] Zhang, H. W., Deng, X. Y., Lin, F., Chen J. Y., and Huang, W. G., 2006, "A Study on the Mechanism of Tip Leakage Flow Unsteadiness in an Isolated Compressor Rotor," ASME Paper No. GT2006-91123.
[13] Adamczyk, J. J., Celestina, M. L., and Greitzer, E. M., 1993, "The Role of Tip Clearance in High-Speed Fan Stall," ASME J. Turbomach., **115**, pp. 28–39.
[14] Strazisar, A. J., Wood, J. R., Hathaway, M. D., and Suder, K. L., 1989, "Laser Anemometer Measurements in a Transonic Axial-Flow Fan Rotor," NASA, Report No. TP 2879.
[15] Geng, S. J., 2007, "Numerical Study on the Unsteady Response of Compressor Tip Leakage Flow to Discrete Micro Tip Injection and Its Effect on Stability Enhancement," Ph.D. thesis, Graduate School of the Chinese Academy of Sciences, Beijing, China.
[16] Vo, H. D., Tan, C. S., and Greitzer, E. M., 2005, "Criteria for Spike Initiated Rotating Stall," ASME Paper No. GT2005-68374.

Experiments and Computations on Large Tip Clearance Effects in a Linear Cascade

Richard Williams
David Gregory-Smith
Li He[1]
Grant Ingram

University of Durham,
South Road,
Durham DH1 3LE, UK

Large tip clearances typically in the region of 6% exist in the high pressure (HP) stages of compressors of industrial gas turbines. Due to the relatively short annulus height and significant blockage, the tip clearance flow accounts for the largest proportion of loss in the HP. Therefore increasing the understanding of such flows will allow for improvements in design of such compressors, increasing efficiency, stability, and the operating range. Experimental and computational techniques have been used to increase the physical understanding of the tip clearance flows through varying clearances in a linear cascade of controlled-diffusion blades. This paper shows two unexpected results. First the loss does not increase with clearances greater than 4% and second there is an increase in blade loading toward the tip above 2% clearance. It appears that the loss production mechanisms of the pressure driven tip clearance jet do not increase as the clearance is increased to large values. The increase in blade force is attributed to the effect of the strong tip clearance vortex, which does not move across the blade passage to the pressure surface, as is often observed for high stagger blading. These results may be significant for the design of HP compressors for industrial gas turbines. [DOI: 10.1115/1.3104611]

1 Introduction

Industrial axial compressors usually have blade rows at low pressure (LP), intermediate pressure (IP), and high pressure (HP) stages. Within the stages there are numerous sources of loss, traditionally "profile loss," "end-wall loss," and "leakage loss." The percentage that each source contributes toward the total loss varies from stage to stage. One such loss source (leakage loss) is the pressure driven tip clearance (TC) flow, which passes from pressure to suction surface over the end of the blades in nonshrouded rows. Within LP stages the TC is usually within 1% of the annulus height and there is a limited effect on the overall loss of the stage at the normal operating condition. However, within the LP stages, the TC flow is widely understood to act as a trip toward stage stall. Due to this and the applicability within aeroengines most TC work has been undertaken for small TC values where the loss is approximately proportional to the TC gap.

In the later stages the TC flow has a larger influence on the overall stage loss, mostly because of the increased relative TC value (typically about 6% span) due to the reduced length of blades. Note that the absolute TC value is not necessarily larger but relative to span it is. The rotor and stator TC flow can create a blockage up to approximately 20% span from the casing and hub, respectively, creating a significant blockage. This blockage affects the mass flow rate that can travel through the HP thus significantly affecting the operating and stability range of the compressor.

As argued by Denton [1] loss sources in turbomachinery are difficult to quantify; therefore, it is important to have a physical understanding of the flow and origins of loss. The motivation for this work is further to understand and model the flow physics with large tip clearance flows; this progresses the work previously undertaken by Williams et al. [2] and Walker et al. [3]. Previously most literature suggests that increasing the TC value has a diminishing effect on stage efficiency above an optimum. However, this paper shows that an increasing tip clearance can have a beneficial effect on the stage loading. This will allow for improved designs aimed at reducing losses and increasing the operating range of the HP compressor, therefore increasing efficiency and the surge/stall limits.

1.1 Tip Clearance Flow Physics.

As is widely known, the tip clearance flow consists of a pressure driven jet, which moves from the pressure surface to the suction surface across the tip of the blade. As discussed by Peacock [4] the strength of the TC jet depends on the blade pressure field close to the tip of the blade. This tip clearance flow rolls up into a tip clearance vortex along the suction surface of the blade, which then moves across the passage toward the pressure surface of the adjacent blade. Storer and Cumpsty [5] found that the point at which this happens is usually at the maximum loading of the blade. They also concluded that the axial position of the highest blade force varies with the TC value; a higher TC value moves the position of the highest loading further downstream thus delaying the roll up of the TC vortex. In HP blades, the vortex remains closer to the suction surface (SS) and so is different to that in LP blades. Although the TC gap size affects the strength of the TC vortex Hunter and Cumpsty [6] found that the trajectory is unaffected.

Gbadebo [7] considered the interaction between tip clearance flows and 3D flows close to the end wall. He found that the tip clearance flow largely removes the 3D secondary flows. This was attributed to the suppression of the leading edge (LE) horseshoe vortex and the interaction of the tip clearance rolling up into a TC vortex. Clearly then an optimum tip clearance will increase the operating range of the stage. The flow within the tip clearance depends on the thickness of the blade. In the case of a compressor with thin blades the flow separates from the tip forming a vena contracta. This separates the flow from the blade tip reducing the effective tip clearance. The work undertaken by Tang and Simpson [8] measured the flow through the tip clearance within a cascade for two different tip gaps. They found a tip separation vortex formed on the tip due to the sudden turning undertaken by the flow entering the TC. Sjolander [9] dedicated a section on large tip clearance flows up to 15% chord and he presented measurements by Saathoff and Stark [10] for a turbine. He suggested that for larger clearances the blade loading is not entirely responsible for the tip clearance flow because of the huge underturning under-

[1]Present address: Department of Engineering Science, Oxford University.

Contributed by the International Gas Turbine Institute of ASME for publication in the JOURNAL OF TURBOMACHINERY. Manuscript received October 14, 2008; final manuscript received November 18, 2008; published online January 20, 2010. Review conducted by David Wisler. Paper presented at the ASME Turbo Expo 2008: Land, Sea and Air (GT2008), Berlin, Germany, June 9–13, 2008.

taken in the end-wall region.

The trajectory of the TC vortex is clearly dependent on the interaction with the mainstream flow. De Cecco et al. [11] investigated the trajectory of the TC vortex with varying inlet angle. They found that as the inlet angle/loading is increased the TC trajectory moves further across the passage thus creating a larger blockage. At stall the TC vortex moves across the LE of the adjacent blade. Therefore for higher loading the TC flows can have a negative axial velocity.

The TC vortex counteracts the secondary/passage vortex and for the larger TC values completely suppresses it. However, it has been found by Van Zante et al. [12] and Williams et al. [2] that for some tip clearance values a counter-rotating vortex is found, which lies on the casing/hub and prevents the movement of the TC vortex across the passage. This applies for smaller TC values while the for larger TC values the counter-rotating vortex is completely suppressed by the tangential TC flow.

One of the main differences between the LP and HP geometries is that HP geometries typically have lower blade loading, i.e., lower stager angle and turning. Therefore the TC flow in the later stages is almost tangential as opposed to the earlier stages where it often has an upstream component due to the high stager angle. The relative Mach numbers (typically 0.4–0.6) are much lower than the LP (typically larger than 1).

Clearly the stage geometry significantly affects the TC vortex; therefore, control of the trajectory and loss should be possible.

This work investigates the TC flow within a linear cascade. There are significant well known differences between cascade testing and rotating machines. Namely, rotating machines have a skewed inlet, twisted blades, radial effects, and moving end walls; and for the real machine are in a multirow/stage environment. Therefore the real case is far more complicated than the idealized linear cascade but the results are still valid and useful. Peacock [4] discussed the differences between cascades and rotating machines and found that the casing motion has a significant effect on the tip clearance flow due to the viscosity of the fluid. The wall's relative motion pulls the fluid through the TC gap. Previously Williams et al. [2] undertook a study, which investigated the difference between moving end walls and the stationery cascade. They concluded that with the same inlet conditions the moving end wall skews the flow within the TC region, which increases the loading on the tip of the blade. Also in the relative frame of the blade the end wall drags the TC flow through the clearance region increasing the flow. This makes the TC vortex stronger and pushes the TC vortex core away from the SS of the blade further across the passage while keeping it closer to the casing thus reducing blockage. In the relative frame the end wall effectively does work on the flow adding energy to the fluid and therefore the overall loss with a moving end wall is reduced.

Real machines are multistage and in the HP the low Mach number means the TC flow has an effect on the adjacent rows. This is mostly the case for the downstream row where the casing/hub section of the stator/rotor will see overturned flow, thus increasing the loading and almost certainly producing a corner stall.

This work shows that large TC values have a beneficial effect on the blade loading of the cascade. This paper strives to further the understanding of large tip clearance flows and so explain the reason behind the beneficial effects with loading. To do this experimental data from a linear cascade are presented and consequently used to assess the capability of a computational code to predict the large TC flows. The computational fluid dynamics (CFD) code is then used to advance the understanding of the TC physics.

2 Experimental Work

This section of the paper shows some of the linear cascade experimental work, which will later be used to assess the CFD code. However, first there is a brief explanation of the wind tunnel, cascade, and measuring equipment.

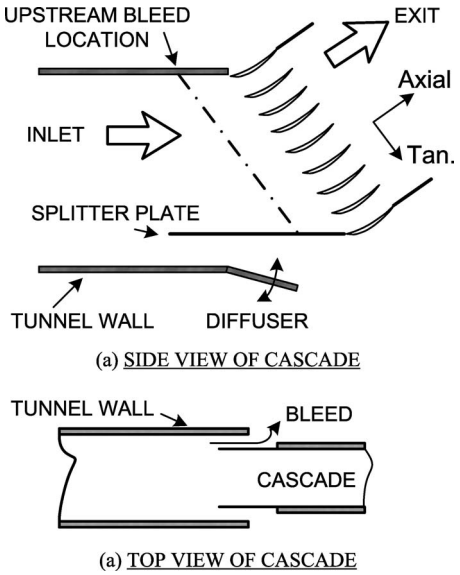

Fig. 1 Cascade details

2.1 Experimental Apparatus. The linear cascade compressor test facility based at the Durham University uses an open flow wind tunnel arrangement, as described by Yang [13]. This consists of a fan, a diffuser, a settling chamber, a gauze screen, a 7.5:1 contraction, a honey comb, and a test section. The flow exits the tunnel through a 0.25×0.8 m^2 section into the cascade.

The cascade located at the wind tunnel exit exhausts to atmosphere one axial chord after the trailing edge. As shown in Fig. 1, seven aerofoils including profiled upper and lower walls give eight passages in total; allowing for reasonably periodic flow. Hinges at the top of the cascade enable the geometric inlet angle to be altered. A bottom splitter plate allows for the vertical change in inlet due to the change in angle; below the splitter plate a bypass exhausts to atmosphere. The bypass is controlled using a movable plate to control the diffusion. A side-wall boundary layer bleed is located one axial chord length upstream of the leading edge. The bleed plate is 3 mm thick ensuring a high quality bleed.

The controlled-diffusion aerofoil used is that as designed by Sanger [14] and intensely tested in open literature including Sanger and Shreeve [15] and Williams et al. [2]. Blade properties are shown in Table 1 and the profile is shown in Fig. 2. Two of the blades are instrumented, these being the central one and one other, which can be moved in to any blade location. There are tappings at various locations along the blade on both surfaces. Passing the blades radially through the hub enables the TC value to be altered.

Table 1 Cascade properties

No. of aerofoil	7
Pitch	0.09 m
Blade span	0.19 m
Stager angle	14.2 deg
Inlet flow angle (nominal)	37.5 deg
Isentropic exit velocity	19.5 m/s
Reynolds number based on chord	195,000
Side-wall bleed location	One axial chord upstream
Pitot-probe location	1Cx upstream
Aerofoil type	Controlled-diffusion blade
Chord length, C	0.15 m
Aspect ratio, h/C	1.27
Maximum thickness	0.07 C
Leading edge radius	0.00132 m
Trailing edge radius	0.00186 m
Solidity, C/S	1.67

Fig. 2 Blade profile

The blades are supported using a 3 mm threaded bar at the tip and supported by the hole in hub at the other end. This tip suspension bar has some effect on the blade loading close to the tip but due to its relatively small size this is a limited effect.

2.2 Instrumentation. Both five-hole probe and blade static pressure measurement instrumentation are available. Two five-hole probe measurement plains were used 0.5*Cx* (50% axial chord) upstream and 0.2*Cx* downstream of the blade row. The probe is moved and held using a traverse gear located downstream of the cascade. The upstream plane is traversed using a kinked probe projected through the blade. A straight probe was used for the downstream traverse. Both probes used had a diameter of 4.5 mm limiting the measurements close to the wall to approximately 3% span.

The probe pressures are measured relative to the upstream total pressure via a Pitot-probe positioned 1.0*Cx* upstream of the cascade. The upstream total to atmospheric pressure is measured as the isentropic dynamic pressure. The traverse gear is operated and the pressures recorded using software developed at Durham University. Calibration of the pressure transducers and probes is accounted for within the software. Probe calibration is undertaken using a calibration rig at Durham University; this process is described by Ingram and Gregory-Smith [16]. The software postprocesses the data including pitch mass averaging thus allowing for a traverse grid of varying density.

The same software system was used to measure the blade static pressures. By controlling a Scanivalve connected to the blade pressure tapings only one transducer was required. The upstream total to downstream static (atmospheric) dynamic pressure was also recorded to enable the values to be made nondimensional.

2.3 Inlet Conditions. The inlet flow to the cascade was conditioned to ensure uniform periodicity and an inlet flow angle of 37.5 deg. The downstream results (Fig. 4) suggest that acceptable periodicity has been obtained. The inlet flow angle, however, was still approximately 5 deg different to the geometrical angle. Good practice was found to include the angle of the bottom plate, the bottom diffuser, and the diffusion of the side-wall bleeding being accurately set. The inlet pitch mass averaged yaw and total pressure can be seen in Fig. 3. It can be seen that there is a significant

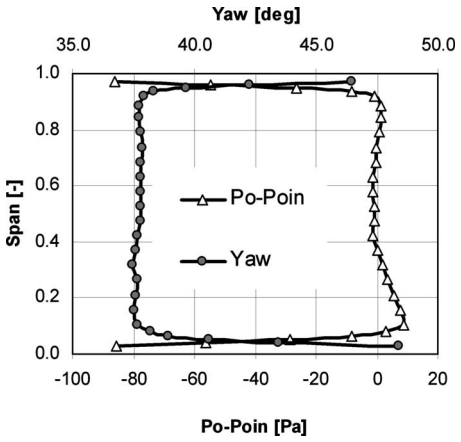

Fig. 3 Cascade inlet conditions

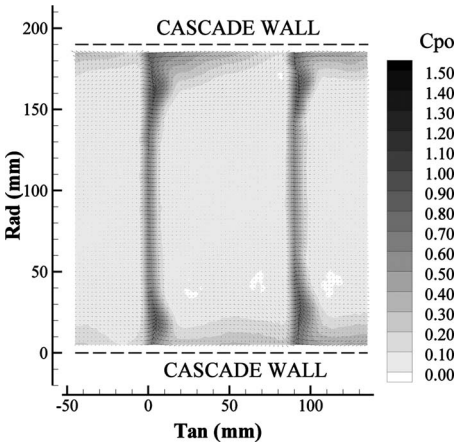

Fig. 4 0% TC, 1.2*Cx*, experimental loss (*Cpo*)

boundary layer with low total pressure and high skew on the walls, which can be attributed to the side-wall bleed pushing the flow down. Considering the multirow case with highly skewed flow at the wall these inlet conditions were deemed acceptable.

Also of note is the increase in total pressure and decrease in yaw toward the hub. However, because only the outer 50% span is of interest this is acceptable.

2.4 Downstream Flow Results. Initially to ensure good periodicity and a base to compare result 0% TC was analyzed across the central two passages for the full span of the cascade. The stagnation pressure loss coefficient is shown in Fig. 4 for the 0% TC case across the full passage.

Four tip clearance values were then evaluated (0%, 1%, 2%, and 6% spans) for both central passages of the cascade but only covering the outer 50% span. *Cpo* loss contour plots are shown in Figs. 4–7. Pitch mass averaged results of yaw and *Cpo* loss can be seen in Figs. 8 and 9. These are referenced to midspan thus highlighting the effects due to the end-wall region secondary flows. Of note are the increase in size of the tip clearance vortex and blockage. The counter-rotating vortex is clearly present and indicated in Fig. 6. For the 6% case it can be seen that higher momentum flow is pulled onto the wall decreasing the *Cpo* loss close to the wall.

2.5 Blade Static Pressure Results. The blade pressure coefficient profiles are shown in Figs. 10–12 for 50%, 90%, and 98% spanwise locations, respectively. Of note is the change in blade loading toward the tip of the blade with increasing tip clearance values. In general with increasing TC value there is a reduction in loading at the leading edge and an increase in loading toward the trailing edge. At 98% span and 6% TC the experimental data show what appears to be a high pressure region on the suction surface at approximately 0.6*Cx*; this is almost certainly an effect of the blade

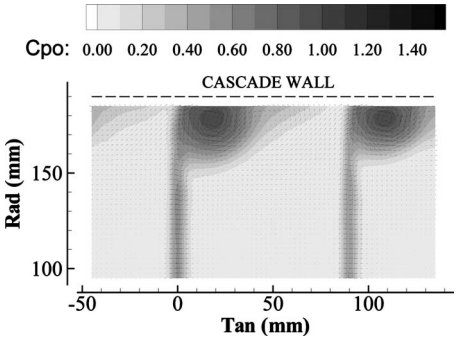

Fig. 5 1% TC, 1.2*Cx*, experimental loss (*Cpo*)

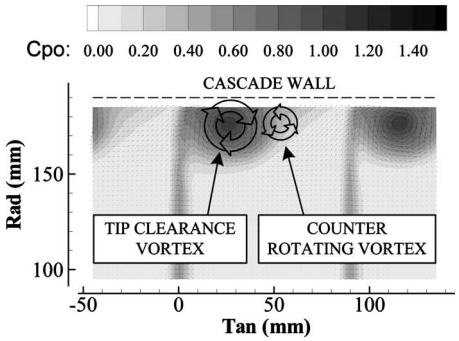

Fig. 6 2% TC, 1.2*Cx*, experimental loss (*Cpo*)

support rod. Integrating the pressure coefficient plots creates a blade force; this can be seen in Fig. 13 where blade force is plotted against distance in blade span from the tip of the blade. Figure 14 shows the overall blade force for each measured TC, and this is shown relative to the zero clearance case. Importantly as will be discussed later this shows an increase in tangential blade loading toward the tip of the blade for the 6% tip clearance.

3 Computation Fluid Dynamics

3.1 CFD Code. This paper uses a code developed by He [17] at Durham University; the same code was used by Williams et al. [2] and Walker et al. [3], and a good description of the code's features can be found in Ref. [17]. The code iteratively solves the Reynolds averaged 3D unsteady compressible Navier–Stokes equations and turbulence closure is achieved by using the Spalart–Allmaras model. The governing equations are discretized in space using the cell centered finite volume scheme, which is integrated in time using the explicit four stage Runge–Kutta method. To accelerate convergence the multigrid technique and local time stepping are used.

The code was run to 5000 time steps; this ensured good convergence with a maximum axial velocity change between time steps <0.001 and the difference between inlet and outlet mass

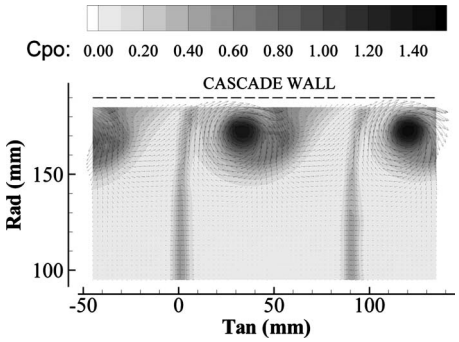

Fig. 7 6% TC, 1.2*Cx*, experimental loss (*Cpo*)

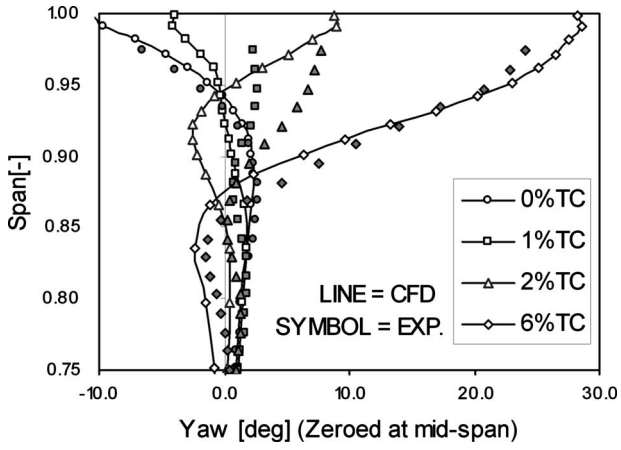

Fig. 8 Pitch mass averaged yaw 1.2*Cx*

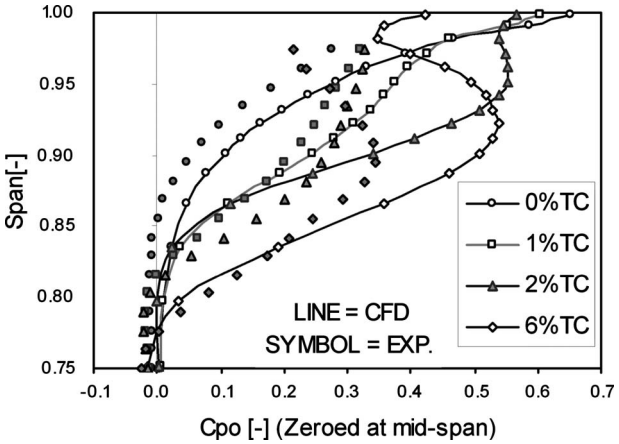

Fig. 9 Pitch mass averaged *Cpo* 1.2*Cx*

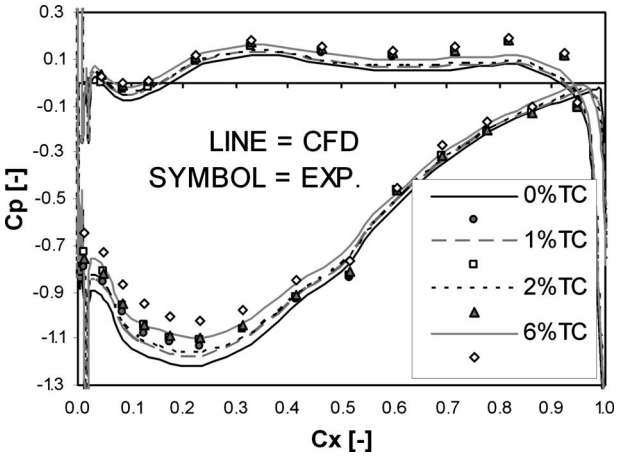

Fig. 10 Blade pressure coefficient (*Cp*) at 50% span

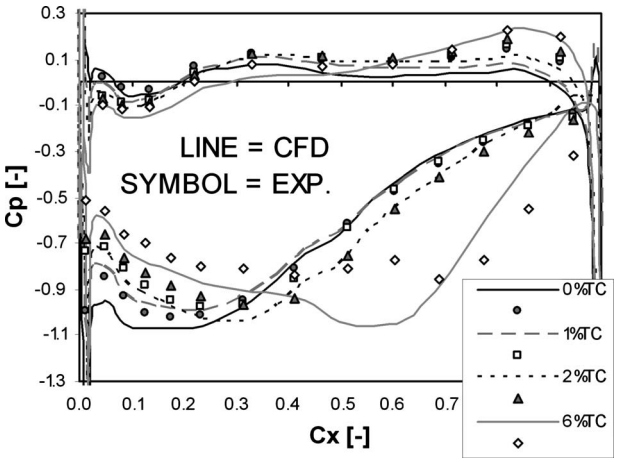

Fig. 11 Blade pressure coefficient (*Cp*) at 95% span

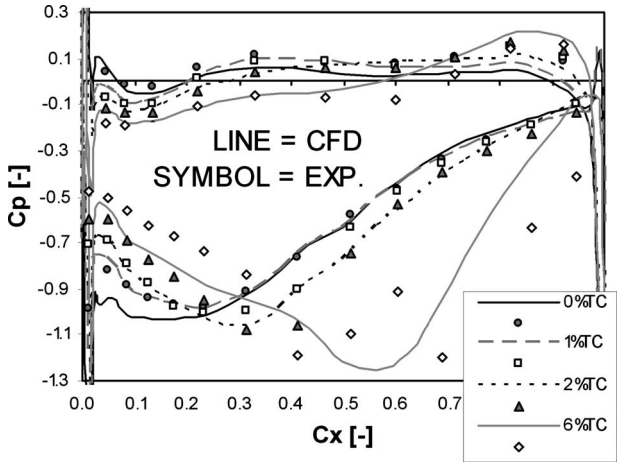

Fig. 12 Blade pressure coefficient (*Cp*) at 98% span

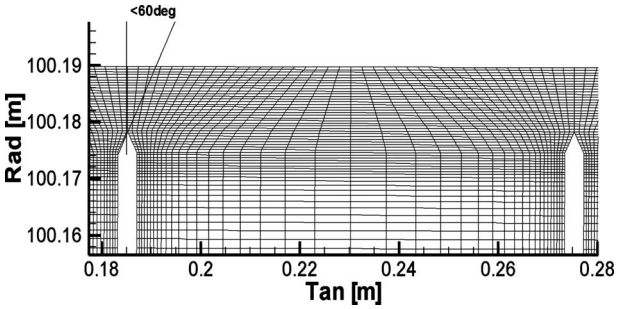

Fig. 15 Example of mesh for 6% TC at 0.9*Cx*

flow <0.05%. Boundary layer trips were located on the blade SS and the casing to ensure a turbulent boundary layer and convergence.

3.2 Grid. A structured H mesh was used for this study and the tip clearance is modeled using the pinch tip method. Several methods for modeling the tip clearance have been proposed throughout literature and these have varying levels of complexity and success. This work used a simple pinch tip model as used by Williams et al. [2] and also reported in various open literatures, e.g., Refs. [12,18]. Although this method is not as accurate as what can be achieved, it has been shown to give a reasonable result without adding complexity and increasing computational time. To ensure the pinch tip does not create numerical instabilities, good practice is to ensure that the tip angle is no larger than 60 deg from the radial direction (as shown in Fig. 15). The tip clearance is defined as the distance between the tip of the pinch and the casing.

Understanding the grid dependency of the solution is crucial to obtain a good quality result. For this reason a mesh dependency study was undertaken to develop a mesh capable of picking up all the physical flows while ensuring convergence and a good quality result using the experimental data as a reference. In general it was found that the grid dependency diminishes with increased tip clearance, i.e., the interaction between the flow on the tip and the casing diminishes. The pitchwise grid was found to have a little effect at the midspan as long as the blade boundary layer mesh size was reasonable. However, to prevent diffusion of the tip clearance vortex, the mesh needs to be as fine as possible close to the casing, and therefore a balance needs to be obtained. Within the tip clearance it was found that if the pitchwise grid is too fine then convergence is poor due to instabilities. Therefore the pitch mesh was made uniform at the casing and then linearly distributed until the start of the pinch, as seen in Fig. 15. The grid dependency study found that there was a 15% change in *Cpo* loss at 1.2*Cx* between the grids investigated.

The radial spacing of the mesh has a large effect on the qualitative result. Thus while ensuring that the *y*+ values were reasonable on the casing the best result was used from that obtained from the grid dependency study. The mesh in general is fine and uniform within the outer 12% span and then expands until the cells are approximately 2.5% span at the hub.

As shown in Fig. 16 in the *k*-plane (constant radius) the inlet mesh follows the inlet flow angle 0.5*Cx* upstream and downstream the mesh extends 2.0*Cx* after the trailing edge approximately at the flow angle, so this allows for any potential boundary effects to be minimized.

The hub was defined as an inviscid wall thus ensuring that only the outer part of the cascade has an effect on the result. To approximate a linear cascade the hub radius is set to 100 m. Therefore there are 6981 blades to ensure the correct pitch of 90 mm although only three passages are solved.

3.3 Boundary Conditions. At the inlet the yaw angle and total pressure are set to be the same as for the experimental inlet conditions for the outer 50%. Closer to the hub the inlet conditions are set the same as at midspan.

At the outlet the static pressure is set at the hub and the spanwise variation is determined by radial equilibrium. The back pressure is set to ensure the velocity is approximately three times

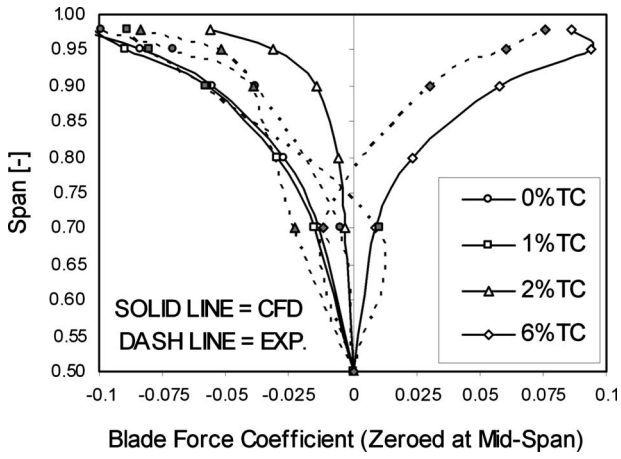

Fig. 13 Blade force coefficient

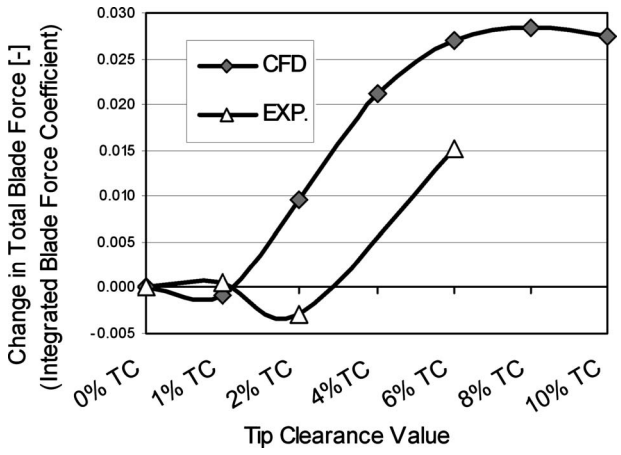

Fig. 14 Total blade force versus TC, CFD, and experimental data

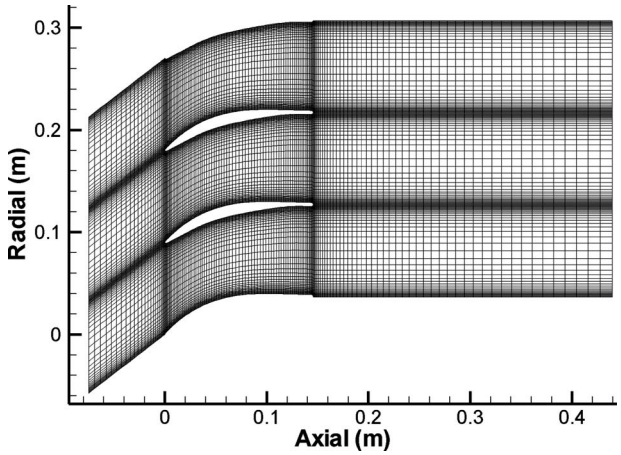

Fig. 16 Example mesh for *k*-plane

higher than for the experimental rig to ensure convergence. However, the Reynolds number is set to be the same as for the experimental cascade ($Re = 1.91 \times 10^5$).

4 CFD Study, Experimental Versus Computational

Seven different TC values have been computationally assessed: 0%, 1%, 2%, 4%, 6%, 8%, and 10%. Often it is more useful to consider the TC in terms of a blade chord so for this case with an aspect ratio of 1.27 the clearances assessed are 0%, 1.27%, 2.53%, 5.07%, 7.6%, 10.13%, and 12.67% of chord.

First it is important to assess CFD against experimentation. Figures 8 and 9 show the pitch mass averaged yaw and *Cpo* for the 0%, 1%, 2%, and 6% tip clearances; 20% axial chord downstream of the trailing edge. Yaw angle is defined relative to the axial direction. Quantitatively the results are reasonable and show a good comparison, especially with the yaw angle although the loss is slightly overpredicted. The 0% and 6% cases show the best comparison with the smaller tip clearances (1% and 2%) showing poorer comparisons. Figures 17–20 show the loss (*Cpo*) contours of the CFD on the 1.2*Cx* plain. These can be compared with the previously presented experimental data (Figs. 4–7). The agreement is reasonable but in general the CFD is more dissipative so that the extent of the loss cores of the tip clearance and profile loss is larger although the peak values are lower for the CFD; this explains the loss overprediction in the CFD solution.

The blade loading as shown in Figs. 10–12 at midspan shows a good agreement with the experimental data. Closer to the tip the computational result varies slightly from the experimental; this is most noticeable for the 6% TC case where two bumps can clearly be seen on the suction surface (Fig. 12). However, as stated above, this is almost certainly attributable to the experimental rig's blade support bar.

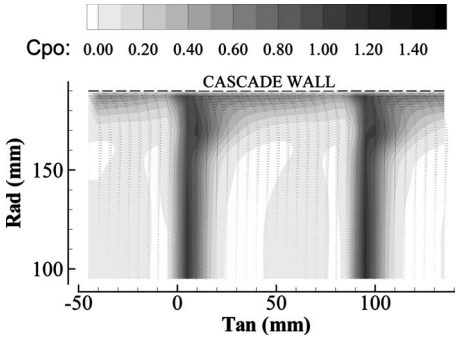

Fig. 17 0% TC, 1.2*Cx*, CFD loss (*Cpo*)

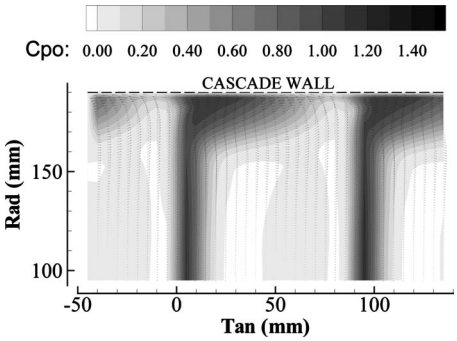

Fig. 18 1% TC, 1.2*Cx*, CFD loss (*Cpo*)

The blade force shown in Fig. 13 shows a good agreement with the 0% and 6% TC cases. Noticeably for both the computational and experimental data there is an increase in blade loading for the larger tip clearance of 6%.

5 Computational Study

Having examined the difference between experimental and computational results it is clear that there is an overprediction in loss, but the yaw is reasonable and qualitatively the results are similar. Therefore Sec. 6 shows the results with varying tip clearance from 0% to 10% span.

Pitch averaged plots of yaw and loss are presented for the various tip clearance values at 0.12*Cx* (Figs. 21 and 22). As shown by Williams et al. [2] the yaw angle for the 0% case shows the classic underturning and overturning, and the loss is increased toward the casing due to the secondary flow and corner stall; in fact, the loss on the casing for the 0% case shows the highest loss peak. The 1% case has less overturning on the casing because the TC flow suppresses the corner stall. For the large tip clearances, 2–10%, the flow undergoes a significant overturning and then underturning caused by the tip clearance vortex. The loss peak at the TC vortex

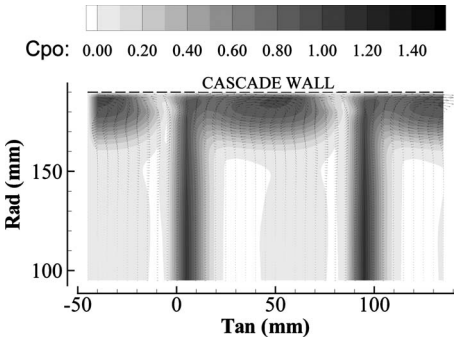

Fig. 19 2% TC, 1.2*Cx*, CFD loss (*Cpo*)

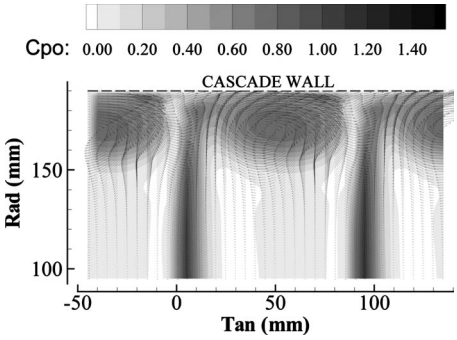

Fig. 20 6% TC, 1.2*Cx*, CFD loss (*Cpo*)

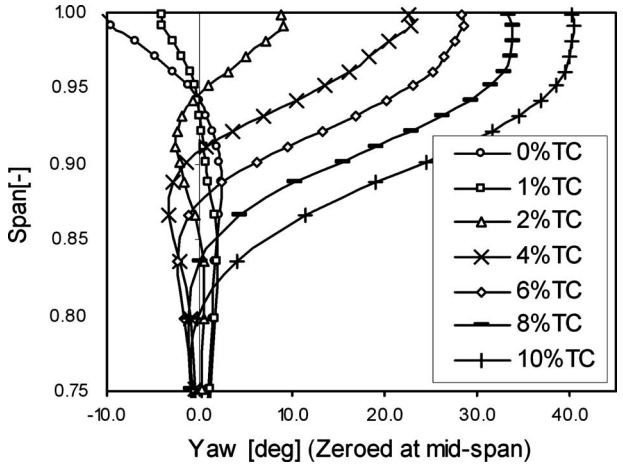

Fig. 21 CFD study, 1.2*Cx* CFD yaw angle with varying TC

core decreases in magnitude with increased TC but the area of loss moves away from the casing, and so it is important to examine the overall loss at 1.2*Cx*. Figure 23 shows the increase in loss from inlet to exit for the outer 50% span, and it can be seen that the overall loss increases until 4% TC and then it falls slightly. A decline in mass flow occurs through the cascade with increased TC and so to eliminate this discrepancy the overall loss between tip clearance values is shown for two different definitions. These use different reference values of dynamic pressure; upstream dynamic pressure and the dynamic pressure across the cascade, i.e., the exit isentropic dynamic pressure. This is important because the mass flow rate is reduced with increased TC (Fig. 24).

Removing the profile loss from the overall loss for the outer 50% span gives the loss attributed to the end-wall secondary flows including the tip clearance; this is shown in Fig. 23. The tip region loss accounts for approximately 45% of the total loss for the smaller TC values (including 0%) and increases to approximately 62% of the total loss for the 10% TC case. The tip clearance flow has mostly mixed out by 1.2*Cx*, although not shown if a plot is made of the loss at 3.0*Cx* then the same pattern is observed as in Fig. 23.

The experimental mass weighted averaged *Cpo* loss is shown in Fig. 23 and follows the same pattern as the CFD results. Experimentally the overall loss is slightly higher than the CFD loss even though the pitch averaged results would not suggest this; this is because the values are mass weighted averaged; therefore, the velocity profile has an effect on the values.

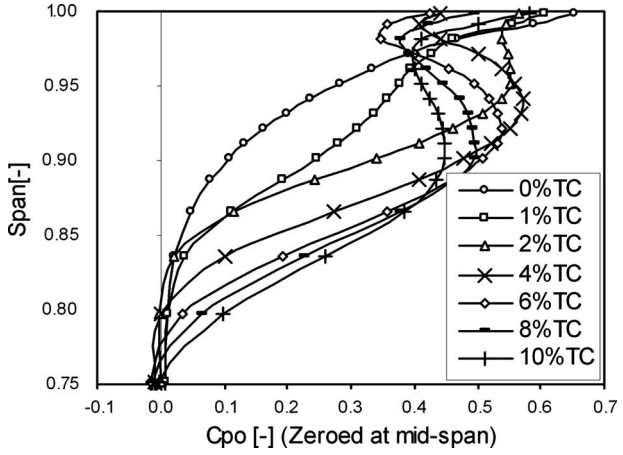

Fig. 22 CFD study, 1.2*Cx* CFD total pressure loss with varying TC

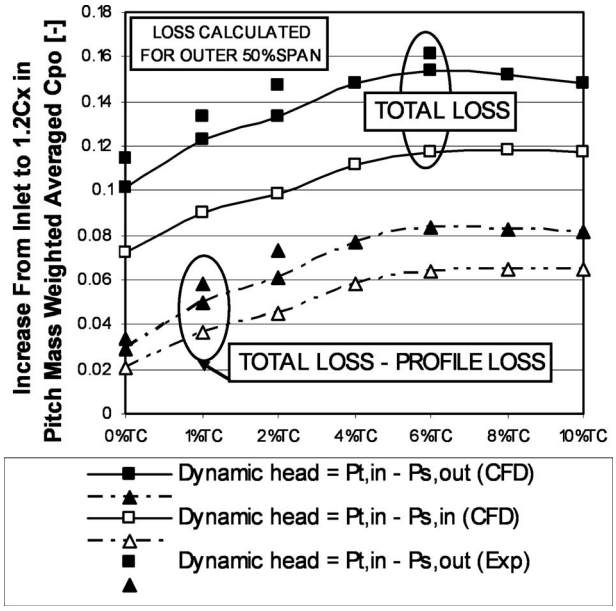

Fig. 23 CFD study, increase in loss through cascade

These results are very similar to Williams et al. [2], even though in this case has a skewed inlet boundary layer, suggesting that the inlet angle within the TC region has a limited effect on the loss and exit angle.

The blade loading integrated becomes the tangential blade force (Fig. 25) and then the blade force integrated along the blade gives the overall tangential blade force (Fig. 14); these are all referenced to midspan. The overall blade force is referenced to the 0% TC case.

It can be seen that the blade loading increases for the larger tip clearances toward the tip of the blade. This is an unexpected result as it shows that the blade force in the outer half of the cascade increases with TC value above 1% TC. This increase in blade loading carries on until 8% TC where the total blade force levels off and appears to start to diminish. Also shown in Fig. 14 are the experimental data; although the loading increase is lower it does show an increase with 6% TC; thus, it can be assumed that this is a valid result. Unfortunately no experimental data were taken above 6% TC so the decline in blade force above 6% TC is not experimentally investigated. The differences between the CFD and experimental blade force can be seen by examining the *Cp* loading plots (Figs. 10–12); in general, on the suction surface,

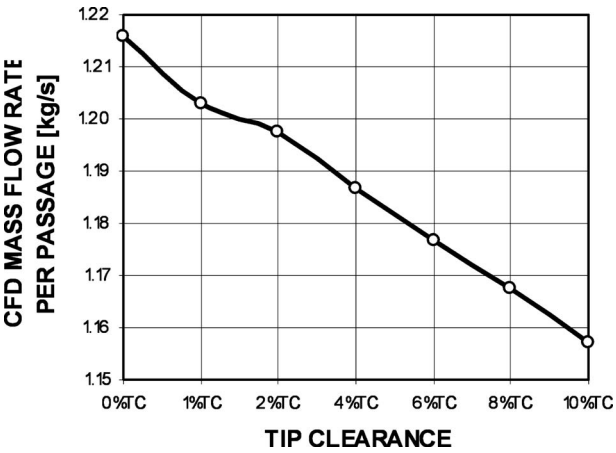

Fig. 24 Mass flow rate per passage

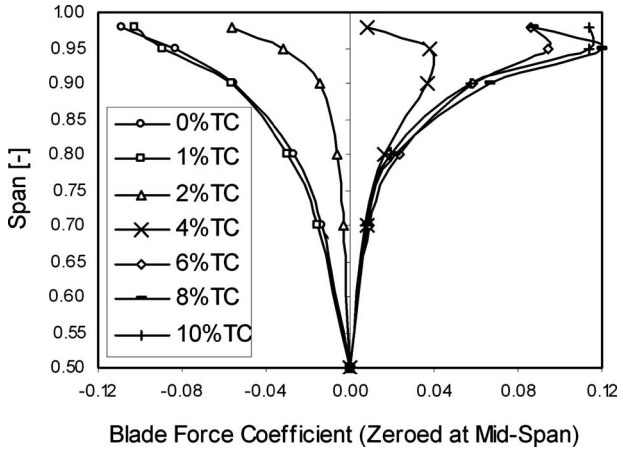

Fig. 25 CFD study, blade force coefficient 6% tip clearance

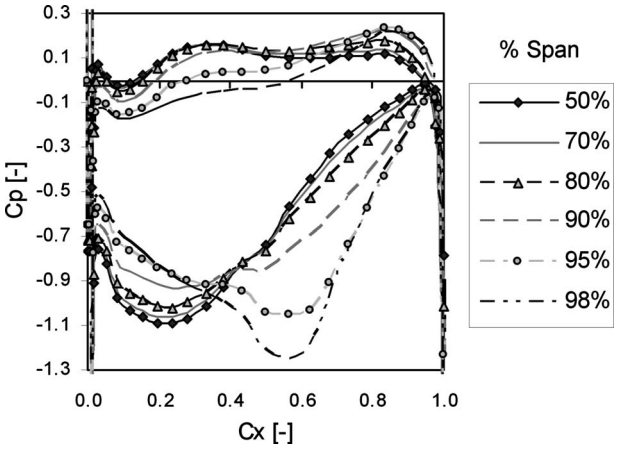

Fig. 27 CFD, 6% TC, blade pressure profile

CFD results are overloaded especially at the leading edge; therefore, the calculated blade force is higher than the experimental force.

Figure 24 shows the mass flow rate per passage versus tip clearance. A linear relationship exists between blockage and tip clearance values above 2% TC. There is a 4.8% reduction in mass flow from 0% to 10%. Therefore for the computational results the mass flow reduction is approximately 0.5% per 1% increase in tip clearance.

In order to investigate the cause of the increase in loading it is useful to look at one TC value in detail, and 6% is examined. Loss contours and velocity vectors through the cascade are shown in Fig. 26, and the blade surface pressure profiles are shown in Fig. 27. The flow features are described through the cascade:

0.0*Cx*. At the inlet to the blade row the inlet boundary layer is skewed and there is already some loss due to the friction on the casing.

0.20*Cx*. Now the blade loading develops and the TC flow accelerates through the clearance. A small separation bubble is present on the tip. Although this is almost certainly due to the pinch tip, a vena contractor over a square blade end would also create such a feature. The blade loading close to the tip has decreased due to the TC flow increasing the pressure on the suction surface and lowering it on the pressure surface.

0.4*Cx*. The blade loading now approaches its maximum and the TC flow has significantly accelerated approximately in the tangential direction. The start of a tip clearance vortex can be seen although it is small and positioned close to the suction surface.

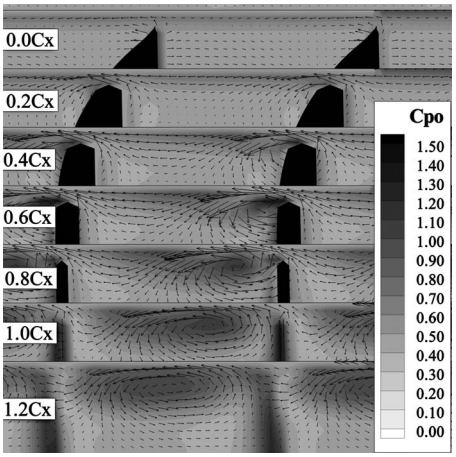

Fig. 26 CFD study, 6% TC *Cpo* loss contour plots

0.6*Cx*. The TC flow has further increased and the vortex starts to move away from the suction surface. Unlike smaller TC values no counter-rotating vortex is seen, although a lower momentum region does exist at the midpassage. The incoming flow is now pushed against the pressure surface and down into the cascade due to the significant blockage created by the TC flows.

0.8*Cx*. The TC vortex continues to move away from the suction surface of the blade. The TC vortex induces lower pressure fluid up the blade toward the tip thus lowering the SS pressure creating a higher blade force. Lower loss fluid is also pulled through the tip clearance reducing the loss on the casing.

1.0*Cx*. The TC vortex has moved away from the SS and now fills the majority of the passage in the outer 20% span. A counter-rotating vortex is just apparent. This is due to the incoming flow interacting with the low momentum fluid in the boundary layer. As found by Williams et al. [2] a relatively rotating casing would suppress the counter-rotating vortex.

6 Discussion

This work shows that there is an unexpected increase in blade loading toward the tip of the blade for the higher values of tip clearance, and that although the loss of the cascade increases with increased tip clearance up to approximately 4% TC, above this the loss levels off and there is no further increase in loss. This section aims to relate these phenomena to the flow physics to further the understanding of large tip clearance flows.

A simple pinch tip model for the tip clearance has been used, which has allowed an investigation of several tip clearances without the use of extensive computer or manpower resources. Experimental measurements have been used to assess the computational work's reliability. It has been found that at 0% and 6% tip clearances, the computation gave good agreement with experiment, particularly for yaw angle (Fig. 8). The 1% and 2% results are not so good, and this is to be expected with the pinch tip model. However, as the thrust of this work is to the larger clearances, the choice of the pinch tip appears justified. As the tip clearance increases the solution becomes less grid dependent; this is because the end wall has a smaller effect on the tip clearance flow. The detailed blade tip modeling and meshing also becomes less influential at a large tip gap. For this reason it can be assumed that the 8% and 10% solutions are valid. The observation from the numerical work so far suggests that if an improved solution to the smaller tip clearance value is required then the use of another tip clearance modeling method would be essential.

The detailed study for 6% TC shows that from the static pressure values on the blade (Fig. 27), at the entry to the blade row the blade loading is significantly reduced for the first 35% chord within 20% span of the casing. This is because the high pressure flow moves from the PS to the SS across the tip, increasing the

pressure on the SS and reducing the pressure on the PS pressure. At midchord the TC vortex starts to roll up close to the SS of the blade. This flow feature creates a blockage reducing the row mass flow rate and forcing the incoming flow toward midspan. The TC vortex induces low pressure fluid up the SS of the blade for 20% span reducing the SS pressure and so increasing the blade force. At approximately 60% chord the TC vortex leaves the suction surface of the blade and moves across the passage, and this coincides with the blade's peak force for the outer 5% blade span. The TC vortex continues to induce fluid along the blade SS into the tip clearance region. Low loss fluid is also pulled through the TC gap from the PS and this serves to reduce the loss on the casing.

An important feature here is that the TC vortex stays relatively close to the suction surface, moving to about midpassage by blade exit. This means that with the high tip clearance, the very strong vortex not so far from the suction side is able to induce the high velocities on the suction surface as noted above. Also the pressure on the pressure surface is raised by the jet stagnating near the tip of the blade.

This lack of movement is in contrast to the movement right across the passage to near the pressure surface usually observed in most of the studies in literature. It does not appear that the high tip clearance is the reason for the lack of movement of the TC vortex, as the lower TC values studied here (Figs. 18 and 19) show that the vortex is also at about midpassage at the exit. The significant feature of this blading is probably the low stagger so that the tip jet is nearly perpendicular to the axial direction.

After 6% TC there is no significant change in blade loading and this suggests that the casing has a decreasing effect on the blade loading and that as the TC value is increased further, the flow around the blade starts to behave independently of the casing. This may help to explain the leveling off of loss with tip clearance, since as the flow crosses the tip as a pressure driven jet there is little further increase in the loss producing mechanisms on the end wall or tip. In effect the flow becomes more like that of a wing tip trailing vortex.

It should be noted that the blade force values shown here (Fig. 14) are dimensionless values based on the span of the actual blade. As the TC increases, of course the blade gets shorter. If the "annulus height" of this linear cascade were used, then an inspection of Fig. 14 shows that the actual force reduces. For instance, at 6% TC, the dimensionless blade force is increased by about 2.7% so that the actual force will reduce by approximately 3.3%, and this is reflected in the large amount of underturning seen in Fig. 21 at higher TC values. Thus the work done by the blade (if it were a rotor) is reduced, but not by as much as might be expected. This coupled with the overall loss becoming independent of the TC value means that the penalties associated with TC values around 4% and above are not as great as might be expected with typical LP blading of high stagger. Unfortunately there is still an increase in blockage so that the mass flow reduces by 0.5% per 1% increase in tip clearance.

With the significant blockage effect, the axial velocity will not be constant at blade inlet, even though the upstream boundary is the same for the different tip clearances. To try and separate the tip clearance flow effects from the blockage effect, the results for angle, loss, and blade force distributions along the span have been referenced to the midspan value. This is perhaps debatable, but it was felt to be most helpful for this study.

It is important to remember that this study is for a linear cascade and that in a rotating machine there will be a number of differences. For instance, in a multirow environment, the inlet boundary layer is skewed and there is relative motion of the end wall. However, the results of Williams et al. [2] showed that the moving end wall did not have much effect for large tip clearances. Thus these cascade results have relevance for HP industrial compressor design.

The aerodynamic designer may find these results interesting; if a design with similar HP blades requires a large tip clearance then the designer who has always strived to reduce the tip clearance value may find that, in fact, the aerodynamic penalty is not as large as previously thought. Therefore cost savings may be made in the mechanical design of the HP stages. The overall blade loading also increases for the larger clearances allowing for slightly higher stage loading.

7 Conclusion

The physics of tip clearance flow for a low stagger cascade of compressor blades has been studied experimentally and computationally. Tip clearances of up to 10% span (12.67% chord) have been studied with application to the HP compressor of an industrial gas turbine. A pinch tip clearance model for the computation was used, and this was found to give satisfactory results for the larger tip clearances. The following conclusions may be drawn.

- Increasing the tip clearance above 4% incurs no further increase in loss and at the same time there is an unexpected increase in blade force toward the tip due to the tip clearance flows.
- The increase in blade force is due to the effect of the strong tip clearance vortex, which does not move across the blade passage to the pressure surface, as is often observed for high stagger blading.
- The leveling off of loss may be attributed to the lack of increasing loss production mechanisms of the pressure driven tip clearance jet as the clearance is increased to large values.
- In general it was found that the CFD overpredicted the loss in the casing region although at midspan there was a very good agreement. The flow angle prediction is very good for the higher tip clearance values although it was not accurate for the smaller clearances.
- These results are significant for the design of HP compressors for industrial gas turbines.

Nomenclature

C = chord, m
Cx = axial chord, m
$Cp = \frac{Ps - Ps_1}{Po_1 - Ps_2}$ = static pressure coefficient
$Cpo = \frac{Po_1 - Po}{Po_1 - Ps_2}$ = total pressure loss coefficient
$C_L = \int_0^C (Cp_{\text{pressure}} - Cp_{\text{suction}})dx$ = blade loading coefficient
Po = total pressure, Pa
Po_1 = inlet total pressure, Pa
Ps = static pressure, Pa
Ps_2 = exit static pressure, Pa
PS = pressure surface
$\text{Re} = VC/\nu$ = Reynolds number
TC = tip clearance, % duct height
X = axial
β = yaw angle (relative to axial)

References

[1] Denton, J. D., 1993, "Loss Mechanisms in Turbomachines," ASME Paper No. 93-GT-435.
[2] Williams, R. J., Gregory-Smith, D., and He, L., 2006, "A Study of Large Tip Clearance Flows in an Axial Compressor Blade Row," ASME Paper No. GT2006-90463.
[3] Walker, M., Gregory-Smith, D., and He, L., 2005, "A Study of Large Tip Clearance in a Row of Low Speed Compressor Blades," *Proceedings of the Sixth European Conference on Turbomachinery*, Lille, Vol. 1, pp. 122–134.
[4] Peacock, R. E., 1982, "A Review of Turbomachinery Tip Gap Effects: Part 1: Cascades," Int. J. Heat Fluid Flow, **3**, pp. 185–193.
[5] Storer, J. A., and Cumpsty, N. A., 1991, "Tip Leakage Flow in Axial Compressors," ASME J. Turbomach., **113**(2), pp. 252–259.
[6] Hunter, I. H., and Cumpsty, N. A., 1982, "Casing Wall Boundary-Layer Development Through an Isolated Compressor Rotor," ASME J. Eng. Gas Turbines Power, **104**(4), pp. 805–818.
[7] Gbadebo, S. A., 2006, "Interaction of Tip Clearance Flow and Three-

Dimensional Separations in Axial Compressors," ASME Paper No. GT2006-90071.
[8] Tang, G., and Simpson, R. L., 2006, "Experimental Study of Tip-Gap Turbulent Flow Features," ASME Paper No. GT2006-90359.
[9] Sjolander, S. A., 1997, "Secondary and Tip-Clearance Flows in Axial Machines," *Physics of Tip Clearance Flows—1* (Lecture Series 1997–01), von Karman Institute for Fluid Dynamics, Rhode-St-Genèse, Belgium.
[10] Saathoff, H., and Stark, U., 2001, "Tip Clearance Flow in a Low-Speed Compressor and Cascade," *Proceedings of the Fourth European Conference on Turbomachinery—Fluid Dynamics and Thermodynamics*, Firenze, Italy, pp. 81–91.
[11] De Cecco, S., Yaras, M. I., and Sjolander, S. A., 1995, "Measurements of the Tip-Leakage Flow in a Turbine Cascade With Large Clearances," ASME Paper No. 95-GT-77.
[12] Van Zante, D. E., Strazisar, A. J., Wood, J. R., Hathaway, M. D., and Okiishi, T. H., 2000, "Recommendations for Achieving Accurate Numerical Simulation of Tip Clearance Flows in Transonic Compressor Rotors," ASME J. Turbomach., **122**(4), pp. 733–742.
[13] Yang, H., 2004, "3D Unsteady Flow in Oscillating Compressor Cascade," Ph.D. thesis, Durham University, Durham, UK.
[14] Sanger, N. L., 1983, "The Use of Optimization Techniques to Design-Controlled Diffusion Compressor Blading," Trans. ASME: J. Eng. Gas Turbines Power, **105**, pp. 256–264.
[15] Sanger, N. L., and Shreeve, R. P., 1986, "Comparison of Calculated and Experimental Cascade Performance for Controlled-Diffusion Compressor Stator Blading," ASME J. Eng. Gas Turbines Power, **108**, pp. 42–50.
[16] Ingram, G., and Gregory-Smith, D., 2006, "An Automated Instrumentation System for Flow and Loss Measurement in a Cascade," *Flow Measurement and Instrumentation*, Elsevier, New York, Vol. 17, pp. 23–28.
[17] He, L., 2000, "Three-Dimensional Unsteady Navier-Stokes Analysis of Stator-Rotor Interaction in Axial-Flow Turbines," Proc. Inst. Mech. Eng., Part A, **214**, pp. 13–22.
[18] Gupta, A., Arif Khalid, S., McNulty, G. S., and Dailey, L., 2003, "Prediction of Low Speed Compressor Rotor Flowfields With Large Tip Clearances," ASME Paper No. GT2003-38637.

Shyy Woei Chang[1]
Professor
Department of Marine Engineering,
Thermal Fluids Laboratory,
National Kaohsiung Marine University,
No. 142, Haijhuan Road, Nanzih District,
Kaohsiung 811, Taiwan, R.O.C.
e-mail: swchang@mail.nkmu.edu.tw

Tong-Miin Liou
Professor
Department of Power Mechanical Engineering,
National Tsing Hua University,
300 Hsinchu, Taiwan, R.O.C.

Tsun Lirng Yang
Associate Professor
National Kaohsiung Marine University,
No. 142, Haijhuan Road, Nanzih District,
Kaohsiung City 81143, Taiwan, R.O.C.

Guo Fang Hong
Marine Engineering,
National Kaohsiung Marine University,
No. 142, Haijhuan Road, Nanzih District,
Kaohsiung City 81143, Taiwan, R.O.C.

Heat Transfer in Radially Rotating Pin-Fin Channel at High Rotation Numbers

Endwall heat transfer measurements for a radially rotating rectangular pin-fin channel with the width-to-height ratio (aspect ratio) of 8 are performed at the parametric conditions of $5000 \leq Re \leq 20{,}000$, $0 \leq Ro \leq 1.4$, *and* $0.1 \leq \Delta\rho/\rho \leq 0.21$. *Centerline heat transfer levels along the leading and trailing endwalls of the rotating pin-fin channel are, respectively, raised to 1.77–3.72 and 3.06–5.2 times of the Dittus–Boelter values. No previous attempt has examined the heat transfer performances for the pin-fin channel at such high rotation numbers. A selection of experimental data illustrates the individual and interactive Re, Ro, and buoyancy number (Bu) effects on heat transfer. Spanwise heat transfer variations between two adjoining pin rows are detected with the averaged Nusselt numbers (Nu) determined. A set of empirical equations that calculates Nu values over leading and trailing endwalls in the developed flow region is derived to correlate all the heat transfer data generated by this study and permits the evaluation of interactive and individual effects of Re, Ro, and Bu on Nu. With the aid of the Nu correlations derived, the operating conditions with the worst heat transfer scenarios for this rotating pin-fin channel are identified.* [DOI: 10.1115/1.3147103]

Keywords: rotor blade cooling, pin-fin rotating channel, high rotating number

1 Introduction

The ever-increased turbine entry temperatures propose serious thermal threats on turbine vanes and blades. The trade-off between aerodynamic efficiencies of a turbine airfoil against cooling requirements results in the thin trailing edge with small wall thickness through which a narrow internal airway is passed. Such structure has made the trailing edge of a turbine blade to be most vulnerable to thermal attacks. The thin trailing edge limits the size and shape of the internal coolant passage, suppresses the thermal inertia of blade wall, and elevates the external heat transfer coefficients. For structural integrity and heat transfer enhancements (HTEs) over the internal coolant passage, the pin-fin array inside a gas turbine blade is prevalent for trailing edge cooling.

A large number of experimental and numerical studies investigated the heat transfer performances over the pin-fins and endwalls in the *static* pin-fin channels [1–14]. With the presence of pin-fin array in a channel, the fluid mixing and unsteadiness from the wakes tripped by pins are enhanced. The protrusion-endwall junctions and the pin-rows trigger a number of complex vortex structures that affect the endwall heat transfer performances. Of the primary importance for endwall cooling performances is the horseshoe vortices that form upstream of each pin at the pin-endwall junction. Regional HTE effects are generated by the secondary advection of horseshoe vortices [1]. Two legs of each horseshoe vortex roll around the adjoining pin and advect downstream to form the pin-fin wakes [2]. Behind each pin, these wakes recirculate the heated coolant and generate low heat transfer regions. After the recirculation zone, flow reattachments of the separated shear layers elevate local heat transfer again. Endwall heat transfer variations along a pin-fin channel are also influenced by the trade-offs between these streamwise enhanced HTE mechanisms against the thickened boundary layers. Such trade-offs elevate heat transfer rates progressively over the first 3–4 pin-rows. The different flow conditions over the surfaces around pin-fins and on the endwalls generate the higher HTE effects on pin surfaces by 35% [3] or 10–20% [4] over those on endwalls. These flow features generalize the heat transfer performances in a *static* pin-fin channel, but the detailed HTE effects vary with the height-to-diameter ratios of pins [5–7], shapes of pin-fin [9], pin-fin arrangements [10–12], and the orientation of pin-array in the cross flow [8,13]. These geometric factors [5–13] are interrelated to affect the endwall cooling performances. Among the various pin-fin geometries, the staggered diamond pin-fin array with pitch ratios of 1.5–2.5 pin-diameters offers the considerable HTE effects, while the elliptical pins offer the higher thermal performance factors [14].

Although the rotating pin-fin channel has a long term history of cooling application to turbine rotor blade, the heat transfer study with rotation is very rare [15], and the detailed flow measurements are not available in the literature. The pioneering heat transfer study for *rotating* pin-fin channel [15] is limited at low rotation rates with no attempt to investigate both rotational buoyancy effects and spanwise heat transfer variations over two opposite rotating endwalls. Heat transfer correlations as the design references for the rotating pin-fin channels are also absent. The lack of experimental heat transfer data and its correlations for rotating pin-fin channels motivate this study. Nevertheless, the evaluations of heat transfer rates in a rotating pin-fin channel need to consider the Coriolis and centrifugal force effects, which act simultaneously and interact with the pin-fins to generate the complex flow structures. The synergistic Coriolis and buoyancy effects modify the endwall cooling performances from the nonrotating conditions in the rotating pin-fin channel; while the degrees and extents of such impacts are the research focus for this study.

In general, Coriolis forces affect mean flows and turbulent fluctuations considerably. The cross-stream Coriolis secondary flows drive the relatively cool fluids from the channel core toward the unstable wall and return to the stable wall after washing the peripheries of a rotating channel. But with the presence of pin-fin

[1]Corresponding author.

Contributed by the International Gas Turbine Institute of ASME for publication in the JOURNAL OF TURBO MACHINERY. Manuscript received August 20, 2008; final manuscript received August 31, 2008; published online January 21, 2010. Review conducted by David Wisler. Paper presented at the ASME Turbo Expo 2008: Land, Sea and Air (GT2008), Berlin, Germany, June 9–13, 2008.

array in the rotating channel, the Coriolis secondary flows are considerably disturbed with less opportunities to generate the three-dimensional Taylor–Görtler roll cells, which normally develop at high rotation rates [16]. However, the mechanism for producing turbulences triggered by the momentum exchange through intensive interactions between the fluctuating streamwise and cross-stream velocities still prevails in a rotating pin-fin channel, within which the turbulent activities are augmented as Coriolis forces act in tandem with these events but are attenuated when the two act in opposition [17]. Heat transfer differences between the stable and unstable endwalls of a rotating pin-fin channel are realized as a result of Coriolis force effects. With heat convection taking place inside a rotating pin-fin channel, the interaction between centrifugal acceleration and density gradients of fluids due to temperature differences vary the volumetric body forces to large extents, since the centrifugal acceleration reaches the order of above 10^4 g. This rotational buoyancy force motivates the warmer and less dense fluids toward the axis of rotation and alters the heat transfer performance by way of distorting the velocity and temperature distributions with turbulence structures modified. Features of the combinative effects between rotating buoyancy and Coriolis secondary flows that interact with the roughness elements, such as surface ribs [18], are highly complicated and interrelated. In this respect, there is no previous attempt available to examine the interactive and individual buoyancy impacts on heat transfer in a rotating pin-fin channel, which will be examined in detail here. Because the buoyancy effects in a rotating channel are relevant to the structures of mean-flow and turbulence, the effects of rotating buoyancy on heat transfer deem to be Reynolds number (Re), rotation number (Ro), and location dependent, as suggested by various research groups [19–26]. But due to the limitation on the range of rotational parameters examined and the various rotating buoyancy effects reported to date [19–26], the impacts of rotating buoyancy on heat transfer at the engine representative conditions remain unclear.

Most of the previous laboratory-scale heat transfer experiments used simplified blade cooling geometry to examine heat transfer performances in these rotating channels at low Ro and low Bu [16–26]. Only a few of the previous studies simulate closely the real engine scenarios by operating experimental tests at conditions of $Ro \geq 1$ [27–29]. This experimental study examines endwall heat transfer performances for a radially rotating rectangular pin-fin channel with an aspect ratio of 8. Local endwall heat transfer measurements along two opposite pairs of streamwise centerlines and spanwise centerlines between two adjacent pin-rows in the developed flow regime are generated with the rotating parameters, namely, Ro and Bu, extended considerably from the past experiences. Heat transfer performances in association with the individual and interactive effects of Re, Ro, and Bu are illustrated along the line of developing the empirical heat transfer correlations. These empirical heat transfer equations not only stand for the entire set of heat transfer data generated with the capabilities to uncouple the individual but mutually interactive Ro and Bu effects on heat transfer but also to determine the spanwise-averaged Nusselt numbers ($\overline{\mathrm{Nu}}$) in the developed flow region. However, this set of $\overline{\mathrm{Nu}}$ correlations is limited to determine the endwall heat transfer performance. The operational conditions with the worst endwall heat transfer scenarios for this rotating pin-fin channel are parametrically identified using the heat transfer correlations generated by this study.

2 Experimental Details

2.1 Rotating Test Rig and Heat Transfer Test Module. The constructional details of this rotating test rig and its instrumentations for measurements of flow rate, heat flux, and temperature, as well as the data acquisition system, have been previously reported [27]. The 420 mm long pin-fin test channel is mounted on the platform of the rotating rig giving the midspan radius (R) of 420 mm. The maximum rotational speed of heat transfer test channel is 500 rev/min. The pressurized and dehumidified test coolant (dry airflow) is channeled through a set of pressure regulator and filter, a pressure transducer, a mass flow meter, and a needle valve that controls the mass airflow rate into the pin-fin test channel. Air flows radially outward through the rotating pin-fin channel. Figure 1(a) depicts the heat transfer test section that shows the assembly of the test module and the geometry of the pin-fin array. The origin of the present X-Y coordinates is located at the midspan of the bottom edge of the endwall, as indicated in Fig. 1(b). The test section is a five-layer sandwiched model consisting of an entry plenum, two supporting flanges, a pin-fin channel, and the existing plenum with choking device. Ten staggered rows of circular pin-fins (1) with the X-wise and Y-wise pin-pitches of two pin-diameters (d_p) are mounted between two Teflon leading (2) and trailing (3) endwalls normal to the flow direction inside the rectangular test section (4). The channel width (136 mm) to channel height (17 mm) (aspect ratio) is 8, which gives the hydraulic diameter (d) of 30.2 mm. The characteristic length selected to define the dimensionless groups is not the pin diameter but the hydraulic diameter of the test channel (d), which is the established convention for pin-fin ducts. Each pin is made of the thermally insulating material (Teflon) with the diameter of 13.5 mm. The additional fin effects provided by this pin-fin array on HTE effectiveness are not included. The Nu data generated here are limited to the endwall heat transfer performance only. The leading or trailing heater surface ((5) and (6)) on which the wall temperatures (T_w) are measured is made of a continuous 27mm wide, 136 mm long, and 0.1 mm thick stainless steel foil. The adjustable dc electrical power is directly fed through the heating foils ((5) and (6)) to simulate the basically uniform heat flux thermal boundary over the leading or trailing endwall. The electrical power for Joule heating is supplied via a variac transformer with the total power consumption metered by a wattmeter. At each tested flow condition, the heating powers are constantly adjusted in order to reach the preset T_w levels and to vary the relative strength of buoyancy level. Two ends of each heating foils ((5) or (6)) are sandwiched between the insulation Teflon plates and the entry and exit copper plates ((7) and (8)) those connect with copper bars to complete the electrical circuit. The leading and trailing endwalls fitted with heating foils and pin-fin array sandwich two Teflon sidewalls ((9) and (10)) to formulate the rectangular pin-fin channel. The complete set of pin-fin test section is tightened by four draw bolts (11) between the entry (12) and exit (13) plenum chambers and two sets of axial bolts (14) through two Teflon sidewalls. The entry plenum chamber (12) with dimensions of $250 \times 180 \times 120$ mm^3 joins with the pin-fin test section (4) to simulate the abrupt entry condition. This abrupt flow entrance with the abrupt area ratio of 19.46 triggers the simultaneous developments of thermal and hydrodynamic boundary layers at the immediate flow entrance of the heat transfer section. Prior to the heat transfer test section (4), honeycombs and steel meshes are installed inside the entry plenum chamber. The temperature of test coolant in the entry plenum chamber (12) is metered by a type K thermocouple (15). Three additional type K thermocouples (16) are equally spaced along the spanwise centerline over the exit plane of the test section to measure the exit fluid temperatures. The measured exit fluid bulk temperature is approximated as the averaged value of these three thermocouple measurements (16). A needle valve (17) is fitted on the convergent exit plenum chamber in order to adjust the pressure level inside the rotating pin-fin channel. Air leakages from the jointed surfaces are prevented by means of a series of "O" ring seals and high temperature sealants. Thermal insulation tapes are wrapped over the external surfaces of the heat transfer assembly in order to minimize the external heat loss. The complete test module is vertically mounted onto the rotating platform with the dynamic balance ensured.

As indicated in Fig. 1(b), nine K-type thermocouples are installed on the back of each leading or trailing heating foil along its

(a)

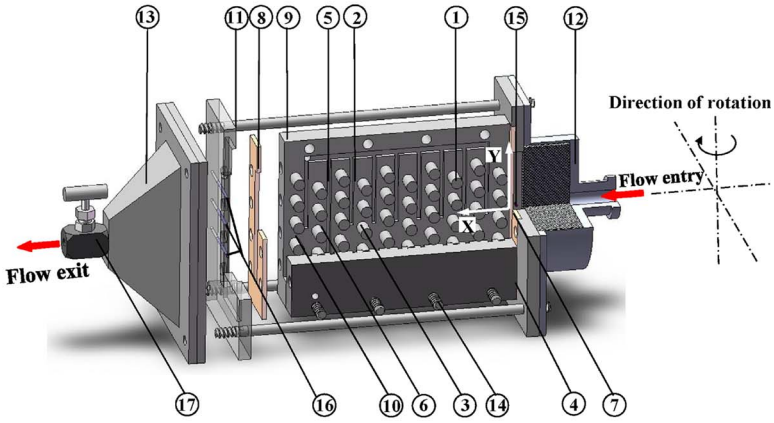

(1) Teflon pin-fins
(2) Leading endwall
(3) Trailing endwall
(4) Rectangular test channel
(5) Heating foil (Leading)
(6) Heating foil (trailing)
(7) Entry copper plates
(8) Exit copper plates
(9) Leading Teflon sidewall
(10) Trailing Teflon sidewall
(11) Draw bolt
(12) Entry plenum chamber
(13) Exit plenum chamber
(14) Axial draw bolts
(15) Thermocouple (entry airflow)
(16) Thermocouple (exit airflow)
(17) Needle valve

(b)

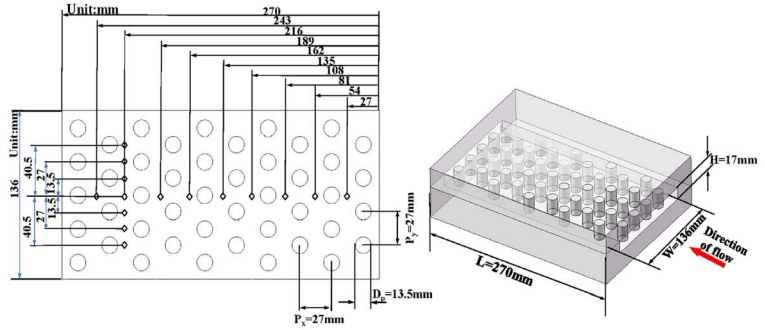

W (channel width) = 136mm
d_p (pin diameter) = 13.5mm
H (pin height) = 17mmP_x (X-wise pin pitch) = 27mm
P_y (Y-wise pin pitch) =27mm
X-wise pitch ratio (Px /d_p) = 2
Y-wise pitch ratio (Py / d_p) = 2
Pin height-to-diameter ratio (H/ d_p)=2
Channel aspect ratio (W/H) = 8

Fig. 1 (*a*) **Test assembly and** (*b*) **channel and thermocouples**

centerline for streamwise T_w measurements. These streamwise thermocouples locate at the midpin positions. Between pin-rows 8 and 9 over the leading or trailing endwall, seven spanwise thermocouples at the pin and midpin locations are installed to detect the spanwise T_w variations in the developed flow regime over the endwall. At each thermocouple junction on the back of the thin heating foil, the ceramic cement is applied to secure its position. Thermocouple wires are taken out of the test assembly via the grooves machined on the Teflon back walls. These temperature measurements are scanned by a PC via the Net-DAQ Fluke Hydra 2640A data logger. All the relevant raw data, such as temperature measurements, airflow rates, pressures, and heater powers, are stored in this PC for the subsequent data processing.

2.2 Parameters, Data Processing, and Program. Experimental studies that determine heat transfer performance in radially rotating channels generally adopt Re, *Ro*, and *Bu* as the controlling parameters with which the parametric coverage of realistic engine conditions are accordingly specified. The rotating buoyancy number (*Bu*) is a combination of density ratio ($\Delta\rho/\rho$ or $\beta[T_w - T_b]$) and the relative centrifuge that formulates the nondimensional group of $\beta(T_w - T_b)Ro^2(R/d)$ with the physical identity of relative strength of rotating buoyancy force. This experimental study is formulated to determine the functional relationships between heat transfer levels, and these controlling parameters for a rotating pin-fin channel are in the form of

$$\text{Nu or } \overline{\text{Nu}} = \Psi\{\text{Re}, Ro, Bu, \text{boundary conditions}\} \quad (1)$$

In Eq. (1), the experimentally defined Nusselt number (Nu) is calculated by Eq. (2). Re, *Ro*, and *Bu* are defined in the nomenclature. The boundary conditions and the coordinate system adopted here are specified by the heat transfer test section, as described in Sec. 2.1

$$\text{Nu} = qd/k(T_w - T_b) \quad (2)$$

The local convective heat flux (q) in Eq. (2) is obtained. by subtracting the external heat loss flux from the total heat flux supplied. The heating area selected to calculate the heat flux is the endwall area with the pin-fin sectional areas deducted. Heat loss calibration tests are performed to generate the correlation between external heat loss fluxes and the wall-to-ambient temperature differences at various rotational speeds. This set of heat loss correlations is incorporated into the data processing program to evalu-

Table 1 Range of dimensionless parameters

Dimensionless parameter	Range
Reynolds number (Re)	5000, 10,000, 15,000, 20,000
Rotation number (Ro)	0–1.4
Buoyancy number $[Bu=\beta(T_w-T_b)Ro^2(R/d)]$	0.004–3.6
Density ratio $[\beta(T_w-T_b)]$	0.1–0.24

Tested Ro for each Re

Re	Ro
5000	0.05, 0.1, 0.15, 0.3, 0.5, 0.7, 1, 1.3, 1.4
10,000	0.05, 0.1, 0.15, 0.3, 0.5, 0.7
15,000, 20,000, 24,000	0.05, 0.1, 0.15, 0.3, 0.5

ate local heat loss fluxes and consequently the local convective heat fluxes. The maximum heat loss flux takes place at the test conditions with the highest rotational speed and wall temperatures, which is about 8.9% of the total heat flux supplied. Having determined the local convective heat flux (q) at each axial station where the wall temperature (T_w) is detected, the local enthalpy balance is accounted to calculate the fluid bulk temperature (T_b) at this particular T_w spot. To check the accuracy of such energy accountancy, the calculated and measured T_b values at the flow exit are constantly compared when the heat transfer tests are performed. Only the raw data can be collected for subsequent processing when the differences between the calculated and measured T_b values are lesser than 10%. All the fluid properties used to define the dimensionless parameters in Eq. (1) are evaluated at these T_b values. Table 1 summarizes the parametric conditions examined here. The maximum Re and Ro in Table 1 are not simultaneously attainable. The present ranges of Ro and Bu are considerably extended from the previous experiences [15–26] by increasing test pressures and the channel hydraulic diameter (d). Test pressures are controlled in the range of 1.1–2.4 bars that allow for the full coverage of the parametric conditions summarized in Table 1.

The present experimental programs perform heat transfer tests at static and rotating conditions with a final phase of deriving $\overline{\mathrm{Nu}}$ correlations. Steady state heat transfer measurements are carried out at both static and rotating conditions. The steady state condition is assumed when the temporal T_w variations after several successive scans are less than $\pm 0.3\,^{\circ}\mathrm{C}$. Generally, the flow and heater power have to be kept for about 45 min in order to satisfy such steady state criterion. The heat transfer results obtained from the static pin-fin channel are compared with the relevant data available for validation. This set of heat transfer data obtained at the zero-rotating speed is treated as the database against which the heat transfer results detected from the rotating channel are compared. Each set of heat transfer data generated by the rotating pin-fin channel is produced at fixed Re and Ro by adjusting the rotational speed, coolant mass flow rate, and the pressure level. At each Re-Ro tested, four heater powers that raise the highest T_w levels to 363 K, 383 K, 403 K, and 423 K are supplied to generate four different steady state conditions with different buoyancy levels. These four sets of heat transfer data are acquired at fixed Re and Ro with four ascending buoyancy levels, which reflect the isolated Bu effect on local Nu. However, adjustments of heat flux vary local T_b values and accordingly vary the fluid properties such as viscosity and thermal conductivity of the test coolant (dry air). To control Re and Ro at the flow entrance within the maximum deviations of $\pm 1\%$ from the targeting values, the mass airflow rates are frequently adjusted so that the changes of fluid properties due to variations in T_b are compensated.

For heat transfer tests, the acquisition of experimental heat transfer data requires the finite wall-to-fluid temperature difference, which inevitably inherits certain degrees of buoyancy impact on heat transfer results. Therefore an additional set of data that is needed to separate Re or Ro impact from Bu interaction is alternatively obtained by extrapolating the rotational heat transfer data into the limiting condition of $Bu=0$, while Re and Ro remain as the targeting test values. This regression process generates a set of Nu data at the zero-buoyancy conditions with which the analysis of individual Re or/and Ro effects on Nu or $\overline{\mathrm{Nu}}$ can be performed. Having realized the individual and intercorrelative relationships between Re, Ro, and Bu on heat transfer, a set of $\overline{\mathrm{Nu}}$ correlations is derived to evaluate the individual and interactive effects of Re, Ro, and Bu on $\overline{\mathrm{Nu}}$ along the leading and trailing endwalls in the developed flow region of the rotating pin-fin channel. Typical HTE effects generated by various surface enhancements for rotating channels are also compared with the present pin-fin channel to reveal the different degrees of rotational impacts on heat transfer. The uncertainty analysis indicates that the most of experimental uncertainties result from the temperature measurements because the fluid properties are estimated from T_b. Applying the method of estimating experimental uncertainties recommended by the editorial board of ASME Journal of Heat Transfer [30], with the values of T_w-T_b in the range of 50–83 K, the estimated maximum uncertainties for Nu, Re, Ro, and Bu are about 8.9%, 5.3%, 4.2%, and 7.6%, respectively.

3 Results and Discussion

3.1 Static Results. In the static channel, the T_w measurements at two opposite leading and trailing endwalls exhibit negligible differences due to the lack of rotational forces. But the axial and spanwise T_w variations generally show the lower T_w value behind the pin relative to its adjacent location in front of the pin. Figure 2(a) typifies such axial T_w variations along leading and trailing centerlines at Re=15,000. The local bulk temperature (T_b) depicted in Fig. 1(a) increases linearly along the test channel. The locations behind and in front of a pin are, respectively, referred to in the notations as BP and FP hereafter. As the experimental heating condition on each of the two opposite leading and trailing endwalls corresponds closely to the uniform heat flux, the axial and spanwise Nu_0 variations reassemble the zigzag pattern of T_w variations with the higher Nu_0 values at the BP locations. By way of normalizing the Nu_0 value with Dittus–Boelter Nusselt number (Nu_∞) [31], the HTE effects generated by the pin-fin array in the static channel are revealed.

Figures 2(b) and 2(c), respectively, show the axial and spanwise variations in $\mathrm{Nu}_0/\mathrm{Nu}_\infty$ at Re=5000, 15,000, and 20,000 with zero Ro. The range of data scatter at each x/d location driven by varying buoyancy levels is small that indicates the negligible buoyancy impact on heat transfer in this static channel. The axial distributions of $\mathrm{Nu}_0/\mathrm{Nu}_\infty$, as seen in Fig. 2($b$) at Re=5000, 10,000, and 15,000, follow a general trend of streamwise increase in the

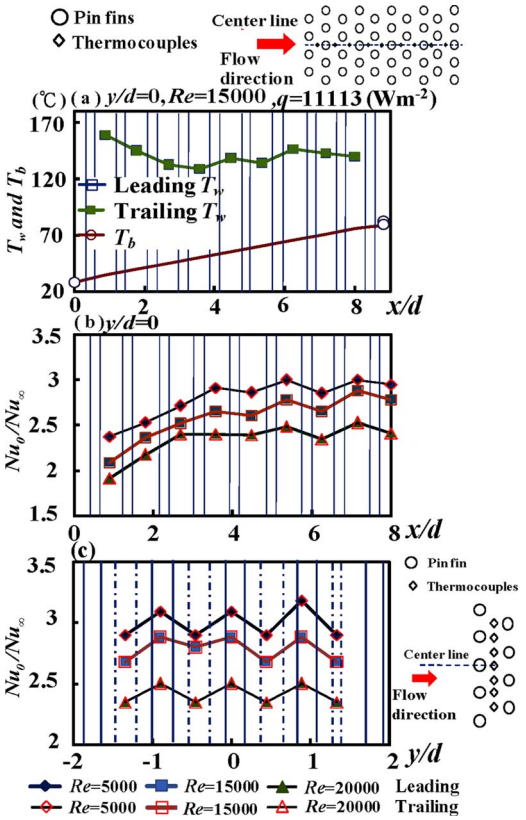

Fig. 2 (a) Axial T_w and T_b variations at Re=15,000 (*b*) axial and (*c*) spanwise distributions of Nu_0/Nu_∞ along leading and trailing walls at Re=5000, 15,000, and 20,000

initial entry region toward the asymptotic values with relatively high Nu_0/Nu_∞ ratios in the developed flow region. This developed flow region takes place after the fourth pin-row ($x/d>4$), where the regular zigzag heat transfer variations with the higher Nu_0/Nu_∞ ratios are constantly observed at the BP locations. With the abrupt flow entrance, the axial Nu_0/Nu_∞ profiles, as shown in Fig. 2(*b*), are in contrast with those in the plain channels where the high heat transfer rates in the initial entry region axially decay toward the asymptotic values in the developed flow region due to the thickened boundary layers in the streamwise direction. The typical axial heat transfer distribution shown in Fig. 2(*b*) agrees with the well known fact for the flows across tube-bundles or a pin-fin array that the fluid mixing and unsteadiness from the wakes tripped by individual rows of tubes or pins increase progressively as the flow traverses further downstream. Heat transfer performances over the first 3–4 rows of pins therefore increase progressively with the three-dimensional advection and turbulence diffusion enhanced further downstream. Although the thickened boundary layers reduce downstream heat transfer rates in the initial entry region, the streamwise enhanced HTE mechanisms tripped by pin-rows offset the effects of thickened boundary layers and produce the axial increases in Nu_0/Nu_∞ ratios in the pin-fin channel.

Figure 2(*c*) depicts the spanwise Nu_0/Nu_∞ variations along the centerline between two adjoining pin-rows 8 and 9, where the flow is considered as developed. Along this spanwise centerline at 7.14 x/d, the zigzag patterns with the higher Nu_0/Nu_∞ ratios at BP locations are consistently found at all the Re tested. Over the entire Re range from 5000 to 20,000, the ratios of Nu_0/Nu_∞ vary in the range of 3.1–2.3. It is worth noting that the addition of heat transfer capacities produced by pin surfaces can significantly elevate the HTE performances from the conditions reported for endwalls only. Also indicated in Figs. 2(*b*) and 2(*c*) are the reduced

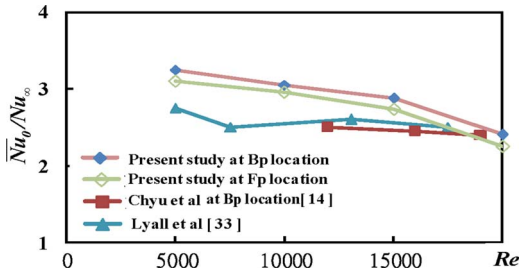

Fig. 3 $\overline{Nu_0}/Nu_\infty$ variations against Re at BP and FP locations

local Nu_0/Nu_∞ ratios as Re increases. Such systematic reductions in Nu_0/Nu_∞ ratios as Re increases indicate that the Re exponent in the Nu_0 correlation for this pin-fin channel is lesser than 0.8 for the Nu_∞ correlation. Consequently, the HTE effect in terms of Nu_0/Nu_∞ attributed from the pin-fin array is Re dependent.

Due to the spatial variations in flow structure in this pin-fin channel, the functional relationship between Nu_0 and Re at each measurement spot is individually examined. As the variations in Pr are negligible over the temperature range covered here, the local Nu_0 values are correlated as $Nu_0=A(x/d)\times Re^{n(x/d)}$. The coefficient A and exponent n vary with the axial and spanwise locations. This set of correlations (not shown here) that evaluates local Nu_0 values is derived to serve as the zero-rotation heat transfer references, against which the rotational Nusselt number (Nu) is compared and normalized. The heat transfer performance in the developed flow region of this pin-fin channel is indexed as $\overline{Nu_0}$, which is acquired by averaging all the spanwise Nu_0 measurements at the BP and FP locations along two opposite centerlines between pin-rows 8 and 9 ($x/d=7.15$) over the leading and trailing endwalls. The varying manner of $\overline{Nu_0}/Nu_\infty$ ratios against Re for BP and LP locations are displayed in Fig. 3 in which the $\overline{Nu_0}/Nu_\infty$ ratios at BP location are consistently higher than those at the FP location.

Also shown in Fig. 3 is the comparable data of Chyu et al. [13] and Lyall et al. [32], which share the similar geometries of pin-fin array and test channel for the purpose of validation. As seen in Fig. 3, the range of differences between the present $\overline{Nu_0}/Nu_\infty$ and those reported in Refs. [13,32] of less than 15% is due to the differences in H/d ratio, channel aspect ratio, and the number of pin-rows of these pin-fin channels. Because the $\overline{Nu_0}/Nu_\infty$ ratios cited in Ref. [32] are the spatially averaged Nu_0 values calculated from the full-surface Nu_0 distributions over the entire endwall, the spanwise-averaged $\overline{Nu_0}$ value defined by this study seems to be close to the spatially averaged Nu_0 value. The validation demonstrated in Fig. 3 seems to be satisfactory. The $\overline{Nu_0}$ correlations at BP and FP locations are, respectively, derived as Eqs. (3) and (4) to level the averaged heat transfer performances in the developed flow region of the present static pin-fin channel

$$\overline{Nu_0}=0.33Re^{0.628} \quad \text{at BP location} \tag{3}$$

$$\overline{Nu_0}=0.144Re^{0.708} \quad \text{at FP location} \tag{4}$$

3.2 Rotational Heat Transfer Results in General. It is a well known fact in this technical community that the Coriolis secondary flows convect the cooler fluids from the duct-core to the trailing edge with the heated coolant flowing along the periphery of the rotating duct toward the leading edge, when the mainstream of airflow is radially outward. This is referred to a major impact of Coriolis forces on mean-flow fields as the so-called Coriolis washing effect. However, in the rotating pin-fin channel, the Coriolis secondary flows are constantly disturbed by the pin-fin array. But the velocity components driven by Coriolis and rotating buoyancy forces can still affect the vortical flows tripped by pin-fins, as well as the turbulent structures. In addition, the

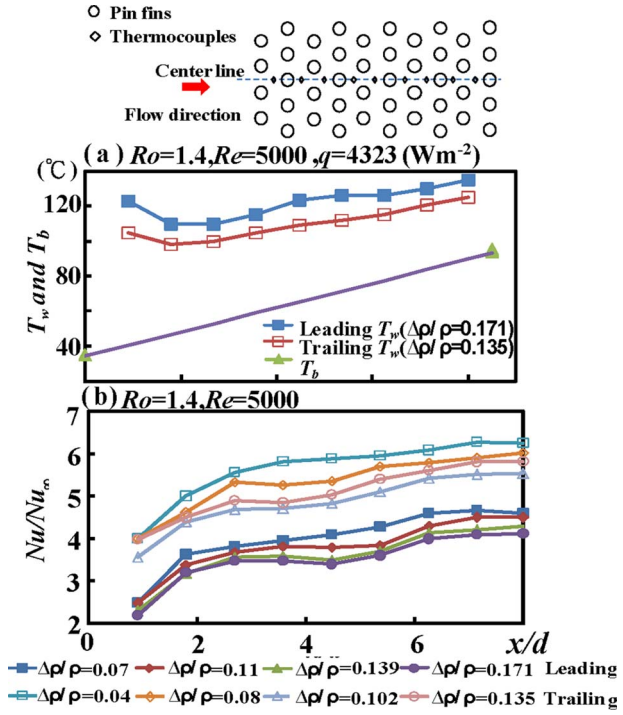

Fig. 4 (*a*) **Axial T_w and T_b variations** (*b*) **axial Nu/Nu_∞ variations along centerlines on leading and trailing endwalls with different $\Delta\rho/\rho$ at Re=5000 and *Ro*=1.4**

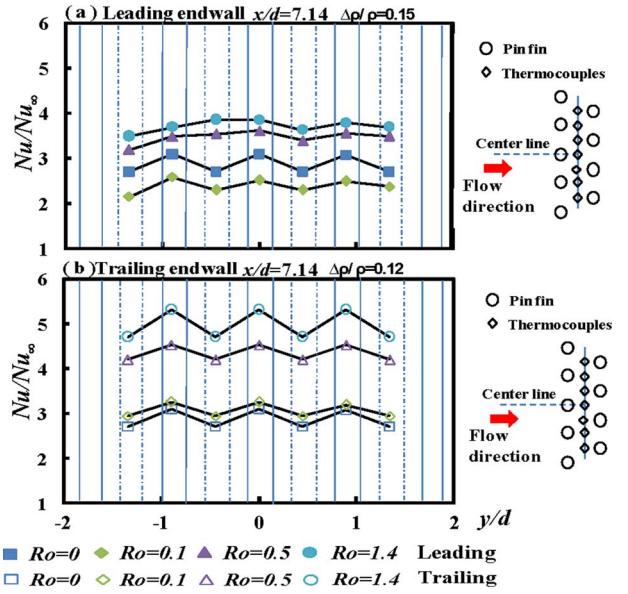

Fig. 5 Spanwise distributions of Nu/Nu_∞ over (*a*) leading and (*b*) trailing endwalls with Re=5000, $\Delta\rho/\rho$=0.15, *Ro*=0, 0.1, 0.5, and 1.4 at 7.14 *x/d* location

Coriolis forces generate the spanwise pressure gradient that modifies the local flow instability phenomena with the turbulence promoted and suppressed at the unstable (trailing) and stable (leading) endwalls, respectively. These interactive effects produce heat transfer differences between the leading and trailing endwalls with the higher heat transfer rates on the trailing endwall. With the basically uniform heat flux heating condition, leading T_w values constantly operate at the higher levels than the trailing counterparts, as typified by Fig. 4(*a*).

By way of normalizing the rotational endwall Nusselt number (Nu) with Nu_∞, the HTE effects produced by the pin-fin array in the rotating channel are revealed. Figure 4(*b*) typifies the axial distributions of Nu/Nu_∞ along two opposite centerlines over leading and trailing endwalls with four different $\Delta\rho/\rho$ ratios at Re=5000 and *Ro*=1.4. The heat transfer levels along the centerline of trailing endwall constantly operate at the higher values than those leading counterparts due to the Coriolis force effects. Unlike the static pin-fin channel in which the buoyancy effect is nonexistent, four pairs of descending Nu/Nu_∞ profiles along each centerline on leading or trailing endwall are driven by increasing $\Delta\rho/\rho$ at the fixed Re and *Ro* shown in Fig. 4(*b*). This clearly demonstrates the impairing buoyancy effect on heat transfer on both leading and trailing endwalls.

Figure 5 depicts the spanwise variations in Nu/Nu_∞ over the leading (a) and (b) trailing endwalls in the developed flow region (x/d=7.14) of the rotating pin-fin channel at Re=5000.

As seen in Fig. 5(*a*) where Nu/Nu_∞ obtained with *Ro*=0, 0.1, 0.5, and 1.4 with $\Delta\rho/\rho \approx 0.15$ are compared, the increase in *Ro* from 0 to 0.1 reduces heat transfer levels from the Nu_0 reference on the leading endwall. Further increasing *Ro* from 0.1 to 0.5, Nu/Nu_∞ starts increasing on the leading endwall. With $Ro > 0.5$, Nu/Nu_∞ increases with the increase in *Ro* on the leading endwall. On the trailing endwall, as shown in Fig. 5(*b*), the increase in *Ro* from 0 to 1.4 produces the consistent heat transfer elevations from the Nu_0 reference. Such heat transfer characteristics found in this rotating pin-fin channel on the leading and trailing endwalls follow those found in the rotating channels operating at high *Ro* [27–29]. It is also worth comparing the attendant variations in the spanwise Nu/Nu_∞ profiles over the leading and trailing endwalls as *Ro* increases. In Fig. 5(*a*), the spanwise zigzag patterns are systematically moderated as *Ro* increases from 0 to 1.4. But such spanwise zigzag Nu/Nu_∞ patterns are persistent over the trailing endwall, as seen in Fig. 5(*b*). It has previously stated that the different heat transfer values at the BP and LP locations are produced due to the endwall vortices tripped by pin-fins. The Coriolis forces directed toward the trailing endwall of this rotating pin-fin channel seem to lift the endwall vortices from the leading wall as *Ro* increases. Because the endwall vortices are lifted over this rotating leading surface, heat transfer differences between BP and LP locations, as shown in Fig. 5(*a*), are accordingly moderated. Acting by the Coriolis forces, the endwall vortices tripped by pin-rows attach firmly on the rotating trailing surface so that the spanwise zigzag Nu/Nu_∞ profiles are persistently found on the trailing endwall, as seen in Fig. 5(*b*). With respect to the Coriolis force effect, which lifts the endwall vortices from the leading surface and results in the heat transfer scenarios depicted in Fig. 5(*a*), is the first time observation that can considerably alter the spatial heat transfer variations over the leading endwall in the rotating pin-fin channel.

Clearly, the presence of rotational forces in the enhanced coolant passages of turbine rotor blades interacts with a variety of HTE elements to produce different flow structures and heat transfer performances. It is interesting to know how and to what extent the different flow interactions between the rotational forces and the flow features induced by various types of surface roughness, such as ribs, pin-fins, and dimples, can affect the cooling performances of these rotating channels. This attempt is realized by comparing the variations in Nu/Nu_∞ against *Ro* for various sets of data collected from the rotating ribbed [22–28], dimpled [26], and pin-fin [15] channels. Such comparison is made in Fig. 6, where the Nu/Nu_∞ data generated by this study are included. The ranges of $\Delta\rho/\rho$ for each data trend compared in Fig. 6 are indicated by the data available in the open literature.

As well as a reconfirmation, the present data agree well with those reported in Ref. [15] for the rotating pin-fin channel in the low *Ro* range ($Ro < 0.3$). It is noticed in Fig. 6 that the different geometries of the channel wall provide various degrees of impact on Nu_0/Nu_∞ in these rotating channels. Among these rotating

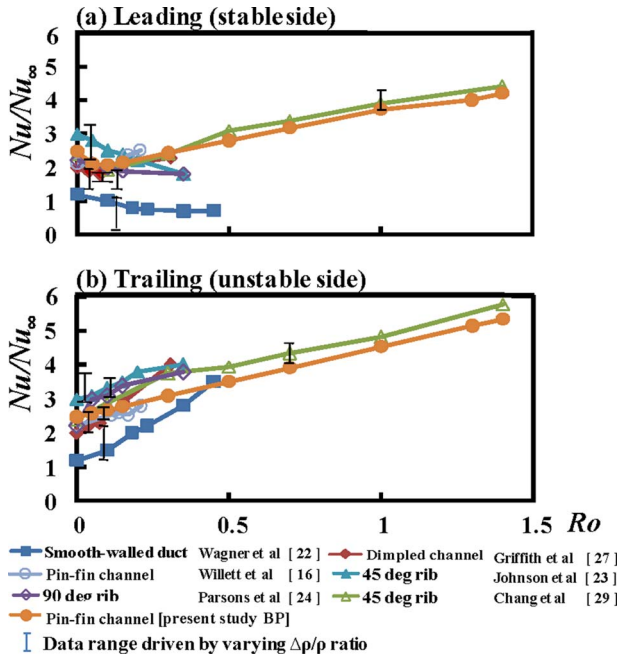

Fig. 6 Variations in Nu/Nu_∞ against *Ro* for rotating channels fitted with surface ribs, dimples, or pin-fins along the centerline of (*a*) leading and (*b*) trailing walls with radially outward flow

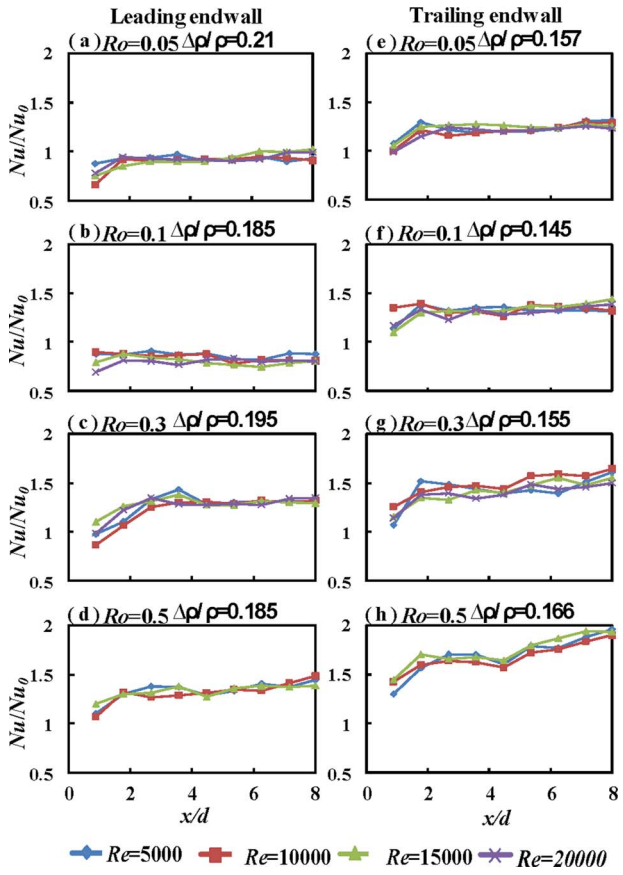

Fig. 7 Axial Nu/Nu_0 profiles with Re=5000, 10,000, 15,000, and 20,000 but at a fixed *Ro* of 0.05, 0.1, 0.15, 0.3, or 0.5 and fixed nominal $\Delta\rho/\rho$ along leading and trailing centerlines

channels with smooth-wall [21], 90 deg [23], and 45 deg ribs [22,28], dimples [26], and pin-fins [15], the smooth duct [21] shows the lowest heat transfer levels but with the largest range of Nu/Nu_0 from 0.45 (leading) to 3.8 (trailing) in the *Ro* range of 0–0.5. The widest varying range of Nu/Nu_0 in the *Ro* range of $0<Ro<0.5$ among the comparative groups collected in Fig. 6 indicates the largest extents of rotational influences on heat transfer in the smooth duct. The endwall Nu/Nu_∞ for the rotating pin-fin channels, as shown by the data from Ref. [15] and present study, is compatible with those in the dimpled channel [26]. With $Ro<1.5$, the range of Nu/Nu_0 between 0.8 (leading) and 2.1 (trailing) for the present pin-fin channel is lesser than the varying range of 0.6(leading)–2.2(trailing) for the square duct roughened by 45 deg ribs [28]. It is worth mentioned that the data points collected in Fig. 6 are affected by *Bu* as well. The ranges of Nu/Nu_0 are subject to the variations from the scenarios depicted in Fig. 6 to some extent at the conditions with the nonexistent buoyancy impact. The lesser extent of rotational influences on the endwall heat transfer due to the presence of pin-fin array is revealed by the comparative study shown in Fig. 6. As described previously, the protruding pin-fins disturb the Coriolis secondary flows in the rotating channel and result in less degree of rotational impacts on endwall heat transfer. Less degree of heat transfer enhancements from the duct roughened by 45 deg ribs [28] result in the lower heat transfer rates in the rotating pin-fin channel over the trailing endwall.

Four sets of Nu/Nu_0 data obtained with Re=5000, 10,000, 15,000 and 20,000 but at a fixed *Ro* with approximately the same values of $\Delta\rho/\rho$ along the leading and trailing centerlines, as indicated in Fig. 7. In each plot of Fig. 7 with *Ro* fixed at 0.05, 0.1, 0.15, 0.3, or 0.5, four sets of axial Nu/Nu_0 profiles along the centerline of leading or trailing wall collapse into a tight data band that validates the feasibility of isolating Re impacts from the rotational effects (synergistic *Ro-Bu* effects) on heat transfer using Nu/Nu_0 data structure. Such result enables the isolation of the Re effect from the synergistic *Ro-Bu* impacts on Nu by presenting the rotational heat transfer data in terms of Nu/Nu_0. The axial Nu/Nu_0 profile displayed in each plot of Fig. 7 can therefore be treated as the streamwise development of the combined *Ro-Bu* effects on Nu. In view of all the plots collected in Fig. 7, the axial Nu/Nu_0 profiles follow a general pattern with an initial fall of Nu/Nu_0 at the flow entry region, where the boundary layers and Coriolis secondary flow both develop. The values of Nu/Nu_0 gradually evolve into the two asymptotic values in the developed flow region after the airflow traverses about four pin-rows, where the vortices tripped by pin-fins are developed. Over the entire length of the rotating pin-fin channel, the higher Nu/Nu_0 ratios consistently develop at the trailing edge relative to its leading counterpart. The leading-wall heat transfer impediments from the nonrotation conditions develop at $Ro=0.05$ and 0.1. These combined *Ro-Bu* impacts on axial Nu/Nu_0 profiles typified by Fig. 7 are followed by all the test results obtained with different heat flux settings.

3.3 Parametric Analysis of Rotational Results. The parametric analysis identifies the functional structures of Nu versus Re, *Bu*, and *Ro* to reflect the heat transfer physics in this rotating pin-fin channel. The individual and interactive Re, *Bu*, and *Ro* impacts on heat transfer have to be examined along with the development of heat transfer correlation. As described previously, the seven spanwise Nu measurements at the BP and FP locations in the developed flow region over the leading or trailing endwall of the rotating pin-fin channel are averaged as Nu. The processes of generating the Nu correlation with the associated heat transfer physics illustrated are summarized in this section. Initially, the isolation of Re impacts generate the synergistic *Ro-Bu* effects on Nu, permitted by presenting the heat transfer data in terms of Nu/Nu_0. This is confirmed by the converged Nu/Nu_0 obtained with different Re but at the same values of *Ro* and *Bu*. With the Re impacts isolated, the individual *Bu* effect on heat transfer is

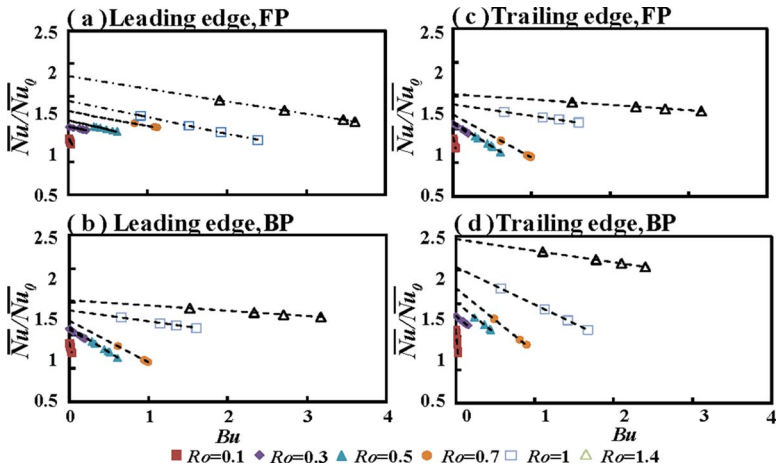

Fig. 8 Variations in $\overline{Nu}/\overline{Nu}_0$ against *Bu* at fixed *Ro* of 0.1, 0.3, 0.5, 0.7, 1, and 1.4

analyzed by plotting $\overline{Nu}/\overline{Nu}_0$ against *Bu* at BP and FP locations on leading and trailing endwalls. Figure 8 depicts the variations in $\overline{Nu}/\overline{Nu}_0$ against *Bu* at *Ro*=0.1, 0.3, 0.5, 0.7, 1, and 1.4.

With each *Ro* tested, the $\overline{Nu}/\overline{Nu}_0$ descends linearly as *Bu* increases. Due to the negative slopes for all the *Ro* controlled data trends, as seen in the plots of Fig. 8, the isolated *Bu* effect impairs heat transfer within the range of parametric conditions tested here. But the magnitude of the slope for each data series, as shown in Fig. 8, systematically decreases as *Ro* increases. The degrees of impairing buoyancy impact on heat transfer in this rotating pin-fin channel are consistently weakened as *Ro* increases. Such an intercorrelative *Ro-Bu* structure needs to be considered in the as correlation.

The subsequent analysis is devised to reveal the individual *Ro* effect on heat transfer. But it is not practical to uncouple the *Bu* effects from the *Ro* controlled thermal physics based on the direct heat transfer measurements as the finite wall-to-fluid temperature differences, and therefore the buoyancy interactions, are inevitable. In this respect, an additional set of zero-buoyancy heat transfer data is generated by extrapolating each *Ro* controlled data series, as seen in the plot of Fig. 8, to the limiting condition of *Bu*=0 using the regressive type of analysis. As the data trend with a fixed *Ro* in each plot of Fig. 8 follows a general trend of linear variation, the extrapolating process adopts the linear curve fitting routine that leads to the generation of $\overline{Nu}/\overline{Nu}_0$ data corresponding to zero $\beta(T_w-T_b)$. These fitted lines, as well as the $\overline{Nu}/\overline{Nu}_0$ ratios at the zero-buoyancy condition, are shown in Fig. 8. The $\overline{Nu}/\overline{Nu}_0$ ratios over the leading and trailing endwalls at the BP and FP locations are accordingly correlated by Eq. (5)

$$\frac{\overline{Nu}_{L,T}}{\overline{Nu}_0} = \phi_1\{Ro\} + \phi_2\{Ro\} \times Ro^2\beta(T_w - T_b)(R/d) \qquad (5)$$

In Eq. (5), ϕ_1 and ϕ_2 are functions of *Ro*. The ϕ_1 function evaluates the $\overline{Nu}/\overline{Nu}_0$ ratios at the zero-buoyancy condition that quantifies the individual Coriolis force effects on heat transfer. The interactive mechanism between the Coriolis forces and rotating buoyancy is captured as the ϕ_2 function by taking into account the various *Ro* controlled slopes for the fitted lines shown in Fig. 8. A physical interpretation of these ϕ_2 values is the various degrees of buoyancy impact on $\overline{Nu}/\overline{Nu}_0$. The negative ϕ_2 values signify the impairing heat transfer impacts; while the magnitudes of ϕ_2 index the degree of *Bu* impacts on heat transfer. Figure 9 displays the varying manner of the ϕ_1 value, which represents the $\overline{Nu}/\overline{Nu}_0$ at zero-buoyancy condition, against *Ro* at BP and FP locations.

The data trends depicted in Figs. 9(*a*) and 9(*b*) restate the heat transfer variations caused by the Coriolis force effects alone. At both BP and FP locations on the leading endwall, the $\overline{Nu}/\overline{Nu}_0$ ratios are initially reduced from the zero-rotation references as *Ro* increases from 0 to 0.1. Such heat transfer impediments on the leading endwall of the rotating pin-fin channel are soon recovered with the $\overline{Nu}/\overline{Nu}_0$ to be kept increasing as *Ro* increases above than 0.1. On the trailing endwall, the $\overline{Nu}/\overline{Nu}_0$ ratios increase linearly as *Ro* increases. It is noticed that, by adding the impeding buoyancy effects, the $\overline{Nu}/\overline{Nu}_0$ ratios are somewhat reduced. Therefore the ϕ_1 curves shown in Fig. 9 limit the upper bound heat transfer performances for in this rotating pin-fin channel. The review of the present data ranges with involvements of the impairing *Bu* effects indicate that the ranges of $\overline{Nu}/\overline{Nu}_0$ on the leading and trailing endwalls are 0.8–1.6 and 1–2.1, respectively. The upper bounds of maximum $\overline{Nu}/\overline{Nu}_0$ ratios on the leading and trailing endwalls defined by the zero-buoyancy performances can reach 1.8 and 2.4, respectively. Converting the entire ranges of $\overline{Nu}/\overline{Nu}_0$ including the zero-buoyancy conditions into the HTE effectiveness in terms of $\overline{Nu}/\overline{Nu}_\infty$ shows the $\overline{Nu}/\overline{Nu}_\infty$ ratios on the leading and trailing endwalls fall in the ranges of 2.6–5.9 and 3.3–6.9 respectively. The comparison of ϕ_1 values between the leading and trailing counterparts, as shown in Fig. 9, clearly indicates the increased heat transfer differences as *Ro* increases due to the enhanced Coriolis effects.

The variations in ϕ_2 versus *Ro* on the leading and trailing endwalls, as seen in Fig. 10, depict a general trend of complex exponential function. The ϕ_2 values remain all negative and increase to asymptotic values. However, the magnitudes of ϕ_2 are reduced as *Ro* increases. Although the date points collected in Fig. 10 reveal a general trend of developing toward the positive ϕ_2 values, all the *Ro* controlled ϕ_2 values still remain negative in the parametric range of $0 < Ro \leq 1.4$. Also the magnitudes of ϕ_2 value on the trailing endwall are consistently larger than the leading counterparts. The trailing wall thus undergoes the more severe impairing buoyancy impacts on heat transfer relative to its leading counterpart in this rotating pin-fin channel. Considering all the data trends revealed in Figs. 8–10, a set of $\overline{Nu}/\overline{Nu}_0$ correlations that can determine $\overline{Nu}$ values at the BP and FP locations in the developed flow region on the leading and trailing endwalls of this rotating pin-fin channel is generated as Eqs. (6)–(9).

For leading (FP),

$$\overline{Nu}/\overline{Nu}_0 = (0.756 + 0.245e^{-29.2Ro}) + (0.882 - 0.604Ro + 76.2e^{-27Ro}) \times Bu \qquad (6)$$

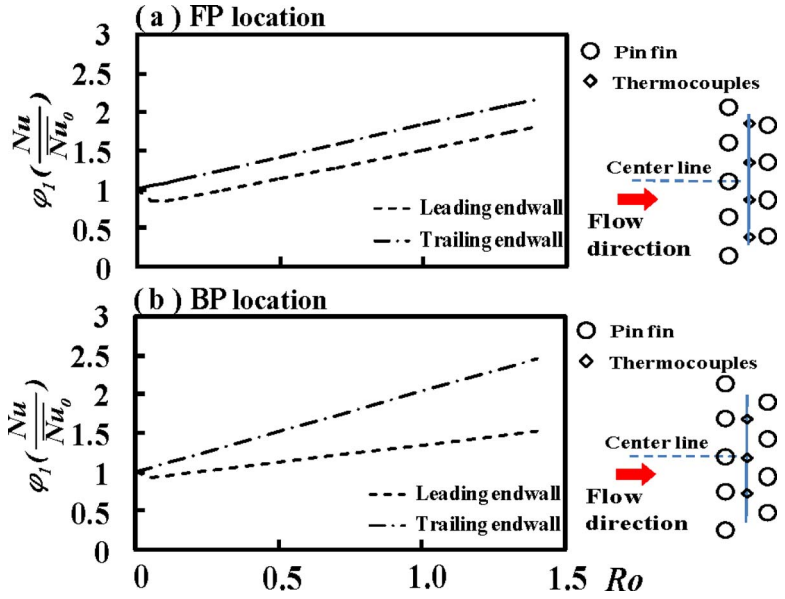

Fig. 9 Variations in $\overline{Nu}/\overline{Nu}_0$ at zero-buoyancy condition against *Ro* at (*a*) FP and (*b*) BP locations

For leading (BP),

$$\overline{Nu}/\overline{Nu}_0 = (0.904 + 0.0962e^{-60.9Ro}) + (0.703 - 0.495Ro + 72.1e^{-15.2Ro}) \times Bu \quad (7)$$

For trailing (FP),

$$\overline{Nu}/\overline{Nu}_0 = (-40.8 + 3.57Ro + 41.9e^{-0.0791Ro}) + (1.09 - 0.681Ro + 183e^{-21.4Ro}) \times Bu \quad (8)$$

For trailing (BP),

$$\overline{Nu}/\overline{Nu}_0 = (-30 + 4.58Ro + 31e^{-0.137Ro}) + (2.43 - 1.62Ro + 311e^{-24.4Ro}) \times Bu \quad (9)$$

Equations (6)–(9) correlate and represent all the $\overline{Nu}/\overline{Nu}_0$ measurements generated here, which can be readily adopted for computational fluid dynamics (CFD) validations. A comparison of all the experimental measurements with the calculated results for $\overline{Nu}$ using Eqs. (6)–(9) is performed. There are 90% of experimental data found to agree with the correlation results within ±30% discrepancies, as shown in Fig. 11. However, the applications of Eqs. (6)–(9) beyond the parametric ranges specified in Table 1 give rise to the extrapolating uncertainties.

With the assistance of the derived $\overline{Nu}_0$ and $\overline{Nu}$ correlations, the charts, which refer to the rotation induced relative heat transfer modifications from the static references in terms of $\overline{Nu}/\overline{Nu}_0$, are constructed for this rotating pin-fin channel. Within the parametric conditions covered by the present study, Fig. 12 depicts the variations in $\overline{Nu}/\overline{Nu}_0$ contours against *Ro* and *Bu* over the leading and trailing endwalls at the FP and BP locations. As the buoyancy interaction impedes heat transfer performances, $\overline{Nu}/\overline{Nu}_0$ consistently decreases as *Bu* increases in the range of $0 < Ro < 1.4$, as seen in each plot of Fig. 12. The minimum $\overline{Nu}/\overline{Nu}_0$ of 0.89 and 0.8 at the BP and FP locations over the leading endwall are, re-

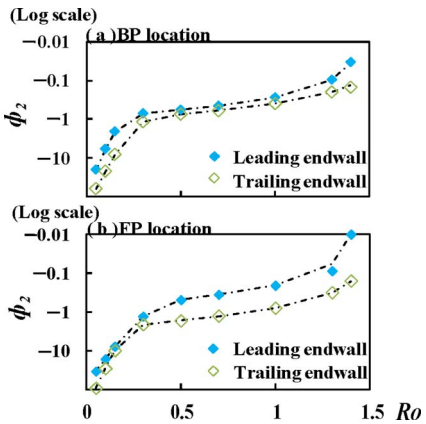

Fig. 10 Variations in ϕ_2 values against *Ro* on the leading and trailing endwalls at (*a*) BP and (*b*) FP locations

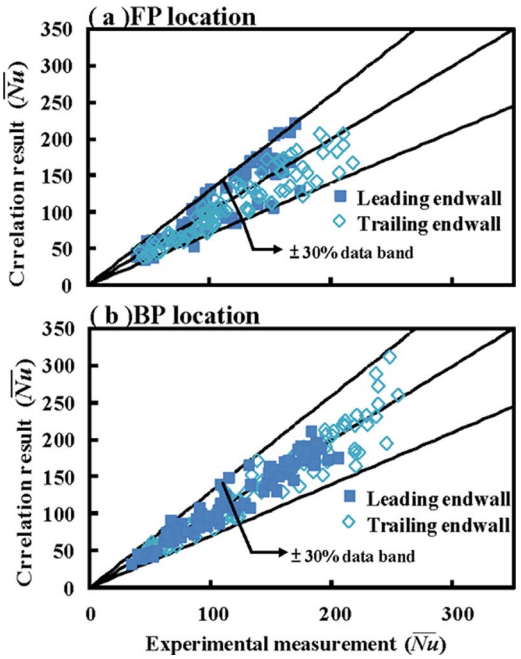

Fig. 11 Comparison of experimental measurements with the calculated results for $\overline{Nu}$

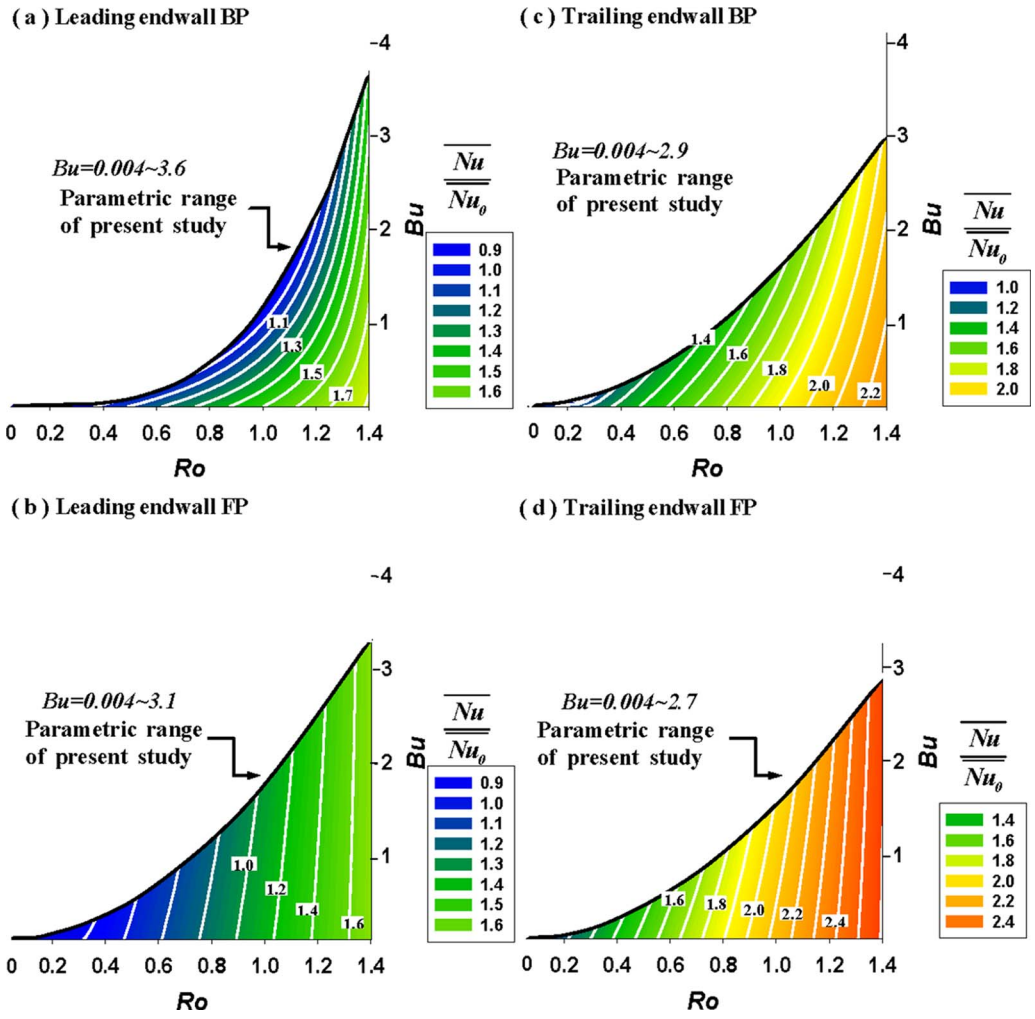

Fig. 12 Variations in $\overline{Nu}/\overline{Nu}_0$ contours against *Ro* and *Bu* over (*a*) and (*b*) leading and (*c*) and (*d*) trailing endwalls at FP and BP locations

spectively, resolved at $Ro=0.1$ on the edge of the parametric limits specified in Figs. 12(*a*) and 12(*b*). On the trailing endwall, $\overline{Nu}/\overline{Nu}_0$ consistently increases with the increase in *Ro* but is reduced as *Bu* increases. Such synergistic *Ro*-*Bu* impacts lead to high $\overline{Nu}/\overline{Nu}_0$ at the bottom right corners of Figs. 12(*c*) and 12(*d*). The maximum $\overline{Nu}/\overline{Nu}_0$ of 2.2 and 2.4 develop at $Ro=1.4$ with the zero-buoyancy condition over the trailing endwall at BP and FP locations respectively. From the viewpoints of design and operation, $\overline{Nu}/\overline{Nu}_0$ is clearly the functions of *Ro* and *Bu* impacts, as shown in Fig. 12. The parametric regime in which $\overline{Nu}/\overline{Nu}_0$ is lesser than unity on the leading endwall needs design precautions in order to prevent the development of hot spots on the rotor blade.

4 Conclusions

This experimental study simulates closely both parametric and geometric conditions of a rotating pin-fin channel with cooling applications to the typical coolant passage inside the trailing edge of a gas turbine rotor blade. The *Ro* range of 0–1.4 examined here considerably extends previous experiences with the first time heat transfer data generated by this study. Several concluding remarks are obtained as follows.

1. Local Nu_0 values over the first 3–4 pin-rows along the pin-fin channel increase progressively toward the asymptotic levels, as the trade-off between the thickened downstream boundary layers and the streamwise enhanced HTE mechanisms tripped by pin-rows. The spanwise heat transfer variations show the zigzag patterns with the higher heat transfer rates at BP locations. With $5000 \leq Re \leq 20{,}000$, the range of Nu_0/Nu_∞ falls between 3.1 and 2.3. The reduced Nu_0/Nu_∞ (HTE ratio) as Re increases indicates that the HTE effect produced by this pin-fin array is Re dependent. The spanwise-averaged $\overline{Nu}_0$ correlations at BP and LP locations are derived as Eqs. (3) and (4).
2. Rotational heat transfer rates on the trailing endwall are constantly higher than those leading counterparts, with the rotating buoyancy effects impairing local heat transfer. The increase in *Ro* from 0 to 0.1 reduces heat transfer levels on leading endwall from the Nu_0 references. But the heat transfer levels on the leading endwall are subsequently increased as *Ro* increases from 0.1 to 1.4. On the trailing endwall, the increase in *Ro* produces consistent heat transfer elevations from the Nu_0 references. Along with these typical rotational effects on local Nu, the spanwise zigzag Nu patterns over the leading endwall are systematically moderated as *Ro* increases; however, the spanwise zigzag Nu patterns are still persistent on the trailing endwall. Acting by the Coriolis forces, the endwall vortices tripped by pin-rows attach firmly on the trailing endwall but are lifted on the leading endwall in this rotating pin-fin channel.
3. Isolation of Re effects from the synergistic *Ro*-*Bu* impacts

on Nu are achieved by representing the rotational heat transfer data in terms of $\overline{Nu}/\overline{Nu}_0$. Due to the combined *Ro*-*Bu* impacts involving the impairing *Bu* effects, the ranges of $\overline{Nu}/\overline{Nu}_0$ on the leading and trailing endwalls are 0.8–1.6 and 1–2.1, respectively. The upper bounds of maximum $\overline{Nu}/\overline{Nu}_0$ develop at the conditions without buoyancy impacts with $\overline{Nu}/\overline{Nu}_0$, respectively, reaching 1.8 and 2.4 on the leading and trailing endwalls. The worst heat transfer scenarios develop on the leading endwall that lead $\overline{Nu}/\overline{Nu}_0$ to 0.89 and 0.8 at the BP and FP locations, respectively.

4. Increasing rotating buoyancy caused a decrease in wall heat transfer at all measurement locations. The relative decrease in heat transfer with buoyancy was greater at low *Ro* and less at the highest *Ro*.
5. A set of heat transfer correlations that permits the evaluation of $\overline{Nu}$ at FP and BP locations in the developed flow regime of present rotating pin-fin channel is derived to represent the experimental heat transfer data generated by this study with the individual and interactive influences of Re, *Ro*, and *Bu* assessed.

Nomenclature

A and n = coefficient
Bu = buoyancy number$=Ro^2\beta(T_w-T_b)(R/d)$
C_p = specific heat of fluid ($Jkg^{-1}\ K^{-1}$)
d = hydraulic diameter of test channel (m)
d_p = pin diameter (m)
H = pin height (m)
k = thermal conductivity of fluid ($W\ m^{-1}\ K^{-1}$)
Nu = rotational Nusselt number$=qd/[k(T_w-T_b)]$
Nu_0 = stationary Nusselt number for pin-fin duct
Nu_∞ = Dittus–Boelter Nusselt number for static smooth duct based on channel hydraulic diameter
$\overline{Nu}$ = spanwise-averaged Nusselt number in the developed flow region
P_X = X-wise pin pitch (m)
P_Y = Y-wise pin pitch (m)
Pr = Prandtl number$=\mu C_p/k$
q = convective heat flux (Wm^{-2})
R = rotating radius at midspan of test duct from rotating axis (m)
Re = Reynolds number$=\rho W_m d/\mu$
Ro = rotating number$=\Omega d/W_m$
T_b = fluid bulk temperature (K)
T_w = wall temperature of test duct (K)
W = channel width (m)
W_m = mean through flow velocity ($m\ s^{-1}$)
X and Y = dimensionless axial and spanwise coordinates$=x/d,\ y/d$
β = thermal expansion coefficient of fluid (K^{-1})
ρ = fluid density ($kg\ m^{-3}$)
μ = fluid dynamic viscosity ($kg\ s^{-1}\ m^{-1}$)
Ω = rotating speed of test duct ($rad\ s^{-1}$)
Ψ, ϕ_1, and ϕ_2 = unknown functions

Subscripts

L = refers to centerline of rotating leading edge
T = refers to centerline of rotating trailing edge
0 = refers to nonrotating situation

References

[1] Chyu, M. K., and Natarajan, V., 1996, "Heat Transfer on the Base Surface of Three-Dimensional Protruding Elements," Int. J. Heat Mass Transfer, **39**, pp. 2925–2935.
[2] Won, S. Y., Mahmood, G. I., and Ligrani, P. M., 2004, "Spatially-Resolved Heat Transfer and Flow Structure in a Rectangular Channel With Pin Fins," Int. J. Heat Mass Transfer, **47**, pp. 1731–1743.
[3] Van Fossen, G. J., 1982, "Heat-Transfer Coefficients for Staggered Arrays of Short Pin-Fins," ASME J. Eng. Power, **104**, pp. 268–274.
[4] Chyu, M. K., Hsing, Y. C., Shih, T. I.-P., and Natarajan, V., 1999, "Heat Transfer Contributions of Pins and Endwall in Pin-Fin Arrays: Effects of Thermal Boundary Condition Modeling," ASME J. Turbomach., **121**, pp. 257–263.
[5] Metzger, D. E., Berry, R. A., and Bronson, J. P., 1982, "Developing Heat Transfer in Rectangular Ducts With Staggered Arrays of Short Pin Fins," ASME J. Heat Transfer, **104**, pp. 700–706.
[6] Simoneau, R. J., and Van Fossen, G. J., 1984, "Effects of Location in an Array on Heat Transfer to a Short Cylinder in Cross Flow," ASME J. Heat Transfer, **106**, pp. 42–48.
[7] Chyu, M. K., 1990, "Heat Transfer and Pressure Drop for Short Pin-Fin Arrays With Pin-Endwall Fillet," ASME J. Heat Transfer, **112**, pp. 926–932.
[8] Mezger, D. E., Fan, C. D., and Haley, S. W., 1984, "Effects of Pin Shape and Array Orientation on Heat Transfer and Pressure Loss in Pin Arrays," ASME J. Eng. Gas Turbines Power, **106**, pp. 252–257.
[9] Sahiti, N., Lemouedda, A., Stojkovic, D., Durst, F., and Franz, E., 2006, "Performance Comparison of Pin Fin in-Duct Flow Arrays With Various Pin Cross-Sections," Appl. Therm. Eng., **26**, pp. 1176–1192.
[10] Sparrow, E. M., Ramsey, J. W., and Altemani, C. A. C., 1980, "Experiments on in-Line Pin Fin Arrays and Performance Comparisons With Staggered Array," ASME J. Heat Transfer, **102**, pp. 44–50.
[11] Jubran, B. A., Hamdan, M. A., and Abdualh, R. M., 1993, "Enhanced Heat Transfer, Missing Pin and Optimization for Cylindrical Pin Fin Arrays," ASME J. Heat Transfer, **115**, pp. 576–583.
[12] Natarajan, V., and Chyu, M. K., 1994, "Effect of Flow Angle-of-Attack on the Local Heat/Mass Transfer From a Wall-Mounted Cube," ASME J. Heat Transfer, **116**, pp. 552–560.
[13] Chyu, M. K., Oluyede, E. O., and Moon, H.-K., 2007, "Heat Transfer on Convective Surfaces With Pin-Fins Mounted in Inclined Angles," ASME Paper No. GT2007-28138.
[14] Sahiti, N., Durst, F., and Geremia, P., 2007, "Selection and Optimization of Pin Cross-Sections for Electronics Cooling," Appl. Therm. Eng., **27**, pp. 111–119.
[15] Willett, F. T., and Bergles, A. E., 2002, "Heat Transfer in Rotating Narrow Rectangular Pin-Fin Ducts," Exp. Therm. Fluid Sci., **25**, pp. 573–582.
[16] Kristoffersen, R., and Anderson, H. I., 1993, "Direct Simulations of Low-Reynolds-Number Turbulent Flow in a Rotating Channel," J. Fluid Mech., **256**, pp. 163–197.
[17] Lezius, D. K., and Johnston, J. P., 1976, "Roll-Cell Instabilities in Rotating Laminar and Turbulent Channel Flows," J. Fluid Mech., **77**, pp. 153–175.
[18] Murata, A., and Mochizuki, S., 2001, "Effect of Centrifugal Buoyancy on Turbulent Heat Transfer in an Orthogonally Rotating Square Duct With Transverse or Angled Rib Turbulators," Int. J. Heat Mass Transfer, **44**, pp. 2739–2750.
[19] Iskakov, K. M., and Trushin, V. A., 1985, "The Effect of Rotation on Heat Transfer in the Radial Cooling Channels of Turbine Blades," Teploenergetika (Moscow, Russ. Fed.), **32**, pp. 52–55.
[20] Harasgama, S. P., and Morris, W. D., 1988, "The Influence of Rotation on the Heat Transfer Characteristics of Circular, Triangular and Square-Sectioned Coolant Passages of Gas Turbine Rotor Blade," ASME J. Turbomach., **110**, pp. 44–50.
[21] Wagner, J. H., Johnson, B. V., and Hajek, T. J., 1992, "Heat Transfer in Rotating Passages With Smooth Walls and Radial Outward Flow," ASME J. Turbomach., **114**, pp. 847–857.
[22] Johnson, B. V., Wagner, J. H., Steuber, G. D., and Yeh, F. C., 1994, "Heat Transfer in Rotating Serpentine Passages With Trips Skewed to the Flow," ASME J. Turbomach., **116**, pp. 113–123.
[23] Parsons, J. A., Han, J. C., and Zhang, Y. M., 1994, "Wall Heating Effect on Local Heat Transfer in a Rotating Two-Pass Square Channel With 90° Rib Turbulators," Int. J. Heat Mass Transfer, **37**, pp. 1411–1420.
[24] Chang, S. W., and Morris, W. D., 1998, "A Comparative Study of Heat Transfer Between Rotating Circular Smooth-Walled and Square Rib-Roughened Ducts With Cooling Application for Gas Turbine Rotor Blades," JSME Int. J., Ser. B, **41**, pp. 302–315.
[25] Chang, S. W., and Morris, W. D., 2003, "Heat Transfer in a Radially Rotating Square Duct Fitted With in-Line Transverse Ribs," Int. J. Therm. Sci., **42**, pp. 267–282.
[26] Griffith, T.S., AI-Hadhrami, L., and Han, J.-C., 2003, "Heat Transfer in Rotating Rectangular Cooling Channels (AR=4) With Dimples," ASME J. Turbomach., **125**, pp. 555–563.
[27] Chang, S.W., Yang, T. L., and Wang, W. J., 2006, "Heat Transfer in a Rotating Twin-Pass Trapezoidal-Sectioned Passage Roughened by Skewed Ribs on Two Opposite Walls," Heat Transfer Eng., **27**, pp. 63–79.
[28] Chang, S. W., Liou, T. M., Yeh, W. H., and Hung, J. H., 2007, "Heat Transfer in a Rotating Square-Sectioned Duct With Two Opposite Walls Roughened by 45 Degree Staggered Ribs at High Rotation Numbers," ASME J. Heat Transfer, **129**, pp. 188–199.

[29] Chang, S. W., Liou, T. M., Chiou, S. F., and Chang, S. F., 2008, "Heat Transfer in High-Speed Rotating Trapezoidal Duct With Rib-Roughened Surfaces and Air Bleeds From the Wall on the Apical Side," ASME J. Heat Transfer, **130**, p. 061702.
[30] Kim, J. H., Simon, T. W., and Viskanta, R., eds., 1993, "Journal of Heat Transfer Policy on Reporting Uncertainties in Experimental Measurements and Results," ASME J. Heat Transfer, **115**, pp. 5–6.
[31] Dittus, F. W., and Boelter, L. M. K., 1930, University of California Publication for Engineering, **2**, p. 443.7.
[32] Lyall, M. E., Thrift, A. A., Thole, K. A., and Kohli, A., 2007, "Heat Transfer for Low Aspect Ratio Pin Fins," ASME Paper No. GT2007-27431.

Investigation of Sand Blocking Within Impingement and Film-Cooling Holes

N. D. Cardwell
Department of Mechanical Engineering,
Virginia Polytechnic Institute,
Blacksburg, VA 24061

K. A. Thole
Department of Mechanical and Nuclear Engineering,
Pennsylvania State University,
University Park, PA 16802

S. W. Burd
Pratt & Whitney,
United Technologies Corporation,
East Hartford, CT 06108

Gas turbines are not generally designed for operation with a particle laden inlet flow but, in fact, are commonly operated in unclean environments resulting in dirt, sand, and other debris ingestion. In addition to the negative effects within the main gas path, for aeroengines these particles are pulled into the coolant system where they can clog cooling passages and erode internal surfaces. Unlike previous research that focused on deposition and erosion within the main gas path, this study evaluated blocking in a double wall liner whereby both impingement and film-cooling holes were simulated. Double wall liners are commonly used in the combustor and turbine for combined internal and external cooling of metal components. Specifically, sand blockages were evaluated through comparisons of measured flowrates for a particular pressure ratio across the liner. Four liner geometries were tested whereby the coolant hole size and orientation were varied in test coupons. At ambient temperature, blocking was shown to be a function of the impingement flow area. A significant rise in blocking was observed as sand and metal temperatures were increased. The overlap between the impingement and film-cooling holes was also found to have a significant effect. [DOI: 10.1115/1.3106702]

1 Introduction

Figure 1 shows two instances of gas turbines operating in dust-laden environments. Complete filtration of the intake air is often deemed infeasible because of the associated pressure drop, filter replacement and cleaning requirements, and overall increase in engine weight. Particle ingestion into a gas turbine can have serious effects on both performance and engine service intervals. While passing through the engine, ingested debris collides with and subsequently erodes the metal surfaces. These particles, which are also pulled into the coolant air bypass, clog the internal channels thereby reducing coolant mass flow and increasing part temperature. Elevated temperatures within the engine can melt the sand, further increasing the likelihood of deposition and blocking within the cooling channels. Two commonly used cooling techniques within a gas turbine are impingement and film-cooling (FC). Impingement cooling is used to cool parts from the inside, as this type of flow would be aerodynamically disruptive within the main gas path. Film-cooling is often employed on the external surface by providing a coolant film along the exterior.

For this study, the combination of impingement and film-cooling holes, often referred to as a double wall liner, was subjected to a sand-laden coolant stream. Measurements of the coolant flow at a given pressure ratio (PR) were made to deduce the reduction in flow that would occur in an engine under sand-laden coolant conditions. The following parameters were investigated: liner geometry, pressure ratio, entering sand temperature, sand amount, and metal temperature. This paper also contains a literature review and description of experimental methods in addition to the experimental results performed at both ambient and engine temperatures.

2 Relevant Past Studies

As stated previously, ingestion of foreign particles can adversely affect a turbine's performance and lifecycle. The past studies review begins with previous research focusing on actual incidents of in-service turbine hardware experiencing debris ingestion. It is followed by a review of simulated experimental and computational studies on the effects of particle ingestion relevant to gas turbine applications.

2.1 Research Motivation. The most common instances of foreign particle ingestion for a commercial aircraft engine arise from entering a volcanic ash cloud. An early instance of this potentially disastrous situation was on the June 24th, 1982 encounter of British Airways 77 where a Boeing 747, powered by Rolls-Royce RB-211 engines, flew into the eruption cloud of Mt. Galunggung near Indonesia [2]. Upon entering the cloud, the aircraft was forced into an emergency landing after all four engines experienced a temporary flameout. Upon investigation after landing, significant erosion and deposition was observed, as shown in Fig. 2. This encounter, along with several others, prompted the aircraft community to address this new danger [4] and instruct pilots on tactics to avoid ash clouds and emergency procedures during an encounter [5]. The most well known instance of volcanic ash ingestion occurred on December 15th, 1989 when a Boeing 747-400, powered by GE CF6-80C2 engines, entered an ash cloud from Mt. Redoubt volcano near Anchorage, AL [6]. All engines experienced a flame-out after being throttled up in an attempt to climb above the debris. After numerous restart attempts and losing more than 10,000 ft in altitude, the crew was finally able to restart the engines and make an emergency landing. Repairs to the aircraft totaled more than 80 million dollars, which included the total replacement of all four engines. These and other instances of aircraft traversing through volcanic dust clouds prompted studies on the effects of ash ingestion for gas turbine engines and also the development of satellite and radar systems to warn pilots of possible encounters. Despite these precautions, the ingestion of volcanic debris is still considered to be a significant danger to commercial airliners.

With regards to military aircraft, helicopter pilots in Desert Shield and Desert Storm were forced to come up with unorthodox operational procedures to help mitigate the negative effects of sand ingestion for virtually all helicopter platforms [7]. One such procedure was lifting the helicopter off before the recommended engine warm-up period and turning off the engines immediately after a landing. This reduced the total amount of sand being in-

Manuscript received February 1, 2009; final manuscript received February 4, 2009; published online January 21, 2010. Review conducted by David Wisler. Paper presented at the ASME Turbo Expo 2008: Land, Sea and Air (GT2008), Berlin, Germany, June 9–13, 2008.

Fig. 1 Gas turbines operated in dust laden environments [1]

gested into the engine while under load, which was primarily being stirred up by the rotors. Pilots also incorporated strict turbine washing regimes after each flight, which removed some of the deposits in the engine by flushing it with high pressure water.

2.2 Studies on Particle Ingestion. Several investigators have performed research as to the effects of particle ingestion with emphasis on gas turbines. The majority of these studies can be grouped into several categories: full-scale engine tests, accelerated erosion and deposition testing, and internal cooling blockage studies.

The earliest full-scale engine studies on dust ingestion were conducted by Batcho et al. [8] and Dunn et al. [9,10] in 1987. For their tests, several engines were operated with a dust-laden inlet stream while monitoring engine performance. After completion of testing, each engine was disassembled and the effects of sand ingestion were documented. They identified the following damage mechanisms that resulted in deterioration of engine performance: compressor erosion, deposition in the high pressure turbine, blockage of cooling holes in the high pressure turbine, and partial combustor fuel nozzle blockage. For their specific tests, however, the turbine inlet temperature was too low to result in sand glassification downstream of the combustor. While the concentration of sand ingested into the engine's environmental control system (ECS) was monitored, no attention was given as to the effects of particles traveling through the coolant bypass and into the combustor and turbine internal cooling geometries.

As a result of the high cost associated with these types of engine tests, a hot section test system (HSTS) was developed by Kim et al. [11] to simulate the exit temperature and flow of a T56 can-type combustor and the more modern F100 annular combustor. Actual engine hardware was installed downstream of the HSTS and different dust blends were introduced upstream of the HSTS for each test. It was concluded that deposition was dependent on sand composition, sand concentration, turbine inlet temperature, and metal surface temperatures. Molten deposition was reported in the turbine when inlet temperature and metal temperature were above 1177°C and 816°C, respectively. An independent cooling system was utilized thereby supplying the turbine components with a dust-free coolant stream, as the study was focused only on the effects of a particle laden main flow through the engine. Another study using the HSTS was performed by Weaver et al. [12]. This study evaluated the effects of cooling hole diameter, hole roughness, turbine inlet temperature, and vane geometry with a dust-laden main flow. Test vanes included Inconel® 617 and Lamilloy film-cooled cylinders as well as F100-PW-220 first stage turbine vanes. Unlike previous studies, the coolant stream was modified to accommodate both clean and dust-laden flows. Inspection after testing showed that the cooling holes or passages had negligible clogging from dust while there was significant deposition on the external surfaces at elevated turbine inlet and metal temperatures.

Fig. 2 Image of turbine nozzle guide vanes after ingestion of volcanic ash [3]

Another subject of study pertaining to dust ingestion is the erosion caused by particle impacts with metal surfaces. Accelerated erosion studies at metal temperatures of up to 815°C have been presented in the literature [13] showing the effects of impingement angle, temperature, particle and eroded surface character, and impact velocity [14,15]. Recently the focus of this group has been investigating the effect of different turbine blade coatings on erosion rates and the resulting surface roughness characteristics. A study by Tabakoff and Simpson [16] compared uncoated turbine and compressor blades to a number of different coatings at elevated temperatures. After testing, the blade weight was taken and compared with the original value. A similar study of coated and uncoated turbine vanes was performed by Hamed et al. [17] with the primary focus being on the resulting vane surface roughness. All of these studies support the argument that particle ingestion causes material erosion and deposition on external compressor and turbine surfaces.

Other researchers have developed a high temperature accelerated deposition facility with emphasis on studying the characteristics and chemical composition of material deposits on turbine surfaces [18]. Jensen et al. [18] recognized the need for accelerated deposition studies as deposit formation could take as much as 25,000 operation hours in an industrial gas turbine. Bons et al. [19] also quantified the surface characteristics and roughness levels for in-service turbine blades and vanes to serve as a basis of comparison for their accelerated tests. The results of the investigation by Bons et al. identified the leading edge region as having the highest levels of external deposition for the evaluated turbine hardware. Another interesting finding of this study was the measurement of substantial deposition on in-service turbine vanes operated at a turbine inlet temperature below 900°C, which was substantially less than the 1177°C threshold for deposition previously stated by Kim et al. [11].

A review of the current research on erosion and deposition in turbomachinery was presented by Hamed et al. [20]. In their paper, the authors presented a review of erosion studies including numerical studies of particle trajectories and collisions for the main gas path. A summary of computational and experimental studies on the mechanisms of particle delivery and deposition was also presented. The authors also addressed the performance and lifecycle reductions, which are associated with erosion and deposition. The paper does not, however, address what effects erosion and deposition have on internal cooling geometries. This is because of the lack of experimental research on internal cooling blockage associated with dirty inlet air.

A numerical study of particles within a square channel having periodically spaced ribs was performed by Tafti and Shah [21]. For their study, 10 μm particles were shown to be more sensitive to large flow structures within the channel. Particle impacts on the rib surfaces were evenly distributed and impacts on the side walls were preferentially concentrated in the region of the top and bottom ribs. This was not true for the 100 μm particles, which showed significantly higher tendency to impact the upstream surface of the rib as well as the reattachment region behind the rib.

Walsh et al. [22] have currently performed the only experimental investigation within the literature directly focusing on the effects of a dust-laden coolant stream. Their study was focused on the effects of metal temperature, coolant temperature, coolant pressure ratio, number of cooling holes, sand amount, and sand diameter on cooling hole blockage for a test coupon with laser drilled film-cooling holes. Walsh et al. concluded that increases in metal temperature had the most significant effect on cooling hole blockage. Walsh et al. reported 1–6% reduction in test coupon

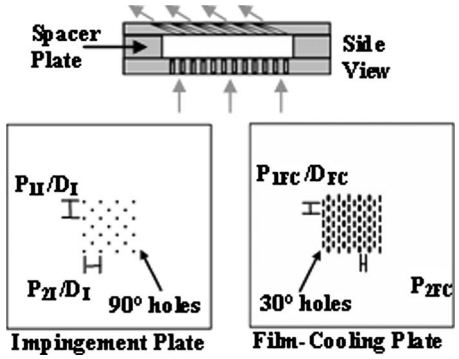

Fig. 3 Representative impingement and film-cooling double wall liner

flow parameter (FP) at engine representative metal and coolant temperatures for a pressure ratio range of 1.1–1.6 across the cooling holes.

3 Geometries of the Double Wall Liners

Combinations representing four different designs of a double wall liner utilizing impingement and film-cooling were chosen as representative of either a combustor liner or blade outer air seal. All liners consisted of an impingement plate, spacer plate, and film-cooling plate, as shown in Fig. 3. A periodic representation of the alignment between impingement and film holes is shown in Fig. 4 for each of the four liners tested. As can be seen, for each double wall liner, there was more or less overlap of the impingement jet locations with respect to the film hole entrances.

A 9×9 cm^2 sheet of Inconel® 625, which is a high nickel superalloy with similar physical properties to metals used within the engine, was used as the material base for each plate. The sheets had a machined finish and the thicknesses of the impingement, film-cooling, and spacer plates were 1.27 mm, 0.89 mm, and 1.65 mm, respectively. The impingement and film-cooling holes were machined 90 deg and 30 deg inclined to the surface, respectively. All cooling holes were created using electron discharge machining (EDM), chosen for its high dimensional tolerance at this scale in comparison to traditional and laser machinings. Each spacer plate was machined with a 3.8 cm^2 hole for the purpose of forming a sealed cavity between the impingement and film plates. All 12 plates were also machined with a six-hole mounting pattern to assure correct alignment for each test. Detailed information on each design is shown in Table 1.

For the geometries shown in Fig. 4, L1 was chosen as representative of an actual engine combustor liner. Each design was varied off of the L1 design to asses the effect of cooling hole diameter, total cooling flow area, and relative alignment between the impingement and film. The number of impingement holes was increased between L1 and L2 while keeping the cooling hole diameter and the number of film-cooling holes constant. This allowed for the investigation of total impingement flow area on sand blocking levels. Cooling hole size was reduced by 20% for L3 while keeping the total film-cooling flow area and impingement hole pattern equal to the values for L1. L4 had an increased cooling hole diameter of 20% above L1 and L2 in addition to a different pattern for the film-cooling and impingement holes.

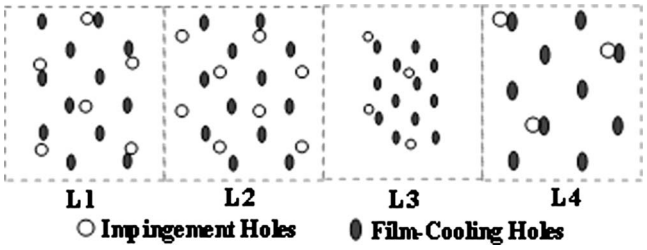

Fig. 4 Overlap between impingement hole exit and film hole entrance (periodic section shown)

4 Experimental Facility and Methodology

The level of hole blockage was quantified through the use of the flow parameter, as was done by Walsh et al. [22]. The FP, shown in the Nomenclature, is a convenient definition of a nondimensional mass flow parameter [23]. In the definition, P_{exit} refers to the discharge pressure of the cooling hole. During testing each liner was exhausted to the ambient laboratory environment, which allowed P_{exit} to be replaced by P_{amb} in the definition of flow parameter. There is one unique flow parameter that results for a given geometry, temperature, and pressure ratio.

The pressure ratio is defined as the ratio of supply pressure upstream for the impingement plate to the exit static pressure of the film-cooling plate. The coolant supply pressure P_{0C} was measured upstream of the impingement plate. If either the film-cooling or impingement holes were partially blocked, one would expect to measure a lower flowrate than for an unblocked hole at the same pressure ratio. This drop in flowrate also corresponded to a drop in flow parameter. Ultimately, matching the flow parameter with engine conditions resulted in a matched air residence time within the liner. For a realistic coolant temperature, matching the air residence time resulted in a particle residence time, which was similar to engine values. Matching the particle and air residence times assured that the thermal response of each particle, set by

Table 1 Double wall liner details

	Film cooling					
Liner No.	N_{FC}	D_{FC} (μm)	A_{FC} (mm^2)	L_{FC}/D	P_{1FC}/D	P_{2FC}/D
L1	64	635	20.3	2.8	7.0	7.1
L2	64	635	20.3	2.8	7.0	7.1
L3	100	508	20.3	3.5	8.8	7.1
L4	52	762	23.7	2.3	5.9	6.5
	Impingement					
Liner No.	N_I	D_1 (μm)	A_I (mm^2)	L_I/D	P_{1I}/D	P_{2I}/D
L1	25	635	7.9	2.0	11.3	11.3
L2	32	635	10.1	2.0	11.3	10.0
L3	25	508	5.1	2.5	14.1	14.2
L4	13	762	5.9	1.7	9.4	13.1

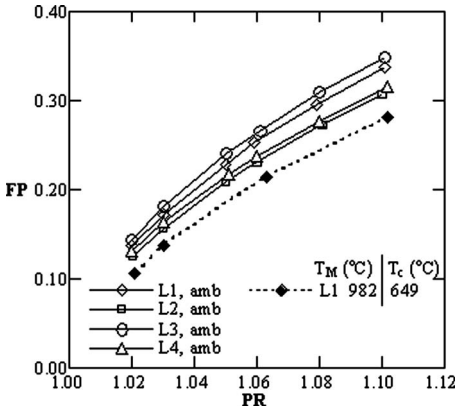

Fig. 5 Baseline flow parameter curves for all liners at ambient conditions and L1 at heated conditions

radiation and convection within the part, was equivalent to that occurring within the engine. It was because of these relationships that matching flow parameter as well as coolant and part temperatures were important for studying the blockage of an internal cooling geometry.

Before sand testing was performed, a baseline flow parameter curve, shown in Fig. 5, was established for each liner at ambient and elevated temperatures. At a given coolant temperature, each liner had a unique relationship between pressure ratio and flow parameter. Varying the coolant temperature changed the fluid viscosity within the liner, resulting in a new relationship between the flow parameter and the pressure ratio, as shown in Fig. 5. Each respective baseline was used to evaluate the total reduction in flow parameter (RFP) for a blocked liner, as shown in the Nomenclature.

Prior to each blockage test where sand was injected into the air stream, the measured baseline flow parameter was repeated to ensure that the hole passages were clear of any sand from the previous test. Note that the blockage was based on the flow parameter that occurred at the final pressure ratio of the clogged liner. This procedure is illustrated in Fig. 6 as a zoomed graph of ambient and heated baseline curves with representative data points. Under experimental conditions, the result of sand blocking with the liner was a sudden increase in pressure ratio and decrease in flow parameter. After clogging with sand, liner flow parameter and pressure ratio remained at their blocked values until the liner was cleaned manually. This method of using the reduction in flow parameter to quantify sand blockage within cooling holes was published in a similar study by Walsh et al. [22].

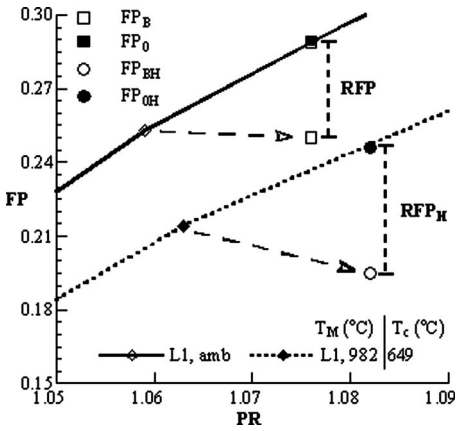

Fig. 6 Testing procedure for calculation of RFP

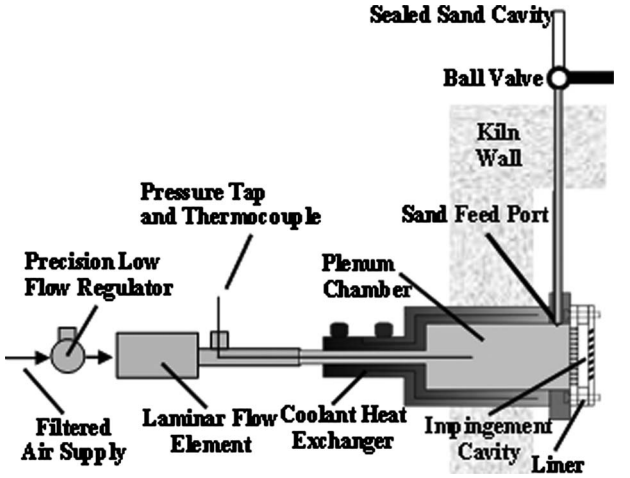

Fig. 7 Test facility used for studying sand blockages in the double wall liner coupons

The reduction in flow parameter can be reported several ways, whether an ambient temperature or a heated test was conducted. The previously defined variable RFP was used to compare the reduction in flow parameter under ambient conditions. For all cold cases, the RFP was based on the difference between the blocked flow parameter FP_B and the equivalent unblocked flow parameter at the blocked pressure ratio FP_0. The calculation of RFP is illustrated in Fig. 6. At heated conditions, the RFP_H was used whereby FP_{0H} was the equivalent unblocked baseline flow parameter at the blocked pressure ratio and FP_{BH} was the blocked value at heated conditions, as shown in Fig. 6.

4.1 Test Facility. Originally constructed by Walsh et al. [22], a test facility that generated a constant pressure upstream of the test coupons was modified to accept the double wall liner coupons, as seen in Fig. 7. High pressure room temperature air was supplied as coolant to the test coupons. This air was supplied to the laboratory, prior to which it was filtered and dried by an auxiliary compressor facility at approximately 550 kPa. A self-adjusting precision pressure regulator was used to control and regulate a constant coolant pressure. Downstream of the pressure regulator was a laminar flow element, having a maximum capacity of 1400 cm^3/s, which measured the total coolant flowrate through each liner. The required flowrate range was 170–830 cm^3/s.

Coolant temperatures were recorded within the center of the plenum chamber using a type K sheathed thermocouple probe as shown in Fig. 7. Coolant pressure was also measured at this location using a 1.6 mm diameter Inconel® tube as a pressure probe. The ratio of plenum diameter to impingement hole diameter varied from 144:1 to 96:1, thus assuring that pressure measured within the chamber was equivalent to the total coolant pressure.

Control of the metal temperature was accomplished by placing the liner and sand feed pipe within an electric kiln. The coolant temperature was controlled with a multipass heat exchanger supplied with ambient temperature compressed air, also shown in Fig. 7. Two fiberglass shielded type K thermocouples were affixed to the film-cooling plate using a high temperature ceramic adhesive to measure the metal temperature of the film-cooling plate. Each thermocouple was located in close proximity to a film-cooling hole, but not within the coolant jet. For each test, the difference in metal temperature measured between the two thermocouples was less than 5 °C. Variation of the metal and coolant temperature was accomplished by changing the kiln power and auxiliary heat exchanger flow for the coolant stream.

An electric oven, set at 150 °C, was used to dry the sand for 4 h before each test. This preliminary drying was performed to

avoid humidity clumping of the sand. Sand delivery to the liner was accomplished using a sealed gravity feed system, shown in Fig. 7. For each test, the prescribed sand amount was loaded above a valve that controlled access to the sand feed pipe. Opening this valve allowed the sand to pass vertically down the feed pipe, which was approximately 10 cm in length. This pipe terminated just upstream of the impingement plate and above the first row of cooling holes. The sand feed pipe was terminated above the cooling holes to insure that it did not disturb the inlet flow into the impingement plate. It is important to note that this resulted in a slightly higher mass loading of sand through the upper holes than through the lower holes. In addition, visual inspection after testing showed only trace amounts of sand within the coolant plenum, which meant that all the sand had become entrained within the coolant flow.

Since the tube supplying the sand was located within the hot portion of the kiln, as shown in Fig. 7, it is important to recognize that there was a significant heat up of the sand prior to entering the test coupon. Heat transfer to the falling sand was driven primarily through radiation from the section of the feed tube, which was exposed to the heated kiln. It is also important to note that the kiln temperature needed to be adjusted to maintain a constant coupon metal temperature for different coolant flowrates. For a constant coolant and kiln temperature, increasing the coolant flowrate to the coupon resulted in a decrease in the part's metal temperature. Because of this, the kiln temperature was varied to maintain a constant metal temperature for the different coolant flowrates. As a result, the supply tube temperature was changing with the kiln temperature. With the tube temperature changing, so did the entering sand temperatures. At elevated temperatures the probability of deposition increased when using heated sand. Therefore a transient calculation was performed for each test to estimate the sand temperature as it flowed into the impingement plate. Reported values of sand temperature were based on the mean particle size and assumed that the supply tube temperature was equal to the kiln temperature.

Each liner plate was affixed in the test setup using a ceramic adhesive and sealant that formed an airtight seal once cured up to 1260°C. Most importantly, the adhesive's coefficient of thermal expansion was similar to that of Inconel® 625, making it an ideal high temperature sealant. Steps were made to ensure each joint was hermetically sealed before and after each test, which was verified through repeating the baseline flow parameter-pressure ratio curve.

4.2 Sand Characterization. The chosen test sand, Arizona road dust, is comprised primarily of crushed quartz [22]. The analysis of each of the sand samples agree with the manufacturer's specification stating that it contains different phases of quartz (SiO_2) up to approximately 68–76%. The other major constituent is aluminum oxide (Al_2O_3) between 10–15%, with traces of iron oxide (Fe_2O_3), sodium silicate (Na_2O), lime (CaO), magnesium oxide (MgO), titanium dioxide (TiO_2), and potassium oxide (K_2O) in descending concentration. Arizona road dust has been used extensively for particle ingestion testing by the aviation, automotive, and filtration industries. Its chemical composition closely matches the types of sand found in arid desertlike climates. In addition to having a wide variation in particle size, this particular sand agglomerates readily forming large particles.

In characterizing the sand, a number of measurement methods were originally used to verify the particle size distribution. To reduce the particle breakup during the sizing measurement, a dry analysis was performed by using a series of mesh sieves ranging from 53 μm to 850 μm. The sieves were stacked thus filtering the sand in different bandwidths. These results are given in Fig. 8. The initial weight of each sieve and the sand were recorded. The entire stack was then lightly agitated for 4 h. After the agitation, each sieve was weighed and the amount of sand within each size band calculated. Several large conglomerates of particles were

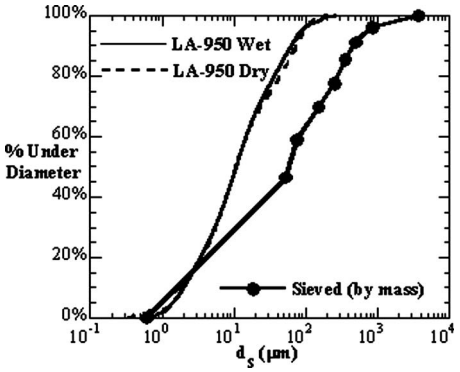

Fig. 8 Size distributions for the test sand obtained by several methods

observed in the 850 μm sieve. The maximum linear dimension of the conglomerates was measured by calipers as ~3000 μm and is listed in Fig. 8 as the 100% data point. A minimum particle diameter of 0.6 μm was measured using a Horiba Partica LA-950 laser diffraction analyzer. The LA-950 utilizes both a wet and dry measurement method, both of which caused significant breakup of particle agglomerations and were therefore deemed unsuitable for measurement of the overall size spectrum. The results of the laser diffraction methods are also included in Fig. 8.

Unless indicated, the amount of sand used was 0.35 g for each of the tests. The 0.35 g corresponded to a particle mass loading of 0.8, which was used by Walsh et al. [22] as representative of actual levels within the engine. Particle mass loading is defined as the mass flux ratio of the dispersed phase to the continuous phase [24]. For these tests the sand and cooling air served as the dispersed and continuous phases, respectively. Walsh et al. determined the appropriate mass loading by comparing the flow parameters of clean turbine components with field-operated components in which sand had entered the coolant stream and blocked cooling holes.

Deposition within the engine is most likely to occur over a longer period of time than the method used in this study in which a slug of sand was introduced to the part. To assure realistic results, several tests were performed to determine if a slug of a given sand amount has the same blocking characteristics as when the given sand amount was divided into portions. It was verified that the cumulative sand amount equaled that used for the single slug tests. Representative results of these comparison tests are shown in Fig. 9. The tests indicate an insensitivity to how the sand

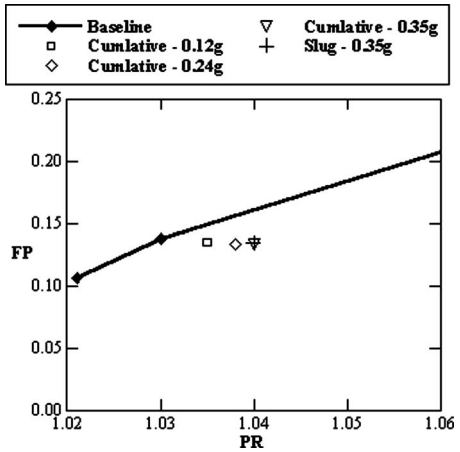

Fig. 9 Cumulative blocking effects versus slug flow for L1 at T_M=982°C and T_c=649°C

Table 2 Parameters used for combustor liner study

	T_M (°C)	T_c (°C)	m_s (g)	PR
L1		20°C	0.21, 0.35, 0.52	1.02, 1.03, 1.06, 1.10
L2			0.35	1.02, 1.03, 1.06, 1.10
L3			0.21, 0.35, 0.52	1.02, 1.03, 1.06, 1.10
L4			0.35	1.02, 1.03, 1.06, 1.10
L1	871, 982	538, 593, 649	0.35	1.03
L2	982	649	0.35	1.03
L3	982	649	0.35	1.03
L4	982	649	0.35	1.03

was introduced into the liner as both the cumulative and slug tests resulted in the same overall blockage.

4.3 Testing Procedure. Before each test, deposited sand from the previous test was removed from the impingement and film-cooling plates. The liner was considered free of previous sand remnants once its original baseline flow parameters could be reproduced.

After confirming the appropriate baseline flow parameter curve, the desired pressure ratio was set between 1.02 and 1.1. For an unheated test, the system was ready for sand injection. When performing a heated test, the test apparatus was placed in the kiln prior to setting the appropriate pressure ratio. The auxiliary cooling air flowrate and kiln power were varied until the desired coolant and metal temperature were set and steady. Required time to reach steady state for a heated test varied from 3–6 h, dependent on the desired test conditions.

With the pressure ratio set and steady-state temperatures achieved, the sand feed valve was quickly opened allowing the prescribed amount of sand to flow through the part. Once the pressure ratio and flow parameter were steady again, which typically took less than a few seconds, the new pressure ratio and flow parameter were recorded. The appropriate reduction in the flow parameter was then calculated relative to the clean liner flow parameter at the blocked pressure ratio. A 25 case repeatability study conducted by Walsh et al. [22] showed that three tests conducted for each case resulted in repeatable results to within 7%. In addition, multiple investigators have performed these studies spanning over 1 year. Their results also indicate that an average of three tests resulted in good repeatability. Each data point presented by this study corresponds to an average of three independent tests.

4.4 Uncertainty Analysis. Uncertainty and repeatability tests conducted by Walsh et al. [22] showed that three tests provided an adequate repeatability for this type of cooling blockage tests. Average variation of RFP between each group of three tests was 2.5% for both ambient and heated conditions. The propagation of uncertainty associated with the measurement methods was calculated for all test conditions, as outlined by Figliola and Beasley [25], to validate the observed results and trends. At both ambient and heated conditions, the uncertainty in flow parameter was approximately ±2% of the measured value for all pressure ratios. At ambient conditions, the overall uncertainty in RFP was 0.11 ± 0.011 at PR=1.02 and 0.16 ± 0.01 at PR=1.10. At heated conditions, the uncertainty in RFP_H was 0.18 ± 0.016 for PR =1.03, T_M=982°C, and T_c=649°C. Negligible variation in uncertainty was calculated between the different liner geometries. In addition, the uncertainty associated with measuring the prescribed sand amount was $0.35\ \text{g} \pm 0.005\ \text{g}$.

4.5 Derivation of the Test Matrix. Significant consideration was given to the generation of the test matrix, shown in Table 2. The nominal coolant temperature chosen for the high temperature testing was 649°C. With respect to external metal temperatures, the combustor liner typically operates in excess of 1000°C. However, a maximum metal temperature of 982°C was chosen because of the material limitations of Inconel® 625 as it melts at a lower temperature than proprietary engine alloys.

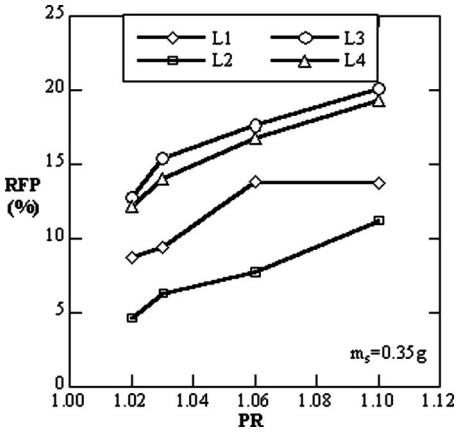

Fig. 10 %RFP verses pressure ratio for all liners at ambient temperature

With regards to entering sand temperature, no information was available as to the levels seen within the engine. Whether entering sand temperature was above or below the coolant temperature value was a function of particle residence time, slip velocity, and wall collision rate. Since realistic engine values for these variables are unknown, the maximum limitations of the testing capabilities were chosen to evaluate this parameter resulting in an entering sand temperature range of 316–760°C. This range was set by the minimum and maximum heated lengths of the sand feed tube within the limitations of the kiln's interior dimensions.

5 Discussion of Results

A number of tests were conducted to analyze the effect of sand being ingested into several double wall liner designs. The experimental results are broken into two sections: ambient temperature and elevated temperature. For the ambient temperature tests, the effects of pressure ratio, liner geometry, and sand amount were investigated. At elevated temperatures, the effects of liner geometry, film-plate metal temperature, and entering sand temperature were evaluated. The ambient results will be discussed prior to the high temperature results. In Secs. 5.1–5.4 and 6, the reduction in flow parameter will be referred to as an increase or decrease in "blockage."

5.1 Ambient Temperature Results. Figure 10 compares the blockage levels for all four liner geometries at a range of pressure ratios given a nominal sand amount of 0.35 g. An increase in pressure ratio from 1.02 to 1.10 resulted in elevated blockage for all liners with a maximum increase in RFP from 12% to 20% for L3. As seen in Fig. 10, at all pressure ratios the liners showed the same performance trend: lowest values of blockage for L2 and highest blocking levels observed with L3. The results show that the cooling hole diameter, both impingement and film, did not solely dictate the level of blocking for a given design. L3, despite having a 33% smaller cooling hole diameter than L4, varied in RFP less than 1% relative to L4. L1 and L2, despite having the same cooling hole size, showed a difference in blockage of approximately 6% at a pressure ratio of 1.06. However, when considering the total flow area through the impingement plate, consistent trends were identified. Figure 11 shows the same data as Fig. 10 but replotted versus the total flow area of each liner's impingement plate. Representing the data in this manner indicates that blocking for a given liner design decreases monotonically with increasing impingement flow area.

It was concluded that blocking levels within the liner, at ambient temperatures, were influenced by several different factors that

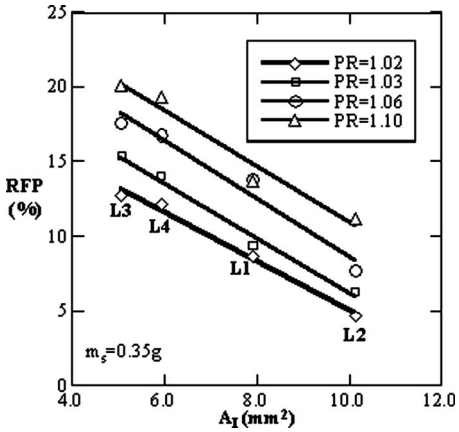

Fig. 11 Ambient temperature results plotted versus impingement flow area for all liners

are unique to a double wall liner design. The two dominant factors were filtration of large particles by the impingement plate before entering the impingement cavity (refer to Figs. 3 and 7) and the breakup of particles, which travel through the impingement holes and impact against the upstream side of the film-cooling plate.

It was observed that the impingement plate acted as a filter for the film-cooling plate with respect to sand particles and agglomerations whose maximum linear dimensions were equal to or greater than the impingement hole diameter. Approximately 7% of the particles tested were above 600 μm in diameter, which was nominally the size of each liner's impingement holes. Particles in this size range blocked within the impingement holes and were therefore unable to convect into the cavity upstream of the film-cooling holes. It is also important to recall that the film-cooling and impingement hole sizes were matched for each liner configuration. For this particular design, the impingement plate was filtering out all of the larger particles, which could have blocked cooling holes within the film-cooling plate.

Particles, which did not stick to the upstream side of the impingement plate or block within the impingement holes, were carried into the impingement cavity by the coolant flow. Upon exiting the impingement holes, the particles impacted on the upstream surface of the film-cooling plate. This impingement broke up the particles, increasing their likelihood to pass through the film-cooling holes. Post-test inspection of the liner confirmed that the particles were impinging on the upstream side of the film-cooling plate, as shown in Fig. 12. The particle impingement velocities were high enough to locally abrade the metal surface, as shown by the dark circles on the upstream side of the film-cooling plate in Fig. 12.

A study by Land et al. [26], performed congruently with this research, confirmed that particle breakup does occur within the double wall liner. The study compared the relative blocking characteristics of a combined impingement and film-cooling liner with a film-cooling only liner. Land et al. [26] reported a ~300% increase in blockage with the film-cooling only configuration when compared with the double wall liner thus verifying that the impingement resulted in a beneficial breakup of the sand particles within the cavity.

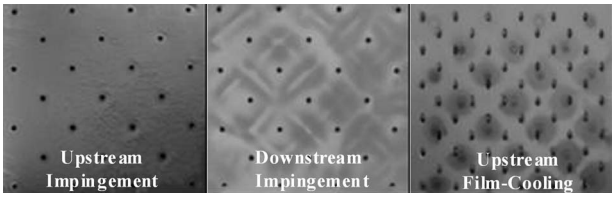

Fig. 12 Post-test images of sand deposition patterns at ambient temperature for L1 at PR=1.03

For the presented research, further visual inspection of the impingement and film-cooling holes showed that the bulk of the blockage occurred at the entrance to and within the impingement holes. Conversely, very little blockage was observed within or around the film-cooling holes. The breakup of impinging particles and impingement plate filtering resulted in significantly higher amounts of blockage in and around the impingement holes when compared with the film-cooling plate.

Since all tests were performed with a nominal amount of sand, it is logical that a liner with less impingement flow area would block at a higher rate than a liner with a large impingement flow area. Impingement flow area and particle breakup do not, however, offer insight into the cause of elevated blocking for all liners as pressure ratio was increased. Blocking sensitivity to pressure ratio results from how well particles follow the coolant flow. As the pressure ratio was increased, so did the mean velocity of air through the part therefore resulting in a decreased time characteristic of the flow τ_f. The particle response time τ_s is commonly used to describe the time required for a particle to respond to a change in velocity. In an average sense, τ_s remained constant for our testing since it was primarily a function of particle density and diameter. Therefore an increased pressure ratio resulted in an increased average particle Stokes number (St).

Stokes number is commonly used to define how well a given particle will follow the fluid surrounding it. Particles with a St $\ll 1$ are assumed to follow the flow perfectly while particles having a St $\gg 1$ are considered ballistic and are mostly unaffected by the fluid [24]. Studies by Tu et al. [27] showed that, for a rebounding flow over a curved wall, increased Stokes numbers were associated with particle trajectories deviating from the fluid streamlines thereby increasing the likelihood of wall collisions.

Calculations were performed to determine the Stokes number of 1 μm and 50 μm sand particles traveling through the liner. The impingement jet velocity and impingement hole diameter were chosen as the characteristic length and velocity of the coolant flow within the cavity. At 50 μm, particle Stokes numbers were above 500 for all pressure ratios. It was therefore assumed that the trajectories of sand particles at this size or larger deviated greatly from the cooling air path. For a 1 μm particle traveling through an impingement hole, Stokes numbers were slightly less than unity for all four liners. Therefore the Stokes number of the 1 μm particles fell within the range where particle motion was significantly affected by the coolant air but did not follow it perfectly. Increasing pressure ratio from 1.02 to 1.10 doubled the particle Stokes number for all particle sizes. We may infer that increases in pressure ratio also corresponded to an increased likelihood that sand particles would collide with the surfaces in and around the cooling holes. The increased number of wall collisions ultimately related to a higher probability of deposition for a given sand amount. Therefore elevated collision and deposition rates were the cause of the increased blocking at higher pressure ratios.

5.2 Ambient Temperature Results With a Varied Sand Amount. As explained previously, L3 exhibited the highest blockage of the four liner designs tested because of its relatively small impingement flow area. Therefore L3 was chosen to evaluate the sensitivity of the blocking to sand amount. As previously described for the nominal case, sand amounts were determined from the studies by Walsh et al. [22] based on comparing clean and field-operated turbine components. The maximum and minimum particle mass loadings from Ref. [22] were matched for the double wall liners resulting in high and low sand amounts of 0.52 g and 0.21 g, respectively. The effect of sand amount on L3 was then evaluated for all pressure ratios, as shown in Fig. 13.

As shown in Fig. 13, a 51% increase in sand amount resulted in an average increase in blocking of 18% across all pressure ratios.

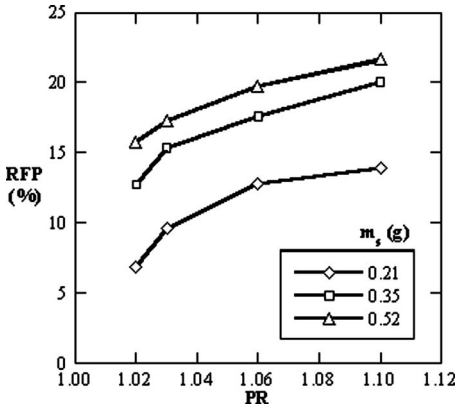

Fig. 13 Effects of sand amount variation for L3 at ambient temperature

Lowering the sand amount by 41% resulted in an average 35% decrease in blocking. At pressure ratios above 1.03, these results agree with the results of Walsh et al. [22], which showed a near linear dependence of blocking on the injected sand amount at a given pressure ratio. It is important to note that the studies by Walsh et al. were conducted at pressure ratios above 1.1. The effect of varying sand amount was also evaluated for another liner at a pressure ratio of 1.06 to assure that the results were not dependent on the film-cooling and impingement geometry. As shown in Fig. 14, L1 exhibits the same trend as L3 with linearly increasing blockage as sand amount was increased.

5.3 Elevated Temperature Results. Each liner was evaluated with a constant metal, coolant, and entering sand temperature at $T_M=982°C$, $T_c=649°C$, and $T_s\sim760°C$. In addition to these tests, as was described previously, the length of the sand delivery pipe was changed such that less of it was inside the kiln to lower the sand temperature for L1 and L2 to $T_s\sim370°C$. As stated previously, a transient heat transfer calculation was performed to estimate the sand temperature flowing into the impingement plate. It is important to note that all elevated temperature tests were performed with a nominal sand amount of 0.35 g.

As discussed previously, the reduction in flow parameter or blockage was calculated differently at heated condition than what was performed for the ambient temperature testing. At heated conditions, the RFP_H was used. In this equation for the reduction in flow parameter, FP_{0H} was defined as the equivalent baseline flow parameter at heated conditions and FP_H was the blocked value at

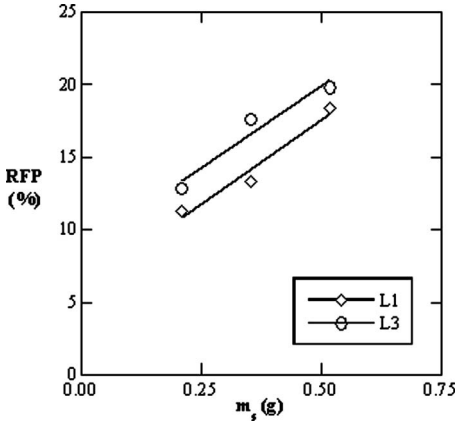

Fig. 14 Sand amounts for L1 and L3 at PR=1.06 at ambient temperature

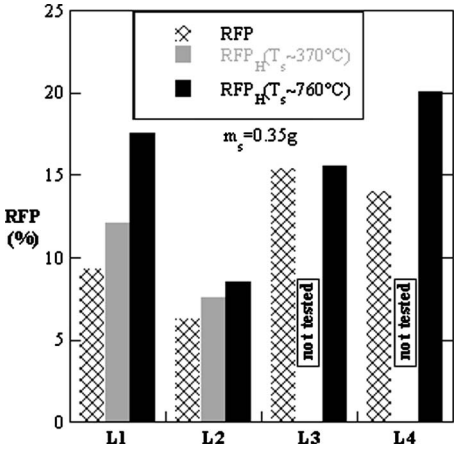

Fig. 15 Comparison of all liners for ambient and heated tests at $T_M=982°C$ and $T_c=649°C$ and two ranges of entering sand temperature at PR=1.03

heated conditions. Figure 6 illustrates the testing procedure and calculation of this parameter at heated conditions.

The high temperature results for each liner are shown in Fig. 15 with the previously reported values of blockage for the ambient temperature results. Each liner showed an increase in blocking at elevated temperatures. L2 performed the best with the lowest values of blockage for both heated and ambient temperatures. L3 had the highest operational flexibility, exhibiting very little change in sand blockage between heated and ambient temperature testings. The largest increase in blockage, by means of an increase in temperature, occurred with L1. Explanation of the elevated temperature results was accomplished by disassembling each liner after testing and noting differences in the sand blocking patterns.

At elevated temperatures, the liner blocking results no longer scaled with impingement area as it did under ambient conditions. Visual inspection after heated testing confirmed that the sand blockage had moved into the film-cooling holes and continued to occur within the impingement plate. Recall that negligible amounts of blocking were observed within the film-cooling holes at ambient conditions. It was apparent that the impingement plate was still acting as a filter for larger particles, but observations of completely blocked film-cooling holes meant there was a new blocking mechanism occurring within the liner for heated conditions.

Under heated conditions, blockages within the film-cooling plate resulted from the sand becoming sticky at elevated temperatures. This stickiness increased the likelihood of sand adhering to the impingement and film-cooling plates as well as within the cooling holes. It was found, as shown in Fig. 16, that the deposited sand takes the shape of small mounds on the upstream side of the film-cooling plate at elevated temperatures. Figure 16 illustrates these sand mounds in comparison to the case under ambient temperatures, as shown in Fig. 12. As shown, each sand mound was centered on the location of the impingement hole exit. These

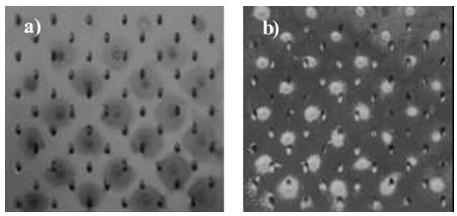

Fig. 16 Upstream side of the L1 film-cooling plate at PR=1.03 for (*a*) ambient and (*b*) $T_M=982°C$, $T_c=649°C$, and $T_s=386°C$

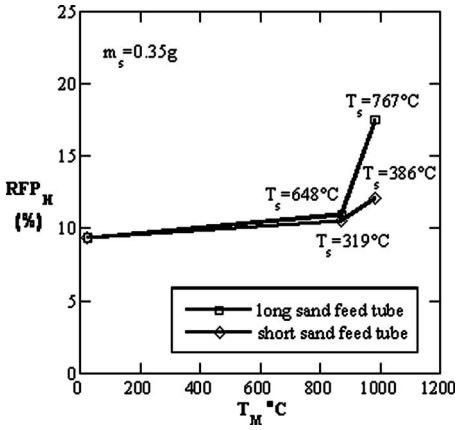

Fig. 17 Blockage associated with varied metals and entering sand temperatures for L1 at a fixed coolant temperature of T_c=649°C and PR=1.03

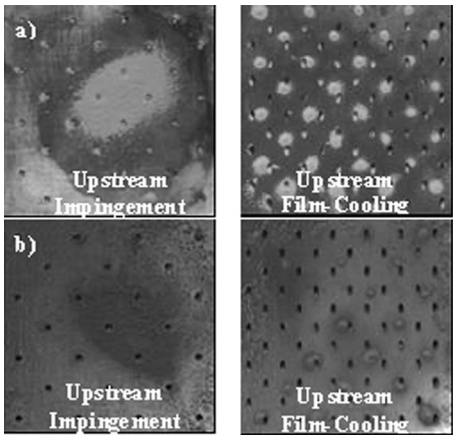

Fig. 18 Post-test images of elevated temperature sand deposition patterns for L1 at T_c=982°C, T_c=649°C, and PR=1.03 having two entering sand temperatures (*a*) T_s=386°C and (*b*) T_s=767°C

mounds formed around and within the entrance to the film-cooling hole when there was overlap between the impingement hole exit and film-cooling hole entrance, thereby contributing to an increase in blocking within the nearby film-cooling holes.

Recalling Fig. 4, L2 and L3 showed little overlap between the impingement and film-cooling holes. The opposite was true for L1 and L4, which had much higher levels of cooling hole overlap. Therefore L2 and L3 were less sensitive than L1 and L4 to operating at elevated temperatures because of the difference in overlap between impingement and film-cooling holes. It was also of note that L4 showed the highest blockage at elevated temperature despite having the largest cooling hole diameter. Again, this was attributed to L4 having the highest level of impingement/film-cooling hole overlap when compared with the other three liners. This result further reinforced the hypothesis that the combination of sand stickiness and the amount of cooling hole overlap were responsible for the increase in blocking observed at elevated temperatures.

5.4 Results With Varied Metal and Sand Temperatures. Varied metal and entering sand temperature tests were conducted with L1 as it showed the greatest sensitivity to being operated at elevated temperatures. The range of metal temperatures tested (871–982°C) correspond to realistic values of metal temperature for the combustor liner. As discussed previously, the range of entering sand temperature was varied to the maximum allowable limitations for the testing setup. This value was set by the heated length of sand feed tube, as discussed previously. All tests were performed with a fixed coolant temperature of T_c=649°C.

The results of this study are shown in Fig. 17 along with the sand temperature entering the liner for each test. The blockage level at ambient conditions is also shown in Fig. 17 to serve as a basis of comparison for the elevated temperature tests. For a relatively low entering sand temperature, the increase in metal temperature from ambient to 871°C resulted in a 13% increase in blocking. An increase of 17% in blocking was observed between ambient and T_M=871°C for a relatively high entering sand temperature. Through visual inspection it was concluded that a metal temperature of 871°C was too low to sufficiently heat the sand as it passed through the liner. However, increasing the liner metal temperature to 982°C resulted in a dramatic effect. As shown in Fig. 17, for a relatively high entering sand temperature blocking increased by 60% compared with T_M=871°C. This corresponded to two times the blocking at ambient conditions. For a relatively low entering sand temperature, blocking increased by 14% when compared with T_M=871°C

The dramatic increase in blockage for a high entering sand temperature occurred because the sand was becoming sticky at higher temperatures. The driving heat transfer mechanism of this effect was radiative heating from the liner's metal surfaces to the sand. Collisions with the surface also aided in the heating up of the sand. With higher temperature, tackier sand was therefore more likely to deposit on the internal surfaces of the liner. After a particle adhered to the surface, it provided an area where subsequent particles could readily adhere. Interparticle collisions of sticky particles also resulted in increasing mean particle size. Agglomeration of colliding particles resulted in an increase in Stokes number, which is a function of the particle diameter. Increasing Stokes numbers corresponded to a greater deviation of particle trajectories from the flow streamlines, thus increasing the likelihood of wall collisions and depositions. Visual inspection of parts after testing, shown in Fig. 18, support the conclusion that the combination of elevated metal temperature and high entering sand temperature was having a significant effect on particle stickiness. At low entering sand temperatures, light color sand was observed, which could be easily removed with high pressure air. At high entering sand temperatures, sand color darkened appreciably and could not be dislodged by high pressure air alone. The dark mounds of sand were difficult to break up and required manual removal.

6 Conclusions

The effects of sand flowing through a combined impingement and film-cooling double wall liner have been presented. Pressure ratio across the liner, sand amount, metal temperature, and sand temperature were used to evaluate four realistic liner geometries. The four liners were designed to investigate what effect the cooling hole diameter, number of cooling holes, total coolant flow area, and relative alignment between the impingement and film-cooling holes had on blockage levels. The study was divided into two sections: ambient and engine representative temperature results.

For all liner geometries tested at ambient conditions, an increasing pressure ratio resulted in an increase in blockage. Since raising the pressure ratio resulted in an overall increase in fluid velocity, it was hypothesized that the increasing deviation of particles from fluid streamlines, described by the Stokes number, resulted in more wall collisions and therefore higher deposition rates. It was found that blocking levels scaled directly with impingement plate area at ambient conditions. At ambient conditions, the liner with the largest impingement flow area exhibited the lowest blocking for all pressure ratios. Each double wall liner design also had a matched diameter of impingement and film-cooling holes, causing the impingement plate to act as a particle filter for the film-cooling plate. It was also observed that particles small enough to travel through the impingement holes subse-

quently impinged on the upstream side of the film-cooling plate. This impingement broke the particles up, allowing them to more easily pass through the film-cooling holes. Because of the particle breakup and filtering by the impingement plate, a negligible buildup of sand was observed within the film-cooling holes or on the upstream surface of the film-cooling plate at ambient conditions.

At elevated temperatures, blocking levels did not scale with impingement area. The amount of blocking increased for all liners as metal temperature was increased. This was found to be a result of the sand becoming sticky at higher temperatures thus increasing the probability of particle deposition. Visual inspection of the liner after testing confirmed that the sand was becoming sticky, which resulted in elevated deposition levels on the upstream side of the film-cooling plate and within the film-cooling holes. This effect was quite different than at ambient conditions, where no sand buildup was observed on the upstream surface of the film-cooling plate. Since sand was depositing in small mounds on the upstream surface of the film-cooling plate downstream of the impingement jets, it was determined that liners with a high amount of overlap between the impingement and film-cooling holes blocked more when compared with staggered impingement and film-cooling holes.

Overall, the liner with the largest impingement flow area and least overlap between the impingement and film-cooling holes exhibited the lowest blocking overall at both ambient and heated conditions. At all operating conditions, the impingement holes were acting as a particle size filter for the film-cooling plate. This study has shown that impingement could be used to breakup larger particles thereby reducing their possibility of blocking within subsequent cooling geometries. In addition, the cooling liners with staggered film and impingement holes were found to be less sensitive to the sand depositing on the upstream side of the film-cooling plate, which occurred at higher temperatures.

Acknowledgment

This research was conducted through funding provided by Pratt & Whitney. The authors graciously acknowledge this support.

Nomenclature

A = cross-sectional area
d = particle diameter
D = cooling hole diameter
FP = $(\dot{m}_{\text{hole}}\sqrt{T_c R})/(P_{\text{exit}} A_{\text{hole}})$
L = length
L_c = characteristic flow length
m = mass
$\dot{m}$ = mass flowrate
n = number of holes
P = pressure
P_1 = pitchwise cooling hole spacing
P_2 = streamwise cooling hole spacing
PR = P_{0C}/P_{exit}
Q = volumetric flowrate
R = air gas constant
RFP = $(\text{FP}_0 - \text{FP}_B)/\text{FP}_0$
RFP_H = $\text{RFP}_H = (\text{FP}_{0H} - \text{FP}_{BH})/\text{FP}_{0H}$
St = Stokes number $= \tau_s/\tau_f$
T = temperature
U = velocity
u = uncertainty

Greek

ρ = density
μ = dynamic viscosity
τ_f = characteristic flow time scale, $\tau_f = L_c/U$
τ_s = particle response time, $\tau_s = (\rho_s d_s^2)/(18\mu_f)$

Subscripts

0 = equivalent unblocked parameter for ambient conditions at the blocked pressure ratio
$0H$ = equivalent unblocked parameter for heated conditions at the blocked pressure ratio
$0C$ = coolant total property
amb = ambient laboratory conditions
B = blocked with sand at ambient conditions
BH = blocked with sand at heated conditions
c = coolant
exit = film-cooling hole exit
hole = relating to a single cooling hole
H = evaluated at heated conditions
I = impingement
M = metal
s = sand

References

[1] United States Department of Defense, 2006, http://www.defenselink.mil/transformation/.
[2] Chambers, J. C., 1985, "The 1982 Encounter of British Airways 77 With the Mt. Galuggung Eruption Cloud," AIAA Paper No. 85-0097.
[3] 1990, Airline Pilot Magazine, 59(6), June/July.
[4] Mitchell, H. J., and Gilmore, F. R., "Dust-Cloud Effects on Aircraft Engines: Emerging Issues and New Damage Mechanisms," Paper No. RDA-TR-120012-001.
[5] Smith, W. S., 1985, "International Efforts to Avoid Volcanic Ash Clouds," AIAA Paper No. 85-0101.
[6] Campbell, E., 1994, "Recommended Flight-Crew Procedures if Volcanic Ash is Encountered," U. S. Geol. Surv. Bull., **2047**, pp. 151–156.
[7] Coons, S., 2006, private communication.
[8] Batcho, P. F., Moller, J. C., Padova, C., and Dunn, M. G., 1987, "Interpretation of Gas Turbine Response Due to Dust Ingestion," ASME J. Eng. Gas Turbines Power, **109**, pp. 344–352.
[9] Dunn, M. G., Padova, C., and Adams, R. M., 1987, "Operation of Gas Turbine Engines in Dust-Laden Environments," AGARD-CP, Paris, France.
[10] Dunn, M. G., Padova, C., Moller, J. E., and Adams, R. M., 1987, "Performance Deterioration of a Turbofan and a Turbojet Engine Upon Exposure to a Dust Environment," ASME J. Eng. Gas Turbines Power, **109**, pp. 336–343.
[11] Kim, J., Dunn, M. G., Baran, A. J., Wade, D. P., and Tremba, E. L., 1993, "Deposition of Volcanic Materials in Hot Sections of Two Gas Turbine Engines," ASME J. Eng. Gas Turbines Power, **115**, pp. 641–651.
[12] Weaver, M.W., Dunn, M.G., and Heffernan, T., 1996, "Experimental Determination of the Influence of Foreign Particle Ingestion on the Behavior of Hot-Section Components Including Lamilloy," Paper No. 96-GT-337.
[13] Tabakoff, W., and Wakeman, T., 1979, "Test Facility for Material Erosion at High Temperature," ASTM Spec. Tech. Publ., **664**, pp. 123–135.
[14] Tabakoff, W., Metwally, M., and Hamed, A., 1995, "High Temperature Coatings for Protection Against Turbine Deterioration," ASME J. Eng. Gas Turbines Power, **117**, pp. 146–151.
[15] Walsh, P. N., Quest, J. M., and Tucker, R. C., Jr., 1995, "Coating for the Protection of Turbine Blades From Erosion," ASME J. Eng. Gas Turbines Power, **117**, pp. 152–155.
[16] Tabakoff, W., and Simpson, G., 2002, "Experimental Study of Deterioration and Retention on Coated and Uncoated Compressor and Turbine Blades," AIAA Paper No. 2002-0373.
[17] Hamed, A. A., Tabakoff, W., Rivir, R. B., Kaushik, D., and Arora, P., 2005, "Turbine Blade Surface Deterioration by Erosion," ASME J. Turbomach., **127**, pp. 445–452.
[18] Jensen, J. W., Squire, S. W., Bons, J. P., and Fletcher, T. H., 2005, "Simulated Land-Based Turbine Deposits Generated in an Accelerated Deposition Facility," ASME J. Turbomach., **127**, pp. 462–470.
[19] Bons, J. P., Taylor, R. P., McClain, S. T., and Rivir, R. B., 2001, "The Many Faces of Turbine Surface Roughness," ASME J. Turbomach., **123**, pp. 739–748.
[20] Hamed, A., Tabakoff, W., and Wenglarz, R., 2006, "Erosion and Deposition in Turbomachinery," J. Propul. Power, **22**, pp. 350–360.
[21] Tafti, D.K., and Shah, A., 2006, "Transport of Particulates in an Internal Cooling Ribbed Duct," Paper No. GT2006-91284.
[22] Walsh, W.S., Thole, K.A., and Joe, C., 2006, "Effects of Sand Ingestion on the Blockage of Film-Cooling Holes," Paper No. GT2006-90067.
[23] Hill, P., and Peterson, C., 1992, *Mechanics and Thermodynamics of Propulsion*, Addison-Wesley, Reading, MA.
[24] Crowe, C., Sommerfeld, M., and Tsuji, Y., 1998, *Multiphase Flows With Droplets and Particles*, CRC, Boca Raton, FL.
[25] Figliola, R. S., and Beasley, D. E., 2006, *Theory and Design for Mechanical Measurements*, Wiley, Hoboken, NJ.
[26] Land, C.L., Thole, K.A., and Joe, C., 2008, "Considerations of a Double Wall Cooling Design to Reduce Sand Blockage," Paper No. GT2008-50160.
[27] Tu, J. Y., Yeoh, G. H., Morsi, Y. S., and Yang, W., 2004, "A Study of Particle Rebounding Characteristics of a Gas-Particle Flow Over a Curved Wall Surface," Aerosol Sci. Technol., **38**, pp. 739–755.

P. Schuepbach[1]
e-mail: schuepbach@lec.mavt.ethz.ch

R. S. Abhari

Department of Mechanical and Process Engineering,
LEC,
Laboratory of Energy Conversion,
ETH Zurich,
Zurich CH-8092, Switzerland

M. G. Rose
Institute of Aeronautical Propulsion,
University of Stuttgart,
70569 Stuttgart, Germany

T. Germain

I. Raab

J. Gier

MTU Aero Engines GmbH,
Dachauer Strasse 665,
80995 München, Germany

Effects of Suction and Injection Purge-Flow on the Secondary Flow Structures of a High-Work Turbine

In high-pressure turbines, a small amount of air is ejected at the hub rim seal to cool and prevent the ingestion of hot gases into the cavity between the stator and the disk. This paper presents an experimental study of the flow mechanisms that are associated with injection through the hub rim seal at the rotor inlet. Two different injection rates are investigated: nominal sucking of −0.14% of the main massflow and nominal blowing of 0.9%. This investigation is executed on a one-and-1/2-stage axial turbine. The results shown here come from unsteady and steady measurements, which have been acquired upstream and downstream of the rotor. The paper gives a detailed analysis of the changing secondary flow field, as well as unsteady interactions associated with the injection. The injection of fluid causes a very different and generally more unsteady flow field at the rotor exit near the hub. The injection causes the turbine efficiency to deteriorate by about 0.6%. [DOI: 10.1115/1.4000485]

1 Introduction

In order to improve the thermal cycle efficiency of gas turbines, turbine entry temperatures have been continuously increased over the past decades. With these increases the ingestion of hot gases into the disk cavities has become an issue, as it can cause overheating of the disks, as well as thermal fatigue of the components. In order to mitigate the adverse effects of ingestion of hot gases, bypassed compressor air is injected through the rim seals between the rotating and stationary parts. The goal is to minimize the amount of injection massflow and to reduce the aerodynamic losses, which can be attributed to the injection. The ingestion of hot gases is driven by both disk pumping, as well as the external nonaxisymmetric pressure field. This has been experimentally investigated in previous studies; Kobashi et al. [1] found that the pressure difference criterion underestimates the minimum cooling flow rate. Chew et al. [2] and Dadkhah et al. [3] also examined the question of the minimum coolant flow that is required to prevent ingestion and where the ingested air would end up in the cavity. The pressure field is however highly unsteady due to stator-rotor interactions. Roy et al. [4], for example, showed that the effect of the unsteady pressure field was much more pronounced inside the cavity than the time-averaged circumferential external pressure field. Recent research has focused on the flow interactions between the cooling air and the mainstream flow. McLean et al. [5,6] tested radial, impingement, and root injection cooling configurations. They observed that root injection had the most pronounced effect on the loss coefficient and total-to-total efficiency. Furthermore they found profound effects on the secondary flows of the following row. Girgis et al. [7] compared radial injection to compound injection, which had both radial and tangential components. They observed that the latter resulted in an efficiency improvement. Ong et al. [8] also concluded that some of the efficiency penalty due to coolant could be regained by introducing a swirl component to the coolant jet. Furthermore they found that most of the coolant is entrained by the downstream blade hub secondary flow. Paniagua et al. [9] reported that there is an intensification of the rotor hub vortex and an enhancement of the radial migration due to injection. In recent studies the importance of the unsteady interaction of the freestream and the cavity were highlighted. Boudet et al. [10] found frequencies that are unrelated to the blade passing frequency. They attributed this to a nonlinear coupling of the blade passing frequency with an instability formed inside the cavity. They concluded that only full annulus and unsteady modeling would capture the experimentally observed flow phenomena. Reid et al. [11] quantified the efficiency penalty caused by the rim seal flow to be about 0.56% for 1.0% of injection massflow. Marini and Girgis [12] in a numerical study examined the effects of the blade leading edge platform and noted that there is a 0.07% stage efficiency benefit and a reduced sensitivity to an increasing cavity massflow.

The present work shows performance sensitivities for purge flow. Intensification of the secondary flows at exit of the rotor and a higher penetration of the secondary flows with purge flow are observed. A detailed time-resolved measurement and analysis with and without purge flow are presented. By a spectral analysis at exit of the rotor with purge, flow subharmonic frequencies are resolved.

2 Experimental Method

2.1 Experimental Turbine Facility. The experimental investigation was performed in the research turbine "LISA" in the Laboratory of Energy Conversion at Swiss Federal Institute of Technology. Recently the existing two-stage, shrouded turbine configuration [13] was redesigned as a one-and-1/2 unshrouded

[1]Corresponding author.

Contributed by the International Gas Turbine Institute (IGTI) of ASME for publication in the JOURNAL OF TURBOMACHINERY. Manuscript received August 20, 2008; final manuscript received August 29, 2008; published online January 21, 2010. Editor: David Wisler.

Table 1 Characteristic geometry

	Stator 1	Rotor
No. of blades	36	54
Inlet angle (midspan) (deg)	0	54
Exit angle (midspan) (deg)	73	−67
Solidity (chord/pitch)	0.87	1.17
Aspect ratio (span/chord)	1.27	1.41
Profile stacking	LE	CoG

turbine that is representative of a high work cooled turbine. Further details of the new design are presented by Behr et al. [14], but its salient features are described below.

The air-loop of the facility is a quasiclosed type and includes a radial compressor, a two-stage water to air heat exchanger and a calibrated venturi nozzle for mass flow measurements. Upstream of the turbine section is a 3 m part with flow straighteners to ensure a homogenous flow field. Additionally the flow undergoes an acceleration ahead of the turbine section in order to reduce the significance of any remaining flow nonuniformities. At the exit of the turbine section the air-loop opens to atmosphere. A dc generator absorbs the turbine power and controls the rotational speed with an indicated accuracy $\pm 0.02\%$ ($\pm 0.5RMP$). A heat exchanger controls the $T_{t,\mathrm{in}}$ to an accuracy of $\pm 0.3\%$. A torquemeter measures the torque on the rotor shaft. With a compressor ratio limited to $\Pi_{c,\max}=1.5$, it is necessary to add a tandem deswirl vane arrangement to recover the static pressure at the exit of the second stator back to the ambient level, in order to reach the intended turbine pressure ratio of $\Pi_{1.5}=1.65$. The turbine is unshrouded with a nominal tip gap of 1% of the span. The variation in the tip gap between builds is less than 1% of the tip gap, which ensures a good repeatability.

Table 1 gives the general geometrical data of the first stage of the investigated turbine. A new air-system was designed to provide the possibility of injection of air through the rotor upstream rim seal. The air is bled off the primary air-loop upstream of the flow conditioning stretch. The bleed air passes through a venturi to measure the bypassed massflow. Finally the bypass flow enters a plenum from where ten plastic pipes lead the flow to ten first nozzle guide vane rows (NGV1s). Through these NGV1s the flow enters the cavity labeled **B** in Fig. 1. From the cavity underneath the NGV1s there are two leakage paths indicated in Fig. 1 as dotted arrows **P** and **S**. One path is through the upstream rim seal into the mainflow **P**. The rest of the gas is ejected through the drum to the ambient after being measured in another venturi called the secondary massflow **S**. The pressure difference over the labyrinth seal leading from the downstream rim seal into the drum is balanced. Under these conditions the net massflow through the downstream rim seal into the drum is assumed to be zero. Thus the injection or purge massflow can be calculated as the difference of the bypass massflow and secondary massflow. Previously it was only possible to run the rig with the upstream rim seal in a sucking mode.

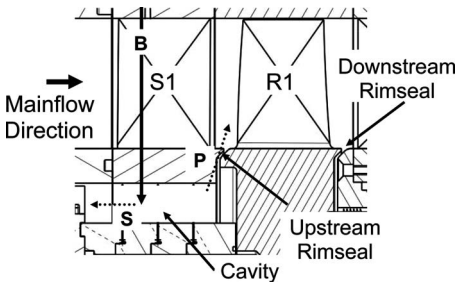

Fig. 1 Illustration of leakage path

Table 2 Operating conditions

$\Pi_{1.5}$	$1.65 \pm 0.4\%$
$T_{t,\mathrm{in}}$	328 ± 0.2 K
$\frac{\dot{m}\sqrt{T_{t,\mathrm{in}}}}{p_{t,\mathrm{in}}}$	$152 \pm 0.2\%$ $\left(\frac{\mathrm{kg\ K^{1/2}}}{\mathrm{s\ bar}}\right)$
$\frac{N}{\sqrt{T_{t,\mathrm{in}}}}$	2.48 ± 0.05 $\frac{\mathrm{rps}}{\mathrm{K^{1/2}}}$

2.2 Measurement Technology. The steady flow field is measured with a miniature cobra-head five-hole probe with a tip diameter of 0.9 mm. The unsteady flow field is measured with a fast response aerodynamic probe (FRAP), which was developed at the LEC [15,16]. The probe is capable of capturing unsteady flow features of up to frequencies of 48 kHz based on measurements including total and static pressures, flow yaw and pitch angles, and Mach number. The frequency bandwidth of the temperature is limited to a frequency of 10 Hz. However the influence of the temperature on the velocity is very modest. The used FRAP probe has a 1.8 mm tip diameter and is equipped with two sensors. The probe is operated in a virtual-four-sensor mode to measure three-dimensional time-resolved flow properties. The measurement grid consisted of 39 radial and 40 circumferential points (covering one stator pitch) with a radial clustering near the endwalls. The data are acquired at a sampling rate of 200 kHz over a period of 2 s. During the data processing a phase lock averaging over 85 rotor revolutions per rotor pitch is used. The postprocessing is done for three consecutive rotor pitches. The sampling rate resolves 82 points per rotor pitch in the relative frame of reference.

3 Results and Discussion

3.1 Operating Conditions. During measurements the turbine 1(1/2) stage total-to-static pressure ratio is kept constant at $\Pi_{1.5}=1.65$. The entry temperature is kept constant to permit an accurate comparison between measurements made on different days. To account for the change in ambient pressure on different measurement days the pressures are nondimensionalized by the respective inlet total pressure. The operating conditions are given in Table 2.

In this paper the data of two different injection rates are compared. The definition of the injection rate is given in Eq. (1).

$$IR = \frac{\dot{m}_{\mathrm{by}} - \dot{m}_{\mathrm{dr}}}{\dot{m}_v} \cdot 100 \tag{1}$$

The tests were conducted with two different IRs −0.14% and 0.9%. At −0.14% the rim seal is nominally in a modest sucking mode, while at 0.9% it is said to be blowing.

3.2 Performance Sensitivity. In this section the sensitivity of the total-to-total efficiency to different injection rates is presented. The definition of efficiency used in this study, accounting for the injection is given in Eq. (2)

$$\eta_{tt} = \frac{\dfrac{\omega \cdot M}{\dot{m}_v \cdot c_p \cdot T_{t,\mathrm{in}}}}{1 - \left(1 - \dfrac{IR}{100}\right) \cdot \left(\dfrac{p_{t,R1\mathrm{ex}}}{p_{t,\mathrm{in}}}\right)^{\gamma-1/\gamma} - \dfrac{IR}{100} \cdot \left(\dfrac{p_{t,R1\mathrm{ex}}}{p_{t,\mathrm{cav}}}\right)^{(\gamma-1)/\gamma}} \tag{2}$$

The efficiency drop is $\Delta\eta_{tt}=0.6\%$ when comparing the sucking case ($IR=-0.14\%$) to the blowing case ($IR=0.9\%$).

Figure 2 shows the circumferentially massflow averaged relative flow yaw angle at the exit of the rotor. The design metal angle is −67 deg over the whole span. At the hub one can see the underturning region between 20% and 30% span.

At 10% span there is the overturning region induced by the hub passage vortex. At 72% span the tip passage vortex introduces

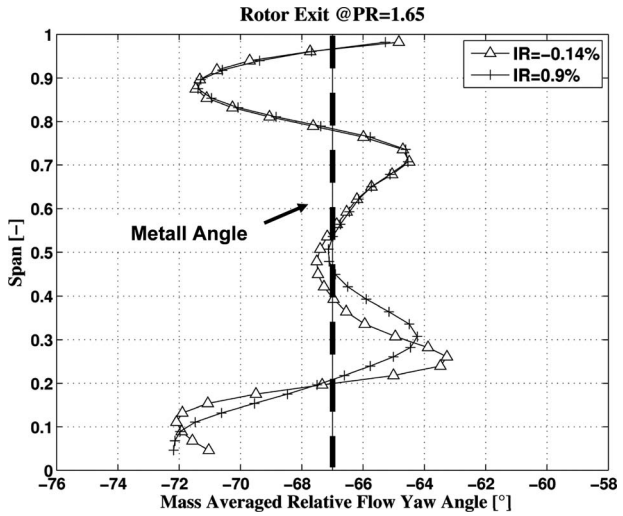

Fig. 2 Mass-averaged relative flow angle traverse plane *R*1ex

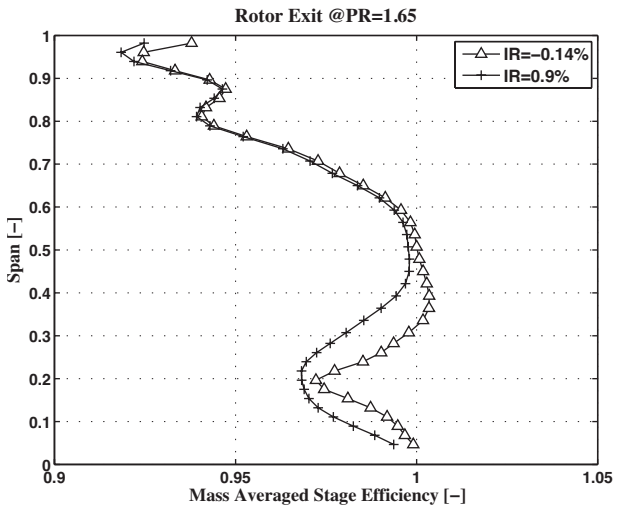

Fig. 3 Mass-averaged total-to-total efficiency traverse plane *R*1ex

underturning. At 88% span there is the combined overturning of the tip passage vortex and the tip leakage vortex. Finally at the casing the underturning part of the tip leakage vortex can be seen. In the outer half of the annulus there is no influence of the injection. At the hub the underturning is reduced by 1.4 deg with purge flow, while it radially migrated outwards by 5% of the span. The overturning is the same in both cases. With purge flow the highest overturning is at a 5% lower span position. With purge flow the signature of the secondary flow is diminished, while it has a larger radial extent.

Figure 3 shows the radial distribution of the total-to-total efficiency. It should be noted that this efficiency is linearly related to the total pressure distribution since the power used to calculate it is only a one-dimensional (1D) value. The efficiency is nondimensionalized with the midheight value of the ($IR=-0.14\%$) sucking case. There is an increasing efficiency deficit toward the hub for the injection case. The suction case has a more pronounced loss core around 20% span, while it is more diffused in the purge flow case.

3.3 Time-Resolved Data. Figure 4 shows the relative total pressure field of the blowing case with an injection rate of 0.9% for two stator pitches at exit of the rotor. As the vane to blade ratio is two to three, the loss systems of three rotor blades can be seen. Figure 4 shows the situation at one instant in time in the absolute frame. The rotor loss features can be identified as the low relative total pressure zones.

From 90% span up to the casing the loss is associated with the tip leakage vortex labeled with 1. Between 65% and 80% span the tip passage vortex loss 2. In between 30% and 65% span the rotor wake can be identified. From 10% to 30% span the low relative total pressure zone shows the rotor hub passage vortex 3. The low momentum purge flow is entrained by the hub passage vortex of the rotor. This results in a large and diffused region at the hub.

Based on the stationary flow field three different interaction zones in the rotor exit flow field can be identified. The centerlines of these regions are seen as radial lines in Fig. 4 labeled with **A**, **B**, and **C**. In the region along traverse **A** the loss features of the upstream nozzle appear. Sharma et al. [17] called this region *minimum interaction time location* as the nozzle flow features pass through the rotor passage with minimal interaction with the rotor leading edge. Traverse **B** is in the middle of a high relative total pressure zone caused by the pressure waves of the downstream nozzle. In the region around traverse **C** there is no interaction of the rotor flow features with either the upstream nozzle or the downstream nozzle. Sharma et al. [17] showed that this region is

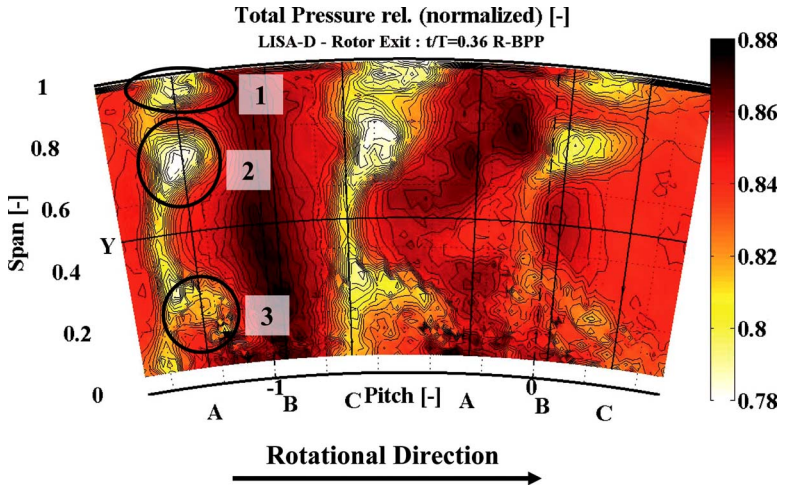

Fig. 4 Relative total pressure for blowing *IR*=0.9% at traverse plane *R*1ex

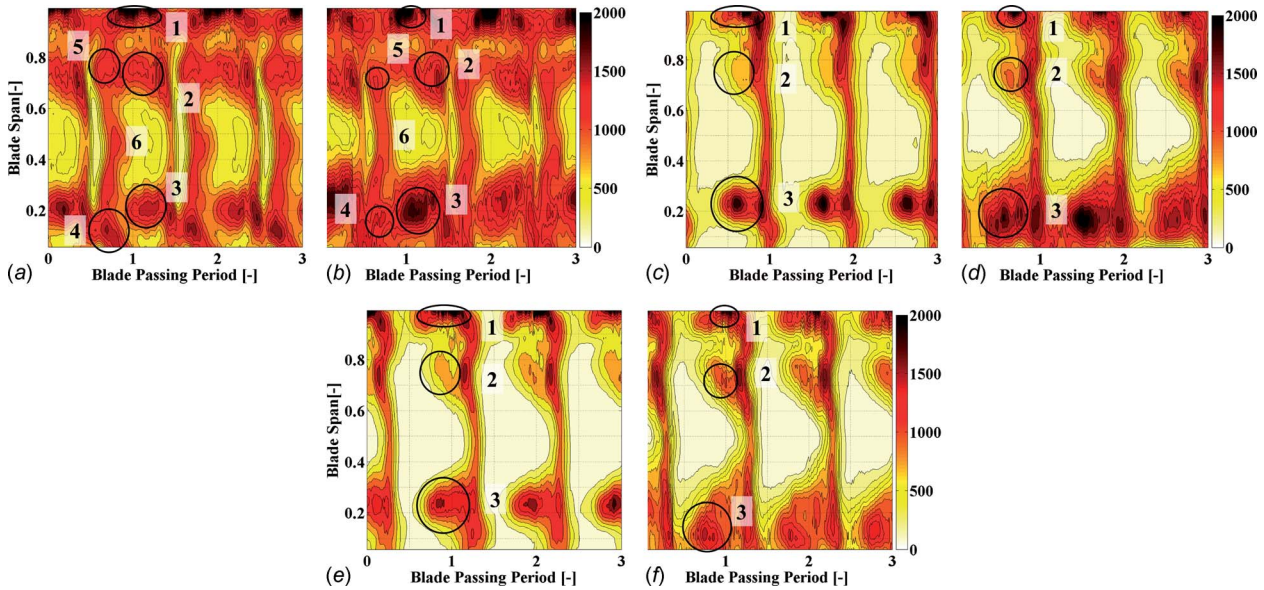

Fig. 5 rms of random part of total pressure at traverse plane *R*1ex (Pa)

characterized by low turbulence values and that the flow field is quite similar to the one, which would be observed in cascade tests. To better understand the different interactions in region **A**, **B**, and **C**, these traverses are plotted against time, as seen in Figs. 5–7.

Figure 5 shows the rms values of the random part of the total pressure signal as a plot of radius against time for the three traverses. Using the triple decomposition of the time-resolved pressure signal as shown in Eq. (3) the random part $p'(t)$ can be evaluated as the difference between the time-resolved pressure $p(t)$ and the phase-locked averaged pressure $\bar{p}+\tilde{p}(t)$. The same

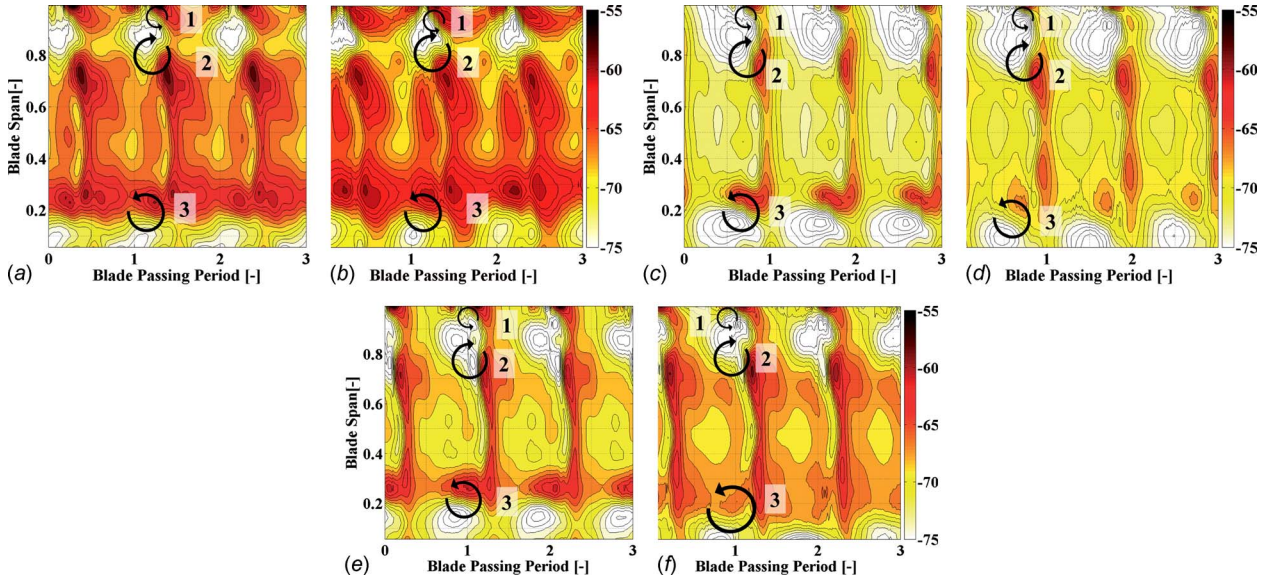

Fig. 6 Relative flow angle traverse plane *R*1ex

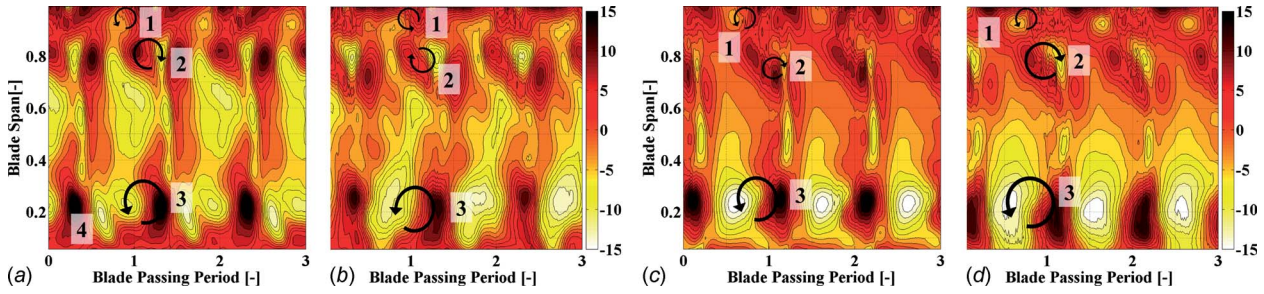

Fig. 7 Pitch angle at traverse plane *R*1ex

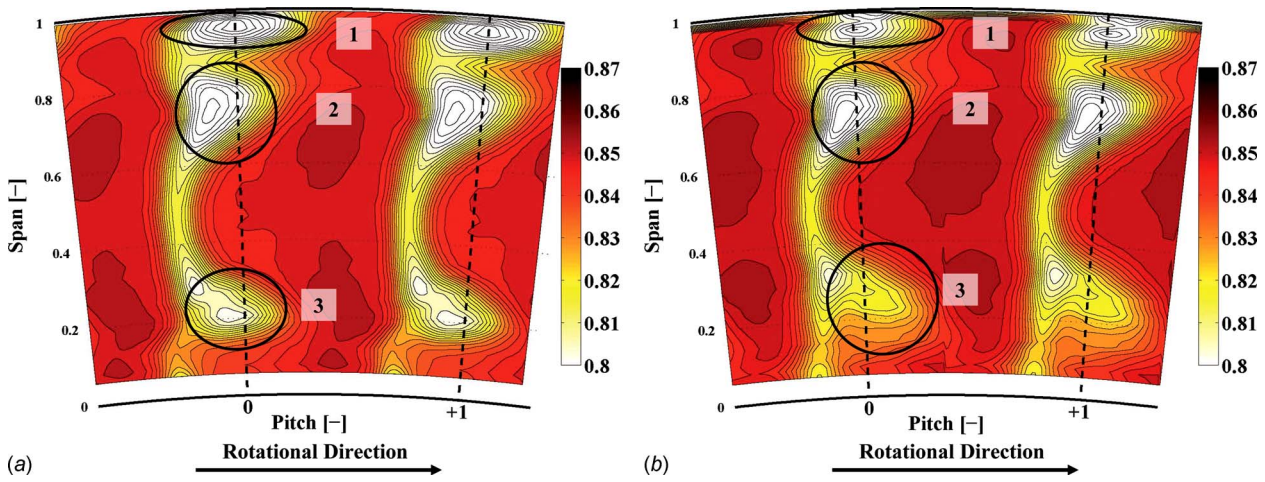

Fig. 8 Time-averaged relative total pressure in the rotor frame of reference at traverse plane *R*1ex

approach was used by Porreca et al. [18] to derive turbulent quantities.

$$p(t) = \bar{p} + \tilde{p}(t) + p'(t) \tag{3}$$

Figures 5(*e*) and 5(*f*) show only minor rotor-stator interactions characterized by the lowest integral rms values. The rotor flow features identified in Fig. 4 can be seen as high rms regions. From 90% span to the tip one can identify the tip leakage vortex labeled with 1 in between 60% and 80% span the rotor tip passage vortex 2, and finally between 15% and 35% span the rotor hub passage vortex 3. With purge flow the highest unsteadiness in the hub passage vortex is constrained to the hub and diffused over a larger area.

In traverse **B** the unsteadiness in the rotor hub passage vortex rises due to the interaction with the downstream stator leading edge. The purge flow case shows a much stronger increase in rms. This could be the signature of a vortex break down.

Along traverse **A** the integral rms values rise once more as additional high rms zones are occurring. These zones show the remains of the upstream vane flow features. There is a high rms zone at the hub labeled 4 associated with the upstream vane hub passage vortex. With purge flow the high rms zone of the rotor hub passage vortex 3 is lifted of the endwall once it starts to interact with the upstream vane hub passage vortex 4. This is probably happening as the leakage fluid has very little momentum.

If streamwise vorticity is present in a flowfield one will find radial gradients of yaw angle, as well as circumferential gradients of pitch angle. As the rotor vorticities travel through the radial traverse, the time gradients are related to the circumferential gradients in the rotating frame. Therefore the strength of the radial yaw angle and the time gradient of the pitch angle are good indicators of the strength of the streamwise vorticity.

Figure 6 shows the relative flow angle in the time-space format. At the hub there is a positive radial gradient of the relative flow angle associated with the hub passage vortex 3. In traverse **B** and **C** this gradient is lowered by a factor of about 5–6 with purge flow present. In traverse **B** it has been reduced from 4.9 deg/mm to 1.0 deg/mm with purge flow and at traverse **C** from 4.6 deg/mm to 0.8 deg/mm. At traverse **A** the gradients are about the same size 1.4 deg/mm and 1.6 deg/mm for both injection cases. This leads to the conclusion that the hub passage vortex of the purge flow case shows a different behavior once the vortex starts to interact with the upstream vane features as seen in traverse **A**. With purge flow the vortex is gaining intensity as it starts to interact with the upstream flow features. Without purge flow the vortex loses intensity.

Figure 7 shows the radial-time diagram for the pitch angle of traverse **A** and **C**. Traverse **C** shows pitch angle variations caused by the rotor flow features. Between 10% and 30% span there is a positive temporal pitch angle gradient, which is the signature of the rotor passage vortex 3. The maximum pitch angle gradient is at 27% in the sucking case and at 21% in the blowing case. The gradient reduced by 2.7 deg per blade passing period with purge flow. This indicates a lower vorticity peak closer to the hub. In traverse **A** the maximum temporal pitch angle gradient can be found at 23% in the sucking case and at 26% in the blowing case. With purge flow the positive gradient at the hub is reduced by 3.5 deg per blade passing period in this circumferential location. With purge flow the rotor hub passage vortex migrates outwards going from traverse **C** to **A**. This reconfirms the observation made further up that the hub passage vortex lifts of the endwall once it starts to interact with the upstream vane flow features, as seen in traverse **A** if purge flow is present.

3.4 Rotating Frame Time-Averaged Results. Figure 8 shows the relative total pressure at the rotor exit time-averaged in the rotating frame of reference. Below 30% span there is the low relative total pressure zone that is associated with the rotor hub passage vortex 3. Between 65% and 80% the tip passage vortex loss core can be identified as 2. Between 90% span and the casing there is the signature of the tip leakage vortex 1. The narrow band of low relative total pressure between 30% and 65% represents the rotor wake. In the purge flow case the hub loss zone is about twice the size of the zone in the sucking case. This loss zone extends from 40% span down to the measurement line closest to the hub

$$Y_{\text{rel}}(r) = \frac{p_{\text{trel,S1ex}}(r) - p_{\text{trel,R1ex}}(r)}{p_{\text{trel,R1ex}}(r) - p_{s,R1\text{ex}}(r)} \cdot 100 \tag{4}$$

Equation (4) gives the definition for the relative total pressure loss coefficient Y_{rel}. Figure 9 shows the radial distribution of Y_{rel} determined with the mass-averaged relative total pressure values at the same radial height. Figure 9 confirms the observations made in Fig. 8. The peak loss in both cases is the same within 1%. The purge flow however shows loss over a much larger radial extent, resulting in an 18% higher integral hub loss.

Figure 10 shows the streamwise vorticity at the rotor exit time-averaged in the rotating frame of reference. The positive streamwise vorticity seen at 20% span and labeled 3 is due to the rotor hub passage vortex. The negative vorticity region 5 can be associated with the trailing edge shed vortex. At 75% the vorticity of the tip passage vortex can be seen in region 2. The tip shed vortex is labeled 4. Along the casing the positive vorticity signature of the tip leakage vortex is seen in region 1. With purge flow the peak vorticity of the hub passage vortex is about halved. This agrees with the observation made in the radial-time plots of the pitch and relative flow angle, as seen Figs. 6 and 7. However the

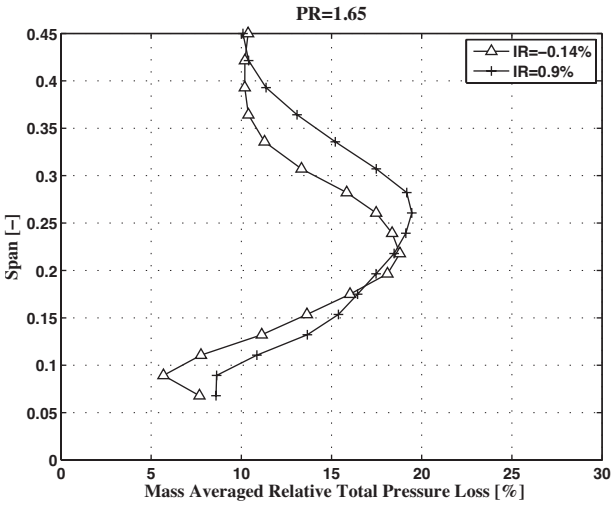

Fig. 9 Time-averaged and circumferentially mass-averaged in the rotor frame of reference relative total pressure loss at traverse plane *R*1ex (%)

integrated circulation is 10% higher with injection. The integrated circulation of the hub trailing shed vortex has increased by 30%. This indicates a greater variation in blade lift with span. Therefore the lift at the hub must have reduced. The purge flow shows no significant influence in the outer annulus half.

Figure 11 shows the time-averaged rms values of the random part of the total pressure signal in the rotating frame of reference. There are three distinct regions of high rms values representing the hub passage vortex (below 40% Span) 3, the tip passage vortex (between 60% and 80% Span) 2 and the leakage vortex (beyond 90% span) 1. Furthermore there is a band of high rms values between 40% and 60% span associated with the rotor wake. The rms plot shows a very diffused hub passage vortex region with purge flow, which has increased in size and reduced in peak intensity compared with the sucking case.

The rate of irreversible heat generation by doing work against the viscous forces is given in Eq. (5) given in Ref. [19]. The parameter Φ is the dissipation function. The viscosity in Eq. (5) is the molecular or laminar viscosity. In order to evaluate the dissipation correctly one would need a very fine spatial resolution. The instantaneous velocity vector with its deterministic and turbulent fluctuations is also needed. In practice the spatial resolution is limited by the traverse grid size and the temporal resolution is only deterministic. For these reasons the calculated dissipation must be regarded with some care as the modest spatial resolution and the deterministic time signature will result in an underestimate of the dissipation

$$dQ_F = dt \cdot \Delta V \cdot \mu \cdot \Phi \tag{5}$$

Φ, the viscous dissipation function, is given in cylindrical coordinates in Eq. (6). The required axial gradients are approximated using a frozen flow structure assumption. The detailed approach can be found in Ref. [20]

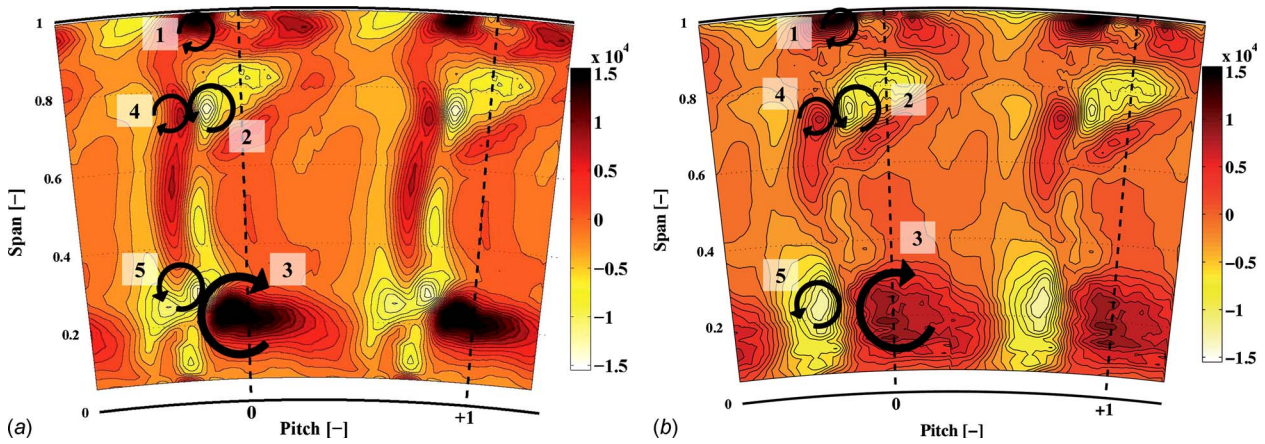

Fig. 10 Time-averaged streamwise vorticity in the rotor frame of reference at traverse plane *R*1ex (1/s)

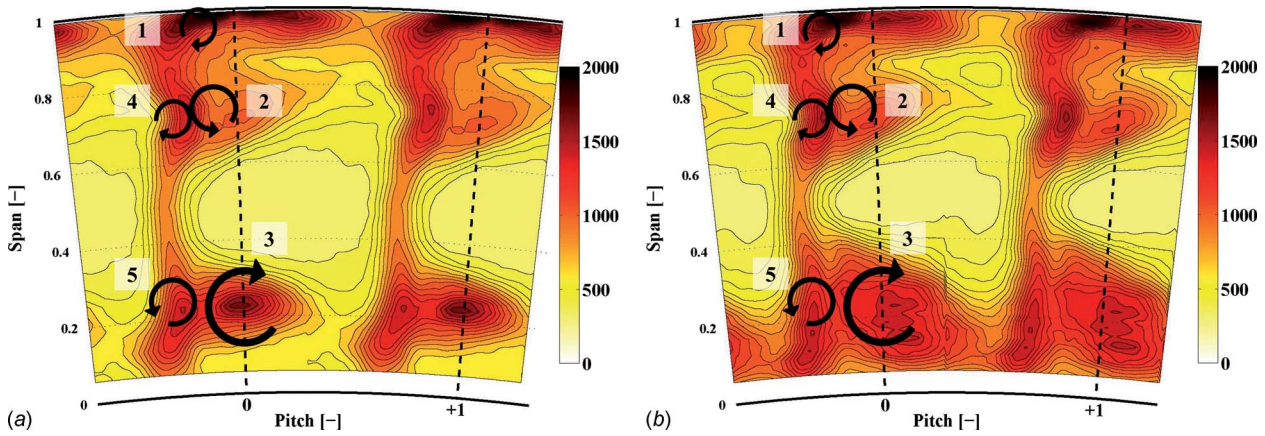

Fig. 11 Time-averaged rms of random part of total pressure in the rotor frame of reference at traverse plane *R*1ex (Pa)

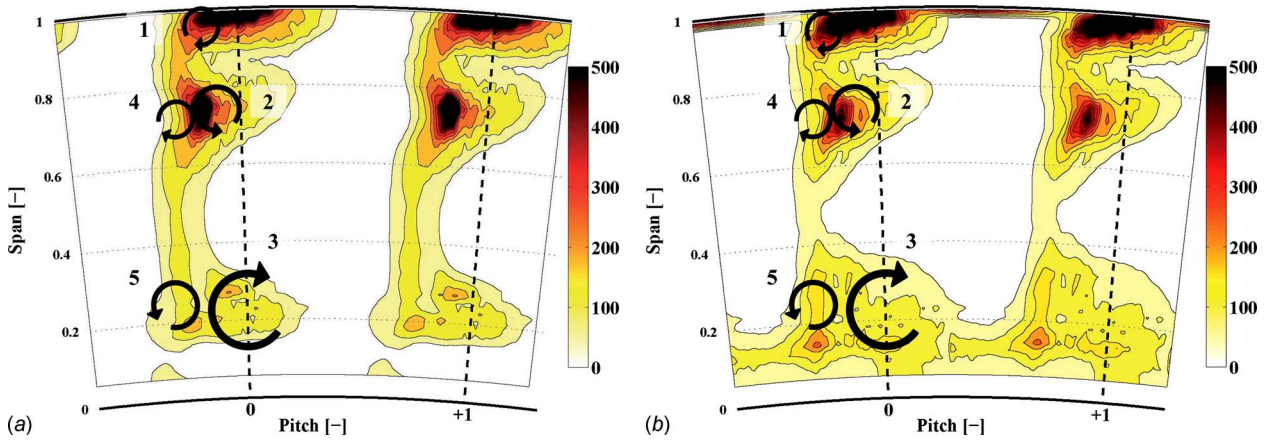

Fig. 12 Time-averaged *D* parameter in the rotor frame of reference at traverse plane *R*1ex (%/s)

$$\Phi = 2\left[\left(\frac{\partial u_r}{\partial r}\right)^2 + \left(\frac{1}{r}\frac{\partial u_\theta}{\partial \theta} + \frac{u_r}{r}\right)^2 + \left(\frac{\partial u_x}{\partial x}\right)^2\right] + \left[r\frac{\partial}{\partial r}\left(\frac{u_\theta}{r}\right) + \frac{1}{r}\frac{\partial u_r}{\partial \theta}\right]^2 + \left[\frac{1}{r}\frac{\partial u_x}{\partial \theta} + \frac{\partial u_\theta}{\partial x}\right]^2 + \left[\frac{\partial u_r}{\partial x} + \frac{\partial u_x}{\partial r}\right]^2 - \frac{2}{3}(\nabla \cdot \underline{u})^2 \tag{6}$$

In order to better quantify the dissipation function, it is normalized by the flux of kinetic energy given in Eq. (7)

$$\dot{m} \cdot \frac{u^2}{2} = \rho \cdot u_x \cdot A_x \cdot \frac{u^2}{2} \tag{7}$$

where

$$u^2 = u_x^2 + u_r^2 + u_\theta^2 \tag{8}$$

Thus we have the semi-nondimensional dissipation function D given in Eq. (9)

$$D = \frac{\mu \cdot \Phi}{\rho \cdot \frac{u^2}{2}} \tag{9}$$

Figure 12 shows the time-averaged D parameter at the rotor exit in the rotating frame of reference. The highest values are measured both in the tip leakage region and in the interaction zone of the tip trailing edge shed vortex 4 and the tip passage vortex 2. The dissipation at the hub is much less pronounced. The peak dissipation values are about the same in both cases. However the extension with purge flow is much larger, resulting in a 39.6 % higher integral dissipation value for the lower annulus half.

3.5 Spectral Analysis. The frequency composition of the flow in the hub loss core is determined from an fast Fourier transform (FFT) of the raw voltage signal of sensor 1 of the FRAP probe, which is directly related to the pressure signal. The amplitude is nondimensionalized by the baseline value at blade passing frequency. The measurements at 16% span and −12.5% pitch are considered. The results are presented in Fig. 13. The blade passing period is 2430 Hz. With $IR=-0.14\%$ there is a distinct peak at the blade passing frequency. With purge flow the peak amplitude at the blade passing frequency is reduced. Furthermore there is a band of relatively high amplitudes centered on the subharmonic of the blade passing frequency. The injection seems to introduce such subharmonic frequencies, as was observed by Boudet et al. [10]. They found that such frequencies result from the nonlinear interactions with cavity instabilities. In the present work no time-resolved cavity data are available. Therefore no conclusive statement on the origin of these frequencies can be made. Alternatively there are possibly some nondeterministic modes of the rotor hub secondary flows influenced by the purge flow.

4 Conclusions

The results with axisymmetric endwalls show a total-to-total efficiency drop of $\Delta\eta_{tt}=0.6\%$ when increasing the injection from the sucking mode $IR=-0.14\%$ to the blowing mode $IR=0.9\%$. With injection and conventional endwalls the hub secondary flows have a larger radial extent. The angles, as well as the vorticity contour plots in the rotor hub passage vortex region, show that the vorticity peak values are reduced by using purge flow. This indicates a reduced rotation of the vortex when the purge flow is entrained into the vortex. However the integrated circulation of the passage vortex with purge flow has increased by 10%. The circulation of the hub trailing shed vortex has increased by 30% with injection through the rotor upstream rim seal. The integrated dissipation function D has increased with purge flow by almost 40% explaining some of the efficiency deficit.

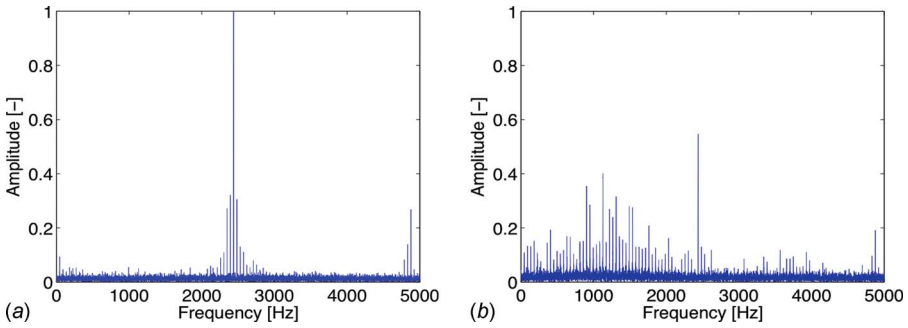

Fig. 13 FFT of the raw voltage signal of the frap probe at 16% span and –12.5% pitch

FFT results show that there is a frequency in the pressure signal of around half the blade passing frequency in the hub region, which could possibly result from a nonlinear combination with some cavity modes. Nevertheless no conclusive statement can be made as there is no time-resolved data from the cavity available.

Acknowledgment

The work leading to the results of this paper was carried out within the joint industrial and academic research program that is part of the "Luftfahrtforschungsprogramm LuFo3" supported by the German Federal Ministry of Economics and Technology.

Nomenclature

A = area (m^2)
D = semi-nondimensional dissipation function (%/s)
c_p = specific heat for constant pressure (J/kg)
IR = injection rate
M = torque (Nm)
$\dot{m}$ = massflow (kg/s)
N = rotational speed (rps)
p = pressure (Pa)
$\bar{p}$ = time mean part of pressure signal (Pa)
$\tilde{p}$ = periodic part of pressure signal (Pa)
p' = random part of pressure signal (Pa)
Q = amount of heat (J)
r = radial coordinate (m)
T = temperature (K)
T = blade period (s)
t = time (s)
u = velocity (m/s)
V = volume (m^3)
x = axial coordinate (m)
Y = total pressure loss coefficient

Greek

γ = isentropic coefficient
η = efficiency
θ = circumferential coordinate
μ = viscosity (kg/m s)
Π = pressure ratio
ρ = density (kg/m^3)
Φ = dissipation function ($1/s^2$)
ω = rotational speed (rad/s)

Subscripts

by = bypass
c,max = compressor
cav = cavity
dr = drum
F = frictional
in = turbine inlet
r = radial coordinate
rel = relative frame
$R1$ex = rotor1 exit
s = static flow quantity
$S1$ex = stator1 exit
t = stagnation flow quantity
tt = total-to-total
v = main venturi
x = axial coordinate
θ = circumferential coordinate
1.5 = total-to-static 1.5 stages

Abbreviations

$R1$ex = rotor1 exit
$S1$ex = stator1 exit

References

[1] Kobayashi, N., Matsumato, M., and Shizuy, M., 1984, "An Experimental Investigation of a Gas-Turbine Disk Cooling System," ASME J. Eng. Gas Turbines Power, **106**(1), pp. 136–141.
[2] Chew, J. W., Dadkhah, S., and Turner, A. B., 1992, "Rim Sealing of Rotor-Stator Wheelspaces in the Absence of External Flow," ASME J. Turbomach., **114**(2), pp. 433–438.
[3] Dadkhah, S., Turner, A. B., and Chew, J. W., 1992, "Performance of Radial Clearance Rim Seals in Upstream and Downstream Rotor-Stator Wheelspaces," ASME J. Turbomach., **114**(2), pp. 439–445.
[4] Roy, R. P., Xu, G., Feng, J., and Kang, S., 2001, "Pressure Field and Main-Stream Gas Ingestion in a Rotor-Stator Disk Cavity," ASME Paper No. 2001-GT-0564.
[5] McLean, C., Camci, C., and Glezer, B., 2001, "Mainstream Aerodynamic Effects Due to Wheelspace Coolant Injection in a High-Pressure Turbine Stage: Part I—Aerodynamic Measurements in the Stationary Frame'," ASME J. Turbomach., **123**(4), pp. 687–696.
[6] McLean, C., Camci, C., and Glezer, B., 2001, "Mainstream Aerodynamic Effects Due to Wheelspace Coolant Injection in a High-Pressure Turbine Stage: Part II—Aerodynamic Measurements in the Rotational Frame," ASME J. Turbomach., **123**(4), pp. 697–703.
[7] Girgis, S., Vlasic, E., Lavoie, J.-P., and Moustapha, S. H., 2002, "The Effect of Secondary Air Injection on the Performance of a Transonic Turbine Stage," ASME Paper No. GT-2002-30340.
[8] Ong, J. H. P., Miller, R. J., and Uchida, S., 2006, "The Effect of Coolant Injection on the Endwall Flow of a High Pressure Turbine," ASME Paper No. GT2006-91060.
[9] Paniagua, G., Denos, R., and Almeida, S., 2004, "Effect of the Hub Endwall Cavity Flow on the Flow-Field of a Transonic High-Pressure Turbine," ASME J. Turbomach., **126**(4), pp. 578–586.
[10] Boudet, J., Hills, N. J., and Chew, J. W., 2006, "Numerical Simulation of the Flow Interaction Between Turbine Main Annulus and Disc Cavities," ASME Paper No. GT-2006-90307.
[11] Reid, K., Denton, J., Pullan, G., Curtis, E., and Longley, J., 2006, "The Effect of Stator-Rotor Hub Sealing Flow on the Mainstream Aerodynamics of a Turbine," ASME Paper No. GT-2006-90838.
[12] Marini, R., and Girgis, S., 2007, "The Effect of Blade Leading Edge Platform Shape on Upstream Disk Cavity to Mainstream Flow Interaction of a High-Pressure Turbine Stage," ASME Paper No. GT2007-27429.
[13] Sell, M., Schlienger, J., Pfau, A., Treiber, M., and Abhari, R. S., 2001, "The 2-Stage Axial Turbine Test Facility LISA," ASME Paper No. 2001-GT-0492.
[14] Behr, T., Kalfas, A. I., and Abhari, R. S., 2007, "Unsteady Flow Physics and Performance of a One-and-1/2-Stage Unshrouded High Work Turbine," ASME J. Turbomach., **129**(2), pp. 348–359.
[15] Kupferschmied, P., Kopperl, O., Gizzi, W. P., and Gyarmathy, G., 2000, "Time Resolved Flow Measurements With Fast Aerodynamic Probes in Turbomachinery," Meas. Sci. Technol., **11**, pp. 1036–1054.
[16] Pfau, A., Schlienger, J., Kalfas, A. I., and Abhari, R. S., 2003, "Unsteady, 3-Dimensional Flow Measurement Using a Miniature Virtual 4 Sensor Fast Response Aerodynamic Probe (FRAP)," ASME Paper No. GT2003-38128.
[17] Sharma, O. P., Butler, T. L., Joslyn, H. D., and Dring, R. P., 1985, "3-Dimensional Unsteady-Flow in an Axial-Flow Turbine," J. Propul. Power, **1**(1), pp. 29–38.
[18] Porreca, L., Hollenstein, M., Kalfas, A. I., and Abhari, R. S., 2007, "Turbulence Measurements and Analysis in a Multistage Axial Turbine," J. Propul. Power, **23**(1), pp. 227–234.
[19] Schlichting, H., 1951, *Grenzschicht-Theorie*, G. Braun, Karlsruhe, Germany.
[20] Schuepbach, P., Rose, M. G., Abhari, R. S., Germain, T., Raab, I., and Gier, J., 2008, "Improving Efficiency of a High-Work Turbine Using Non-Axisymmetric Endwalls. Part II: Time-Resolved Flow Physics," ASME Paper No. GT2008-50470.